8-2009

Laser Machining of Structural Ceramics: Computational and Experimental Analysis

Anoop Samant
University of Tennessee - Knoxville

To the Graduate Council:

I am submitting herewith a dissertation written by Anoop Samant entitled "Laser Machining of Structural Ceramics: Computational and Experimental Analysis." I have examined the final electronic copy of this dissertation for form and content and recommend that it be accepted in partial fulfillment of the requirements for the degree of Doctor of Philosophy, with a major in Mechanical Engineering.

Narendra B. Dahotre,, Major Professor

We have read this dissertation and recommend its acceptance:

Craig A. Blue, Peter K. Liaw, Rao V. Arimilli

Accepted for the Council:
Dixie L. Thompson

Vice Provost and Dean of the Graduate School

(Original signatures are on file with official student records.)

To the Graduate Council:

I am submitting herewith a dissertation written by Anoop N. Samant entitled "Laser Machining of Structural Ceramics: Computational and Experimental Analysis". I have examined the final electronic copy of this dissertation for form and content and recommend that it be accepted in partial fulfillment of the requirements for the degree of Doctor of Philosophy, with a major in Materials Science and Engineering.

Dr. Narendra B. Dahotre, Major Professor

We have read this dissertation
and recommend its acceptance:

Dr. Craig A. Blue

Dr. Peter K. Liaw

Dr. Rao V. Arimilli

Accepted for the Council:

Carolyn R. Hodges,
Vice Provost and Dean of the Graduate School

(Original signatures are on file with official student records.)

LASER MACHINING OF STRUCTURAL CERAMICS: COMPUTATIONAL AND EXPERIMENTAL ANALYSIS

A Dissertation
Presented for the
Doctor of Philosophy
Degree
The University of Tennessee, Knoxville

Anoop N. Samant
August 2009

Dedicated to

My Parents

And

Teachers

ACKNOWLEDGEMENT

I wish to thank all those who helped me complete my degree of Doctor of Philosophy in Materials Science and Engineering. Firstly, I would like to thank Dr. Narendra B. Dahotre for his constant guidance and support throughout this project. I would also like to extend my gratitude to Dr. Craig A. Blue, Dr. Peter K. Liaw, and Dr. Rao V. Arimilli for agreeing to serve on my doctoral committee. I am extremely grateful to all my family and friends, whose suggestions and motivation made this work feasible. I would also like to thank Dr. Adrian Sabau from ORNL for his guidance and support in the early stages of my study.

Lastly, I acknowledge the financial support from Oak Ridge National Laboratory (ORNL), Oak Ridge, TN, the Center for Materials Processing (CMP), Knoxville, TN, the Department of Materials Science and Engineering (MS&E) at the University of Tennessee, Knoxville, TN, the Center for Laser Applications (CLA) at the University of Tennessee Space Institute (UTSI), Tullahoma, TN and from the Elsie L. Crenshaw Student Aid Fund offered by the Center for International Education (CIE) at the University of Tennessee, Knoxville, TN in various stages of my doctoral program.

ABSTRACT

Outstanding mechanical and physical properties like high thermal resistance, high hardness and chemical stability have encouraged use of structural ceramics in several applications. The brittle and hard nature of these ceramics makes them difficult to machine using conventional techniques and damage caused to the surface while machining affects efficiency of components. Laser machining has recently emerged as a potential technique for attaining high material removal rates. Major focus of this work is to understand the material removal mechanisms during laser machining of structural ceramics such as alumina (Al_2O_3), silicon nitride (Si_3N_4), silicon carbide (SiC) and magnesia (MgO). A 1.06 μm wavelength pulsed Nd:YAG laser was used for machining cavities of variable dimensions in these ceramics and an *ab-initio* computational model was developed to correlate attributes of machined cavities with laser processing conditions.

Material removal in Al_2O_3, Si_3N_4 and SiC takes place by a combination of melting, dissociation and evaporation while dissociation followed by evaporation is responsible for material removal in MgO. Temperature measurement at high temperatures being difficult, thermocouples were used to measure temperatures in the low temperature regime (700- 1150K). A thermal model was then iterated to obtain trends in absorptivity variation below phase transition temperature for these ceramics. Following this, measured machined depths were used as a benchmark to predict absorptivity transitions at higher temperatures (> 1150K) using the developed thermal model. For temperatures below phase transition, due to intraband absorption, the absorptivity decreases with increase in temperature until the surface temperature reaches the melting point in case of Al_2O_3, Si_3N_4 and SiC and the vaporization temperature in case of MgO. The absorptivity then continues to follow increasing trend with increasing temperature due to

physical entrapment of laser beam in the cavity evolved during machining of certain depth in the ceramic. Rate of machining was predicted in terms of material removed per unit time and it increased with increase in heating rate.

Such a composite study based on computational and experimental analysis would enable advance predictions of laser processing conditions required to machine cavities of desired dimensions and thus assist in controlling the laser machining process more proficiently.

TABLE OF CONTENTS

LIST OF TABLES

Table **Page**

LIST OF FIGURES

Figure **Page**

NOMENCLATURE

A	Cross sectional area of laser beam
AWJM	Abrasive water jet machining
a	Absorptivity of material
a’	Distance traveled by laser beam in x direction between two adjacent pulses
a_1	Absorptivity corresponding to T_{max} = MP at t_{res}
a_2	Absorptivity corresponding to T_{max} = VT at t_{res}
a_3	Absorptivity for which corresponding predicted depth matched measured machined depth
b’	Distance traveled by laser beam in y direction between two adjacent passes
c	Speed of light
CM	Chemical Machining
CMM	Chemical-Mechanical Machining
$C_p(T)$	Temperature dependent specific heat
CW	Continuous wave
d	Laser beam diameter
$d_{ablation}$	Depth of ablation
d_{end}	Beam diameter at end of a pass
d_{start}	Beam diameter at beginning of a pass
e	Pulse energy

EBM	Electron Beam Machining
ECDM	Electro-chemical discharge machining
ECM	Electrochemical machining
$E_{dissociation}$	Dissociation energy loss
EDM	Electrical-discharge machining
$E_{effective}$	Total effective energy incident on a spot area
E_f	Energy of the final state in the upper band
E_i	Ionization energy
E_l	Energy of the electron in the lower band
erf()	Error function
f	Pulse repetition rate
g_a	Degeneracy of states for atoms
g_i	Degeneracy of states for ions
H	Thickness of sample
h	Planck's constant
h(T)	Temperature dependent heat transfer coefficient
$\hbar\omega$	Photon energy
I_o	Laser power density
j_e	Rate of evaporation
k	Boltzmann constant
k(T)	Temperature dependent thermal conductivity
L	Length of cavity
LAM	Laser Assisted Machining

LM	Laser Machining
L_v	Latent heat of vaporization
M^2	Beam quality parameter
MEMS	Micro-electro-mechanical systems
MP	Melting point
MRM	Material removal mechanism
MRR	Material removal rate
$MRR_{measured}$	Measured material removal rate
$MRR_{predicted}$	Predicted material removal rate
m_v	Mass of vapor molecule
N	Total number of pulses required to machine a single track
N_a	Number densities of atoms
N_d	Number of pulses required to machine a spot area
N_e	Number densities of electrons
N_{moles}	Number of moles
n	Number of pulse
n_r	Number of reflections
$\hat{n}$	Normal direction
P	Number of passes
PM	Pulsed mode
p	Pulse width
$p(T_s)$	Saturation pressure
p_0	Ambient pressure

p_{recoil}	Recoil pressure
Q	Incident laser power
Q_a	Absorbed laser power
Q_{th}	Threshold laser power
R_a	Surface roughness
r_c	Reflection coefficient
r_{eff}	Effective beam radius
r_{tip}	Distance between center of laser beam and thermocouple tip
s	Overlap
s_{pulse}	Overlap of each pulse over a single spot area
s_x	Overlap in x direction
s_y	Overlap in y direction
T	Temperature
T_1	Transition temperature
T_i	Temperature during heating of pulse i
T'_{i-1}	Temperature during cooling of earlier pulse
T_{max}	Maximum surface temperature
T_o	Ambient temperature
t	Time
$t_{cooling}$	Total time it takes for laser beam to come back to starting point for laying next pass
t_d	Total time of interaction for N_d pulses
t_{off}	Pulse off time

t_p	On time for laser
$t_{processing}$	Time required for machining entire volume of cavity
t_{res}	Residence time
t_{return}	Time for which laser is switched off during return
t_{scan}	Time for machining a single track
USM	Ultrasonic machining
V	Scanning speed
V_{diss}	Volume of cavity formed by dissociation
$V_{evaporation}$	Velocity of liquid-vapor interface
v_{exp}	Velocity of expulsion
VT	Vaporization / dissociation temperature
W	Width of machined cavity
X	Aspect ratio
Z	Depth of machined cavity
z_{ava}	Available melt depth
z_{eff}	Effective melt depth
z_{eva}	Evaporated depth
$z_{expelled}$	Expelled melt depth
z_m	Total melt depth
z_t	Depth of machined cavity
$\alpha(T)$	Temperature dependent thermal diffusivity
β	Surface tension coefficient
ΔG	Gibbs free energy

ΔT_{eva}	Drop in temperature by evaporation
δ_f	Focal length
ε	Emissivity for thermal radiation
θ	Angle cavity wall makes with normal direction
λ	Wavelength of laser
μ_a	Absorption coefficient
ξ	Degree of ionization
ρ	Density
σ	Stefan-Boltzman constant
σ_{dc}	Electrical conductivity of material

CHAPTER I
LASER MACHINING OF STRUCTURAL CERAMICS - AN OVERVIEW[1]

Introduction

Structural materials can be classified as ceramics, metals or polymers with each type of material having its own advantages and drawbacks. Even though metals are strong, cheap and tough, they are chemically reactive, heavy and have limitations on the maximum operating temperature. Polymers are easy to fabricate and light, but they can be used at temperatures only below 573 K. The characteristic features of ceramics compared to others make them more suitable for some applications. In comparison with metals and polymers, most ceramics possess useful features such as high-temperature strength, superior wear resistance, high hardness, lower thermal and electrical conductivity and chemical stability [1]. Retention of these properties by structural ceramics at high temperatures present these materials as an exclusive solution to several engineering application problems [2].

Commonly used structural ceramics are zirconia (ZrO_2), boron carbide (B_4C), alumina (Al_2O_3), silicon carbide (SiC), silicon nitride (Si_3N_4), sialon (Si-Al-O-N), berylia (BeO), magnesia (MgO), titanium carbide (TiC), titanium nitride (TiN), titanium diboride(TiB_2), zirconium nitride (ZrN) and zirconium diboride (ZrB_2). In general, these structural ceramics fall into two major groups: conductive ceramics such as carbides (TiC and SiC), borides (TiB_2 and ZrB_2**)** or nitrides (TiN and ZrN) and ceramics that are a mixture of dielectric (semiconductive) materials and electrically conductive materials such as Si_3N_4-TiN, sialon-TiN, and Si_3N_4-SiC [3]. The applications of some of the structural ceramics are presented in Table 1.1.

[1] The content of this chapter is originally from Reference [1].

Table 1.1 Applications of different structural ceramics [1]

Application	Performance advantages	Examples
Wear Parts: seals, bearings, valves, nozzles	High hardness, low friction	SiC, Al_2O_3
Cutting Tools	High strength, hardness	Si_3N_4
Heat Engines : diesel components, gas turbines	Thermal insulation, high temperature strength, fuel economy	ZrO_2, SiC, Si_3N_4
Medical Implants: hips, teeth, joints	Biocompatibility, surface bond to tissue, corrosion resistance	Hydroxyapatite, bioglass, Al_2O_3, ZrO_2
Construction: highways, bridges, buildings	Improved durability, lower overall cost	Advanced cements and concrete

Al_2O_3 is also used in making machine tool inserts, heat-resistant packings, electrical and electronic components and attachments to melting ducts and refractory linings [4]. Zirconium diboride (ZrB_2) possesses a high melting point, low density, and excellent resistance to thermal shock and oxidation compared to other non-oxide structural ceramics. Hence, it is used as an ultra-high-temperature ceramic (UHTC), for refractory materials and as electrodes or crucible materials [5]. MgO is a very stable oxide used in refractory linings, brake linings, thin film semi-conductors, for housing thermocouples in aggressive environments, in making crucibles in chemical and nuclear industry where high corrosion resistance is required and in making thin-film substrates and laser parts [6, 7]. In addition to the above mentioned structural ceramics and their engineering applications, there are several other fields where these ceramics are significantly used. These advanced high-performance materials have certain limitations such as difficulty in fabrication, high cost, and poor reproducibility as seen in next section.

Fabrication Techniques

Many features (high hardness) that make structural ceramics attractive for particular uses also make them difficult to fabricate by traditional methods based on mechanical grinding and machining. Strength and efficiency of the components can be affected by the damage caused on the surface of the ceramics machined by conventional methods. A crucial step in manufacturing ceramic components is their cost-effective machining with excellent quality. Massive research efforts have been conducted on the precision machining of ceramic components over the past few decades, developing several advanced machining technologies without affecting the beneficial properties of the surface [2]. Some of these techniques are summarized in Fig. 1.1 and briefly described below.

Mechanical Machining

In mechanical machining, material removal takes place when the ceramic is subjected to some mechanical force / impingement of abrasive particles. Commonly used techniques under this category are abrasive machining / grinding, ultrasonic machining, and abrasive water jet machining.

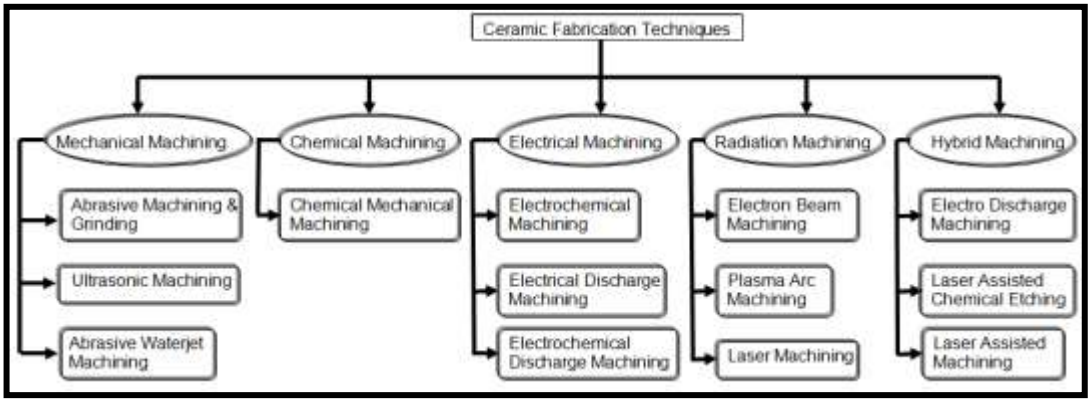

Fig. 1.1 Ceramic fabrication techniques [1].

Abrasive Machining / Grinding

The machining takes place by using grinding wheels that are bonded abrasives used for producing several complex shapes [8]. Even though the needs for dimensional accuracy and surface finish are satisfied by conventional grinding, long machining times and high machining costs accounts for 60-90% of the final cost of the finished product. This poses a major hindrance for the grinding process [9, 10] and ground products also generate surface and subsurface cracks [11, 12], pulverization layers [13], some plastic deformation [14] and significant residual stresses [15].

Ultrasonic Machining (USM)

Ultrasonically vibrated abrasive particles remove material in ultrasonic machining at generally low material removal rates. A transducer / booster combination converts electrical energy into mechanical vibrations and causes the tool to vibrate along its longitudinal axis at high frequency [16]. As the mechanism of material removal is not properly documented, process optimization is difficult [17].

Abrasive Water Jet Machining (AWJM)

In abrasive water jet machining, a blast of abrasive-laden water stream impinges on the surface of the material and results in erosive wear. This process is advantageous over the grinding process as it reduces tool wear and machining time [18]. At high speeds, surface fracture results in kerf formation because of the hydrodynamic forces within the water jet.

Chemical Machining (CM)

Chemical machining using etchants is the oldest of the machining processes, wherein chemicals attack the materials and remove small amounts from the surface. Sharp corners, deep

cavities and porous workpieces cannot be easily machined as this method is only suitable for shallow removal of material (up to 12mm) [8].

Chemical-Mechanical Machining (CMM)

This technology is widely used in surface patterning in semiconductors and micro-electro-mechanical systems (MEMS). Initially, the chemical absorption on the surface of the material produces a chemically reacted layer with physical properties different from the original material. This is followed by mechanical machining to generate the desired pattern on the surface. High costs and several steps involved in patterning commonly used materials such as silicon can be minimized by using KOH solution that can change hard brittle material surface of silicon into a hydrated layer which makes machining easier. Furthermore, this technique also offers flexibility and controllability in the processes [19].

Electrical Machining

Electrical energy in the form of pulse or continuous in isolation or in combination with chemicals is used to erode the material. It is highly effective for machining electrically conductive and semi conductive materials. Electrochemical Machining (ECM), Electrical-Discharge Machining (EDM) and Electro-Chemical Discharge Machining (ECDM) are the commonly used electrical machining techniques.

Electrochemical Machining (ECM)

Electrochemical Machining is the reverse of electroplating used for machining complex cavities in high-strength materials. As the electrolyte has a tendency to erode away sharp profiles, this method is not suitable for generating sharp corners.

Electrical-Discharge Machining (EDM)

EDM is an abrasionless method used for machining conductive ceramics such as boron carbide (B_4C) and SiC [20]. This method is not affected by the hardness of the material, but requires an electrical resistivity of less than 100 Ω cm [2].

Electro-Chemical Discharge Machining (ECDM)

This technique has the combined features of EDM and ECM and is capable of machining high strength electrically non-conductive ceramics. This process is inefficient because a significant portion of the total heat developed is dissipated for increasing the temperature and the corresponding material removed while machining is less [21].

Radiation Machining

Radiation machining is a non-contact machining process where the dimension of the hole or the groove can be controlled by the energy supply to the work piece. The energy can be provided by an electron beam, plasma arc or by lasers. These non-contact machining techniques are not affected by the abrasion of the tools and they are independent of electrical resistivity of the materials being machined.

Electron Beam Machining (EBM)

The energy source in EBM is high-speed electrons that strike the surface of the work piece generating heat [8]. Since the beam can be positioned rapidly by a deflection coil, high machining speeds are possible. This machining process has the drawback that the width of the machined cavity increases while machining at high speeds due to the beam defocusing effect [22].

Plasma Arc Machining

Ionized gas is used for machining the ceramic at very high temperatures leading to smaller kerf widths and good surface finish. As the vacuum chambers have limited capacity, the size of the components should closely match the size of the vacuum chamber [8].

Laser Machining (LM)

The source of energy in LM is a laser (acronym for Light Amplification by Stimulated Emission of Radiation). High density optical energy is incident on the surface of the work piece and the material is removed by melting, dissociation / decomposition (broken chemical bonds causes the material to dissociate / decompose), evaporation and material expulsion from the area of laser-material interaction. The vital parameters governing this process are the different properties of the ceramic such as reflectivity, thermal conductivity, specific heat and latent heats of melting and evaporation. The schematic representation of the laser machining process is made in Fig. 1.2 [23]. Laser machining of structural ceramics and the associated physical phenomena will be discussed extensively in the later part of this chapter.

Hybrid Machining

Hybrid machining uses a combination of two or more of the above techniques for machining the ceramic such as Electrical Discharge Grinding , Laser-Assisted Chemical Etching and machining using lasers and cutting tool / Laser Assisted Machining (LAM).

Electrical Discharge Grinding

This method combining the advantages of grinding and electrical discharge machining (EDM) has low equipment cost and high efficiency [24, 25]. Material is removed from the ceramic surface by recurring spark discharges between the rotating wheel and the work piece [8].

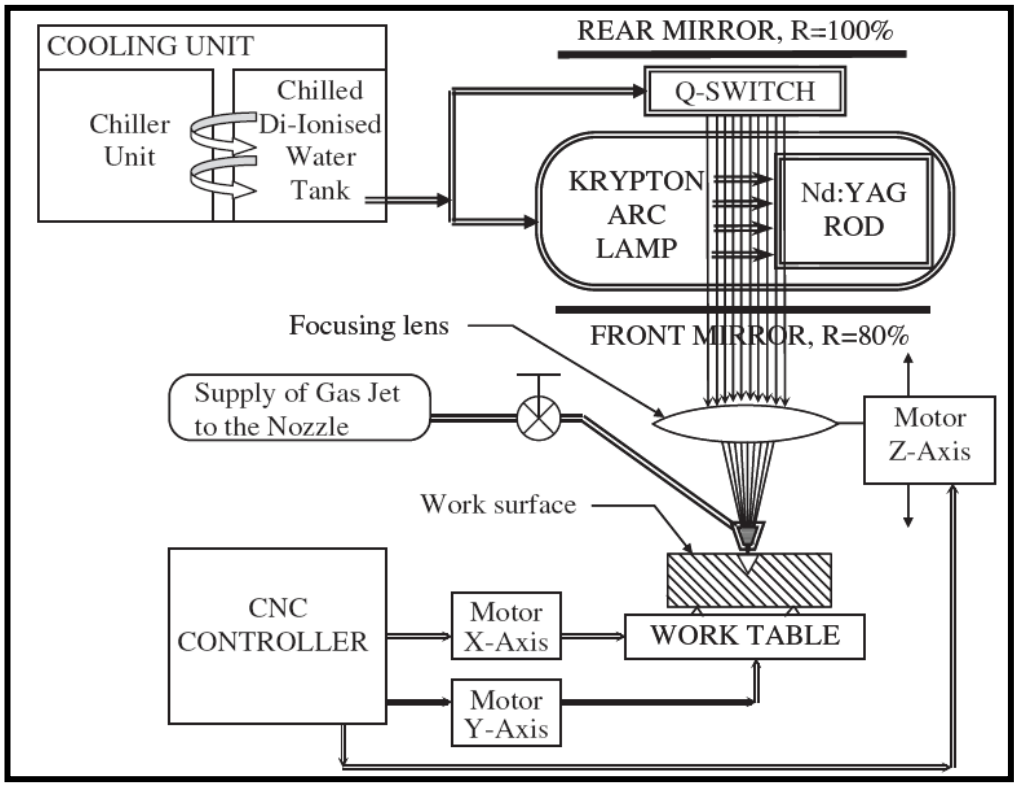

Fig. 1.2 Schematic of laser machining [23].

Laser-Assisted Chemical Etching

Material removal is carried out by using suitable etchant in combination with selective laser irradiation. The laser radiation influences the reaction between the material and the etchant by exciting the etchant molecules and/or the material surface [26] and the etch rate is significantly affected by the laser fluence.

Laser Assisted Machining (LAM)

In Laser Assisted Machining (LAM), the material is locally heated by an intense laser source prior to material removal, without melting or sublimation of the ceramic. This technique has been successfully used for machining Si_3N_4 and the corresponding work piece temperature, tool wear and surface integrity have been measured [27-32]. Magnesia-partially-stabilized

zirconia was machined with a polycrystalline cubic boron nitride tool and it was found that the tool life increased with material removal temperatures [33].

LAM effectively reduced the cutting force and improved the surface finish of the finished products made from Al_2O_3 [34]. In LAM, after the laser is used to change the ceramic deformation behavior from brittle to ductile, material removal takes place with a conventional cutting tool. Unlike LAM, in Laser Machining (LM), actual material removal takes place by the laser beam. The physical phenomena taking place during the LAM of structural ceramics is different from LM and will not be a part of this study. The difference in the two processes is demonstrated in Fig. 1.3.

Laser Machining

Lasers can replace mechanical material removal methods in several engineering applications because of their following salient features [36]:

i) Non-contact process: Energy transfer from the laser to the ceramic through irradiation eliminates cutting forces, tool wear and machine vibration. Furthermore, the material

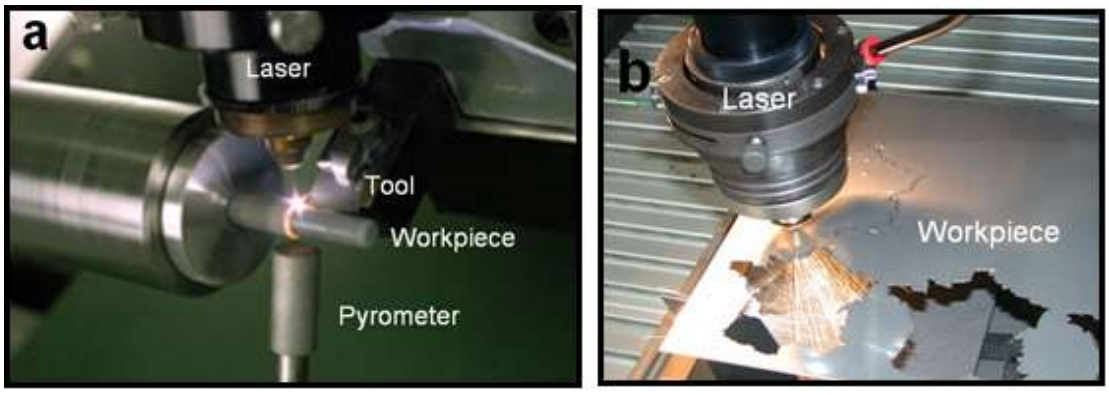

Fig. 1.3 a) Laser assisted machining [32] b) Laser machining [35].

removal rate is not affected by the maximum tool force, tool chatter or built-up edge formation, but can be controlled by varying the laser processing parameters such as input energy and processing speed.

ii) Thermal process: The efficiency of laser machining depends on the thermal and, to some extent on the optical properties of the material. This makes hard or brittle materials such as structural ceramics with low thermal diffusivity and conductivity suitable for machining.

iii) Flexible process: In combination with a multi-axis positioning system or robot, lasers can be used for drilling, cutting, grooving, welding and heat treating on the same machine without any necessity to transport the parts for processing them with specialized machines. In-process monitoring during the laser machining process can allow key parameters to be measured and a high level of reproducibility can be attained [37]. Relative economic comparison of laser machining with other machining processes is made in Table 1.2.

Different types of lasers such as CO_2, Nd:YAG and excimer lasers are used for machining of structural ceramics with each type of laser having its own wavelength of absorption and machining applications. CO_2 lasers are molecular lasers (subgroup of gas lasers) that use gas molecules (combination of carbon dioxide, nitrogen and helium) as the lasing medium, whereby the excitation of the carbon dioxide is achieved by increasing the vibrational energy of the molecule. The actual pumping takes place by an AC or DC electrical discharge and this laser emits light at a wavelength of 10.6 μm in the far infrared region of the electromagnetic spectrum. CO_2 lasers are widely used in industry for applications in laser machining, heat treatment and welding [36].

Table 1.2 Relative economic comparisons of different machining processes [38]

	Parameter Influencing Economy				
Machining process	Capital investment	Toolings/ Fixtures	Power requirements	Removal efficiency	Tool wear
Conventional Machining	Low	Low	Low	Very low	Low
Ultrasonic Machining	Low	Low	Low	High	Medium
Electrochemical Machining	Very high	Medium	Medium	Low	Very low
Chemical Machining	Medium	Low	High	Medium	Very low
Electric Discharge Machining	Medium	High	Low	High	High
Plasma Arc Machining	Very low	Low	Very low	Very low	Very low
Laser Machining	Medium	Low	Very low	Very high	Very low

On the other hand, Nd:YAG lasers are solid state lasers that use dopants (Neodinium (Nd^{3+})) dispersed in a crystalline matrix (complex crystal of Yttrium-Aluminum-Garnet (YAG) with chemical composition $Y_3Al_5O_{12}$) to generate laser light. Excitation is attained by krypton or xenon flash lamps and an output wavelength of 1.06 μm in the near infrared region of the spectrum can be obtained. Nd:YAG fibre lasers are used in applications requiring low pulse repetition rate and high pulse energies (up to 100J per pulse) such as hole piercing and deep keyhole welding applications [36].

Excimer lasers are an increasingly popular type of gas lasers made up of a compound of two identical species that exist only in an excited state. Commonly used excimer complexes include argon fluoride (ArF), krypton fluoride (KrF), xenon fluoride (XeF) and xenon chloride (XeCl) with the output wavelengths varying from 0.193 to 0.351 μm in the ultraviolet to near-

ultraviolet spectra. These compounds can be formed by inducing the noble gas (Ar, Kr, or Xe) of the compound into an excited state with an electron beam, an electrical discharge or a combination of the two. Excimer lasers are used for machining solid polymer workpieces, removing metal films from polymer substrates, micromachining ceramics and semiconductors, and marking thermally sensitive materials [36].

The different types of lasers can be operated in either the continuous wave, CW or the pulsed mode, PM (nano, pico and femto second lasers). In CW lasers, continuous pumping of the laser emits incessant light, while in a pulsed laser, there is a laser power-off period between two successive pulses [39]. Pulsed lasers are preferred for machining ceramics as the processing parameters can be more effectively controlled compared to continuous wave mode [40]. The next section looks at the important physical processes that assist in laser machining of ceramic and discusses the different types of laser machining.

Absorption of Laser Energy and Multiple Reflections

The physical phenomena that take place when the laser beam is incident on the ceramic surface are reflection, absorption, scattering and transmission (Fig. 1.4). Absorption, the vital of all the effects, is the interaction of the electromagnetic radiation with the electrons of the material and it depends on both the wavelength of the material and the spectral absorptivity characteristics of the ceramic being machined [36, 40]. The absorptivity is also influenced by the orientation of the ceramic surface with respect to the beam direction and reaches a maximum value for angles of incidence above 80^{o} [36]. For machined cavities with high aspect ratios, multiple beam reflections along the wall of cavity also affect the amount of absorbed energy [41, 42]. The multiple reflections in a machined cavity is schematically represented in Fig.1.5 where I_o is the incident laser energy, I_{a1}, I_{a2} and I_{a3} are the first, second and third absorptions respectively and

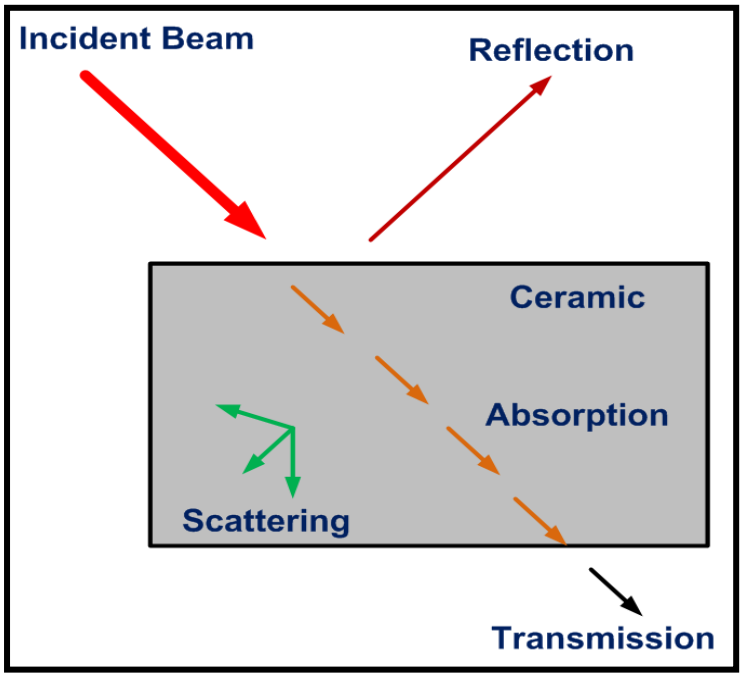

Fig.1.4 Interactions of incident laser beam with ceramic [1].

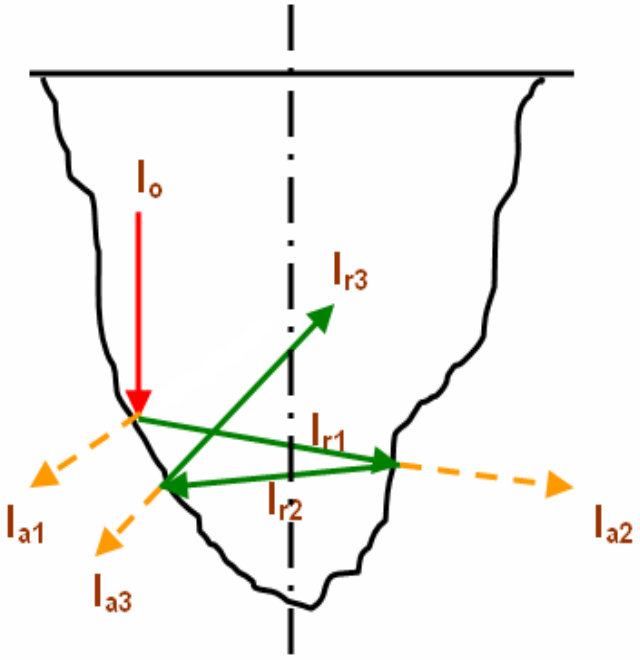

Fig.1.5 Multiple reflections in a machined cavity [43].

I_{r1}, I_{r2} and I_{r3} are the first, second and third reflections respectively [43]. There will be many more reflections taking place during actual ceramic machining than illustrated in Fig.1.5. The phenomenon of multiple reflections has been incorporated into the machining process in several ways [44-48]. The laser power Q_a absorbed by the ceramic after n_r reflections is [49]:

$$Q_a = Q(r_c)^{n_r} \tag{1.1}$$

where Q is incident laser power, r_c is angle-dependent reflection coefficient of the ceramic, and n_r is number of multiple reflections given by:

$$n_r = \frac{\pi}{4\theta} \tag{1.2}$$

where θ is angle the cavity wall makes with normal direction. Moreover, as the thermal conductivity of structural ceramics is generally less than that of majority of metals, the energy absorption takes place faster in ceramics and 100% of incident energy is expected to be immediately absorbed by the ceramic for machining high aspect ratio cavities [50, 51]. Thus the absorbed energy depends on properties of the ceramic (reflection coefficient), magnitude of incident laser energy, output wavelength of processing laser and wall angle. This energy is converted into heat and its ensuing conduction into the material establishes the temperature distribution within the material which in turn affects machining effects.

Thermal Effects

The excitation energy provided by the laser is rapidly converted into heat and this is followed by various heat transfer processes such as conduction into the materials, convection and radiation from the surface [49]. The conduction of heat into the ceramic is governed by the following law:

$$\frac{\partial T(x,y,z,t)}{\partial t} = \alpha(T)\left[\frac{\partial^2 T(x,y,z,t)}{\partial x^2} + \frac{\partial^2 T(x,y,z,t)}{\partial y^2} + \frac{\partial^2 T(x,y,z,t)}{\partial z^2}\right] \quad (1.3)$$

where T is temperature field, t is time and x, y and z are spatial directions. The term $\alpha(T)$ is temperature dependent thermal diffusivity of the material which is given by $k(T)/\rho C_p(T)$, where ρ is density of ceramic, $C_p(T)$ and $k(T)$ are temperature dependent specific heat and thermal conductivity of the ceramic respectively. The balance between the absorbed laser energy at the surface and the radiation losses is given by:

$$-k(T)\left(\frac{\partial T}{\partial \hat{n}}\right) = \frac{\delta a Q}{A} - \varepsilon\sigma\left(T(x,y,0,t)^4 - T_0^4\right)$$

$$\delta = 1 \qquad if\ 0 \le t \le t_p$$

$$\delta = 0 \qquad if\ t > t_p \quad (1.4)$$

where a is absorptivity of material elaborately discussed later in Chapters II to V, ε is emissivity for thermal radiation, T_o is ambient temperature, t_p is on time for laser, σ is Stefan-Boltzman constant (5.67×10^{-8} W/m^{2}K^4) , $\hat{n}$ is normal direction and A is cross sectional area of the beam. The term δ takes a value of 1 when time, t is less than laser on-time, t_p and it is 0 when time, t exceeds laser on-time. Thus the value of δ depends on time, t and ensures that the energy is input to the system only when the laser is on and cuts off the energy supply when the laser is switched off. The convection taking place is given by:

$$-k(T)\left(\frac{\partial T}{\partial \hat{n}}\right) = h(T)\left(T(x,y,H,t) - T_0\right), \quad (1.5)$$

where H is thickness of the sample being processed, $h(T)$ is temperature dependent heat transfer coefficient. The temperature distribution within the material as a result of these heat transfer processes depends on the thermo- physical properties of the material (density, absorptivity, emissivity, thermal conductivity, specific heat, thermal diffusivity), dimensions of sample

(thickness) and laser processing parameters (absorbed energy, beam cross-sectional area). The magnitude of temperature rise due to heating governs the different physical effects in the material such as melting, sublimation, vaporization, dissociation, plasma formation and ablation responsible for material removal / machining as discussed next. (Fig. 1.6) [49, 52, 53]. Incorporation of above mentioned fundamental modes of heat transfer (Eqs. (1.3) – (1.5)) into a thermal model to predict machining effects based on the material removal mechanism (MRM) is described in next chapter.

Melting and Sublimation

At high laser power densities (I_o>10^5 W/cm^2), the surface temperature of the ceramic T (predicted using Eqs. (1.1) – (1.5)) may reach the melting point T_m and material removal takes place by melting as considered by Salonitis et.al [54]. As indicated in Fig. 1.7a, the surface temperature increases with increasing irradiation time, reaches maximum temperature T_{max} at laser on time t_p and then decreases [49].

The temperatures reached and the corresponding irradiation times are: $T_1 < T_m$ at time $t_1 < t_p$, T_m at time t_2, T_{max} at time t_p, T_m at time $t_3 > t_p$, and finally T_1 at time $t_4 > t_p$. The corresponding temperature profiles in the depth of the material for various times during laser irradiation are presented in Fig. 1.7b. The solid-liquid interface can be predicted by tracking the melting point in temperature versus depth (z) plots (Fig. 1.7b). For example, it can be seen from Fig. 1.7b that at time t_p, the position of the solid-liquid interface (melt depth) corresponds to z_{max}. Before initialization of surface evaporation, maximum melt depth increases with laser power density I (power per unit area) at constant pulse time (Fig. 1.8a) while at a constant laser power density, maximum depth of melting increases with increasing pulse time. (Fig. 1.8b) Prediction of melt depth using temperature profiles obtained from Eqs. (1.1) – (1.5) assists in determining depth of

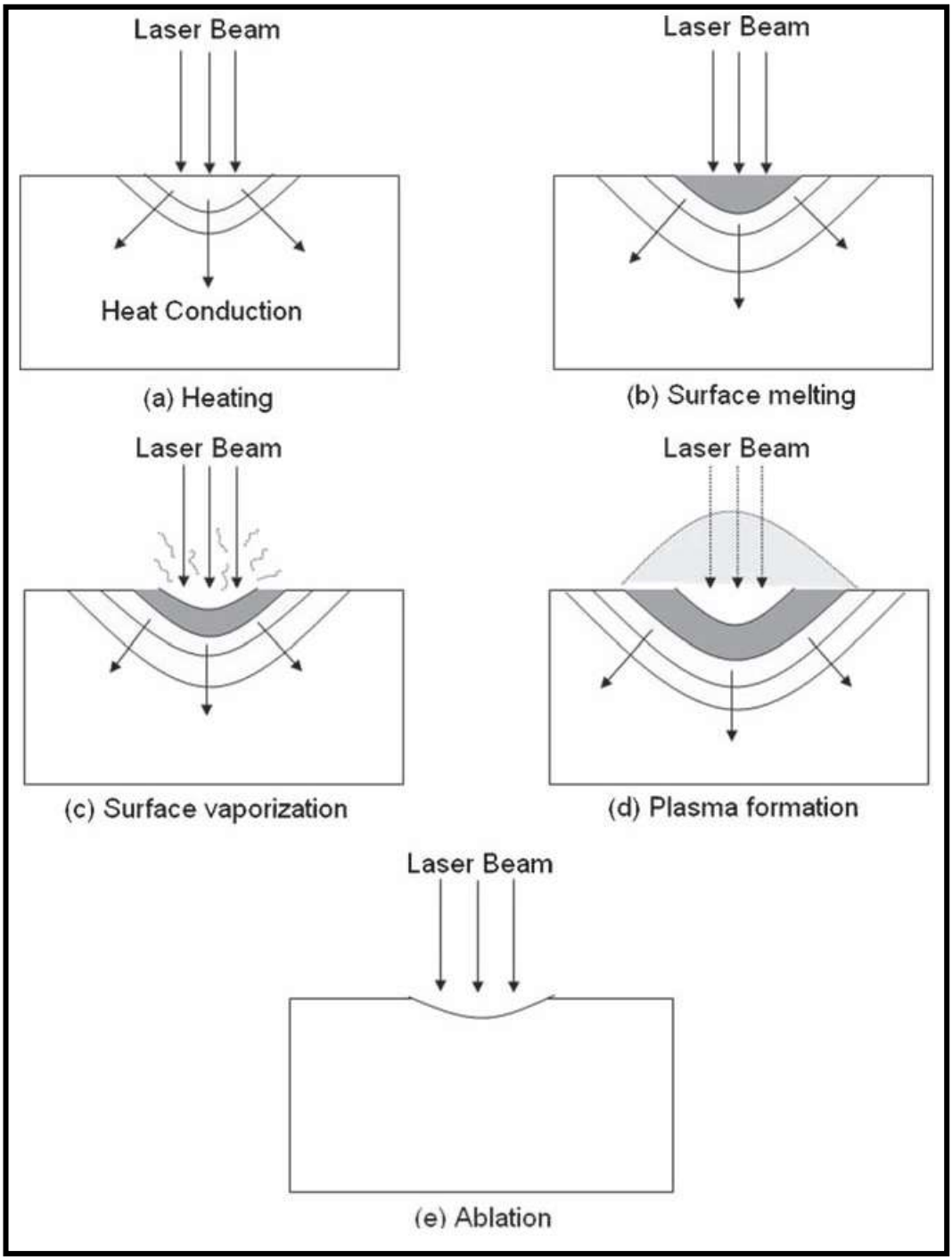

Fig.1.6 Various physical phenomena during laser-ceramic interaction [49].

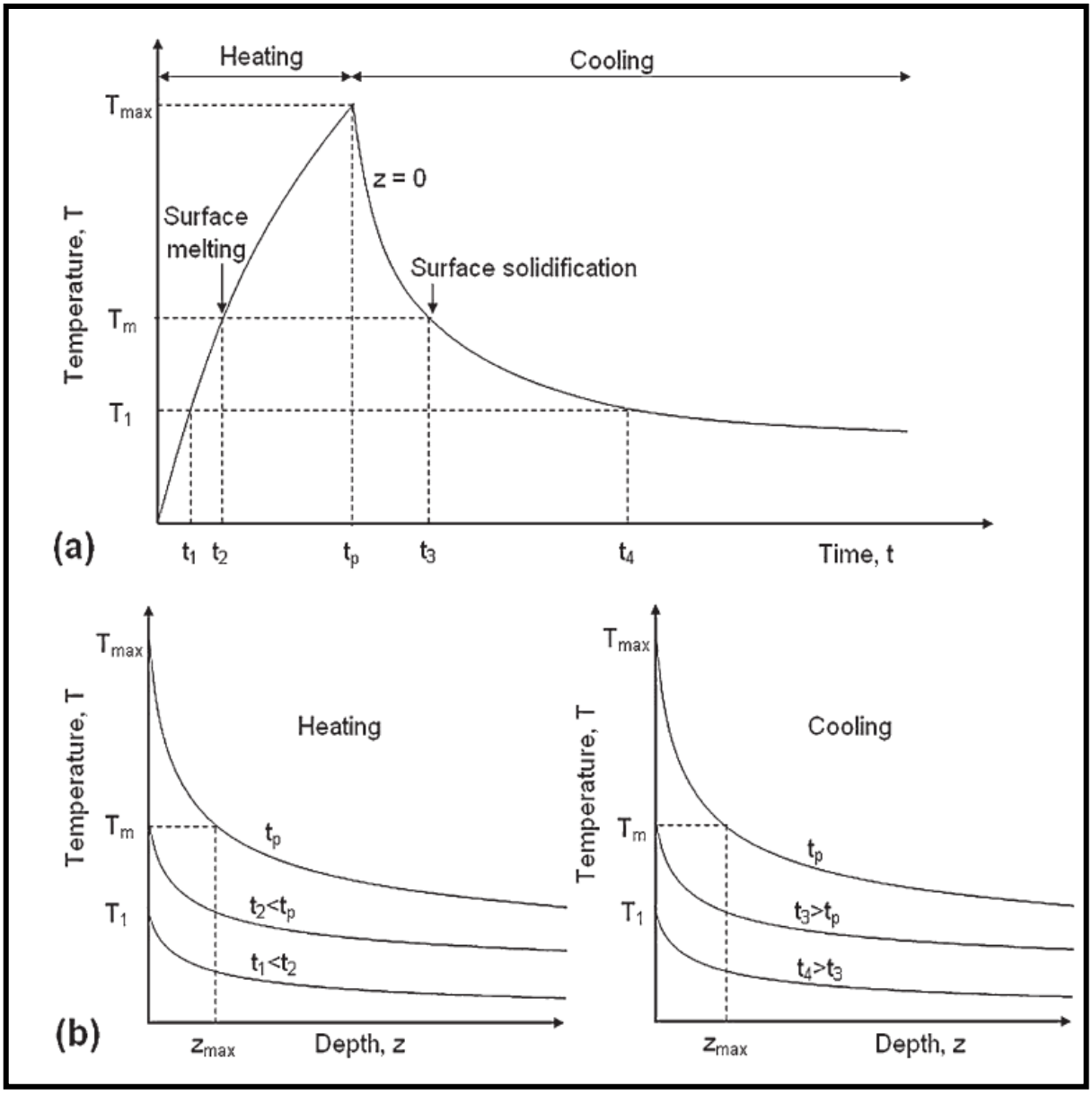

Fig.1.7 Calculation of temporal evolution of melt depth a) surface temperature as a function of time b) temperature as a function of depth below the surface during heating and cooling [49].

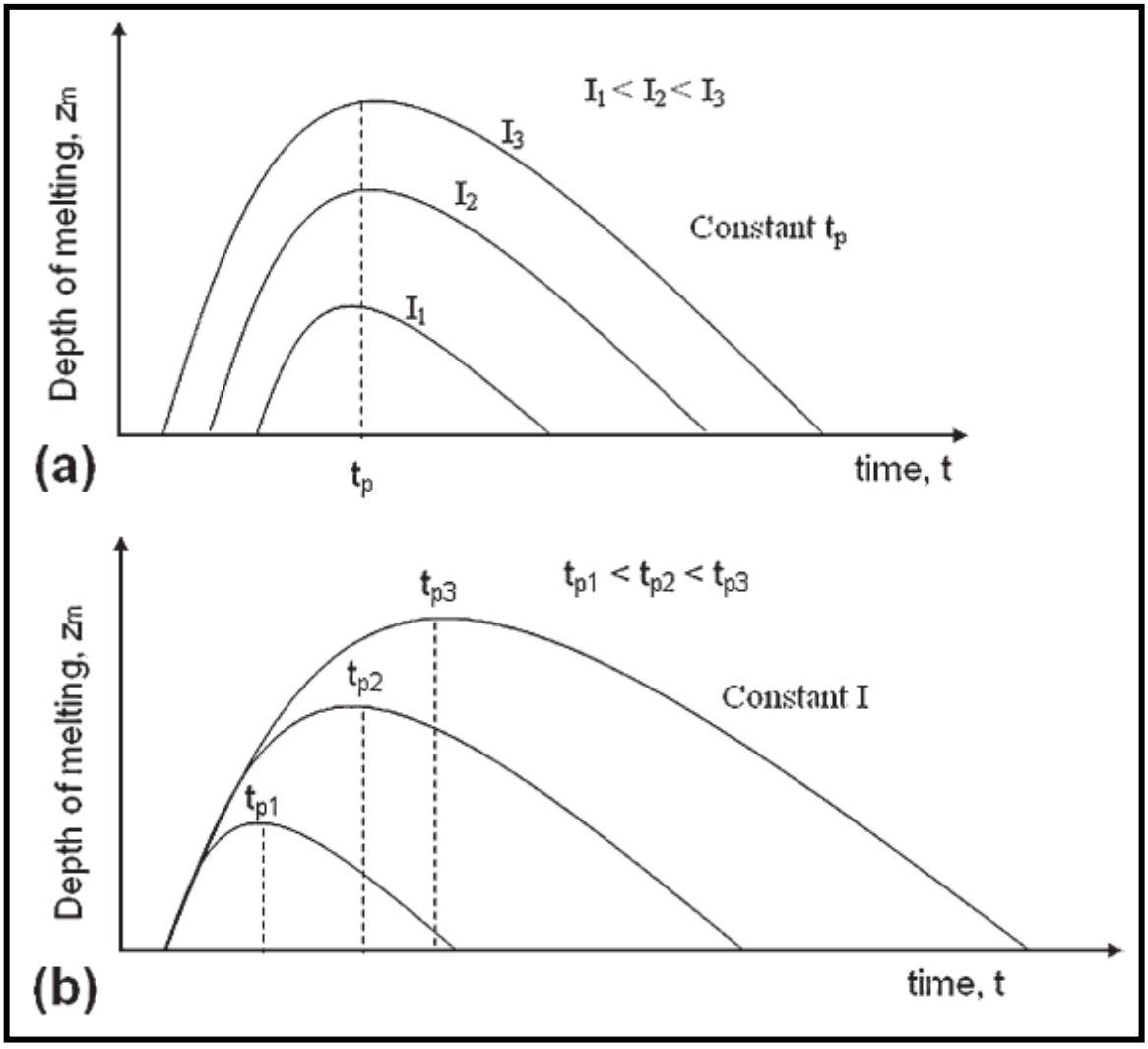

Fig.1.8 Variation of melt depth during laser irradiation a) effect of laser power density at constant pulse time b) effect of laser pulse time at constant laser power density [49].

machined cavity in those ceramics in which material removal takes place entirely or in part by melting [49].

Some structural ceramics like Si_3N_4 do not melt but sublime, emitting N_2 and depositing a recast layer of silicon on the machined surface [2]. Attempts have been made to machine Si_3N_4 in water by Q-switched YAG lasers that can generate high peak powers (above 50 kW) from very short duration pulses (~ 100 ns) at high frequency (~ 10 kHz). As seen in Fig. 1.9, by machining Si_3N_4 in air, a recast layer about 20 μm thick is formed and microcracks are spread within this layer. In contrast, by processing in water, no recast layers and cracks were observed. As YAG lasers retain high transmittance through water, removal of material (Si_3N_4) was possible without the formation of recast layer or micro-cracks [55, 56]. The water also solidified the Si vapor and flushed away the micro-particles, thus preventing the vapor from reaching the saturation level.

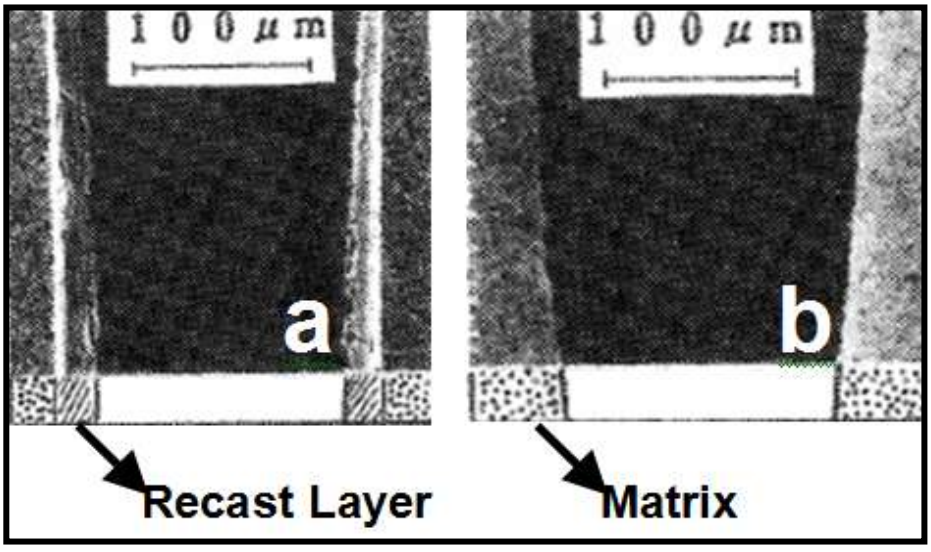

Fig. 1.9 Cross section of Si_3N_4 ceramic machined in a) air and b) water [55].

Vaporization and Dissociation

As the surface temperature of ceramic reaches the boiling point, further increase in laser power density or pulse time removes the material by evaporation instead of melting. After vaporization starts at the material surface, the liquid-vapor interface moves further inside the material with supply of laser energy and material is removed by evaporation from the surface above the liquid-vapor interface [49]. The velocity of liquid-vapor interface, $V_{evaporation}$ and corresponding vaporization depth, $d_{evaporation}$ are given by [52]:

$$V_{evaporation} = \frac{Q_a}{\rho(cT_b + L_v)} \tag{1.6}$$

$$d_{evaporation} = \frac{Q_a t_p}{\rho(cT_b + L_v)} \tag{1.7}$$

where c is speed of light, T_b is boiling point of the ceramic and L_v is latent heat of vaporization. Several works in the past have considered material removal only through this direct evaporation mechanism [57-61]. In such cases, the depth of evaporation (Eq. (1.7)) corresponding to depth of machined cavity depends on the laser conditions (processing time and absorbed laser energy) and material properties such as density, latent heat of vaporization, and boiling point.

As seen in next chapter, certain ceramics dissociate / decompose into several stoichiometric and/or non-stoichiometric species depending on the thermodynamic conditions prevailing during laser machining. The dissociation reaction forms different species that are expelled / removed during machining process and dissociation energy losses also affect the input laser energy and thus the temperature distribution, dimensions of machined cavity and machining time [62-66].

The evolving vapor from the surface applies recoil pressure (p_{recoil}) [67, 68] on the surface given by [69] :

$$\frac{Ap_{recoil}}{Q_a} = \frac{1.69}{\sqrt{L_v}}\left(\frac{b}{1+2.2b^2}\right) \tag{1.8}$$

where $b^2 = kT_{max} / m_v L_v$, T_{max} is surface temperature, k is the Boltzmann constant (1.38065×10^{-23} J/K) and m_v is the mass of vapor molecule. As seen in next chapter, the absorbed laser energy (Eqs. (1.1) and (1.2)) and associated surface temperatures predicted using Eqs. (1.3) - (1.5) affect the recoil pressure which plays a vital role in material removal in molten state during machining of some ceramics such as SiC, Al_2O_3 and Si_3N_4. The total enthalpy required for laser-induced vaporization being greater than that required for melting, the energy required for laser machining by melting is much less than the energy required for machining by vaporization [26].

Plasma Formation

When the laser energy density surpasses a certain threshold limit, the material immediately vaporizes, gets ionized and forms plasma having temperatures as high as 50,000 K and pressures up to 500 MPa [70]. The degree of ionization (ξ) depends on the surface temperatures (predicted from Eqs. (1.1) – (1.5)) and is given by the Saha equation [26]

$$\frac{\xi^2}{1-\xi} = \frac{2g_i}{g_a N_g}\left(\frac{2\pi m_v kT_s}{h^2}\right)^{3/2} exp\left(-\frac{E_i}{kT_s}\right) \tag{1.9}$$

where $\xi = N_e/N_g$ and $N_g = N_e + N_a$. N_e and N_a are the number densities of electrons and atoms/molecules respectively, g_i and g_a are the degeneracy of states for ions and atoms/molecules, E_i is the ionization energy and h is Planck's constant (6.626×10^{-34} m^2 kg/s). The plasma plume forms a shield over the machining area and reduces the energy available to the

work piece when the surface temperature exceeds a certain threshold value. Aerosols formed due to the condensation of ionized material vapor stick to the surface and reduces the efficiency of machined components for applications dominated by wear or tear load. Hence the degree of ionization is an important parameter which gives an indication whether plasma will be formed during the machining process and accordingly, necessary efforts to overcome the harmful effects of plasma could be undertaken. A special gas nozzle designed by Tönshoff et. al [71] (Fig. 1.10) prevents the deposition of aerosols and this technique has been successfully applied to machine SiC ceramic surfaces without any debris [70]. The additional gas stream obtained by combining a process gas stream and an exhaust stream transports the vaporized material and avoids radial distribution of the plasma.

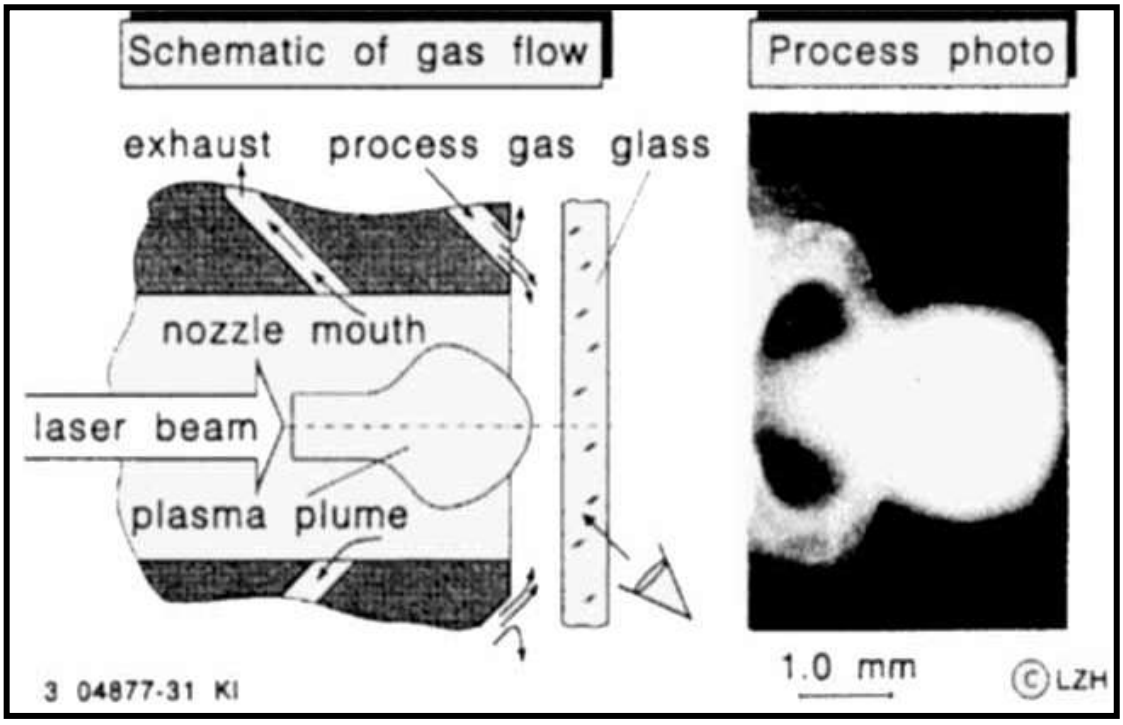

Fig. 1.10 Formation of plasma plume and its suction by gas nozzle [71].

A technique developed at the Integrated Manufacturing Technologies Institute (IMTI), National Research Council Canada (NRC) minimizes the harmful effects of the plasma and provides a precise control over the material removal rate and surface finish. This technique controls the pulse duration and energy per pulse such that majority of the energy in a pulse instantaneously vaporizes a given quantity of the material from the surface. Continuous application of laser pulses ensures that each successive spot is adequately displaced to reduce the plasma absorption effects. Furthermore, short duration pulses reduce the recast layer thickness, eliminate micro-cracks and the material removed per pulse increases with increasing energy density while machining TiN/Si_3N_4 and SiC/Si_3N_4 materials. (Fig. 1.11) [72].

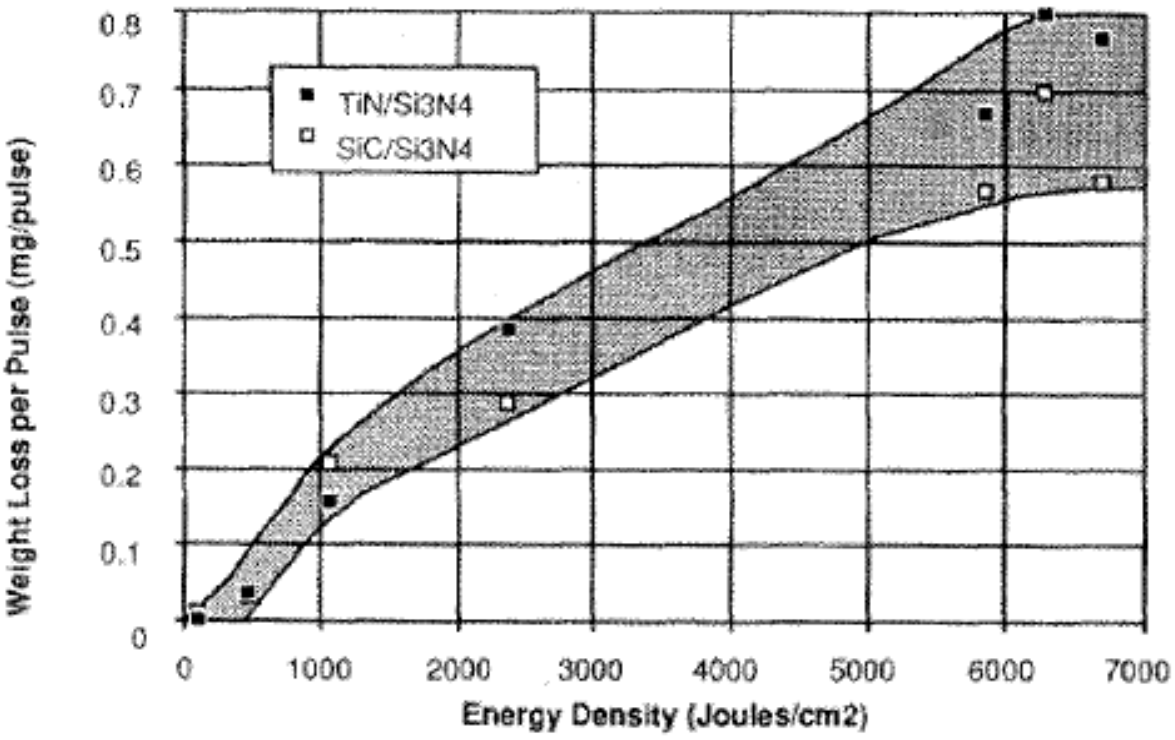

Fig. 1.11 Variation of material removal rate with energy density [72].

Ablation

When the material is exposed to sufficiently large incident laser energy, the temperature of the surface exceeds the boiling point of the material causing rapid vaporization and subsequent material removal by the process referred to as thermal ablation [26]. Ablation takes place when laser energy exceeds the characteristic threshold laser energy which represents the minimum energy required to remove material by ablation. The complex laser-material interaction during ablation depends on the interaction between the photo-thermal (vibrational heating) and photo-chemical (bond breaking) processes. Above ablation threshold energy, material removal is facilitated by bond breaking, whereas thermal effects take place below ablation threshold energy. Absorption properties of the ceramic and incident laser parameters determine the location at which the absorbed energy reaches the ablation threshold, thus determining the depth of ablation, $d_{ablation}$ given by [49]:

$$d_{ablation} = \frac{1}{\mu_a} ln\left(\frac{Q_a}{Q_{th}}\right) \tag{1.10}$$

where μ_a is absorption coefficient of ceramic and Q_{th} is threshold laser power. The ablation rates and associated machined depths are governed by laser energy Q_a (predicted from Eq. (1.1)), pulse duration, number of pulses and pulse repetition rate. Yttrium stabilized Si-Al-O-N (Y-sialon) was irradiated by an Kr-F-excimer laser at a fluence of 850 mJ/cm^2, pulse repetition rate varying from 2 to 20 Hz and by applying different number of pulses [73]. The material removal in Y-sialon under the above processing conditions was by ablation. The variation of ablation depth and a Y-sialon sample ablated by laser irradiation is presented in Fig. 1.12a and Fig.1.12b respectively.

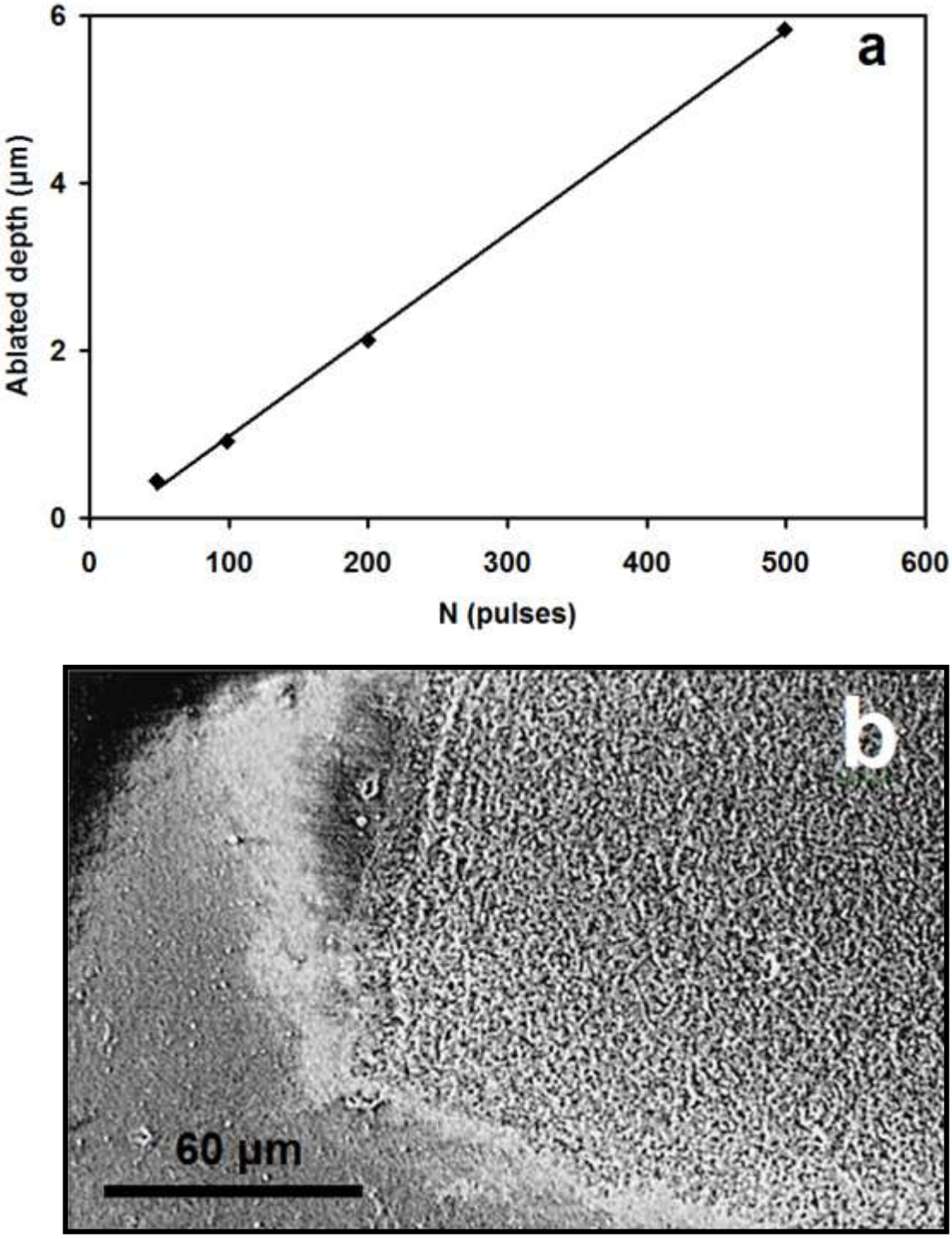

Fig. 1.12 a) Ablation profile of Y-sialon under irradiation b) ablated region in Y-sialon [73].

Types of Machining

Based on the kinematics of the front in the area where material removal takes place, laser machining is classified into one, two, and three dimensional machining. The laser beam is considered as a one-dimensional line source with line thickness given by the diameter for circular and the major axis for elliptical beam cross sections. Laser drilling (one-dimensional) machining (Fig. 1.13a) discussed later in Chapter II can be achieved by keeping the ceramic workpiece as well as the laser beam stationary. On the other hand, motion of laser beam or ceramic in only one direction leads to cutting (two-dimensional machining) (Fig. 1.13b) in the ceramic and is seen later in Chapters IV and V. Motion of one or more laser beams or the workpiece in more than one direction leads to three-dimensional machining and complex geometries can be machined (Fig. 1.13c) as described in Chapter VI.

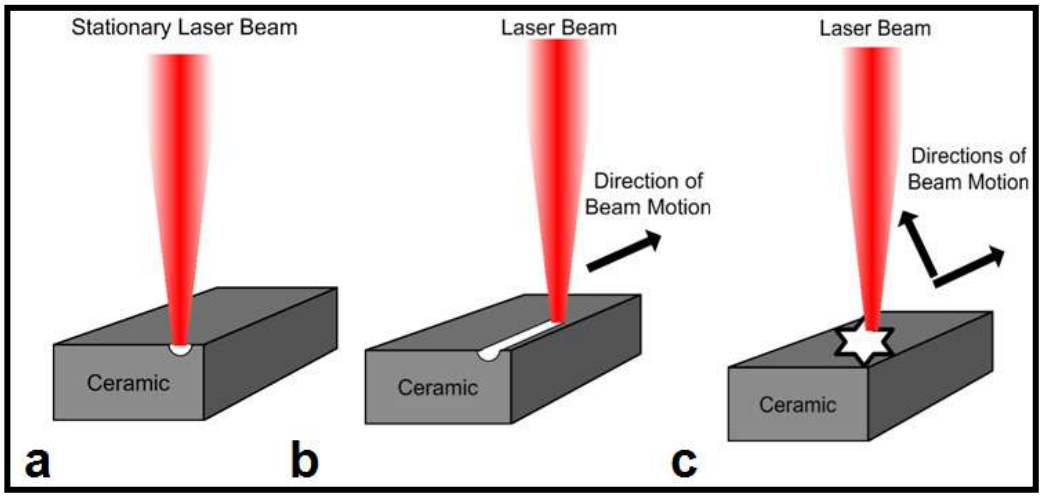

Fig. 1.13 Schematic of basic laser machining processes a) laser drilling (one-dimensional machining), b) laser cutting (two-dimensional machining), c) engraving a star by laser beam (three- dimensional machining) [1].

One-dimensional Laser Machining

Drilling is a one-dimensional laser machining process where the laser beam is fixed relative to the workpiece. The material removal rate is governed by the velocity of the erosion front in the direction of the laser beam. The hole taper is a measure of the dimensional accuracy for laser drilling and it can be minimized to an insignificant order of appearance by using a lens of long focal length with longer focal waist. A schematic of the laser drilling process and a hole drilled in SiC with associated microstructural features is presented in Fig. 1.14 and Fig. 1.15 respectively [74]. The drilling in SiC was carried out using a pulsed CO_2 laser (λ = 10.6 μm) with a pulse duration of 2 ms, a power of 0.5kW and the lens had a focal length of 31.8mm.

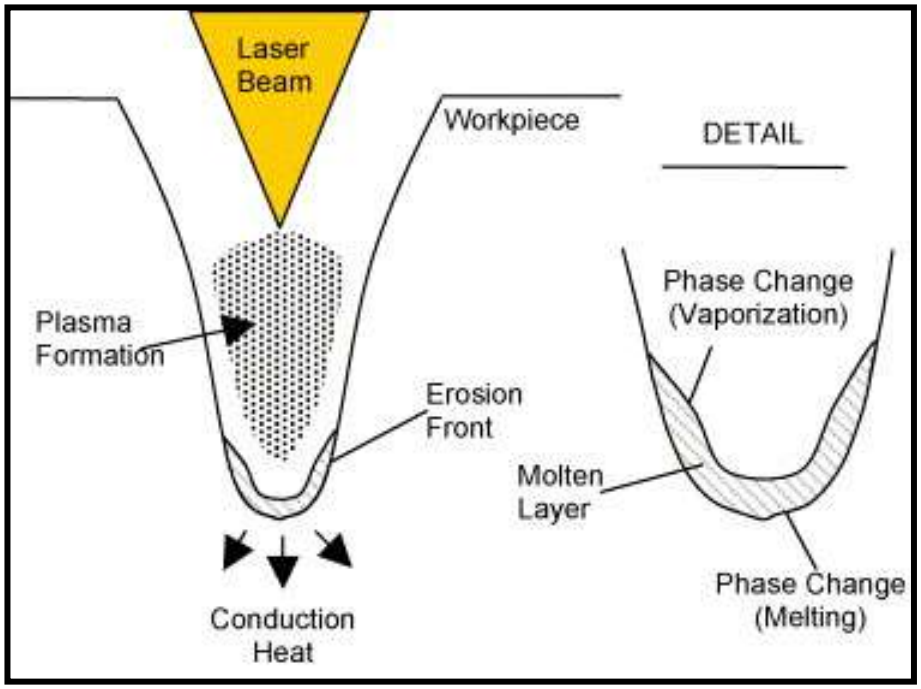

Fig.1.14 Schematic of laser drilling process [36].

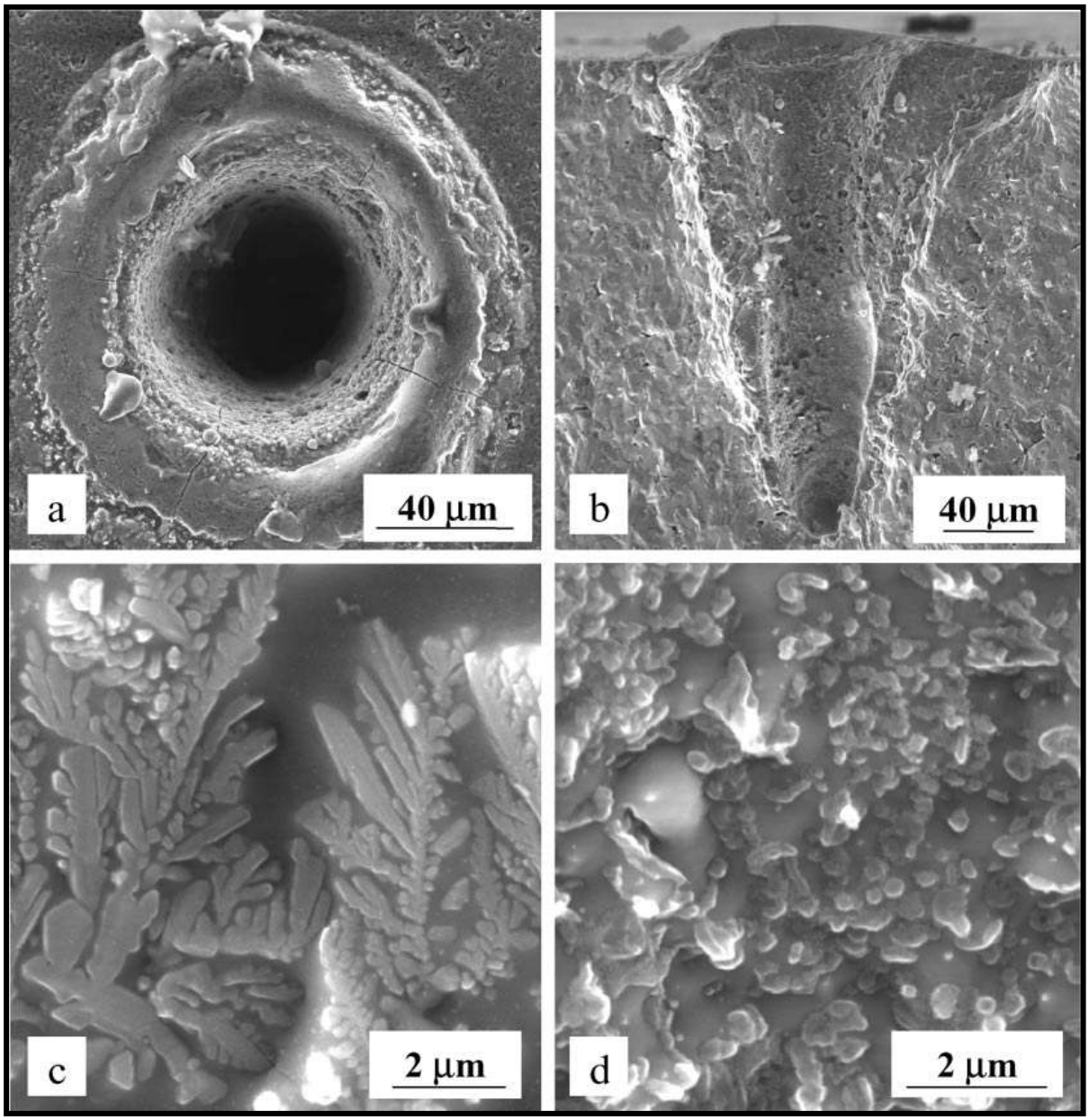

Fig. 1.15 Microstructural features of hole in SiC a) hole entry b) hole section c) silicate- like dendrite crystals on debris area d) hole inside walls [74].

Two-dimensional Laser Machining

In two-dimensional laser machining (cutting), the laser beam is in relative motion with respect to the workpiece (Fig. 1.16). A cutting front is formed when the laser beam melts / vaporizes the material throughout the thickness or the depth. In addition to removal of the molten material, the pressurized gas jet also assists in enhanced material removal by chemical reactions such as oxidation. Cutting of the material then proceeds by the motion of the cutting front across the surface of the material [75].

Brittle ceramics such as Al_2O_3 are mostly machined by the controlled fracture technique where the incident laser energy generates localized thermal stresses that cause the material to separate by crack extension with controllable fracture growth. The energy requirement is less

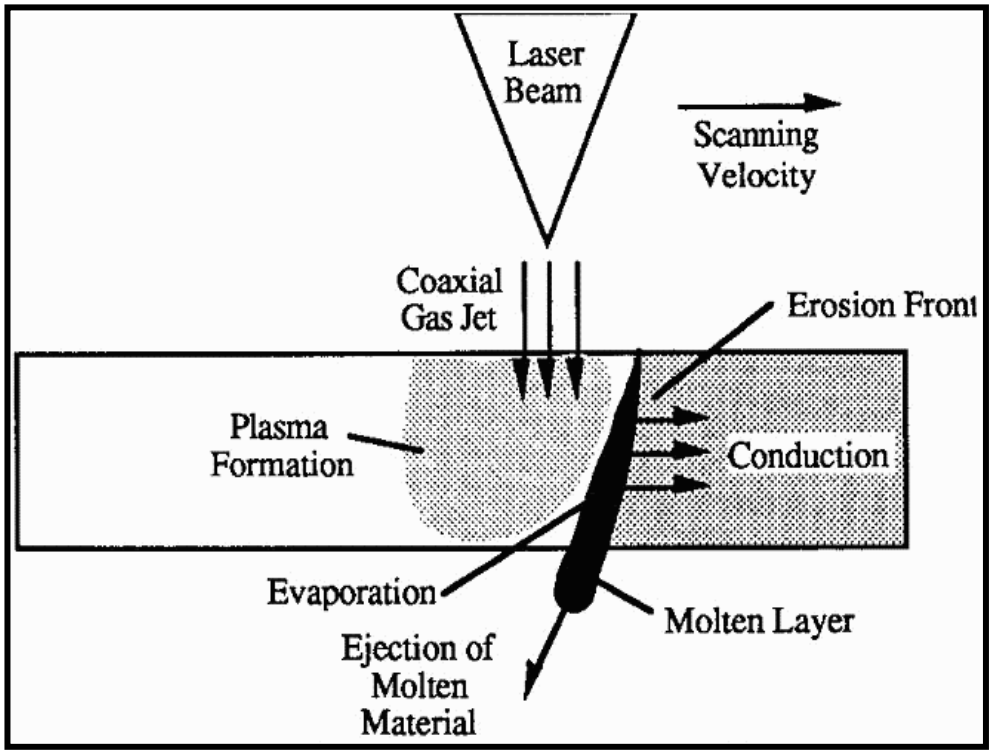

Fig. 1.16 Schematic of laser cutting process [36].

compared to conventional evaporative laser cutting as the material removal is by crack propagation. The experimental setup in Fig. 1.17a consists of a personal computer, a CO_2 laser, a Nd:YAG laser and a XYZ positioning table. The focused Nd:YAG laser having a focal plane on the surface of the substrate and the beam orthogonal to the surface is used to scribe a groove on the ceramic surface. The defocused CO_2 laser inclined to the Nd:YAG laser beam induces localized thermal stresses in the substrate. Both the laser beams are applied simultaneously on the ceramic surface in a continuous mode of operation. The stress concentration at the groove tip assists in extending the crack through the substrate followed by controlled separation along the moving path of the laser beam [76]. The four distinct regions: evaporation, columnar grain, intergranular fracture, and transgranular fracture regions of the Al_2O_3 ceramic cut by controlled fracture technique is presented in Fig. 1.17b.

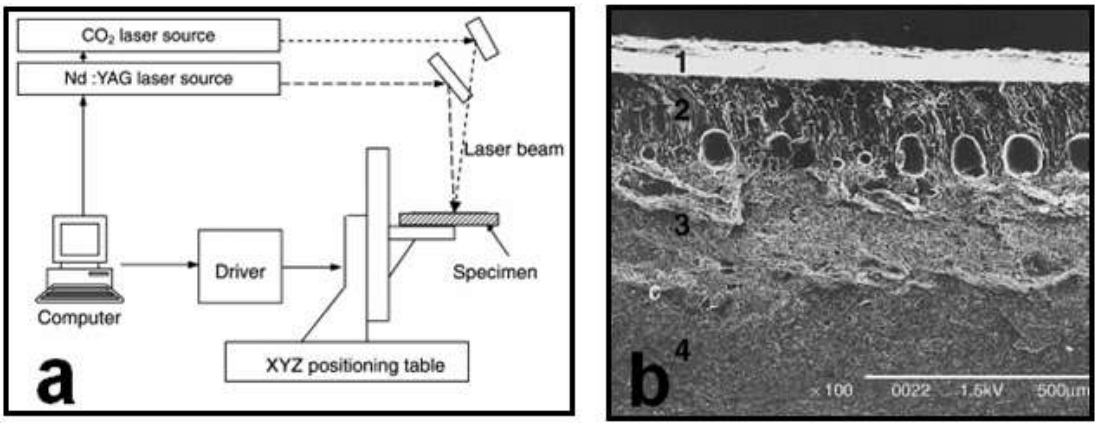

Fig. 1.17 a) Configuration of laser cutting using controlled fracture technique. b) fracture surface of Al_2O_3 substrate [76].

Three-dimensional Laser Machining

Two or more laser beams are used for three-dimensional machining and each beam forms a surface with relative motion with the workpiece (Fig. 1.18). The erosion front for each surface is located at the leading edge of each laser beam. When the surfaces intersect, the three-dimensional volume bounded by the surfaces is removed and machining takes place. Laser turning and milling are commonly used three-dimensional laser machining techniques useful for machining complex geometries such as slots, grooves, threads, and complex patterns in ceramic workpieces. Laser machining has been used to turn threads in Si_3N_4 ceramic (Fig. 1.19a) [77] and also to cut gears from SiC_ω/Al_2O_3 composite (Fig. 1.19b) [72].

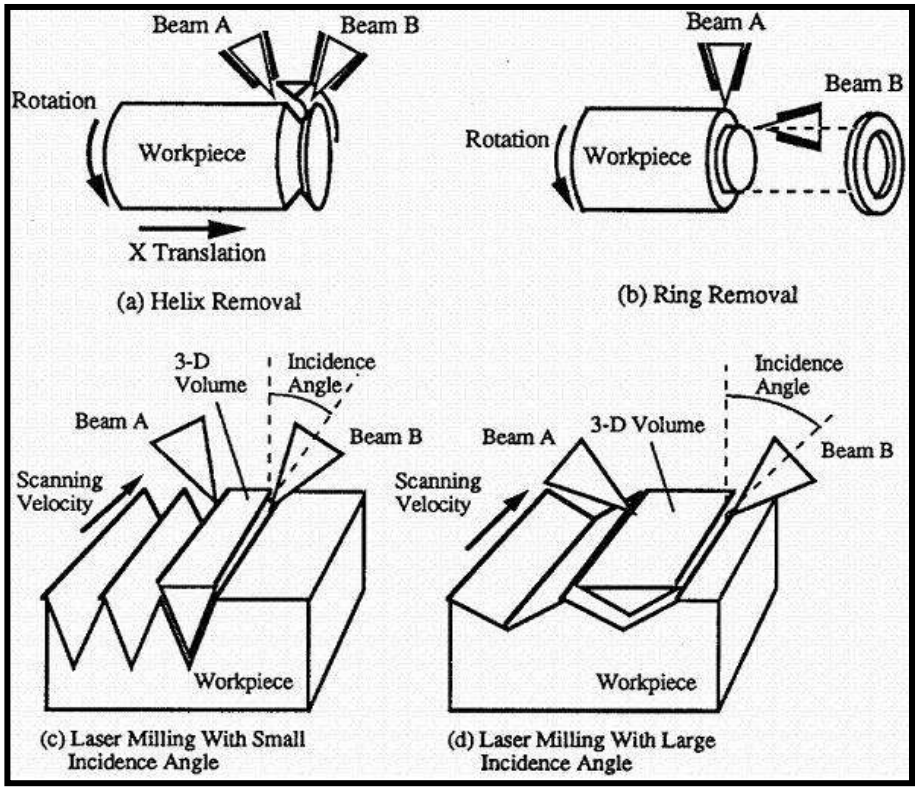

Fig. 1.18 Three dimensional laser machining [36].

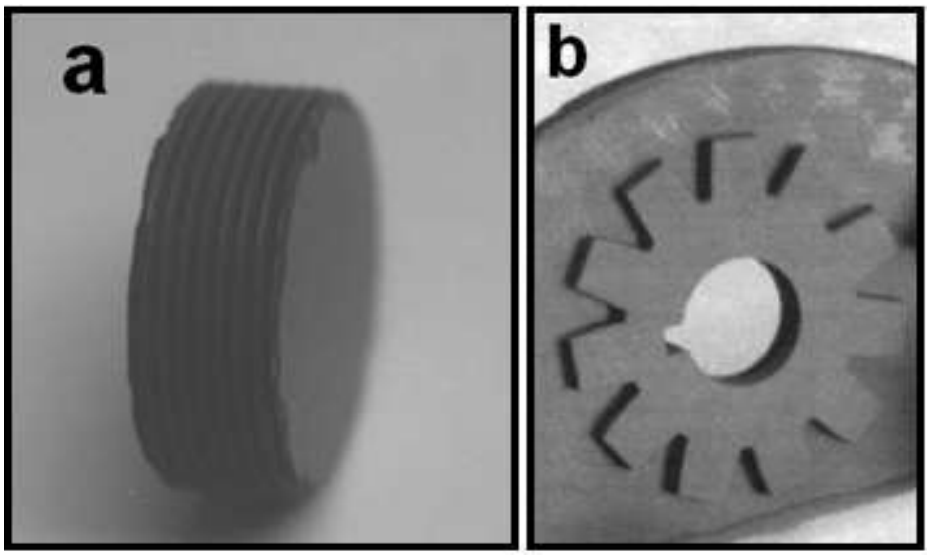

Fig.1.19 a) Turning of threads in Si_3N_4 [77] b) a gear shape cut in SiC_ω/Al_2O_3 composite [72].

State of the Art

So far it has been covered in this chapter that temperature dependent thermo-physical properties and laser processing conditions govern the physical phenomena that can machine ceramics in one, two or three dimensions. Even though a few structural ceramics have been briefly mentioned earlier only to explain key concepts of laser machining, this section presents the detailed state of the art in machining by lasers of some commonly used structural ceramics such as Al_2O_3 , Si_3N_4, SiC, and MgO.

Al_2O_3

Besides the applications mentioned earlier, Al_2O_3 is also used as a substrate in hybrid circuits as it possesses excellent dielectric strength, thermal stability and conductivity [78]. CO_2

lasers have been adapted for drilling holes in thin Al_2O_3 plates used as substrates for thin film circuits in electronic switching systems. Hole diameters varying from 0.125 to 0.3 mm were drilled by changing the lenses and the pulse duration [79]. Laser scribing (drilling a series of holes in a line) was carried out by Saifi and Borutta [80] with a pulsed CO_2 laser for separating individual thin film circuits on a large substrate. It was observed that for shorter pulse length, the heat affected zone was small with a corresponding rapid temperature drop. On the other hand, the development of microcracks in the scribed region reduced the flexural strength of the scribed substrates.

The threshold energy density (the minimum energy density required for material removal) for drilling gold coated Al_2O_3 by ruby lasers (400 J/cm^2) was less than the energy density for drilling uncoated Al_2O_3 (750 – 1000 J/cm^2). This drop in energy density could be attributed to the relatively high thermal conductivity of gold [81]. Drilling of 0.25 mm diameter holes in 0.1 mm thick Al_2O_3 workpiece was performed by Coherent, Inc at a machining speed of 0.1 seconds per hole using a pulsed CO_2 laser at a pulse frequency of 500 Hz and pulse duration of 200ms [82]. Chryssolouris and Bredt [83] drilled blind holes (depths varying from 0.02cm to 1 cm) using a 1.2 kW CW CO_2 laser with energy densities ranging from 2kJ/cm^2 to 500 kJ/cm^2. CO_2 and Nd:YAG lasers with power densities between 10^6 and 10^8 W/cm^2 were used to drill holes in Al_2O_3 upto 0.25mm diameter and it was found that the holes drilled by CO_2 laser showed a noticeable taper compared to the holes made by Nd:YAG laser [84].

Common defects associated with laser drilling (microcracks and spatter [85-88]) were prevented by a drilling technique based on gelcasting [89]. For gelcasting, the ceramic slurry made by dispersing the powders in a pre-mixed monomer solution is cast in a mold of desired shape. After addition of a suitable initiator, the entire system is polymerized *in situ* and green

bodies with improved mechanical properties are produced. As the green body has relatively loose structures compared with sintered ceramics, spatter-free holes with more uniform shapes and without microcracks can be drilled (Fig. 1.20).

A computer controlled Nd:YAG Laser was used to obtain good quality kerfs and cuts without cracks in Al_2O_3 substrates for embedded MCM-Ds (Multi Chip Modules, deposited) and water-cooled heat sinks for single chips, multichip modules or laser diodes. A laser energy of 1.7J, pulse duration of 0.4 ms, pulse frequency of 250 Hz, nitrogen as process gas and a feed rate of 150 mm/min were used for machining these substrates [90]. Al_2O_3 has also been machined with a KrF excimer laser with laser fluence (1.8 and 7.5 J/cm^2), pulse duration (25 ns), number of pulses (1 to 500), frequency (1 to 120 Hz), and the corresponding microstructural changes were examined [91]. At low fluence (1.8 J/cm^2), the melting / resolidification produced scales on the surface while at high fluence (7.5 J/cm^2), there were no continuous scales as the material was removed by vaporization. The depth of material removed was directly proportional to the number of pulses.

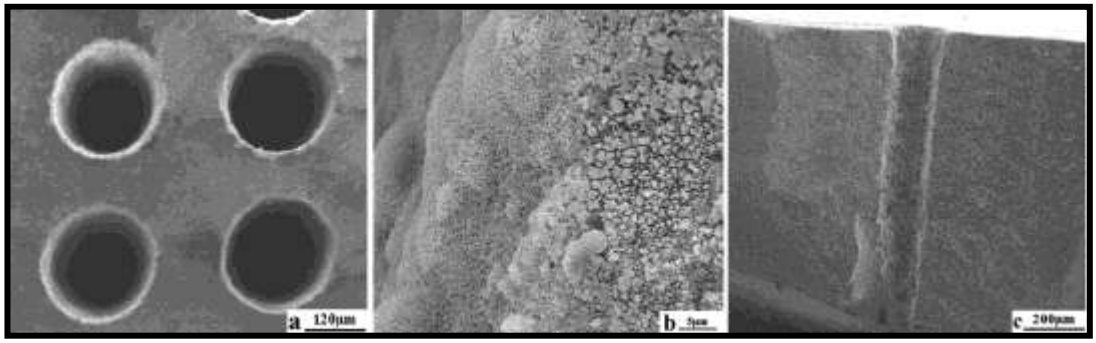

Fig. 1.20 Holes drilled on gelcast green body of Al_2O_3. a) top view, b) hole edge, c) cross section of hole [89].

However, this laser treatment was not suitable for reducing the roughness as can be seen from Fig. 1.21 that the values of R_a (surface roughness) and R_t (peak-to-valley distance) varied slightly compared to the starting values. Moreover, femtosecond near infra red (NIR) optical pulses have been used for microstructuring Al_2O_3 with improved edge quality at scanned intensities less than 50 W/cm^2 [78]. The surface showed no discoloration unlike the processing done by nanosecond UV lasers at 248 nm wavelength by Sciti et. al [91].

3D Laser Carving is an emerging technique in industries for manufacturing ceramic components of complex shapes. Initially, a 3D CAD model is sliced in a particular direction to obtain profile information of the slice. The focused laser beam is then used for scanning and engraving the ceramic surface as per the profile information, producing two-dimensional layer patterns. Finally, the Z-axis of the table is raised to a designated height to locate the carving surface at the focal plane. This process is repeated several times until the whole model is completely sliced and the 3D graphics is engraved on the workpiece (Fig. 1.22) [92]. Thus, Al_2O_3 ceramic has been laser machined in one, two and three dimensions by using different types of lasers for several applications.

Si_3N_4

Si_3N_4 is widely used for machining purposes in automotive, semiconductor and aerospace industries. Cams, bearings, piston rings and rocker arms can be made by machining this ceramic [93, 94]. A 0.1 mm hole drilled at the Integrated Manufacturing Technologies Institute (IMTI), National Research Council Canada (NRC) through a 6mm thick Si_3N_4 cutting tool insert is presented in Fig. 1.23 [72]. Harrysson et. al. drilled holes in Si_3N_4 using CO_2 and Nd:YAG lasers. High thermal stresses produced intense cracking in CO_2 laser drilled samples

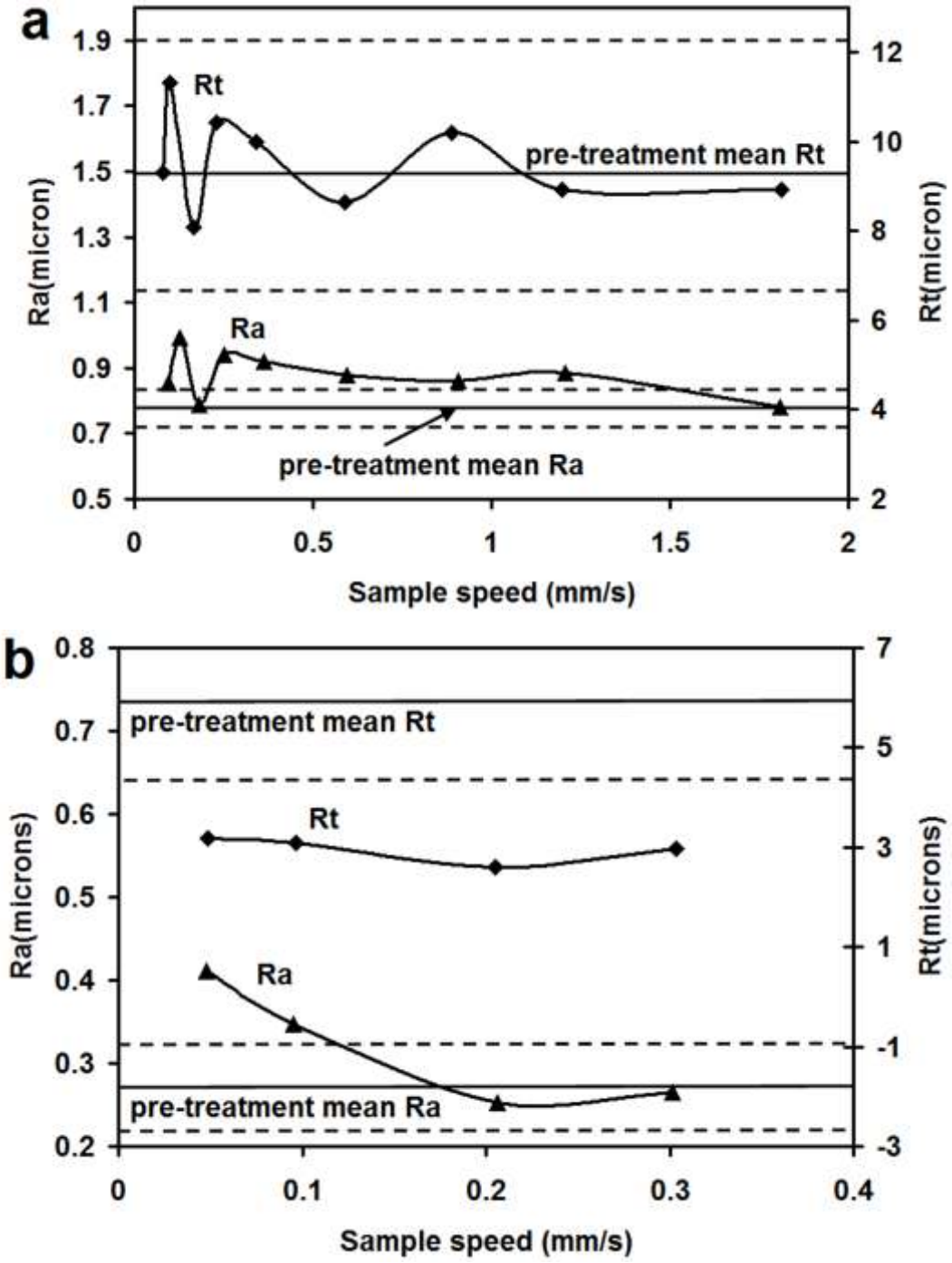

Fig. 1.21 Surface roughness after laser treatment for a) raw Al_2O_3 at fluence of 1.8 J/cm^2 and b) polished Al_2O_3 at fluence of 7.5 J/cm^2 [91].

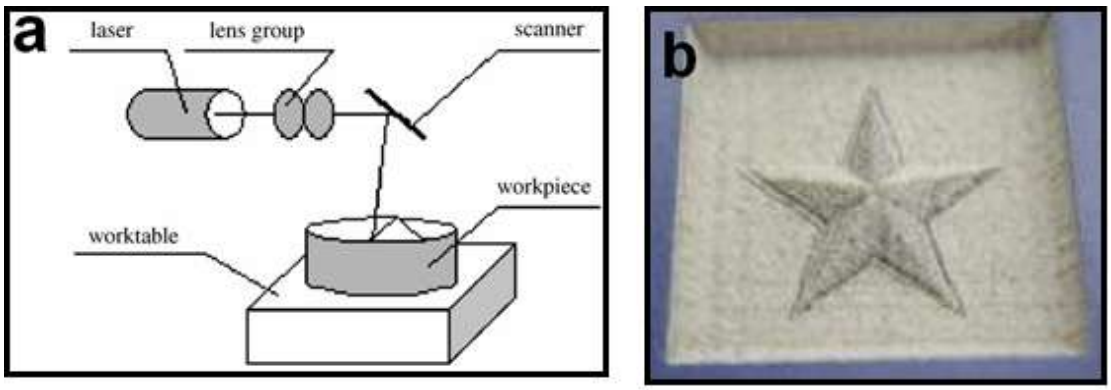

Fig. 1.22 Laser carving a) schematic layout and b) 3D star in Al_2O_3 ceramic [92]

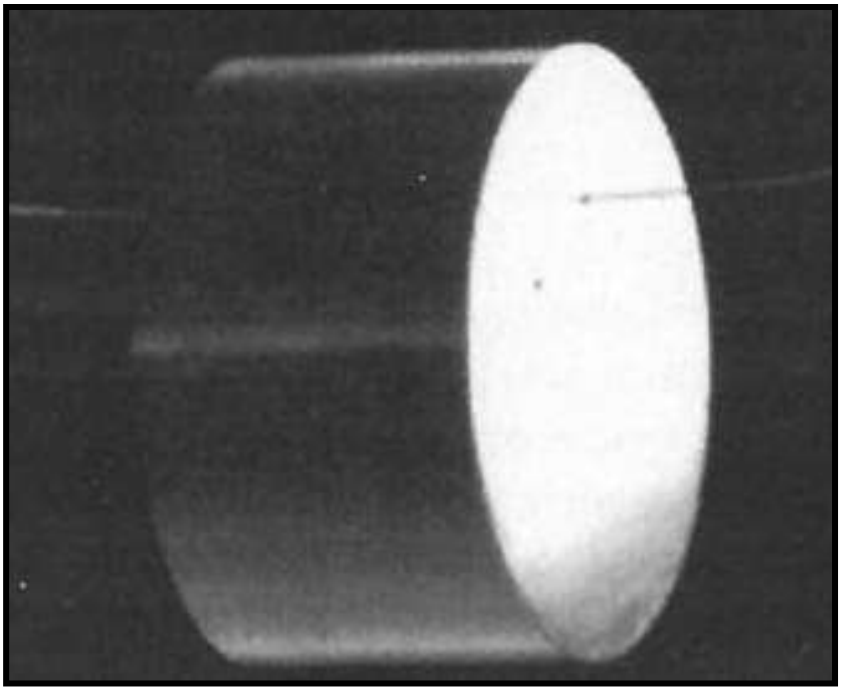

Fig.1.23 A 0.1 mm diameter hole drilled in 6 mm thick Si_3N_4 cutting tool insert. Wire passing through the hole is also seen [72].

while the cracking was limited only to the re-cast layer (about 0.02 mm) by using a Nd:YAG laser [95].

CO_2 laser was operated in continuous and pulsed mode for cutting Si_3N_4 and it was found that deep and narrow cuts were produced by pulsed mode as compared to continuous mode of operation. Reducing the traverse speed avoided fracture of the ceramic and it was more effective than increasing the laser power for machining thicker plates (6 to 8 mm) [96]. Firestone et. al used a 15 kW CO_2 laser to machine Si_3N_4 without fracturing at 1269 K and the machining rates achieved were ten times that of conventional diamond grinding [97]. This ceramic has also been machined by Lavrinovich et. al in two regimes: with free generation where the width of the laser pulse was 4 ms and with Q-factor modulation where the pulse width was 3×10^{-7} sec [98]. Q-factor modulation was able to form an oxide film on the surface when exposed to a defocused laser beam. This method also helped to minimize the residual microcracks.

Apart from the above applications of laser machining of Si_3N_4, laser milling is a newly developed method of producing wide variety of complex parts from ceramics such as Si_3N_4 directly using the CAD data, thus making it possible to machine Si_3N_4 in one, two and three dimensions [99].

SiC

SiC is another structural ceramic that has been widely machined by lasers for different purposes. Sciti and Bellosi used a pulsed CO_2 laser with laser powers of 0.5 and 1 kW for drilling the ceramic surface [74]. The beam was incident on the surface at an angle of 90º and three different focal lengths of 95.3, 63.5, and 31.8 mm were used for machining. The hole depth increased with the pulse duration and also the input power for a given focal length because of increase in laser light intensity. Even though the hole diameters remained constant with pulse

duration, they were affected by the lens focal length that governed the size of the laser spot (Fig. 1.24). A 400W Nd:YAG laser with pulse frequencies upto 200Hz and pulse width of 250ms to 1000ms was capable of drilling holes (0.25 to 1.5 mm diameter) in 3 to 3.5 mm thick SiC plates along with other ceramics such as Si_3N_4 and Al_2O_3 [100]. It was found that SiC required the highest pulse energy of all ceramics and corresponding holes produced had the most irregular shape.

Affolter et. al. cut 5mm thick SiC plates with a 10kW Nd:YAG laser at a cutting speed of 40 mm/min [101] while a 15 kW CW CO_2 laser with a spot diameter of 2.7 mm was used by Firestone et. al [97] for the cutting process. The workpieces were initially heated to 1673 K in a furnace to reduce the cracks and a gas jet minimized oxidation and plasma formation [97]. For SiC processed by KrF excimer lasers, ablation depth varied linearly with number of pulses and the surface showed flat as well as rough areas, debris deposit and thin scale formation [91].

Three dimensional contours have been made on SiC ceramic by a 450W CW CO_2 laser by machining overlapping grooves for material removal. The grooves were formed by directing the beam tangential to the workpiece. Decreasing the groove depth on successive overlapping passes controlled the surface roughness of the finished components. This technique is similar to electrical-discharge machining (EDM) and was used for generating flat or threaded surfaces on the workpiece [102].

MgO

To the best of the present knowledge based on available literature, no significant work has been carried out in the laser machining of pure MgO ceramic and some data on the laser machining of MgO can be found in laser machining handbooks [103]. Hence as seen later in

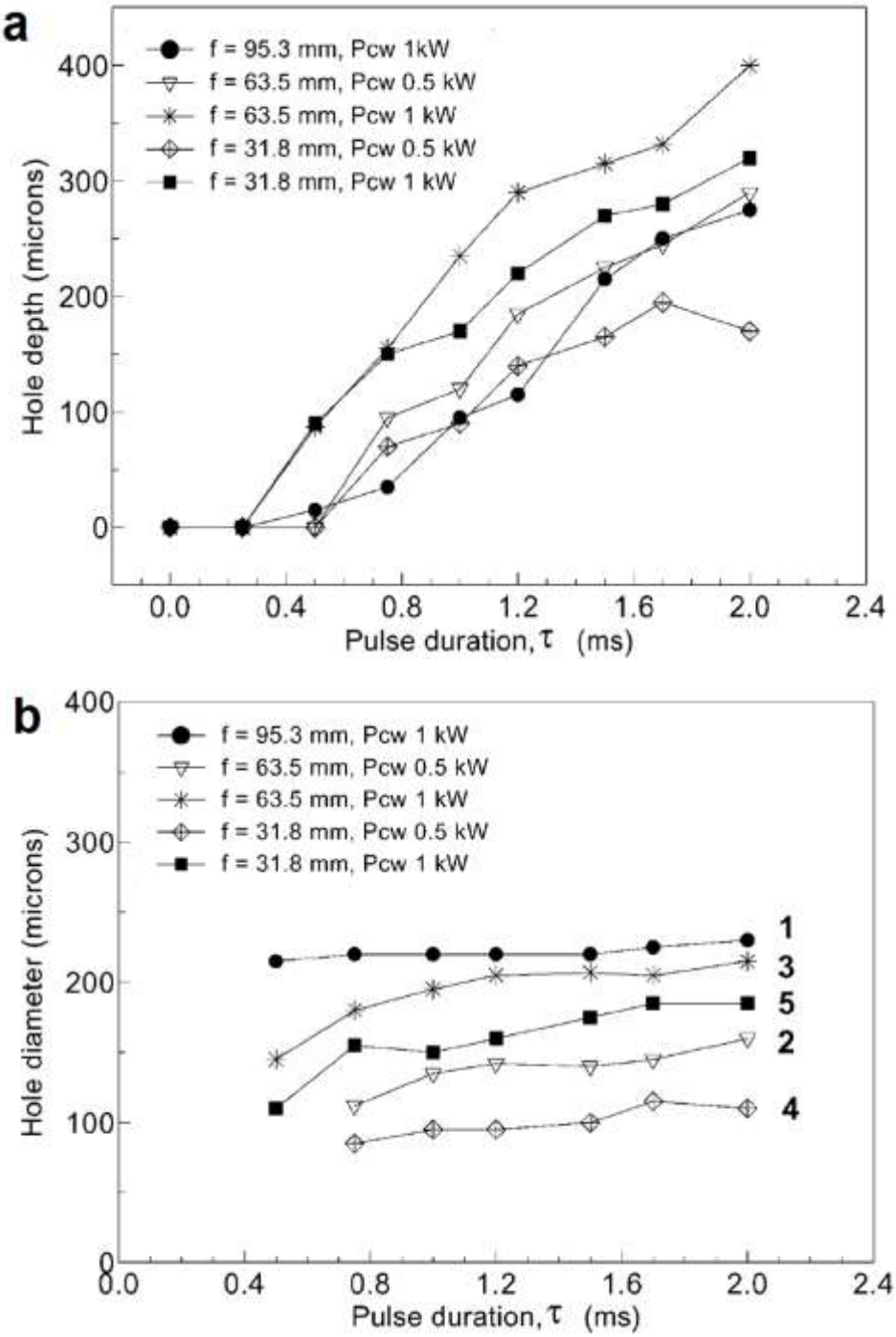

Fig. 1.24 Variation of a) hole depth and b) hole diameter with pulse duration for SiC drilling [74].

Chapters II-VI, an attempt will be made to machine this ceramic with a pulsed Nd:YAG laser and the material removal mechanism will be elaborately discussed.

Thus this chapter explains different physical phenomena that occur when a laser beam interacts with a ceramic surface and provides state of the art in machining different ceramics such as Al_2O_3, Si_3N_4, SiC and MgO. As none of the above mentioned examples have developed a correlation between machined attributes and corresponding material removal mechanism, this study aims at understanding the MRMs for these ceramics and attempts to develop a computational model based on experimental observations that would enable advance predictions of laser processing parameters to achieve desired machining effects. This study would thus enable to develop a system with an optimum material removal rate to machine a cavity of any complex shape and size, thus saving considerable amount of energy and time.

Hence in order to understand basic material removal mechanisms in above mentioned ceramics, one-dimensional laser machining (drilling) is first studied in the next (second) chapter and a fundamental machining model is built. As seen in subsequent chapters, this knowledge of MRMs will then be applied to two and three dimensional laser machining of these ceramics leading to a progressive development of the computational model.

CHAPTER II
ONE- DIMENSIONAL LASER MACHINING[1]

As mentioned in Chapter I, one-dimensional machining (drilling) is a process in which laser beam is fixed relative to workpiece. The experimental procedure for machining (drilling) Al_2O_3, Si_3N_4, SiC, and MgO is first explained in this chapter followed by an understanding of the MRM in these ceramics. Discrimination and incorporation of these physical processes into a hydrodynamic machining model to predict different machining parameters is also presented. The model provides an outstanding tool for advance prediction of thermal energy and time required for machining desired depth of material and it can also predict the depth machined in a given time.

Experimental Procedure

Coupons of variable geometry and dimensions (Table 2.1) were made from dense Al_2O_3, Si_3N_4, SiC and MgO. These coupons were obtained from a commercial source (Coorstek, Golden, CO for Al_2O_3, Advanced Ceramics Manufacturing, Tucson, AZ for Si_3N_4, Saint Gobain Advanced Ceramics, Niagara Falls, NY for SiC and Ozark Technical Ceramics, Inc, Webb City, MO for MgO) and hence details of methods used for manufacturing these coupons were not available. The surface of all coupons was exposed to a JK 701 pulsed Nd:YAG laser (1.064 μm wavelength) from GSI Lumonics, Rugby, England. The laser offered pulse energies from 0.1-55 J, repetition rates from 0.2-500 Hz, and the pulse width from 0.3-20 ms. By varying pulse repetition rate, peak power and pulse width in different combinations, a set of parameters were

[1] The content of this chapter is originally from References [62] - [66].

Table 2.1 Geometry and physical attributes of ceramic coupons used for one-dimensional machining

Ceramic	Geometry	Physical attributes	Number of pulses
Al_2O_3	Circular disc	89mm diameter and 4mm thick	5, 10, 20 and 30
Si_3N_4	Rectangular plate	12mm x 15mm and 3.5mm thick	3, 6, 10 and 20
SiC	Rectangular plate	12mm x 15mm with thicknesses of 2mm and 3mm	25 and 125
MgO	Rectangular plate	12mm x 15mm and 3mm thick	3, 6, 9 and 20

recognized that generated adequate interaction between the laser beam and the ceramic surface for required machining of ceramic coupons. A fiber optic system and a 120 mm focal length convex lens delivered a defocused laser beam of spot diameter, *d* of approximately 0.5 mm on the surface. For Al_2O_3, Si_3N_4 and MgO, pulse energy, *e* of 4 J, pulse repetition rate, *f* of 20 Hz and pulse width, *p* of 0.5 ms was capable of generating reasonable interaction between the laser and ceramic surface and a cavity could be machined. The average power used for laser processing in these ceramics was 80W (*e* (4J) x *f* (20Hz)). Processing conditions for SiC were slightly different and will be discussed later. A pulse repetition rate of 20 Hz implied that 20 pulses were incident on surface per second and duration of each pulse (total on and off time) was 1/20 = 0.05 s. In addition, as *p* was 0.5 ms, each pulse was on for only 0.5 ms (t_p) and corresponding off time for each pulse (t_{off}) was 0.05s – 0.5 ms = 0.0495 s and the pulse intensity distribution shape was 'top hat' type.

For the set of laser parameters mentioned above for each ceramic, several pulses (Table 2.1) were applied on the ceramic surface. The given number of pulses were chosen based on

prior experience to machine blind cavities of various depths and also a cavity through the entire thickness of plate. Three runs for each number of pulses were conducted and for each case, the mean value of the machined depth was reported by taking five measurements from the optical cross sectional views (Fig.2.1a, Fig. 2.1b and Fig. 2.1d) by Image J^{TM} software. The figures also include top views of cavities machined on the top surface of ceramic. The average value of the machined depths measured using this method for these ceramics has been listed in Table 2.2 along with standard deviation corresponding to the scatter in each case. Thus the measurements were statistically analyzed by considering the average and the standard deviation of the measured depths. As there was no feedback system to monitor the formation of a through cavity, some extra (stray) pulses could have been supplied even after the through cavity was formed. Even though experiments were conducted using air as an assist gas, the effect of assist gas on the machined depth was not the focus of this study and can be considered for future work on this topic.

One of the basic principles of any statistical design of experiments is randomization. Randomization means that the order in which individual runs of the experiment are to be performed are determined randomly. This assists in averaging out the effects of extraneous factors (lurking variables) that may be present such as relative humidity and surrounding temperature [104]. Hence, in this study, the number of pulses were applied in a random order for the different runs. For example in MgO, the number of pulses varied from 3-6-9-20 for the first run, from 9-20-6-3 for the second run and from 20-3-9-6 for the third run and the standard procedure of randomization of experimental runs was thus implemented.

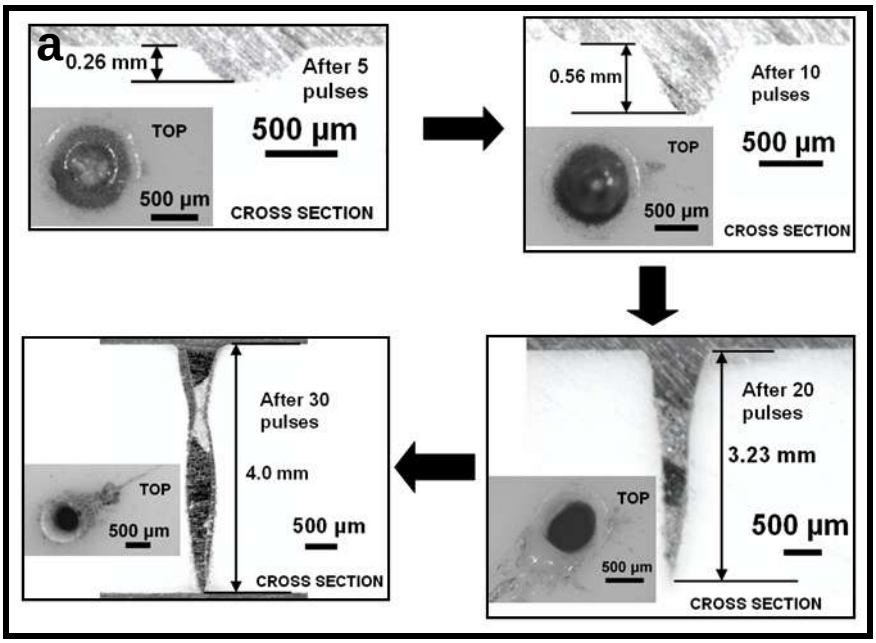

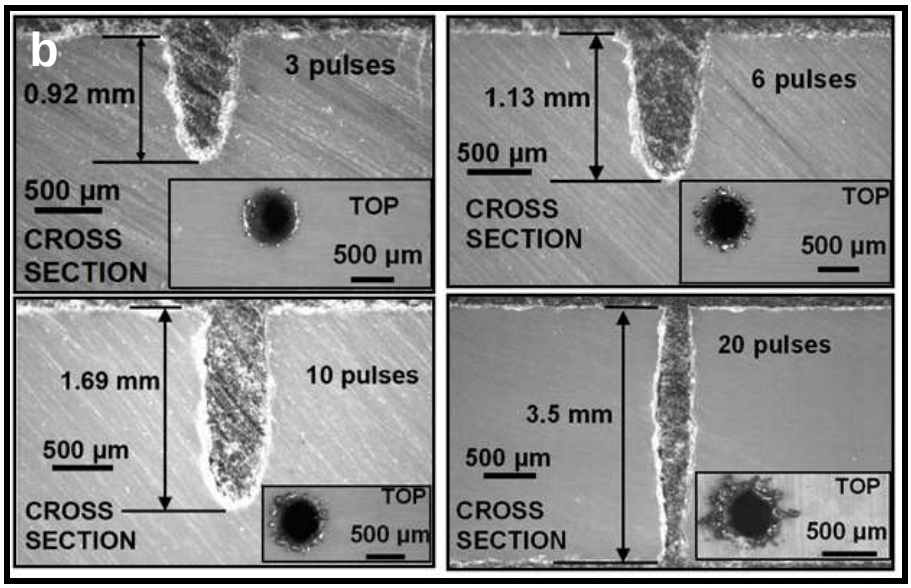

Fig. 2.1 One-dimensional laser machining of a) Al_2O_3 [63] b) Si_3N_4 [62] c) SiC [66] d) MgO [65].

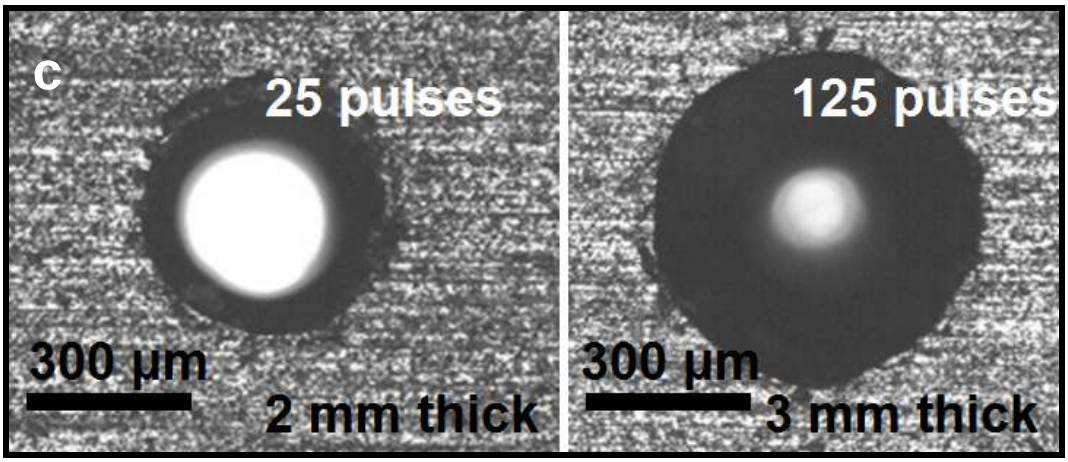

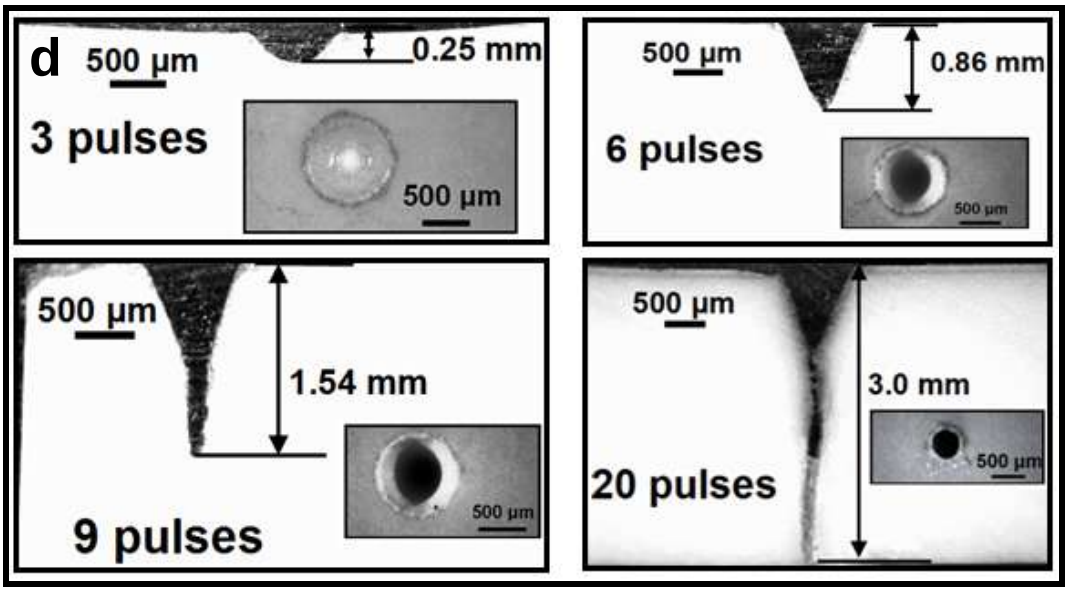

Fig. 2.1 Continued.

Table 2.2 Machined depths and machining energy for Al_2O_3, Si_3N_4, SiC and MgO.

Ceramic	Number of pulses	Machined depth(mm)	Machining energy (J)
Al_2O_3	5	0.26 ± 0.013	0.20
	10	0.56 ± 0.040	0.40
	20	3.23 ± 0.232	0.80
	30	4.0 ± 0.050	1.20
Si_3N_4	3	0.92 ± 0.020	0.12
	6	1.13 ± 0.110	0.24
	10	1.69 ± 0.040	0.40
	20	3.5 ± 0.049	0.80
SiC	25	2.0 ± 0.083	3.75
	125	3.0 ± 0.035	18.75
MgO	3	0.25 ± 0.057	0.12
	6	0.86 ± 0.040	0.24
	9	1.54 ± 0.027	0.36
	20	3.0 ± 0.061	0.80

Attempts were made to reduce tapering effect by machining the cavities with a lens of longer focal length and longer focal waist. A uniform beam distribution in both temporal and spatial evolution was obtained from the configuration of focusing lens assembly and it was assumed that energy was evenly distributed across the pulse. For the simplicity of the model described later, beam was assumed to be temporally uniform. The corresponding machining energy required for machining a cavity of desired dimensions in any ceramic was given by Eq. (2.1) below and has also been listed in Table 2.2:

$$\begin{aligned} \textit{Machining Energy} &= \textit{Total on time} \times \textit{Average Power} \\ &= \textit{Total number of pulses} \times \textit{Pulse Width} \times \textit{Average Power} \end{aligned} \quad (2.1)$$

On the other hand, *e* of 6J, *p* of 0.5 ms, and *f* of 50 Hz was required for machining cavities in SiC. The average power used for laser machining of SiC was 300W (*e* (6J) x *f* (50Hz)). For this set of laser processing parameters, multiple pulses were applied until a through cavity was machined in the 2mm and 3mm thick SiC plates (Fig. 2.1c). A through cavity in the 2 mm thick SiC plate could be machined in approximately 0.5 s while under the same conditions a through cavity in the 3 mm thick plate was produced in approximately 2.5 s. Under the set of parameters employed in the present work, the repetition rate of 50 Hz over 0.5 s corresponded to 25 pulses while over 2.5 s it was equivalent to 125 pulses (Table 2.2). The corresponding machining energies for 25 and 125 pulses were 3.75 and 18.75 J respectively (Table 2.2). The visual observations ensured the creation of cavities (Fig. 2.1c) with 25 and 125 pulses in 2 mm and 3 mm thick SiC plates respectively.

Foresighting the exact number of pulses required to machine a certain cavity depth or predicting the depth machined in a given time for any ceramic is an exigent task. Hence, developing a mathematical model based on the material removal mechanism for each ceramic is the most suitable approach as discussed in next section.

Computational Modeling

During laser processing, the changes in surface temperature with absorption of laser energy and associated thermal gradient within the material have an effect on the machined depth and machining time. The heating during pulse on and the subsequent cooling during pulse off over the entire time of machining operation were considered for determining the heating curve by taking into account the on and off times during machining under present set of laser parameters. As this study does not focus on the microstructure evolution after the pulsing was

stopped, the cooling curves have not been discussed. The schematic illustrating the pulse on-off is shown in Fig.2.2 and it was necessary to start the computations with predictions of surface temperature profiles.

Temperature Evolution

The maximum temperature reached at the end of first pulse was predicted by using a model developed in COMSOL™ 's heat transfer transient mode [105, 106] which obtained the emperature distribution within the material using the finite element approach. This model solved the fundamental Fourier's second law of heat transfer subjected to convection and radiation boundary conditions (Eqs. (1.3) – (1.5)) [107-109].

Six vital modes were used to solve the problem. In the draw mode, the geometry and dimensions of the coupon (Table 2.1) were specified. The boundary mode permitted specification of all boundary conditions (Eqs. (1.3) – (1.5)) as discontinuous functions that were used to model the heating and the cooling processes. As mentioned earlier in Chapter I (Eq. (1.4)), energy was input to the system during t_p of 0.5 ms (corresponding to heating) and was cut off during t_{off} of 0.0495 s (corresponding to cooling). In order to incorporate this effect, the energy was input as a discontinuous function.

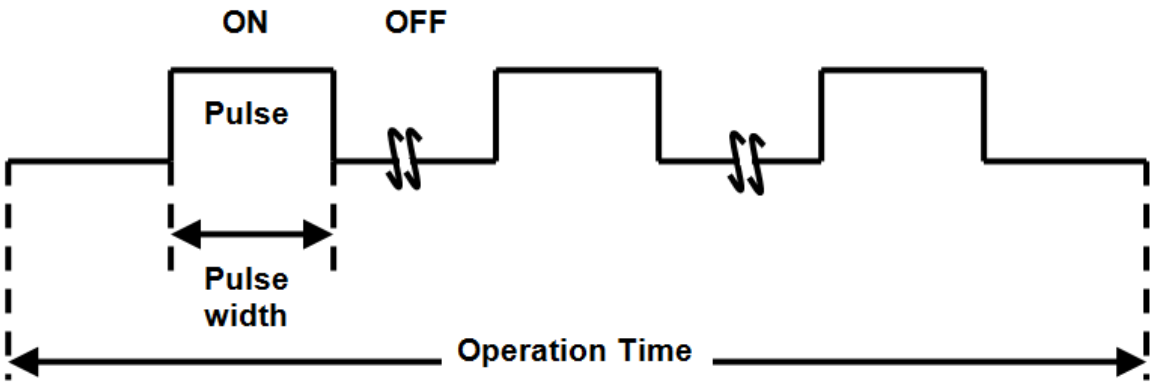

Fig. 2.2 Schematic of pulse on-off [63].

Terms involved in the governing equations that defined different material properties were presented by the subdomain mode. Laser induced machining is a rapid heating and cooling process due to which the thermophysical properties of materials exposed to the laser beam change rapidly in a large temperature range. Changes in thermal conductivity and specific heat as a function of temperature [110] (Fig.2.3) were incorporated to provide better accuracy in calculations. The latent heat was accounted for by incorporating the variation of specific heat as a function of temperature. This took into consideration the phase change due to melting/ vaporization. Density of Al_2O_3, Si_3N_4, SiC and MgO was 3800, 2370, 3100, and 3580 kg/m^3 respectively [110] and it was also input to the model along with thermal conductivity and

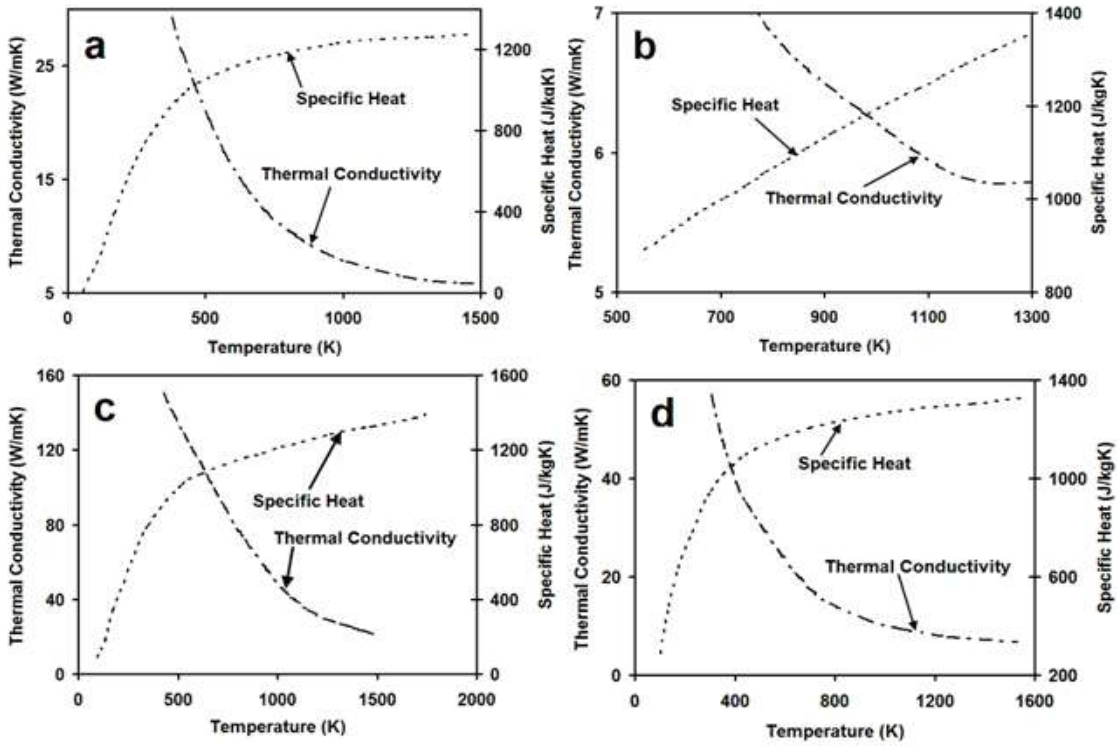

Fig. 2.3 Variation of thermophysical properties with temperature of a) Al_2O_3, b) Si_3N_4, c) SiC , and d) MgO [110]

specific heat. In addition, even though it is difficult to find in open literature, attempts were made to include the heat transfer coefficient as a function of temperature [111].

The characteristics of the finite element mesh were specified in the mesh mode, and a free mesh containing tetrahedral elements was generated. A non-uniform grid was used for simulations with a finer mesh under the laser beam as compared to the rest of the geometry where temperatures and their gradients are highest [112]. The grid independence test was conducted and mesh size of approximately 30,000 elements resulted in a grid independent solution. The actual number of elements varied with the geometry and dimensions of the coupons. The parameters of the solver and the solver type were set in the solver mode. The temperature profiles were obtained by running the simulations with extremely small time steps of 1μs and the 'time dependent' solver was used in COMSOL^{TM}. This developed model was a time based model and as seen later, the temperature evolution with time was correlated with machined depth. Hence kinetics of the material removal mechanism was inherently built in.

Finally, the postprocessing mode was used to analyze the results given by the solver. The temperature distribution and the temperature gradient were visualized in this mode. It should be noted that this study aims at correlating machined attributes with laser processing conditions and hence uses modeling only as a tool to achieve this goal. Studying the effect of change of modeling parameters such as element type, mesh size, type of solver, and time steps will however not be discussed here and can be considered for future study. A schematic of the steps involved in the generation of temperature profiles is represented in Fig. 2.4.

The solution of above described model gave maximum surface temperature reached after the first pulse which was input in Eq. (2.2), below to predict the temperature reached after the laser is switched off [54]:

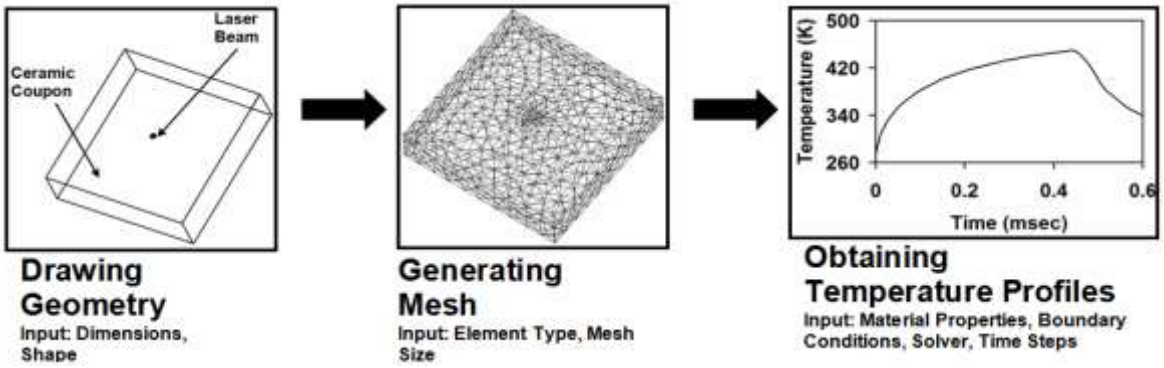

Fig. 2.4 Flow chart for temperature determination in COMSOL™.

$$T_i^{'} = T_i + (T_0 - T_i)\left[1 - \left[\exp\frac{h(T)^2\,\alpha(T)\,t_{off}}{k(T)^2}\right]\left[1 - erf\left(\frac{h(T)\sqrt{\alpha(T)t_{off}}}{k(T)}\right)\right]\right] \tag{2.2}$$

where T_i is the temperature during heating of pulse i (K), and *erf()* is the error function.

When the laser is active, the surface temperature is given by [54]:

$$T_i = T_{i-1}^{'} + \frac{8aQ}{\pi d^2}\frac{\sqrt{\alpha(T)t_p/\pi}}{k(T)} \tag{2.3}$$

where $T_{i-1}^{'}$ is the temperature during cooling of the earlier pulse (K) predicted from Eq. (2.2), above and Q is 80W for Al_2O_3, Si_3N_4 and MgO and 300 W for SiC. The temperatures reached during the on and off periods of the successive pulses were determined by repeatedly solving Eqs. (2.2) and (2.3) till desired number of pulses were completed or till the end of machining time. Due to extremely short time scale associated with the laser processing, the heat transfer in direction orthogonal to laser beam was neglected in Eqs. (2.2) and (2.3) used in the current study. This assumption was valid because in a rapid process like laser-material interaction, the heat transfer was confined to the laser beam and spatial distribution outside the beam was negligible. Only the centerline of the machined cavity was examined and an estimate of the corresponding

machining time and number of pulses was made. Furthermore, the width of the machined cavity was not predicted in this study and it was assumed to be the same as the out of focus beam diameter on the surface of sample. This was also a reasonable assumption because width of machined cavities was approximately the same as the out of focus beam diameter of 0.5 mm (Fig. 2.1) due to the negligible spatial distribution beyond the beam diameter as mentioned before. Thus it may be noted here that the model considered in this study is a 3D model [105] with width of the machined cavity in X and Y directions assumed to be constant and equal to the out of focus beam diameter (as also seen from Fig. 2.1).

Absorptivity

For cavities shown in Fig.2.1, as mentioned earlier in Chapter I, the transfer of energy from laser to surface of ceramic is affected by the multiple reflections within the machined cavity [41]. It was found by Bang and Modest [42] that multiple reflections increase the effective absorptivity of material and in the processes such as high aspect ratio laser machining, the value is expected to reach 100% instantaneously as also assumed by Andrew et. al [50] and Mazumdar et. al.[51]. Furthermore, it can be seen from Fig. 2.3 that as thermal conductivity of these ceramics is far less than metals (Al: 247 W/mK, Cu: 398 W/mK, Au: 315 W/mK [65]), the rate at which losses due to conduction take place will be less than the rate at which the laser energy is absorbed. This effect together with the effect of multiple reflections from the wall of machined cavity rapidly raises the absorption of incident energy to the level of 100%. In light of this, in this high aspect ratio one-dimensional machining study, the absorptivity value for all ceramics was taken to be 1 corresponding to 100% energy absorption and was used in Eqs. (1.3) – (1.5) and Eq. (2.3). The emissivity was also assumed to be 1 because for a given material and processing condition, the absorptivity is equal to the emissivity [113].

Furthermore, although conducting in-situ absorptivity measurements in a very short duration high energy dynamic process like laser material interaction is extremely challenging, efforts were made for actual absorptivity measurements under processing conditions similar to the ones used in this study and they are incorporated in later stages of this work (Chapters III to VI). Solution of Eqs. (1.3) – (1.5) and Eqs. (2.2) – (2.3) lead to the evolution of temperature with time for all the ceramics (Al_2O_3, Si_3N_4, SiC and MgO). As seen in the next section, dissociation and evaporation losses have an effect on the surface temperature of these ceramics and hence the final surface temperature profiles will be presented later in the chapter.

Material Removal Mechanisms

This section discusses the material removal mechanisms (MRM) relevant for each ceramic and it will be observed that a combination of different physical processes mentioned in Chapter I affect the machining of a certain ceramic rather a single predominant process.

By tracking the depth at which the melting point or decomposition temperature of Al_2O_3 (2323K [114]) was reached, the total melt depth (z_m) from the surface at any instant was estimated from the heating curves discussed above and ensuing depth calculations were based on this depth. At temperatures above 3250 K, dissociation of Al_2O_3 ceramic yields different species such as $AlO_{(g)}$, $Al_{(g)}$, $Al_2O_{(g)}$ and $AlO_{2(g)}$ [115]. Expulsion of the liquid phase formed due to melting above 2323K followed by the dissociation process above 3250 K (most likely by reaction in Eq. (2.4)) was responsible for laser machining in Al_2O_3.

$$Al_2O_3 = 2Al + \frac{3}{2}O_2 \tag{2.4}$$

However, some material was lost at the surface due to evaporation and the rate of evaporation j_e (kg/m^{2}s) was given by [116]:

$$j_e = p(T_s)\left[\frac{m_v}{2\pi kT_{max}}\right]^{1/2} \tag{2.5}$$

where $p(T_s)$ is the saturation pressure given by Clausius-Clapeyron equation:

$$p(T_s) = p_0 \exp\left[L_v / kT_e \left(1 - T_e / T_s\right)\right] \tag{2.6}$$

where p_0 is ambient pressure (1.013 x 10^5 N/m^2), L_v is 108.74 kJ/mol for Al_2O_3 [117] and T_e is the vaporization temperature (3250K [118]). The losses due to evaporation begin to take place after the surface temperature exceeds the vaporization temperature of Al_2O_3 after a certain number of pulses. The corresponding depth of material evaporated at a given instant was predicted from the rate of evaporation by the relation:

$$z_{eva} = \frac{j_e \times increment\ in\ time}{\rho} \tag{2.7}$$

where ρ for Al_2O_3 is 3800 kg/m^3 [110]. The evaporated depth (z_{eva}) was subtracted from the total melt depth (z_m) to give the available melt pool (z_{ava}). The corresponding drop in temperature at any instant at the surface because of the cooling of the melt pool by evaporation was given by [119]:

$$\Delta T_{eva} = \frac{2z_{eva}\rho L_v}{k(T)\,t\,d\pi^{3/2}} arc\,tg\,\frac{4\sqrt{\alpha(T)\times(increment\ in\ time)}}{d} \tag{2.8}$$

This drop in temperature was subtracted from the temperature predicted by Eqs. (1.3) – (1.5) and Eqs. (2.2) – (2.3).

Furthermore, at temperatures above dissociation temperature, the Gibbs free energy (ΔG) associated with the dissociation reaction (Eq. (2.4) was – 2372.6 kJ/mol at 3250K [120] and was used to determine the energy loss due to dissociation. The volume of the machined cavities was measured from Fig. 2.1 and it was found to be equivalent to a cylinder of diameter *d*, where *d*

was width of the machined cavity (equal to beam diameter of 0.5 mm as mentioned before). Hence, for the set of processing conditions considered in this study, it was assumed that the machined cavity had a cylindrical cross section of volume:

$$V_{diss} = \frac{\pi d^2 z_{ava}}{4} \tag{2.9}$$

where z_{ava} is available melt depth explained earlier. This volume was equivalent to $N_{moles} = V / 22.4 \times 10^{-3}$ moles and the loss of energy corresponding to dissociation of this volume of machined cavity above dissociation temperature was estimated by:

$$E_{dissociation} = \Delta G \times N \tag{2.10}$$

At temperatures above dissociation temperature, this energy loss was deducted from the input laser energy to give the effective laser energy available in subsequent laser pulses for raising the surface temperature and to generate corresponding machined depth. The final variation of surface temperature with time obtained by considering all above mentioned phenomena are represented in Fig. 2.5 for different number of pulses. The heating curve meanders because the temperature drops during off time and rises during on time of laser. The inset in Fig. 2.5 corresponding to heating curve for 20 pulses represents this rise and fall in temperature and this trend holds true for all cases in different ceramics considered in this study.

In laser machining, material removal takes place primarily in the liquid and vapor phases. As mentioned earlier in Chapter I, expulsion of the molten material is driven by the recoil pressure stimulated due to the evaporation of the melt surface exposed to the laser beam [121]. The recoil pressure stimulates ejection of the melt flow from the interaction zone at very high velocities [122]. The effective melt depth (z_{eff}) will be available for expulsion for the next time instant and it would be the portion remaining after a fraction of z_{ava} was expelled by p_{recoil}

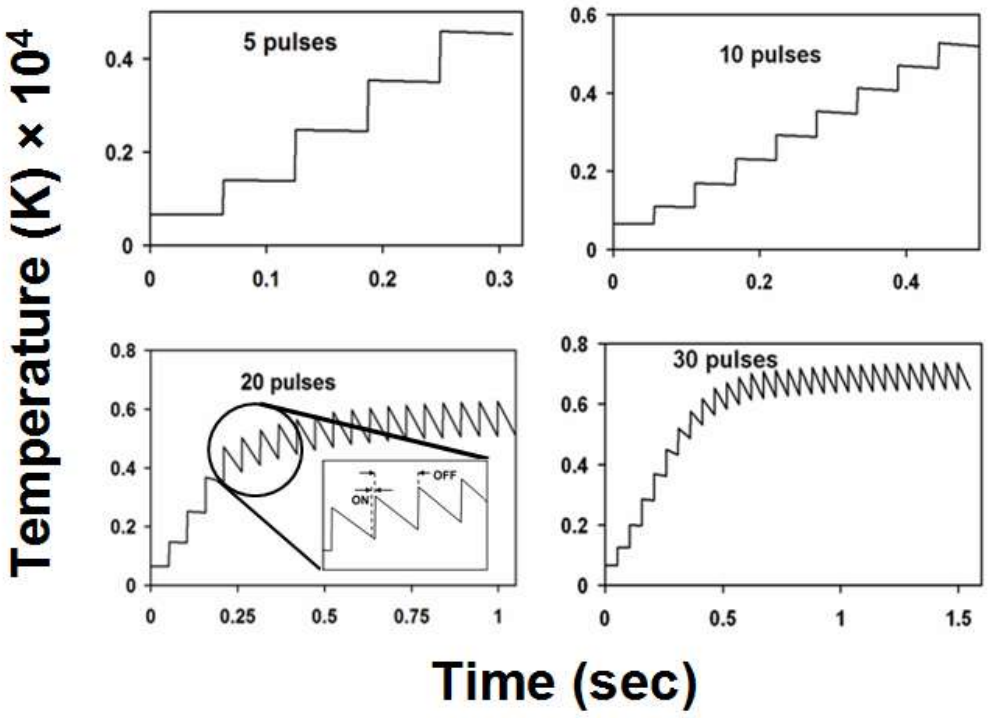

Fig. 2.5 Heating curves for different number of pulses in Al_2O_3 [63].

(Eq. (1.8)). Predictions of this fraction of the melt pool that is expelled by the recoil pressure will follow later in this section. In the absence of this recoil pressure, the thin film of molten material formed around the machined cavity would be responsible for closing the cavity. Thus the predicted temperature field assisted in determining the evaporation-provoked recoil pressure at the surface during machining through the ceramic using the physical model of melt hydrodynamics proposed by Anisimov who also experimentally verified the same [69]. According to Anisimov, when the surface temperature exceeds the boiling point or the decomposition temperature, the recoil pressure becomes $0.55p_s$, where p_s is the saturated vapor pressure (1.013.25 N/m^2). Under typical materials processing conditions such as those

encountered in machining, this recoil pressure exceeds the highest surface tension pressure and plays a vital role in removal of material in molten state.

It has been observed in the past that besides recoil pressure, surface tension also affects the melt pool shape [123] due to which it was necessary to consider the effect of surface tension as it was responsible for modifying the pressure on the melt and thus affecting the depth of the machined cavity. The laser beam gets defocused and effective beam radius which changes with evolution of machined cavity is given by [54, 124]:

$$r_{eff} = \frac{d}{2}\left[1+\left(M^2\frac{4\lambda(z_t+\delta_f)}{\pi d^2}\right)^2\right]^{1/2} \tag{2.11}$$

where M^2 is beam quality parameter assumed to be 1 for a perfect beam profile, δ_f is focal length of 120mm, λ is laser wavelength of 1.064 μm and z_t is depth of machined cavity which is zero at beginning of the machining process and is predicted later for successive time steps. Beam quality factor represents the beam quality which is a measure of the focusability of the laser used. All real beams tend to have an M^2 value greater than 1. Incorporation of actual M^2 values will take into account the complex distribution of energy during the laser machining process. However, in this study, the effect of defocusing of laser beam was accounted for by using the effective beam radius (Eq. (2.11) above).

The surface tension pressure depends on this effective beam radius and the melt available at the axis of the beam was expelled with a velocity v_{exp} given by [121]:

$$v_{exp}(t) = \frac{1}{\rho}\frac{p_{recoil}-\beta/r_{eff}}{r_{eff}}t \tag{2.12}$$

where β is the surface tension coefficient of liquid Al_2O_3 given by

$$\beta = 0.65\times(1-\omega(T_s-2500)) \tag{2.13}$$

where ω= 6 x 10^{-5} K^{-1} is the surface tension temperature coefficient [125]. As the temperature reached after the first few pulses is less than the melting point of Al_2O_3, there will be no material expulsion. Hence the expression for expulsion velocity (Eq. (2.12)) above does not imply for the first few pulses which are responsible for just raising the temperature of the material till the melting point is reached, after which the material expulsion process begins as governed by Eq. (2.12). Where as in case of through the depth machining, during application of final pulses, as explained later, only a very thin layer of the material remains which is simply pushed down from bottom by the recoil pressure. Eq. (2.12), therefore, does not apply to the later set of pulses during machining of a through cavity. Instead, the expression is only applied for the range of pulses where the material removal mechanism remains the same and is through expulsion. Integration of the expelled velocity over time (Eq. (2.14)) gave the fraction of the effective melt depth that was expelled at a certain time instant ($z_{expelled}$) and the depth of machined cavity z_t was given by Eq. (2.15) [126].

$$z_{expelled} = \int_0^t v_{exp}(t)\, dt \tag{2.14}$$

$$z_t = \sum_0^t z_{expelled} \tag{2.15}$$

Thus material removal in Al_2O_3 is a combined effect of melt expulsion, dissociation and evaporation. A flow chart for attaining the final machined depth using the process parameters and material properties will be presented later in this chapter after discussing the MRMs for all ceramics considered in this study. The computational predictions of temporal evolution of cavity machined in Al_2O_3 along with the schematic of different stages of cavity formation are represented in Fig. 2.6a and Fig. 2.6b respectively. The temporal evolution of the depth of the

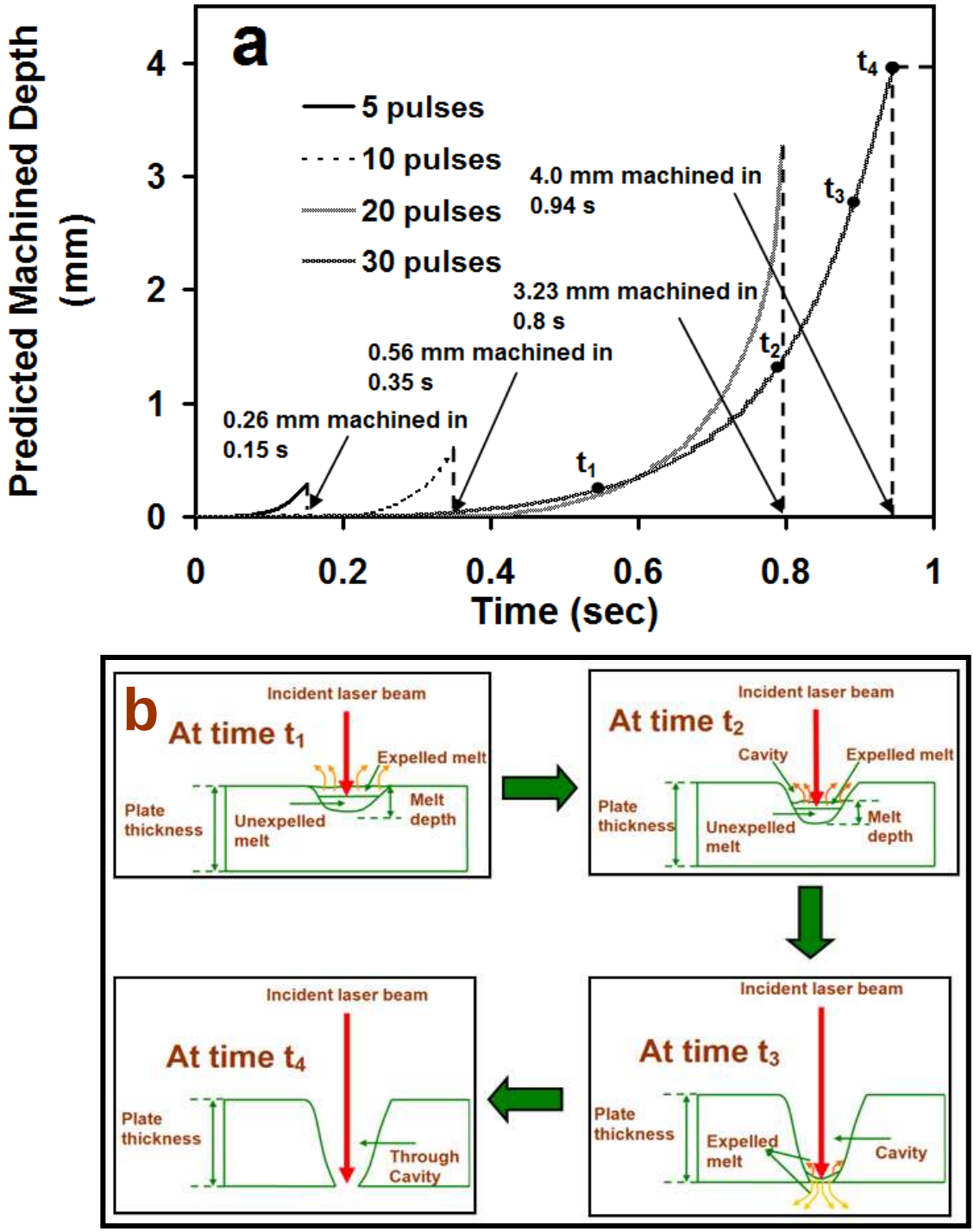

Fig. 2.6 Temporal evolution of machined depth during laser machining of Al_2O_3 a) computational predictions b) schematic for progression of cavity formation [63].

machined cavity for a given material thickness depends on the interaction time i.e. the number of pulses to which the material is exposed because it governs the amount of energy going into the material. Hence, the evolution profile was different for different number of pulses.

From this profile (Fig. 2.6a), comparison between experimental and predicted number of pulses and time required for machining a certain depth of material was made in Table 2.3[63]. The corresponding machining energy for predicted number of pulses was also calculated from Eq. (2.1) and compared with experimental machining energy values (Table 2.2) in Table 2.3. The table also compares experimental and predicted attributes of cavities machined in SiC and MgO which will however be discussed later. Also, as seen later, in Si_3N_4, the model was used to determine depth machined in a certain time rather than predicting time required to machine desired depth. This demonstrated feasibility of the developed model to determine different

Table 2.3 Comparison between experimental and predicted attributes of machined cavities in Al_2O_3, SiC and MgO [63, 65, 66].

Ceramic	Depth of machined cavity (mm)	$Pulses_{experimental}$ (Time, sec)	$Pulses_{predicted}$ (Time, sec)	$Machining\ energy_{experimental}$ (J)	$Machining\ energy_{predicted}$ (J)
Al_2O_3	0.26	5 (0.25)	3 (0.15)	0.20	0.12
	0.56	10 (0.5)	7 (0.35)	0.40	0.28
	3.23	20 (1.0)	16 (0.8)	0.80	0.64
	4	30 (1.5)	19 (0.94)	1.20	0.76
SiC	2	25(0.5)	21(0.41)	3.75	3.15
	3	125(2.5)	103(2.05)	18.75	15.45
MgO	0.25	3 (0.15)	2 (0.11)	0.12	0.08
	0.86	6 (0.3)	4 (0.2)	0.24	0.16
	1.54	9 (0.45)	5 (0.25)	0.36	0.20
	3	20 (1)	16 (0.8)	0.80	0.64

attributes of machined cavity in any ceramic and a comparison between experimental and predicted machined depths in Si_3N_4 will be done later in a separate table.

It can be observed from Table 2.3 that predicted number of pulses and machining energy for Al_2O_3 were close to the experimentally measured values (Table 2.2). However, the predicted number of pulses (and corresponding machining energy) was less than those experimentally detected for machining because the number of pulses were chosen based on prior experience in laser processing. Furthermore, as mentioned before, due to lack of a feedback system to monitor the formation of a through cavity, the material could have been exposed to few extra pulses even after a cavity through entire thickness of the ceramic coupon was machined. Some error could also have been introduced due to limitations of technique used for measuring machined depth from micrographs (Fig. 2.1). In addition to the above considered physical phenomena, there could be some other mechanisms as mentioned later which are not incorporated in this study that could have had an effect on the predicted number of pulses. Thus the presented model can assist to determine the number of pulses required for machining a certain depth in a given material under a certain set of other laser parameters.

In the initial stages of machining (until around time instant t_2 in Fig. 2.6b), the recoil pressure expelled the material in the upward direction and continued to do so for increased depth of the machined cavity as the time progressed. Eventually, when a very thin layer of the material remained in the bottom (at around time instant t_3), the recoil pressure was able to push most of the material in the downward direction thereby reversing the direction of material expulsion in the final stages of machining. This happened due to least resistance to recoil pressure by the small mass of supporting material at the bottom. Finally, at around time instant t_4, all the rest of molten material was expelled and a clean through cavity was formed.

Such a comprehensive approach differentiated the current work from earlier work such as that of Salonitis et. al [54] and Miyazaki et. al [127] who considered the machining mechanism as comprised of melting and subsequent material removal by melt expulsion where as Atanasov et. al [128] considered the machining of Al_2O_3 merely by a single step material evaporation without any melting. On the contrary, in the present study, the material removal during the machining process takes place due to a combination of melt expulsion, dissociation and evaporation processes. Furthermore, the past studies [54, 127, 128] have also neglected the effect of multiple reflections on the absorbed laser energy. Thus the systematic approach considered in this study is an advancement of the existing computational approach to machining of ceramics.

After determining the temperature distribution (Eqs. (1.3) – (1.5) and Eqs. (2.2) – (2.3)), the procedure for predicting attributes of machined cavities in Si_3N_4 and SiC discussed below was the same as used for Al_2O_3 (Eq. (2.5) – (2.12), and Eq. (2.14)- (2.15)) because the MRMs were same for all these ceramics. However, as seen later, melting is not involved in material removal in MgO and hence only vaporization temperature was tracked in the corresponding temperature profiles to determine machined depth in MgO.

The sublimation / dissociation temperature of Si_3N_4 is 2,173 K [114, 129] at which it dissociates into liquid silicon and nitrogen (Eq. (2.16)) [130] and the laser machining took place due to expulsion of this liquid silicon by evaporation induced recoil pressure (Eq.(1.8)).

$$Si_3N_4 = 3Si_{(l)} + 2N_{2(g)} \tag{2.16}$$

Dissociation temperature of Si_3N_4 was tracked in the temperature profiles obtained by solving Eqs. (1.3) – (1.5) and Eqs. (2.2) – (2.3) to determine the melt depth from the surface at any

instant which was then used for further depth predictions as described above for Al_2O_3. Evaporation also assists in material removal (Eq. (2.5) – (2.8)) and melting, dissociation and evaporation together lead to machining in Si_3N_4 [62]. The latent heat of evaporation for Si_3N_4 was 336.94 kJ/mol [131] and it was used to determine the recoil pressure (Eq. (1.8)) and temperature drop due to evaporation (Eq. (2.8)). To determine energy loss due to dissociation (Eq. (2.9) and Eq. (2.10)), Gibbs free energy of -1309.42 kJ/mol at 2151K [120] associated with Eq. (2.16) was used. The machined depth was also affected by the effective beam radius (Eq. (2.11) due to laser beam defocusing and by surface tension (Eq. (2.12)). As the thermophysical properties of Si_3N_4 control the dissociation of Si_3N_4 into its species, the Si_3N_4 properties were considered only till Si_3N_4 dissociated into liquid Si after which the properties of Si melt were taken into account. In light of this, the surface tension coefficient of liquid Si (0.843 N/m for liquid Si [132]) was considered as it affects the expulsion velocity (Eq. (2.12)) and hence depth of machined cavity (Eq. (2.15)).

The evolution of surface temperature (using thermal model described above) and machined cavity with time for application of different number of pulses in Si_3N_4 is presented in Fig. 2.7 and a comparison between predicted (Fig. 2.7b) and actual machined depth (Fig. 2.1) in a given time is presented in Table 2.4[62]. In most of the cases seen in Table 2.4, there was a reasonable match between machined depth estimated by model and depth actually measured. Discrepancy in some values could be attributed to the same causes as mentioned before such as limitations of depth measurement technique (using optical micrographs) and lack of feedback system for indicating the onset of a through cavity. Thus, the computational model could also be used to predict depth machined in any ceramic in a given time in addition to determination of time (number of pulses) required for machining a certain depth as demonstrated earlier for

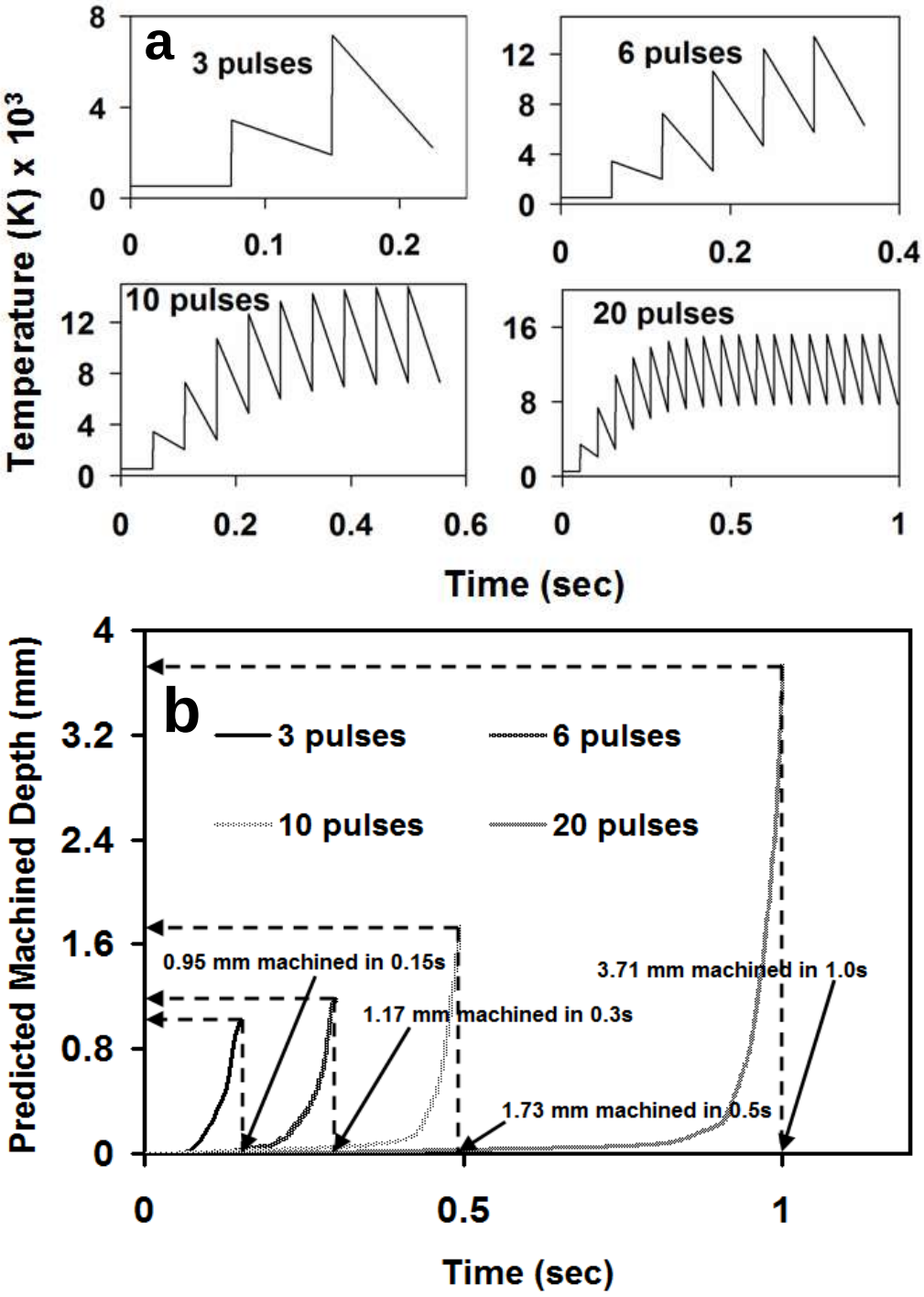

Fig. 2.7 Evolution of a) surface temperature and b) machined depth with time in Si_3N_4 [62].

Table 2.4 Comparison between experimental and predicted attributes of machined cavities in Si_3N_4 [62].

Pulses (Time,s)	Machined depth $_{experimental}$ (mm)	Machined depth $_{predicted}$ (mm)	Machining energy$_{experimental}$ (J)	Machining energy$_{predicted}$ (J)
3 (0.15)	0.92	0.95	0.12	0.12
6 (0.3)	1.13	1.17	0.24	0.24
10 (0.5)	1.69	1.73	0.40	0.40
20 (1.0)	3.5	3.71	0.80	0.80

Al_2O_3. The time required to machine a certain depth was not predicted for Si_3N_4. On the contrary, depth machined in a given time was predicted. Hence, total number of pulses (experimental and predicted) for a given depth were same and corresponding machining energy for any given number of pulses was also same (Eq. (2.1)).This study on one- dimensional laser machining of Si_3N_4 was different from prior machining work on this ceramic [72, 95-97] who did not attempt to understand the material removal mechanisms.

Depending upon the thermodynamic conditions prevailing during laser machining, decomposition of SiC may produce several species such as $Si_{(g)}$, $Si_{2(g)}$, $SiC_{2(g)}$, $Si_{(l)}$, $C_{(s)}$, $Si_{(s)}$, $Si_2C_{(g)}$, $C_{(g)}$, and $Si_{3(g)}$ [74] at the decomposition temperature of SiC (3,103 K) [114]. *In-situ* detection of formation of these species during extremely dynamic and short duration laser machining process is a challenging task and can be considered in future. However, the most likely reaction to produce liquid species available for expulsion is :

$$SiC = Si_{(l)} + C_{(s)} \tag{2.17}$$

Decomposition temperature of SiC (3,103 K) was traced in the generated temperature profiles to predict the melt depth from the surface at any instant. Similar to Al_2O_3 and Si_3N_4, some loss of

material also occurs due to evaporation and a combination of melting, evaporation (Eq. (2.7) and Eq. (2.8)), and dissociation (Eq.(2.9) and Eq. (2.10)) contributes to machining in SiC. Latent heat of evaporation was 530 kJ/mol for SiC [133] and was used to predict recoil pressure and evaporation losses. The Gibbs free energy associated with this reaction (Eq. (2.17)) was -335.96 kJ/mol at 3259K [120] and it determined dissociation energy losses. Similar to Si_3N_4, the surface tension coefficient of liquid Si (0.843 N/m) was considered to determine depth of machined cavity (Eq. (2.15)) in SiC. The variation of temperature for the 2 and 3mm thick SiC plates is represented in Fig. 2.8a while evolution of machined depth with time for SiC is represented in Fig. 2.8b. It can be observed from Fig. 2.8b that a 2 mm thick plate was machined through its entire depth in 0.41 s while it took 2.05 s to machine through the entire thickness of a 3 mm thick plate (Table 2.3). Thus, only 21 pulses for a 2 mm plate and 103 pulses for a 3 mm plate were required to machine through the entire thickness. A comparison between experimental (Table 2.2) and predicted machining energy (obtained from Eq. (2.1) by using predicted number of pulses) is also made in Table 2.3[66].

Computationally predicted number of pulses (and corresponding machining energy) was less than those experimentally identified and this discrepancy is due to the fact that selection of number of pulses during actual machining was based on prior practical experience in laser-materials interactions and visual observations. This study on single dimensional machining of SiC was diverse from prior work by Sciti et. al. [74] who only considered the microstructural surface modification of SiC as a function of laser processing parameters without considering the actual physical phenomena such as effect of recoil pressure, evaporation losses and dissociation energy losses responsible for cavity formation as considered in present study. The progression of

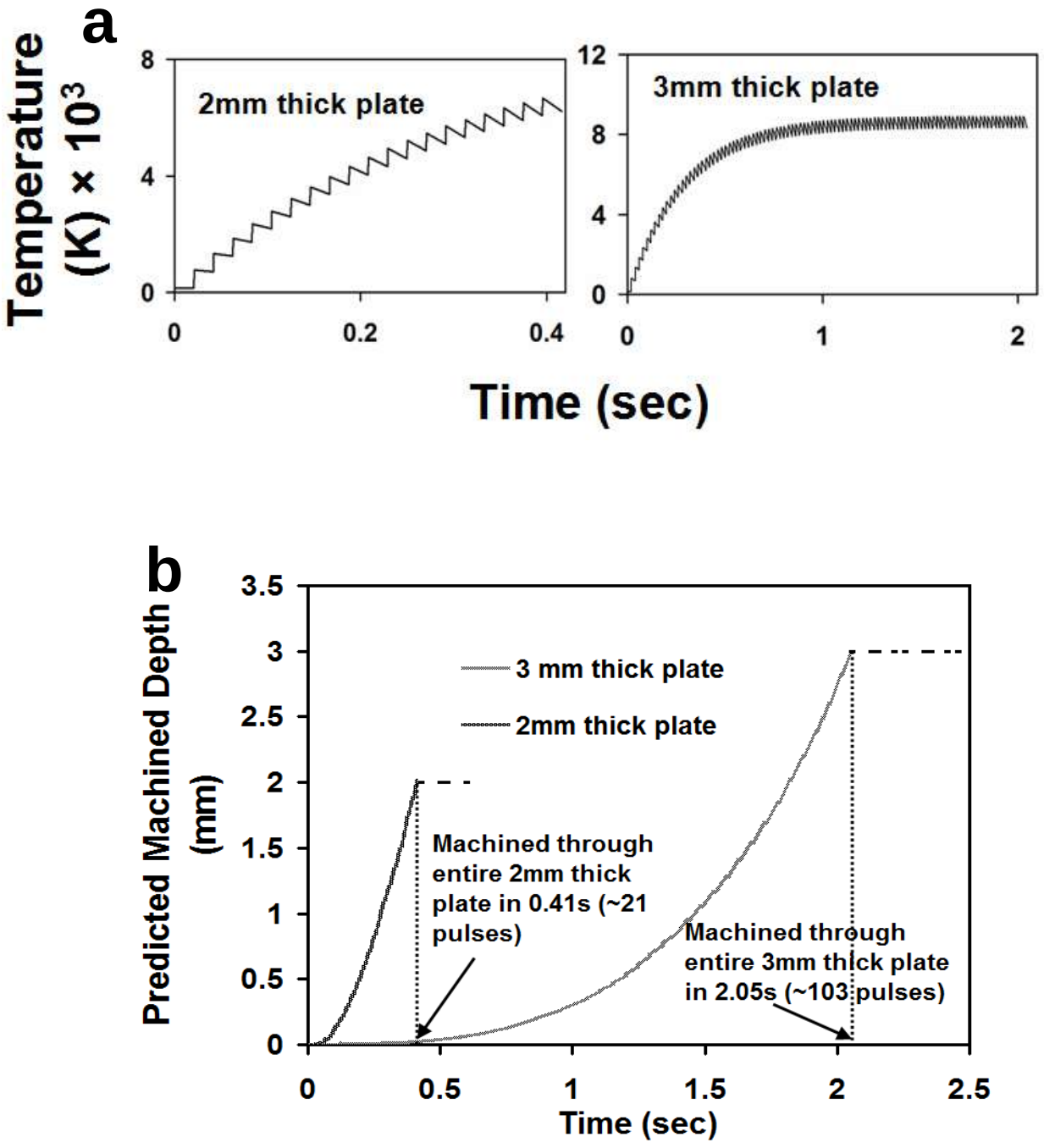

Fig. 2.8 a) Heating curves for 2 and 3 mm thick plates and b) evolution of machined depth with time in SiC [66].

cavity evolution illustrated in Fig. 2.6b for Al_2O_3 would be applicable to Si_3N_4 and SiC as material removal mechanisms are same for all these ceramics.

The dissociation of MgO takes place as per the following reaction [134, 135]:

$$MgO \rightarrow Mg + O \tag{2.18}$$

The melting and vaporization temperatures of magnesium are 922K [136] and 1363K [137] respectively. Thus, at temperatures above the melting/decomposition/vaporization temperature of MgO (3123K [114]), material losses take place purely by evaporation of magnesium formed due to the above dissociation reaction. Thus machining in MgO takes place due to dissociation of the ceramic via above mentioned reaction (Eq. (2.18)) followed by evaporation of the material exposed to laser fluence. This mechanism is in contrast to the machining of Al_2O_3, Si_3N_4 or SiC ceramics using the same laser based technique where material removal is a combination of melt expulsion and evaporation [62, 63, 66] as elaborately discussed above. A schematic illustrating evolution of machined cavity in MgO at different time instants is shown in Fig. 2.9 where depth of cavity increases with increase in time from t_1 to t_4 as more material vaporizes. A very thin layer of material remains in the final stages of through machining which falls down from the bottom due to gravity.

The Gibbs free energy associated with the dissociation reaction (Eq. (2.18)) was -974.1 kJ/mol at 3533K [120] and it was used to predict dissociation energy losses (Eq. (2.9) and Eq. (2.10)). The amount of material evaporated was predicted by obtaining the temperature profiles (presented in Fig. 2.10 below) from the procedure described above (Eqs. (1.3) – (1.5), Eqs. (2.2) – (2.3), Eq. (2.9) and Eq. (2.10)) and then tracking depth from surface at which decomposition temperature of MgO was reached. In general, it can be observed from the heating curves (Fig.

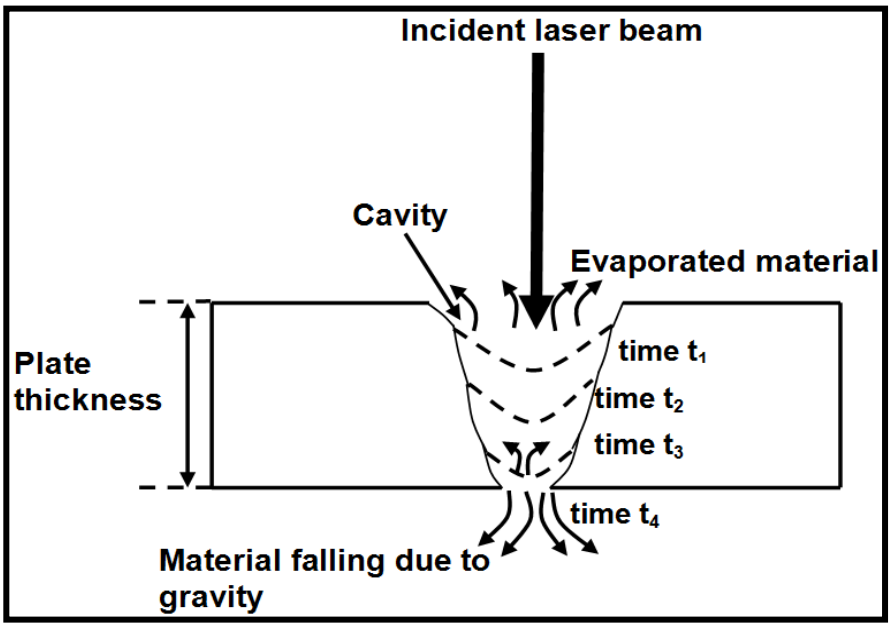

Fig. 2.9 Progression of cavity in MgO.

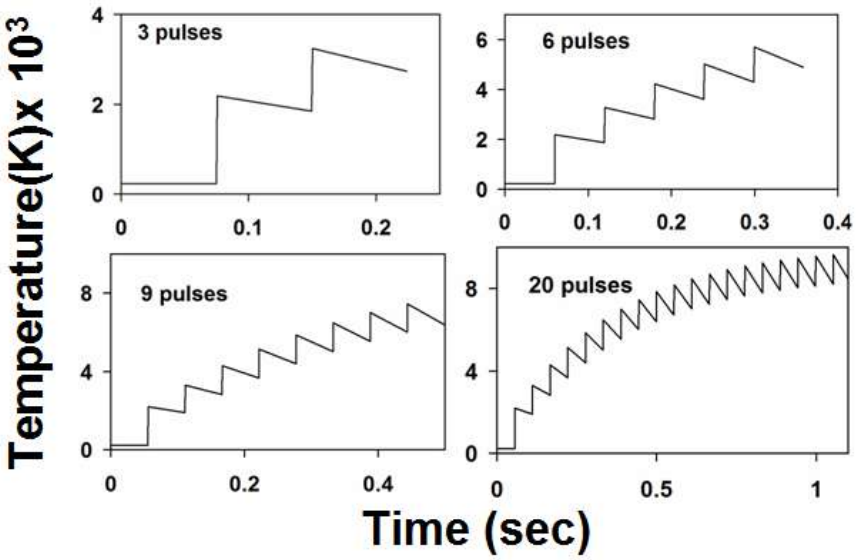

Fig. 2.10 Heating curves for different number of pulses incident on MgO ceramic [65].

2.5, 2.7a, 2.8a, and 2.10) that maximum surface temperatures were high in these ceramics. It should be noted that even though temperatures were high enough for such a short duration process, they were mostly limited to the surface for an extremely short duration with a probability of some material loss by ablation. These high temperatures immediately drop below melting point within the sub-surface region and further lower values in the substrate material due to self quenching.

The evolution of machined depth with time is represented in Fig. 2.11 and a comparison between experimental and predicted number of pulses and machining time is made in Table 2.3 [65] which also compares corresponding machining energies. The number of pulses, machining time and energy predicted for different machining depths were close to the actual values. Thus this study is a novel effort in understanding the material removal mechanism in MgO as not much work has been carried out in the past in that direction.

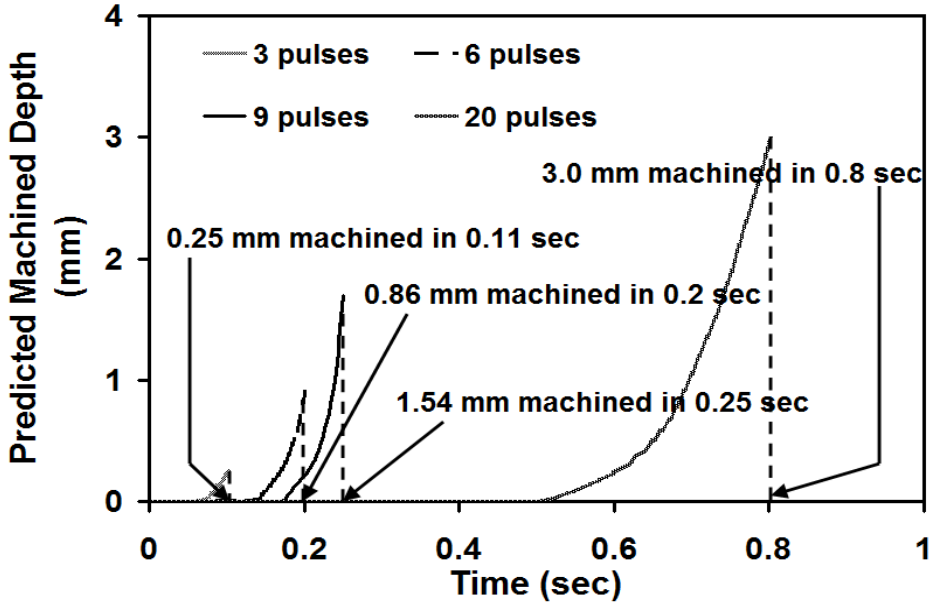

Fig. 2.11 Evolution of machined cavity with time in MgO [64, 65].

Thus it can be seen from this chapter that prediction of exact number of pulses (for that matter pulse duration, laser energy, etc.) to drill a required depth or predicting depth machined when a given number of pulses are incident on a certain type of material under chosen set of laser processing parameters would be extremely advantageous to conserve substantial energy and time. The governing mechanisms in different ceramics considered in this study are summarized in Table 2.5 and a general flow chart for predicting the desired machining parameter based on such computational model using the process parameters and material properties is represented in Fig.2.12. The nature of the structural ceramic will govern the physical phenomena (Table 2.5) that can be incorporated into the mathematical model (Fig. 2.12).

In addition to the physical processes considered in this study, the different physical phenomena that could possibly have an effect on the machining process are: a) plasma formation and associated ionization, b) ablation, and c) effect of assist gas pressure and flow rate on the machined depth. These processes are not considered in the present study and can affect the predicted attributes of machined cavities. Moreover, it has been mentioned by Modest [47] that the increase in absorptivity is affected by the number of pulses, i.e. for a small number of pulses

Table 2.5 Mechanisms governing material removal in Al_2O_3, Si_3N_4, SiC and MgO (✓- phenomena present; × - phenomena not present) [64].

Physical process ↓ / Material →	Al_2O_3	Si_3N_4	SiC	MgO
Melting	✓	✓	✓	×
Dissociation	✓	✓	✓	✓
Evaporation	✓	✓	✓	✓

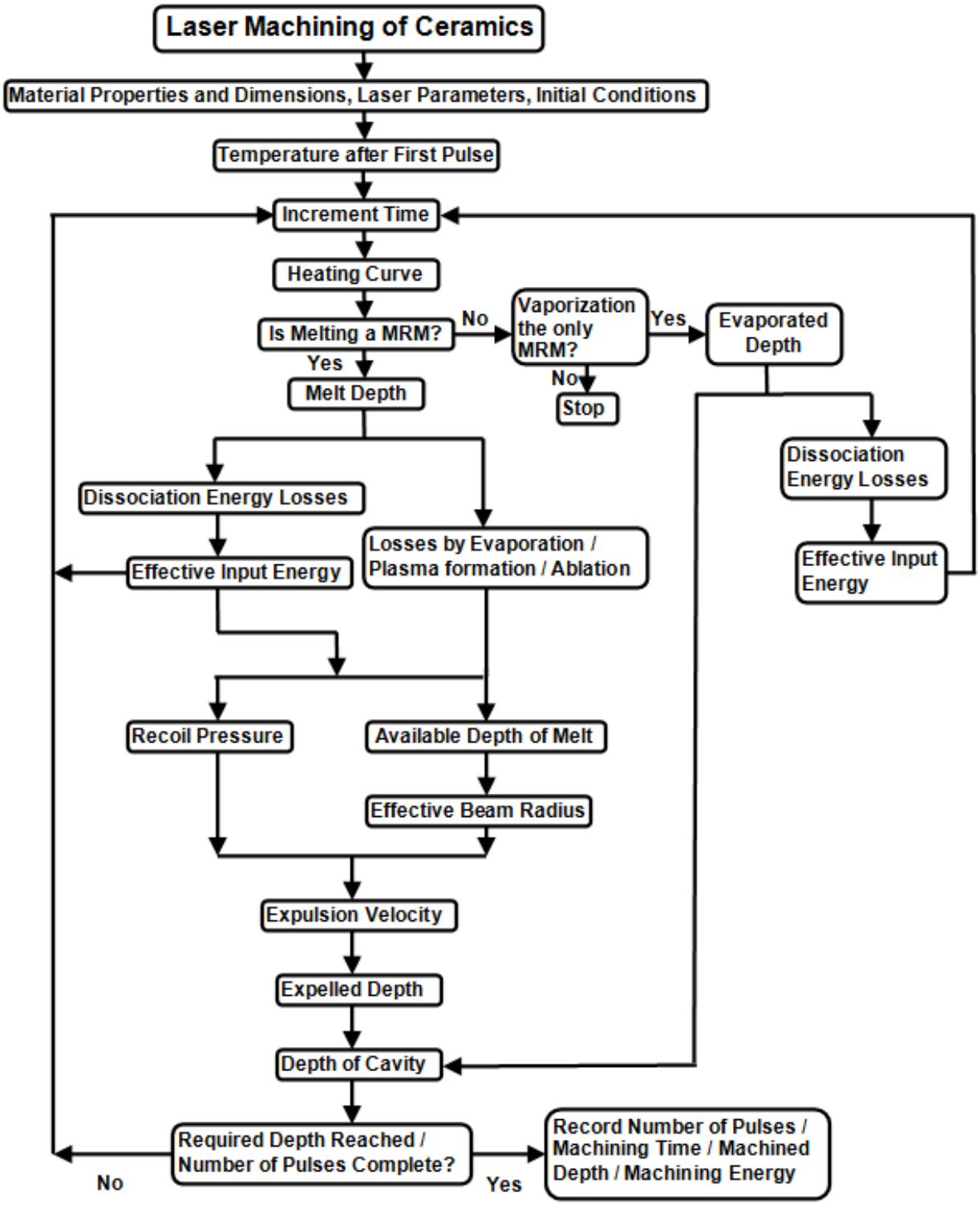

Fig. 2.12 Stepwise procedure for prediction of attributes of machined cavities.

the absorptivity is increased only slightly. Hence, the assumption of 100% absorption of incident laser energy due to multiple reflections for the entire range of pulses employed in the present work may have produced the differences between predicted and measured machining parameters for all ceramics (Table 2.3 and Table 2.4). In light of this, in order to improve accuracy of calculations, an attempt was made to predict actual absorptivity values during laser machining of these ceramics under conditions similar to the ones used in this study and this approach will be presented in the next chapter on *in-situ* surface absorptivity measurements.

CHAPTER III
IN-SITU SURFACE ABSORPTIVITY PREDICTIONS[1]

The laser beam incident on ceramic surface is absorbed, reflected, transmitted, and scattered (Fig. 1.4). Significant of all these effects is absorption which depends on the wavelength of laser used for processing, spectral absorptivity characteristics of the ceramic being machined, surface roughness, orientation of the material surface with respect to beam direction and temperature attained during processing [36, 40]. Absorptivity, *a* is defined as ratio of absorbed part of incoming radiation to total incoming radiation and it varies between the values 0 and 1 [103]. As mentioned in Chapters I and II, the amount of energy absorbed by the ceramic surface governs the temperature evolution and it is high enough to cause material removal at surface and sub surface region. The ensuing effects such as machined depth, machining time and energy required for machining a certain depth will be governed by this temperature evolution. Thus the energy absorbed by the surface decides if machining is likely to take place.

In light of this, in order to efficiently predict these effects and corresponding machining parameters, it is critical to determine variation of absorptivity with temperature during laser processing. To the best of author's knowledge, except for LIA Handbook of Laser Materials Processing [103], there is paucity of data in open literature representing the variation of absorptivity with temperature for these structural ceramics processed at wavelength of 1.06 μm. Hence, an attempt was made in this study to predict the absorptivity of Al_2O_3, Si_3N_4, SiC and MgO as a function of temperature by measuring in-situ machining temperatures with the aid of thermocouples and correlating them with temperatures predicted from the thermal model described in Chapter II [138].

[1] The content of this chapter is originally from Reference [138].

Furthermore, the energy absorbed at the surface is maximum and it decays because of several phenomena as it propagates through the bulk of the material. In certain ceramics which have a multi- crystalline nature, the incident energy will be multiply scattered inside the material and this would affect the variation of absorptivity with depth. However, laser processing being an extremely rapid process (interaction time of the order of a few ms), it is extremely difficult to determine decay of absorptivity in bulk material. Prediction of absorptivity decay (drop in absorptivity per unit length) is not a focus of this study and can be considered in the future.

In this study, the temperatures were measured for the workpiece machined with low aspect ratio (depth to width <1) because for cavities with high aspect ratios (>1), multiple beam reflections along the cavity wall affect the amount of absorbed energy [41, 42] and the surface absorptivity rapidly changes to 1 as seen earlier in Chapter II. Moreover, thermal conductivity of ceramics generally being less than majority of metals, the portion of absorbed incident energy builds up rapidly to raise the temperature within surface and subsurface regions for machining of ceramics via various physical processes such as melting, dissociation/decomposition and vaporization as seen in Chapter II. Also, due to phase change (solid-liquid transformation above melting point or liquid-vapor/solid-vapor transformation above vaporization/dissociation temperature of ceramic), the absorptivity rapidly increases through multiple reflections and physical entrapment of beam by the molten material/ vapor in the cavity. Hence, although the absorptivity was predicted for low aspect ratio machining of the ceramic, the respective values can be very useful for estimating absorbed energy and corresponding machining parameters in the initial stages of any machining where there is no phase change. The absorptivity transitions above the phase transition temperature will be predicted and discussed in next chapter. It should be noted in this study that even though the workpiece was assumed to be multi- crystalline and

not a single crystal, the complex phenomenon of scattering (reflections) at the several interfaces was not incorporated.

Experimental Procedure

Coupons of dimensions 5mm × 5mm × 8mm were made from dense Al_2O_3, Si_3N_4, SiC, and MgO. In order to sense the temperature rise during laser interaction, a K-type thermocouple with a bead diameter of ~ 800 μm was glued to the coupons using a high temperature ceramic adhesive (Ceramabond^{TM} 516 from Aremco Products, Inc) followed by curing at 373K for one hour. K-type thermocouple is a nickel based alloy composed of chromel (90 wt% Ni and 10 wt% Cr) and alumel (95 wt% Ni, 2 wt% Mn, 2 wt% Al, and 1 wt% Si) with capability to sense temperatures as high as 1623K [139]. The thermocouple was calibrated using an electronically controlled furnace. The temperature recorded by the thermocouple for a preset temperature of the furnace is presented in Fig. 3.1. The linear fit law ($T_{actual} = 0.9768\ T_{thermocouple} + 10.241$) was used to convert the measured temperature into actual temperature. Slope of linear fit (0.9768) was close to 1 and these set of temperature values differed only maximum of 2 % from each other.

JK 701 pulsed Nd:YAG laser (1.06 μm wavelength) was used to machine the ceramic coupon with a low aspect ratio (<1) cavity during thermocouple based temperature measurement by applying different number of pulses (400 to 700 pulses) with *p* of 2.0 ms, *f* of 20Hz, and *e* of 4 J corresponding to an average power of 80W (*f* (20Hz) × *e* (4J)). Three temperatures were recorded for each set of pulses to minimize errors. The number of pulses were applied in a random sequence (500,700,600,400 followed by 700,400,500,600 and then 400,600,500,700 pulses) and thus the principle of randomization explained earlier in Chapter II was implemented.

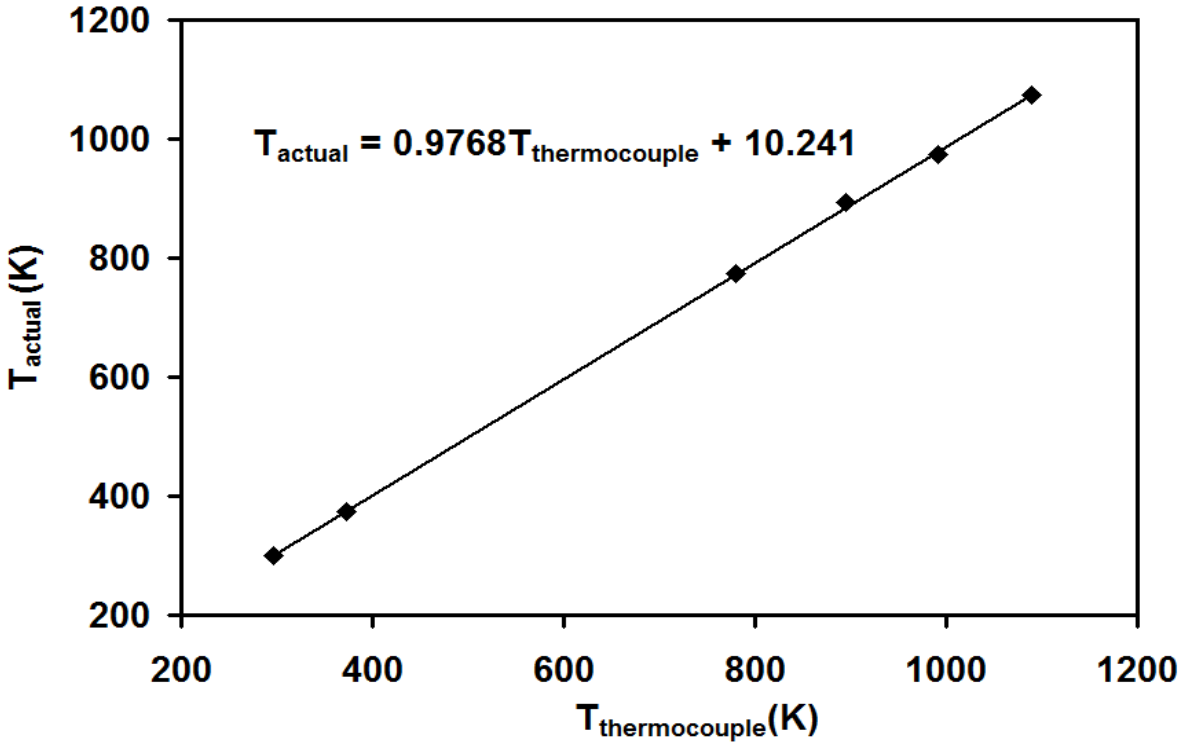

Fig.3.1 Thermocouple calibration [138].

Absorptivity was predicted for each case using the procedure elaborated later. The laser beam was defocused on the surface and pulses were applied as close as possible to the thermocouple tip to minimize losses of heat to the surrounding environment and enable effective sensing of the maximum temperatures attained during machining. A very small fraction of the incident energy is scattered towards the thermocouple tip and magnitude of energy directly absorbed by the tip is extremely small. Hence no significant temperature rise can be caused due to scattering and subsequent direct absorption of incident energy by thermocouple tip at the surface. The out of focus beam diameter, d and distance between center of laser beam and thermocouple tip, r_{tip} were measured from the top views of the machined ceramic coupons (Fig.3.2) and are represented in Table 3.1.

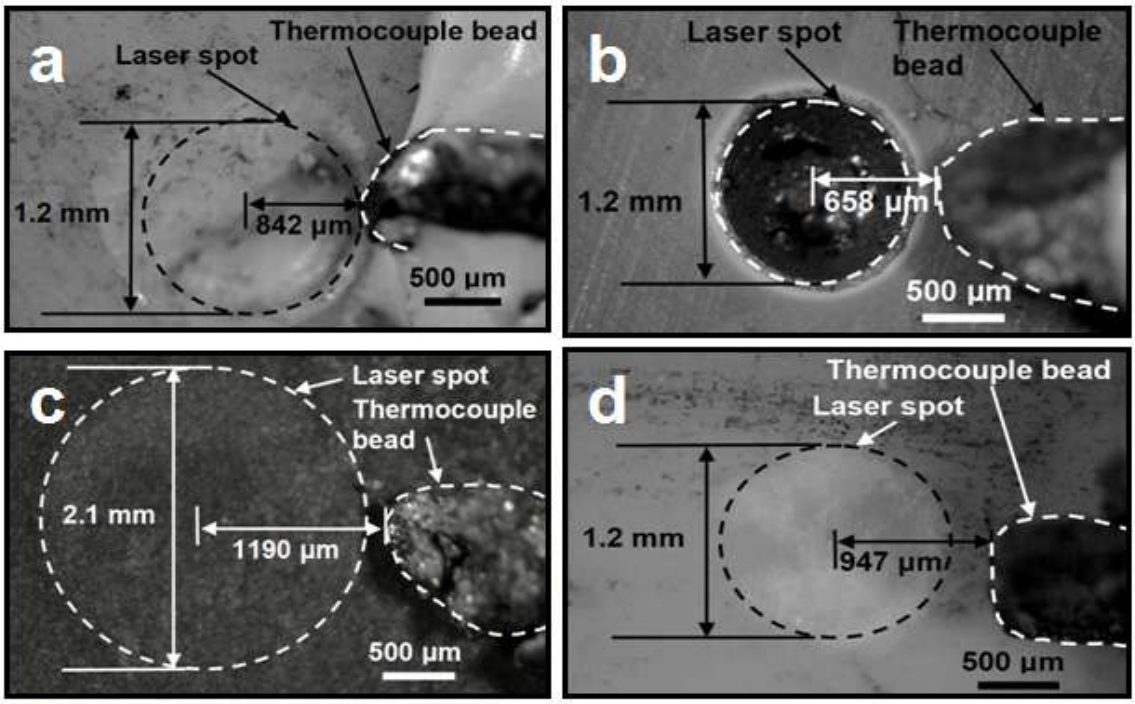

Fig.3.2 Top views of thermocouple glued to the ceramic surface in a) Al_2O_3, b) Si_3N_4, c) SiC, and d) MgO[138].

Table 3.1 Physical parameters corresponding to experimental conditions and ceramics used in computational model [138].

Ceramic	Out of focus beam diameter d (mm)	Distance of thermocouple tip from laser beam center r_{tip} (µm)	Surface roughness R_a (µm)
Al_2O_3	1.2	842	0.913 ± 0.154
Si_3N_4	1.2	658	0.249 ± 0.096
SiC	2.1	1190	0.283 ± 0.024
MgO	1.2	947	0.527 ± 0.121

As the laser beam was positioned near the thermocouple by mere visual observation and judgement, r_{tip} between the center of the laser beam and the thermocouple tip was not the same for all ceramics.

Furthermore, a surface becomes more absorptive (less reflective) as the roughness increases because the incident laser beam may undergo multiple reflections off local peaks and valleys (resulting in increased absorption) before leaving the surface of workpiece into an off-specular direction [103]. Thus, as surface roughness affects absorptivity of the ceramic, it was measured for all ceramics using a Mahr Federal Perthometer (Model M1) with a tip scan distance of 5.6 mm and these values have also been represented in Table 3.1. The absorptivities predicted later were corresponding to these roughness values and they may change significantly with roughness. As long as surface roughness is less than beam wavelength (1.06 μm), the incident beam will not suffer multiple reflections as mentioned above and the surface will be considered to be flat [52]. However, for higher roughness values, the effect of surface roughness on absorptivity could be a very complex phenomena and absorptivity could differ by more than an order of magnitude depending on magnitude of surface roughness. The effect of change of surface roughness on absorptivity was not the focus of this study.

The laser beam was defocused on the surface of ceramic to achieve the formation of low aspect ratio (<1) machined cavity. In case of Al_2O_3, MgO, and Si_3N_4 such defocused beam diameter that raised the surface temperature sufficiently high was 1.2 mm whereas it was 2.1 mm for SiC due to its inherently high absorption characteristic for 1.06 μm wavelength laser beam [103]. The in-situ machining temperatures were recorded using LabVIEW (Laboratory Virtual Instrument Engineering Workbench); a commercially available package for data acquisition and visualization [140]. A schematic of the entire setup used for temperature measurement is

represented in Fig. 3.3. The maximum temperature measured by the thermocouple at the surface for each ceramic was used as a benchmark for predicting temperatures using the thermal model (Eq. (1.3) – (1.5)) explained in Chapter I and iteration method [141] described in next section. Similar approach can be extended for bulk absorptivity determination by inserting the thermocouple at different depths and then iterating the thermal model to predict absorptivity as function of depth. However, the present study assumes a constant absorptivity through the bulk of material and only considers variation of absorptivity at the surface as function of temperature.

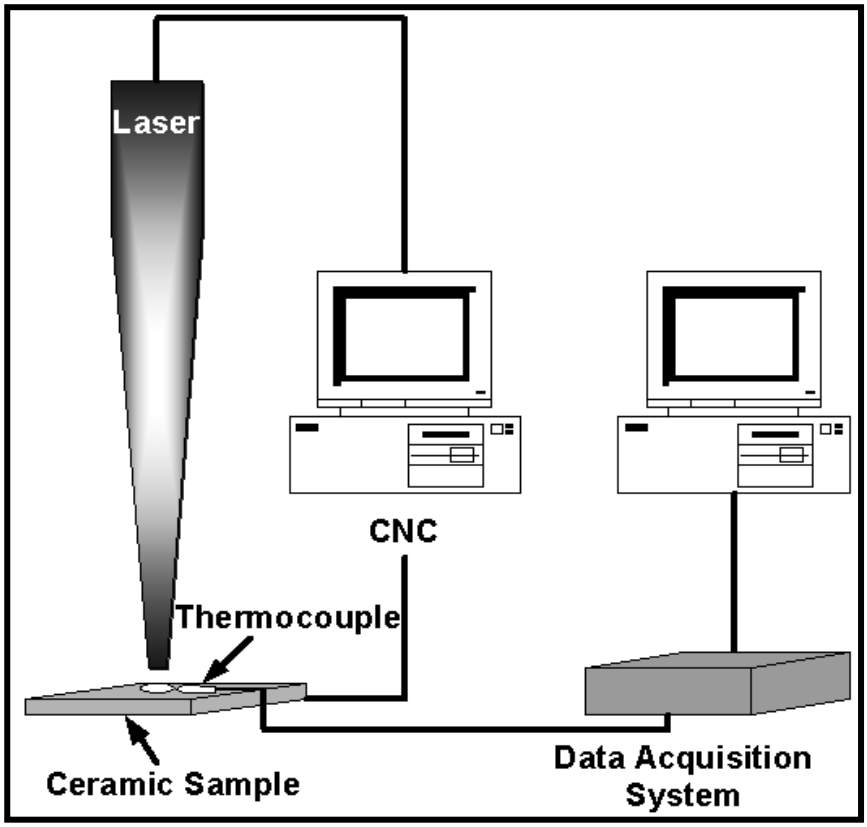

Fig.3.3 Setup for temperature measurement using thermocouple [138].

Computational Modeling

As mentioned earlier, during laser machining, the ceramic surface absorbs a part of incident energy and this affects the temperature distribution and machining parameters. The temperature evolution was predicted by using the heat transfer model in COMSOL^{TM} which has been elaborately explained in Chapters I and II (Eqs. (1.3) – (1.5)). The temperature dependent thermophysical properties (Fig.2.3) [110], heat transfer coefficient [111], density of ceramic (3800, 2370, 3100, and 3580 kg/m^3 for Al_2O_3, Si_3N_4, SiC and MgO) [110] were input to the model. In addition, the incident average power was 80W and the beam was assumed to have circular cross section with *d* measured from Fig. 3.2 and listed in Table 3.1. Furthermore, the total time t_p for which pulses were applied was 20, 25, 30 and 35 seconds for 400, 500, 600 and 700 pulses respectively (number of pulses/ pulse repetition rate). Even though a pulsed laser was used in this study, it was assumed that drop in temperature during the pulse off-time was negligible for these ceramics as seen from Fig. 2.5, 2.7a, 2.8a, and 2.10 in Chapter II [62-66] and also from the work of Salonitis et. al. [54] and it did not have any significant effect on the temperature profile. The value of *a* (absorptivity) was iterated in the set of equations (Eqs. (1.3) to (1.5)) to obtain a solution for the maximum predicted surface temperature at distance r_{tip} from the laser beam center that matched the temperature measured by the thermocouple at the same distance for any given number of pulses [141]. The absorptivity for the maximum surface temperature corresponding to a particular number of pulses was thus obtained and is presented in the following section. These predicted absorptivity values govern the temperature evolution which can be tracked for melting/ dissociation/ evaporation based material removal (machining) as elaborately discussed in Chapter II.

Absorptivity

The variation of absorptivity of different ceramics with temperature is represented in Fig. 3.4 along with corresponding governing law for each ceramic [138]. As mentioned above, three temperature measurements were made for each set of pulses and corresponding absorptivity was predicted. The average maximum surface temperature for each case along with standard deviation in absorptivity is presented in Table 3.2. For all the ceramics, it was seen that there was no significant variation in absorptivity predicted for the different readings corresponding to a given number of pulses. This ensured that the temperature measurements for the processing conditions used in this study were repeatable. Under the processing conditions used in this study, the maximum surface temperatures recorded for determining absorptivity in Al_2O_3, Si_3N_4, SiC and MgO were 1101, 1135, 914 and 965 K respectively as further higher temperatures was causing the thermocouple tip to come off the ceramic surface due to melting (foaming) of the applied ceramic glue. The absorptivity of SiC was the highest of all the structural ceramics considered in this study (varying from 0.66 to 0.85 with change in temperature from 914 to 735K). This high absorptivity of SiC, as mentioned earlier, made it essential for the beam on the surface to defocus more (2.5 mm diameter) compared to that for Al_2O_3, MgO, and Si_3N_4 (1.2 mm diameter) without creating a cavity of high aspect ratio (>1).

Contrary to many established notions, a very interesting fact was observed that for the 1.06 μm wavelength of laser beam used in this study, absorptivity of all structural ceramics decreased with increase in temperature as also noticed by Riethof et. al in some other ceramics [142]. In reality, there is a wavelength for which the absorptivity is constant with temperature and this wavelength is termed as X-point beyond which an opposite trend is observed and

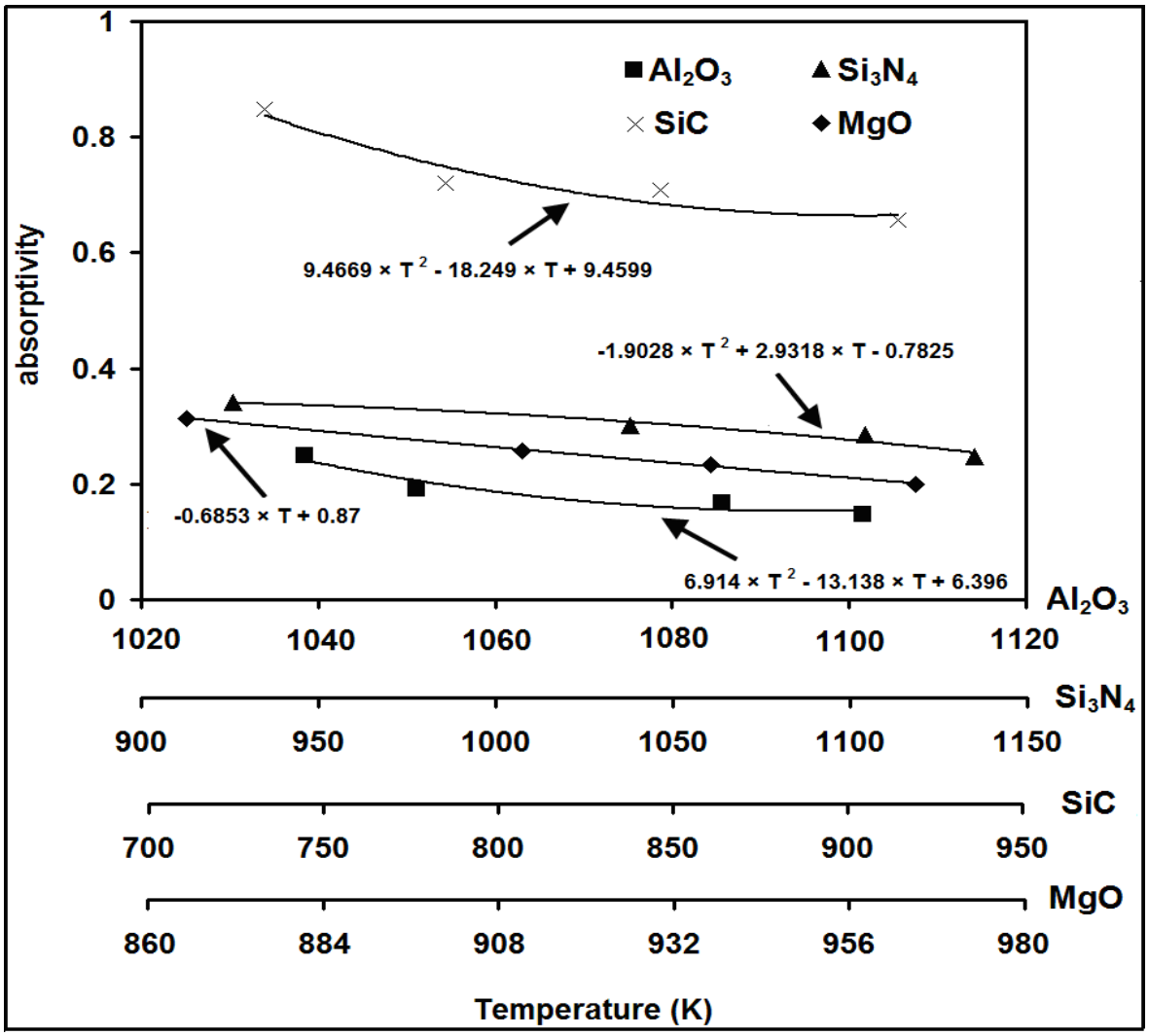

Fig.3.4 Variation of absorptivity with temperature for Al_2O_3, Si_3N_4, SiC, and MgO and corresponding governing laws [138].

Table 3.2 Computed values of absorptivity corresponding to experimentally measured temperature for Al_2O_3, Si_3N_4, SiC and MgO [138].

Ceramic	Number of pulses	$T_{average}$ (K)	Absorptivity
Al_2O_3	400	1039	0.25 ± 0.002
	500	1051	0.19 ± 0.001
	600	1086	0.17 ± 0.001
	700	1102	0.15 ± 0.001
Si_3N_4	400	927	0.34 ± 0.020
	500	1039	0.30 ± 0.004
	600	1105	0.29 ± 0.003
	700	1136	0.25 ± 0.001
SiC	400	735	0.85 ± 0.022
	500	787	0.72 ± 0.031
	600	847	0.71 ± 0.018
	700	914	0.66 ± 0.006
MgO	400	866	0.32 ± 0.007
	500	912	0.26 ± 0.002
	600	938	0.23 ± 0.003
	700	965	0.20 ± 0.002

absorptivity increases with rise in temperature [143]. However, machining the ceramics at a wavelength greater than 1.06 μm for observing the trend in absorptivity variation and predicting X-point was not a part of this study. As discussed next, the mechanism of energy absorption depends on the wavelength of processing energy (laser beam) and it governs the trend observed in variation of absorptivity with temperature.

The free carrier absorption mechanism (intraband absorption) plays a dominant role in energy absorption in ceramics in the short wavelength range while in the long wavelength range (> 10 μm), photons contribute to absorptivity changes (interband absorption) [144,145]. In any solid (ceramics), free carriers / electrons are relegated to bands that are separated from each other by energy gaps. Incompletely filled bands are termed conduction bands while the full bands are valence bands [146]. In intraband absorption, the free carriers are transferred to higher energy levels in the same band (conduction or valence) by absorption of incident radiation and this mechanism is dominant for absorption of radiations with frequencies lower than those which give rise to interband transitions [147]. Decrease in half-width of absorption band of free carriers with increase in temperature at short wavelength leads to a drop in absorptivity. Furthermore, due to the increase in vibrations of free carriers with temperature, the mean free path also increases for short wavelength of incident energy [148]. This reduces the associated scattering of the laser beam and the absorptivity.

On the other hand, in interband absorption observed at longer wavelengths of processing, the electron jumps from the band at lower energy to the one above it by absorbing a photon [147,149]. The conservation of energy for the interband transition is given by:

$$E_f = E_I + \hbar\omega \tag{3.1}$$

where E_l is energy of the electron in the lower band, E_f is energy of the final state in the upper band, and $\hbar\omega$ is the photon energy. The number of photons increases with temperature and this causes more number of electrons to transit from lower to higher energy band and an increase in absorptivity with temperature is observed. This is also in accordance with the Hagen-Rubens relationship which postulates that absorptivity is proportional to $1/\sqrt{\sigma_{dc}}$ where σ_{dc} is electrical conductivity of the material which is approximately inversely proportional to the temperature. Thus, the absorptivity is proportional to the square root of absolute temperature for longer wavelengths, and an increase in absorptivity with temperature is observed [103].

It can be seen from this chapter that mechanism of absorption of energy depends on wavelength of processing laser beam. Laser machining is a thermal process and different machining parameters such as machining time, depth of machined cavity, and number of pulses are heavily dependent on the temperature evolution which is a function of the absorbed energy. Such a study would assist in better designing of the laser machining process and similar approach can also be extended to determine the absorptivity at the surface or the bulk of other structural ceramics or materials (metals, polymers, composites or inter-metallic compounds). It should be noted that the time delay in thermocouple measurements was not included in this study and can be implemented in future study by calibrating the thermocouple dynamically.

Below the first phase change temperatures (melting / vaporization / sublimation / dissociation temperature depending on the type of ceramic) and for low aspect ratio cavity machining, the absorbed energy can be calculated using the predicted absorptivity values (Fig. 3.4 and Table 3.2). Above this temperature and for high aspect ratio machining, absorptivities of these ceramics increase with increase in temperature for reasons mentioned above (multiple reflections, low thermal conductivity of ceramics, physical entrapment of beam). Hence, in order

to determine absorptivity transitions at temperatures above first phase change temperature, two-dimensional machining was considered and will be discussed in the next chapter. Two-dimensional machining was preferred for predicting the absorptivity transitions instead of one-dimensional machining because contrary to one-dimensional machining, 100% of incident energy cannot be absorbed because the laser beam propagates along a cutting front and a portion of it is reflected or transmitted through the open kerf [103]. Thus two-dimensional machining would provide a better insight into absorptivity transitions.

CHAPTER IV
SINGLE PASS TWO-DIMENSIONAL LASER MACHINING[1]

This chapter focuses on predicting absorptivity transitions at temperatures above first phase change temperature based on material removal mechanisms discussed in Chapters I and II. The absorptivity values were evaluated through in-situ experimental measurements (Chapter III) at low temperatures (700-1150 K) and computational thermal model (Chapters I and II) at high temperatures (> 1150K) [150].

Experimental Procedure

Coupons of dimensions 25.4 mm × 25.4 mm × 4.5 mm were made from dense Al_2O_3, Si_3N_4, SiC and MgO. JK 701 pulsed Nd:YAG laser (1.06 μm wavelength) was used to machine (cut) these ceramics by a single pass of the laser beam with *p* of 0.5 ms, *f* of 20 Hz, and *e* of 4 J at scanning speeds, *V* of 5 in/min (2.11 mm/s), 10 in/min (4.23 mm/s), 12 in/min (5.08 mm/s) and 15 in/min (6.35 mm/s) using air as a cover gas at a pressure of 80 psi (5.5 bar). These speeds were chosen based on prior experience because reasonable cuts without fracture were produced at these speeds and this study can be extended to any desired processing speed with appropriate combination of remaining laser processing parameters. Similar to one-dimensional machining, a fiber optic system and a 120 mm focal length convex lens delivered a defocused laser beam of spot diameter of approximately 0.5 mm on the surface. For the same input energy, a focused beam with a reduced cross-sectional area causes a very high intensity beam to be incident on ceramic surface compared to a defocused beam and this may lead to cracking of ceramic. On the other hand, for a focused laser beam, the input energy needs to be substantially reduced to

[1] The content of this chapter is originally from References [138] & [150].

produce same effect (machining without cracks) as that of a higher energy defocused beam leading to higher machining times to attain the same depth of cut without any cracking. Furthermore, the depth machined and corresponding volume of material removed by a focused low energy laser beam would also be less compared to a defocused high energy beam. Hence a defocused spot was used as opposed to focusing the beam on surface.

Three coupons of each ceramic were machined under these processing conditions and were used for further analysis. The coupons were processed at different speeds in random sequence (2.11, 5.08, 4.23, 6.35 mm/s for first coupon followed by 5.08, 6.35, 2.11, 4.23 mm/s for second and then 4.23, 2.11, 6.35, 5.08 mm/s for the third coupon) and the principle of randomization was implemented. In this chapter, the experimentally derived low temperature (700-1150K) absorptivity values in Chapter III are further supplemented with the high temperature (> 1150K) values of absorptivity computed using thermal model. Such integrated approach was based on reliability of thermocouple measurements at low temperatures and detection of any possible transition in the trend of absorptivity as function of temperature over a wide range (700 K- melting/vaporization).

The machined coupons were cross sectioned to measure depth of cut from the cross sectional views (Fig. 4.1) at three different locations in each coupon by ImageJ^{TM} software and mean value was reported for each processing condition**.** The surface was characterized by a Hitachi S4300N SEM and these SEM images are shown in the insets in Fig. 4.1. To determine the aspect ratio X (depth to width), width of the cuts was also measured from cross sections and it was found that all cuts had a low aspect ratio ($0.23 < X < 1.41$) for this study. The laser processing speed, corresponding depth of cut along with scatter in data and associated aspect

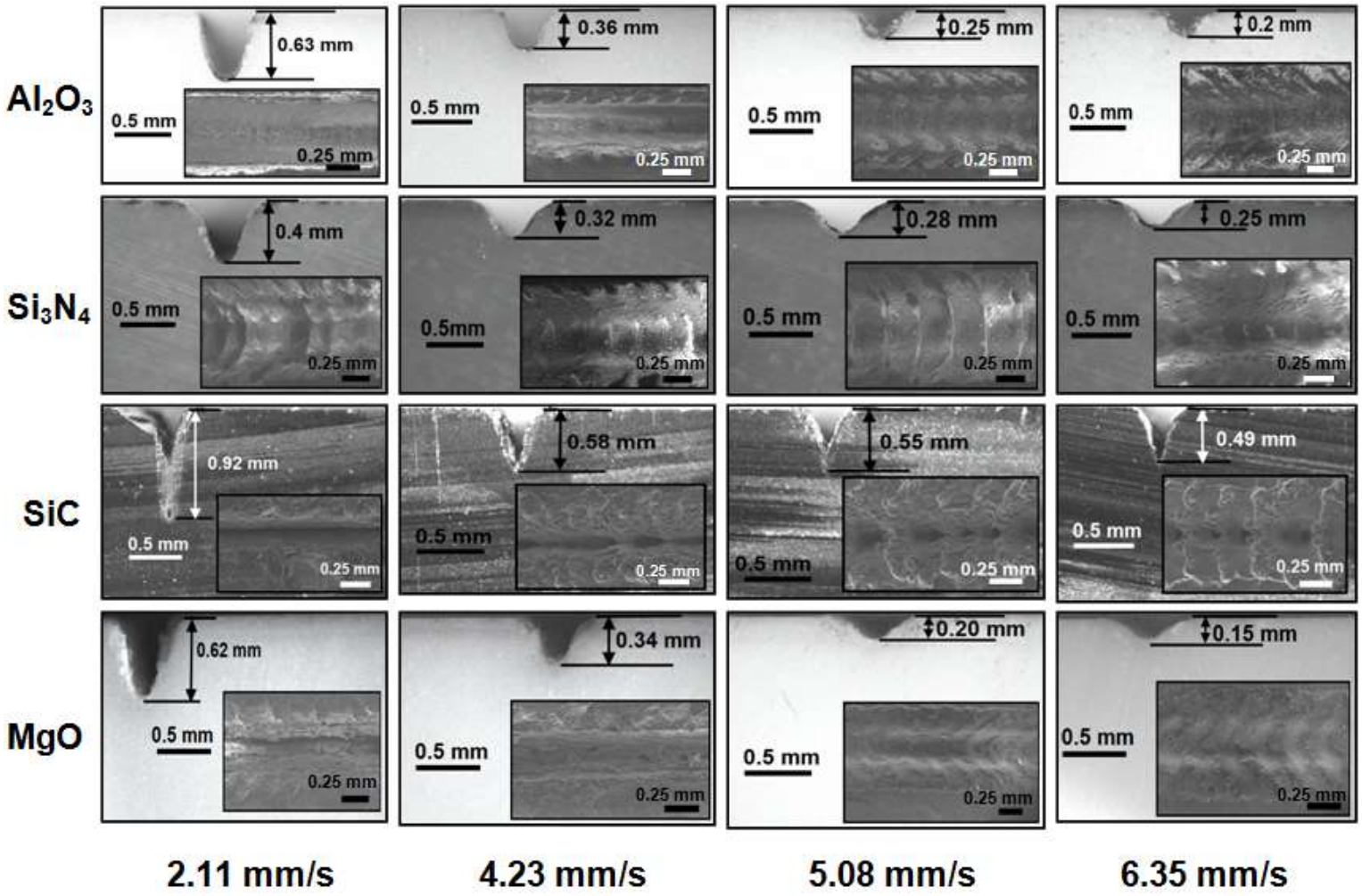

Fig.4.1 Cross- sectional views and SEM images (inset) of cavities machined in Al_2O_3, Si_3N_4, SiC, and MgO at various processing speeds[150].

ratio for all ceramics are listed in Table 4.1. There was only negligible scatter (maximum of ~ 3.4 %) in the measured machined depth values. It is noteworthy that same machining effects as produced by a pulsed laser may not be produced by a continuous wave (CW) laser. The off time between successive pulses in pulsed laser machining assists cooling and hence reduces heat build up. On the contrary, as energy is continuously being supplied to the material in CW processing, there is no time for cooling and cracks are more likely to be produced in ceramics machined by CW laser. This study however aims to predict absorptivity transitions during pulsed laser machining only by correlating depth of cut with laser processing conditions based on the MRM as discussed later.

For this purpose, the thermal model built in COMSOL's ™ heat transfer transient mode and discussed in Chapters I and II was used. Attempts to compare observed and predicted width of cut will be made in the next chapter where the effect of multiple laser passes and associated preheating on features of machined cavity will be discussed.

Laser-Ceramic Interaction: Temporal Evolution and Governing Mechanisms

As mentioned in Chapter III, total absorption (100 % of incident energy) is not possible during low aspect ratio laser machining considered in this chapter [103]. On the other hand, as seen in Chapter II, for machined cavities with high aspect ratios ($X >> 1$), multiple beam reflections along the wall of the machined cavity influences energy absorption and 100% of the energy is immediately absorbed [41, 42].

The time of exposure of the surface to laser energy (residence time) controls the temperature evolution. The pulse width, p (0.5 ms) and pulse repetition rate, f (20 Hz) of the laser beam of diameter, d (0.5 mm) were considered to predict the residence time, t_{res} as there

Table 4.1 Physical parameters corresponding to experimental conditions and values of absorptivity and transition temperatures predicted by computational model for Al_2O_3, Si_3N_4, SiC and MgO [150].

Ceramic	Processing speed (mm/s)	Depth (mm)	Aspect ratio, X	a_1	a_2	a_3	T_1(K)
Al_2O_3	2.11	0.63 ± 0.034	1.1	0.041	0.05	0.32	1165
	4.23	0.36 ± 0.017	0.75	0.063	0.09	0.33	1150
	5.08	0.25 ± 0.02	0.57	0.061	0.08	0.22	1151
	6.35	0.20 ± 0.01	0.4	0.084	0.12	0.32	1135
Si_3N_4	2.11	0.40 ± 0.011	0.52	0.031	0.07	0.19	1723
	4.23	0.32 ± 0.005	0.45	0.025	0.08	0.33	1738
	5.08	0.28 ± 0.011	0.39	0.031	0.1	0.28	1723
	6.35	0.25 ± 0.021	0.36	0.08	0.12	0.44	1600
SiC	2.11	0.92 ± 0.005	1.34	0.054	0.07	0.79	1473
	4.23	0.58 ± 0.005	1.31	0.08	0.11	0.68	1443
	5.08	0.55 ± 0.01	1.41	0.08	0.11	0.63	1443
	6.35	0.49 ± 0.005	1.07	0.114	0.13	0.73	1413
MgO	2.11	0.62 ± 0.011	0.99	-	0.06	0.25	1263
	4.23	0.34 ± 0.015	0.61		0.07	0.2	1228
	5.08	0.20 ± 0.015	0.37		0.08	0.17	1200
	6.35	0.15 ± 0.014	0.23		0.1	0.17	1178

was a power off period between two successive pulses [151]:

$$Residence\ time = \frac{Pulse\ Repetition\ \ rate \times Pulse\ width \times Beam\ diameter}{Scanning\ \ speed} = \frac{f\,p\,d}{V} \tag{4.1}$$

Laser scanning speeds of 2.11 mm/s, 4.23 mm/s, 5.08 mm/s, and 6.35 mm/s corresponded to residence times of 2.36 ms, 1.18 ms, 0.98 ms, and 0.79 ms respectively. It can be seen from Fig. 4.1 and Table 4.1 that for all ceramics, the deepest cut was obtained at the slowest speed of 2.11 mm/s due to maximum interaction between laser and ceramic at this speed (longer residence time) compared to higher processing speeds (shorter residence time). Furthermore, energy input to the system depends on the time for which it is incident on the surface (residence time) and this input energy also has an effect on the temperature profiles. Hence, the residence time for different speeds was input to the model along with peak power density per unit beam cross sectional area given by:

$$Peak\ power\ density = \frac{Pulse\ energy}{Pulse\,width \times Area\ of\ incident\ beam} = \frac{e}{p\frac{\pi}{4}d^2} \tag{4.2}$$

Considering a uniform beam distribution in both the temporal and spatial evolution, the power density corresponding to e of 4 J, p of 0.5 ms and A of 0.196 mm^2 (for a d of 0.5 mm) was 4.07 × 10^{10} W/m^2. Giving this peak power density as an input to the thermal model along with the residence times for which it was incident on the surface incorporated the control of residence time in the energy input. In this study, the laser beam was considered as a quasi- stationary heat source with coordinate system translating with it and the effect of a moving laser beam was equivalent to that of a stationary beam interacting with surface for a time equal to residence time [112, 152,153]. The values of absorptivity in the temperature range (700 – 1150K) for all ceramics considered in the current work are already presented in Fig. 3.4 [138]. The decreasing

trend observed in variation of absorptivity with increasing temperature for low aspect ratio short wavelength (1.06 μm) laser processing used in this study and corresponding governing mechanism have been elaborately discussed in Chapter III. However, in the present attempt to determine absorptivity transitions, this trend is assumed to exist until the first phase change temperature (melting/ vaporization/ sublimation/ dissociation temperature depending on the type of ceramic) and as later proved, the absorptivity does not continuously decrease with increasing temperature. An attempt is also made to predict the temperature T_1 at which such a transition occurs for increase in absorptivity during laser machining (cutting) of the ceramics considered in the present work.

The temperature evolves with time (Eqs. (1.3) – (1.5)) and different material removal mechanisms (melting, dissociation, evaporation, recoil pressure driven melt expulsion) come into effect depending on the type of ceramic and temperature regime as elaborately discussed in Chapter II. It should be noted that the developed thermal model is valid only for longer pulse lengths (pulse duration of microsecond and above) where material removal was primarily based on phase transitions (melting/ dissociation/ sublimation/ evaporation). However, for shorter pulse lengths (nano, pico or femtosecond pulse length) material removal takes place far from equilibrium and is based on thermal or non-thermal microscopic mechanisms [26]. Nanosecond laser material removal/ ablation can be due to thermal activation, direct bond breaking (photochemical ablation) or by a combination of both these mechanisms (photophysical ablation). On the contrary, for ultrashort pulses (pico and femtosecond duration pulses), desorption of excited species, avalanche breakdown, multiphoton ionization, phenomena related to overcritical heating, non-linear optical absorption, and non-equilibrium effects related to electronic and/or vibrational excitations contribute to material removal [26,154-158]. Thus based

on pulse length regime, different material removal mechanisms become significant and same model developed here will not hold true. Understanding material removal mechanisms for these shorter pulse lengths (nano, pico or femtosecond pulse length) is not a focus of this study. Furthermore, as temperatures encountered in ionization processes are extremely high, corresponding absorptivity would also be high because absorptivity increases with increase in temperature above phase transition temperature as proved later. Unlike the use of thermocouples in this study to measure temperature, plasma temperatures encountered in short pulse length regimes (nano, pico or femtosecond pulse length) can be determined spectroscopically from ratio of line intensity to underlying continuum, from ratio of integrated line intensities, and from shape of continuum spectrum [159, 160]. The best way to determine the technique to be employed for plasma temperature measurement depends on the material under consideration and processing conditions.

Absorptivity Transitions

The experimental absorptivity values and corresponding governing law for each ceramic (Fig. 3.4) can be extended to predict the energy absorbed until the surface temperature reaches the first phase change temperature mentioned above. However, in order for material removal (machining) to take place, temperature attained at the end of laser beam residence (exposure) time is expected to reach at least equal to or higher than the phase change temperature. Under the selected set of laser processing parameters this can only occur with increase in input energy with increased absorptivity indicating the transition of absorptivity at the phase transition temperature. Furthermore, as mentioned in Chapter III, physical entrapment and multiple reflections of the beam are dominant mechanisms contributing to the trend of increasing absorptivity observed at

temperatures above the first phase change temperature. Depending on the governing material removal mechanism (MRM) in a ceramic [64], the absorptivity transition temperature T_1 was determined using the thermal model (Eqs. (1.3) – (1.5)). As seen in Chapter II, in ceramics such as Al_2O_3, Si_3N_4, and SiC, material removal takes place by a combination of melting, dissociation and vaporization where as dissociation followed by evaporation is responsible for material removal in MgO [62-66]. The different temperature regimes in which each MRM plays a role and corresponding absorptivity transitions for these ceramics are described in the following section.

As seen in Chapter II, in Al_2O_3, melting and expulsion of the molten liquid at temperatures above 2323 K followed by dissociation and evaporation above 3250 K leads to material removal [64]. The absorptivity first drops according to the polynomial law for Al_2O_3: $6.914 \times T^2 - 13.13 \times T + 6.396$ (Fig. 3.4) to a value a_1 corresponding to T_1 attained at a time $t < t_{res}$. The value a_1 was obtained by iterating the thermal model (Eqs. (1.3) – (1.5)) such that the corresponding maximum surface temperature, T_{max} at the end of laser beam exposure (t_{res}) was the melting point (MP) of Al_2O_3 (2323 K) as seen in Fig. 4.2a. This ensured that material removal started taking place by melting and gave the absorptivity transition temperature T_1.

As dissociation and vaporization followed melting, surface temperature had to increase for further material removal to take place. In light of this, absorptivity was also enhanced in gradual increments of 0.01 and maximum surface temperature was monitored for each iteration. That value of a_2 was reported for which corresponding T_{max} at t_{res} was the vaporization / dissociation temperature (VT) of Al_2O_3 (3250K) and vaporization was included as a MRM in addition to melting (Fig. 4.2b).

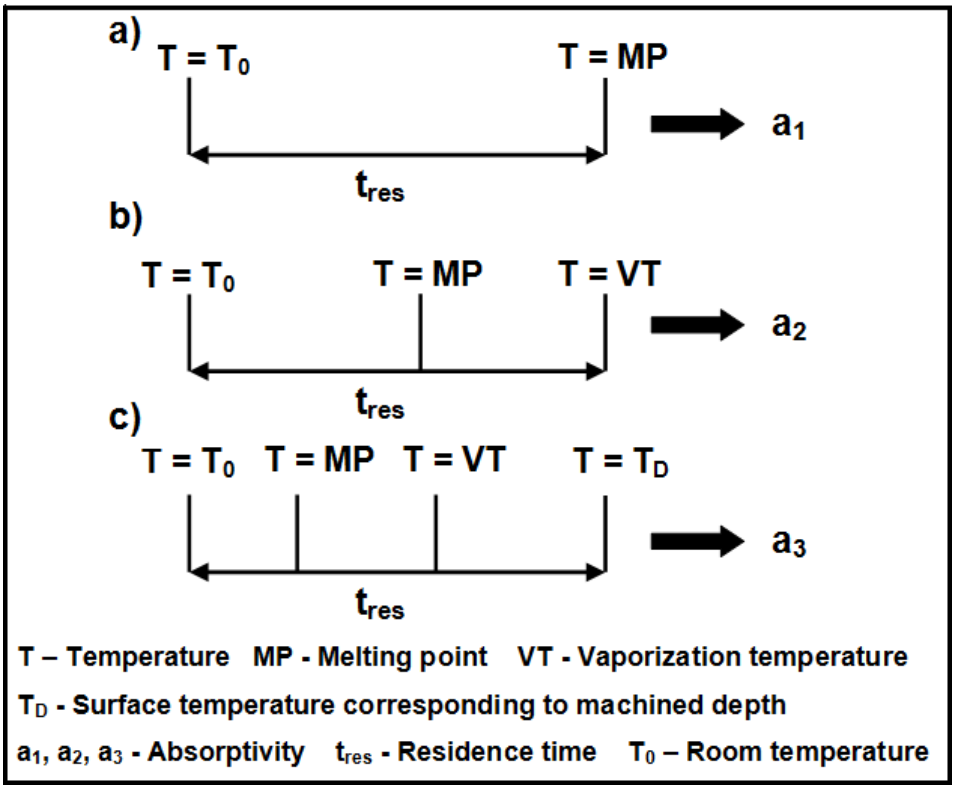

Fig.4.2 Schematic illustrating the procedure for determining absorptivity values for ceramics with melting and vaporization as MRM [150].

Predicting a_1 and a_2 above only initiated the process of machining. In order to achieve the desired depth of cut, more energy (higher absorptivity) had to be input to the system. For this purpose, in the model the absorptivity was again given increments of 0.01 and corresponding temperature evolution was scrutinized. A value $a_3 > a_2$ was identified such that the predicted depth of cut at the end of t_{res} , obtained by tracking the highest phase change temperature (VT, 3250K) during iteration of the thermal model to the depth that matched the depth measured from optical micrographs in Fig. 4.1 and mentioned in Table 4.1 (Fig. 4.2c). The temperature versus

depth plot for Al_2O_3 is shown in Fig. 4.3 which was obtained by using a_1 and a_2 predicted through procedures described above in Fig. 4.2a and 4.2b. The value of a_3 corresponding to this plot was the one that machined a depth equal to measured depth in residence time (Fig. 4.2c). The absorptivity values (a_1, a_2, a_3) and the transition temperature T_1 for Al_2O_3 are listed in Table 4.1.

For the processing conditions used in this study, the actual time in which MP and VT are attained in Fig. 4.2c during material removal was much less than the total residence time as was considered in Fig. 4.2a and Fig. 4.2b. The melting point and vaporization temperature were assumed to be attained at end of residence time in Fig. 4.2a and Fig. 4.2b respectively in order to

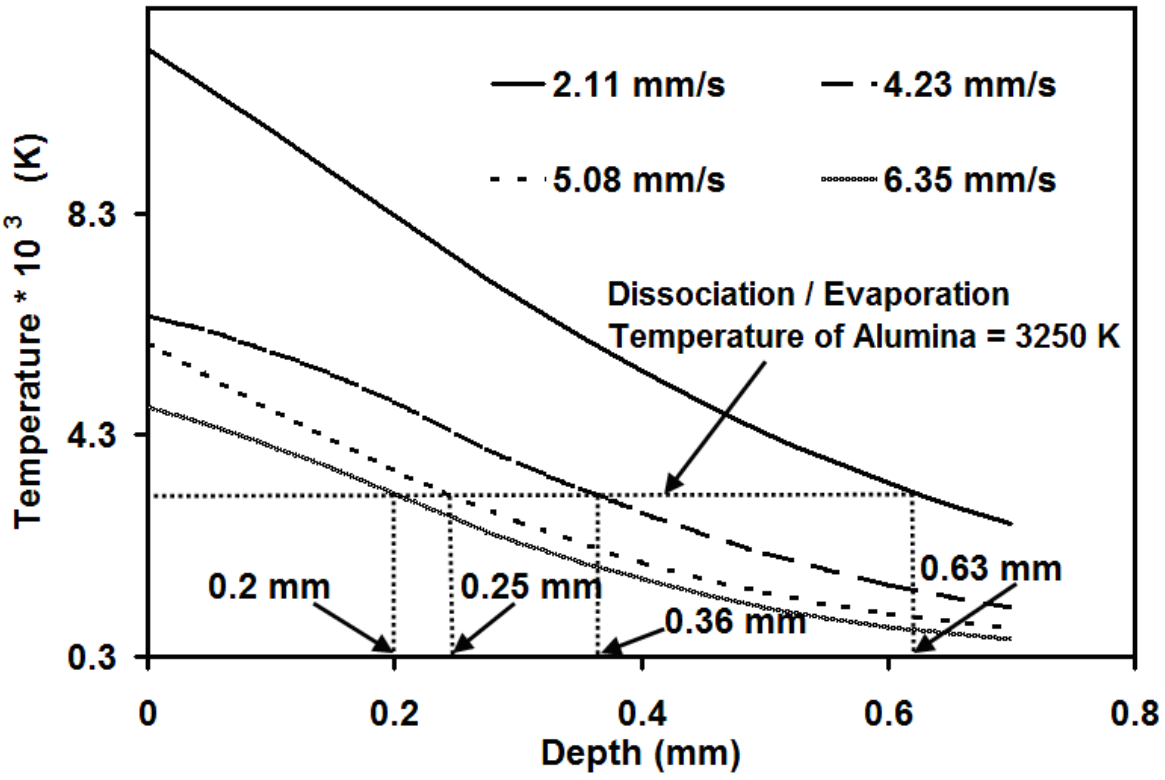

Fig.4.3 Temperature versus depth profiles for Al_2O_3 at various processing speeds [150].

ensure that material removal started taking place by these mechanisms and would definitely be a part of the final material removal process in Fig. 4.2c where these two MRMs together machined the final depth. The procedure for predicting a_1, a_2 and a_3 in Si_3N_4 and SiC discussed below was the same as used above for Al_2O_3. However, as seen later, melting is not involved in material removal in MgO and hence only vaporization temperature was tracked to determine absorptivity transitions in MgO.

It can be seen from Eq. (2.16) that liquid Si formed during the dissociation of Si_3N_4 gets expelled and at temperatures above boiling point of silicon (3514 K [161]), liquid Si vaporizes and material removal in Si_3N_4 thus takes place by a combination of melting, dissociation and evaporation [162,163]. Hence, in the thermal model (Eqs. (1.3) – (1.5)), absorptivity first decreased as per the polynomial law for Si_3N_4: $-1.90 \times T^2 + 2.93 \times T - 0.7825$ (Fig. 3.4) to a value a_1 at T_1 (Fig. 4.2a) and then it rises to a_2 (Fig. 4.2b) followed by a_3 (Fig. 4.2c). The boiling point of silicon (3514 K) was tracked for the depth that was equal to the measured depth (Fig. 4.1 and Table 4.1) during iteration of the thermal model to obtain final a_3. The final temperature versus depth plot for Si_3N_4 was obtained similar to Al_2O_3 (by using a_1 and a_2 predicted above and iterating a_3 so that predicted depth matched measured depth) and is shown in Fig. 4.4. The predicted absorptivity values and transition temperature are listed in Table 4.1.

As seen in Chapter II, the liquid Si (Eq. (2.17)) generated by the melting/ decomposition of SiC at 3103 K get continuously expelled and at temperatures greater than 3514 K (boiling point of Si [161]), vaporization of Si contributes to machining. Melting, dissociation and evaporation appears to be the governing mechanisms for machining in SiC [64]. In the thermal model (Eqs. (1.3) – (1.5)) the absorptivity first decreased to a_1 associated with T_1 (Fig. 4.2a) (in consensus with the law for SiC: $9.47 \times T^2 - 18.24 \times T + 9.46$ (Fig. 3.4)) and then it increased to

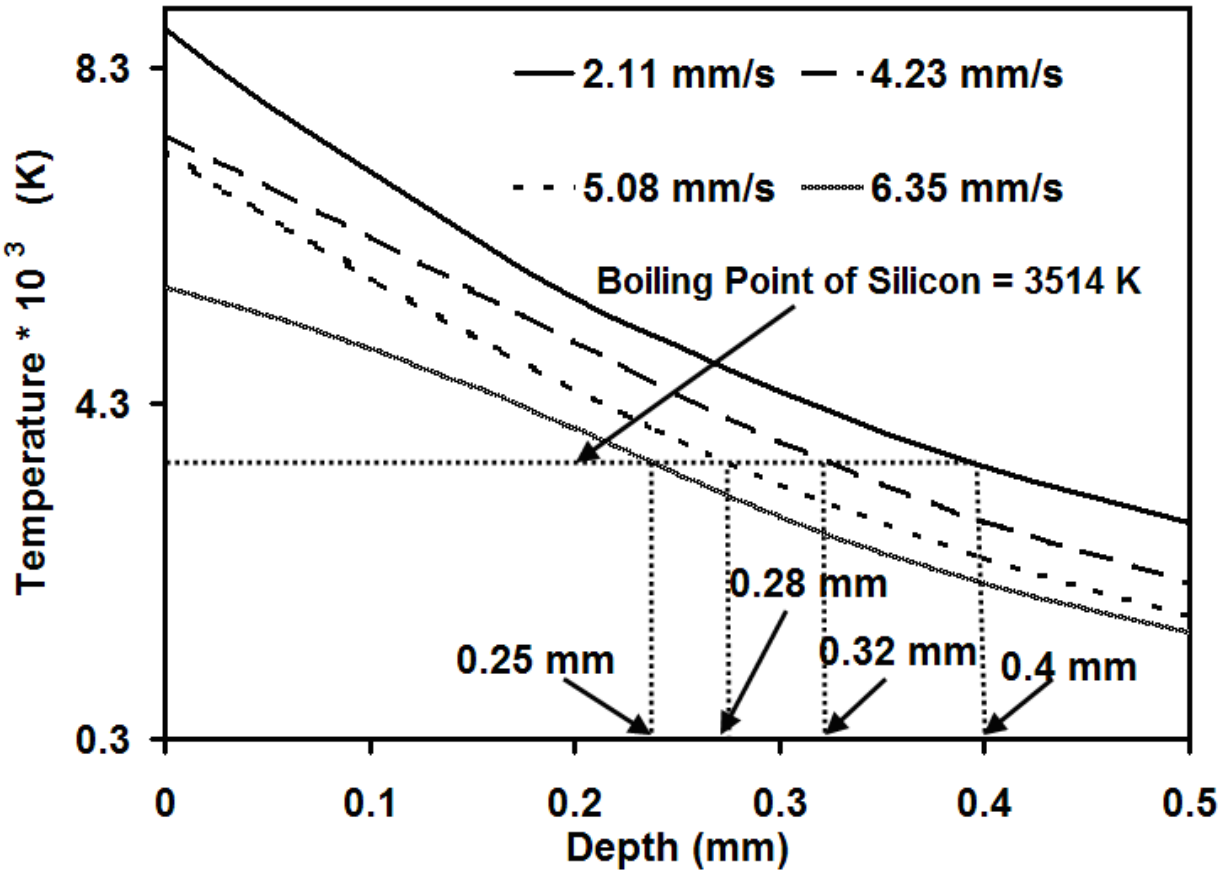

Fig.4.4 Temperature versus depth profiles for Si_3N_4 at various processing speeds [150].

a_2 (Fig. 4.2b) and then a_3 (Fig. 4.2c). Similar to Si_3N_4, the boiling point of silicon (3514 K) was traced to the depth that was equal to the measured depth (Fig. 4.1 and Table 4.1) for predicting a_3. Obtained in a manner similar to Al_2O_3 and Si_3N_4 above (by first predicting a_1 and a_2 (Fig. 4.2a and 4.2b) and then iterating a_3 so that predicted depth matched measured depth (Fig. 4c)), the temperature versus depth plot for SiC is represented in Fig. 4.5 and corresponding absorptivity values and transition temperature is listed in Table 4.1.

As extremely high heating rates (of the order of ~ 10^6 - 10^7 K/s) are encountered in laser machining, the temperature immediately rises from melting to vaporization temperature (in a

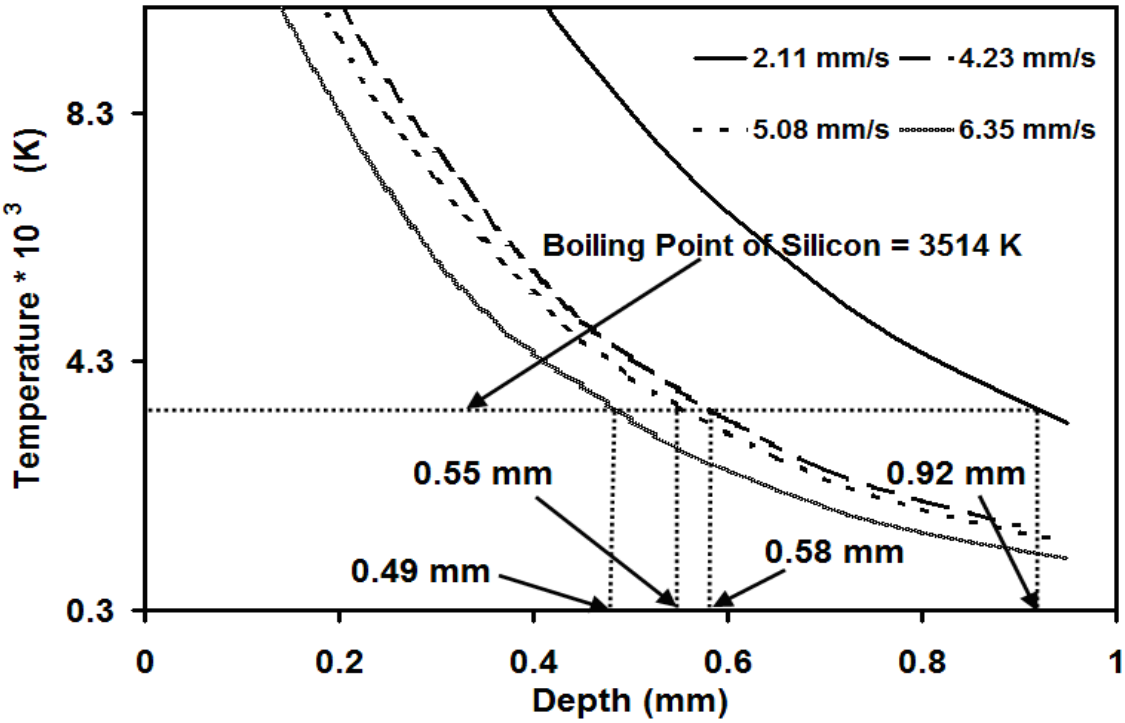

Fig.4.5 Temperature versus depth profiles for SiC at various processing speeds[150].

few microseconds). Hence, it was assumed in this study that final machined depth was due to vaporization only (phenomena occurring at the highest phase change temperature) as the high heating rates made it difficult to separate the portions of the machined depth that were generated by melting and expulsion. However, predicting the absorptivity value a_1 accounted for contribution of melting to the machining process as illustrated in Fig. 4.2.

Instantaneous temperatures attained at the surface during laser machining are extremely high (> 3123 K, the VT of MgO [114]) and at such high temperatures, material removal in MgO takes place exclusively by dissociation of the ceramic followed by evaporation [65]. In light of this MRM, in the thermal model (Eqs. (1.3) – (1.5)) the absorptivity first

decreases to a value a_2 in accordance with the linear law for MgO: $-0.68 \times T + 0.87$ (Fig. 3.4) corresponding to T_1 attained at a time $t < t_{res}$. The value of a_2 was obtained by iterating the thermal model with T_{max} at t_{res} equal to the vaporization/ dissociation temperature of MgO (3123K) (Fig. 4.6a). This was followed by an increase in absorptivity to a_3 and machining of desired depth. In Fig. 4.6b, to determine a_3, several iterations were carried out in the thermal model by systematically increasing a_3 in steps of 0.01 and a value $a_3 > a_2$ was recognized such that depth estimated by tracking the vaporization/ decomposition temperature of MgO (3123 K) to the depth that was equal to the measured depth (Fig. 4.1 and Table 4.1). The actual time in which VT is reached during actual material removal in Fig. 4.6b was much less than residence time and it does not take the entire residence time to attain VT for the processing conditions used

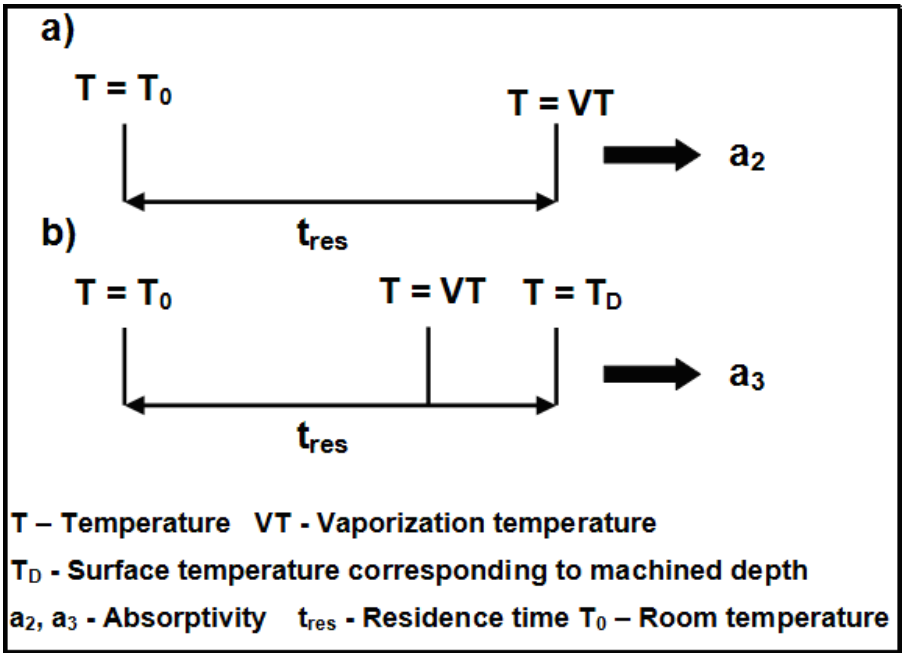

Fig.4.6 Schematic illustrating the procedure for determining absorptivity values for ceramics with only vaporization as MRM [150].

in this study. It was so assumed in Fig. 4.6a in order to make sure that vaporization would definitely be a part of the actual material removal process. It should be noted that as a linear curve better fits the absorptivity data in low temperature range for MgO (860- 980K) it was preferred over the polynomial fit used for other ceramics in this study (Al_2O_3, Si_3N_4 and SiC).

The temperature versus depth plot for MgO is represented in Fig. 4.7. In this plot, the value of a_2 was the one determined by the above procedure (Fig. 4.6a) while the value of a_3 was such that predicted depth at end of residence time was equal to the measured depth (Fig. 4.6b). The values of a_2 and a_3 are listed in Table 4.1 along with the transition temperature for MgO. A flow chart summarizing the general procedure followed to determine different absorptivity values and transition temperature depending on the type of ceramic is represented in Fig. 4.8.

Similar to Figs. 2.5, 2.7a, 2.8a, and 2.10, it can be observed from Figs. 4.3, 4.4, 4.5 and 4.7 that maximum surface temperatures were high in these ceramics. As mentioned in Chapter II,

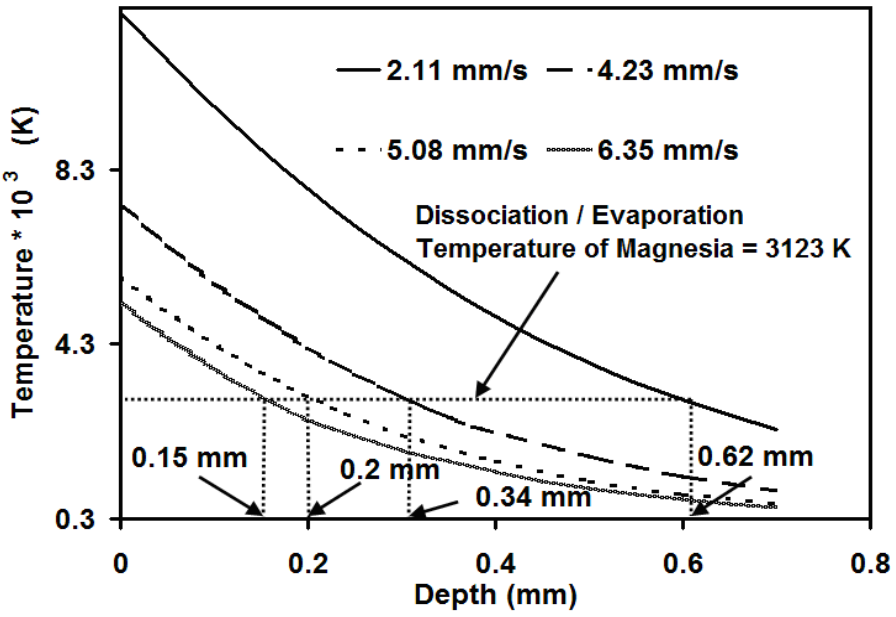

Fig.4.7 Temperature versus depth profiles for MgO at various processing speeds[150].

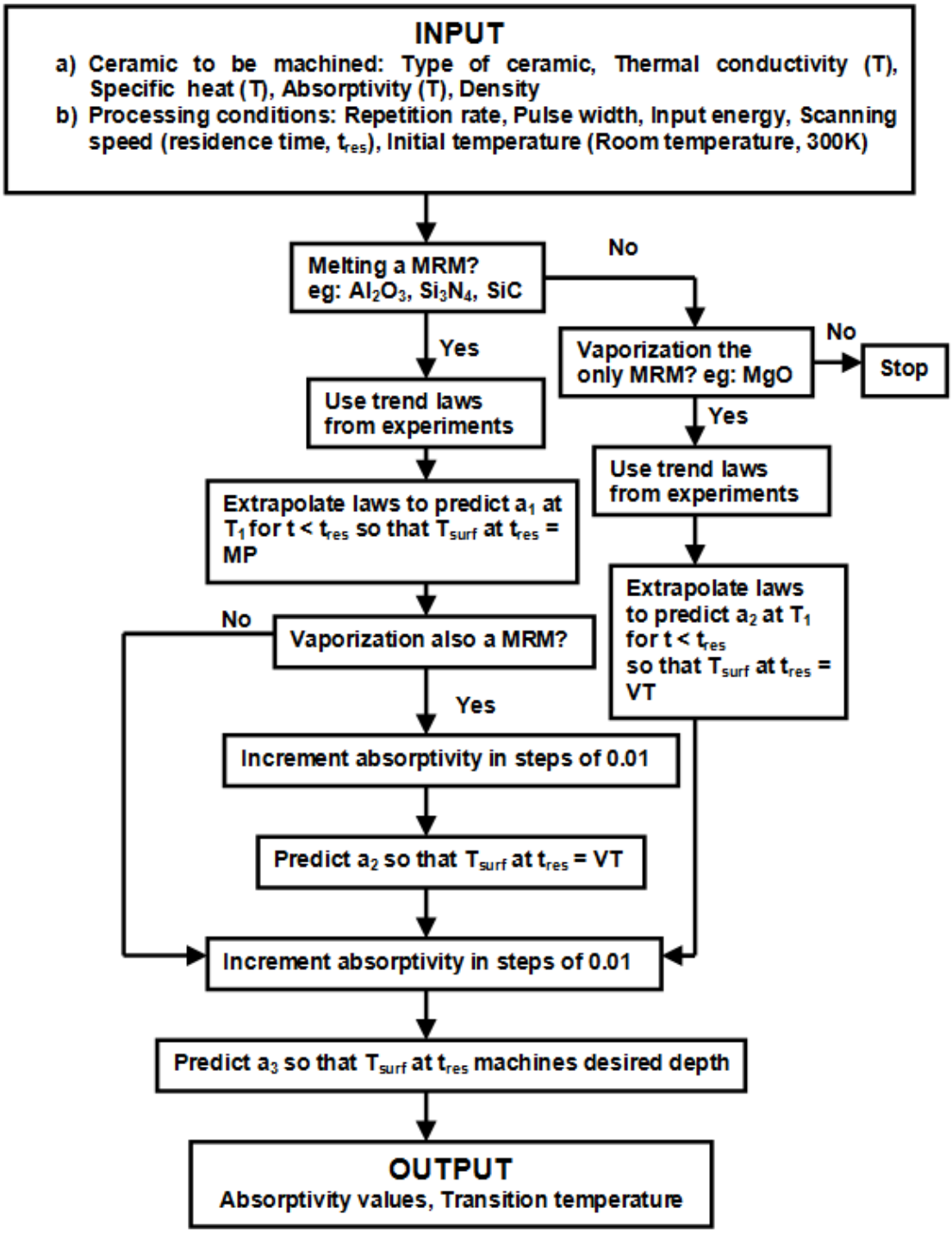

Fig.4.8 Flowchart for predicting absorptivity transitions based on MRM for ceramics[150].

in a short duration process like laser processing, these high temperatures immediately drop below melting point due to self quenching. Furthermore, as SiC has the highest absorptivity compared to Al_2O_3, Si_3N_4 and SiC [138], it absorbed more energy compared to other ceramics. Higher absorbed energy machined deeper cuts in SiC for a given processing speed and also the value of a_3 required to attain the final depth was more than other ceramics (Table 4.1).

Thus it can be seen from this study that the portion of incident energy absorbed by the ceramic during machining continuously changes depending on type of the ceramic and governing material removal mechanisms. Unlike in the past [46, 47, 54, 62-66, 128, 164,165], the present work considered the transient nature of absorptivity during predictions of machined depths using the thermal model. The model developed was implemented for three-dimensional laser machining of these structural ceramics (Al_2O_3, Si_3N_4 , SiC and MgO) and an attempt was made to determine material removed per unit time (material removal rate (MRR)) using predicted machined depth for a given set of laser processing conditions and they showed a reasonable match with measured MRR as seen later in Chapter VI [166]. This approach can also be extended for machining of other structural ceramics or materials in general. In general, such a study would enable efficient designing of the laser machining process as amount of energy to be input to the system for a given set of laser processing conditions can be predicted in advance based on absorptivity variations.

It should be noted that the high energy single laser pass discussed in this chapter would induce large thermal stresses and cracking of ceramic. Hence multiple laser passes would be preferred for generating deeper cavities. In light of this, the model developed for single pass laser machining was further extended to multiple pass two-dimensional laser machining and predicted attributes were compared with measured values as seen in next chapter.

CHAPTER V
MULTIPASS TWO-DIMENSIONAL LASER MACHINING[1]

Even though, in two-dimensional laser machining, desired depth of cavity in a given ceramic can be attained by a single pass of the laser beam with different processing conditions (varying scanning speed, pulse repetition rate, pulse energy, pulse width), scanning ceramic surface with multiple laser passes with appropriate parameters is, however, likely to machine the ceramic for the same dimensions with minimal thermal stresses and cracking. In Chapters I to IV, various physical effects that stir up during laser machining such as phase transition, variation of thermophysical properties and absorptivity with temperature, and heat transfer via the three basic modes (conduction, convection and radiation) were incorporated into a thermal model. In this chapter, this model was further enhanced by including additional effects such as preheating due to multiple tracks and defocusing of laser beam with increased machined depth and an attempt was made to predict depth and width of cavity generated in a ceramic after exposure to multiple passes of the laser beam under a given set of processing conditions [167].

Experimental Procedure

Dense Al_2O_3, Si_3N_4, SiC and MgO coupons (25.4 mm × 25.4 mm × 4.5 mm) were exposed to a 1.06 μm wavelength JK 701 pulsed Nd:YAG laser. Initially, a 15 mm long cavity was machined by scanning the surface with a single pass of the laser beam at repetition rate, f of 20 Hz, pulse energy, e of 4 J, pulse width, p of 0.5 ms and scanning speed, V of 5 in/min (2.11 mm/s) with air as cover gas at a pressure of 80 psi (5.5 bar). This was followed by exposing the

[1] The content of this chapter is originally from References [138], [150] & [167].

cavity to different number of laser passes (3, 5 and 7 passes for Al_2O_3, 2, 3 and 4 passes for Si_3N_4, 2, 3 and 5 passes for SiC, and 3, 4 and 5 passes for MgO) under the same set of machining parameters as that employed for single cavity machining in order to study effect of multiple passes on dimensions of depth and width of machined cavity with minimal thermal stresses. However, evaluation of thermal stress is not a part of present study and can be considered in future. For every subsequent pass, the laser beam was again brought to same position on the ceramic surface from where the preceding cavity was started. A CNC program developed in FlashCut CNC^{TM} was used to facilitate repeated to and from motion of laser beam.

Similar to one-dimensional machining (Chapter II) and single pass two-dimensional laser machining (Chapter IV), the laser beam was delivered by a fiber optic system and a 120 mm focal length convex lens so that a defocused spot diameter of roughly 0.5 mm was generated on the surface at the beginning of first pass. Although, in the present study, the scanning speed, *V* of 5 in/min (2.11 mm/s) was chosen based on prior experience, the approach adopted in the study can be extended to any desirable processing speed. A schematic of effect of multiple pass laser processing on depth and width evolution of cavity on the surface of a ceramic is represented in Fig. 5.1.

The laser beam starts processing from point A for every pass and one pass is complete when the laser reaches point B. Then, the laser is switched off and no processing is done when the laser returns back with the same scanning speed from point B to point A. It is observed that machined depth and width increases with increase in number of passes. The physical phenomena responsible for this trend will be discussed in detail in later part of this study. Although, the number of passes chosen for different ceramics were based on prior experience and for the purpose to demonstrate feasibility of the approach in predicting the dimensions of machined

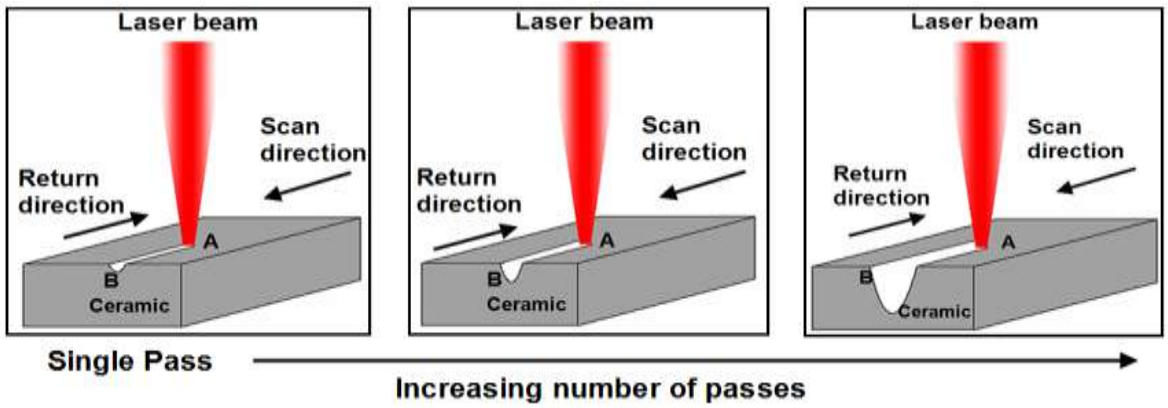

Fig.5.1 Schematic illustrating the effect of multiple passes on the attributes of machined cavity (depth and width) [167].

cavity, the approach can be extended to machining a cavity of desired dimensions and corresponding number of passes in any ceramic.

In order to incorporate the principle of randomization mentioned in Chapter II, three coupons of each ceramic were machined under these laser conditions with three cavities machined in each coupon by different number of passes in random sequence (for example in Al_2O_3, 3, 5, 7 passes in first coupon followed by 3, 7, 5 passes in second and then 7, 5, 3 passes in the third coupon). The machined cavities were then cross-sectioned to measure depth and width using ImageJ^{TM} software (Fig. 5.2). Cavities machined in some ceramics for a certain number of passes (3, 5 passes in SiC and for 4, 5 passes in MgO) were a little asymmetric around the bottom tip of the cavity and a portion of the cavity also chipped off from top. This cracking can be attributed to thermal stresses generated in some of these brittle ceramics under certain set of laser machining parameters. In light of this, as seen in Fig. 5.2, in order to determine actual width of these cavities, their profile was reconstructed by assuming symmetry around the marked centerline and corresponding width was reported. On the other hand, cavities in Al_2O_3 and Si_3N_4

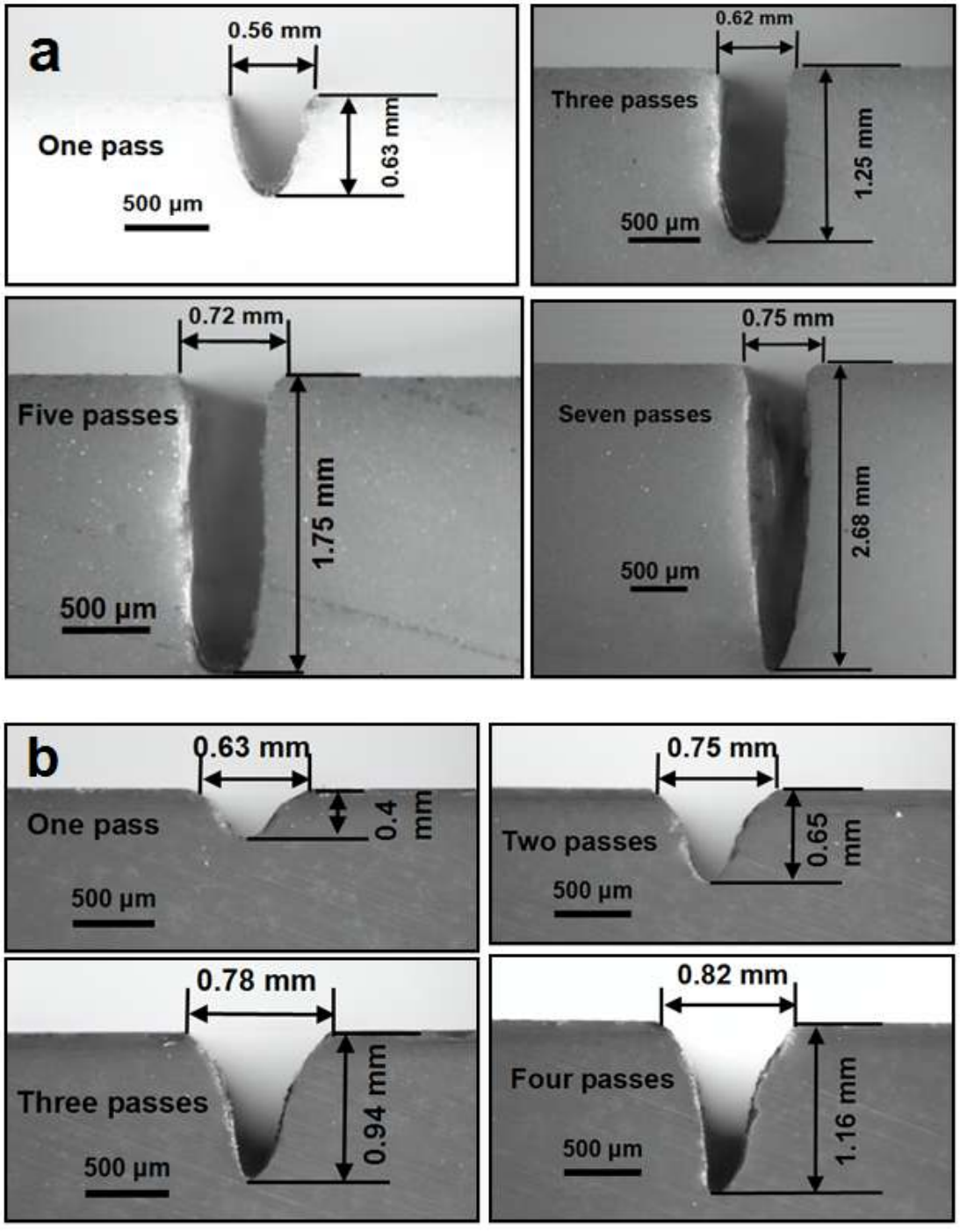

Fig.5.2 Cross- sectional views of cavities machined in a) Al_2O_3, b) Si_3N_4, c) SiC, and d) MgO for different number of passes [167].

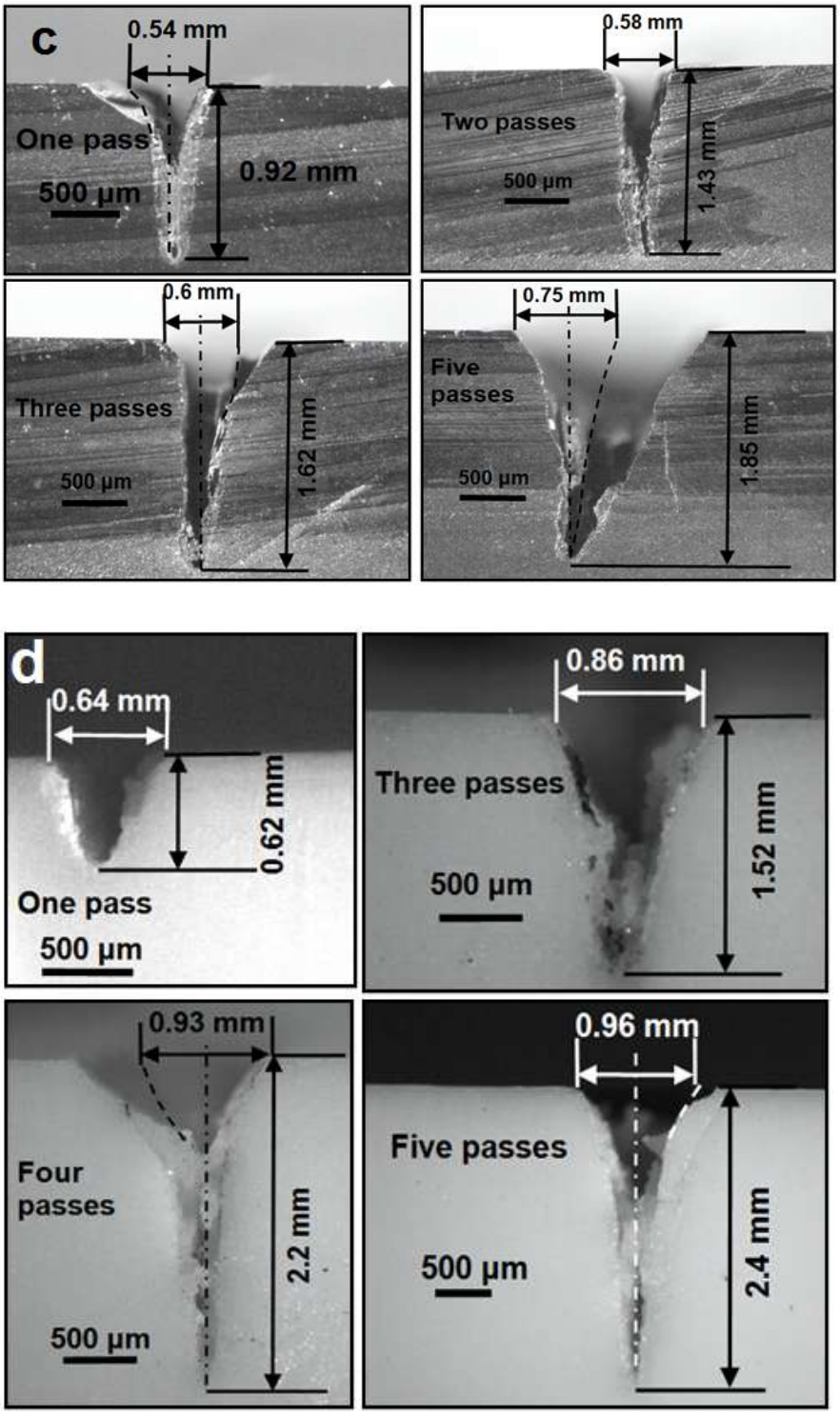

Fig. 5.2 Continued.

did not experience thermal stress cracking under the present machining conditions. The depth and width of cavities for different number of passes are marked in Fig. 5.2 and also listed in Table 5.1 along with the scatter in measured data.

Multiple Pass Machining

As schematically illustrated in Fig. 5.1 earlier, for all ceramics, the machined depth increased with increase in number of passes as each pass removed material by absorbing energy and added to the total machined depth. Furthermore, as discussed later, the laser beam became defocused with the evolution of machined cavity and diameter of beam on the bottom surface of the cavity at the end of a given pass (assumed to be equal to the width of cavity) increased with multiple passes as also presented in Fig. 5.1 [54]. Experimentally determined absorptivity values in the low temperature range (700- 1150K) [138] presented in Chapter III and the absorptivity transitions predicted at high temperatures (> 1150K) discussed in Chapter IV for two-dimensional laser machining by a single pass of the laser beam [150] were used as a basis for this study on multi pass laser machining. Under the processing conditions used in this study, the residence time was 2.36 ms (Eq. (4.1)) and peak power density was 4.07×10^{10} W/m^2 (Eq. (4.2)) for the first pass and corresponding to a beam diameter of 0.5 mm at the surface. For improved accuracy in calculations, thermophysical properties (Fig. 2.3) [110] and laser beam (1.06 μm wavelength) absorptivity were included as a function of temperature (Fig. 3.4, Table 4.1) [138,150]. Furthermore, as mentioned in Chapters II, III and IV, material removal mechanisms during laser based machining of the ceramic are influenced by various physical processes. In light of this, the absorptivity transitions for Al_2O_3, Si_3N_4, SiC, and MgO have been elaborately

Table 5.1 Measured and predicted attributes of machined cavity (depth and width) for different number of passes in Al_2O_3, Si_3N_4, SiC and MgO [167].

Ceramic	Number of passes	$Depth_{measured}$ (mm)	$Depth_{predicted}$ (mm)	$Width_{measured}$ (mm)	$Width_{predicted}$ (mm)
Al_2O_3	1	0.63 ± 0.034	0.63	0.56 ± 0.060	0.60
	3	1.25 ± 0.015	1.70	0.62 ± 0.090	0.70
	5	1.75 ± 0.021	2.69	0.72 ± 0.046	0.77
	7	2.68 ± 0.030	3.59	0.75 ± 0.067	0.82
Si_3N_4	1	0.4 ± 0.011	0.40	0.63 ± 0.10	0.57
	2	0.65 ± 0.020	0.69	0.75 ± 0.07	0.66
	3	0.94 ± 0.015	0.92	0.78 ± 0.05	0.69
	4	1.16 ± 0.005	1.27	0.82 ± 0.07	0.72
SiC	1	0.92 ± 0.005	0.92	0.54 ± 0.040	0.61
	2	1.43 ± 0.010	1.75	0.58 ± 0.066	0.66
	3	1.62 ± 0.040	2.65	0.60 ± 0.033	0.70
	5	1.85 ± 0.025	3.40	0.75 ± 0.120	0.77
MgO	1	0.62 ± 0.011	0.62	0.64 ± 0.008	0.59
	3	1.52 ± 0.060	1.50	0.86 ± 0.025	0.70
	4	2.20 ± 0.030	1.89	0.93 ± 0.074	0.74
	5	2.40 ± 0.045	2.27	0.96 ± 0.150	0.78

discussed in Chapter IV for different processing speeds. However, in this chapter, single pass machining (20 Hz, 0.5 ms, 4J and 2.11 mm/s) was considered as the precursor for multiple pass machining and corresponding absorptivity transition values and transition temperatures mentioned in Table 4.1 for all ceramics are used for further calculations.

In multiple pass machining, the laser first interacts with ceramic surface for time equivalent to residence time (Eq. (4.1) for laying first track on the surface. Then the laser is switched off and it returns back to starting point (point A in Fig. 5.1) for laying next track by again moving till the end of the track (point B in Fig. 5.1). This to and from motion is controlled by the CNC program. As seen later, the total time taken by the beam to come back to the starting point (from the instant it starts laying the preceding track) to lay the next track is summation of time for machining a single track (t_{scan}) and time for which laser is switched off during return (t_{return}). The heat transfer phenomena, associated material removal mechanisms (melting, dissociation, vaporization based on the type of ceramic) and absorptivity transitions mentioned in Chapters II, III and IV for Al_2O_3, Si_3N_4, SiC and MgO occur during each laser pass on that ceramic and can be implemented for every pass by using the computational model developed in these chapters. In addition, few additional effects such as beam defocusing and surface preheating play a role in multiple pass machining and will be incorporated in the existing model as discussed in next section. It should be noted that a certain depth of cavity achieved by multiple laser passes can also be attained by a single laser pass with large energy input. However, as the high energy single laser pass would induce large thermal stresses and cracking of ceramic as mentioned above, multiple laser passes are preferred for machining deeper cavities [167].

Laser Beam Defocusing

As the machined cavity evolves with successive passes, the beam gets defocused on the bottom surface of each cavity with increase in machined depth [54] and does not remain of the same size as it was at the beginning of that pass, d_{start}. The diameter at the end of a pass, d_{end} (> d_{start}) is given by [54]:

$$d_{end} = d_{start}\left[1+\left(\frac{4\lambda(z_t+\delta_f)}{\pi d_{start}^2}\right)^2\right]^{1/2} \tag{5.1}$$

where z_t is predicted depth of cavity at the end of that pass. As mentioned earlier, width of cavity and beam diameter at the bottom of the cavity at the end of a given pass, d_{end} were assumed to be same and the successive pass was processed with d_{end}. The diameter of beam at beginning of first pass was adjusted to 0.5 mm as an out of focus beam diameter on the surface. The diameter of the beam, d_{end} predicted by Eq. (5.1) above for each (i^{th}) pass was used to predict the residence time and peak power density for the next (($i+1$)th) pass using Eq. (4.1) and Eq. (4.2) respectively. These values were constantly updated at the end of each pass and were input for consecutive passes. Thus defocusing of the beam reduced the peak power density input to the system and increased the residence time for successive passes.

Preheating Effect

A series of pulses are incident on the ceramic surface when one complete track is machined. The total number of pulses required to machine a cavity of given length, L (15 mm in this case) was given by dividing the length of machined cavity by beam diameter for that pass (d_{end}). The overlap between successive pulses was neglected in this study and as each pulse was active for residence time (2.36 ms), the total on time for the laser (t_{scan}) was given by multiplying

the total number of pulses by residence time. However, as seen later in Chapter VI, while predicting the machining rate in three-dimensional laser machining, the overlap between consecutive pulses was incorporated and the number of pulses required to cover a distance equal to beam diameter and thus the cavity length was determined. As mentioned earlier, the laser is switched off after machining a track and the time it takes to come back to machine the next track (t_{return}) was obtained by dividing the length of cavity, L by return speed (same as scanning speed, V (2.11 mm/s) in this study). The total time it takes for laser beam to come back to starting point was summation of t_{scan} and t_{return}. Thus, after i^{th} pass, laser beam comes back to starting point (point A in Fig. 5.1) for the next $(i+1)^{th}$ pass in a time, $t_{cooling}$ given by:

$$t_{cooling} = t_{scan} + t_{return} = \frac{L \times t_{res}}{d_{end}} + \frac{L}{V} \tag{5.2}$$

The temperature at the start of this $(i+1)^{th}$ pass is temperature of staring point of i^{th} pass (point A in Fig. 5.1) at time equal to $t_{cooling}$. This temperature was noted from the cooling curve of i^{th} pass at $time = t_{cooling}$ and input as an initial temperature for $i+1^{th}$ pass.

Computations were then carried out by using this initial temperature along with residence time and peak power density updated after considering a defocused laser beam (Eq. (4.1) and (4.2)). The depth machined by each laser pass was predicted by tracking maximum phase transition temperature for different ceramics as described in Chapter IV [150]. Once the depth was estimated, the corresponding width of cavity was also predicted by determining the changed diameter of laser beam, d_{end} and considering it to be equal to the cavity width as mentioned above (Eq. (5.1). The final depth at the end of multiple passes was the summation of depths machined after individual passes.

Thus the region where the $i+1^{th}$ track will be machined is preheated by earlier i^{th} track and temperature at beginning of a pass (except for the first one) is greater than room temperature (300 K) due to this preheating effect. The temperature at the beginning of first pass was assumed to be equal to room temperature. This preheating facilitates machining of deeper cavities for the same input energy as surface is already heated prior to next interaction with laser thereby saving the energy utilized in further raising surface temperature. Incorporation of laser beam defocusing and preheating effect into computations is illustrated in a flow chart in Fig. 5.3.

Considering experimentally determined absorptivity values for low temperatures (700-1150K) [138] followed by transitions in absorptivity at higher temperatures (> 1150K) [150] and incorporating beam defocusing and surface preheating effects mentioned above, the total predicted depth machined for different number of passes on all ceramics and corresponding predicted width are listed in Table 5.1. Furthermore, a comparison between predicted and measured depth and width of cavity has also been made in Fig. 5.4 and Fig. 5.5 respectively.

The measured and predicted depth machined by a single laser pass on all ceramics (Fig. 5.4) showed a perfect match because of the procedure described in Chapter IV in determining final absorptivity required to machine a certain depth in a single pass [150]. For other passes, some deviation in values (depth and/or width) can be attributed to limitations of method employed in measuring machined parameters from optical micrographs using ImageJ^{TM} software as mentioned above. It should be noted that even though physical phenomena occurring in every laser pass are same, the depth machined at the end of each pass was different (Table 5.1 and Fig. 5.4). As discussed above, a defocused beam reduces energy input to the system while on the contrary, preheating saves energy by removing more material for same input energy. Thus, the depth machined by any laser pass is governed by the resultant of these two counter effects. In

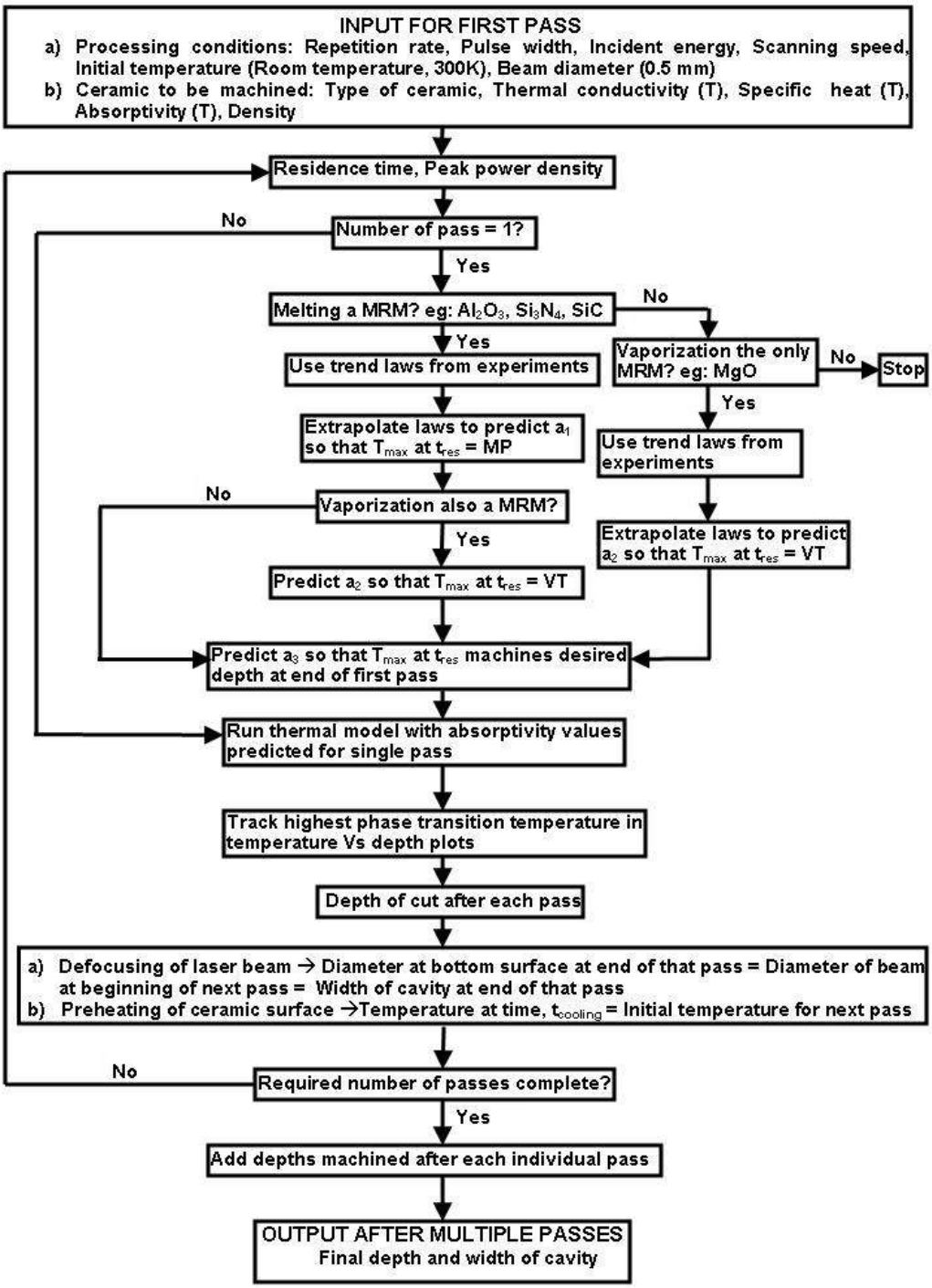

Fig.5.3 Flowchart for predicting depth and width of machined cavity after multiple laser passes [167].

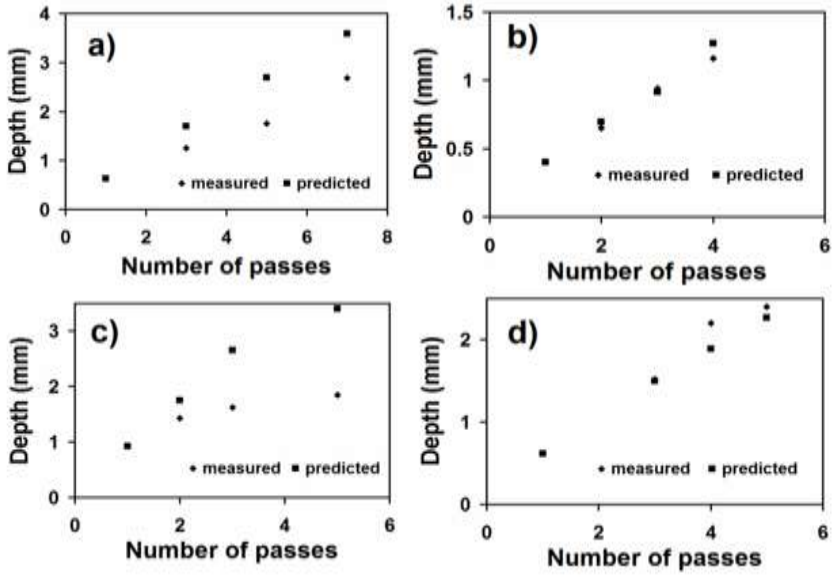

Fig.5.4 Comparison between predicted and measured depth of cavity in a) Al_2O_3, b) Si_3N_4, c) SiC, and d) MgO for different number of passes [167].

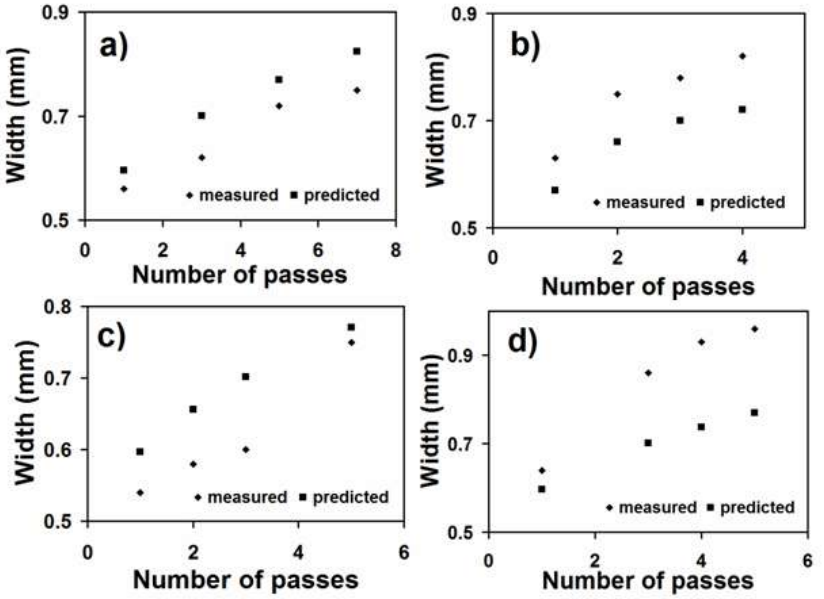

Fig.5.5 Comparison between predicted and measured width of cavity in a) Al_2O_3, b) Si_3N_4, c) SiC, and d) MgO for different number of passes [167].

addition to heat transfer, preheating, phase changes, transition in absorptivity, and beam defocusing, there could be some other phenomena that are unknown at this time and not considered in this study which may affect cavity dimensions (depth and width). In general, this study enables in advance prediction of the laser processing parameters and number of passes required for machining desired depth in any ceramic.

Moreover, it can be seen in next chapter that for three-dimensional laser machining of certain ceramics such as MgO, multiple passes are more beneficial to develop a better finish of cavities without cracking thus making the study of multiple laser passes essential. Finally, the progressive machining model developed so far from Chapters I through V will finally be applied in the next chapter on three-dimensional laser machining to predict material removal (machining) rate in any ceramic for any desired scanning speed for a given set of other laser processing parameters.

CHAPTER VI
THREE-DIMENSIONAL LASER MACHINING[1]

It was mentioned in Chapter I that 3D Laser Carving on Al_2O_3 has been carried out by Wang et. al. [92] while threads and gears have been cut in Si_3N_4 ceramic [77] and SiC_ω/Al_2O_3 composite [40] respectively. However, all of these studies were confined to qualitative analysis of machining process and its effects on machined ceramics. On the contrary, this chapter deals with material removal rate (MRR) based on MRM during three-dimensional laser machining of structural ceramics. The computational model discussed so far was further enhanced to predict and compare machining effects.

Experimental Procedure

Cavities 10 mm wide (W) and of variable length (L) and depth (Z) were machined in dense Al_2O_3, Si_3N_4, SiC and MgO coupons by overlapping laser pulses in x direction (with overlap, s_x) and also in y direction (with overlap, s_y). Overlap s in any direction is defined as a ratio of overlap distance (beam diameter – distance traveled by laser beam) to beam diameter [168]. For machining the cavities, e of 4 J, f of 20 Hz, p of 0.5 ms and V of 3 in/min (1.27 mm/sec) with air as cover gas at a pressure of 80 psi (5.5 bar) were used for processing. Cavities were machined through the entire length of ceramic coupons and an overlap s_y of 0.25 was used for overlapping successive laser passes in order to scan a width of 10 mm. As mentioned in earlier chapters, a fiber optic system and a 120 mm focal length convex lens delivered a defocused laser beam of spot diameter of roughly 0.5 mm on the surface.

A schematic of 3D- machining is represented in Fig. 6.1 where a rectangular cavity of

[1] The content of this chapter is originally from Reference [166].

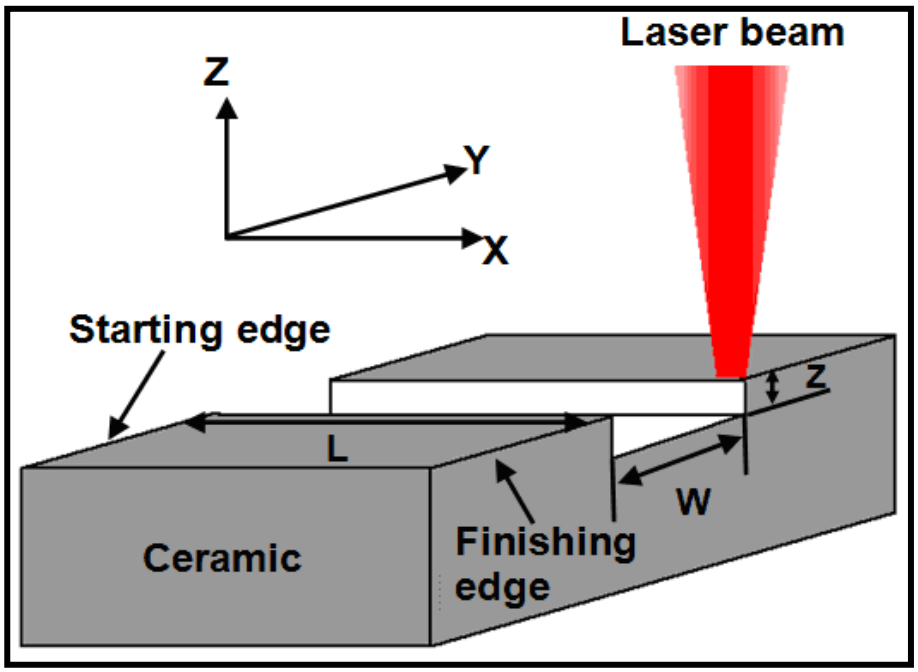

Fig.6. 1 Schematic illustrating three-dimensional laser machining of structural ceramics [166].

dimensions *L*, *W* and *Z* is machined in the ceramic by motion of laser beam in x and y directions. The x, y and z axes were assumed to be along the length, width, and depth of machined cavity respectively. As shown in Fig. 6.1, the laser beam started scanning from starting edge and moved to finishing edge in *x* direction covering a distance *L* following which laser was switched off and the beam returned back to the starting edge. Next pass was laid after the beam advanced a distance in y direction (predicted later) corresponding to an overlap of 0.25 and this process was repeated till entire width *W* of cavity was machined. The actual cavities machined in Al_2O_3, Si_3N_4, SiC and MgO are shown in Fig. 6.2 [166]. It can be clearly seen from Fig. 6.2 that crack free cavities were formed in different ceramics using above mentioned laser processing conditions. Determination of thermal stresses generated during laser machining was however not

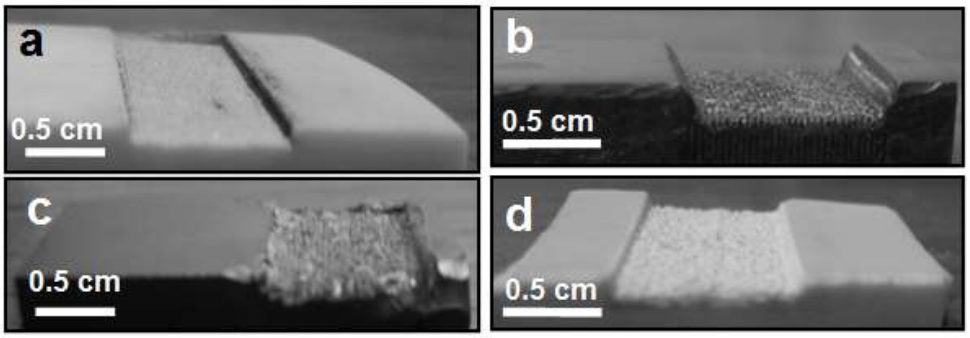

Fig.6.2 Three-dimensional cavities machined in a) Al_2O_3, b) Si_3N_4, c) SiC, and d) MgO [166].

a focus of this study and can be considered in future.

Even though based on prior experience, a V of 3 in/min (1.27 mm/sec) and s_y of 0.25 were chosen in the present study, the same approach can also be extended to any other appropriate combinations of processing parameters (speed, overlap, and energy) to produce cavities of variable dimensions without introduction of thermal stresses and cracking. Furthermore, as under certain set of laser processing conditions, a single high energy laser pass may introduce large thermal stresses and cracking of ceramic [167], multiple laser passes were preferred for machining deeper cavities in some of these ceramics such as MgO and SiC.

In order to predict volume of machined cavities and hence measured $MRR_{measured}$, depths of different cavities, Z were measured by MicroXAM interferometer which is a non-contact interferometric microscope and allows precise depth measurements without necessity for cross sectioning coupons. Surface roughness of all ceramics was also measured by this interferometer across length of laser track to cover entire machined surface area. Due to uneven surface of machined cavities, depth and roughness were measured at five different locations and mean value was reported along with scatter in the data. The experimentally measured physical

attributes of the rectangular cavities (L, W and Z) corresponding to a volume of $L \times W \times Z$) machined in Al_2O_3, Si_3N_4, SiC and MgO are listed in Table 6.1 and will be used to determine $MRR_{measured}$ as discussed in next section. Surface roughnesses for all ceramics are also listed in Table 6.1 and will be used to correlate measured and predicted material removal rates as discussed later.

Material Removal Rate

As mentioned above, dimensions of machined cavities were used to determine $MRR_{measured}$. On the contrary, a thermal model incorporating various material removal mechanisms for laser machining developed in Chapters I to V was adopted to predict the depth machined under a given set of laser processing parameters and hence corresponding volume loss

Table 6.1 Experimentally evaluated attributes of machined cavities related to Al_2O_3, Si_3N_4, SiC and MgO [166].

Ceramic	Length L (mm)	Width W (mm)	Measured machined depth Z (mm)	Surface roughness R_a (μm)	Total processing time $t_{processing}$ (sec)	$MRR_{measured}$ (mg/sec)
Al_2O_3	23	10	0.76 ± 0.013	2.75 ± 0.95	5.01	132.24 ± 2.37
Si_3N_4	10	10	0.86 ± 0.114	2.68 ± 1.02	2.14	95.06 ± 12.70
SiC	13	10	0.76 ± 0.064	4.22 ± 0.87	2.81	108.65 ± 9.28
MgO	25	10	0.58 ± 0.166	1.65 ± 0.59	5.45	95.57 ± 27.36

and $MRR_{predicted}$ in different ceramics. The procedure for determining these MRRs ($MRR_{measured}$ and $MRR_{predicted}$) , comparison between their values and factors affecting material removal are discussed in the following sections.

Measured Material Removal Rate ($MRR_{measured}$)

As laser beam is incident on ceramic surface, in addition to overlap between adjacent pulses (s_x) within a single pass of length L there is also an overlap between successive passes (s_y) to machine the entire width W of cavity. This process is represented in Fig. 6.3 and the distance, a' traveled by laser beam in x direction between two adjacent pulses or the distance, b' traveled by laser beam between two adjacent passes (tracks) is given by [168]:

$$\textit{Distance traveled by laser beam} = d\,(1 - s) \tag{6.1}$$

where s is overlap in either direction (s_x or s_y) as defined above.

Overlap s_x between adjacent pulses is schematically depicted in Fig.6.4. For machining a cavity of length L, this s_x depends on scanning speed, pulse repetition rate and beam diameter and is given by [92,168]:

$$s_x = 1 - \frac{V}{f\,d} \tag{6.2}$$

where V is 1.27 mm/sec, f is 20 Hz and d is 0.5 mm. For laser processing conditions used in this study, the overlap s_x was 0.873 (Eq.(6.2)) and distance a' traveled by laser beam in x direction (Fig.6.3) was 0.0635 mm (Eq. (6.1)). The overlap s_x between adjacent pulses and distance a' was same for all ceramics because cavities in all ceramics were machined under same processing conditions. As seen in Fig. 6.3, desired length L of a single machined track is equal to the distance between center of first pulse and center of last pulse. The total number of pulses, N

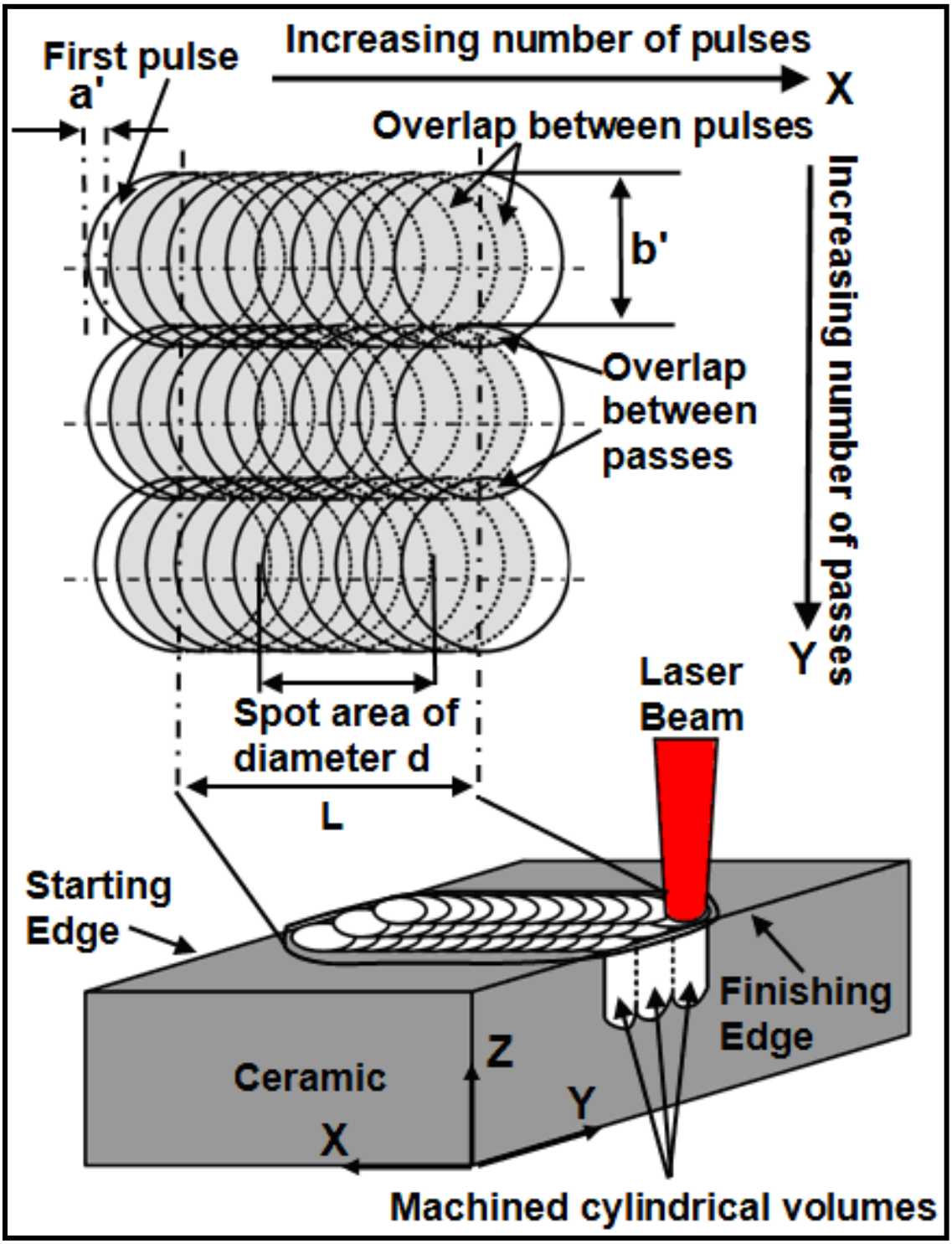

Fig.6.3 Schematic illustrating overlap in x and y directions and cylindrical volume machined per spot area [166].

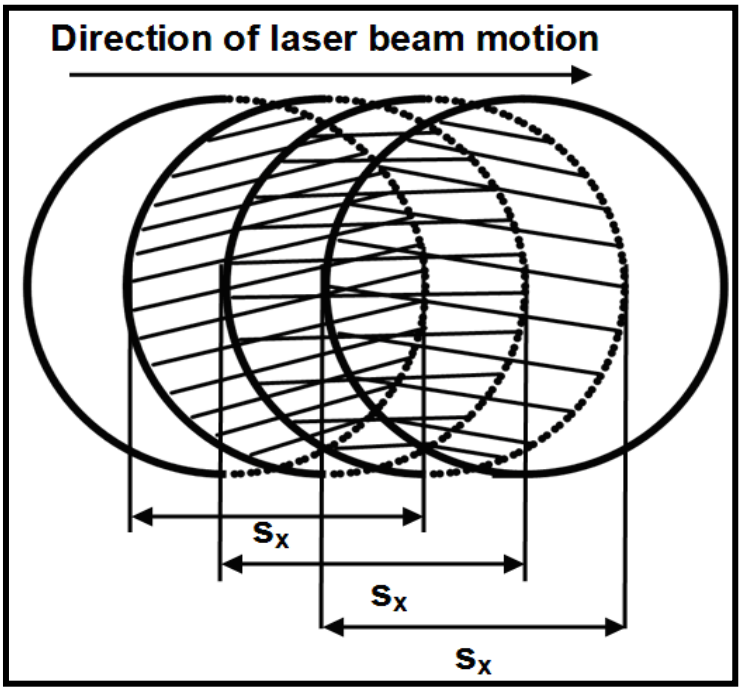

Fig.6.4 Overlap between adjacent laser pulses [166].

required to machine a single track of this length in ceramic is given by:

$$N = \frac{L}{a'} \tag{6.3}$$

Furthermore, as seen in Fig.6.3, multiple laser pulses are required to process an area equivalent to a single laser spot of diameter d and number of pulses N_d required to machine this area is obtained by replacing L with d in Eq. (6.3). For processing conditions employed in this study, N_d was found to be 8 pulses and this value will be used in next section on predicted material removal rate.

Distance b' traversed by laser beam in y direction (Fig. 6.3) for an overlap s_y of 0.25 after completing one pass in x direction (equal to length L of machined cavity) (Fig. 6.1) was 0.375 mm (b' = 0.5(1- 0.25) in Eq. (6.1)). As all ceramics were machined with a constant overlap s_y of

0.25, this distance *b'* was also same for all ceramics and number of passes, *P* required to machine width *W* was given by:

$$P = W/b' \tag{6.4}$$

Thus 27 passes (P = 10/0.375) were required to scan a width of 10mm (same for all ceramics) and total processing time, $t_{processing}$ (Table 6.1) required for machining entire volume of cavity was given by:

$$t_{processing} = N \times p \times P \tag{6.5}$$

The total number of pulses, *N* incident per pass is different for each ceramic as length of cavity machined in every ceramic was different (Eq. (6.3). Thus material removal rate ($MRR_{measured}$) listed in Table 6.1 was given by:

$$MRR_{measured} = \frac{\rho \times L \times W \times Z}{t_{processing}} \tag{6.6}$$

$MRR_{measured}$ varied from (95.06 ± 12.70) mg/sec for Si_3N_4 to (132.24 ± 2.37) mg/sec for Al_2O_3. Even though pulse overlap in x and y direction is evident in laser processing and has been covered in the past [92, 168], it was considered extensively in the present study as it has a significant effect on the material removal rates. As described in the following section, $MRR_{measured}$ thus calculated will be compared with predicted material removal rate $MRR_{predicted}$.

Predicted Material Removal Rate ($MRR_{predicted}$)

The various physical phenomena occurring when the laser beam interacts with the ceramic surface, different material removal mechanisms affecting machining, observed absorptivity trends, and transition temperatures have been elaborately discussed in Chapters I to V [1, 62-66,138, 150]. As shown in Fig. 6.3, it was assumed that volume of cavity machined (corresponding to a certain depth in z direction) per unit spot area (defined above in relation to

Eq. (6.3)) by these physical phenomena was equivalent to a cylinder of diameter, *d* (beam diameter of 0.5 mm on surface of ceramic being machined) [65]. Translation of laser beam in x and y directions (Fig.6.1 and Fig. 6.3) lead to material removal in all three directions (x, y and z) and a three- dimensional cavity was formed as seen in Fig.6.2. All these above mentioned effects and corresponding equations have been integrated into an *ab-initio* computational model for prediction of temperature rise [150]. As explained later, in order to predict material removal rate ($MRR_{predicted}$), the machined depth corresponding to a single spot area of diameter *d* was predicted using this thermal model [150].

The total area corresponding to a single pass of length *L* is composed of several individual spot areas. In the present case, this length being different for each ceramic, number of such spot areas of diameter *d* covering a length *L* under the set of processing parameters employed in this study (4J, 20 Hz, 0.5 ms pulse width, 1.27 mm/sec) will be different for each ceramic. Thus, due to symmetrical/ repetitive nature of material removal process, only rate of material removal for a single spot area or corresponding single cylindrical volume is determined in this study and it is considered to be a representative of $MRR_{predicted}$ for a given ceramic. The temperature evolution (necessary for depth predictions) was governed by effective energy input to system and time for which this energy was incident as discussed in next section.

Effective Energy Per Spot Area

The laser beam moves with a constant *V*, therefore, as schematically illustrated in Fig. 6.5, a single spot area is covered by several pulses. The overlap of each pulse over this area is given by:

$$s_{pulse} = \frac{d - (n-1)a'}{d} \tag{6.7}$$

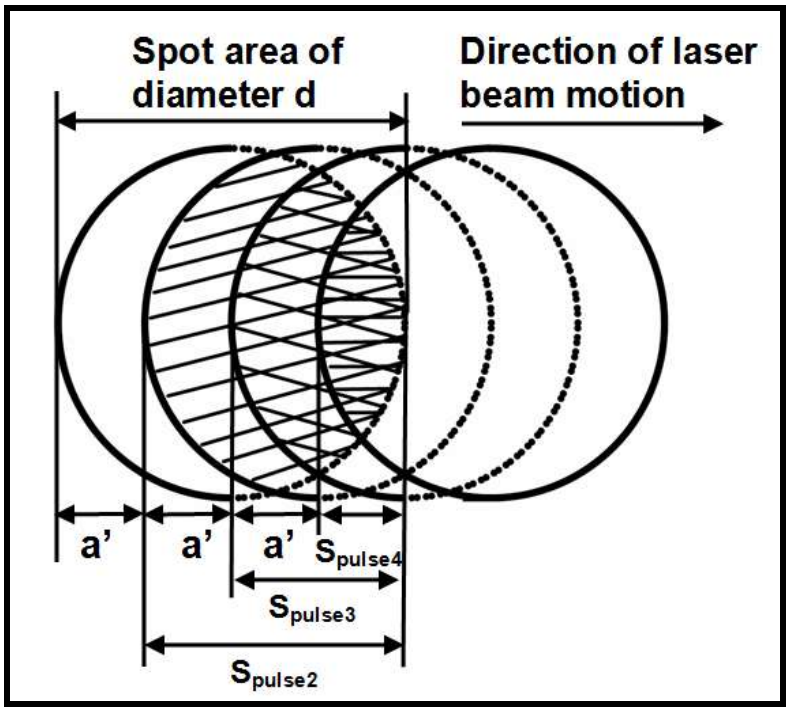

Fig.6.5 Overlap of successive laser pulses over a single spot area [166].

where *n* is the number of the pulses ranging from 1 to 8 for this study (predicted for a travel distance equal to the beam diameter, *d* from Eq. (6.3)), *a'* is predicted above as 0.0635 mm from Eq. (6.1) and Eq. (6.2). Even though Eq. (6.3) predicts number of pulses in entire length of track, same equation can be used to predict number of pulses in a spot area by replacing *L* with *d*. The number of pulses overlapping one spot area was same for all ceramics considered in this study as they were machined under same set of processing conditions. However, as seen in Fig.6.5, the overlap s_{pulse} was different for each pulse (s_{pulse2}, s_{pulse3}, and s_{pulse4} corresponding to overlap of second, third and fourth pulse respectively over spot area of first pulse). The contribution of each of these pulses to effective energy falling on every spot area [92] was $s_{pulse} \times e$ where *e* is energy

of individual laser pulse (4J). From Eq. (6.7), total effective energy incident on a spot area due to N_d pulses is given by:

$$E_{effective} = \sum_{n=1}^{N_d} \left[\frac{d-(n-1)a'}{d} \right] e \tag{6.8}$$

In Eq. (6.8), n represents the incremental pulses (varying from 1 to 8 pulses) while N_d represents final number of pulses covering a spot area (8 pulses for all ceramics considered in this study). Total time of interaction for N_d pulses (t_d) is given by $N_d \times p$ where p is 0.5 ms. Beam distribution in temporal and spatial evolution being uniform, peak power density within a single spot area is given by:

$$\text{Effective peak power density} = \frac{\text{Effective energy per spot area}}{N_d \times \text{Pulse width} \times \text{Area of incident beam}}$$

$$= \frac{\sum_{n=1}^{N_d} \left[\frac{d-(n-1)a'}{d} \right] e}{N_d\, p \left(\frac{\pi d^2}{4} \right)} \tag{6.9}$$

Under the processing conditions used in this study, the peak power density is 2.01×10^{10} W/m^2 corresponding to a beam diameter of 0.5 mm at surface and this energy was incident for time t_d equal to 4.0 ms.

To determine depth machined per spot area in time t_d by effective peak power density (Eq. (6.9)), thermophysical properties (density [110], temperature dependent absorptivity [138,150], thermal conductivity and specific heat [110]) of the ceramics, heat transfer coefficient as a function of temperature [111], laser processing conditions (t_d, and effective peak power density (Eq. (6.9)), and dimensions of coupon were input to computational model [150]. As mentioned in Chapter IV, the corresponding depth machined was predicted by tracking highest

phase change temperature (melting, dissociation, or evaporation based on type of ceramic) at end of t_d. The predicted machined depths, z_t for Al_2O_3, Si_3N_4, SiC and MgO are listed in Table 6.2. Total predicted volume loss per unit time was given by:

$$Predicted\ volume\ loss\ per\ unit\ time = \frac{(\pi d^2 z_t / 4)}{t_d} \qquad (6.10)$$

Finally, the predicted material removal rate ($MRR_{predicted}$) listed in Table 6.2 was obtained by multiplying volume loss per unit time (Eq. (6.10)) by density of ceramic (3800, 2370, 3100, and 3580 kg/m^3 for Al_2O_3, Si_3N_4, SiC and MgO respectively [110]). $MRR_{predicted}$ so obtained varied from 63.98 mg/sec for Si_3N_4 to 136.95 mg/sec for SiC. It can be seen that Si_3N_4 demonstrated lowest value of $MRR_{measured}$ (95.06 ± 12.70 mg/sec) and also $MRR_{predicted}$ (63.98 mg/sec). Even though SiC had highest $MRR_{predicted}$ (136.95 mg/sec), it did not demonstrate highest value of $MRR_{measured}$. On the contrary, $MRR_{measured}$ for Al_2O_3 was highest (132.24 ± 2.37 mg/sec). This discrepancy could be attributed to uneven/ rough surface (R_a = 4.22 ± 0.87 μm) of cavities machined in SiC (Table 6.1, Fig. 6.2c).

Thus the developed computational model assisted in predicting machined depth and associated material removal rate (mg/sec) and a flow chart illustrating the steps to be followed to

Table 6.2 Predicted attributes of machined cavities related to Al_2O_3, Si_3N_4, SiC and MgO [166].

Ceramic	Predicted machined depth z_t (mm)	Heating rate × 10^6 (K/sec)	$MRR_{predicted}$ (mg/sec)
Al_2O_3	0.57	3.10	106.32
Si_3N_4	0.55	1.86	63.98
SiC	0.9	5.02	136.95
MgO	0.47	2.26	82.59

achieve $MRR_{measured}$ and $MRR_{predicted}$ is represented in Fig. 6.6. The model was also able to predict heating rates (K/sec) from the slope of temperature vs. time profiles at different time instants. The average heating rate for the ceramics machined in the present work has been listed in Table 6.2 and the correlation with MRR is discussed in next section.

Material Removal Rate and Heating Rate

As mentioned above, temperature changes are responsible for material removal by different MRMs based on type of ceramic. Higher heating rates imply rapid rise in temperature per unit time leading to more material removal per unit time and corresponding higher machining rate. This effect can also be seen in Fig. 6.7 where the variation of measured (Table 6.1) and predicted (Table 6.2) material removal rate showed an increasing trend with increase in heating rate (Table 6.2).

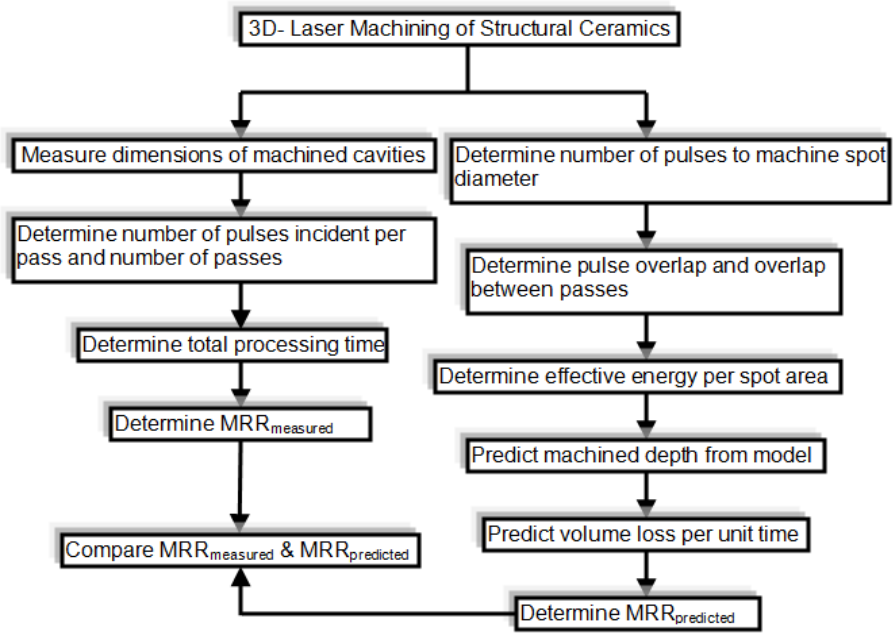

Fig.6. 6 Flowchart for determining material removal rate (MRR) during three-dimensional laser machining of structural ceramics.

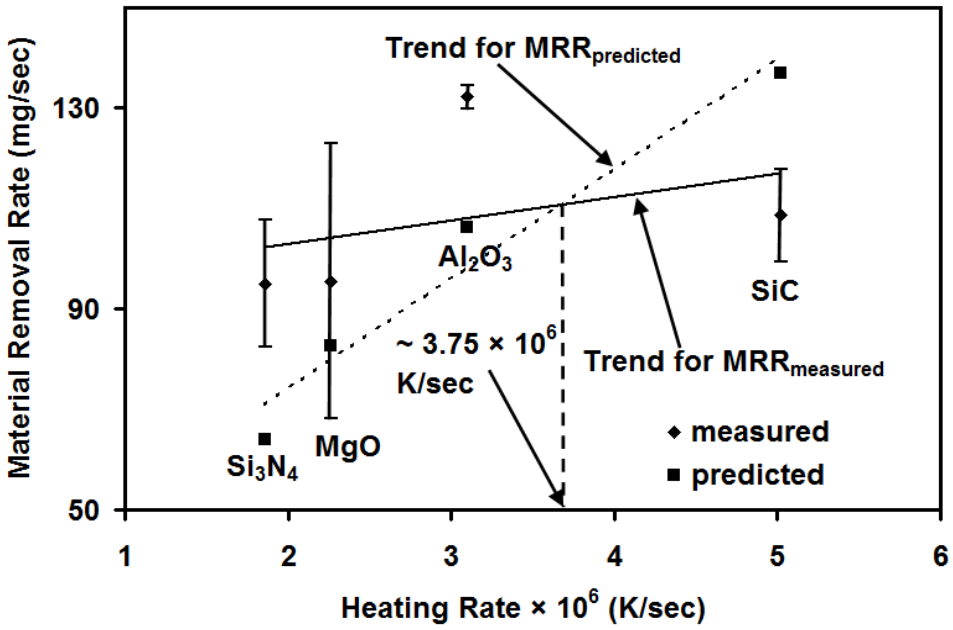

Fig.6.7 Variation of material removal rate with heating rate for Al_2O_3, Si_3N_4, SiC, MgO [166].

However, a crossover of trend lines for $MRR_{predicted}$ and $MRR_{measured}$ was observed around a heating rate of ~3.75 × 10^6 K/s. This cross over is due to difference in predicted and measured MRR values of SiC and can be attributed to highly rough (R_a = 4.22 ± 0.87 μm) machined surface of SiC (Table 6.1, Fig. 6.2c). The sharp peaks (raised portions) on such rough surfaces could lead to a measured depth (hence corresponding volume losses and $MRR_{measured}$) lower than its actual value.

Furthermore, as heating rate was predicted through computational model [150], it accounted for all properties of ceramic (density, specific heat, thermal conductivity, absorptivity), the phase transition temperature (melting point, dissociation temperature, or boiling point depending on ceramic), material removal mechanism (melting, sublimation,

dissociation, or evaporation based on type of ceramic) in addition to laser processing conditions (scanning speed, pulse repetition rate, pulse width, input energy, beam cross sectional area). The heating rate thus represented combined effect of type of ceramic (thermophysical properties) and laser processing parameters on material removal rate. As a result of this study, an efficient control on material removal rate can be obtained by altering laser processing parameters and selecting appropriate materials to attain desired heating rates.

It should be noted that besides heating rate there could be some additional factors that are not considered in this study and could have an effect on material removal rate. Recognition and inclusion of these physical processes in prediction of machining rate can be dealt with in the future. In general, such a study would enable advance foresight into laser processing conditions (such as scanning speed for a given set of other processing parameters) to machine a cavity of desired dimensions at an optimum rate to save considerable amount of energy and time.

CHAPTER VII
CONCLUSIONS AND FUTURE WORK

Conclusions

- Feasibility of laser machining of structural ceramics such as Al_2O_3, Si_3N_4, SiC and MgO in one, two and three dimensions was demonstrated by using a pulsed Nd:YAG laser.
- For pulse energy of 4 J, pulse repetition rate of 20 Hz and pulse width of 0.5 ms, the machined depth increased from 0.26 to 4mm, 0.92 to 3.5 mm and from 0.25 to 3.0 mm with increase in number of pulses from 5 to 30, 3 to 20 and from 3 to 20 for Al_2O_3, Si_3N_4 and MgO respectively.
- For pulse energy of 6J, pulse duration of 0.5 ms, and pulse repetition rate of 50 Hz, 25 and 125 pulses were required for machining thicknesses of 2 and 3 mm respectively in SiC.
- Material removal in Al_2O_3, Si_3N_4 and SiC took place by a combination of melting, recoil pressure driven melt expulsion, dissociation and evaporation while dissociation followed by evaporation was responsible for material removal in MgO.
- An *ab-initio* computational machining model incorporating temperature evolution and material removal mechanisms was developed to correlate laser processing parameters with attributes of machined cavities.
- Intraband absorption was the cause for drop in absorptivity with increasing temperature for short wavelength while the opposite trend of rise in absorptivity with increase in temperature at long wavelength (> 10 μm) could be attributed to interband absorption.
- SiC had the highest absorptivity of all the ceramics considered in this study (0.85 at a temperature of 735K). On the other hand, for the observed range of temperatures, it was seen

that maximum absorptivity for Al_2O_3, MgO, and Si_3N_4 were 0.25 at 1039 K, 0.32 at 866 K, and 0.34 at 927 K, respectively.

- At the slowest processing speed of 2.11 mm/s considered in this study, the deepest cuts of 0.63, 0.4, 0.92, and 0.62 mm were obtained in Al_2O_3, Si_3N_4, SiC and MgO respectively due to maximum interaction of ceramic with the laser as compared to higher processing speeds.
- For the speeds used for processing (2.11, 4.23, 5.08 and 6.35 mm/s), the transition temperature T_1 for Al_2O_3, Si_3N_4 , SiC and MgO varied from 1135 – 1165 K, 1600 – 1738 K, 1413 – 1473 K and 1178 – 1263 K respectively.
- Cavities were machined with depths varying from 0.63 to 2.68 mm (for number of passes varying from 1 to 7) in Al_2O_3 and from 0.4 to 1.16 mm (for variation in number of passes from 1 to 4) in Si_3N_4. Corresponding widths varied from 0.56 to 0.75 mm in Al_2O_3 and from 0.63 to 0.82 mm Si_3N_4.
- Cavities 0.9 to 1.85 mm (for variation from 1 to 5 passes) and 0.62 to 2.4 mm (for variation from 1 to 5 passes) deep were machined in SiC and MgO respectively. Widths of these cavities varied from 0.54 to 0.75 mm in SiC and from 0.64 to 0.96 mm in MgO.
- Predicted heating rates for Al_2O_3, Si_3N_4, SiC and MgO were 3.1×10^6, 1.86×10^6, 5.02×10^6, and 2.26×10^6 K/sec respectively and corresponding predicted material removal rates were 106.32, 63.98, 136.95, and 82.59 mg/sec.
- Measured material removal rates for Al_2O_3, Si_3N_4, SiC and MgO were 132.24 ± 2.37, 95.06 ± 12.70, 108.65 ± 9.28, and 95.57 ± 27.36 mg/sec respectively and corresponding surface roughness were 2.75 ± 0.95, 2.68 ± 1.02, 4.22 ± 0.87 and 1.65 ± 0.59 μm respectively.

- For processing conditions employed in this study, cavities machined in Al_2O_3, Si_3N_4 and MgO had a smoother surface (R_a varying from 1.65 ± 0.59 for MgO to 2.75 ± 0.95 μm for Al_2O_3) compared to cavities machined in SiC (R_a = 4.22 ± 0.87 μm).

Future Work

This study mainly focused on understanding the material removal mechanisms in machining of structural ceramics and a computational model was developed that correlated the laser processing conditions with attributes of machined cavities. A comprehensive flow chart illustrating different stages of this work is presented in Fig. 7.1. This study would assist in predicting the laser parameters required to obtain a cavity of desired dimensions at an optimum machining rate. Having illustrated the viability of laser machining of structural ceramics and understanding the physical phenomena involved in material removal, following directions for future work are proposed:

- The laser processing conditions should be varied and effect on surface roughness should be studied and this correlation should be incorporated into the machining model.
- The effect of change of assist gas pressure and type on the attributes of machined cavities should be studied and the gas providing optimum machining rates and surface finish should be selected.
- In order to further improve accuracy of calculations, an attempt should be made to estimate the decay of absorptivity within the bulk of material by extending the present approach of using thermocouples to measure surface temperatures.
- A systematic parametric study should be conducted by varying the laser parameters (pulse repetition rate, pulse width, input energy and beam diameter) and using statistical methods

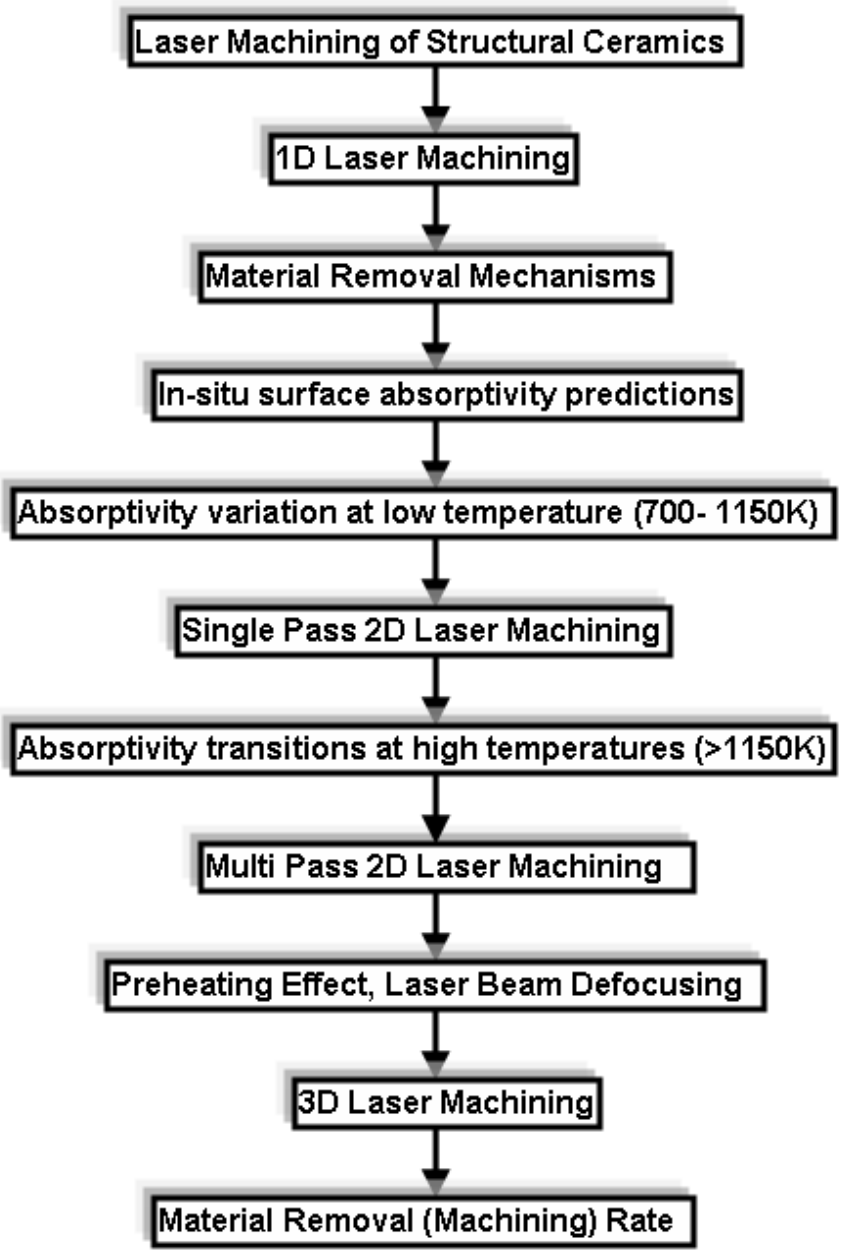

Fig.7.1 Comprehensive flow chart for laser machining of structural ceramics.

such as Design of Experiments (DOE), Analysis of Variance (ANOVA) and Taguchi method to come up with a set of parameters to provide optimum surface finish and depth of machined cavities.

- The effect of laser parameters on the microstructure of the machined cavities should be studied and an attempt should be made to correlate the processing conditions with the microstructure evolution by using the cooling curves and associated cooling rates predicted by the thermal model.
- Efforts should also be made to study the thermal stresses generated in the surface and sub-surface regions by the laser machining process and attempts should be made to reduce and gradually eliminate them.

LIST OF REFERENCES

[1] Samant, A. N., and Dahotre, N. B., Laser machining of structural ceramics – A review. *J. Eur. Ceram. Soc.*, 2009, **29**, 969-993.

[2] Tuersley, I.P., Jawaid, A., and Pashby, I.R., Review: Various methods of machining advanced ceramic materials. *J. Mater. Process. Technol.*, 1994, **42**(4), 377-390.

[3] Schwartz, M., *Handbook of Structural Ceramics*, McGraw-Hill, New York, 1992.

[4] Vikulin, V., Kelina, I., Shatalin, A. and Rusanova, L., Advanced ceramic structural materials. *Refractories and Industrial Ceramics*, 2004, **45,** 383-386.

[5] Wang, H., Wang, C.A., Yao, X. and Fang, D., Processing and mechanical properties of zirconium diboride-based ceramics prepared by spark plasma sintering. *J. Am. Ceram. Soc*, 2007, **90**, 1992-1997.

[6] Kim, J. D., Lee, E. S. and Lee, C. Y., Crack generation and the effect of in-process electro-discharge dressing in grinding single crystal MgO. *Int. J. Mech. Sci.*, 1995, **37,** 569-583.

[7] Kim, J.D. and Lee, E.S., A study on the mirror-like grinding of MgO single crystal with various diamond wheels. *J. Mater. Process. Technol.*, 1997, **72**, 1-10.

[8] Kalpakjian, S. and Schmid, S.R., *Manufacturing Engineering and Technology*, Prentice Hall, Upper Saddle River, NJ, 2001.

[9] König, W. and Wagemann, A., Machining of ceramic components - process-technological potentials. *Machining of Advanced Materials, NIST Special Publication*, 1990, **847**, 3–16.

[10] Chryssolouris, G., Anifantis, N. and Karagiannis, S., Laser assisted machining: an overview. *J. Manuf. Sci. Eng.*, 1997, **119** (4B), 766-769.

[11] Koepke, B.G. and Stokes, R.J., A study of grinding damage in magnesium oxide single crystals. *J. Mater. Sci.*, 1970, **5**(3), 240-247.

[12] Kirchner, H.P., Damage penetration at elongated machining grooves in hot-pressed Si_3N_4. *J. Am. Ceram. Soc*, 1984, **67**(2), 127-132.

[13] Zhang, B., Precision grinding regime of advanced ceramics. In *Proceedings of Annual Meeting of American Society of Precision Engieering, Seattle, WA*, 1993. p. 225-229.

[14] Xu, H.H.K. and Jahanmir, S., Microfracture and material removal in scratching of alumina. *J. Mater. Sci.*, 1995, **30**(9), 2235-2247.

[15] Zhang, B., Zheng, X.L., Tokura, H., and Yoshikawa, M., Grinding induced damage in ceramics. *J. Mater. Process. Technol.*, 2003, **132**, 353-364.

[16] Thoe, T.B., Aspinwall, D.K. and Wise, M.L.H., Review on ultrasonic machining. *Int. J. Mach. Tools Manuf*, 1998, **38**(4), 239-255.

[17] Choi, J.P., Jeon, B.H., and Kim, B.H., Chemical-assisted ultrasonic machining of glass. *J. Mater. Process. Technol.*, 2007, **191**(1-3), 153-156.

[18] Gudimetla, P., Wang, J., and Wong, W., Kerf formation analysis in the abrasive waterjet cutting of industrial ceramics. *J. Mater. Process. Technol.*, 2002, **128**(1-3), 123-129 .

[19] Park, J.M., Jeong, S.C., Lee, H.W., Jeong, H.D. and Lee, E., A study on the chemical mechanical micro-machining (C3M) process and its application. *J. Mater. Process. Technol.*, 2002, **130-131**, 390-395.

[20] Puertas, I. and Luis, C.J., A study on the electrical discharge machining of conductive ceramics. *J. Mater. Process. Technol.*, 2004, **153-154**, 1033-1038.

[21] Chak, S.K. and Rao, P. V., Trepanning of Al_2O_3 by electro-chemical discharge machining (ECDM) process using abrasive electrode with pulsed DC supply. *Int. J. Mach. Tools Manuf*, 2007, **47**(14), 2061-2070.

[22] Horio, K., Terabayashi, T. and Taniguchi, N., Beam defocus effect in electron beam machining of green ceramic sheet. *CIRP Annals - Manufacturing Technology*, 1987, **36**(1), 95-98.

[23] Kuar, A.S., Doloi, B. and Bhattacharyya, B., Modelling and analysis of pulsed Nd:YAG laser machining characteristics during micro-drilling of zirconia (ZrO_2). *Int. J. Mach. Tools Manuf*, 2006, **46(**12-13), 1301-1310.

[24] Jia, Z. X., Zhang, J.H. and Ai, X., High quality machining of engineering ceramics. *Key Eng. Mater.*, 1995, **108-110,** 155-164.

[25] Shih, H. and Shu, K., A study of electrical discharge grinding using a rotary disk electrode. *Int. J. Adv. Manuf. Technol.*, 2008, **38**, 59-67.

[26] Bäuerle, D., *Laser Processing and Chemistry*, Springer, New York, 2000.

[27] Lei, S., Shin, Y.C. and Incropera, F.P., Experimental investigation of thermo-mechanical characteristics in laser-assisted machining of silicon nitride ceramics. *J. Manuf. Sci. Eng.*, 2001, **123,** 639-646.

[28] Rozzi, J.C., Pfefferkorn, F.E., Incropera, F.P. and Shin, Y.C., Transient, three-dimensional heat transfer model for the laser assisted machining of silicon nitride: I. Comparison of predictions with measured surface temperature histories. *Int. J. Heat Mass Transfer*, 2000, **43(**8), 1409-1424.

[29] Rozzi, J.C., Pfefferkorn, F.E., Incropera, F.P. and Shin, Y.C., Transient thermal response of a rotating cylindrical silicon nitride workpiece subjected to a translating laser heat source, Part I: Comparison of surface temperature measurements with theoretical results. *J. Heat Transfer*, 1998, **120**, 899-906.

[30] Rozzi, J.C., Incropera, F.P. and Shin, Y.C. , Transient thermal response of a rotating cylindrical silicon nitride workpiece subjected to a translating laser heat source, Part II: Parametric effects and assessment of a simplified model. *J. Heat Transfer*, 1998, **120,** 907-915.

[31] Rozzi, J.C., Incropera, F.P. and Shin, Y.C., Transient, three-dimensional heat transfer model for the laser assisted machining of silicon nitride: II. Assessment of parametric effects. *Int. J. Heat Mass Transfer*, 2000, **43**(8), 1425-1437.

[32] Lei, S., Shin, Y.C. and Incropera, F.P. , Deformation mechanisms and constitutive modeling for silicon nitride undergoing laser-assisted machining. *Int. J. Mach. Tools Manuf*, 2000, **40**(15), 2213-2233.

[33] Pfefferkorn, F.E., Shin, Y.C., Tian, Y. and Incropera, F.P., Laser-assisted machining of magnesia-partially-stabilized zirconia. *J. Manuf. Sci. Eng.*, 2004, **126**, 42-51.

[34] Chang, C.W. and Kuo, C.P., An investigation of laser-assisted machining of Al_2O_3 ceramics planning. *Int. J. Mach. Tools Manuf*, 2007, **47**(3-4), 452-461.

[35] www.lasercheval.fr/eng/subcontracting.php

[36] Chryssolouris, G., *Laser Machining Theory and Practice*, Springer-Verlag, New York, 1991.

[37] Albright, C., *Laser Welding, Machining and Materials Processing*, IFS (Publications) Ltd and Springer-Verlag, New York, 1985.

[38] Pandey, P.C. and Shan, H.S., *Modern Machining Processes*, McGraw Hill, New Delhi, 1980.

[39] Sun, S., Durandet, Y. and Brandt, M., Parametric investigation of pulsed Nd: YAG laser cladding of stellite 6 on stainless steel. *Surf. Coat. Technol.*, 2005, **194**(2-3), 225-231.

[40] Islam, M.U. and Campbell, G., Laser machining of ceramics: A review. *Mater. Manuf. Processes*, 1993, **8**(6), 611 - 630.

[41] Ki, H., Mohanty, P.S. and Mazumder, J., Multiple reflection and its influence on keyhole evolution. *J. Laser Appl.*, 2002, **14**, 39-45.

[42] Bang, S.Y. and Modest, M.F., Multiple reflection effects on evaporative cutting with a moving CW laser. *J. Heat Transfer,* 1991, **113,** 663-669.

[43] Zhao, J., Numerical Simulation of High Intensity Laser Drilling of Metals. Masters Thesis. The University of Tennessee: Knoxville,TN, 1999.

[44] Minamida, K. , Takafuji, H. , Hamada, N., Haga, H. and Mizuhashi, N., Wedge shape welding with multiple reflection effects of high power CO_2 laser beam. In *Proceedings of the 5th Int. Congress on Applications of Lasers and Electro-optics, Arlington, VA,* 1986. p. 97-104.

[45] Rahman, F. A., Takahashi, K. and Teik, C. H., Theoretical analysis of coupling between laser diodes and conically lensed single-mode fibres utilising ABCD matrix method. *Opt. Commun.*, 2003, **215**(1-3), 61-68.

[46] Bang, S.Y., Roy, S. and Modest, M.F. , CW laser machining of hard ceramics-II. Effects of multiple reflections. *Int. J. Heat Mass Transfer*, 1993, **36**(14), 3529-3540.

[47] Modest, M.F., Effects of multiple reflections on hole formation during short-pulsed laser drilling. *J. Heat Transfer*, 2006, **128(**7), 653-661.

[48] Baily, A.W. and Modak, A., Numerical simulation of laser ablation with cavity reflections. *J. Thermophys. Heat Transfer*, 1989, **3**, 42-45.

[49] Dahotre, N. B. and Harimkar, S.P., *Laser Fabrication and Machining of Materials*, Springer, New York, NY, 2008.

[50] Andrews, J.G. and Atthey, D.R., Hydrodynamic limit to penetration of a material by a high-power beam. *J. Phys. D: Appl. Phys.,* 1976, **9,** 2181-2194.

[51] Mazumdar, J. and Steen, W.M., Heat transfer model for CW laser material processing. *J.Appl.Phys,* 1980, **51**, DOI : 10.1063/1.327672.

[52] Steen, W.M., *Laser Materials Processing,* Springer, London, 1991.

[53] Dubey, A.K. and Yadava, V., Experimental study of Nd:YAG laser beam machining-An overview. *J. Mater. Process. Technol.*, 2008, **195(**1-3), 15-26.

[54] Salonitis, K., Stournaras, A., Tsoukantas, G., Stavropoulos, P. and Chryssolouris, G., A theoretical and experimental investigation on limitations of pulsed laser drilling. *J. Mater. Process. Technol.*, 2007, **183**(1), 96-103.

[55] Morita, N., Ishida, S., Fujimori, Y. and Ishikawa, K., Pulsed laser processing of ceramics in water. *Appl. Phys. Lett.*, 1988, **52**(23), 1965-1966.

[56] Kovalenko, V.S. and Laurinovich, A.V. , Laser machining of ceramic materials. In *Proceedings of 6th Int. Conf. on Production Engineering, Osaka, Japan,* 1987. p. 627-631.

[57] Kim, M.J., 3D Finite element analysis of evaporative laser cutting. *Appl. Math. Modelling,* 2005, **29**(10), 938-954.

[58] Kim, M.J. and Zhang, J., Finite element analysis of evaporative cutting with a moving high energy pulsed laser. *Appl. Math. Modelling,* 2001, **25**(3), 203-220.

[59] Modest, M.F. and Abakian, H., Heat conduction in a moving semi-infinite solid subjected to pulsed laser irradiation. *ASME J. Heat Transfer,* 1986, **108,** 602–607.

[60] Abakian, H. and Modest, M.F., Evaporative cutting of a semi-transparent body with a moving CW laser. *ASME J. Heat Transfer,* 1988, **110**,924–930.

[61] Modest, M., Laser machining of ablating / decomposing materials through cutting and drilling models. *J. Laser Appl.*, 1997, **9**,137-145.

[62] Samant, A.N. and Dahotre, N.B., Ab initio physical analysis of single dimensional laser machining of silicon nitride. *Adv. Eng. Mater.*, 2008, **10**, 978- 981.

[63] Samant, A.N. and Dahotre, N.B. , Computational predictions in single dimensional laser machining of alumina. *Int. J. Mach. Tools Manuf.*, 2008, **48**, 1345-1353.

[64] Samant, A. N. and Dahotre, N.B., Differences in physical phenomena governing laser machining of structural ceramics. *Ceram. Int.*, 2009, **35**, 2093-2097.

[65] Samant, A. N. and Dahotre, N.B., An integrated computational approach to single dimensional laser machining of magnesia. *Opt. Lasers Eng.*, 2009, **47**, 570- 577.

[66] Samant, A. N., Daniel, C., Chand, R.H., Blue, C. A. and Dahotre, N.B., Computational approach to photonic drilling of silicon carbide. *Int. J. Adv. Manuf. Technol*, in press, DOI: 10.1007/s00170-009-2004-0.

[67] Semak, V.V., Knorovsky, G.A., MacCallum, D.O. and Roach, R.A., Effect of surface tension on melt pool dynamics during laser pulse interaction. *J.Phys. D: Appl. Phys.*, 2006, **39**,590-595.

[68] Semak, V.V., Knorovsky, G.A. and MacCallum, D.O. , On the possibility of microwelding with laser beams. *J. Phys. D: Appl. Phys.*, 2003, **36**, 2170-2174.

[69] Anisimov, S.I., Vaporization of metal absorbing laser radiation. *Sov. Physics JETP*, 1968, **27**, 182-183.

[70] Tönshoff, H.K. and Kappel, H., Surface modification of ceramics by laser machining. *CIRP Annals – Manuf. Technol.*, 1998, **47**(1), 471-474.

[71] Tönshoff, H.K., Hesse, D. and Gonschior, M., Microstructuring with excimer lasers and reduction of deposited ablation products using a special gas nozzle with a vacuum system. In *Proceedings of ICALEO, Orlando, FL*, 1994. p. 333-342.

[72] Islam, M.U., An overview of research in the fields of laser surface modification and laser machining at the Integrated Manufacturing Technologies Institute, NRC. *Adv. Perform. Mater.*, 1996, **3,** 215-238.

[73] Laude, L.D., Ogeret, C., Jadin, A. and Kolev, K., Excimer laser ablation of Y-SiAlON. *Appl. Surf. Sci.*, 1998, **127-129**, 848-851.

[74] Sciti, D. and Bellosi, A., Laser-induced surface drilling of silicon carbide. *Appl. Surf. Sci.*, 2001, **180**, 92-101.

[75] Dubey, A.K. and Yadava, V., Optimization of kerf quality during pulsed laser cutting of aluminium alloy sheet. *J. Mater. Process. Technol.*, 2008, **204**(1-3), 412-418.

[76] Tsai, C.H. and Chen, H.W. , Laser cutting of thick ceramic substrates by controlled fracture technique. *J. Mater. Process. Technol.*, 2003, **136**(1-3), 166-173.

[77] Liu, J.S., Li, L.J. and Jin, X.Z., Accuracy control of three-dimensional Nd:YAG laser shaping by ablation. *Opt. Laser Technol.*, 1999, **31,** 419-423.

[78] Perrie, W., Rushton, A., Gill, M., Fox, P. and O'Neill, W., Femtosecond laser micro-structuring of alumina ceramic. *Appl. Surf. Sci.*, 2005, **248**(1-4), 213-217.

[79] Longfellow, J., High speed drilling in alumina substrates with a CO_2 laser. *Am. Ceram. Soc. Bull.*, 1971, **50(3)**, 251-253.

[80] Saifi, M.A. and Borutta, R. , Optimization of pulsed CO_2 laser parameters for Al_2O_3 scribing. *Ceram. Bull.*, 1975, **54,** 986-989.

[81] Wagner, R.E., Laser Drilling Mechanics. *J. Appl. Phys.*, 1974, **45**(10), 4631-4637.

[82] Coherent, Inc.,*Lasers-Operation, Equipment, Application, and Design*, McGraw Hill, New York, 1980.

[83] Chryssolouris, G. and Bredt, J., Machining of ceramics using a laser lathe. In *Proceedings of Intersociety Symp. on Machining of Adv. Ceram. Mater. and Components*. ed. R.E. Barks, K. Subramanian, and K.E. Ball, *Pittsburgh, PA*, 1987. p. 70-72.

[84] Hamann, C. and Rosen, H. , Laser machining of ceramic and silicon. *SPIE-High Power Lasers and Their Industrial Applications*, 1987, **801,** 130-137.

[85] Tönshoff, H.K. and Emmelmann, E., Laser processing of ceramics. *International Power Beam Conference, San Diego, CA*, 1988.

[86] Tönshoff, H.K. and Semrau, H., Laser beam machining in new fields of application. *Conference on Research and Technology Development in Non-Traditional Machining, ASME, Chicago, IL*, 1988.

[87] Tönshoff, H.K. , Butje, R. , Konig, W. and Trasser, F.J., Excimer laser in material processing. *Annals of the CIRP*, 1988, **37**(2), 681-684.

[88] Tönshoff, H.K. and Emmelmann, E., Laser cutting of advanced ceramics. *Annals of the CIRP*, 1989, **38**(1), 219-222.

[89] Guo, D., Cai, K., Yang, J. and Huang, Y., Spatter-free laser drilling of alumina ceramics based on gelcasting technology. *J. Eur. Ceram. Soc.*, 2003, **23(**8), 1263-1267.

[90] Glaw, V., Hahn, R., Paredes, A., Hein, U., Ehrmann, O. and Reichl, H., Laser machining of ceramics and silicon for MCM-D applications. In *Proceedings of the 3rd International Symposium on Adv. Packaging Mater, Braselton, Georgia*, 1997. p. 173-176.

[91] Sciti, D., Melandri, C. and Bellosi, A., Excimer laser-induced microstructural changes of alumina and silicon carbide. *J. Mater. Sci.*, 2000, **35**, 3799-3810.

[92] Wang, C. and Zeng, X., Study of laser carving three-dimensional structures on ceramics: Quality controlling and mechanisms. *Opt. Laser Technol.*, 2007, **39**(7), 1400-1405.

[93] Kelly, A. and Macmillan, N.H., *Strong Solids*, Oxford University Press, New York 1986.

[94] Wachtman, J.B., *Mechanical Properties of Ceramics*, John Wiley & Sons, New York, 1996.

[95] Harrysson, R. and Herbertsson, H., Machining of high performace ceramics and thermal etching of glass by laser. In *Proceedings of the 4th International Conference on Lasers in Manufacturing, Birmingham,UK*, 1987. p. 211-219.

[96] Yamamoto, J. and Yamamoto, Y., Laser machining of silicon nitride. In *Proceedings of LAMP' 87, Osaka, Japan*, 1987. p. 297.

[97] Firestone, R.F., and Vesely. Jr., E.J., High power laser beam machining of structural ceramics, In *Proceedings of the ASME Symposium on Machining of Adv. Ceram. Mater. & Components, Chicago, IL*, 1988. p. 215-227.

[98] Lavrinovich, A.V., Kryl, Y.A. , Androsov, I.M. and Artemyuk, S.A. , Effect of dimensional laser machining on the structure and properties of silicon nitride. *Powder Metall. Met. Ceram.*, 1990, **29**(4), 328-332.

[99] Pham, D.T., Dimov, S.S. and Petkov, P.V. , Laser milling of ceramic components. *Int. J. Mach. Tools Manuf*, 2007, **47**(3-4), 618-626.

[100] Polk, D.H. , Banas, C.M. , Frye, R.W. and Gragosz, R.A., Laser processing of materials. *Industrial Heat Exchangers*, 1986, 357-364.

[101] Affolter, P. and Schmid, H.G., Processing of new ceramic materials with solid state laser radiation. *SPIE-High Power Lasers and Their Industrial Applications*, 1987, **801**, 120-129.

[102] Copley, S., Bass, M., Jau, B. and Wallace, R., Shaping materials with lasers. *Laser Mater. Proc.*, 1983, 297-336.

[103] Ready J.F., *LIA Handbook of Laser Materials Processing*, Magnolia Publishing, Inc., 2002.

[104] Montgomery D. C., *Design and analysis of experiments,* Wiley ,New York, 1997.

[105] Harimkar, S.P., Samant, A.N. and Dahotre, N.B., Temporally evolved recoil pressure driven melt infiltration during laser surface modifications of porous alumina ceramic. *J. of Appl. Phys*., 2007**, 101**, 054911.

[106] Harimkar, S. P., Samant, A. N., Khangar, A. A. and Dahotre, N. B., Prediction of solidification microstructures during laser dressing of alumina based grinding wheel material. *J. Phys. D: Appl. Phys.*, 2006, **39,** 1642-1649.

[107] Shuja, S . Z. and Yilbas, B.S., 3- Dimensional conjugate laser heating of a moving slab. *Appl. Surf. Sci.*, 2000, **167**,134- 148.

[108] Modest, M. F., Laser through-cutting and drilling models for ablating/decomposing materials. *J. Laser Appl.*, 1997, **9**, 137-145.

[109] Modest, M. F. and Abakians, H., Evaporative cutting of a semi-infinite body with a moving CW laser. *J. Heat Transfer*, 1986, **108**, 602-607.

[110] Touloukian, Y.S. ,*Thermophysical Properties of High Temperature Materials*, IFI/Plenum, New York, 1967.

[111] Incropera F. P. and Dewitt, D. P., *Fundamentals of Heat and Mass Transfer,* J. Wiley, New York, 2002.

[112] Patwa, R., Shin, Y. C., Predictive modeling of laser hardening of AISI5150H steels. *Int. J. Mach. Tools. Manuf.*, 2007, **47**, 307- 320.

[113] Sturge, M. D., *Statistical and Thermal Physics, Fundamentals and Applications*, A.K.Peters Ltd., Natick, 2003.

[114] Bhushan, B., Gupta, B., *Handbook of Tribology (Materials, Coatings and Surface Treatments)*, Mc Graw Hill, New York, 1991.

[115] Ananthapadmanabhan, P.V., Thiyagarajan, T.K., Sreekumar, K.P. and Venkatramani, N., Formation of nano-sized alumina by in-flight oxidation of aluminium powder in a thermal plasma reactor. *Scr. Mater.*, 2004, **50**(1), 143-147.

[116] Duley, W. W., *Laser Welding.*,Wiley Interscience Publication, New York, NY, 1998.

[117] Gitzen, W. H., *Alumina as a Ceramic Material*, The American Ceramic Society, Westerville, OH, 1970.

[118] Baker, M., MSDS. Aluminum Oxide: Material Safety Data Sheet.

[119] Allmen, M. V., Blaser, P., Affolter, K. and Strumer, E., Absorption phenomena in metal drilling with Nd-lasers. *IEEE J. Quantum Electron.*, 1978, **14**, 85-88.

[120] Barin, I., Knacke, O., *Thermochemical properties of inorganic substance*, Springer, New York, 1973.

[121] Matsunawa, A., Semak, V., The simulation of front keyhole wall dynamics during laser welding. *J. Phys. D: Appl. Phys.*, 1997, **30**, 798–809.

[122] Semak, V., Matsunawa, A., The role of recoil pressure in energy balance during laser materials processing. *J.Phys. D:Appl. Phys.*, 1997, **30**, 2541-2552.

[123] Han, L., Liou, F. W., Musti, S., Thermal behavior and geometry model of melt pool in laser material process, *J. Heat Transfer*, 2005, **127**, 1005-1014.

[124] Kogelnik, H., and Li, T., Laser Beams and Resonators. *Appl. Opt.*, 1956, **5**, 1550-1565.

[125] Glorieux, B., Millot, F., Rifflet, J. C. , Surface tension of liquid alumina from contactless techniques. *Int. J. Thermophys.*, 2002, **23**, 1249-1257.

[126] Semak, V. V., Knorovsky, G. A., MacCallum, D. O., Roach, R. A., Effect of surface tension on melt pool dynamics during laser pulse interaction. *J. Phys. D: Appl. Phys.*, 2006, **39**, 590–595.

[127] Miyazaki, T., Yoshioka, S. and Kimura, T., Ejection of molten material produced by pulsed electron and laser beams. *Precision Engineering* , 1988, **10**, 141-146.

[128] Atanasov, P. A., Eugenieva, E. D. and Nedialkov, N.N., Laser drilling of silicon nitride and alumina ceramics: A numerical and experimental study. *J. of Appl. Phys*., 2001, **89**, DOI: 10.1063/1.1334367.

[129] Perry, D. L., Phillips, S. L., *Handbook of Inorganic Compounds* , CRC Press INC, Florida, 1995.

[130] Murray, J. P., Flamant, G., Roos, C. J., Silicon and solar-grade silicon production by solar dissociation of Si_3N_4. *Solar Energy*, 2006, **80,** 1349- 1354.

[131] Kosolapova, T. Ya., *Handbook of High Temperature Compounds: Properties, Production, Applications*, Hemisphere Publishing Corporation, New York, 1990.

[132] Yuan, Z. F., Mukai, K., and Huang, W. L., Surface temperature and its temperature coefficient of molten silicon at different oxygen potentials. *Langmuir*, 2002,**18,** 2054-2062.

[133] Reitano, R. and Baeri, P., Nanosecond laser-induced thermal evaporation of silicon carbide. *Int. J. Thermophys.*, 1996, **17**, 1079-1087.

[134] Yabe, T., Mohamed, M.S., Uchida, S., Baasandash, C., Sato, Y., Tsuji, M., Mori, Y., Noncatalytic dissociation of MgO by laser pulses towards sustainable energy cycle. *J.Appl.Phys.*, 2007, **101,** DOI: 10.1063/1.2743730.

[135] Brewer, L. and Porter, R.F., A thermodynamic and spectroscopic study of gaseous Magnesium Oxide. *J. Chem. Phys.*, 1954, **22**, 1867-1877.

[136] Weimin, Z., Yong, S., Haipeng, L., Chunyong, L., The effects of some elements on the igniting temperature of magnesium alloys. *Mater. Sci. Eng., B*, 2006, **127,** 105-107.

[137] Massalski, T.B., Okamoto, H., Subramanian, P.R. and Kacprzak, L., *Binary alloy phase diagrams*. ASM International, Materials Park, OH, 1990.

[138] Samant, A. N. and Dahotre, N. B. In-situ absorptivity prediction during low aspect ratio 1.06 μm wavelength laser machining of structural ceramics. *Phys. Status Solidi*, in press, DOI: 10.1002/pssa.200925108.

[139]Buttsworth, D.R., Assessment of effective thermal product of surface junction thermocouples on millisecond and microsecond time scales. *Exp. Therm Fluid Sci.*, 2001, **25**, 409- 420.

[140] Kim, K.D., Rizwan-uddin, A web-based nuclear simulator using RELAP5 and LabVIEW. *Nucl. Eng. Des.*, 2007, **237**, 1185-1194.

[141] Singh, R., Alberts, M. J., Melkote, S. M., Characterization and prediction of the heat-affected zone in a laser-assisted mechanical micromachining process. *Int. J. Mach. Tools Manuf.*, 2008, **48**, 994-1004.

[142] Riethof, T. R. and DeSantis, V.J., *Measurement of thermal radiation properties of solids* edited by J. C. Richmond, National Aeronautics and Space Administration, Washington, D.C., 1963.

[143] Price, D. J., The temperature variation of the emissivity of metals in the near infra-red. *Proc. Phys. Soc.*, 1947, **59**, 131- 138.

[144] Ravindra, N. M., Abedrabbo, N. M., Chen, W. , Tong, F. M., Nanda, A. K. and Speranza, A. C., Temperature-dependent emissivity of silicon-related materials and structures. *IEEE Trans. Semicond. Manuf.* , 1998, **11**, 30- 39.

[145] Ravindra, N. M., Tong, F.M., Abedrabbo, S., Chen, W., Schmidt, W., Nanda, A., Speranza, T. and Tello, T., Applications of spectral emissometry to silicon relater materials. In: *Proceedings of Fourth Int. Conf. Rapid Thermal Processing*, Boise, ID, 1996, p 190-204.

[146] Barsoum, M. W., *Fundamentals of Ceramics*, Institute of Physics Publishing, Philadelphia, PA, 1997.

[147] Wu, C. C., Tsai, J., Lin, C. J., Free-carrier absorption in n-type gallium arsenide in quantizing magnetic fields, *Phys. Rev. B*, 1991, **43**, 7328- 7331.

[148] Kingery, W. D., Bowen, H. K., Uhlmann, D.R., *Introduction to Ceramics*, J Wiley & Sons, New York, 1976.

[149] Fox, M., *Optical Properties of Solids,* Oxford University Press Inc., New York, 2001.

[150] Samant, A. N., and Dahotre, N. B., Absorptivity transition in 1.06 μm wavelength laser machining of structural ceramics. *Int. J. Appl. Ceram. Technol.*, in press.

[151] Samant, A. N., Harimkar, S. P., and Dahotre, N. B., Laser beam operation mode dependent grain morphology of alumina. *J. Appl. Phys.*, 2007, **102**, 123105.

[152] Ahlström, J., Karlsson, B. and Niederhauser, S., Modeling of laser cladding of medium carbon steel- a first approach. *J. Phys. IV France*, 2004, **120**, 405- 412.

[153] Arnold, N., Kullmer, R. and Bäuerle, D., Simulation of growth in pyrolytic laser- CVD of microstructures-I. One-dimensional approach. *Microelectron. Eng.*, 1993, **20**, 31-41.

[154] Liu, X., Du, D. and Mourou, G., Laser ablation and micromachining with ultrashort laser pulses. *Quantum Electron.*, 1997, **33,** 1706-1716.

[155] Pronko, P. P. , Dutta, S. K., Squier, S. K., Rudd, J. V. , Du, D. and Mourou, G., Machining of sub-micron holes using a femtosecond laser at 800 nm. *Opt. Commun.*, 1995, **114**, 106-110.

[156] Shirk, M.D. and Molian, P. A., A review of ultrashort pulsed laser ablation of materials. *J. Laser Appl.*, 1998, **10**, 18-28.

[157] Jandeleit, J., Horn, A., Weichenhain, R., Kreutz, E.E. and Poprawe, R., Fundamental investigations of micromachining of nano-and picosecond laser radiation. *Appl. Surf. Sci.*, 1998, **127-129**, 885-891.

[158] Chen, X., Liu, X., Short pulsed laser machining: How short is short enough. *J. Laser Appl.*, 1999, **11(6)**, 268-272.

[159] Harilal, S. S., Bindhu, C.V., Issac, R. C., Nampoori, V. P. N. and Vallabhan, C.P.G., Electron density and temperature measurements in a laser produced carbon plasma. *J. Appl. Phys.*, 1997, **82(5)**, 2140-2146.

[160] Griem, H.R., *Plasma Spectroscopy*, McGraw Hill, New York, 1964.

[161] Yaws, C. L., *Chemical Properties Handbook*, Mc Graw Hill, New York, 1991.

[162] Copley, S.M., Laser shaping of materials. In *Proceedings of ASM Conference on Lasers in Materials Processing*, Los Angeles, CA, 1983.

[163]Copley, S.M., Shaping ceramics with lasers. *Interdisciplinary Issues in Material Processing and Manufacturing*, 1987, 631.

[164] Modest, M. F., Transient model for CW and pulsed laser machining of ablating/decomposing materials—approximate analysis. *J. Heat Transfer*, 1996, **118 (3),** 774–780.

[165]Modest,M.F.,Three-dimensional, transient model for laser machining of ablating/decomposing materials. *Int. J. Heat Mass Transfer*, 1996, **39 (2)**, 221–234.

[166] Samant, A. N., and Dahotre, N. B., Three- dimensional laser machining of structural ceramics. *J. Manuf . Processes*, under review.

[167] Samant, A. N., and Dahotre, N. B., Physical effects of multipass two dimensional laser machining of structural ceramics. *Adv. Eng. Mater.*, in press, DOI: 10.1002/adem.200900056.

[168] Gilbert, T., Krstic, V. D. and Zak, G., Machining of aluminum nitride with ultra-violet and near-infrared Nd:YAG lasers. *J. Mater. Process. Technol.*, 2007, 189, 409-417.

APPENDICES

APPENDIX A:
List of publications produced during the course of study by the author

Journal Publications

[1] **Samant, A.N.**, Harimkar, S.P. and Dahotre, N.B., Laser beam operation mode dependent grain morphology of alumina. *J. Appl. Phys.* 2007, **102**, 123105

[2] Kurella, A., **Samant, A.N.**, Dahotre, N.B., Laser surface multilevel self assembly of CaP-TiO_2 particles. *J. Appl. Phys.*, 2009, **105**, 014913 (*selected for the January 26, 2009 issue of Virtual Journal of Nanoscale Science & Technology)*

[3] Harimkar, S.P., **Samant, A.N.**, Dahotre, N.B., Temporally evolved recoil pressure driven melt infiltration during laser surface modifications of porous alumina ceramic. *J. Appl. Phys*, 2007, **101**, 054911.

[4] **Samant, A.N.**, and Dahotre, N.B., Multilevel residual stress evaluation in laser surface modified alumina ceramic. *Appl. Phys. A*, 2008, **90**, 493–499.

[5] Harimkar, S.P., **Samant, A.N.**, Khangar, A.A., Dahotre, N.B., Prediction of solidification microstructures during laser dressing of alumina-based grinding wheel material. *J.Phys.D:Appl.Phys.* , 2006, **39,** 1642-1649.

[6] **Samant, A.N.**, Harimkar, S.P., and Dahotre, N.B., The laser surface modification of advanced ceramics – A modeling approach. *JOM*, 2007, **59(8)**, 35-38

[7] **Samant, A.N.**, Paital, S.R. and Dahotre, N.B., Process optimization in laser surface structuring of alumina. *J. Mater. Process. Technol.* 2008, **203,** 498-504.

[8] **Samant, A.N.**, and Dahotre, N.B., Computational predictions in single dimensional laser machining of alumina. *Int. J. Mach. Tools Manuf* ., 2008, **48,** 1345-1353.

[9] **Samant, A.N.**, and Dahotre, N.B., Ab initio physical analysis of single dimensional laser machining of silicon nitride. *Adv. Eng. Mater.*, 2008, **10,** 978-981.

[10] **Samant, A.N.**, and Dahotre, N.B., An integrated computational approach to single dimensional laser machining of magnesia. *Opt. Lasers Eng.*, 2009, **47,** 570-577.

[11] **Samant, A.N.**, and Dahotre, N.B., Differences in physical phenomena governing laser machining of structural ceramics. *Ceram. Int.*, 2009, **35**, 2093-2097.

[12] **Samant, A.N.**, and Dahotre, N.B., Laser machining of structural ceramics- A review., *J. Eur. Ceram. Soc.* 2009, **29**, 969-993.

[13] **Samant, A.N.**, Dahotre, N.B., Computational prediction of grain size during rapid laser surface modification of Al-O ceramic. *Phys. Status Solidi RRL* , 2006, DOI: 10.1002.

[14] Du, B., **Samant, A.N.**, Paital, S.R., and Dahotre, N.B. Pulsed laser synthesis of ceramic-metal composite coating on steel. *Appl. Surf. Sci.*, 2008, **255,** 3188-3194.

[15] Chen, Y., **Samant, A.**, Balani, K., Dahotre, N.B., and Agarwal, A., Laser melting of plasma sprayed aluminum oxide coatings reinforced with carbon nanotubes. *Appl. Phys. A.*, 2009, **94,** 861-870.

[16] Basu, A., **Samant, A.N.**, Harimkar, S.P., Majumdar, J.D., Manna, I., Dahotre, N.B., Laser surface cladding of Fe-Cr-Mo-Y-B-C bulk metallic glass on AISI 4041 steel. *Surf. Coat. Technol.* , 2008, **202**, 2623– 2631.

[17] Engleman, G.P., Kurella, A., **Samant, A.N.,** Blue, C.A., Dahotre, N.B. ,The application of laser- induced multi- scale surface texturing. *JOM* , 2005, **57**, 46-50.

[18] **Samant, A.N.**, Daniel, C., Chand, R.H., Blue, C.A., and Dahotre, N.B., Computational approach to photonic drilling of silicon carbide. *Int. J. Adv. Manuf. Technol.*, in press, DOI: 10.1007/s00170-009-2004-0.

[19] **Samant, A.N.**, Du, B., Paital, S.R., Kumar, S., and Dahotre, N.B., Pulsed laser surface treatment of magnesium: Correlation between thermal model and experimental observations. *J. Mater. Process. Technol.*, 2009, **209**, 5060-5067.

[20] **Samant, A.N.**, and Dahotre, N.B., Physical effects of multipass two dimensional laser machining of structural ceramics. *Adv. Eng. Mater.*, in press, DOI: 10.1002/adem.200900056.

[21] **Samant, A.N.**, and Dahotre, N.B., Absorptivity transition in 1.06 μm wavelength laser machining of structural ceramics. *Int. J. Appl. Ceram. Technol.*, in press.

[22] **Samant, A.N.**, Du, B., and Dahotre, N.B., In-situ surface absorptivity prediction during 1.06 μm wavelength low aspect ratio machining of structural ceramics. *Phys. Status Solidi.*, in press, DOI: 10.1002/pssa.200925108.

[23] **Samant, A.N.**, and Dahotre, N.B., Three-dimensional laser machining of structural ceramics. *J. Manuf . Processes*, under review.

[24] Dahotre, N. B., Paital, S.R., **Samant, A.N.**, Daniel, C., Wetting behavior of laser synthetic surface micro textures on Ti-6Al-4V for bioapplication. *Philosophical Transactions of Royal Society-A*, under review.

Conference Proceedings

[1] **Samant, A.N.**, and Dahotre, N.B., Laser-assisted rapid surface microstructuring of alumina ceramic. In: Proceedings of 2009 NSF Engineering Research and Innovation Conference, Honolunu, Hawaii, June 2009.

Presentations and Posters

[1] **Samant, A.N.** and Dahotre, N.B., Laser micro-machining of structural ceramics, invited talk at the *MSE Graduate Seminar* in the Department of Materials Science & Engineering, University of Tennessee, Knoxville, TN, February 2009

[2] **Samant, A.N.** and Dahotre, N.B., Ab-initio computational approach to laser micro-machining of structural ceramics, oral presentation at the *Annual Sigma Xi Student Competition*, University of Tennessee, Knoxville, TN, April 2009

[3] **Samant, A.N.** and Dahotre, N.B., Process optimization in laser processing of ceramics, oral presentation at *TMS Annual Meeting & Exhibition*, New Orleans, LA, March 2008

[4] **Samant, A.N.** and Dahotre, N.B., Photonic machining of structural ceramics, oral presentation at *MS&T 08 Conference*, Pittsburgh, PA, October 2008

[5] **Samant, A.N.** and Dahotre, N.B., Laser- assisted rapid surface microstructuring of alumina ceramic, poster presented at the *NSF CMMI Research and Innovation Conference*, Honolunu, HI, June 2009

[6] **Samant, A.N.** and Dahotre, N.B., Laser Processing of Ceramics: A Modeling Approach, poster presented at the *Oak Ridge Chapter of ASM, the Materials Information Society and the Smoky Mountain Chapter of the Society of Plastic Engineers*, Knoxville, TN, November 2007

[7] **Samant, A.N.** and Dahotre, N.B., Laser machining of structural ceramics, poster presented at *MS&T 08 Conference*, Pittsburgh, PA, October 2008 & *the Oak Ridge Chapter of ASM, the Materials Information Society and the Smoky Mountain Chapter of the Society of Plastic Engineers*, Knoxville, TN, November 2008

[8] **Samant, A.N.** and Dahotre, N.B., Laser-ceramic interaction: A modeling approach, poster presented at *TMS Annual Meeting & Exhibition*, New Orleans, LA, March 2008

[9] Harimkar, S.P., **Samant, A.N.**, Khangar, A.A., Dahotre, N.B., Transient thermal and microstructural evolutions in alumina during laser surface modification, poster presented at the *Oak Ridge Chapter of ASM, the Materials Information Society and the Smoky Mountain Chapter of the Society of Plastic Engineers*, Knoxville, TN, November 2005

APPENDIX B: Journal articles related to the subject matter by the author

International Journal of Machine Tools & Manufacture 48 (2008) 1345–1353

Contents lists available at ScienceDirect

International Journal of Machine Tools & Manufacture

journal homepage: www.elsevier.com/locate/ijmactool

Computational predictions in single-dimensional laser machining of alumina

Anoop N. Samant, Narendra B. Dahotre *

Department of Materials Science and Engineering, The University of Tennessee, Knoxville, TN 37996, USA

ARTICLE INFO

Article history:
Received 25 January 2008
Received in revised form
15 May 2008
Accepted 25 May 2008
Available online 7 July 2008

Keywords:
Machining
Alumina
Pulsed mode laser
Recoil pressure

ABSTRACT

Machining of alumina was investigated in this study by using a JK 701 pulsed Nd:YAG laser. A hydrodynamic machining model was developed which incorporated the effect of multiple reflections on the amount of laser energy absorbed, the thermal effects for melting the material, vapor pressure effect for expelling out the molten material, material losses due to evaporation and the inverse effect of surface tension on the expelled depth .The model also incorporated the transient effect of laser beam de-focusing due to change in machined depth as a function of expelled material during machining for precise estimation of the melted depth during each pulse. It was observed that the material removal was a combination of melt expulsion and evaporation processes. The developed model would be an excellent tool for advance prediction of the total thermal energy and time required for removal and/or machining of desired depth of material.

1. Introduction

Outstanding mechanical and physical properties like high hardness, chemical stability and high thermal resistance have encouraged the use of engineering ceramics such as alumina, silicon nitride, zirconia and silicon carbide in several applications. These ceramics are widely used for making machine tools, valves, rotors, optical and electronic devices [1–5] and in medical applications for components such as artificial joints [6,7].

High hardness and brittleness make the ceramics difficult to machine using conventional techniques that are mostly based on mechanical grinding and fracturing (cutting). The damage caused on the surface by the machining of ceramics employing these techniques can affect the strength and efficiency of the components thereby creating a hurdle in their widespread utilization in above-mentioned applications. Hence, a vital step in the manufacturing of ceramic components is their cost-effective machining with excellent quality. Extensive research on precision machining of ceramic components has been conducted over the past several years, developing numerous advanced technologies in grinding, cutting and polishing. Out of all the techniques for ceramic machining, grinding is still considered to be the most desirable and reliable [8]. Although conventional grinding fulfills the necessities for dimensional accuracy and surface finish, prohibitively longer times to machine them and high machining costs amounting to 60–90% of the final cost of the end product pose a major drawback for the grinding process [9,10]. Furthermore, ground products often demonstrate surface and subsurface cracks [11–13], some amount of plastic deformation [14], pulverization layers [15,16] and significant surface residual stresses [17]. Hence, there is a requirement for ceramic processing techniques which can reduce tool wear, enhance the material removal rates and improve the surface finish of the components.

Ultrasonic machining removes materials by the impact motion of ultrasonically vibrated abrasive particles. However, the mechanism of material removal is not very well documented, thus making the process optimization difficult [18]. Recent developments in the field of electrical discharge machining (EDM) have permitted the use of this technology for manufacturing conductive ceramic materials [19]. Electro-chemical discharge machining (ECDM) which has combined features of EDM and electrochemical machining (ECM) is capable of machining high strength electrically non-conductive materials. However, as a significant portion of the total heat developed is dissipated for increasing the temperature of the electrolyte, the material removed while machining is less, thus making the process incompetent [20].

Over the past few years, laser machining (LM) has been considered as a potential technique for acquiring high material removal rates in machining ceramic materials [6]. Laser machining is an operation similar to laser drilling subsequently conducted on neighboring locations. Both the processes involve material removal via melting or decomposition, and vaporization and physical expulsion of these phases from the region of laser–material interaction. Thus the physical phenomena governing both machining and drilling are similar. The temporally and spatially intense and restricted heat source of laser power provides an extremely efficient method to increase the

* Corresponding author. Tel.: +1 865 974 3609; fax: +1 865 974 4115.
E-mail address: ndahotre@utk.edu (N.B. Dahotre).

0890-6955/$ - see front matter © 2008 Elsevier Ltd. All rights reserved.
doi:10.1016/j.ijmachtools.2008.05.004

temperature of the work piece making the machining process convenient.

Escalating interest in the use of lasers for manufacturing can be attributed to the several benefits such as non-contact processing, capability of automation, reduced manufacturing costs, efficient material utilization, reduced heat-affected zone (HAZ), high productivity and eradication of finishing operations [21,22]. Laser machining of ceramics is widely used in the aerospace industry for generating closely spaced holes in turbine engine components and also in the micro-electronics industry for drilling holes with high aspect ratios at designated locations [23]. Pulsed lasers can be successfully used to carry out micro-drilling on zirconia and the process parameters can be controlled to drill holes in the zirconia ceramic [21] which can be used in bearings, oxygen sensors, fuel cells and pH meters [24]. The hole diameter at the entry is more than the diameter at the exit leading to a positive taper to several of the drilled holes. However, this effect can be minimized by using a lens of long focal length with longer focal waist. As laser drilling has tremendous applications, understanding the drilling mechanism is extremely vital in order to efficiently control the processing parameters and thus the associated surface features.

Alumina is widely used as a substrate in hybrid circuits as it possesses high dielectric strength and thermal stability [25,26]. Due to its high hardness, strength and corrosion resistance at high temperature, machining of alumina is carried out for different applications. During laser machining, the phenomena occurring in the area of interaction between the laser beam and the ceramic such as but not limited to material removal, ablation, melting, evaporation, absorption of energy by the solid, and reflection of energy from the surface depend on the processing parameters (energy, repetition rate, pulse duration and peak power of the laser) and on the chemical and physical properties of the material. Hence, the present study aims at understanding the physical phenomena underlying the machining of alumina ceramic by pulsed Nd:YAG laser and develops a computational approach to predict the effect of the laser processing parameters on the depth of the machined region. In this approach, single-dimensional laser machining of ceramics for applications such as drilling has been demonstrated. Multidimensional laser machining of ceramics by the linear or non-linear movement of the laser beam for applications such as cutting will be discussed in future work.

2. Laser processing

Dense alumina ceramic obtained from a commercial source (Coorstek, Golden, CO) in the form of disc of 89 mm diameter and 4 mm thickness was used for the machining purpose. The alumina surface was exposed to a JK 701 pulsed Nd:YAG laser (1064 nm wavelength) from GSI Lumonics, Rugby, England. The laser offered pulse energies from 0.1 to 55 J, repetition rates from 0.2 to 500 Hz, and the pulse width from 0.3 to 20 ms. By varying the repetition rate, peak power and pulse width in different combinations, a set of parameters were recognized that generated adequate interaction between the laser beam and the ceramic surface for required machining of alumina disc. For a pulse energy of 4 J, repetition rate of 20 Hz and a pulse width of 0.5 ms, reasonable interaction was observed between the laser and the ceramic surface that was capable of machining a cavity. Hence for this set of parameters, several pulses (5, 10, 20 and 30) were applied on the ceramic surface and the corresponding depth in the cross-section of machined cavity was measured from the optical micrograph (Fig. 1). The figure also includes the top views of machined cavities on the top surface of the alumina disc. The given number of pulses were chosen to machine blind cavities of various depths and also a cavity through the entire thickness of plate. The number of pulses were applied to the ceramic randomly and not in any systematic order in order to avoid the influence of lurking variables such as change of surrounding temperature, relative humidity and so on that could affect the drill depth to some extent. Thus the standard procedure of randomizing the experimental runs was implemented in this study. It was observed that under the present set of laser parameters (4 J, 20 Hz, 0.5 ms) application of 30 pulses machined through the entire thickness of the alumina disc (4 mm). However, foresighting the exact number of pulses required to machine a certain cavity depth is an exigent task. Hence, developing a mathematical model

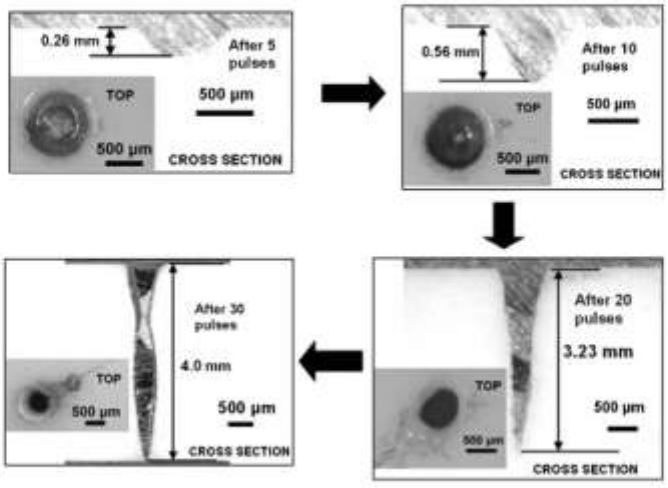

Fig. 1. Cross-sectional and top views of the cavities machined in alumina disc with different number of pulses.

based on the processing data for such predictions is the most suitable approach.

3. Computational predictions

Laser machining is accomplished when the work piece absorbs laser energy and this photon energy gets converted into thermal energy. The magnitude of the laser energy absorbed depends on the initial absorptivity of the material and the amount of multiple reflections within the machined cavity. The temperature at the surface of the ceramic changes because of this absorbed energy. When the temperature rises beyond the melting point or the decomposition temperature, the phase of the material changes and it melts and/or evaporates [27]. The high peak intensity of the pulse generates strong evaporation pressure which is responsible for ejection of this molten material and material loss at the surface due to evaporation for generation of machined depth. However, the surface tension of molten material reduces the depth of penetration to some extent [28]. Although, in the past majority of works have considered material removal only through direct evaporation [29–32] in the present work the material removal will be based on a mixed phenomenon comprising of both the melt expulsion and evaporation. The above-mentioned effects will be systematically considered in the present study. A complete model of material removal (machining) by laser beam interaction with the ceramic surface could consider many more phenomena than those considered here. Complexities generated by other physical processes during laser–material interactions will be demonstrated in subsequent publications. As the physical processes occurring along the depth are entirely different from those occurring at the surface, this study aims at predicting only the depth rather than estimating the width (diameter of a machined cavity) of material removed/machined at the surface. Efforts are on going to predict the width of material machined (diameter) and will be incorporated in due course of time.

3.1. Temporal evolution

To estimate the depth of machined region for a given set of laser processing parameters considering the above mentioned effects, the temperature at the surface and the corresponding thermal gradient within the material were predicted. The heating during pulse on and the subsequent cooling during pulse off over the entire time of machining operation were considered for determining the heating curve by taking into account the ON and OFF times during machining under present set of laser parameters. The schematic illustrating the pulse ON–OFF is shown in Fig. 2 while the process parameters and the corresponding machined depths measured optically are represented in Table 1.

There is a temperature drop when the laser is switched off after the first pulse which is followed by a temperature rise when the laser is switched on again for the next pulse. The simulations were run till the operation time was completed for each case. A detailed procedure explaining the predictions of depth of material removed (machined) from the alumina disc will be explained in the later sections. The computations were started with estimation of the maximum temperature reached after the first pulse by using a three-dimensional heat transfer flow model developed in COMSOL's heat transfer mode [33] using Fourier's second law of heat transfer:

$$\frac{\partial T(x,y,z,t)}{\partial t} = \alpha(T)\left[\frac{\partial^2 T(x,t)}{\partial x^2} + \frac{\partial^2 T(y,t)}{\partial y^2} + \frac{\partial^2 T(z,t)}{\partial z^2}\right] \tag{1}$$

where T is the temperature field, t is the time and x, y and z are the spatial directions. The term $\alpha(T)$ is the temperature-dependent thermal diffusivity of the material which is given by $k(T)/\rho C_p(T)$, where ρ is the density (3.8 g/cm^3) [34], $C_p(T)$ is the temperature-dependent specific heat of the material (J/kg K) and $k(T)$ is the temperature-dependent thermal conductivity of the material (W/m K) [35]. At time $t = 0$, the initial temperature of $T = T_0 = 300$ K was applied. The equilibrium between the laser energy absorbed at the surface and the losses due to radiation is given by

$$-k(T)\left(\frac{\partial T(x,y,0,t)}{\partial x} + \frac{\partial T(x,y,0,t)}{\partial y} + \frac{\partial T(x,y,0,t)}{\partial z}\right) = \delta\alpha I - \varepsilon\sigma(T(x,y,0,t)^4 - T_0^4)$$

$$\delta = 1 \quad \text{if} \quad 0 \leq t \leq t_p$$
$$\delta = 0 \quad \text{if} \quad t > t_p \tag{2}$$

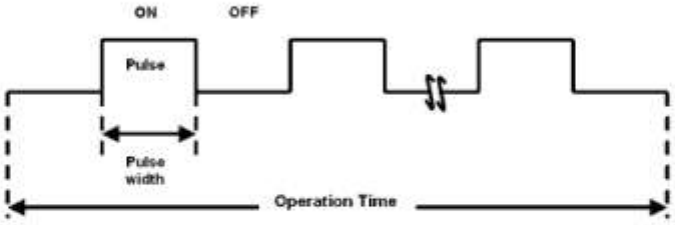

Fig. 2. Schematic of pulse ON–OFF.

Table 1
Parameters of laser processing

Number of pulses	Operation time (s)	Pulse width (ON time) (ms)	OFF time (ms)	Total ON time (ms)	Total OFF time (ms)	Cavity depth (mm)
5	0.25	0.5	49.5	2.5	247.5	0.26
10	0.5	0.5	49.5	5.0	495.0	0.56
20	1.0	0.5	49.5	10.0	990.0	3.23
30	1.5	0.5	49.5	15.0	1485.0	4.0

where k is the thermal conductivity of the material (W/m K), ε is emissivity for thermal radiation (0.7) [35], α is the absorptivity of the material (0.8) [34], I is laser power intensity, t_p is the operation time and σ is the Stefan–Boltzmann constant (5.67×10^{-8} W/m^2 K^4). Laser-induced machining is a rapid heating and cooling process due to which the thermophysical properties of materials exposed to the laser beam change rapidly in a large temperature range. Changes in thermal conductivity and specific heat as a function of temperature [35] (Fig. 3) were incorporated to provide better accuracy in calculations. The latent heat of fusion was taken into account by including the variation of specific heat as a function of temperature.

Multiple reflections of the laser beam are extremely important for high aspect ratio drill cavities (Fig. 1) and they govern the flow of energy from the laser to the surface of the material being machined [36]. This phenomenon has been incorporated into the machining process in different ways [37–41]. Bang and Modest [42] found that the effective absorptivity of the material is increased due to the phenomena of multiple reflections and in process such as high aspect ratio laser drilling it is expected to instantaneously reach the value of 100% [43,44]. Nonetheless, accurate in-situ absorptivity measurements being difficult for rapid process like laser processing, in this study, for comparison purpose the computations were conducted by considering three different values of absorptivity that included the literature value of 0.8 mentioned above [34], 0.9 and 1 (corresponding to an absorption of 100%). The resultant effect of these absorptivity values on the machined depth is discussed later. Although it is very difficult in an extremely short duration high-energy density dynamic process like laser–material interaction to accurately conduct in-situ absorptivity measurements, attempts are going on in parallel to measure the actual absorptivity values under the laser processing conditions similar to the ones employed in the present work and they will be incorporated in the future calculations. The convection occurring at the bottom surface of the disc is given by

$$-k(T)\left(\frac{\partial T(x,y,L,t)}{\partial x}+\frac{\partial T(x,y,L,t)}{\partial y}+\frac{\partial T(x,y,L,t)}{\partial z}\right) = h(T(x,y,L,t)-T_0) \tag{3}$$

where L is the thickness of the disc (4 mm) and $h(T)$ is the heat transfer coefficient (W/m^2 K) considered as a function of temperature. It was assumed that no heat loss took place through the other surfaces. The variation of heat transfer coefficient was also included as a function of temperature [45]. After solving this model, the maximum surface temperature reached after the first pulse was determined which was input in Eq. (4) below to predict the temperature reached after the laser is switched off [27]:

$$T_i' = T_i + (T_0 - T_i)\left[1 - \left[\exp\frac{t_{off}\alpha(T)h(T)^2}{k(T)^2}\right] \times \left[1 - \mathrm{erf}\left(\frac{h\sqrt{t_{off}\alpha(T)}}{k(T)}\right)\right]\right] \tag{4}$$

where T_i is the temperature during heating of pulse i (K), T_0 is the ambient temperature of 300 K, t_{off} is the OFF period between successive pulses and erf ( ) is the error function. When the laser is active, the surface temperature is given by [27]

$$T_i = T_{i-1}' + \frac{2\alpha W\sqrt{t_{on}\alpha(T)/\pi}}{\pi r^2 k(T)} \tag{5}$$

where T_{i-1}' is the temperature during cooling of the earlier pulse (K) predicted from Eq. (4) above, W is the incident beam power, t_{on} is the pulse duration and r is the beam radius (0.12 mm). The temperatures reached during the ON and OFF periods of the successive pulses were determined by repeatedly solving Eqs. (4) and (5) till the operation time was reached.

As this study does not focus on the microstructure evolution after the pulsing was stopped, the cooling curves have not been discussed. By tracking the depth at which the melting point or decomposition temperature of alumina (2323 K [46]) was reached, the melt depth (z_c) from the surface at any instant was estimated from the heating curves and further depth calculations were based on this depth. Alumina is stable up to the melting point after which it melts and forms the liquid which is stable till about 3500 K. Due to the dissociation of alumina at temperatures above 3250 K, sub-oxides of aluminum, aluminum metal vapor and oxygen gas are formed. The majority of the stable species formed above 3250 K comprises of $AlO_{(g)}$ and $Al_{(g)}$ while minor amounts of $Al_2O_{(g)}$ and $AlO_{2(g)}$ are formed. At temperatures above 5000 K, the sub-oxides dissociate completely forming aluminum vapor and atomic oxygen [47]. Laser machining takes place due to the expulsion of the liquid phase formed during the dissociation process as can be seen from the presence of several droplets or humps of solidified material around the drilled hole. (Fig. 1)

However, some material was lost at the surface due to evaporation and the rate of evaporation j_e (kg/m^2 s) was given by

$$j_e = p(T_s)\left[\frac{m_v}{2\pi kT_s}\right]^{1/2} \tag{6}$$

where m_v is mass of vapor molecule (molecular weight of alumina/Avogadro's number = 1.693×10^{-25} kg/at), k is the Boltzmann constant (1.38065×10^{-23} J/K), T_s is the surface temperature and $p(T_s)$ is the saturation pressure given by Clausius–Clapeyron equation:

$$p(T_s) = p_0 \exp\left[\frac{L_e/kT_e}{1 - T_e/T_s}\right] \tag{7}$$

where p_0 is the ambient pressure (1.013×10^5 N/m^2), L_v is latent heat of evaporation (10665 J/g) [34] and T_e is the vaporization temperature (3253 K [48]). The corresponding depth of material evaporated at a given instant was predicted from the rate of evaporation by the relation:

$$z_{eva} = \frac{j_e \times \text{increment in time}}{\rho} \tag{8}$$

The cumulative evaporated depths (for 100% absorption) at different time instants is represented in Fig. 4. The evaporated depth (z_{eva}) was subtracted from the melt depth (z_c) to give the available melt pool (z_{eva}). The corresponding drop in temperature at any instant at the surface because of the cooling of the melt pool by evaporation was given by [49]

$$\Delta T_{eva} = \frac{2z_{eva}\rho L_v}{k(T)\pi d\varepsilon^{3/2}}\,\mathrm{arc\,tg}\,\frac{4\sqrt{\alpha(T)\times(\text{increment in time})}}{d} \tag{9}$$

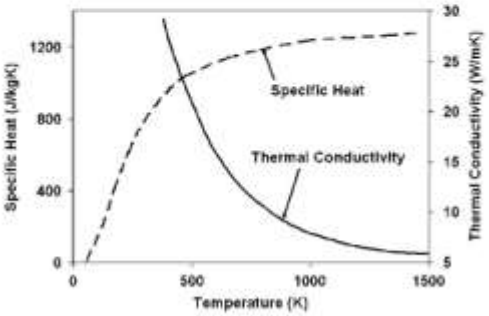

Fig. 3. Variation in specific heat and thermal conductivity with temperature [35].

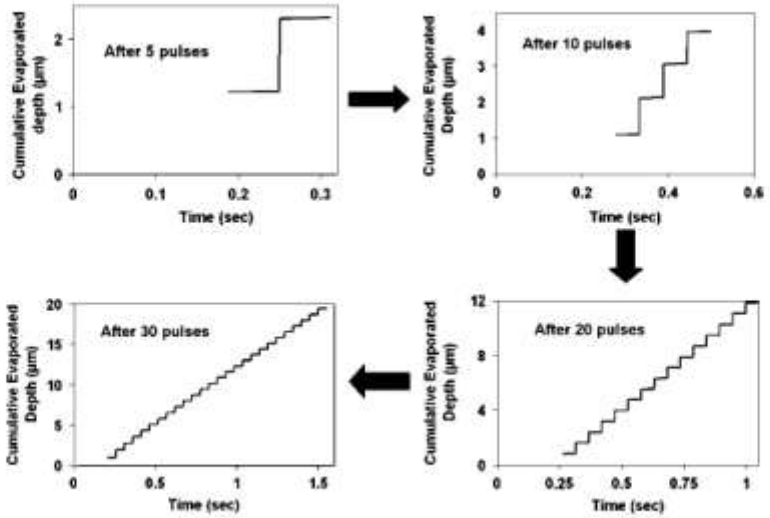

Fig. 4. Cumulative evaporated depth (for 100% absorption).

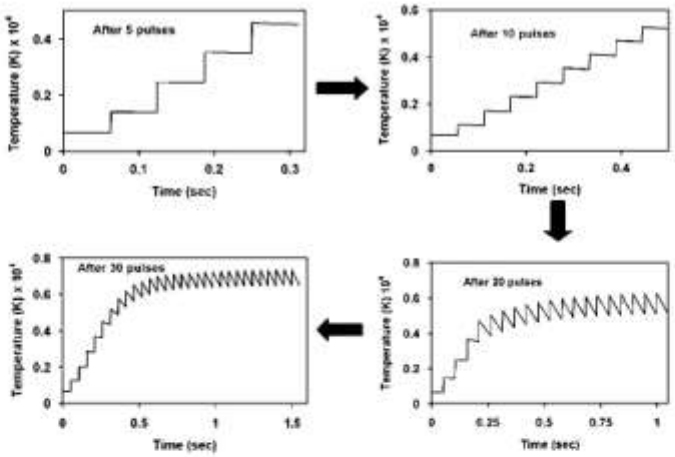

Fig. 5. Heating curves for different number of pulses (for 100% absorption).

This drop in temperature was subtracted from the temperature predicted by Eqs. (4) and (5) above to give the actual surface temperature (for 100% absorption) at any given time instant as represented in Fig. 5 which has a winding nature because the temperature drops during the OFF time and rises during the ON time of the laser. As the evaporation losses represented in Fig. 4 were a function of the surface temperature, the increase in the cumulative evaporated depth was more (steeper slope) during the ON time due to rise in temperature compared to the increase in the cumulative evaporated depth during the OFF time when the temperature drop leads to a gentle slope during the OFF time. The losses due to evaporation begin to take place after the surface temperature exceeds the vaporization temperature of alumina (3253 K [48]) after a certain number of pulses.

3.2. Recoil pressure and surface tension effects

In laser machining, material removal takes place primarily in the liquid and vapor phases. The expulsion of the molten material is driven by the recoil pressure stimulated due to the evaporation of the melt surface exposed to the laser beam [50]. The recoil

pressure stimulates ejection of the melt flow from the interaction zone at very high velocities [51]. The effective melt depth (z_{eff}) will be available for expulsion for the next time instant and it would be the portion remaining after a fraction of the available melt depth (z_{ava}) was expelled by the recoil pressure p_r given by [52]

$$\frac{\pi r^2 p_r}{aW} = \frac{1.68}{\sqrt{L_v}}\left(\frac{m}{1+2.2m^2}\right) \tag{10}$$

where L_v is latent heat of evaporation (1066.5 J/g) [34], and $m^2 = kT_s/m_v L_v$, where m_v is mass of the vapor molecule (1.693×10^{-25} kg/at) [34] and T_s is the surface temperature. Predictions of this fraction of the melt pool that is expelled by the recoil pressure will follow later in this section. In the absence of this recoil pressure, the thin film of molten material formed around the machined cavity would be responsible for closing the cavity. Thus the temperature field predicted in Section 3.1 above assisted in determining the evaporation-provoked recoil pressure at the surface during laser machining of alumina ceramic using the experimentally verified physical model of melt hydrodynamics proposed by Anisimov [52] (Eq. (10)).

It has been observed in the past that besides the recoil pressure, the surface tension also affects the melt pool shape [53] due to which it was necessary to consider the effect of surface tension as it was responsible for modifying the pressure on the melt and thus affecting the depth of the machined cavity. The laser beam gets defocused with the change in the depth of the machined cavity and the laser power density is reduced due to the increasing distance of the material surface from the focal plane [27] and the effective beam radius is given by [27,54]

$$r_{eff} = r\left[1+\left(M^2\frac{\lambda(z_{ava}+\delta_f)}{\pi r^2}\right)^2\right]^{1/2} \tag{11}$$

where M^2 is the beam quality parameter assumed to be 1 for a perfect gaussian beam profile, δ_f is the focal length of 120 mm, λ is the laser wavelength of 1064 nm and z_{ava} is the available melt depth explained earlier. Beam quality factor represents the beam

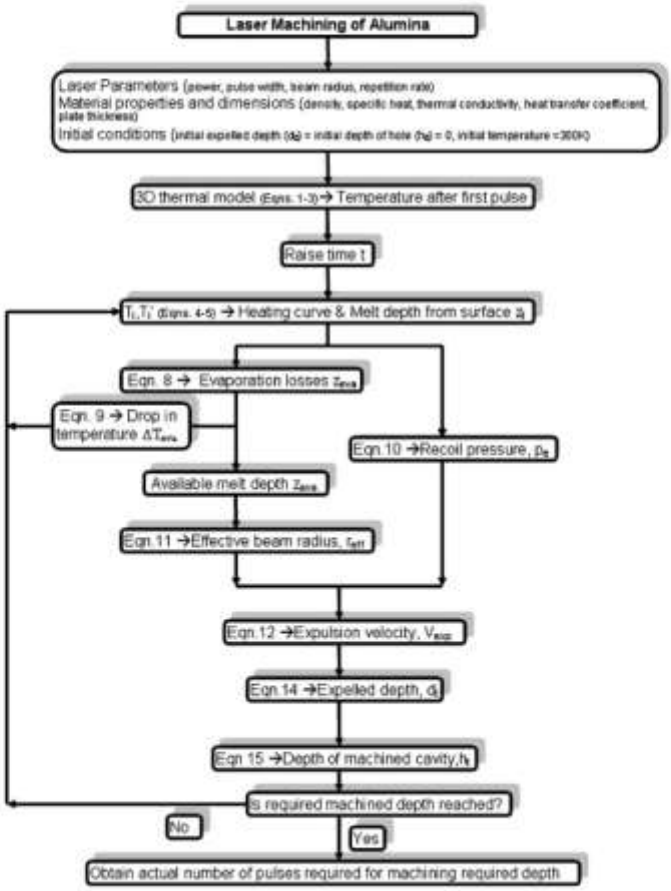

Fig. 6. Flowchart showing procedure for prediction of machined depth.

quality which is a measure of the focusability of the laser used. It was assumed in this study that the beam is initially at full focus, thus corresponding to a beam quality factor of 1. Attempts are ongoing to accurately determine M^2 and it will be incorporated in due course of time. Incorporation of actual M^2 values will take into account the complex distribution of energy taking place during the laser machining process. However, currently, the effect of the defocusing of the laser beam was accounted for by using the effective beam radius (Eq. (11) above). The surface tension pressure depends on this effective beam radius [50] and the melt available at the axis of the beam was expelled with a velocity v_{exp} given by [50]

$$v_{exp}(t) = \frac{1}{\rho}\frac{p_b - \beta/r_{eff}}{r_{eff}}t \tag{12}$$

where β is the surface tension coefficient given by

$$\beta = 0.65 \times (1 - \omega(T_s - 2500))\,\mathrm{J/m^2} \tag{13}$$

where $\omega = 6 \times 10^{-5}\,\mathrm{K^{-1}}$ is the surface tension temperature coefficient [55], r_{eff} is the effective beam radius determined above in Eq. (11) and t is the time. As the temperature reached after the first few pulses is less than the melting point of alumina, there will be no material expulsion. Hence, the expression for expulsion velocity (Eq. (12)) above does not imply for the first few pulses which are responsible for just raising the temperature of the material till the melting point is reached, after which the material expulsion process begins as governed by Eq. (12). Where as in case of through the depth machining, during application of final pulses, as explained later, only a very thin layer of the material remains which is simply pushed down from bottom by the recoil pressure. Eq. (12), therefore, does not apply to the later set of pulses during machining of a through cavity (hole). Instead, the expression is only applied for the range of pulses where the material removal mechanism remains the same and is through expulsion. Integration of the expelled velocity over time (Eq. (14)) gave the fraction of the effective melt depth that was expelled at a certain time instant, d_t, and the depth of machined cavity h_t was given by Eq. (15) [56]

$$d_t = \int_0^t v_{exp}(t)\,\mathrm{d}t \tag{14}$$

$$h_t = \sum_0^t d_t \tag{15}$$

The flow chart for attaining the final machined depth using the process parameters and material properties is presented in Fig. 6 and the computational predictions of temporal evolution of cavity machined (for 100% energy absorption) along with the schematic of different stages of cavity formation are represented in Fig. 7a and b, respectively.

The temporal evolution of the depth of the machined cavity for a given material thickness depends on the interaction time, i.e. the number of pulses to which the material is exposed because it governs the amount of energy going into the material. Hence, the evolution profile is different for different number of pulses. From this profile (Fig. 7a), comparison between experimental and predicted number of pulses and the time required for machining a certain depth of material was made in Table 2 for different absorptivity values (0.8, 0.9 and 1.0). The predicted number of pulses/machining time for absorptivity values of 0.8 and 0.9 were similar because at these two absorptivity values, the rise in temperature due to increase in input laser energy was compensated by the drop in temperature due to evaporation, thus yielding similar surface temperatures for both the cases. Hence, no significant effect was seen on the predicted number of pulses/machining time because the expulsion velocity and the machined depth were a function of the surface temperature (Eqs. (9)–(15) above).

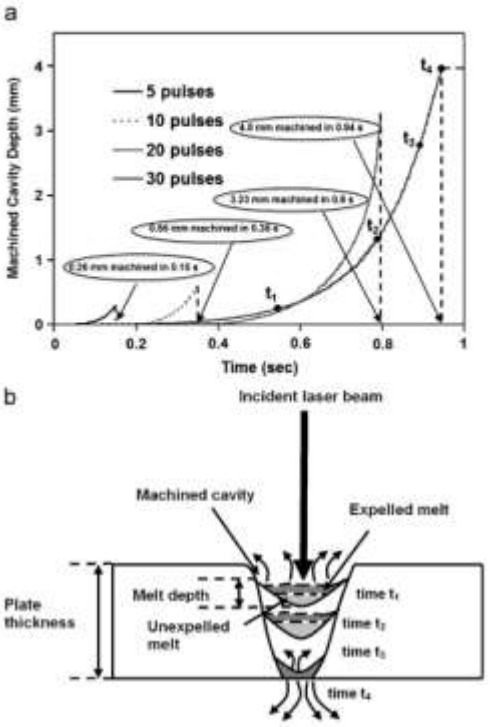

Fig. 7. Temporal evolution of machined depth during laser machining of ceramic: (a) computational predictions (for 100% absorption) and (b) schematic for progression of cavity formation.

Table 2
Comparison between number of pulses for a particular depth of machined cavity for different absorptivity values

Depth of machined cavity (mm)	Pulses$_{experimental}$ (time, s)	Pulses$_{model}$ ($a = 0.8, 0.9$) (time, s)	Pulses$_{model}$ ($a = 1.0$) (time, s)
0.26	5 (0.25)	4 (0.24)	3 (0.15)
0.56	10 (0.5)	9 (0.49)	7 (0.35)
3.23	20 (1.0)	20 (1.0)	16 (0.8)
4.0	30 (1.5)	24 (1.2)	19 (0.94)

It can also be seen from Table 2 that the number of pulses predicted from the model for absorptivity of 1.0 (considering multiple reflection phenomena) were less than those predicted by considering theoretical absorptivity value of 0.8 and 0.9. This could be attributed to the fact that when 100% energy absorption was considered, more energy was input to the material in the same amount of time thus machining more material in a shorter time. However, for all the absorptivity values considered in the present study, the predicted number of pulses was close to those actually required to machine depths of 0.26, 0.56, 3.23 and 4.0 mm. The predicted number of pulses was less than those

experimentally detected for machining because the number of pulses were chosen based on prior experience in laser processing and hence the material could have been exposed to few extra pulses even after the desired depth of the material was machined. Some error could also have been introduced while measuring the machined depth from the micrographs (Fig. 1). In addition to the above considered physical phenomena, there could be some other mechanisms which are not incorporated in this study that could have had an effect on the predicted number of pulses. Thus the presented model can assist to determine the number of pulses required for machining a certain depth in a given material under a certain set of other laser parameters.

The recoil pressure expelled the material in the upward direction and continued to do so for increased depth of machined cavity till around time instant t_2, (Fig. 7b) At around time instant t_3, when a very thin layer of the material remained in the bottom, the recoil pressure was able to push most of the material in the downward direction due to which the direction of material expulsion was reversed in the final stages of machining. In case of through depth machining, such reversal in material expulsion was because of minimum resistance to the recoil pressure by the small mass of supporting material at the bottom. Finally, all the rest of molten material was expelled and a clean through cavity was formed passing through the entire thickness of the material at around time instant t_4. Thus the prediction of exact number of pulses to machine a required depth in a given type of material under chosen set of laser processing parameters would be extremely advantageous to save significant amount of energy and time. Although in this work, other than the number of pulses all laser machining parameters were kept constant, because of their interdependence, the present computational model can be configured to predict these parameters under various combinations of processing.

4. Conclusion

Machining of different depths of alumina ceramic was successfully carried out using pulsed laser, thus demonstrating the capabilities of lasers in machining ceramics. Multiple reflections within the high aspect ratio machined cavities were responsible for increasing the amount of energy absorbed. The thermal effects were responsible for melting and evaporating the material while the recoil pressure and surface tension was responsible to expel the molten material to machine a cavity of desired depth. All these effects were integrated in a computational model and the predictions were compared with experimentally detected pulses for machining different depths of alumina disc which showed a reasonable match, thus proving the model's efficiency in foreseeing the number of pulses required for machining desired depth in a material. It was found that for increase in energy absorption from 80–90% to 100% (due to multiple reflections) by the alumina ceramic, the number of pulses required to machine depths of 0.26, 0.56, 3.23 and 4.0 mm reduced to 4, 9, 20, 24 and 3, 7, 16, 19 pulses, respectively, which were less than the number of pulses experimentally determined (5, 10, 20, and 30, respectively) to machine the same depths.

Such a comprehensive approach differentiated the current work from earlier work such as that of Miyazaki et al. [57] and Salonitis et al. [27] who considered the drilling mechanism as comprised of melting and subsequent material removal by melt expulsion where as Atanasov et al. [58] considered the drilling of alumina merely by a single-step material evaporation without any melting. On the contrary, in the present study, the material removal during the drilling process takes place due to a combination of melt expulsion and evaporation processes. Furthermore, the past studies [27,57,58] have also neglected the effect of multiple reflections on the absorbed laser energy which, has a subsequent effect on the predicted number of pulses as seen in the present study. Thus, the systematic approach considered in this study is an advancement of the existing computational approach to drilling/machining of ceramics.

References

[1] B.W. Davidge, Mechanical Behavior of Ceramics, Cambridge University Press, Cambridge, 1979.
[2] T. Warren Liao, Flexural strength of creep feed ground ceramics: general pattern, ductile–brittle transition and MLP modeling, International Journal of Machine Tools & Manufacturing 38 (4) (1998) 257–275.
[3] S. Reschke, C. Bogdanow, Engineering ceramics: new perspectives through value-added (multi-) functionality, Key Engineering Materials 175–176 (1999) 1–10.
[4] Q.H. Zhang, J.H. Zhang, D.M. Sun, G.D. Wang, Study on the diamond tool drilling of engineering ceramics, Journal of Materials Processing Technology 122 (2002) 232–236.
[5] C. Tsutsumi, K. Okano, T. Soto, High quality machining of ceramics, Journal of Materials Processing Technology 37 (1993) 639–654.
[6] C.W. Chang, C.P. Kuo, An investigation of laser-assisted machining of Al_2O_3 ceramics planning, International Journal of Machine Tools & Manufacture 47 (2007) 452–461.
[7] R.L. Allor, S. Jahanmir, Current problems and future directions for ceramic machining, Journal of the American Ceramic Society Bulletin 75 (7) (1996) 60–63.
[8] J.Y. Shen, C.B. Luo, W.M. Zeng, X.P. Xu, Y.S. Gao, Ceramics grinding under the condition of constant pressure, Journal of Materials Processing Technology 129 (2002) 176–181.
[9] W. Konig, A. Wagemann, Machining of ceramic components: process technological potentials, Machining of Advanced Materials, NIST Special Publication 847 (1990) 3–16.
[10] G. Chryssolouris, N. Anifantis, S. Karagiannis, Laser assisted machining: an overview, Journal of Manufacturing Science and Engineering, ASME 119 (1997) 766–769.
[11] B.G. Koepke, R.J. Stokes, A study of grinding damage in magnesium oxide single crystals, Journal of Materials Science 5 (1970) 240–247.
[12] H.P. Kirchner, Damage penetration at elongated machining grooves in hot-pressed Si_3N_4, Journal of the American Ceramic Society 67 (5) (1984) 127–132.
[13] J.C. Conway, H.P. Kirchner, Crack branching as a mechanism of crushing during grinding, Journal of the American Ceramic Society 69 (1986) 603–607.
[14] H.K. Xu, S. Jahanmir, Microfracture and material removal in scratching of alumina, Journal of Materials Science 30 (1995) 2235–2247.
[15] B. Zhang, Precision grinding regime of advanced ceramics, in: Proceedings of the 1993 Annual Meeting of American Society of Precision Engineering, Seattle, Washington, DC, November 7–12, 1993, pp. 225–229.
[16] B. Zhang, T.D. Howes, Material removal mechanisms in grinding ceramics, Annals of CIRP 43 (1994) 305–308.
[17] B. Zhang, X.L. Zheng, H. Tokura, M. Yoshikawa, Grinding induced damage in ceramics, Journal of Materials Processing Technology 132 (2003) 353–364.
[18] J.P. Choi, B.H. Jeon, B.H. Kim, Chemical-assisted ultrasonic machining of glass, Journal of Materials Processing Technology 191 (2007) 153–156.
[19] I. Puertas, C.J. Luis, A study on the electrical discharge machining of conductive ceramics, Journal of Materials Processing Technology 153–154 (2004) 1033–1038.
[20] S.K. Chak, P.V. Rao, Trepanning of Al_2O_3 by electro-chemical discharge machining (ECDM) process using abrasive electrode with pulsed DC supply, International Journal of Machine Tools & Manufacture 47 (2007) 2061–2070.
[21] A.S. Kuar, B. Doloi, B. Bhattacharyya, Modelling and analysis of pulsed Nd:YAG laser machining characteristics during micro-drilling of zirconia (ZrO_2), International Journal of Machine Tools & Manufacture 46 (2006) 1301–1310.
[22] C. Bagger, F.O. Olsen, Pulsed mode laser cutting of sheets for tailored blank, Journal of Materials Processing Technology 115 (2001) 131–133.
[23] D.K.Y. Low, L. Li, P.J. Byrd, Spatter prevention during the laser drilling of selected aerospace materials, Journal of Materials Processing Technology 139 (2003) 71–76.
[24] X. Yahong Liang, S.P. Dutta, Application trend in advanced ceramic technologies, Technovation 21 (2001) 61–65.
[25] W. Perrie, A. Rushton, M. Gill, P. Fox, W. O'Neill, Femtosecond laser microstructuring of alumina ceramic, Applied Surface Science 248 (2005) 213–217.
[26] C. Barnes, P. Shrotriya, P. Molian, Water-assisted laser thermal shock machining of alumina, International Journal of Machine Tools & Manufacture 47 (2007) 1864–1874.
[27] K. Salonitis, A. Stournaras, G. Tsoukantas, P. Stavropoulos, G. Chryssolouris, A theoretical and experimental investigation on limitations of pulsed laser drilling, Journal of Materials Processing Technology 183 (2007) 96–103.
[28] J.G. Andrews, D.R. Atthey, Hydrodynamic limit to penetration of a material by a high-power beam, Journal of Physics D: Applied Physics 9 (1976) 2181–2194.

[29] M.F. Modest, H. Abakian, Heat conduction in a moving semi-infinite solid subjected to pulsed laser irradiation, ASME Journal of Heat Transfer 108 (1986) 602–607.
[30] M.F. Modest, H. Abakian, Evaporative cutting of a semi-infinite body with a moving CW laser, ASME Journal of Heat Transfer 108 (1986) 597–601.
[31] H. Abakian, M.F. Modest, Evaporative cutting of a semi-transparent body with a moving CW laser, ASME Journal of Heat Transfer 110 (1988) 924–930.
[32] M. Modest, Laser machining of ablating/decomposing materials through cutting and drilling models, Journal of Laser Applications 9 (1997) 137–145.
[33] S.P. Harimkar, A.N. Samant, N.B. Dahotre, Temporally evolved recoil pressure driven melt infiltration during laser surface modifications of porous alumina ceramic, Journal of Applied Physics 101 (2007) 054911.
[34] W.H. Gitzen, Alumina as a Ceramic Material, The American Ceramic Society, Westerville, OH, 1970.
[35] Y.S. Touloukian, Thermophysical Properties of High Temperature Materials, IFI/Plenum, New York, 1967.
[36] H. Ki, P.S. Mohanty, J. Mazumder, Multiple reflection and its influence on keyhole evolution, Journal of Laser Applications 14 (2002) 39–45.
[37] K. Minamida, H. Takafuji, N. Hamada, H. Haga, N. Mizuhashi, Wedge shape welding with multiple reflection effects of high power CO_2 laser beam, in: Fifth International Congress on Applications of Lasers and Electro-optics, 1986, pp. 97–104.
[38] F.A. Rahman, K. Takahashi, C.H. Teik, Theoretical analysis of coupling between laser diodes and conically lensed single-mode fibres utilizing ABCD matrix method, Optics Communications 215 (2003) 61–68.
[39] S.Y. Bang, S. Roy, M.F. Modest, CW Laser machining of hard ceramics – II. Effect of multiple reflections, International Journal of Heat and Mass Transfer 36 (1993) 3529–3540.
[40] M.F. Modest, Effect of multiple reflections on hole formation during short pulsed laser drilling, Journal of Heat Transfer 128 (2006) 653–661.
[41] A.W. Baily, A. Modak, Numerical simulation of laser ablation with cavity reflections, Journal of Thermophysics and Heat Transfer 3 (1989) 42–45.
[42] S.Y. Bang, M.F. Modest, Multiple reflection effects on evaporative cutting with a moving CW laser, Journal of Heat Transfer 113 (1991) 663–669.
[43] J.G. Andrews, D.R. Atthey, Hydrodynamic limit to penetration of a material by a high-power beam, Journal of Physics D – Applied Physics 9 (1976) 2181–2194.
[44] J. Mazumdar, W.M. Steen, Heat transfer model for CW laser material processing, Journal of Applied Physics 51 (1980).
[45] F.P. Incropera, D.P. Dewitt, Fundamentals of Heat and Mass Transfer, Wiley, New York, 2002.
[46] B. Bhushan, B. Gupta, Handbook of Tribology (Materials, Coatings and Surface Treatments), McGraw-Hill, New York, 1991.
[47] P.V. Ananthapadmanabhan, T.K. Thiyagarajan, K.P. Sreekumar, N. Venkatramani, Formation of nano-sized alumina by in-flight oxidation of aluminium powder in a thermal plasma reactor, Scripta Materialia 50 (2004) 143–147.
[48] M. Baker, MSDS: Aluminum Oxide: Material Safety Data Sheet.
[49] M.V. Allmen, P. Blaser, K. Affolter, E. Strumer, Absorption phenomena in metal drilling with Nd-lasers, IEEE Journal of Quantum Electronics 14 (1978) 85–88.
[50] A. Matsunawa, V. Semak, The simulation of front keyhole wall dynamics during laser welding, Journal of Physics D – Applied Physics 30 (1997) 798–809.
[51] V. Semak, A. Matsunawa, The role of recoil pressure in energy balance during laser materials processing, Journal of Physics D – Applied Physics 30 (1997) 2541–2552.
[52] S.I. Anisimov, Vaporization of metal absorbing laser radiation, Soviet Physics JETP 27 (1968) 182–183.
[53] L. Han, F.W. Liou, S. Musti, Thermal behavior and geometry model of melt pool in laser material process, Journal of Heat Transfer 127 (2005) 1005–1014.
[54] H. Kogelnik, T. Li, Laser beams and resonators, Applied Optics 5 (1956) 1550–1565.
[55] B. Glorieux, F. Millot, J.C. Rifflet, Surface tension of liquid alumina from contactless techniques, International Journal of Thermophysics 23 (2002) 1249–1257.
[56] V.V. Semak, G.A. Knorovsky, D.O. MacCallum, R.A. Roach, Effect of surface tension on melt pool dynamics during laser pulse interaction, Journal of Physics D – Applied Physics 39 (2006) 590–595.
[57] T. Miyazaki, S. Yoshioka, T. Kimura, Ejection of molten material produced by pulsed electron and laser beams, Precision Engineering 10 (1988) 141–146.
[58] P.A. Atanasov, E.D. Eugenieva, N.N. Nedialkov, Laser drilling of silicon nitride and alumina ceramics: a numerical and experimental study, Journal of Applied Physics 89 (2001).

ADVANCED ENGINEERING MATERIALS

DOI: 10.1002/adem.200800146

Ab initio Physical Analysis of Single Dimensional Laser Machining of Silicon Nitride

By Anoop N. Samant and Narendra B. Dahotre*

High wear resistance, low electrical conductivity, high thermal stability and hardness are some of the vital properties that make silicon nitride one of the crucial engineering ceramics used for machining purposes in the aerospace, automotive and semiconductor industries.[1–3] Cams, piston rings, rocker arms and bearings can be made by machining silicon nitride. Non contact processing, effective material utilization, low manufacturing costs and high productivity have led to the increased use of lasers for machining a wide range of materials including ceramics such as alumina, silicon carbide and silicon nitride.[4–6] The laser processing conditions and the material properties significantly affect the physical processes such as energy absorption, ablation, melting, material removal and evaporation taking place during laser machining. This work demonstrates single dimensional laser machining of ceramics for applications such as drilling and generates a computational model to estimate the effect of laser processing parameters on the depth of the machined region. An insight into the depth of material machined by the application of certain number of pulses can be obtained from such a comprehensive model. The physical phenomena taking place at the surface and along the depth being different, predictions of the width of the cavity at the surface are not included in this study and will be presented in future.

Experimental

Dense Si_3N_4 obtained from a commercial source (Advanced Ceramics Manufacturing, Tucson, AZ) in the form of plates (12 mm × 15 mm and 3.5 mm thick) was exposed to a JK 701 pulsed Nd:YAG laser (1064 nm wavelength) from GSI Lumonics, Rugby, England. As pulse energy of 4 J, pulse width of 0.5 ms and a repetition rate of 20 Hz produced reasonable interaction between the laser and the ceramic surface, several pulses (3, 6, 10 and 20) were randomly applied to the Si_3N_4 surface and the resultant depth in cross-section of machined cavity was measured from the optical micrograph (Fig. 1) The bird's eye views of machined cavities on the top surface are also shown. In order to reduce the tapering effect, the holes/cavities were drilled/machined with a lens of longer focal length and longer focal waist.

Computational Approach

The surface temperature and the corresponding thermal gradient within the material were predicted in order to estimate the depth of machined region for a given set of laser processing parameters. The simulations began with the prediction of the maximum temperature reached after the first pulse by using a heat transfer flow model in COMSOL's heat transfer mode based on Fourier's second law of heat transfer.[7] The temperature rise during the ON time and the following temperature drop during the OFF time were estimated using Equations 1 and 2[7] which were valid as the heat transfer occurring in the direction perpendicular to the laser beam could be neglected for the short time scale used in laser processing.

$$T'_j = T_j + (T_0 - T_j)\left[1 - \left[\exp\frac{h(T)^2 t_{off}}{\rho C_p(T)k(T)}\right]\left[1 - \mathrm{erf}\left(h(T)\sqrt{\frac{t_{off}}{\rho C_p(T)k(T)}}\right)\right]\right] \quad (1)$$

$$T_j = T'_{j-1} + \frac{8aQ}{\pi d^2}\sqrt{\frac{t_{on}}{\rho C_p(T)k(T)\pi}} \quad (2)$$

where T_j is temperature during heating of pulse j(K), T'_{j-1} is the temperature during cooling of the earlier pulse (K), T_0 is ambient temperature (300 K), t_{off} is OFF time between successive pulses (sec), erf() is the error function, $k(T)$ is the temperature dependent thermal conductivity (W/mK)[8], $h(T)$ is the temperature dependent heat transfer coefficient (W/m^{2}K), ρ is density (2370 kg/m^3),[8] $C_p(T)$ is the temperature dependent specific heat,[8] d is the beam diameter (0.24 mm), t_{on} is the pulse duration (ON time), Q is the incident beam power and a is the absorptivity of the material (0.74).[8] Accurate in-situ absorptivity measurements being difficult for rapid processes like laser processing, a value commonly found in literature was used for this study.

The sublimation/decomposition temperature of Si_3N_4 is 2,173 K[9–10] at which it dissociates into liquid silicon and

[*] A. N. Samant, Dr. N. B. Dahotre,
Department of Materials Science & Engineering
The University of Tennessee
Knoxville, TN 37996, USA
E-mail: ndahotre@utk.edu

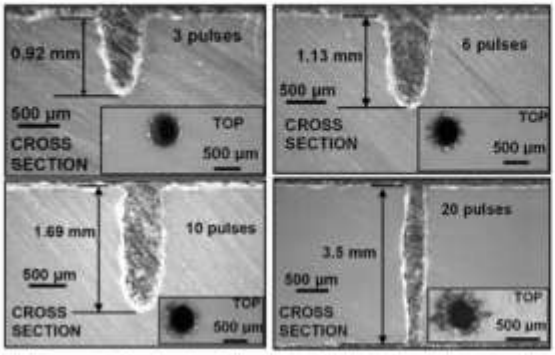

Fig. 1. Cross sectional and top views of the cavities machined in Si_3N_4 with different number of pulses.

nitrogen (Eq. 3)[11–13] and the laser machining took place due to the expulsion of this liquid silicon.

$$Si_3N_4 = 3Si(l) + 2N_2(g) \quad (3)$$

The depth from the surface at which the decomposition temperature was reached was the melt depth (z_s) and was used for further calculations. The rate of material loss at the surface due to evaporation (kg/m^{2}s) was given by:[13]

$$\dot{m}_{evaporated} = p(T_s)\left[\frac{m_v}{2\pi kT_s}\right]^{1/2} \quad (4)$$

where T_s is the surface temperature predicted above, k is the Boltzmann constant (1.38065×10^{-23} J/K), m_v is mass of the vapor molecule (Molecular weight of Si_3N_4/Avogadro's number = 2.3284×10^{-22} kg/at for Si_3N_4), and $p(T_s)$ is the saturation pressure given by the Clausius-Clapeyron equation:

$$p(T_s) = p_0 \exp[(L_v/kT_s)(1 - T_e/T_s)] \quad (5)$$

where p_0 is the ambient pressure (1.013×10^5 N/m^2), L_v is latent heat of evaporation (336.94 kJ/mol for Si_3N_4)[14] and T_e is the decomposition temperature. The depth of evaporated material ($z_{evaporated}$) at a given instant which was predicted by Equation 6 was subtracted from the melt depth (z_s) at that instant to give the available depth of melt pool (z_{ava}).

$$z_{evaporated} = \frac{\dot{m}_{evaporated} \times \text{increment in time}}{\rho} \quad (6)$$

The cumulative evaporated depth at different time instants is represented in Figure 2(a). The drop in temperature at the surface due to the cooling of the melt pool by evaporation (Eq. 7)[15] was subtracted from the temperature predicted by Equations 1 and 2 above to give the actual surface temperature at any given time instant. (Fig. 2(b))

$$\Delta T_{eva} = \frac{2\dot{m}_{evaporated}L_v}{k(T)d\pi^{1/2}} \text{arc tg} \frac{4\sqrt{k(T) \times (\text{increment in time})}}{\sqrt{\rho C_p(T)d}} \quad (7)$$

Again, the winding nature of the heating curve (Fig. 2(b)) was due to the temperature rise and drop during the ON and OFF time respectively. As the material loss due to evaporation was a function of the surface temperature, the increase in the cumulative evaporated depth was more (steeper slope) during the ON time due to rise in temperature compared to the increase in the cumulative evaporated depth during the OFF time when the temperature drop leads to a gentle slope during the OFF time (Fig. 2(a)). The losses due to evaporation begin to take place only after the sublimation/decomposition temperature of Si_3N_4 (2,173 K) is reached within the few initial pulses. The machined cavities with minimum taper were assumed to have a cylindrical cross section of volume,

$$V = \frac{\pi d^2 z_{ava}}{4} \quad (7a)$$

(equivalent to $N = V/22.4 \times 10^{-3}$ moles). The Gibbs free energy (ΔG) associated with the dissociation of Si_3N_4 (Eq. 3) was –1309.42 kJ/mol at 2151 K[16] and the energy loss due to dissociation for this volume of the machined cavity was predicted by $E_{diss} = (\Delta G \times N)$ J. This energy loss increased with time as it was a function of the melt depth which also increased with time. The energy loss was subtracted from the input laser energy to give the effective laser energy available in subsequent pulses and thus the corresponding temperature and available melt depth.

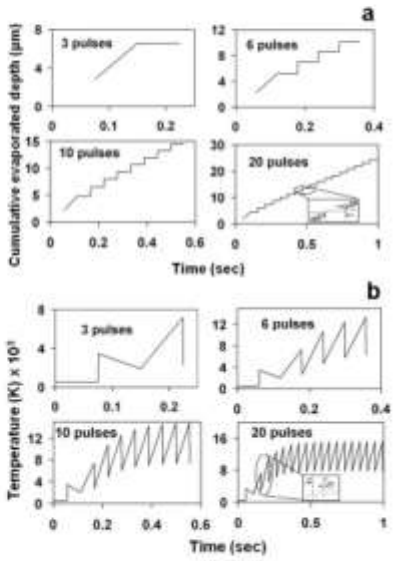

Fig. 2. a) Cumulative evaporated depth b) Heating curves.

Evaporation induced recoil pressure p_r (Eq. 8)[17] stimulated by some of the dissociated species was responsible for expulsion of the pool of liquid Si formed due to the dissociation[18–19] and the effective melt depth (z_{eff}) was available for expulsion at the next instant after a part of the available melt depth (z_{ava}) was expelled by the recoil pressure.

$$\frac{\pi d^2 p_r}{4\alpha Q} = \frac{1.69}{\sqrt{L_v}}\left(\frac{b}{1+2.2b^2}\right) \tag{8}$$

where $b^2 = \kappa T_v / m_v L_v$. The plasma pressure was neglected as the laser intensity was 3.3×10^3 W/cm which was less than 10^8 W/cm, typically required for the material to be expelled by pure evaporation.[20] The shape of the melt pool changes with the surface tension pressure[21] which depends on the effective beam radius[16] (Eq. 9)[7] which changes as the machined cavity evolves.

$$r_{eff} = \frac{d}{2}\left[1 + \left(M^2 \frac{4\lambda(z_{ava} + \delta_f)}{\pi d^2}\right)^2\right]^{1/2} \tag{9}$$

where δ_f is the focal length (120 mm), λ is the laser wavelength (1,064 nm), M is the beam quality parameter assumed to be 1 for a perfect Gaussian beam profile[22] and z_{ava} is the available melt depth explained earlier, which is expelled by velocity $v_{expulsion}$ (Eq. 10).[21]

$$v_{expulsion}(t) = \frac{1}{\rho}\frac{p_r - \tau/r_{eff}}{r_{eff}} t \tag{10}$$

where τ is the surface tension coefficient of liquid Si (843 dyne/cm[23]) as liquid Si is available through the dissociation of Si_3N_4. Integration of the expulsion velocity over time gave the fraction of the available melt depth that was expelled in a given time and the depth of the machined cavity was given by the summation of the additional depths expelled in successive time steps. The flow chart showing the attainment of the final depth starting with material properties and processing parameters is represented in Figure 3 while the evolution of the machined cavity for the application of different number of pulses is presented in Figure 4. A comparison between the predicted machined depth (Fig. 4) and the actual machined depth measured from the optical micrographs (Fig. 1) is presented in Table 1.

In most of the cases, there was a reasonable match between the machined depth estimated by the model and the depth actually measured. Discrepancy in some values could be due to slight error in measurement of actual machined depth. Also, while machining through the entire thickness of the Si_3N_4 plate (3.5 mm), the material could have been exposed to some extra pulses even after the through cavity was formed. These extra pulses could have attributed to increase in the actual machined depth.

Fig. 3. Stepwise procedure for machined cavity depth prediction.

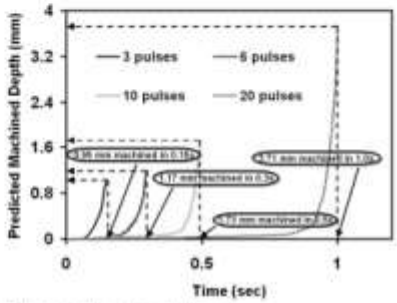

Fig. 4. Evolution of machined cavity with time.

Table 1. Comparison between depths of machined cavity for a given number of pulses.

Pulses (time, s)	Machined depth$_{experimental}$ (mm)	Machined depth$_{model}$ (mm)
3 (0.15)	0.92	0.95
6 (0.3)	1.13	1.17
10 (0.5)	1.69	1.73
20 (1.0)	3.50	3.71

Conclusions

Silicon Nitride (Si_3N_4) ceramic was machined using a JK 701 pulsed Nd:YAG laser. A machining model accounting for the decomposition of the ceramic, material loss due to evaporation and recoil pressure provoked expulsion of molten material was developed. This model had capabilities to predict the depth machined for a certain number of pulses in a given material under a given set of other laser parameters.

Received: May 05, 2008
Final version: May 21, 2008
Published online: October 07, 2008

[1] A. Kelly, N. H. Macmillan, *in Strong Solids*, Oxford University Press, New York **1986**.
[2] J. B. Wachtman, *in Mech. Properties of Ceram.* John Wiley & Sons, New York **1996**.
[3] A. J. Pyzik, D. F. Carroll, *Annu. Rev. Mater. Sci.* **1994**, *24*, 189.
[4] A. S. Kuar, B. Doloi, B. Bhattacharyya, *Int. J. Mac. Tools & Manuf.* **2006**, *46*, 1301.
[5] C. Bagger, F. O. Olsen, *J. Mater. Process. Tech.* **2001**, *115*, 131.
[6] S. P. Harimkar, A. N. Samant, N. B. Dahotre, *J. of Appl. Phys.* **2007**, *101*, DOI: 054911.
[7] K. Salonitis, A. Stournaras, G. Tsoukantas, P. Stavropoulos, G. Chryssolouris, *J. Mater. Process. Tech.* **2007**, *183*, 96.
[8] Y. S. Touloukian, *in Thermophys. Properties of High Temp. Mater.* IFI/Plenum, New York **1967**.
[9] B. Bhushan, B. K. Gupta, *in Handbook of Tribol. Mater. Coatings and Surf. Treatments*. Mc Graw Hill, New York **1991**.
[10] D. L. Perry, S. L. Phillips, *in Handbook of Inorg. Compds.* CRC Press INC, Florida **1995**.
[11] J. P. Murray, G. Flamant, C. J. Roos, *Solar Energy* **2006**, *80*, 1349.
[12] C. Boberski, R. Hamminger, M. Peuckert, F. Aldinger, R. Dillinger, J. Heinrich, J. Huber, *Angew. Chem. Int. Ed. Adv. Mater.* **1989**, *28*, 1560.
[13] W. W. Duley, *in Laser Weld.* Wiley Interscience Publication, New York, NY **1998**.
[14] T. Ya. Kosolapova, *in Handbook of High Temp. Compds: Properties, Production, Appl.* Hemisphere Publishing Corporation, New York **1990**.
[15] M. V. Allmen, P. Blaser, K. Affolter, E. Strumer, *IEEE Journal of Quantum Electron.* **1978**, *14*, 85.
[16] I. Barin, O. Knacke, *in Thermochem. Properties of Inorg. Substance*, Springer, New York **1973**.
[17] S. I. Anisimov, *Sov. Phys. JETP* **1968**, *27*, 182.
[18] A. Matsunawa, V. Semak, *J. Phys. D: Appl. Phys.* **1997**, *30*, 798.
[19] V. Semak, A. Matsunawa, *J. Phys. D: Appl. Phys.* **1997**, *30*, 2541.
[20] V. N. Anisimov, R. V. Arutyunyan, V. Yu. Baranov, L. A. Bolshov, E. P. Velikhov, V. A. Dolgov, A. I. Ilyin, A. M. Kovalevich, V. S. Kraposhin, D. D. Malyuta, L. A. Matveeva, V. S. Mezhevov, V. D. Pismennyi, A. Yu. Sebrant, Yu. Yu. Stepanov, M. A. Stepanova, *Appl. Opt.* **1984**, *23*, 18.
[21] L. Han, F. W. Liou, S. Musti, *J. Heat Trans.* **2005**, *127*, 1005.
[22] A. E. Siegman, *Proc. SPIE* **1993**, *1868*, 2.
[23] Z. F. Yuan, K. Mukai, W. L. Huang, *Langmuir* **2002**, *18*, 2064.

Optics and Lasers in Engineering 47 (2009) 570–577

Contents lists available at ScienceDirect

Optics and Lasers in Engineering

journal homepage: www.elsevier.com/locate/optlaseng

An integrated computational approach to single-dimensional laser machining of magnesia

Anoop N. Samant, Narendra B. Dahotre *

Department of Materials Science and Engineering, The University of Tennessee, 326 Dougherty Engineering Building, Knoxville, Tennessee 37996, USA

ARTICLE INFO

Article history:
Received 4 July 2008
Received in revised form
13 September 2008
Accepted 10 October 2008
Available online 21 November 2008

Keywords:
Lasers
Multiple reflections
Magnesia
Machining efficiency

ABSTRACT

Magnesia (MgO) ceramic was machined using a pulsed Nd:YAG laser. A mathematical model was developed to predict machined effects. The model took into account the physical phenomena taking place during machining of the ceramic such as multiple reflections influencing the absorbed laser energy, thermal effects in vaporizing the material, dissociation energy losses and effect of vapor pressure in producing a cavity through the ceramic. The laser fluence, machining time and number of pulses required for machining a certain depth of cavity and the efficiency of machining in terms of the specific machining depth were estimated and compared with the experimental data, thus making the model useful for advance energy predictions and enhancement of machining efficiency.

1. Introduction

Magnesium oxide (MgO) or magnesia possesses excellent properties such as high corrosion resistance, intermediate hardness, low electrical conductivity and good refractoriness. MgO is a very stable oxide that is used in a wide range of technological applications [1] such as refractory linings, thermocouple housings in aggressive environments, brake linings, thin film semiconductors, crucibles in chemical and nuclear industry where high corrosion resistance is required [2] and laser parts [3].

Several materials processing techniques such as (a) mechanical machining: conventional grinding [4], ultrasonic machining [5], abrasive water jet machining [6]; (b) electrical machining: electrical discharge machining [7], electro-chemical discharge machining (ECDM) [8]; (c) machining by radiation: electron beam [9] and laser processing [10]; and (d) hybrid machining: electric discharge grinding [11], and laser-assisted machining [12] have been employed for processing ceramics. However, of all the processing techniques, laser machining of ceramics is gaining prominence as it is a non-contact process and the material is utilized efficiently leading to reduced processing costs and increased productivity [13]. This technique is being used for producing holes in the micro-electronics industry [14] and has been extensively investigated using either experimental or advanced mathematical methods such as finite element analysis or even molecular dynamics [15–24].

Based on the present knowledge from available open literature, limited work has been carried out in laser machining of MgO ceramic and some data on the laser machining of MgO can be found in laser machining handbooks [25]. Hence, this study aims at understanding the physical phenomena during laser–ceramic (MgO) interaction and develops a numerical tool that will enable advance prediction of number of pulses, machining time and laser fluence (energy per unit area) required for machining a given depth of cavity in a ceramic under a given set of laser processing conditions. As the physical phenomena occurring along the depth of the material are different from those taking place at the surface, it was assumed in the present study that the width of the machined cavity was equivalent to the out of focus laser-spot diameter [26] on the surface of sample being machined. Efforts are ongoing to include the physical processes taking place at the surface into the model and they will be presented in future publications.

2. Experimental

JK 701 pulsed Nd:YAG laser (1064 nm wavelength) from GSI Lumonics, Rugby, England was used for processing the coupons ($1.2 \times 1.5\,cm^2$ and 0.3 cm) which were cut from 99.4% pure and fully dense MgO plates ($7.6 \times 11.4 \times 0.3\,cm^3$) obtained from a commercial source (Ozark Technical Ceramics, Inc., Webb City, MO). As the laser interacted well with the ceramic for pulse energy of 4J, under the combination of pulse width of 0.5 ms and a repetition rate of 20 Hz, several pulses (3, 6, 9 and 20) were

* Corresponding author. Tel.: +1 865 974 3609; fax: +1 865 974 4115.
E-mail address: ndahotre@utk.edu (N.B. Dahotre).

0143-8166/$ - see front matter © 2008 Elsevier Ltd. All rights reserved.
doi:10.1016/j.optlaseng.2008.10.001

applied to the MgO surface. The average power used for laser processing was 80 W (pulse energy, 4 J × repetition rate, 20 Hz) and the out of focus laser beam diameter, d on the surface of sample being machined was 0.05 cm. Three runs for each number of pulses were conducted and for each case, five measurements of the depth of the machined cavity were made from the optical cross-sectional views (Fig. 1) by Image J™ software. The average value of the machined depths measured using this method has been represented in Table 1 along with the standard deviation corresponding to the scatter in each case. Thus the measurements were statistically analyzed by considering the average and the standard deviation of the measured depths. As there was no feedback system to monitor the formation of a through cavity, some extra (stray) pulses could have been supplied even after the through cavity was formed. Even though experiments were conducted using air as an assist gas, the effect of assist gas on the machined depth was not the focus of this study and it will be presented in due course of time.

One of the basic principles of any statistical design of experiments is randomization. Randomization means that the order in which the individual runs of the experiment are to be performed are determined randomly. This assists in averaging out effects of extraneous factors (lurking variables) that may be present, such as relative humidity and surrounding temperature [27]. Hence, in this study, the number of pulses was not applied in the same order for the different runs (for example from 3-6-9-20 pulses). Instead, different runs (three) for each case were conducted with a random sequence of the number of pulses and then the mean value of the measured machined depth was reported. If several runs were conducted with the same order of the number of pulses (say, from 3-6-9-20), then the lurking variables could affect the machined depth. Thus, in order to avoid the effect of these variables, runs were conducted with the number of pulses applied in random sequence. This implemented the standard procedure of randomization of experimental runs. The top surface views of the machined cavities are also shown in Fig. 1. The attempts were made to reduce the tapering effect by machining the cavities with a lens of longer focal length and longer focal waist.

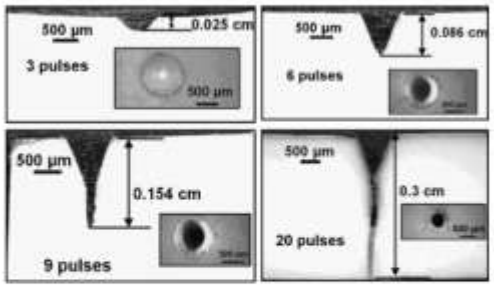

Fig. 1. Cross-sectional and top views of cavities machined in MgO ceramic for different number of pulses.

Table 1
Number of pulses and resulting machined depths.

Number of pulses	Machined depth (cm)
3	0.025 ± 0.0057
6	0.086 ± 0.004
9	0.154 ± 0.0027
20	0.3 ± 0.0061

3. Computational

During laser processing, the changes in surface temperature with the absorption of laser energy and associated thermal gradient within the material have an effect on the machined depth. Hence, it was necessary to start the computations with predictions of surface temperature profiles.

3.1. Temporal evolution

The maximum temperature reached at the end of first pulse was predicted by using a model based on Fourier's second law of heat transfer in COMSOL's™ heat transfer transient mode [28]. The rise in temperature during ON time and corresponding drop in temperature during OFF time for the successive pulses were predicted using Eqs. (1) and (2) below Ref. [29]. Changes in thermal conductivity, heat transfer coefficient and specific heat were included as a function of temperature for improved accuracy in calculations.

$$T'_i = T_i + (T_0 - T_i)\left[1 - \left[\exp\frac{h(T)^2 t_{off}}{\rho C_p(T) k(T)}\right]\right]\left[1 - erf\left(h(T)\sqrt{\frac{t_{off}}{\rho C_p(T) k(T)}}\right)\right] \quad (1)$$

$$T_i = T'_{i-1} + \frac{8\alpha P}{\pi d^2}\sqrt{\frac{t_{on}}{\rho C_p(T) k(T) \pi}} \quad (2)$$

where T_i is temperature during heating of pulse i (K), T'_{i-1} is the temperature during cooling of the earlier pulse (K), $erf(\cdot)$ is the error function, t_{off} is OFF time between successive pulses (s), T_0 is ambient temperature (27 °C), t_{on} is the pulse duration (ON time), $k(T)$ is the temperature-dependent thermal conductivity (W/mK) [30], $C_p(T)$ is the temperature-dependent specific heat [30], ρ is density (3580 kg/m^3) [31], $h(T)$ is the temperature-dependent heat transfer coefficient (W/m^{2}K) [32], P is the incident average beam power predicted above (80 W) and α is the absorptivity of the material which depends on the multiple reflections within the machined cavity as explained below. The variation of thermal conductivity and specific heat with temperature is represented in Fig. 2 Ref. [30].

Due to extremely short time scale associated with the laser processing, the heat transfer in direction orthogonal to the laser

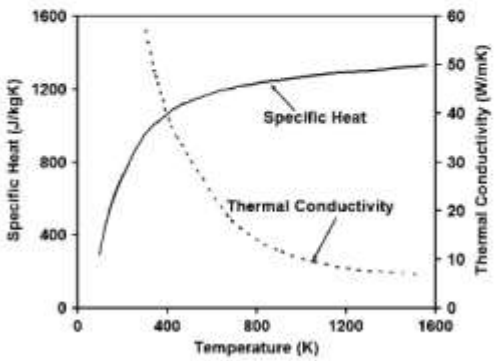

Fig. 2. Variation of thermophysical properties of MgO with temperature [30].

beam was neglected in Eqs. (1) and (2) used in the current study. This assumption was valid because in a rapid process like laser–material interaction, the heat transfer was confined to the laser beam and spatial distribution outside the beam was negligible. Only the centerline of the machined cavity was examined and an estimate of the corresponding machining time and number of pulses was made. As mentioned earlier, the width of the machined cavity was not predicted in this study and it was assumed to be the same as the out of focus beam diameter on the surface of the sample. This was also a reasonable assumption because the width of the machined cavities was approximately the same as the out of focus beam diameter of 0.05 cm (Fig. 1). Furthermore, from the variation of thermal conductivity with temperature (Fig. 2), it appears that the maximum thermal conductivity of MgO is 57 W/mK at 304 K. The thermal conductivity of some of the commonly used metals is shown in Table 2 Ref. [33]. Thus it can be seen from Table 2 and Fig. 2 that thermal conductivity of MgO is far less than values for commonly used metals due to which no significant thermal losses will take place on the surface thereby justifying the assumption of neglecting the heat transfer in direction orthogonal to laser beam. It may also be noted here that the model considered in this study is a three-dimensional (3D) model [28,34] with the width of the machined cavity in X and Y directions assumed to be constant and equal to the out of focus beam diameter (as also seen from Fig. 1).

3.2. Multiple reflections

For cavities shown in Fig. 1, the transfer of energy from laser to the surface of MgO is affected by the multiple reflections within the machined cavity [35] and this phenomena has been handled in several different ways [36–40]. It was found by Ilang and Modest [41] that multiple reflections increase the effective absorptivity of the material and in the processes such as high aspect ratio laser machining, the value is expected to reach 100% instantaneously as also assumed by Andrew et al. and Mazumdar et al. [42,43]. Furthermore, it can be seen from Fig. 2 and Table 2 that as the thermal conductivity of MgO is far less than metals, the rate at which losses due to conduction take place will be less than the rate at which the laser energy is absorbed. This effect together with the effect of multiple reflections from the wall of machined cavity rapidly raises the absorption of incident energy to the level of 100%. In light of this, in this study, the absorptivity value was taken to be 1 corresponding to 100% energy absorption. Further justification for this assumption has been given later in Section 3.4 where the effect of low value of absorptivity of MgO (0.1 at 1064 nm wavelength, Ref. [30]) on the machining time and number of pulses has been discussed. Some losses of energy due to dissociation of the ceramic are explained later. Although conducting in-situ absorptivity measurements in a very short duration high energy dynamic process like laser–material interaction is extremely challenging, parallel efforts are ongoing for actual absorptivity measurements and they will be incorporated in future stages of the work.

Table 2
Thermal conductivity of some commonly used metals [33].

Metal	Thermal conductivity (W/mK)
Aluminum	247
Copper	398
Iron	80
Magnesium	156
Gold	315
Nickel	90

3.3. Dissociation energy losses

The dissociation of MgO takes place as per the following reaction [44,45]:

$$MgO \rightarrow Mg_{(g)} + O_{(g)} \quad (3)$$

The melting and vaporization temperatures of magnesium are 649 °C [46] and 1090 °C [47], respectively. Thus, at temperatures above the melting/decomposition/vaporization temperature of MgO (2850 °C [31]), material losses take place purely by evaporation of magnesium formed in solid form due to the above dissociation reaction. The amount of material evaporated (machined depth, $z_{evaporated}$) was predicted by tracking the depth from the surface at which the decomposition temperature (2850 °C) of MgO was reached. The material generated vapor pressure acts in the upward direction and was mainly responsible for material removal. Additionally, the gravitational force may also have an effect in the formation of a cavity, especially in the case of machining through the entire thickness (0.3 cm) of the ceramic plate by expelling the material out through the opening at the bottom towards the end of process. As the mechanism of material removal depends on the type of ceramic, in the case of MgO, machining takes place due to dissociation of the ceramic via above-mentioned reaction followed by evaporation of the material exposed to laser fluence. This mechanism is in contrast to the machining of alumina or silicon nitride ceramic using the same laser-based technique where material removal is a combination of melt expulsion and evaporation as studied by Samant and Dahotre [34,48].

The Gibbs free energy (ΔG) associated with the dissociation reaction (Eq. (3)) is −974.1 kJ/mol at 3260 °C [49]. The volume of the machined cavities was measured from Fig. 1 and it was found to be equivalent to a cylinder of diameter, $d_{cyl} = d/\sqrt{3}$, where d was the width of the machined cavity which was equal to the out of focus beam diameter of 0.05 cm on the surface of the sample being machined (as also seen from Fig. 1) due to the fact that spatial distribution beyond the beam diameter was negligible. Hence, for the set of processing conditions considered in this study, it was assumed that the machined cavity has an equivalent cylindrical cross section of volume, $V = \pi d_{cyl}^2 z_{evaporated}/4$ (equivalent to $N = V/22.4 \times 10^{-3}$ mol). The loss of energy corresponding to dissociation of this volume of machined cavity is estimated by $E_{dissociation} = (\Delta G \times N)$]. This energy loss was deducted from the input laser energy to give the effective laser energy available in subsequent laser pulses for raising the surface temperature and to generate corresponding evaporated/machined depth.

The temperature profiles obtained by considering 100% absorption of this effective laser energy (Fig. 3) show a winding nature because the temperature rises during pulse ON time and falls during pulse OFF time. It was observed that the maximum surface temperature increased to almost 9000 °C when 20 pulses were applied to the ceramic. Although temperatures were very high for such a short duration process, they were mostly confined to the surface for an extremely short time with a possibility of small amount of material loss by ablation. However, these high temperatures rapidly drop below melting point within the subsurface region and to further lower temperature in the substrate material due to self quenching.

3.4. Effect of absorption on machining time and number of pulses

In literature, commonly found absorptivity value for MgO at a wavelength of 1064 nm (the wavelength used for laser processing in this study) is 0.1 (corresponding to 10% absorption of effective laser energy) [30]. The temperature profiles for $a = 0.1$ obtained

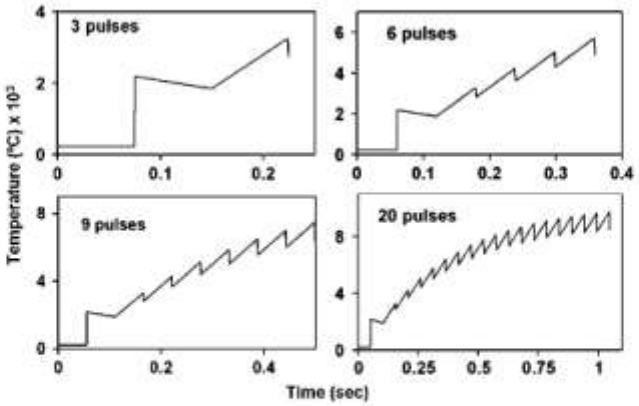

Fig. 3. Heating curves corresponding to laser machining of MgO with various number of pulses corresponding to 100% energy absorption ($a = 1$).

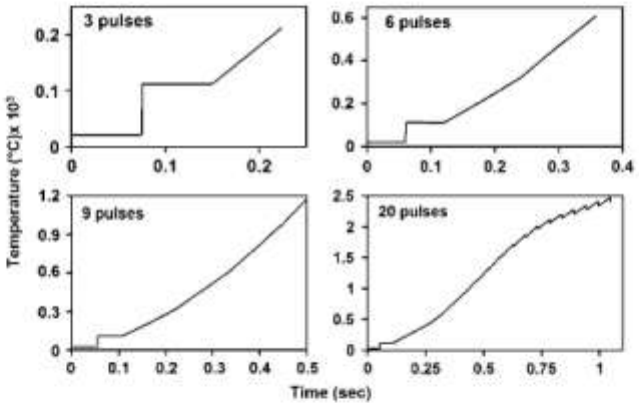

Fig. 4. Heating curves corresponding to laser machining of MgO with various number of pulses for 10% energy absorption (absorptivity, $a = 0.1$).

by using the thermal model described above are represented in Fig. 4. As mentioned earlier, material losses in MgO take place purely by evaporation of magnesium formed during the dissociation of MgO. The maximum surface temperature for 3, 6, 9 and 20 pulses for $a = 0.1$ was less than the decomposition temperature of MgO (2850 °C [31]) and hence no depth could be machined for these combination of number of pulses and absorptivity. On the contrary, there is visual evidence from the cross-sectional views in Fig. 1 that machining does take place at these number of pulses. This clearly establishes that the actual energy absorbed was greater than the theoretical energy absorption of 10%.

The machining time and the number of pulses required for machining depths of 0.025, 0.086, 0.154 and 0.3 cm for absorptivity value of 0.1 were computed using the model described earlier and compared with experimental values in Table 3 which also includes predictions for $a = 1$ (corresponding to 100% absorption of effective laser energy) that are discussed in detail later. The input energy being less for absorptivity value of 0.1, predicted number of pulses was much higher than the number of pulses experimentally observed to machine a given depth; this reinforces the fact that the actual absorptivity is much higher than mentioned in the literature. On the contrary, it is also noteworthy that even for $a = 1$, although the predicted values of number of pulses are much closer to the experimental values they are still smaller than the experimental values.

Thus assumption of 100% absorption ($a = 1$) under the present set of laser processing and materials parameters is justified with these verifications and additional reasons stated in Section 3.2. Nonetheless, attempts are ongoing for *in-situ* temperature and absorptivity measurement adopting various approaches and they will be incorporated in future publications on similar topic.

4. Predictions and comparison of machining effects

The computations for 10% energy absorption were made in the earlier section only to justify the assumption of 100% energy absorption due to multiple reflections within the sufficiently deep

Table 3
Comparison between actual and predicted number of pulses and machining time for different absorptivity values ($\alpha = 0.1$ and 1.0).

Machined depth (cm)	Pulses $_{Actual}$ (time, s)	Pulses $_{Predicted}$ (time, s) ($\alpha = 0.1$)	Pulses $_{Predicted}$ (time, s) ($\alpha = 1.0$)
0.025	3 (0.15)	28 (1.38)	2 (0.11)
0.086	6 (0.3)	42 (2.1)	4 (0.2)
0.154	9 (0.45)	50 (2.49)	5 (0.25)
0.3	20 (1)	130 (6.45)	16 (0.8)

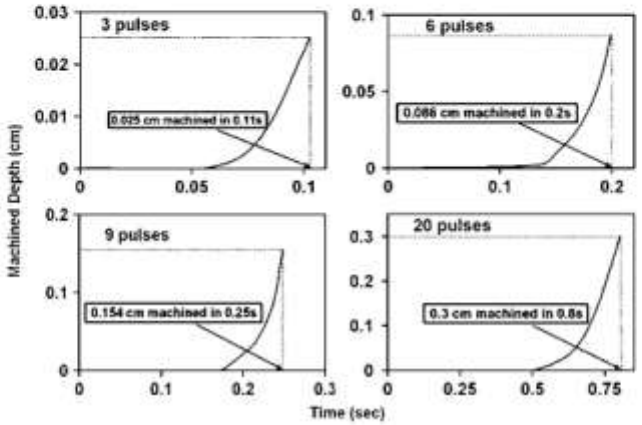

Fig. 5. Evolution of machined cavity at different time instants for $\alpha = 1$.

cavities machined in this study. The associated machining effects corresponding to this absorptivity value (0.1) will not be further discussed while the evolution of machined cavity with time and predictions of corresponding laser fluence, machining time, number of pulses and machining efficiency for 100% energy absorption are discussed in the following section. Furthermore, these predicted parameters were compared with experimental observations as discussed below.

4.1. Number of pulses, machining time and machining energy

Evolution of machined depth with time for 100% energy absorption is represented in Fig. 5, while a comparison between the actual (Table 1) and predicted number of pulses and time (Fig. 5) required for machining a certain depth (Fig. 1) for $\alpha = 1$ (100% energy absorption) is also presented in Table 3 along with the corresponding values for $\alpha = 0.1$ that are discussed earlier. The number of pulses and machining time predicted for different machining depths by considering 100% absorption are close to the actual values. It has been mentioned by Modest [38] that the increase in absorptivity is affected by the number of pulses, i.e. for a small number of pulses the absorptivity is increased only slightly. Hence, the assumption of 100% absorption for the entire range of pulses employed in the present work may have produced the differences between predicted and measured machining time. Some discrepancy in the values can also be contributed to limits of the technique employed to measure machined depth from the micrographs (Fig. 1). Moreover, in addition to the physical processes considered in this study, the different physical phenomena that could possibly have an effect on the machining process are: (a) plasma formation and associated ionization, (b) ablation and (c) effect of assist gas pressure and flow rate on the machined depth. These processes are not considered in the present study and can also affect the predicted number of pulses and machining time. The laser fluence (J/cm^2) employed for machining is given by

$$\text{Laser fluence (J/cm}^2\text{)} = \frac{\text{Average power (W)} \times \text{Number of pulses} \times \text{Pulse width(s)}}{\text{Area of incident beam(cm}^2\text{)}} \quad (4)$$

The area of incident beam is $\pi d^2/4$ where d is the out of focus beam diameter (0.05 cm) on the sample surface. The actual and predicted number of pulses for $\alpha = 1$ (Table 3) were used to determine the actual and predicted laser fluences, respectively (Table 4). Higher laser fluence was required for machining deeper cavities as the energy requirement for removal of larger volume of material is increased with increased machined depth. Direct proportionality between laser fluence and number of pulses (Eq. (4)) resulted in predicted fluences being less than the actual values.

Table 4
Comparison between actual and predicted laser fluences for different machined depths.

Machined depth (cm)	Laser fluence $_{Actual}$ (J/cm^2)	Laser fluence $_{Predicted}$ (J/cm^2) ($\alpha = 1$)
0.025	265	177
0.086	531	354
0.154	796	442
0.3	1768	1415

4.2. Vapor pressure and gravitational pressure effects

As the material removal in MgO takes place by evaporation, the removed material (vapor) exerts a force over the machined area and drives out the material. The magnitude of this force is proportional to the laser fluence required for machining a certain depth. The corresponding pressure (vapor pressure) acting upwards is

$$\text{Vapor pressure} = \frac{\text{Laser fluence}}{\text{Machined depth}} \tag{5}$$

In addition, as mentioned before, the evaporated material could be subjected to the gravitational force in the downward direction that may retain the material at the bottom of the blind cavity or expel out from the opening at the bottom in case of machining through the entire depth of the sample. This gravitational pull was given by $\rho g h$, where g is the acceleration due to gravity (9.8 m/s^2) and h is the machined depth (Table 1). The vapor pressure and gravitational pressure for various machined depths are represented in Table 5.

The vapor pressure based on actual and predicted laser fluence (corresponding to $a = 1$) decreased from 106×10^9 dynes/cm^2 to 51.68×10^9 dynes/cm^2 and from 70.7×10^9 dynes/cm^2 to 28.7×10^9 dynes/cm^2, respectively, as the depth of the machined cavity increased from 0.025 to 0.154 cm. During machining, the cumulative machined/evaporated depth increased with time, but actual amount of material removed in successive pulses did not increase significantly. Increase in the machined depth only increased the free volume to be occupied causing the vapor pressure during subsequent laser pulses to decrease for all depths except for through machining. In the case of through machining (0.3 cm), the vapor pressure was more than that corresponding to the preceding depth (0.154 cm) because for a constant depth of 0.3 cm, there was a loss of energy due to the stray pulses and a corresponding increase in vapor pressure as also seen from Eq. (5) above. It was observed from Table 5 that, for all the machined depths, the vapor pressure (actual and predicted) acting upwards was several orders of magnitude (10^9) more than the gravitational pressure acting downwards ensuring formation of a clean cavity as also seen in Fig. 1. This comparison between the gravitational and vapor pressure clearly indicated that the gravitational force is not an important factor in laser machining of MgO under the set of materials and processing parameters employed in the present work.

4.3. Machining efficiency

Laser-based machining of ceramics is a complex process involving combination of various material and process parameters. The effectiveness of the process, however, can be best realized in terms of machining efficiency expressed in various following ways.

4.3.1. Specific machining depth

The machining efficiency (actual and predicted) was represented in terms of the specific machining depth [50] and expressed in Eq. (6) below as the amount of material removed (depth machined) per unit laser energy.

$$\text{Specific machining depth (cm/J)} = \frac{\text{Machined depth (cm)}}{\text{Laser fluence (J/cm}^2) \times \text{area of incident beam (cm}^2)} \tag{6}$$

The actual and predicted laser fluences were used to determine the actual and predicted specific machining depths, respectively.

4.3.2. Depth ratio

The depth ratio, R was the ratio of depths machined for consecutive processing conditions. In order to set the minimum limit for R, it was assumed that the depth machined for the first processing condition was 0.025 cm (the smallest depth of the cavity machined under the present set of laser processing conditions) and the depth machined for the immediately next processing condition was hypothetically taken to be the same (0.025 cm). Thus the minimum limit for R was 1 (0.025/0.025 cm) (for no change in machined depth even after supplying energy). For the maximum limit of R, the depths machined for consecutive processing conditions (supply of laser energy) were hypothetically taken to be 0.025 cm (smallest depth machined) and 0.3 cm (corresponding to the formation of through cavity of 0.3 cm at the next instant of supply of energy), respectively. This yielded a maximum R value of 12 (0.3/0.025 cm) for the present set of processing conditions. Thus the limits for R were obtained by taking the ratios of depths machined under consecutive processing conditions.

4.3.3. Fluence ratio

The ratio of predicted fluences required for machining different depths under successive processing conditions (supply of laser fluence) was the fluence ratio, F. To determine the minimum limit of F, it was hypothetically considered that the fluence of 177 J/cm^2 (required for machining 0.025 cm) was supplied for two consecutive processing conditions, thus providing a lower limit of 1 (177/177 J/cm^2) for F. On the other hand, for the maximum limit of F, the energy supplied for the first processing condition was assumed as 177 J/cm^2, while the fluence of 1415 J/cm^2 (corresponding to through machining) was hypothetically supplied for the next processing condition. The corresponding maximum limit of F was 8 (1415/177 J/cm^2). Similar to R, the limits of F were also predicted by considering consecutive processing conditions.

The specific machining depth estimated the amount of material machined per unit increase in laser fluence. The proportion in which the laser fluence and corresponding machined depth increased was different. In certain cases, the proportion of increase in machined depth was more compared to the proportion of increase in the laser fluence, and vice versa in some other cases. The depth ratio, R, and the fluence ratio, F, were calculated from parameters (machined depth and laser fluence, respectively) corresponding to consecutive processing conditions and they measured the effect of change in laser fluence on machined depth. Both these ratios were correlated and had an effect on the specific machining depth (Eq. (6)), as discussed below. The comparison between actual and predicted specific machining depths is

Table 5
Vapor pressure (corresponding to actual and predicted fluence) and gravitational pressure for different machined depths.

Machined depth (cm)	Vapor pressure $_{Actual} \times 10^9$ (dynes/cm^2)	Vapor pressure $_{Predicted} \times 10^9$ (dynes/cm^2) ($a = 1$)	Gravitational pressure (dynes/cm^2)
0.025	106	70.7	87.7
0.086	61.7	41.1	302
0.154	51.68	28.7	540.8
0.3	58.9	47.1	1053.5

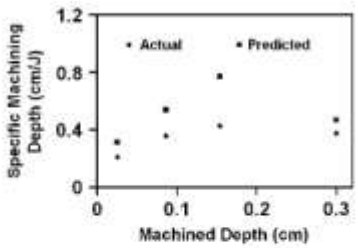

Fig. 6. Comparison between actual and predicted specific machining depth for $a = 1$.

presented in Fig. 6. It may be noted that Fig. 6 is not a variation of the machined depth but a variation of efficiency in terms of depth machined per unit energy supplied for 100% absorption.

Since the predicted number of pulses (Table 3) and corresponding laser fluences (Table 4) for 100% energy absorption were less than the actual values required for machining a given depth, it was predicted that more material would be machined per unit energy. This led to higher values of the predicted specific machining depth than that for actual specific machining depth for all depths (Fig. 6). Increase in machined depth from 0.025 to 0.086 cm and then to 0.154 cm decreased R from 3.44 (0.086/0.025 cm) to 1.79 (0.154/0.086 cm). The corresponding actual and predicted fluence ratios, F decreased from 2 (531/265 J/cm^2) to 1.5 (796/531 J/cm^2) and from 2 (354/177 J/cm^2) to 1.25 (442/354 J/cm^2), respectively. Higher magnitudes of R (3.44 and 1.79) corresponding to lower magnitudes of F (actual: 2 and 1.5 and predicted: 2 and 1.25) are indicative of higher proportional increase in machined depth compared to proportional increase in the corresponding laser fluence. Hence, the specific machined depth increased as the machined depth increased from 0.025 to 0.154 cm (Fig. 6). On the contrary, while machining through the cavity of 0.3 cm, the stray pulses rendered the magnitude of R (0.3/0.154 cm = 1.94) less than the corresponding magnitude of actual F (1768/796 J/cm^2 = 2.2) or predicted F (1415/442 J/cm^2 = 3.2). This led to the indication of drop in actual and predicted specific machining depths and corresponding machining efficiencies in case of through machining as seen in Fig. 6. In light of this, the machining efficiency can be improved with a provision of an optical feedback system that sends a signal to the laser at the onset of a through cavity formation and stop the further delivery of unwarranted laser pulses to the ceramic. Incorporation of such a feedback into the machining process is currently ongoing and will be described in the future work.

The computational model discussed in this study would enable advance predictions of the number of pulses and machining time required for machining a desired depth in any material. The model has additional capabilities of predicting the laser fluence required for machining a given depth of material. Thus the model can assist in advance energy predictions and providing means of improving the efficiency of laser machining process.

5. Conclusions

The ability of machining MgO for different depths was successfully demonstrated using pulsed Nd:YAG laser. It was found that 3, 6, 9 and 20 pulses corresponding to laser fluences of 265, 531, 796 and 1768 J/cm^2 were required for machining cavities of 0.025, 0.086, 0.154 and 0.3 cm depths, respectively. Multiple reflections and energy losses associated with MgO dissociation affected the total amount of the laser energy absorbed. The evaporation of the ceramic was responsible for material removal and the vapor pressure ensured the formation of a clean cavity. A systematic multi-step machining model based on above-mentioned various physical phenomena allowed close prediction of laser parameters and their effects. It was found that for 100% energy absorption, fewer pulses (2, 4, 5 and 16) and corresponding lesser laser fluences (177, 354, 442 and 1415 J/cm^2) were sufficient for machining cavities of above-mentioned depths (0.025, 0.086, 0.154 and 0.3 cm), respectively. The vapor pressure proportional to the force exerted by the removed material (vapor) is responsible for driving out the material. The vapor pressure based on the actual and predicted laser fluence (for 100% energy absorption) varied from 51.68×10^9 dynes/cm^2 to 106×10^9 dynes/cm^2 and from 28.7×10^9 dynes/cm^2 to 70.7×10^9 dynes/cm^2, respectively. This model had the capabilities of advance predictions of number of pulses, machining time and laser fluence required for machining a certain depth in a ceramic under a given set of laser processing conditions and also provided an insight into the machining efficiency. Thus this study was a novel computational approach to the machining of MgO where limited work in the open literature has been reported.

References

[1] Raj AME, Som T, Ganesan V, Jayachandran M, Selvan G, Swaminathan V, et al. Tailoring optical and electrical properties of MgO thin films by 1.5 MeV H^+ implantation to fluences. Nuclear Instruments and Methods in Physics Research B 2008.
[2] http://www.azom.com/details.asp?ArticleID = 54.
[3] Kim JD, Lee ES. A study on the mirror-like grinding of MgO single crystal with various diamond wheels. J Mater Process Technol 1997;72:1–10.
[4] Shen JY, Luo CB, Zeng WM, Xu XP, Cao YS. Ceramics grinding under the condition of constant pressure. J Mater Process Technol 2002;129:176–81.
[5] Choi JP, Jeon BH, Kim BH. Chemical-assisted ultrasonic machining of glass. J Mater Process Technol 2007;191:153–6.
[6] Godlmetla P, Wang J, Wong W. Kerf formation analysis in the abrasive waterjet cutting of industrial ceramics. J Mater Process Technol 2002;128:123–9.
[7] Puertas I, Luis CJ. A study on the electrical discharge machining of conductive ceramics. J Mater Process Technol 2004;153–154:1033–8.
[8] Chak SK, Rao PV. Trepanning of Al_2O_3 by electro-chemical discharge machining (ECDM) process using abrasive electrode with pulsed DC supply. Int J Mach Tools Manuf 2007;47:2061–70.
[9] Horio K, Terahayashi T. Beam defocus effect in electron beam machining of green ceramic sheet. Ann CIRP 1987;36:95–8.
[10] Kuar AS, Doloi B, Bhattacharyya B. Modelling and analysis of pulsed Nd:YAG laser machining characteristics during micro-drilling of zirconia (ZrO_2). Int J Mach Tools Manuf 2006;46:1301–10.
[11] Shih HR, Shu KM. A study of electrical discharge grinding using a rotary disk electrode. Int J Adv Manuf Technol 2008;38:59–67.
[12] Rozzi JC, Pfefferkorn FE, Incropera FP, Shin YC. Transient thermal response of a rotating cylindrical silicon nitride workpiece subjected to a translating laser heat source, part I: comparison of surface temperature measurements with theoretical results. J Heat Transfer 1998;120:899–906.
[13] Bagger C, Olsen FO. Pulsed mode laser cutting of sheets for tailored blanks. J Mater Process Technol 2001;115:131–5.
[14] Low DKY, Li L, Byrd PJ. Spatter prevention during the laser drilling of selected aerospace materials. J Mater Process Technol 2003;139:71–6.
[15] Salonitis K, Stavropoulos P, Stournaras A, Chryssolouris G. CO_2 Laser cutting of aluminium. In: Proceedings of the fifth laser-assisted net shape engineering. Erlangen, Germany; 2007. p. 825–35.
[16] Stavropoulos P, Salonitis K, Stournaras A, Euthimiou K, Chryssolouris G. Molecular dynamics simulation of laser ablation of iron. In: Proceedings of the tenth CIRP international workshop on modeling of machining operations. Calabria, Italy; 2007. p. 549–53.
[17] Stournaras A, Salonitis K, Stavropoulos P, Chryssolouris G. Finite element thermal analysis of pulsed laser drilling process. In: Proceedings of the tenth CIRP international workshop on modeling of machining operations. Calabria, Italy; 2007. p. 563–70.
[18] Zhigilei LV. Dynamics of the plume formation and parameters of the ejected clusters in short-pulse laser ablation. Appl Phys A 2003;76:339–50.
[19] Zhigilei LV, Yingling YG, Itina TE, Schoolcraft TA, Garrison BJ. Molecular dynamics simulations of matrix assisted laser desorption: connections to Experiment. Int J Mass Spectrom 2003;226:85–106.
[20] Zhigilei LV, Dongare AM. Multiscale modeling of laser ablation: applications to nanotechnology. CMES: Computer Modeling in Engineering & Sciences 2002;3:539–55.

[21] Zeifman MI, Garrison BJ, Zhigilei LV. Combined molecular dynamics–direct simulation Monte Carlo computational study of laser ablation plume evolution. J Appl Phys 2002;92:2181–93.
[22] Chryssolouris G, Yablon A. Depth prediction in laser machining with the aid of surface temperature measurements. CIRP Annals–Manufacturing Technology 1993;42:205–7.
[23] Roy S, Modest MF. CW laser machining of hard ceramics—I. Effects of three-dimensional conduction, variable properties and various laser parameters. Int J Heat Mass Transfer 1993;36:3515–28.
[24] Ramanathan S, Modest MF. Single and multiple pass cutting of ceramics with a moving CW laser. In: Proceedings of the XXII ICHMT Int Symp Manuf Mater Process, Dubrovnik, Yugoslavia; 1990.
[25] Ready JF. LIA handbook of laser materials processing. Magnolia Publishing; 2002.
[26] Ng GKL, Crouse PL, Li L. An analytical model for laser drilling incorporating effects of exothermic reaction, pulse width and hole geometry. Int J Heat Mass Transfer 2006;49:1358–74.
[27] Montgomery DC. Design and analysis of experiments. New York: Wiley; 1997.
[28] Harimkar SP, Samant AN, Dahotre NB. Temporally evolved recoil pressure driven melt infiltration during laser surface modifications of porous alumina ceramic. J Appl Phys 2007;101 [Doi:054911].
[29] Salonitis K, Stournaras A, Tsoukantas G, Stavropoulos P, Chryssolouris G. A theoretical and experimental investigation on limitations of pulsed laser drilling. J Mater Process Technol 2007;183:96–103.
[30] Touloukian YS. Thermophysical properties of high temperature materials. New York: IFI/Plenum; 1967.
[31] Bhushan B, Gupta BK. Handbook of tribology (materials, coatings and surface treatments). New York: Mc Graw Hill; 1991.
[32] Incropera FP, Dewitt DP. Fundamentals of heat and mass transfer. New York: Wiley; 2002.
[33] Callister WD. Materials science and engineering—an introduction. New York: Wiley; 2000.
[34] Samant AN, Dahotre NB. Computational predictions in single-dimensional laser machining of alumina. Int J Mach Tools Manuf 2008;48:1345–53.
[35] Ki H, Mohanty PS, Mazumder J. Multiple reflection and its influence on keyhole evolution. J Laser Appl 2002;14:39–45.
[36] Rahman FA, Takahashi K, Teik CH. Theoretical analysis of coupling between laser diodes and conically lensed single-mode fibres utilizing ABCD matrix method. Opt Commun 2003;215:61–8.
[37] Baily AW, Modak A. Numerical simulation of laser ablation with cavity reflections. J Thermophys Heat Transfer 1989;3:42–5.
[38] Modest MF. Effect of multiple reflections on hole formation during short-pulsed laser drilling. J Heat Transfer 2000;122:653–61.
[39] Minamida K, Takafuji H, Hamada N, Haga H, Mizuhashi N. Wedge shape welding with multiple reflection effects of high power CO_2 laser beam. 5th International Congress on Applications of Lasers and Electro-optics 1986:97–104.
[40] Bang SV, Roy S, Modest MF. CW Laser machining of hard ceramics—II. Effect of multiple reflections. Int J Heat Mass Transfer 1993;36:3529–40.
[41] Bang SV, Modest MF. Multiple reflection effects on evaporative cutting with a moving CW laser. J Heat Transfer 1991;113:663–9.
[42] Andrews JG, Atthey DR. Hydrodynamic limit to penetration of a material by a high-power beam. J Phys D: Appl Phys 1976;9:2181–94.
[43] Mazumdar J, Steen WM. Heat transfer model for CW laser material processing. J Appl Phys 1980;51:941–7.
[44] Yabe T, Mohamed MS, Uchida S, Baasandash C, Sato Y, Tuuji M, et al. Noncatalytic dissociation of MgO by laser pulses towards sustainable energy cycle. J Appl Phys 2007;101, doi:10.1063/1.2743730.
[45] Brewer L, Porter RF. A thermodynamic and spectroscopic study of gaseous Magnesium Oxide. J Chem Phys 1954;22:1867–77.
[46] Weimin Z, Yong S, Haipeng L, Chunyong L. The effects of some elements on the igniting temperature of magnesium alloys. Mater Sci Eng B 2006;127:105–7.
[47] Massalski TB, Okamoto H, Subramanian PR, Kacprzak L. Binary alloy phase diagrams. Materials Park, OH: ASM International; 1990.
[48] Samant AN, Dahotre NB. Ab initio physical analysis of single-dimensional laser machining of silicon nitride. Adv Eng Mater 2008;10:978–83.
[49] Barin I, Knacke O. Thermochemical properties of inorganic substance. New York: Springer; 1973.
[50] Beyer H, Ross W, Rudolph R. Interaction of CO_2 laser pulses of microsecond duration with Al_2O_3 ceramic substrates. J Appl Phys 1991;70:75–81.

Int J Adv Manuf Technol
DOI 10.1007/s00170-009-2004-0

ORIGINAL ARTICLE

Computational approach to photonic drilling of silicon carbide

Anoop N. Samant · Claus Daniel · Ron H. Chand · Craig A. Blue · Narendra B. Dahotre

Received: 9 June 2008 / Accepted: 3 March 2009

Abstract The ability of lasers to carry out drilling processes in silicon carbide ceramic was investigated in this study. A JK 701 pulsed Nd:YAG laser was used for drilling through the entire depth of silicon carbide plates of different thicknesses. The laser parameters were varied in different combinations for a well-controlled drilling through the entire thickness of the SiC plates. A drilling model incorporating effects of various physical phenomena such as decomposition, evaporation-induced recoil pressure, and surface tension was developed. Such comprehensive model was capable of advance prediction of the energy and time required for drilling a hole through any desired depth of material.

Keywords Nd:YAG laser · Silicon carbide · Ceramic · Drilling

1 Introduction

Laser beams are extensively used in the manufacturing industry for drilling, cutting, micromachining, welding, sintering, and marking [1]. The high density of the beam and excellent focusing characteristics of Nd:YAG lasers have made it suitable for drilling different materials [2]. Very small holes as well as holes with high aspect ratios can be drilled by lasers. As it is a noncontact process, tool wear is minimal compared to mechanical drilling and only present in the form of laser maintenance [3].

The workpiece absorbs the incident laser energy which is transformed mainly into heat. The material undergoes phase transformations when the temperature increases above decomposition temperature, decomposition products melt, and recoil forces are produced, thus generating a hole. Generation of the taper is a vital feature during the drilling operation due to the intrinsic focusing characteristic of the laser beam [4]. The diameter of the hole at entry is larger than that at the exit giving a positive taper to most of the drilled holes. Through engineering approaches such as utilization of a lens of long focal length with longer focal waist, such a taper can be minimized to an insignificant order of appearance. Some of the ejected material can resolidify and accumulate around the hole periphery forming the spatter which is one of the undesirable effects of laser drilling and requires subsequent finishing operations [5]. Innovative laser drilling techniques based on gel casting methods have been developed for reducing the deposition of spatter and strong alumina parts were successfully produced by this technique [6].

Lasers in pulsed mode offer high peak powers in a short time period, increasing thermal impact and enabling drilling through thicker material [1]. Lasers are used for industrial precision drilling for applications such as cooling holes in gas turbine components [7]. Drilling of SiC is particularly interesting to the semiconductor industry for the production of cooling plates. Metals, alloys, organic as well as inorganic nonmetals, ceramics, and composites can be drilled by lasers [8]. Recently, excimer lasers have been widely used for drilling purposes as each pulse eliminates only a thin layer of the material leading to precise control over the drill depth

A. N. Samant · C. Daniel · N. B. Dahotre (✉)
Department of Materials Science and Engineering,
The University of Tennessee,
Knoxville, TN 37996, USA
e-mail: ndahotre@utk.edu

C. Daniel · R. H. Chand · C. A. Blue
Materials Science and Technology Division,
Oak Ridge National Laboratory,
Oak Ridge, TN 37831, USA

Published online: 14 March 2009

and eliminating mechanical impact which poses a particular problem to composites. Nd:YAG lasers have been used for drilling holes in ceramics such as zirconia, which could be used for making ornaments such as necklaces and earrings. The effect of processing parameters on the heat affected zone (HAZ) thickness, and tapering of the holes drilled in zirconia ceramic has been studied [9]. As the ceramics are very brittle, drilling of ceramics is associated with fracture and crack generation [10]. Of the different available ceramics, silicon carbide (SiC) has long been considered as an outstanding material for high temperature, high power, and high frequency applications [11]. Due to its high thermal conductivity, mechanical hardness, excellent chemical resistance, and low thermal expansion coefficient, drilling of SiC is gaining popularity for different industrial needs. Besides Sciti et al. [12], not much work has been reported on the laser drilling of SiC. Hence, the present study aims at understanding the physical phenomena underlying the drilling of SiC ceramic by pulsed Nd:YAG laser and presents a mathematical model for predicting the effect of laser processing parameters on the depth of the drilling hole.

2 Experimental part

Conventional chemical vapor deposited (CVD) silicon carbide plates of 2 and 3 mm thickness were used for the drilling study. A JK 701 pulsed Nd:YAG laser (1064 nm wavelength) from GSI Lumonics, Rugby, England was used to drill SiC plates of 2 and 3 mm thicknesses. The laser had the capabilities to provide repetition rates varying from 0.2 to 500 Hz, pulse energy in the range of 0.1–55 J, and the pulse width ranging from 0.3–20 ms. The laser processing parameters such as peak power, pulse width, and repetition rate were varied in several different combinations until identification of a set of parameters that provided sufficient interaction between the laser beam and the ceramic surface for required through drilling of SiC plates. For this set of laser processing parameters, multiple pulses were applied until a through hole was drilled in SiC plates. It was observed that for a power of 300 W, pulse duration of 0.5 ms, and repetition rate of 50 Hz, a through hole in the 2 mm thick plate could be drilled in approximately 0.5 s, while under the same conditions, a through hole in the 3-mm thick plate was produced in approximately 2.5 s. De-focusing of the laser through a thicker plate decreases the actual fluence (energy density) at the material front, and needed pressure to eject the molten fraction of decomposed species increases with the hole depth, thus leading to a decreased material removal rate while proceeding through the thickness. Therefore, the drilling time is not a linear function of the thickness.

Under the set of parameters employed in the present work, the repetition rate of 50 Hz over 0.5 s corresponded to 25 pulses, while over 2.5 s, it was equivalent to 125 pulses. The visual observations ensured the creation of holes (Fig. 1) with 25 and 125 pulses in 2 and 3 mm thick plates, respectively. As mentioned earlier, these holes were drilled with a lens of longer focal length and longer focal waist to minimize the tapering effect. But experimentally observed prediction of the exact number of pulses required to produce through hole during such laser-based rapid process remains a challenging task. In light of this, development of a computational model for such predictions is the most appropriate approach. Furthermore, the computational model can be extended to predict drilling parameters for plates of other thicknesses. The physical processes taking place along the depth are entirely different from those occurring at the surface. Efforts are ongoing to incorporate them in the computational model which will enable to predict the hole diameter at the surface, and this will be presented in due course of time. However, for the present study, the hole diameter is assumed to be equivalent to the laser-spot diameter [13].

3 Computational approach: temporal evolution, recoil pressure, and surface tension effects

During the drilling process, temperature at the surface of the ceramic changes because of the absorbed laser energy. To predict the depth of drilled hole, the surface temperature profiles and associated thermal gradient within the material were calculated. In order to estimate the temperature rise during the ON time and the following temperature drop during the OFF time, the ON and OFF times during drilling under the present set of laser parameters were calculated and along with the process parameters employed in the present study are represented in Table 1. Table 1 also represents the actual drilling energy required (3.75 J for the 2-mm thick plate and 18.75 J for the 3 mm thick plate), which was calculated by multiplying the power (300 W) by the total ON time (12.5 ms for the 2 mm thick plate and 62.5 ms for the 3 mm thick plate).

The computations were run until the hole was drilled through the entire thickness of the plate (2 and 3 mm) and were started with calculation of the maximum temperature reached after the first pulse employing a three-dimensional heat transfer flow model which was developed in COMSOL's heat transfer mode [14] and was based on Fourier's second law of heat transfer:

$$\frac{\partial T(x,y,z,t)}{\partial t} = \frac{k(T)}{\rho C_p(T)}\left[\frac{\partial^2 T(x,t)}{\partial x^2} + \frac{\partial^2 T(y,t)}{\partial y^2} + \frac{\partial^2 T(z,t)}{\partial z^2}\right] \quad (1)$$

where $k(T)$ and $C_p(T)$ are the variations in thermal conductivity and specific heat as a function of temperature,

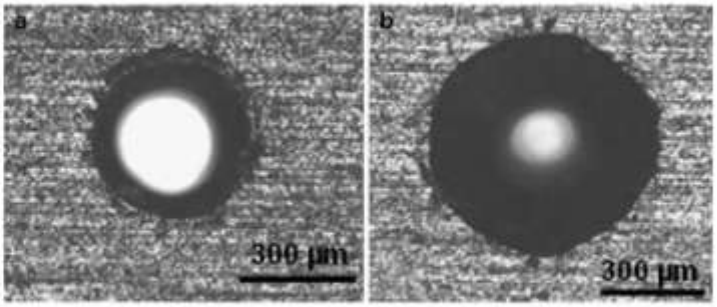

Fig. 1 Front surface showing drilled holes in **a** 2 mm and **b** 3 mm SiC plates

ρ is the density of SiC (3,100 kg/m^3) [15], T is the temperature field, t is time, and x, y, and z are the spatial directions. For improving the accuracy of calculations, variation of thermal conductivity and specific heat as a function of temperature (Fig. 2) were taken into account in the model, and these properties were assumed to be constant after about 1,700 K [15] The latent heat of solidification was accounted for by considering the variation of specific heat as a function of temperature. At time t=0, the initial temperature of T=T_0=300 K was applied. The balance between the absorbed laser energy at the surface and the radiation losses was given by:

$$-k(T)\left(\frac{\partial T(x,y,0,t)}{\partial x}+\frac{\partial T(x,y,0,t)}{\partial y}+\frac{\partial T(x,y,0,t)}{\partial z}\right)=\delta\alpha I-\varepsilon\sigma\left(T(x,y,0,t)^4-T_0^4\right)$$
$$\delta=1 \quad \text{if } 0\le t\le t_{on}$$
$$\delta=0 \quad \text{if } t>t_{on} \tag{2}$$

where $k(T)$ is the temperature dependent thermal conductivity of the material (W/mK), ε is emissivity for thermal radiation (0.7) [15], I is the laser power intensity, t_{on} is the ON time, σ is Stefan Boltzman constant (5.67×10^{-8} W/m^{2}K^4), and α is the absorptivity of the material. The term δ takes a value of 1 when the time, t, is less than the pulse on-time, t_{on}, and it is 0 when the time, t, exceeds the pulse on-time. Thus, the value of δ depends on the time, t, and ensures that the energy is input to the system only during the pulse on-time and cuts off the energy supply during the following pulse off-time.

SiC has a very high absorptivity of 0.95 at 1,064 nm wavelength (for Nd:YAG laser used in present case) and 1,298 K [15], and this value increases with temperature as the depth of the drilled hole increases. The drilled hole is partially filled with decomposed liquid and vapor species, and the laser beam undergoes multiple reflections and absorption within the cavity and these phases (melt and vapor species) for increased absorption of laser energy. Due to a very high absorptivity of SiC (0.95) coupled with further increased absorption due to these physical changes within the laser substrate interaction region, the resultant absorption of the ceramic is almost instantaneously expected to reach nearly 100%. Earlier, similar explanations and assumptions during laser processing of a variety of materials are adopted [16, 17]. Furthermore, for an extremely short duration, high-energy density dynamic process like laser material interaction, it has been extremely difficult to accurately conduct in situ measurements for the instant at which the ceramic starts absorbing all the input energy. In light of this, in the present study, it was reasonable to consider the drilled hole as a black body with 100% absorption. The convection taking place at the bottom surface of the sample was given by:

$$-k(T)\left(\frac{\partial T(x,y,L,t)}{\partial x}+\frac{\partial T(x,y,L,t)}{\partial y}+\frac{\partial T(x,y,L,t)}{\partial z}\right)=h(T(x,y,L,t)-T_0), \tag{3}$$

where L is the thickness of the sample which was taken as 2 and 3 mm for the two different SiC plates used in the present study, and h is the heat transfer coefficient (W/m^{2}K) which was included as a function of temperature [18]. In the short time scale used for laser processing, the heat flow in the direction orthogonal to the laser beam can be neglected. Thus, Eqs. 1, 2, and 3, above could be considered to represent the heat flow, radiation losses, and

Table 1 Parameters for laser processing

Plate thickness (mm)	Operation time (s)	Number of pulses	Drilling energy (J)	Pulse width (ON time) (ms)	OFF time (ms)	Total ON time (ms)	Total OFF time (ms)
2	0.5	25	3.75	0.5	19.5	12.5	487.5
3	2.5	125	18.75	0.5	19.5	62.5	2437.5

convection, respectively, taking place only along the z direction, neglecting these phenomena in the x and y directions. Incorporation of these effects in the x and y directions will be dealt in subsequent work and will be presented in the future. The solution of this model gave the maximum surface temperature reached after the first pulse which was input in Eq. 4, below to predict the temperature reached after the laser is switched off [2]:

$$T_i' = T_i + (T_0 - T_i)\left[1 - \left[\exp\frac{h(T)^2\alpha(T)t_{off}}{k(T)^2}\right]\left[1 - \mathrm{erf}\left(\frac{h(T)\sqrt{\alpha(T)t_{off}}}{k(T)}\right)\right]\right] \tag{4}$$

where T_i is the temperature during heating of pulse i (K), T_0 is the ambient temperature of 300 K, t_{off} is the OFF time between successive pulses (Table 1) and erf() is the error function. The term $\alpha(T)$ is the temperature-dependent thermal diffusivity of the material given by $k(T)/\rho C_p(T)$. When the laser is active, the surface temperature is given by [2]:

$$T_i = T_{i-1}' + \frac{8aP}{\pi d^2}\frac{\sqrt{\alpha(T)t_{on}/\pi}}{k(T)} \tag{5}$$

where T_{i-1}' is the temperature during cooling of the earlier pulse (K) predicted from Eq. 4, above, a is the absorptivity of the material mentioned above, P is the incident beam power (300 W), d is the beam diameter (0.24 mm), and t_{on} is the pulse duration (ON time). The temperatures reached during the ON and OFF periods of the successive pulses were determined by repeatedly solving Eqs. 4 and 5, until the thickness of the plate was reached. The expressions for the temperatures reached during the ON and OFF periods (Eqs. 4 and (5), above) were valid as the heat transfer occurring in the direction perpendicular to the laser beam was not considered. As mentioned above, the processing time being extremely small, these assumptions were justified.

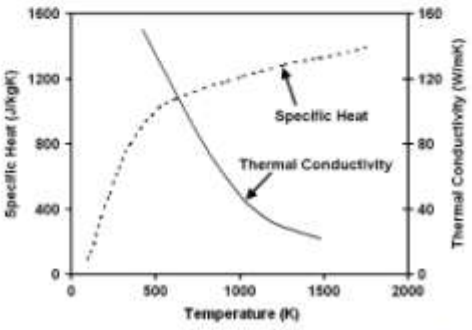

Fig. 2 Variation of thermophysical properties with temperature [15]

The decomposition temperature of SiC is 3,103 K [19] at which decomposition products immediately melt. The melt depth (z_t) from the surface at any instant was predicted from the temperature profiles by tracking the depth at which this decomposition temperature was reached. This depth was used as a starting point for further calculations. However, there was some loss of material at the surface due to evaporation and the rate of evaporation j_d (kg/m^{2}s) [20] is given by:

$$j_d = p(T_s)\left[\frac{m_v}{2\pi kT_s}\right]^{1/2} \tag{6}$$

where m_v is mass of the vapor molecule (6.641×10^{-26} kg/at for SiC), T_s is the surface temperature, k is the Boltzmann constant (1.38065×10^{-23} J/K), and $p(T_s)$ is the saturation pressure given by the Clausius–Clapeyron equation:

$$p(T_s) = p_0\exp[(L_v/kT_e)(1 - T_e/T_s)] \tag{7}$$

where p_0 is the ambient pressure (1.013×10^5 N/m^2), L_v is latent heat of evaporation (530 kJ/mol for SiC) [21], and T_e is the evaporation/decomposition temperature. The equivalent depth of material evaporated was predicted from the rate of evaporation by the relation:

$$z_{eva} = \frac{j_d \times \text{increment in time}}{\rho} \tag{8}$$

where ρ is the constant value of density of SiC (3,100 kg/m^3) [15] mentioned above, and this evaporated depth (z_{eva}) (Fig. 3) was subtracted from the melt depth (z_t) to give the

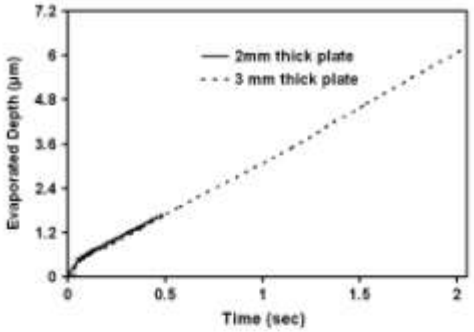

Fig. 3 Material evaporation with time for SiC drilling

available melt pool (z_{eva}). The amount of material evaporated increased with time, as it depends on the surface temperature which also increased with time during the ON time of each pulse. At the same time, there is a drop in temperature at any instant at the surface due to cooling of the melt pool by evaporation which is predicted by [22]:

$$\Delta T_{eva} = \frac{2z_{eva}\rho L_v}{k(T)\pi\, d\pi^{3/2}} \operatorname{arc\,tg} \frac{4\sqrt{\alpha(T) \times \text{increment in time}}}{d} \tag{9}$$

where z_{eva} is the depth of material evaporated as predicted from Eq. 8, above, $k(T)$ is the temperature dependent thermal conductivity of the material (W/mK) [15] mentioned above, and the term $\alpha(T)$ is the temperature dependent thermal diffusivity of the material given by $k(T)/\rho C_p(T)$. This drop in temperature was subtracted from the temperature predicted by Eqs. 4 and 5 above to give the actual surface temperature at any given time instant as represented in Fig. 4. The heating curve meanders because the temperature drops during the OFF time and rises during the ON time of the laser even after a drop due to the evaporation. The maximum surface temperature reached, while drilling the 2-mm thick plate was more compared to the maximum surface temperature reached for drilling through the 3-mm thick plate as more number of pulses (more time) were required for drilling through the 3-mm plate compared to the 2-mm thick plate.

Depending upon the thermodynamic conditions prevailing during laser drilling, the decomposition of SiC may produce several stoichiometric and/or nonstoichiometric species such as $Si_{(l)}$, $C_{(s)}$, $C_{(g)}$, $Si_{(g)}$, $Si_{3(g)}$, $Si_{2(g)}$, $SiC_{2\ (g)}$, $Si_2C_{(g)}$, and $Si_{(s)}$ [12]. In situ detection of formation of these species during extremely dynamic and short duration laser drilling process is a challenging task and will be considered in future efforts. However, the most likely reaction to

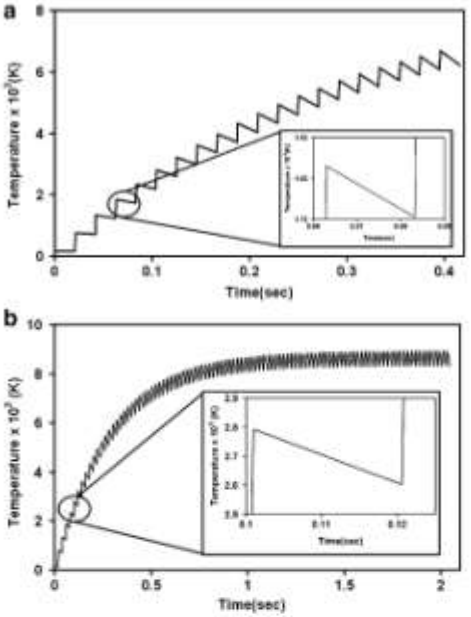

Fig. 4 Heating curves for **a** 2 mm thick plate and **b** 3 mm thick plate

produce liquid species at the decomposition temperature is the following reaction.

$$SiC = Si_{(l)} + C_{(s)} \tag{10}$$

The Gibbs free energy associated with this reaction (−335.96 kJ/mol at 3259 K [23]) was used to determine the energy loss due to dissociation. Due to the presence of a minimum taper as mentioned above, the hole could be assumed to have a cylindrical cross section (of volume $V_{pool} = \frac{\pi\left(0.24\times10^{-3}\right)^2 z_{eva}}{4}\,\mathrm{m}^3$. As 1 mol of a substance corre-

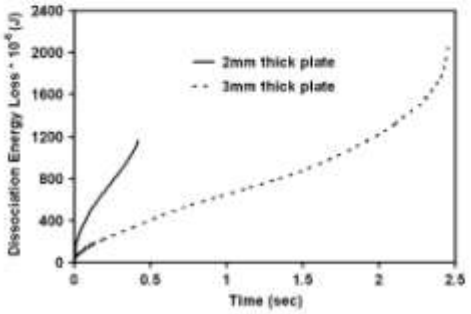

Fig. 5 Dissociation Energy loss during SiC drilling

sponds to 22.4×10^{-3} m^3, there will be $2.019\times10^{-6}\times z_{ava}$ moles in the volume V_{pool} of the melt and the energy loss due to dissociation (Fig. 5) is expressed as

$$E_{diss} = (0.6783 \times z_{ava})J \tag{11}$$

This energy loss was subtracted from the input laser energy to give the effective laser energy for subsequent pulses. The dissociation energy losses increased with time, as it was a function of the melt depth which also increased with time.

The ejection of the molten material can take place either by the reactive recoil pressure due to the vapor or plasma of the ambient medium and cannot take place by both the mechanisms. At laser intensities of the order of 10^9 W/cm, the purely evaporational mechanism of material removal takes place [24]. Thus the mechanism for material removal is dictated by the laser beam intensity. However, for an incident beam power of 300 W and beam diameter of 0.24 mm used in the present study, the laser intensity was 1.25×10^4 W/cm which was far less than the intensity required for the plasma pressure effect on material removal. Hence, the effect of plasma pressure was neglected and only the effect of evaporation induced recoil pressure on material removal was considered.

As mentioned earlier, a melt pool comprising of liquid Si produced due to the decomposition of SiC during the laser irradiation is formed below the vaporization front, and the expulsion of this molten material at very high velocities is driven by the recoil pressure stimulated by some of the decomposed species [25, 26]. However, the entire melt pool measured from the surface was not available for expulsion. Only the portion remaining after a fraction of the available melt depth (z_{ava}) was expelled by the recoil pressure would be the effective melt depth (z_{eff}), and it will be available for expulsion for the next time instant. The fraction of the melt pool that is expelled by the recoil pressure will be predicted in the later part of this section. The evaporation-induced recoil pressure p_r is given by [27]:

$$\frac{\pi d^2 p_r}{4aP} = \frac{1.69}{\sqrt{L_v}}\left(\frac{b}{1+2.2b^2}\right) \tag{12}$$

where $b^2 = kT_s/m_vL_v$. Thus, the predicted temperature field assisted in determining the evaporation-provoked recoil pressure at the surface during drilling through the SiC ceramic using the physical model of melt hydrodynamics proposed by Anisimov who also experimentally verified the same [27]. According to Anisimov, when the surface temperature exceeds the boiling point or the decomposition temperature, the recoil pressure becomes $0.55p_s$, where p_s is the saturated vapor pressure (1.01325×10^5 N/m^2). Under typical materials processing conditions such as those encountered in drilling, this recoil pressure exceeds the highest surface tension pressure and plays a vital role in removal of material in molten state.

It can be seen from the heating curves shown above in Fig. 4 that the maximum surface temperature reached for drilling through the entire depth of 3 mm plate was more than that reached while drilling through the 2-mm plate. However, the maximum recoil pressure attained (Fig. 6) was almost the same for both the cases ($\sim3.73\times10^5$ Pa). It can be observed from Eq. 12 that the recoil pressure depends not only on the maximum surface temperature but also on the laser power which was the same in both the cases (300 W). The recoil pressure does not continuously increase with surface temperature. Once a certain maximum surface temperature was reached after some pulses and the corresponding maximum recoil pressure was attained, then the recoil pressure ceases to increase any further. After the maximum recoil pressure was reached, even though there was a slight drop in the recoil pressure, it was sufficient to continue expulsion of the fraction of the molten part of the decomposed species available at different time instants.

The melt pool shape is affected by the surface tension in addition to the presence of recoil pressure [28]. It was necessary to consider the surface tension effect, as it modifies the pressure on the melt and affects the depth of the drilled hole. The surface tension pressure depends on the effective beam radius [25], which changes as it gets defocused with the changes in the hole depth and is given by [2]:

$$r_{eff} = \frac{d}{2}\left[1+\left(M^2\frac{4\lambda(Z_{eff}+\delta_f)}{\pi d^2}\right)^2\right]^{1/2} \tag{13}$$

where λ is the laser wavelength (1,064 nm), δ_f is the focal length (120 mm), M^2 is the beam quality parameter assumed to be 1 for a perfect Gaussian beam profile, and z_{eff} is the effective melt depth explained earlier. Beam

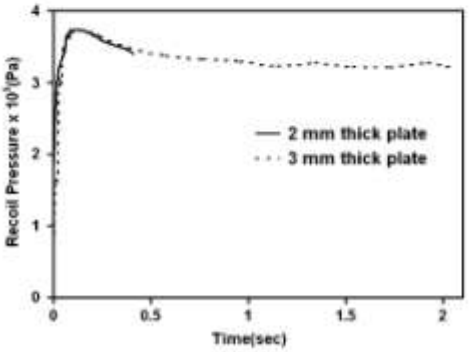

Fig. 6 Recoil pressure variations with time for SiC drilling

quality is a measure of the focusability of the laser used, and beam quality factor is a standard measure used for the same. In this study, it is assumed that the beam is initially at full focus corresponding to a beam quality factor of 1. All real beams tend to have an M^2 value greater than 1. Attempts are ongoing for accurate M^2 determination, and they will be incorporated in future work. However, the effect of the defocusing of the laser beam is taken into account by determining the effective beam radius from Eq. 13 above. The melt available at the axis of the beam was expelled with a velocity v_{exp} given by [25]:

$$v_{exp}(t) = \frac{1}{\rho}\frac{p_r - \tau/r_{eff}}{r_{eff}}t \tag{14}$$

where r_{eff} is the effective beam radius determined above in Eq. 13, t is the time, and τ is the surface tension coefficient. As the thermophysical properties of SiC control the dissociation of SiC into its species, the SiC properties were considered only until SiC dissociated into liquid Si after which the properties of Si melt were taken into account. Hence, the surface tension coefficient of liquid Si (843 dyne/cm for liquid Si [29]) was considered as it affects the expulsion velocity and hence the depth of the drilled hole. The fraction of the effective melt depth that was expelled at a certain time instant, d_t, was obtained by integrating the expelled velocity over time (Eq. 15) and the depth of the hole was given by Eq. 16 [30],

$$d_t = \int_0^t v_{exp}(t)\,dt \tag{15}$$

$$h_t = \sum_0^t d_t \tag{16}$$

The step-wise procedure followed to achieve the final depth is presented in Fig. 7, where it can be seen that the material properties and dimensions along with the laser processing parameters were used to solve the fundamental heat transfer equation to obtain the preliminary temperature profiles and melt depth predictions. The input energy, melt depth, and heating curves were altered due to the losses taking place during the dissociation and evaporation processes. The modified temperature profiles then assisted in determining the recoil pressure and associated velocity of expulsion of the melt leading to the final determination of the hole depth and prediction of required number of pulses. The evolution of the drilled hole with time and the different stages of its formation are schematically represented in Fig. 8a, b, respectively.

It can be observed from Fig. 8a that a 2-mm thick plate was drilled through its entire depth in 0.41 s, while it took 2.05 s to drill through the entire thickness of a 3-mm

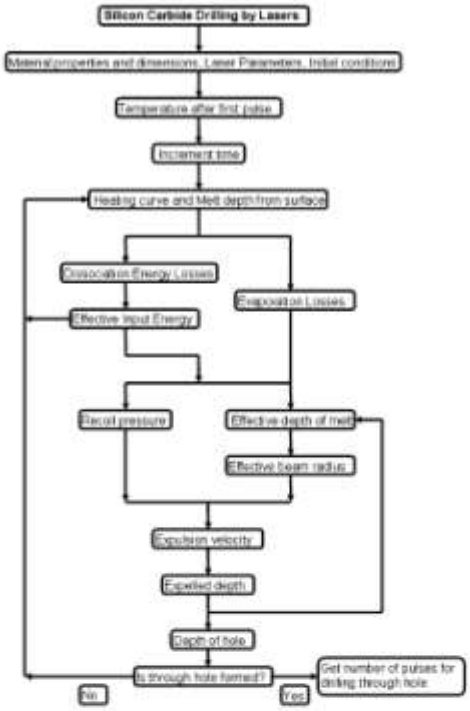

Fig. 7 Flowchart showing procedure for prediction of drilled depth

thick plate. Thus, only 21 pulses for a 2-mm plate and 103 pulses for a 3-mm plate were required to drill through the entire thickness. The predicted total ON time (for a pulse duration of 0.5 ms) corresponding to 21 pulses and 103 pulses was 10.5 and 51.5 ms, respectively. The corresponding predicted drilling energy was obtained by multiplying the power (300 W) by the total predicted ON times for the 2 and 3 mm thick plates, and these drilling energies have also been compared in Table 2. Therefore, as can be seen from Table 2, computationally predicted number of pulses and drilling energy was less than those experimentally identified [25 pulses (3.75 J) for the 2 mm plate and 125 pulses (18.75 J) for the 3-mm plate]. This discrepancy is due to the fact that selection of number of pulses during actual drilling was based on prior practical experience in laser–materials interactions and visual observations. It can be observed from Fig. 8b that in the initial stages of drilling (until around time instant t_2), the recoil pressure expelled the material in the upward direction and continued to do so for increased depth of the drilled hole as the time progressed. Eventually, when a

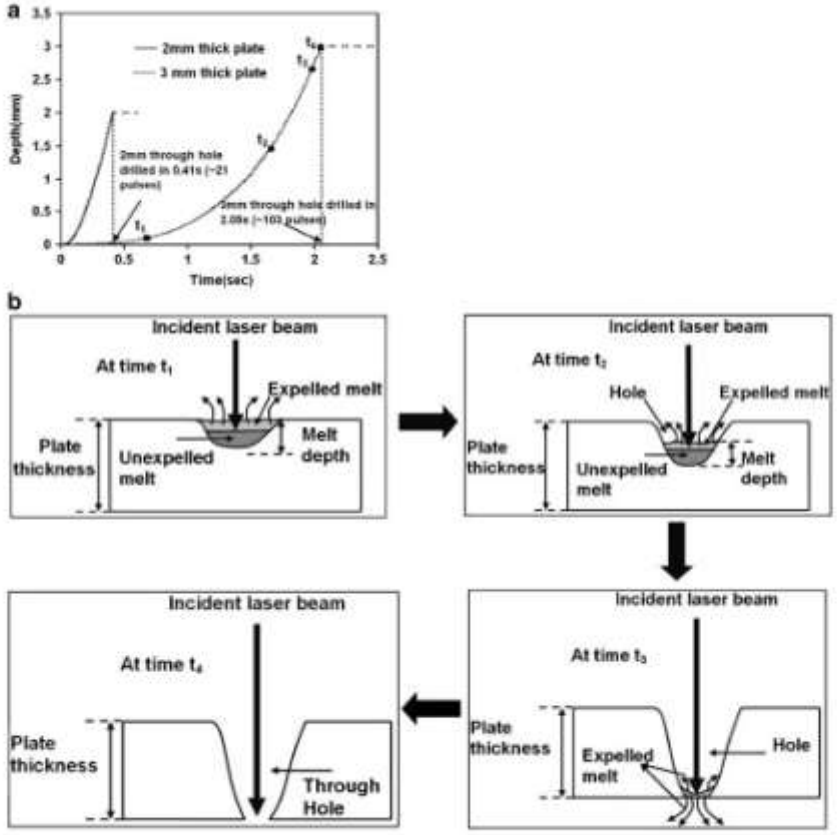

Fig. 8 a Evolution of drill depth with time. **b** Schematic for progression of hole formation during through drilling of ceramic

very thin layer of the material remained in the bottom (at around time instant t_3), the recoil pressure was able to push most of the material in the downward direction thereby reversing the direction of material expulsion in the final stages of drilling. This happened due to the least resistance to the recoil pressure by the small mass of supporting material at the bottom. Finally, at around time instant t_4, all the rest of molten material was expelled and a clean through hole was formed. Thus, the prediction of exact number of pulses (for that matter pulse duration, laser energy, etc.) to drill a required depth in a given type of material under chosen set of laser processing parameters would be extremely advantageous to conserve substantial energy and time.

Table 2 Comparison between measured and predicted number of pulses and drilling energy

Plate thickness (mm)	Number of pulses$_{measured}$	Number of pulses$_{predicted}$	Drilling energy$_{measured}$ (J)	Drilling energy$_{predicted}$ (J)
2	25	21	3.75	3.15
3	125	103	18.75	15.45

4 Conclusion

Through drilling of silicon carbide was successfully carried out using pulsed Nd:YAG laser. A comprehensive theoretical model incorporating the thermal effects in decomposing material, the effect of evaporation induced recoil pressure, surface tension in expelling molten part of the decomposed species, cooling of the surface due to evaporation, and loss in energy due to dissociation assisted in prediction of a drill depth under given processing conditions. Such comprehensive approach distinguished the model from many earlier works including that of Salonitis et al. [2] who considered the drilling mechanism as the melting and subsequent removal of a material volume and Sciti et al. [12] who only considered the microstructural surface modification of SiC as a function of laser processing parameters without considering the actual physical phenomena such as the effect of recoil pressure, evaporation losses, and dissociation energy losses responsible for hole formation as considered in the present study.

In the present study, the computational model specifically indicated that although 25 pulses (3.75 J) and 125 pulses (18.75 J) were employed, only 21 pulses (3.15 J) and 103 pulses (15.45 J) were sufficient for drilling through the entire thickness of 2 and 3 mm plates, respectively, under the present laser processing conditions. The maximum recoil pressure of $\sim 3.73 \times 10^5$ Pa predicted by the model was responsible for expulsion of the melt pool during drilling. Even though the loss of material due to evaporation at the surface contributed to only a small fraction of the total depth drilled through the SiC plate, it was essential to be considered as its magnitude depends on the thermophysical properties of the material and the processing conditions, and these losses could be significant in the drilling of some other materials. Thus, the model is capable of providing an advance estimate of the number of pulses required to drill a desired depth in a given material.

Acknowledgement Claus Daniel acknowledges financial support from the Eugene P. Wigner Fellowship Program at Oak Ridge National Laboratory, managed by UT-Battelle, LLC, for the U.S. Department of Energy under contract no. DE-AC05-00OR22725.

References

1. Dubey AK, Yadava V (2008) Experimental study of Nd:YAG laser beam machining—an overview. J Mater Process Tech 195:15–26. doi:10.1016/j.jmatprotec.2007.05.041
2. Salonitis K, Stournaras A, Tsoukantas G, Stavropoulos P, Chryssolouris G (2007) A theoretical and experimental investigation on limitations of pulsed laser drilling. J Mater Process Tech 183:96–103. doi:10.1016/j.jmatprotec.2006.09.031
3. Srinivasa MJ (1994) Investigation of the drilling dynamics and melt expulsion mechanisms during the laser drilling of Ti-6Al-4V using high speed photography Masters Thesis University of Tennessee
4. Ghoreishi M, Low DKY, Li L (2002) Comparative statistical analysis of hole taper and circularity in laser percussion drilling. Int J Mach Tools Manuf 42:985–995. doi:10.1016/S0890-6955(02)00038-X
5. Low DKY, Li L, Byrd PJ (2003) Spatter prevention during the laser drilling of selected aerospace materials. J Mater Process Tech 139:71–76. doi:10.1016/S0924-0136(03)00184-5
6. Guo D, Cai K, Yang J, Huang Y (2003) Spatter-free laser drilling of alumina ceramics based on gelcasting. J Eur Ceram Soc 23:1263–1267. doi:10.1016/S0955-2219(02)00299-6
7. Yeo CY, Tam SC, Jana S, Lau MWS (1994) A technical review of the laser drilling of aerospace materials. J Mater Process Tech 42:15–49. doi:10.1016/0924-0136(94)90073-6
8. Meijer J (2004) Laser beam machining (LBM), state of the art and new opportunities. J Mater Process Tech 149:2–17. doi:10.1016/j.jmatprotec.2004.02.003
9. Kuar AS, Doloi B, Bhattacharyya B (2006) Modelling and analysis of pulsed Nd:YAG laser machining characteristics during micro-drilling of zirconia (ZrO2). Int J Mach Tools Manuf 46:1301–1310. doi:10.1016/j.ijmachtools.2005.10.016
10. Nedialkov N, Sawczak M, Jendrzejewski R, Atanasov P, Martin M, Śliwiński G (2007) Analysis of surface and material modifications caused by laser drilling of AlN ceramics. Appl Surf Sci 254:893–897. doi:10.1016/j.apsusc.2007.07.151
11. Zeppel S, Farsari M, Mertz R, Zehetner J, Stangl G, Reider GA et al (2006) Laser micro machining of 3C–sic single crystals. Microelectron Eng 83:1400–1402
12. Sciti D, Bellosi A (2001) Laser-induced surface drilling of silicon carbide. Appl Surf Sci 180:92–101. doi:10.1016/S0169-4332(01)00330-0
13. Ng GKL, Crouse PL, Li L (2006) An analytical model for laser drilling incorporating effects of exothermic reaction, pulse width and hole geometry. Int J Heat Mass Transfer 49:1358–1374. doi:10.1016/j.ijheatmasstransfer.2005.10.002
14. Harimkar SP, Samant AN, Dahotre NB (2007) Temporally evolved recoil pressure driven melt infiltration during laser surface modifications of porous alumina ceramic. J Appl Phys 101:054911.1–054911.7. doi:054911
15. Touloukian YS (1967) Thermophysical Properties of High Temperature Materials. IFI/Plenum, New York
16. Andrews JG, Atthey DR (1976) Hydrodynamic limit to penetration of a material by a high-power beam. J Phys D Appl Phys 9:2181–2194. doi:10.1088/0022-3727/9/15/009
17. Mazumdar J, Steen WM (1980) Heat transfer model for cw laser material processing. J Appl Phys 51:941–947. doi:10.1063/1.327672
18. Incropera FP, Dewitt DP (2002) Fundamentals of heat and mass transfer. Wiley, New York
19. Bhushan B, Gupta BK (1991) Handbook of Tribology Materials, Coatings and Surface Treatments. Mc Graw Hill, New York
20. Duley WW (1998) Laser welding. Wiley, New York, NY
21. Reitano R, Baeri P (1996) Nanosecond laser-induced thermal evaporation of silicon carbide. Int J Thermophys 17:1079–1087. doi:10.1007/BF01441996
22. Allmen MV, Blaser P, Affolter K, Strumer E (1978) Absorption phenomena in metal drilling with Nd-lasers. IEEE J Quantum Electron 14:85–88. doi:10.1109/JQE.1978.1069739
23. Barin I, Knacke O (1973) Thermochemical properties of inorganic substance. Springer, New York
24. Anisimov VN, Arutyunyan RV, Bannov VY et al (1984) Applied Optics 23:18–24

25. Matsunawa A, Semak V (1997) The simulation of front keyhole wall dynamics during laser welding. J Phys D Appl Phys 30:798–809. doi:10.1088/0022-3727/30/5/013
26. Semak V, Matsunawa A (1997) The role of recoil pressure in energy balance during laser materials processing. J Phys D Appl Phys 30:2541–2552. doi:10.1088/0022-3727/30/18/008
27. Anisimov SI (1968) Vaporization of metal absorbing laser radiation. Sov Phys JETP 27:182–183
28. Han L, Liou FW, Musti S (2005) Thermal behavior and geometry model of melt pool in laser material process. J Heat Transf 127:1005–1014. doi:10.1115/1.2005275
29. Yuan ZF, Mukai K, Huang WL (2002) Surface temperature and its temperature coefficient of molten silicon at different oxygen potentials. Langmuir 18:2054–2062
30. Semak VV, Knorovsky GA, MacCallum DO, Roach RA (2006) Effect of surface tension on melt pool dynamics during laser pulse interaction. J Phys D Appl Phys 39:590–595. doi:10.1088/0022-3727/39/3/025

Available online at www.sciencedirect.com
ScienceDirect
Ceramics International 35 (2009) 2093–2097
CERAMICS INTERNATIONAL
www.elsevier.com/locate/ceramint

Short communication

Differences in physical phenomena governing laser machining of structural ceramics

Anoop N. Samant, Narendra B. Dahotre *

Department of Materials Science and Engineering, The University of Tennessee, Knoxville, TN 37996, United States

Received 18 August 2008; received in revised form 23 September 2008; accepted 9 November 2008
Available online 3 December 2008

Abstract

Several structural ceramics such as alumina, silicon nitride, silicon carbide and magnesia were machined using a pulsed Nd:YAG laser. Laser processing conditions and temperature dependent thermo-physical properties govern the physical phenomena that machine these ceramics. Melting, dissociation and evaporation are some of the vital mechanisms associated with material removal. Discrimination and incorporation of these physical processes into a hydrodynamic machining model to predict different machining parameters was conducted. The model provides an outstanding tool for advance prediction of thermal energy and time required for machining desired depth of material.

Keywords: D. Al_2O_3; D. Si_3N_4; D. SiC; D. MgO

1. Introduction

Exceptional properties like high hardness, high thermal resistance and chemical stability have increased the use of structural ceramics such as alumina (Al_2O_3), silicon carbide (SiC), silicon nitride (Si_3N_4) and magnesia (MgO) for several electronic, automotive and medical applications [1]. Al_2O_3 is used in making seals, valves, medical implants, and as a substrate in hybrid circuits. Piston rings, bearings, cams are made by machining Si_3N_4 while MgO is used in brake linings, thermocouple housings and in thin film semi-conductors. SiC is also gaining popularity for high temperature, high frequency and high power applications. Hard and brittle nature of these ceramics pose a hindrance in the use of traditional methods based on mechanical grinding and fracturing for machining them. Recently, Laser Machining (LM) has transpired to be one of the widely desired machining techniques on account of its contact less processing, low production costs, efficient material utilization and automation [2–5]. This study aims at understanding the physical phenomena behind the material removal process during machining the above mentioned structural ceramics by a JK 701 pulsed Nd:YAG laser (1064 nm wavelength). The intention of this paper is just to discriminate various mechanisms such as melting, dissociation and evaporation which could be responsible for machining of the different structural ceramics. However, the details of the physical processes and computational results associated with machining of each individual ceramic are separately described elsewhere [6–9].

2. Laser–ceramic interaction

Once the laser beam is incident on the ceramic surface, absorption, reflection, refraction, transmission, and scattering are the different physical phenomena that take place. The majority of the energy is absorbed and this absorption depends on the wavelength and spectral absorptivity characteristics of the material being machined [10]. For machined cavities with high aspect ratios as considered in this study, the multiple beam reflections along the wall of the cavity also influence the energy absorption and 100% of the energy is immediately absorbed [11].

2.1. Temporal evolution

The laser energy converted into heat conducts into the material according to Fourier's second law of heat transfer (Eq. (1)), and simultaneously radiates (Eq. (2)) and convects

* Corresponding author. Tel.: +1 865 974 3609; fax: +1 865 974 4115.
E-mail address: ndahotre@utk.edu (N.B. Dahotre).

0272-8842/$34.00
doi:10.1016/j.ceramint.2008.11.013

(Eq. (3)) from the surface [12].

$$\frac{\partial T(x,y,z,t)}{\partial t} = \alpha(T)\left[\frac{\partial^2 T(x,y,z,t)}{\partial x^2} + \frac{\partial^2 T(x,y,z,t)}{\partial y^2} + \frac{\partial^2 T(x,y,z,t)}{\partial z^2}\right] \quad (1)$$

where $k(T)$ and $C_p(T)$ are variations in thermal conductivity and specific heat as a function of temperature, ρ is density of ceramic, T is temperature field, t is time and x, y and z are spatial directions.

$$-k(T)\left(\frac{\partial T(x,y,0,t)}{\partial x} + \frac{\partial T(x,y,0,t)}{\partial y} + \frac{\partial T(x,y,0,t)}{\partial z}\right) - \frac{4\delta a Q}{\pi d^2} - \varepsilon\sigma\left(T(x,y,0,t)^4 - T_0^4\right) \quad (2)$$

$\delta = 1$ if $0 \le t \le t_{on}$; $\delta = 0$ if $t > t_{on}$

where ε is emissivity for thermal radiation, Q is incident beam power, d is beam diameter, T_0 is ambient temperature, t_{on} is the pulse ON time, σ is Stefan-Boltzman constant (5.67×10^{-8} W/m^2 K^4) and a is absorptivity of the material. In the present case, the values of absorptivity were obtained from previously published references in the open literature. Although it is very difficult in an extremely short duration high energy density dynamic process like laser–material interaction to accurately conduct in situ absorptivity measurements, efforts are going on in parallel for in situ measurement of actual absorptivity values under laser processing conditions similar to the ones employed in the present work. The term δ takes a value of 1 when the time, t is less than t_{on} and it is 0 when the time, t exceeds t_{on}. Thus the value of δ depends on the time, t and ensures that the energy is input to the system only during the pulse on-time and cuts off the energy supply during the following pulse off-time.

$$-k(T)\left(\frac{\partial T(x,y,D,t)}{\partial x} + \frac{\partial T(x,y,D,t)}{\partial y} + \frac{\partial T(x,y,D,t)}{\partial z}\right) = h(T(x,y,D,t) - T_0) \quad (3)$$

where D is the thickness of the ceramic being machined and $h(T)$ is the heat transfer coefficient as a function of temperature. The temperature rise and fall during the ON and OFF time, respectively, also affect the temporal and spatial evolution of temperature within the ceramic body which in turn influences the material removal mechanism [13] (Eq. (4 and 5)).

$$T_i' = T_i + (T_0 - T_i) \times \left[1 - \left[\exp\frac{h(T)^2\alpha(T)t_{off}}{k(T)^2}\right]\left[1 - \operatorname{erf}\left(\frac{h(T)\sqrt{\alpha(T)t_{off}}}{k(T)}\right)\right]\right] \quad (4)$$

where T_i is the temperature during heating of pulse i, t_{off} is the OFF time between successive pulses and erf() is the error function. The term $\alpha(T)$ is the temperature dependent thermal diffusivity of the material given by $k(T)/\rho\, C_p(T)$.

$$T_i = T_{i-1}' + \frac{8aQ}{\pi d^2}\frac{\sqrt{\alpha(T)t_{on}/\pi}}{k(T)} \quad (5)$$

where T_{i-1}' is the temperature during cooling of the earlier pulse predicted from Eq. (4) above.

2.2. Governing physical mechanisms

When the surface temperature reaches the melting point of the ceramic, material removal occurs by melting and the solid–liquid interface can be interpreted by tracing the melting point in the temperature versus depth plots. As the surface temperature further increases with pulse time or laser intensity and reaches the vaporization point of the material, material removal takes place by evaporation instead of melting. The rate of material loss at the surface (kg/m^2 s) due to evaporation is given by [14]:

$$\dot{m}_{evaporated} = p(T_s)\left[\frac{m_v}{2\pi k T_s}\right]^{1/2} \quad (6)$$

where T_s is the surface temperature, k is the Boltzmann constant (1.38065×10^{-23} J/K), m_v is mass of the vapor molecule, and $p(T_s)$ is the saturation pressure given by the Clausius-Clapeyron equation. The evolving vapor from the surface applies recoil pressure on the surface (Eq. (7)) which plays an important role in material removal in molten state during machining of certain ceramics as seen later [15].

$$\frac{\pi d^2 P_{recoil}}{4aQ} = \frac{1.69}{\sqrt{L_v}}\left(\frac{b}{1 + 2.2b^2}\right) \quad (7)$$

where $b^2 = kT_s/m_v L_v$, and L_v is the latent heat of vaporization. Even though thermo-physical properties mentioned above such as thermal conductivity, specific heat, heat transfer coefficient and thermal diffusivity vary with temperature, the latent heat of vaporization is a constant value independent of temperature.

Based on the thermodynamic conditions prevalent during laser machining, certain ceramics dissociate/decompose into various stoichiometric/non-stoichiometric species that are expelled/removed during the machining process. Assuming the machined cavities with minimum taper to have a cylindrical cross-section of volume $V = \pi d^2 z/4$ (equivalent to $N = V/22.4 \times 10^{-3}$ mol), the loss of energy corresponding to dissociation of this volume of machined cavity is estimated by $E_{dissociation} = \Delta G \times N$, where ΔG is Gibbs free energy and z is depth of machined cavity. This dissociation energy loss reduces the effective laser energy available in subsequent pulses and thus the corresponding temperature. As described below, a combination of the different physical processes mentioned above affect the machining of a certain ceramic rather a single predominant process (Table 1).

3. Machining of structural ceramics

Structural ceramics such as alumina (Al_2O_3), silicon nitride (Si_3N_4), silicon carbide (SiC) and magnesia (MgO) were machined using a JK 701 pulsed Nd:YAG laser. Processing conditions and governing physical phenomena for machining of these ceramics are only briefly discussed here for the sole purpose of comparison in this section. As mentioned before,

Table 1
Governing mechanisms in some structural ceramics (✓—phenomena present; ✗—phenomena not present).

Physical Process ↓ / Material →	O_3	Si_3N_4	SiC	MgO
Melting	✓	✓	✓	✗
Dissociation	✓	✓	✓	✓
Evaporation	✓	✓	✓	✓

however, detailed analysis of the machining mechanisms in these ceramics has already been conducted by Samant and Dahotre and separately presented elsewhere [6–9].

3.1. Alumina

At a pulse energy of 4 J, repetition rate of 20 Hz and pulse width of 0.5 ms, 5, 10, 20 and 30 pulses were required for machining depths of 0.26, 0.56, 3.23, and 4.0 mm in Al_2O_3 (Fig. 1a) [6]. $AlO_{(g)}$, $Al_{(l)}$, $Al_{(g)}$, $Al_2O_{(g)}$ and $AlO_{2(g)}$ are some of the species formed due to the dissociation of Al_2O_3 [16]. Recoil pressure provoked expulsion of the liquid phase formed during the dissociation process (most likely by reaction in Eq. (8)) is responsible for laser machining in alumina.

$$Al_2O_3 \rightarrow 2Al_{(l)} + \frac{3}{2}O_{2(g)} \quad (8)$$

Moreover, there is some loss of material due to evaporation (Eq. (6)) and the machining in alumina is a combined effect of melt expulsion, dissociation and evaporation.

3.2. Silicon nitride

For the same set of laser processing parameters as used for machining alumina, 3, 6, 10 and 20 pulses were able to machine depths of 0.92, 1.13, 1.69 and 3.5 mm, respectively, in Si_3N_4 (Fig. 1b) [7]. The dissociation/sublimation of Si_3N_4 into Si liquid and N_2 gas (Eq. (9) [17]) at the sublimation temperature of Si_3N_4 followed by the expulsion of liquid silicon by evaporation induced recoil pressure (Eq. (7)) was proposed as the material removal mechanism.

$$Si_3N_4 \rightarrow 3Si_{(l)} + 2N_{2(g)} \quad (9)$$

Evaporation also assists in material removal and melting, dissociation and evaporation together lead to machining in Si_3N_4 [7].

3.3. Silicon carbide

Using a pulse energy of 6 J, pulse duration of 0.5 ms, and repetition rate of 50 Hz, a through cavity was machined in a 2 mm thick SiC plate in approximately 25 pulses while it took about 125 pulses to machine through the entire thickness of a 3 mm thick plate (Fig. 1c) [8]. Decomposition of SiC may produce several species such as $Si_{(g)}$, $Si_{2(g)}$, $SiC_{2(g)}$, $Si_{(l)}$, $C_{(s)}$, $Si_{(s)}$, $Si_2C_{(g)}$, $C_{(g)}$, and $Si_{3(g)}$. The most likely reaction to produce liquid species available for expulsion is:

$$SiC \rightarrow Si_{(l)} + C_{(s)} \quad (10)$$

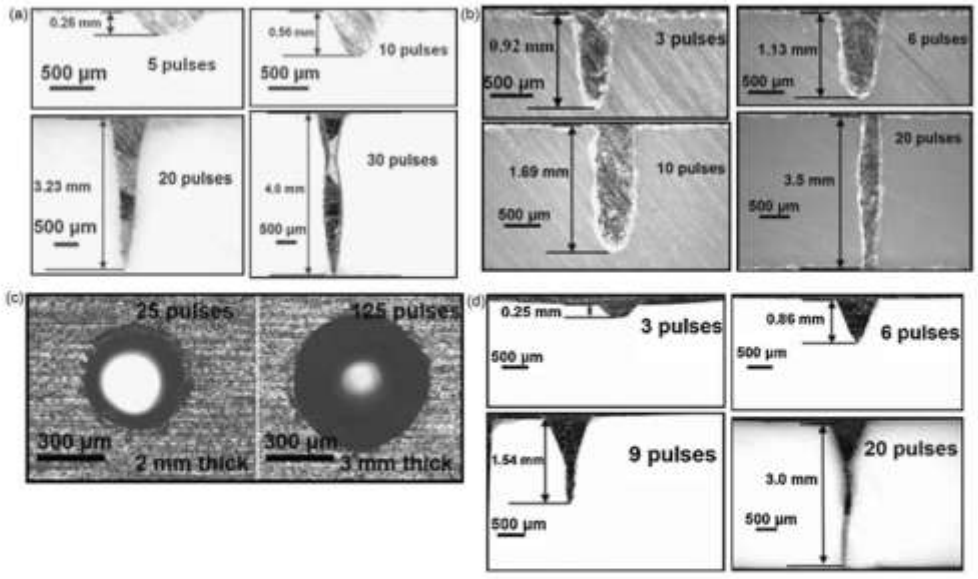

Fig. 1. Laser machining of (a) Al_2O_3, (b) Si_3N_4, (c) SiC and (d) MgO.

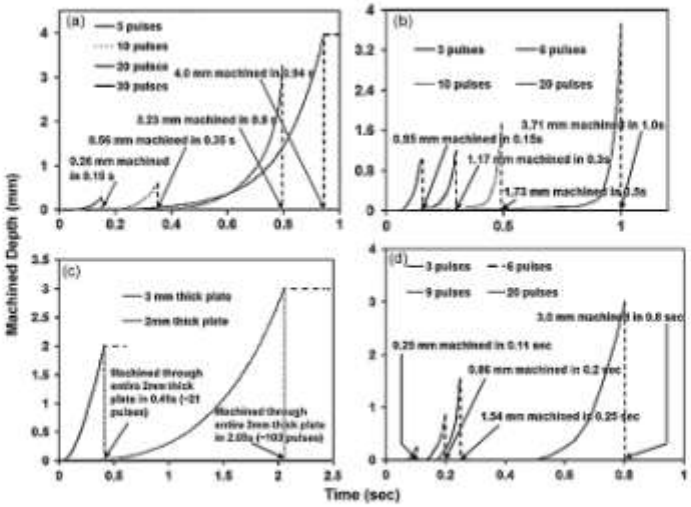

Fig. 2. Machined depth evolution for (a) Al_2O_3, (b) Si_3N_4, (c) SiC and (d) MgO.

Similar to alumina and silicon nitirde, some loss of material also occurs due to evaporation and a combination of melting, dissociation and evaporation contributes to machining in silicon carbide.

3.4. Magnesia

Finally, under the combination of a pulse energy of 4 J, pulse width of 0.5 ms and a repetition rate of 20 Hz, several pulses (3, 6, 9 and 20) were applied to the MgO surface and depths of 0.25, 0.86, 1.54 and 3.0 mm were machined (Fig. 1d) [9]. MgO dissociates as per the following reaction [18]:

$$MgO \rightarrow Mg_{(s)} + O_{(g)} \quad (11)$$

The melting and vaporization temperatures of magnesium (922 K and 1363 K, respectively) being less than the dissociation temperature of MgO (3123 K), the solid magnesium formed due to the dissociation reaction (Eq. (11)) immediately evaporates and material losses in MgO take place solely by evaporation. Dissociation along with evaporation of the ceramic exposed to laser fluence causes material removal in MgO. This mechanism is in contrast to the machining of Al_2O_3, Si_3N_4 and SiC using the same laser based technique. As the material evaporates, the removed material (vapor) exerts a force over the machined area and drives out the material. This force acting upwards is proportional to the laser fluence (energy per unit area) essential for machining a certain depth, z and is given by:

$$\text{Vapor pressure} = \frac{\text{Laser fluence}}{\text{Machined depth}} \quad (12)$$

This vapour pressure (Eq. (12)) is different from the recoil pressure mentioned above (Eq. (7)) and is exerted only during the machining of ceramics such as MgO where the entire material goes directly into vaporization without any melting involved. On the other hand, recoil pressure (Eq. (7)) is experienced in those ceramics in which machining takes place by a combination of melting and evaporation. Simultaneously,

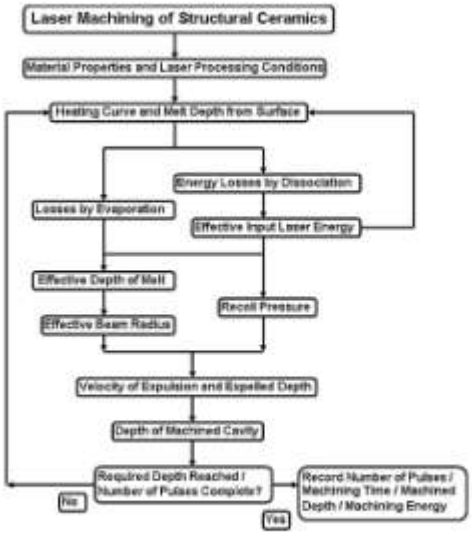

Fig. 3. Stepwise procedure for prediction of machining parameters.

the gravitational pull (ρgz, where g is acceleration due to gravity) acts downwards and the extent of cavity formation is governed by these counterbalancing pressures. A clean cavity is formed when the vapour pressure exceeds the gravitational pull.

4. Computational model

The above described physical processes along with the material properties and laser processing conditions can be incorporated into a computational model for prediction of several machining parameters such as machining time, number of pulses, dimensions of machined cavity and machining energy. In light of this, an ab initio physical model was developed by Samant and Dahotre and used for predicting the number of pulses and corresponding time required for machining a certain depth in Al_2O_3 (Fig. 2a) [6] and for estimating depth of machined cavity when a certain number of pulses were applied to Si_3N_4 (Fig. 2b) [7]. The model was also applied for advance prediction of number of pulses and corresponding energy necessary for machining SiC ceramic (Fig. 2c) [8] and to determine the number of pulses and corresponding time required for machining a certain depth in MgO (Fig. 2d) [9].

As the details of modeling have been elaborately explained by Samant and Dahotre in references [6] to [9], only a general flow chart for predicting the desired machining parameters is represented in Fig. 3. The nature of the structural ceramic governs the physical phenomena that can be incorporated into the mathematical model and it was found that the predictions were within acceptable range of the actual observations.

5. Conclusion

This study demonstrates the feasibility of lasers in machining some of the commonly used structural ceramics and establishes the fact that the material removal mechanism depends on the type of ceramic. Based on this concept, a computational tool was developed that was capable of advance predictions of the machining parameters. It was observed that even though the laser processing conditions were identical for most of the ceramics, the depth of the machined cavity was different for all of them because the machining process was a function of the thermo-physical properties of the ceramic such as thermal conductivity, specific heat, latent heat and density. Furthermore, this study is different from earlier work such as that of Salonitis et al. [13] who considered the machining mechanism as comprised of only melting and subsequent material removal by melt expulsion and Atanasov et al. [19] who thought of machining as a single step material evaporation without any melting.

References

[1] I.P. Tuersley, A. Jawaid, I.R. Pashby, Review: various methods of machining advanced ceramic materials, J. Mater. Process. Technol. 42 (4) (1994) 377–390.

[2] G. Chryssolouris, Laser Machining: Theory and Practice, Springer-Verlag, New York, 1991.

[3] K. Salonitis, P. Stavropoulos, A. Stournaras, G. Chryssolouris, CO_2 Laser cutting of aluminium, in: Proceedings of the 5th Laser Assisted Net Shape Engineering, Erlangen, Germany, 2007, pp. 825–835.

[4] P. Stavropoulos, K. Salonitis, A. Stournaras, K. Eleftheriou, G. Chryssolouris, Molecular dynamics simulation of laser ablation of iron, in: Proceedings of the 10th CIRP International Workshop on Modeling of Machining Operations, Calabria, Italy, 2007, pp. 549–553.

[5] A. Stournaras, K. Salonitis, P. Stavropoulos, G. Chryssolouris, Finite element thermal analysis of pulsed laser drilling process, in: Proceedings of the 10th CIRP International Workshop on Modeling of Machining Operations, Calabria, Italy, 2007, pp. 563–570.

[6] A.N. Samant, N.B. Dahotre, Computational predictions in single dimensional laser machining of alumina, Int. J. Mach. Tools Manuf. 48 (2008) 1345–1353.

[7] A.N. Samant, N.B. Dahotre, Ab initio physical analysis of single dimensional laser machining of silicon nitride, Adv. Eng. Mater. 10 (2008) 978–981.

[8] A.N. Samant, C. Daniel, R.H. Chand, C.A. Blue, N.B. Dahotre, Computational approach to photonic drilling of silicon carbide, Int. J. Adv. Manuf. Technol., under review.

[9] A.N. Samant, N.B. Dahotre, An integrated computational approach to single dimensional laser machining of magnesia, Opt. Lasers Eng., in press, doi:10.1016/j.optlaseng.2008.10.001.

[10] M.U. Islam, G. Campbell, Laser machining of ceramics: a review, Mater. Manuf. Processes. 8 (6) (1993) 611–630.

[11] H. Ki, P.S. Mohanty, J. Mazumder, Multiple reflection and its influence on keyhole evolution, J. Laser Appl. 14 (2002) 39–45.

[12] S.P. Harimkar, A.N. Samant, N.B. Dahotre, Temporally evolved recoil pressure driven melt infiltration during laser surface modifications of porous alumina ceramic, J. Appl. Phys. 101 (2007) DOI: 054911.

[13] K. Salonitis, A. Stournaras, G. Tsoukantas, P. Stavropoulos, G. Chryssolouris, A theoretical and experimental investigation on limitations of pulsed laser drilling, J. Mater. Process. Technol. 183 (1) (2007) 96–103.

[14] W.W. Duley, Laser Welding, Wiley Interscience Publication, New York, NY, 1998.

[15] V.V. Semak, G.A. Knorovsky, D.O. MacCallum, R.A. Roach, Effect of surface tension on melt pool dynamics during laser pulse interaction, J. Phys. D: Appl. Phys. 39 (2006) 590–595.

[16] P.V. Ananthapadmanabhan, T.K. Thiyagarajan, K.P. Sreekumar, N. Venkatramani, Formation of nano-sized alumina by in-flight oxidation of aluminium powder in a thermal plasma reactor, Scr. Mater. 50 (1) (2004) 143–147.

[17] J.P. Murray, G. Flamant, C.J. Roos, Silicon solar-grade silicon production by solar dissociation of Si_3N_4, Sol. Energy 80 (10) (2006) 1349–1354.

[18] T. Yabe, M.S. Mohamed, S. Uchida, C. Baasandash, Y. Sato, M. Tsuji, Y. Mori, Noncatalytic dissociation of MgO by laser pulses towards sustainable energy cycle, J. Appl. Phys. 101 (2007) DOI: 10.1063/1.2743730.

[19] P.A. Atanasov, E.D. Eugenieva, N.N. Nedialkov, Laser drilling of silicon nitride and alumina ceramics: a numerical and experimental study, J. Appl. Phys. 89 (2001) DOI: 10.1063/1.1334367.

Available online at www.sciencedirect.com
ScienceDirect
Journal of the European Ceramic Society 29 (2009) 969–993
www.elsevier.com/locate/jeurceramsoc

Review

Laser machining of structural ceramics—A review

Anoop N. Samant, Narendra B. Dahotre *

Department of Materials Science Engineering, The University of Tennessee, Knoxville, TN 37996, United States

Received 24 July 2008; received in revised form 11 November 2008; accepted 13 November 2008
Available online 6 January 2009

Abstract

Outstanding mechanical and physical properties like high thermal resistance, high hardness and chemical stability have encouraged use of structural ceramics in several applications. The brittle and hard nature of these ceramics makes them difficult to machine using conventional techniques and damage caused to the surface while machining affects efficiency of components. Laser machining has recently emerged as a potential technique for attaining high material removal rates. This review paper aims at presenting the state of the art in the field of laser machining of structural ceramics and emphasizes on experimental and computational approaches in understanding physical nature of the complex phenomena.

Keywords: SiC; Al_2O_3; MgO; Si_3N_4; Traditional ceramics

Contents

* Corresponding author. Tel.: +1 865 974 3609; fax: +1 865 974 4115.
E-mail address: ndahotre@utk.edu (N.B. Dahotre).

0955-2219/$ – see front matter © 2008 Elsevier Ltd. All rights reserved.
doi:10.1016/j.jeurceramsoc.2008.11.010

1. Introduction

Structural materials can be classified as ceramics, metals or polymers with each type of material having its own advantages and drawbacks. Even though metals are strong, cheap and tough, they are chemically reactive, heavy and have limitations on the maximum operating temperature. Polymers are easy to fabricate and light, but they can be used at temperatures only below 300 °C. The characteristic features of ceramics compared to others make them more suitable for some applications. In comparison with metals and polymers, most ceramics possess useful features such as high-temperature strength, superior wear resistance, high hardness, lower thermal and electrical conductivity and chemical stability.[1] Retention of these properties by structural ceramics at high temperatures presents these materials as an exclusive solution to several engineering application problems.[2] Commonly used structural ceramics are zirconia (ZrO_2), boron carbide (B_4C), alumina (Al_2O_3), silicon carbide (SiC), silicon nitride (Si_3N_4), sialon (Si–Al–O–N), berylia (BeO), magnesia (MgO), titanium carbide (TiC), titanium nitride (TiN), titanium diboride (TiB_2), zirconium nitride (ZrN) and zirconium diboride (ZrB_2). In general, these structural ceramics fall into two major groups: conductive ceramics such as carbides (TiC and SiC), borides (TiB_2 and ZrB_2) or nitrides (TiN and ZrN) and ceramics that are a mixture of dielectric (semi-conductive) materials and electrically conductive materials such as Si_3N_4–TiN, sialon-TiN, and Si_3N_4–SiC.[3] The applications of some of the structural ceramics are presented in Table 1 below.

Alumina is also used in making machine tool inserts, heat-resistant packings, electrical and electronic components and attachments to melting ducts and refractory linings.[4] Zirconium diboride (ZrB_2) possesses a high melting point, low density, and excellent resistance to thermal shock and oxidation compared to other non-oxide structural ceramics. Hence, it is used as an ultra-high-temperature ceramic (UHTC), for refractory materials and as electrodes or crucible materials.[5] Magnesia is a very stable oxide used in refractory linings, brake linings, thin-film semi-conductors, for housing thermocouples in aggressive environments, in making crucibles in chemical and nuclear industry where high corrosion resistance is required and in making thin-film substrates and laser parts.[6,7] In addition to the above-mentioned structural ceramics and their engineering applications, there are several other fields where these ceramics are significantly used. As applications of structural ceramics are not the main focus of this study, they will not be discussed in further detail here. These advanced high-performance materials have certain limitations such as difficulty in fabrication, high cost, and poor reproducibility as seen below.

2. Fabrication techniques

Many features (high hardness) that make structural ceramics attractive for particular uses also make them difficult to fabricate by traditional methods based on mechanical grinding and machining. Strength and efficiency of the components can be affected by the damage caused on the surface of the ceramics machined by conventional methods. A crucial step in manufacturing ceramic components is their cost-effective machining with excellent quality. Massive research efforts have been conducted on the precision machining of ceramic components over the past few decades, developing several advanced machining technologies without affecting the beneficial properties of the surface.[2] Some of these techniques are summarized in Fig. 1 and briefly described below.

2.1. Mechanical machining

In mechanical machining, material removal takes place when the ceramic is subjected to some mechanical force/impingement of abrasive particles. Commonly used techniques under this category are abrasive machining/grinding, ultrasonic machining, and abrasive water jet machining.

2.1.1. Abrasive machining/grinding

The machining takes place by using grinding wheels that are bonded abrasives used for producing several complex shapes.[8]

Table 1
Applications of different structural ceramics[7].

Application	Performance advantages	Examples
Wear parts: seals, bearings, valves, nozzles	High hardness, low friction	SiC, Al_2O_3
Cutting tools	High strength, hardness	Si_3N_4
Heat engines: diesel components, gas turbines	Thermal insulation, high-temperature strength, fuel economy	ZrO_2, SiC, Si_3N_4
Medical implants: hips, teeth, joints	Biocompatibility, surface bond to tissue, corrosion resistance	Hydroxyapatite, bioglass, Al_2O_3, ZrO_2
Construction: highways, bridges, buildings	Improved durability, lower overall cost	Advanced cements and concrete

Even though the needs for dimensional accuracy and surface finish are satisfied by conventional grinding, long machining times and high machining costs account for 60–90% of the final cost of the finished product. This poses a major hindrance for the grinding process[9,10] and ground products also generate surface and subsurface cracks,[11,12] pulverization layers,[13] some plastic deformation[14] and significant residual stresses.[15]

2.1.2. Ultrasonic machining (USM)

Ultrasonically vibrated abrasive particles remove material in ultrasonic machining at generally low material removal rates. A transducer/booster combination converts electrical energy into mechanical vibrations and causes the tool to vibrate along its longitudinal axis at high frequency.[16] As the mechanism of material removal is not properly documented, process optimization is difficult.[17]

2.1.3. Abrasive water jet machining (AWJM)

In abrasive water jet machining, a blast of abrasive-laden water stream impinges on the surface of the material and results in erosive wear. This process is advantageous over the grinding process as it reduces tool wear and machining time.[18] At high speeds, surface fracture results in kerf formation because of the hydrodynamic forces within the water jet.

2.2. Chemical machining (CM)

Chemical machining using etchants is the oldest of the machining processes, wherein chemicals attack the materials and remove small amounts from the surface. Sharp corners, deep cavities and porous workpieces cannot be easily machined as this method is only suitable for shallow removal of material (up to 12 mm).[8]

2.2.1. Chemical–mechanical machining (CMM)

This technology is widely used in surface patterning in semiconductors and micro-electro-mechanical systems (MEMS). Initially, the chemical absorption on the surface of the material produces a chemically reacted layer with physical properties different from the original material. This is followed by mechanical machining to generate the desired pattern on the surface. High costs and several steps involved in patterning commonly used materials such as silicon can be minimized by using KOH solution that can change hard brittle material surface of silicon into a hydrated layer which makes machining easier. Furthermore, this technique also offers flexibility and controllability in the process.[19]

2.3. Electrical machining

Electrical energy in the form of pulse or continuous in isolation or in combination with chemicals is used to erode the material. It is highly effective for machining electrically conductive and semi-conductive materials. Electrochemical machining (ECM), electrical-discharge machining (EDM) and electrochemical discharge machining (ECDM) are the commonly used electrical machining techniques.

2.3.1. Electrochemical machining (ECM)

Electrochemical machining is the reverse of electroplating used for machining complex cavities in high-strength materials. As the electrolyte has a tendency to erode away sharp profiles, this method is not suitable for generating sharp corners.

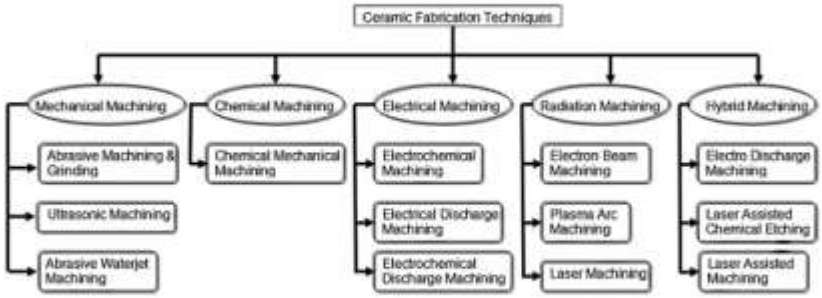

Fig. 1. Ceramic fabrication techniques.

2.3.2. Electrical-discharge machining (EDM)

EDM is an abrasionless method used for machining conductive ceramics such as boron carbide (B_4C) and silicon carbide (SiC).[20] This method is not affected by the hardness of the material, but requires an electrical resistivity of less than 100 Ω cm.[2]

2.3.3. Electro-chemical discharge machining (ECDM)

This technique has the combined features of EDM and ECM and is capable of machining high strength electrically non-conductive ceramics. This process is inefficient because a significant portion of the total heat developed is dissipated for increasing the temperature and the corresponding material removed while machining is less.[21]

2.4. Radiation machining

Radiation machining is a non-contact machining process where the dimension of the hole or the groove can be controlled by the energy supply to the work piece. The energy can be provided by an electron beam, plasma arc or by lasers. These non-contact machining techniques are not affected by the abrasion of the tools and they are independent of electrical resistivity of the materials being machined.

2.4.1. Electron beam machining (EBM)

The energy source in EBM is high-speed electrons that strike the surface of the work piece generating heat.[8] Since the beam can be positioned rapidly by a deflection coil, high machining speeds are possible. This machining process has the drawback that the width of the machined cavity increases while machining at high speeds due to the beam defocusing effect.[22]

2.4.2. Plasma arc machining

Ionized gas is used for machining the ceramic at very high temperatures leading to smaller kerf widths and good surface finish. As the vacuum chambers have limited capacity, the size of the components should closely match the size of the vacuum chamber.[8]

2.4.3. Laser machining (LM)

The source of energy in LM is a laser (acronym for Light Amplification by Stimulated Emission of Radiation). High density optical energy is incident on the surface of the work piece and the material is removed by melting, dissociation/decomposition (broken chemical bonds causes the material to dissociate/decompose), evaporation and material expulsion from the area of laser–material interaction. The vital parameters governing this process are the different properties of the ceramic such as reflectivity, thermal conductivity, specific heat and latent heats of melting and evaporation. The schematic representation of the laser machining process is made in Fig. 2. Laser machining of structural ceramics and the associated physical phenomena will be discussed extensively in the later part of this review.

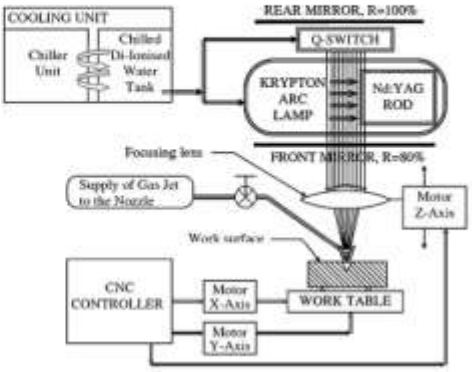

Fig. 2. Schematic of laser machining. (After Knar et al.[23] with permission. Copyright Elsevier.)

2.5. Hybrid machining

Hybrid machining uses a combination of two or more of the above techniques for machining the ceramic such as electrical discharge grinding, laser-assisted chemical etching and machining using lasers and cutting tool/laser assisted machining (LAM).

2.5.1. Electrical discharge grinding

This method combining the advantages of grinding and electrical-discharge machining has low equipment cost and high efficiency.[24,25] Material is removed from the ceramic surface by recurring spark discharges between the rotating wheel and the work piece.[8]

2.5.2. Laser-assisted chemical etching

Material removal is carried out by using suitable etchant in combination with selective laser irradiation. The laser radiation influences the reaction between the material and the etchant by exciting the etchant molecules and/or the material surface[26] and the etch rate is significantly affected by the laser fluence.

2.5.3. Laser assisted machining (LAM)

In laser assisted machining, the material is locally heated by an intense laser source prior to material removal, without melting or sublimation of the ceramic. This technique has been successfully used for machining silicon nitride and the corresponding work piece temperature, tool wear and surface integrity have been measured.[27–32] Magnesia-partially-stabilized zirconia was machined with a polycrystalline cubic boron nitride tool and it was found that the tool life increased with material removal temperatures.[33] LAM effectively reduced the cutting force and improved the surface finish of the finished products made from Al_2O_3.[34] In LAM, after the laser is used to change the ceramic deformation behavior from brittle to ductile, material removal takes place with a conventional cutting tool. Unlike LAM, in laser machining (LM), actual material removal takes place by

Fig. 3. (a) Laser assisted machining. (After Lei et al.[32] with permission. Copyright Elsevier.) (b) Laser machining.[35]

the laser beam. The physical phenomena taking place during the LAM of structural ceramics is different from LM and will not be a part of this study. The difference in the two processes is demonstrated in Fig. 3.

3. Laser machining

Lasers can replace mechanical material removal methods in several engineering applications because of their following salient features:[36]

(i) Non-contact process: Energy transfer from the laser to the ceramic through irradiation eliminates cutting forces, tool wear and machine vibration. Furthermore, the material removal rate is not affected by the maximum tool force, tool chatter or built-up edge formation, but can be controlled by varying the laser processing parameters such as input energy and processing speed.
(ii) Thermal process: The efficiency of laser machining depends on the thermal and, to some extent on the optical properties of the material. This makes hard or brittle materials such as structural ceramics with low thermal diffusivity and conductivity suitable for machining.
(iii) Flexible process: In combination with a multi-axis positioning system or robot, lasers can be used for drilling, cutting, grooving, welding and heat treating on the same machine without any necessity to transport the parts for processing them with specialized machines. In-process monitoring during the laser machining process can allow key parameters to be measured and a high level of reproducibility can be attained.[37] Relative economic comparison of laser machining with other machining processes is made in Table 2.

Different types of lasers such as CO_2, Nd:YAG and Excimer lasers are used for machining of structural ceramics with each type of laser having its own wavelength of absorption and machining applications. CO_2 lasers are molecular lasers (subgroup of gas lasers) that use gas molecules (combination of carbon dioxide, nitrogen and helium) as the lasing medium, whereby the excitation of the carbon dioxide is achieved by increasing the vibrational energy of the molecule. The actual pumping takes place by an AC or DC electrical discharge and this laser emits light at a wavelength of 10.6 μm in the far infrared region of the electromagnetic spectrum. CO_2 lasers are widely used in industry for applications in laser machining, heat treatment and welding.[36]

On the other hand, Nd:YAG lasers are solid state lasers that use dopants (Neodinium (Nd^{3+})) dispersed in a crystalline matrix (complex crystal of Yttrium–Aluminum–Garnet (YAG) with chemical composition $Y_3Al_5O_{12}$) to generate laser light. Excitation is attained by krypton or xenon flash lamps and an output wavelength of 1.06 μm in the near-infrared region of the spectrum can be obtained. Nd:YAG fibre lasers are used in applications requiring low pulse repetition rate and high pulse energies (up to 100 J/pulse) such as hole piercing and deep keyhole welding applications.[36]

Excimer lasers are an increasingly popular type of gas lasers made up of a compound of two identical species that exist only in an excited state. Commonly used excimer complexes include argon fluoride (ArF), krypton fluoride (KrF), xenon fluoride (XeF) and xenon chloride (XeCl) with the output wavelengths varying from 0.193 to 0.351 μm in the ultraviolet to near-ultraviolet spectra. These compounds can be formed by inducing the noble gas (Ar, Kr, or Xe) of the compound into an excited state with an electron beam, an electrical discharge or a combination of the two. Excimer lasers are used for machining solid polymer workpieces, removing metal films from polymer substrates, micromachining ceramics and semi-conductors, and marking thermally sensitive materials.[36]

The different types of lasers can be operated in either the continuous wave, CW or the pulsed mode, PM (nano, pico and femto second lasers). In CW lasers, continuous pumping of the laser emits incessant light, while in a pulsed laser, there is a laser power-off period between two successive pulses.[39] Pulsed lasers are preferred for machining ceramics as the processing parameters can be more effectively controlled compared to continuous wave mode.[40] The next section looks at the important physical processes that assist in laser machining of ceramic and discusses the different types of laser machining.

Table 2
Relative economic comparisons of different machining processes[38].

Machining process	Parameter influencing economy				
	Capital investment	Toolings/fixtures	Power requirements	Removal efficiency	Tool wear
Conventional machining	Low	Low	Low	Very low	Low
Ultrasonic machining	Low	Low	Low	High	Medium
Electrochemical machining	Very high	Medium	Medium	Low	Very low
Chemical machining	Medium	Low	High	Medium	Very low
Electrical-discharge machining	Medium	High	Low	High	High
Plasma arc machining	Very low	Low	Very low	Very low	Very low
Laser machining	Medium	Low	Very low	Very high	Very low

3.1. Absorption of laser energy and multiple reflections

The physical phenomena that take place when the laser beam is incident on the ceramic surface are reflection, absorption, scattering and transmission (Fig. 4). Absorption, the vital of all the effects, is the interaction of the electromagnetic radiation with the electrons of the material and it depends on both the wavelength of the material and the spectral absorptivity characteristics of the ceramic being machined.[36,40] The absorptivity is also influenced by the orientation of the ceramic surface with respect to the beam direction and reaches a maximum value for angles of incidence above 80°.[36] For machined cavities with high aspect ratios, multiple beam reflections along the wall of cavity also affect the amount of absorbed energy.[41,42] The multiple reflections in a machined cavity are schematically represented in Fig. 5 where I_o is the incident laser energy, I_{a1}, I_{a2} and I_{a3} are the first, second and third absorptions, respectively, and I_{r1}, I_{r2} and I_{r3} are the first, second and third reflections, respectively.[43] There will be many more reflections taking place during actual ceramic machining than illustrated in Fig. 5. The phenomenon of multiple reflections has been incorporated into the machining process in several ways.[44–48] The laser beam energy Q_a absorbed by the ceramic after n reflections is:[49]

$$Q_a = Q(r)^n \tag{1}$$

where Q is incident laser beam energy, r is angle-dependent reflection coefficient of the ceramic, and n is number of multiple reflections given by:

$$n = \frac{\pi}{4\theta} \tag{2}$$

where θ is angle the cavity wall makes with normal direction. Moreover, as the thermal conductivity of structural ceramics is generally less than that of majority of metals, the energy absorption takes place faster in ceramics and 100% of incident energy is expected to be immediately absorbed by the ceramic for the machining process.[50,51] Thus the absorbed energy depends on properties of the ceramic (reflection coefficient), magnitude of incident laser energy, output wavelength of processing laser and wall angle. This energy is converted into heat and its ensuing conduction into the material establishes the temperature distribution within the material which in turn affects machining time and depth of machined cavity.

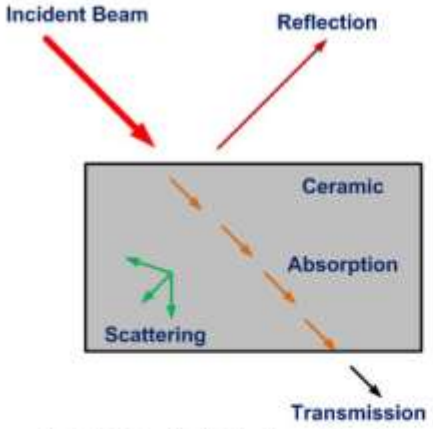

Fig. 4. Interactions of incident laser beam with ceramic.

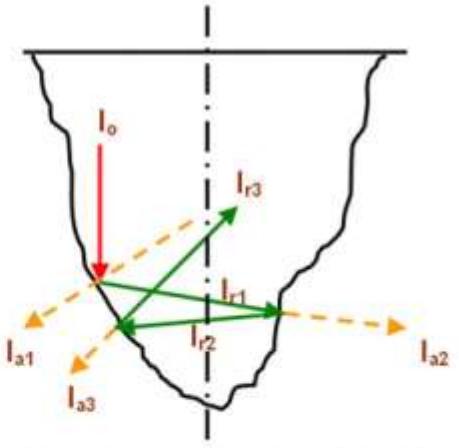

Fig. 5. Multiple reflections in a machined cavity. (After Zhao[43] with kind permission of J. Zhao's Major Professor, Dr. Vladimir V. Semak.)

3.2. Thermal effects

The excitation energy provided by the laser is rapidly converted into heat and this is followed by various heat transfer processes such as conduction into the materials, convection and radiation from the surface.[49] The conduction of heat into the ceramic is governed by Fourier's second law of heat transfer:

$$\frac{\partial T(x,y,z,t)}{\partial t} = \alpha(T)\left[\frac{\partial^2 T(x,y,z,t)}{\partial x^2} + \frac{\partial^2 T(x,y,z,t)}{\partial y^2} + \frac{\partial^2 T(x,y,z,t)}{\partial z^2}\right] \quad (3)$$

where T is temperature field, t is time and x, y and z are spatial directions. The term $\alpha(T)$ is temperature dependent thermal diffusivity of the material which is given by $k(T)/\rho C_p(T)$, where ρ is density of ceramic, $C_p(T)$ and $k(t)$ are temperature dependent specific heat and thermal conductivity of the ceramic, respectively. The balance between the absorbed laser energy at the surface and the radiation losses is given by:

$$-k(T)\left(\frac{\partial T(x,y,0,t)}{\partial x} + \frac{\partial T(x,y,0,t)}{\partial y} + \frac{\partial T(x,y,0,t)}{\partial z}\right) = \frac{\delta Q_a}{A} - \varepsilon\sigma(T(x,y,0,t)^4 - T_o^4) \quad (4)$$

$\delta = 1$ if $0 \le t \le t_p$

$\delta = 0$ if $t > t_p$

where Q_a is absorbed laser power (predicted by considering multiple reflections and material properties), ε is emissivity for thermal radiation, T_o is ambient temperature, t_p is ON-time for laser, σ is Stefan–Boltzmann constant (5.67×10^{-8} W/m^2 K^4) and A is cross-sectional area of the beam. The term δ takes a value of 1 when time, t is less than laser ON-time, t_p and it is 0 when time, t exceeds laser ON-time. Thus the value of δ depends on time, t and ensures that the energy is input to the system only when the laser is ON and cuts off the energy supply when the laser is switched off. The convection taking place at the bottom

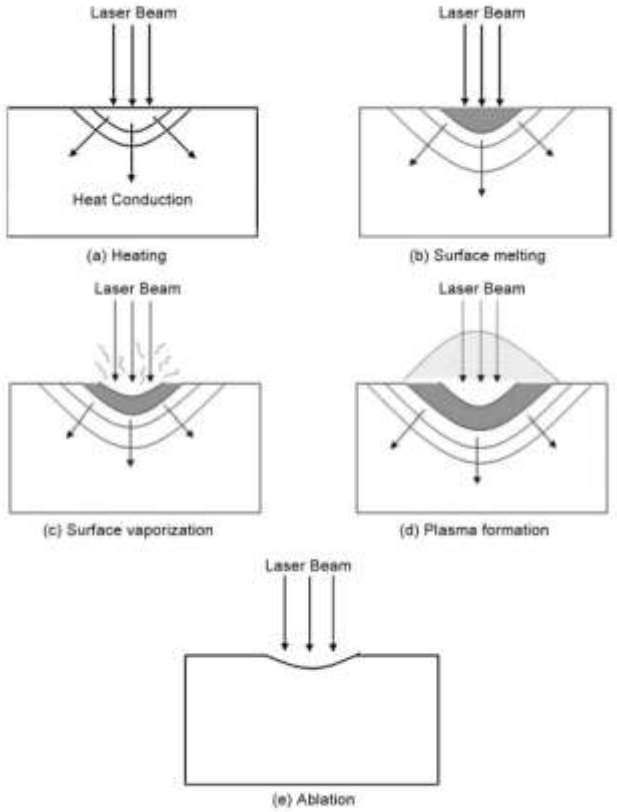

Fig. 6. Various physical phenomena during laser–ceramic interaction. (After Dahotre and Harimkar[49] with kind permission of Springer Science + Business Media.)

surface of the sample is:

$$-k(T)\left(\frac{\partial T(x,y,L,t)}{\partial x}+\frac{\partial T(x,y,L,t)}{\partial y}+\frac{\partial T(x,y,L,t)}{\partial z}\right) = h(T(x,y,L,t)-T_0), \quad (5)$$

where L is thickness of the sample being processed, h is temperature dependent heat transfer coefficient and T_0 is ambient temperature. The temperature distribution within the material as a result of these heat transfer processes depends on the thermophysical properties of the material (density, emissivity, thermal conductivity, specific heat, thermal diffusivity), dimensions of sample (thickness) and laser processing parameters (absorbed energy, beam cross-sectional area). The magnitude of temperature rise due to heating governs the different physical effects in the material such as melting, sublimation, vaporization, dissociation, plasma formation and ablation responsible for material removal/machining as discussed next (Fig. 6).[49,52,53]

3.2.1. Melting and sublimation

At high laser power densities ($I_0 > 10^5$ W/cm^2), the surface temperature of the ceramic T (predicted using Eqs. (1)–(5)) may reach the melting point T_m and material removal takes place by melting as considered by Salonitis et al.[54] As indicated in Fig. 7a, the surface temperature increases with increasing irradiation time, reaches maximum temperature T_{max} at laser ON-time t_p and then decreases.[49]

The temperatures reached and the corresponding irradiation times are: $T_1 < T_m$ at time $t_1 < t_p$, T_m at time t_2, T_{max} at time t_p, T_m at time $t_3 > t_p$, and finally T_1 at time $t_4 > t_p$. The corresponding temperature profiles in the depth of the material for various times during laser irradiation are presented in Fig. 7b. The solid–liquid interface can be predicted by tracking the melting point in temperature versus depth (z) plots (Fig. 7b). For example, it can be seen from Fig. 7b that at time t_p, the position of the solid–liquid interface (melt depth) corresponds to z_{max}. Before initialization of surface evaporation, maximum melt depth increases with laser power density I (power per unit area) at constant pulse time (Fig. 8a) while at a constant laser power density, maximum depth of melting increases with increasing pulse time (Fig. 8b). Prediction of melt depth using temperature profiles obtained from Eqs. (1)–(5) assists in determining depth of machined cavity in those ceramics in which material removal takes place entirely or in part by melting.[49]

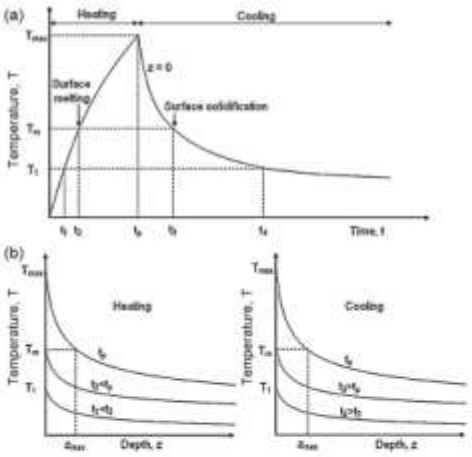

Fig. 7. Calculation of temporal evolution of melt depth (a) surface temperature as a function of time (b) temperature as a function of depth below the surface during heating and cooling. (After Dahotre and Harimkar[49] with kind permission of Springer Science + Business Media.)

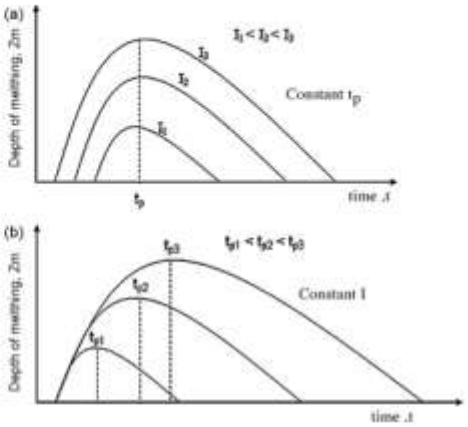

Fig. 8. Variation of melt depth during laser irradiation (a) effect of laser power density at constant pulse time (b) effect of laser pulse time at constant laser power density. (After Dahotre and Harimkar[49] with kind permission of Springer Science + Business Media.)

Some structural ceramics like Si_3N_4 do not melt but sublime, emitting N_2 and depositing a recast layer of silicon on the machined surface.[2] Attempts have been made to machine Si_3N_4 in water by Q-switched YAG lasers that can generate high peak powers (above 50 kW) from very short duration pulses (~100 ns) at high frequency (~10 kHz). As seen in Fig. 9, by machining

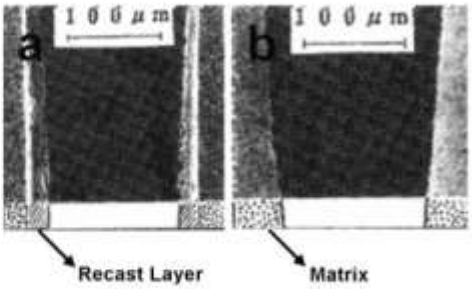

Fig. 9. Cross-section of Si_3N_4 ceramic machined in (a) air and (b) water. (After Morita et al.[55] with permission. Copyright American Institute of Physics.)

Si_3N_4 in air, a recast layer about 20 μm thick is formed and microcracks are spread within this layer. In contrast, by processing in water, no recast layers and cracks were observed. As YAG lasers retain high transmittance through water, removal of material (Si_3N_4) was possible without the formation of recast layer or micro-cracks.[55,56] The water also solidified the Si vapor and flushed away the micro-particles, thus preventing the vapor from reaching the saturation level.

3.2.2. Vaporization and dissociation

As the surface temperature of ceramic reaches the boiling point, further increase in laser power density or pulse time removes the material by evaporation instead of melting. After vaporization starts at the material surface, the liquid–vapor interface moves further inside the material with supply of laser energy and material is removed by evaporation from the surface above the liquid–vapor interface.[49] The velocity of liquid–vapor interface, $V_{evaporation}$ and the corresponding vaporization depth, $d_{evaporation}$ are given by:[52]

$$V_{evaporation} = \frac{Q_a}{\rho(cT_b + L_v)} \quad (6)$$

$$d_{evaporation} = \frac{Q_a t_p}{\rho(cT_b + L_v)} \quad (7)$$

where Q_a is absorbed laser energy (Eq. (1)), ρ is density of the ceramic, c is the speed of light, T_b is the boiling point of the ceramic, L_v is the latent heat of vaporization and t_p is ON-time for laser (time for which the ceramic surface is exposed to incident laser energy). Several works in the past have considered material removal only through this direct evaporation mechanism.[57–61] In such cases, the depth of evaporation (Eq. (7)) corresponding to depth of machined cavity depends on the laser conditions (processing time and absorbed laser energy) and material properties such as density, latent heat of vaporization, and boiling point.

Certain ceramics such as SiC, MgO directly dissociate/decompose into several stoichiometric and/or non-stoichiometric species depending on the thermodynamic conditions prevailing during laser machining. Alumina, on the other hand is stable up to 2327 K after which it melts and forms liquid. This liquid remains stable from 2327 to 3500 K and sub-oxides of aluminum, aluminum metal vapor and gaseous oxygen are formed due to the dissociation above 3250 K. The dissociation reaction forms different species that are expelled/removed during machining process and dissociation energy losses also affect the input laser energy and thus the temperature distribution, dimensions of machined cavity and machining time.[62–66]

The evolving vapor from the surface applies recoil pressure (p_{recoil})[67,68] on the surface given by:[69]

$$\frac{Ap_{recoil}}{Q_a} = \frac{1.69}{\sqrt{L_v}}\left(\frac{b}{1 + 2.2b^2}\right) \quad (8)$$

where $b^2 = kT_s/m_v L_v$, T_s is surface temperature, k is the Boltzmann constant (1.38065×10^{-23} J/K), m_v is the mass of vapor molecule, A is beam cross-sectional area, Q_a is absorbed laser energy, and L_v is the latent heat of vaporization. The absorbed laser energy (Eqs. (1) and (2)) and the associated surface temperatures predicted using Eqs. (3)–(5) affect the recoil pressure which plays a vital role in material removal in molten state during machining of some ceramics such as SiC, Al_2O_3 and Si_3N_4.

Table 3
Physical phenomena governing machining in some structural ceramics (√ – phenomena present; × – phenomena not present)[68].

Material	Physical process		
	Melting	Dissociation	Evaporation
Silicon carbide (SiC)	√	√	√
Alumina (Al_2O_3)	√	√	√
Silicon nitride (Si_3N_4)	√	√	√
Magnesia (MgO)	×	√	√

The total enthalpy required for laser-induced vaporization being greater than that required for melting, the energy required for laser machining by melting is much less than the energy required for machining by vaporization.[26] It was reported by Samant and Dahotre[62–66] that a combination of the different physical phenomena mentioned above was responsible for machining rather than any single predominant process. The machining mechanisms depending on the nature of some of the commonly used structural ceramics are represented in Table 3 and will be discussed elaborately in the later part of this study.

3.2.3. Plasma formation

When the laser energy density surpasses a certain threshold limit, the material immediately vaporizes, gets ionized and forms plasma having temperatures as high as 50,000 °C and pressures up to 500 MPa.[70] The degree of ionization (ξ) depends on the surface temperatures (predicted from Eqs. (1)–(5)) and is given by the Saha equation:[26]

$$\frac{\xi^2}{1-\xi} = \frac{2g_i}{g_a N_g}\left(\frac{2\pi m_v k T_s}{h^2}\right)^{3/2} \exp\left(-\frac{E_i}{kT_s}\right) \quad (9)$$

where $\xi = N_e/N_g$ and $N_g = N_e + N_a$. N_e and N_a are the number densities of electrons and atoms/molecules respectively, g_i and g_a are the degeneracy of states for ions and atoms/molecules, E_i is the ionization energy, m_v is the mass of vapor molecule, k is the Boltzmann constant (1.38065×10^{-23} J/K), T_s is surface temperature, and h is Planck's constant (6.626×10^{-34} m^2 kg/s). The plasma plume forms a shield over the machining area and reduces the energy available to the work piece when the surface temperature exceeds a certain threshold value. Aerosols formed due to the condensation of ionized material vapor stick to the surface and reduces the efficiency of machined components for applications dominated by wear or tear load. Hence the degree of ionization is an important parameter which gives an indication whether plasma will be formed during the machining process and accordingly, necessary efforts to overcome the harmful effects of plasma could be undertaken. A special gas nozzle designed by Tönshoff et al.[71] (Fig. 10) prevents the deposition of aerosols and this technique has been successfully applied to machine SiC ceramic surfaces without any debris.[70] The additional gas stream obtained by combining a process gas

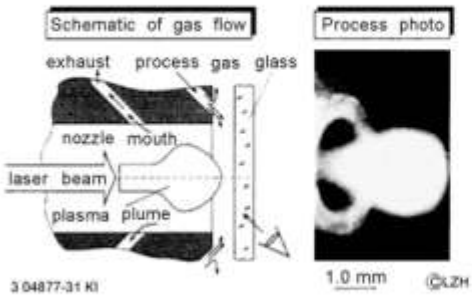

Fig. 10. Formation of plasma plume and its suction by gas nozzle. (After Tönshoff and Kappel[70] with permission. Copyright Elsevier.)

stream and an exhaust stream transports the vaporized material and avoids radial distribution of the plasma.

A technique developed at the Integrated Manufacturing Technologies Institute (IMTI), National Research Council Canada (NRC) minimizes the harmful effects of the plasma and provides a precise control over the material removal rate and surface finish. This technique controls the pulse duration and energy per pulse such that majority of the energy in a pulse instantaneously vaporizes a given quantity of the material from the surface. Continuous application of laser pulses ensures that each successive spot is adequately displaced to reduce the plasma absorption effects. Furthermore, short duration pulses reduce the recast layer thickness, eliminate micro-cracks and the material removed per pulse increases with increasing energy density while machining TiN/Si_3N_4 and SiC/Si_3N_4 materials (Fig. 11).[72]

3.2.4. Ablation

When the material is exposed to sufficiently large incident laser energy, the temperature of the surface exceeds the boiling point of the material causing rapid vaporization and subsequent material removal by the process referred to as thermal ablation.[26] Ablation takes place when laser energy exceeds the characteristic threshold laser energy which represents the minimum energy required to remove material by ablation. The complex laser–material interaction during ablation depends on the interaction between the photo-thermal (vibrational heating) and photo-chemical (bond breaking) processes. Above ablation threshold energy, material removal is facilitated by bond breaking, whereas thermal effects take place below ablation threshold energy. Absorption properties of the ceramic and incident laser parameters determine the location at which the absorbed energy reaches the ablation threshold, thus determining the depth of ablation, $d_{ablation}$ given by:[49]

$$d_{ablation} = \frac{1}{\mu_a} \ln\left(\frac{Q_s}{Q_{th}}\right) \quad (10)$$

where μ_a is absorption coefficient of ceramic and Q_{th} is threshold laser energy. The ablation rates and associated machined depths are governed by laser energy Q_s (predicted from Eq. (1)), pulse duration, number of pulses and pulse repetition rate. Yttrium stabilized Si–Al–O–N (Y-sialon) was irradiated by an Kr-F-excimer laser at a fluence of 850 mJ/cm^2, pulse repetition rate varying from 2 to 20 Hz and by applying different number of pulses.[73] The material removal in Y-sialon under the above processing conditions was by ablation. The variation of ablation depth and a Y-sialon sample ablated by laser irradiation is presented in Fig. 12a and b, respectively.

The above described physical processes can be incorporated into a computational model and used to predict the maximum temperatures attained during machining in addition to several

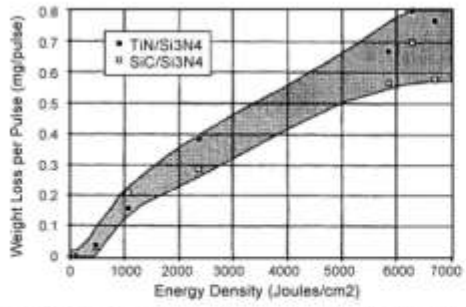

Fig. 11. Variation of material removal rate with energy density. (After Islam[72] with kind permission of Springer Science + Business Media.)

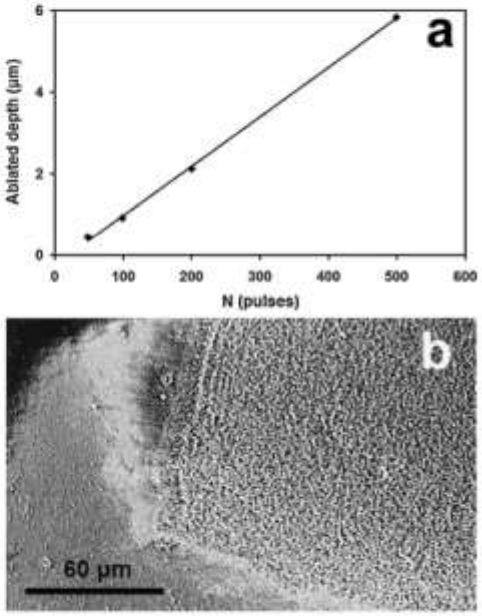

Fig. 12. (a) Ablation profile of Y-sialon under irradiation (b) ablated region in Y-sialon. (After Laude et al.[73] with permission. Copyright Elsevier.)

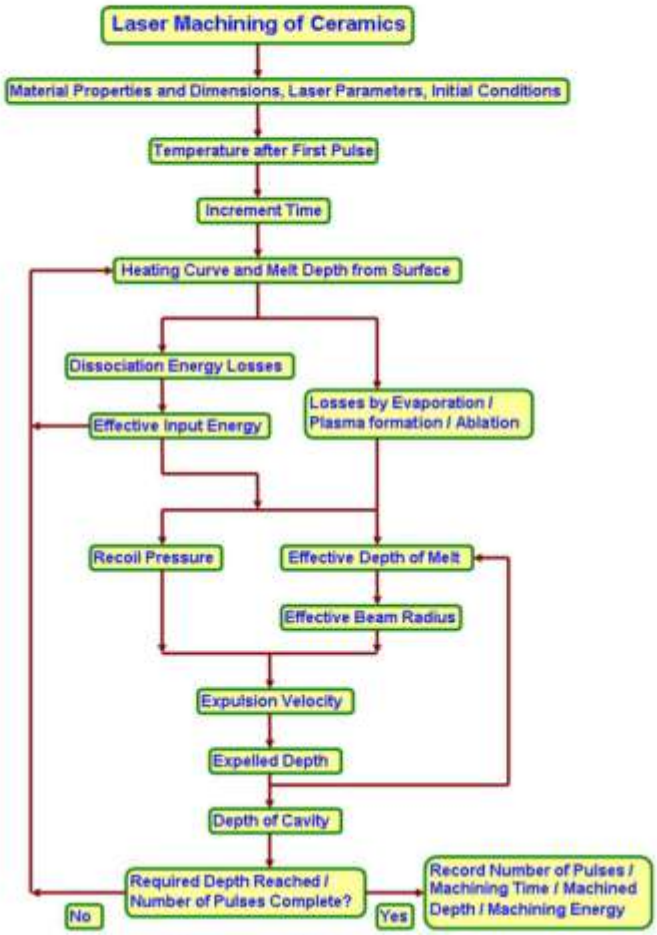

Fig. 13. Stepwise procedure for prediction of machining parameters.

other parameters such as machining time, number of pulses, dimensions of machined cavity and machining energy. In light of this, an ab initio physical model was developed by Samant and Dahotre and used for predicting depth of machined cavity when a certain number of pulses was applied to Si_3N_4[62] and also for advance prediction of number of pulses and energy necessary for machining SiC ceramic.[66] The model was also applied to determine the number of pulses and corresponding time required for machining a certain depth in Al_2O_3[63] and MgO.[65] A general flow chart for predicting the desired machining parameter based on such computational model using the process parameters and material properties is represented in Fig. 13. The nature of the structural ceramic will govern the physical phenomena that can be incorporated into the mathematical model.

3.3. Types of machining

Based on the kinematics of the front in the area where material removal takes place, laser machining is classified into one-, two-, and three-dimensional machining. The laser beam is considered as a one-dimensional line source with line thickness given by the diameter for circular and the major axis for elliptical beam cross-sections. Laser drilling (one-dimensional) machining (Fig. 14a) can be achieved by keeping the ceramic workpiece as well as the laser beam stationary while the motion of the laser beam or the ceramic in only one direction leads to cutting (two-dimensional machining) (Fig. 14b) in the ceramic. Motion of one or more laser beams or the workpiece in more than one direction leads to

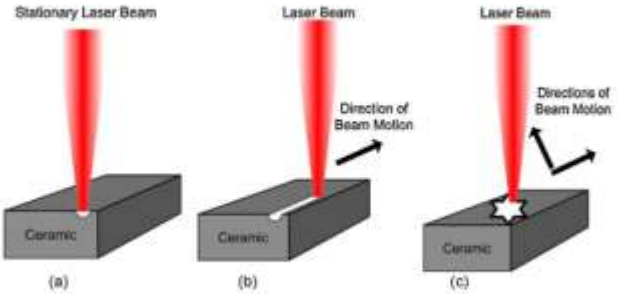

Fig. 14. Schematic of basic laser machining processes (a) laser drilling (one-dimensional machining), (b) laser cutting (two-dimensional machining), (c) engraving a star by laser beam (three-dimensional machining).

three-dimensional machining and complex geometries can be machined (Fig. 14c).

3.3.1. One-dimensional laser machining

Drilling is a one-dimensional laser machining process where the laser beam is fixed relative to the workpiece. The material removal rate is governed by the velocity of the erosion front in the direction of the laser beam. The hole taper is a measure of the dimensional accuracy for laser drilling and it can be minimized to an insignificant order of appearance by using a lens of long focal length with longer focal waist. A schematic of the laser drilling process and a hole drilled in SiC with associated microstructural features is presented in Figs. 15 and 16, respectively.[74] The drilling in SiC was carried out using a pulsed CO_2 laser ($\lambda = 10.6\,\mu m$) with a pulse duration of 2 ms, a power of 0.5 kW and the lens had a focal length of 31.8 mm.

3.3.2. Two-dimensional laser machining

In two-dimensional laser machining (cutting), the laser beam is in relative motion with respect to the workpiece (Fig. 17). A cutting front is formed when the laser beam melts/vaporizes the material throughout the thickness or the depth. In addition to removal of the molten material, the pressurized gas jet also assists in enhanced material removal by chemical reactions such as oxidation. Cutting of the material then proceeds by the motion of the cutting front across the surface of the material.[75] The four main techniques associated with laser cutting are evaporative laser cutting, fusion cutting, reactive fusion cutting and controlled fracture technique. The selection of the machining method depends on the thermo-physical properties of the material, workpiece thickness and type of laser used.

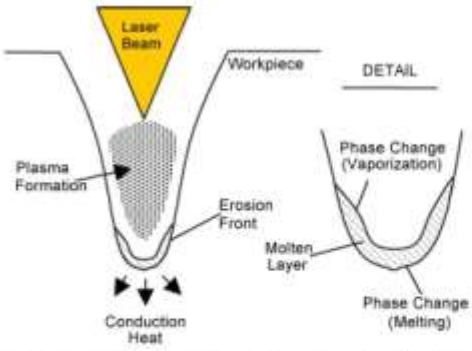

Fig. 15. Laser drilling process schematic. (After Chryssolouris[16] with kind permission of Springer Science + Business Media.)

Brittle ceramics such as alumina are mostly machined by the controlled fracture technique where the incident laser energy generates localized mechanical stresses that cause the material to separate by crack extension with controllable fracture growth. The energy requirement is less compared to conventional evaporative laser cutting as the material removal is by crack propagation. The experimental setup in Fig. 18a consists of a personal computer, a CO_2 laser, a Nd:YAG laser and a XYZ positioning table. The focused Nd:YAG laser having a focal plane on the surface of the substrate and the beam orthogonal to the surface is used to scribe a groove on the ceramic surface. The defocused CO_2 laser inclined to the Nd:YAG laser beam induces localized thermal stresses in the substrate. Both the laser beams are applied simultaneously on the ceramic surface in a continuous mode of operation. The stress concentration at the groove tip assists in extending the crack through the substrate followed by controlled separation along the moving path of the laser beam.[76] The four distinct regions: evaporation, columnar grain, intergranular fracture, and transgranular fracture regions of the alumina ceramic cut by controlled fracture technique is presented in Fig. 18b.

3.3.3. Three-dimensional laser machining

Two or more laser beams are used for three-dimensional machining and each beam forms a surface with relative motion with the workpiece (Fig. 19). The erosion front for each surface is located at the leading edge of each laser beam. When the surfaces intersect, the three-dimensional volume bounded by the surfaces is removed and machining takes place. Laser turning and milling are commonly used three-dimensional laser machining techniques useful for machining complex geometries such as

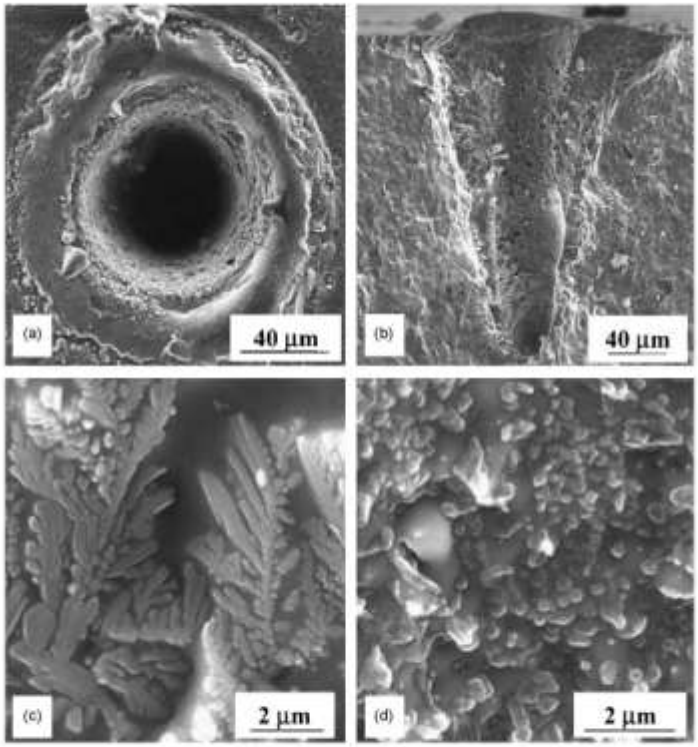

Fig. 16. Microstructural features of hole obtained in SiC (a) hole entry (b) hole section (c) silicate-like dendrite crystals obtained on debris area (d) hole inside walls. (After Sciti and Bellosi[74] with permission. Copyright Elsevier.)

slots, grooves, threads, and complex patterns in ceramic workpieces. Laser machining has been used to turn threads in Si_3N_4 ceramic (Fig. 20a)[77] and also to cut gears from SiC_w/Al_2O_3 composite (Fig. 20b).[72]

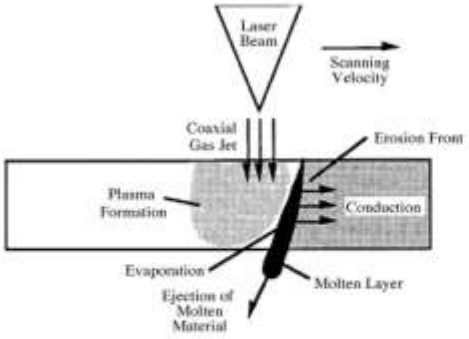

Fig. 17. Schematic of laser cutting process. (After Chryssolouris[76] with kind permission of Springer Science + Business Media.)

4. State of the art

So far it has been covered in this study that temperature dependent thermo-physical properties and laser processing conditions govern the physical phenomena that can machine ceramics in one, two or three dimensions. Even though a few structural ceramics have been briefly mentioned earlier only to explain key concepts of laser machining, this section presents the detailed state of the art in machining by lasers of some commonly used structural ceramics such as Al_2O_3, Si_3N_4, SiC, AlN, ZrO_2, and MgO.

4.1. Alumina

Besides the applications mentioned earlier, alumina is also used as a substrate in hybrid circuits as it possesses excellent dielectric strength, thermal stability and conductivity.[78] CO_2 lasers have been adapted for drilling holes in thin alumina plates used as substrates for thin-film circuits in electronic switching systems. Hole diameters varying from 0.125 to 0.3 mm were drilled by changing the lenses and the pulse duration.[79] Laser

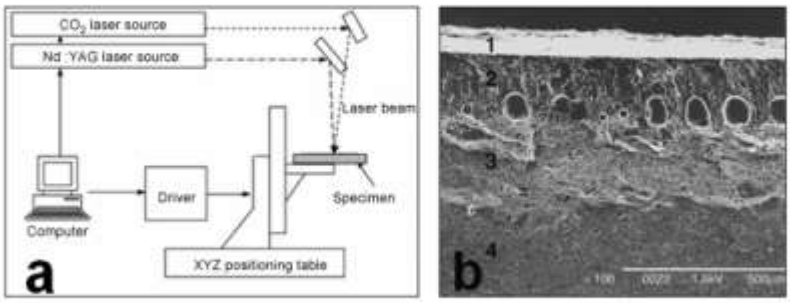

Fig. 18. (a) Configuration of laser cutting using controlled fracture technique. (b) Fracture surface of alumina substrate. (After Tsai and Chen[76] with permission. Copyright Elsevier.)

scribing (drilling a series of blind holes in a line) was carried out by Saifi and Borutta[80] with a pulsed CO_2 laser for separating individual thin-film circuits on a large substrate. It was observed that for shorter pulse length, the heat-affected zone was small with a corresponding rapid temperature drop. On the other hand, the development of microcracks in the scribed region reduced the flexural strength of the scribed substrates.

Holes of variable depths were drilled in dense alumina ceramic using a pulsed Nd:YAG laser (1064 nm wavelength) by applying different number of pulses at a pulse energy of 4 J, repetition rate of 20 Hz and a pulse width of 0.5 ms (Fig. 21). Laser fluences of 442, 884, 1768 and 2652 J/cm^2 were required for drilling depths of 0.26, 0.56, 3.23, and 4.0 mm.[63] As mentioned earlier, alumina liquid is formed at 2327 K which is stable till 3500 K. At temperatures above 3250 K, dissociation of the ceramic yields different species such as AlO(g), Al(l), Al(g), $Al_2O(g)$ and $AlO_2(g)$.[51] At temperatures above 5000 K, dissociation is complete and aluminum vapor and atomic oxygen are formed. Recoil pressure provoked expulsion of the liquid phase formed due to melting between 2327 and 3500 K and the dissociation process above 3250 K (most likely by reaction in Eq. (11)) is responsible for laser machining in alumina.

$$Al_2O_3 = 2Al(l) + \frac{3}{2}O_2(g) \tag{11}$$

There was also some material loss at the surface by evaporation and the machining in alumina was a combined effect of melt expulsion, dissociation and evaporation.[63]

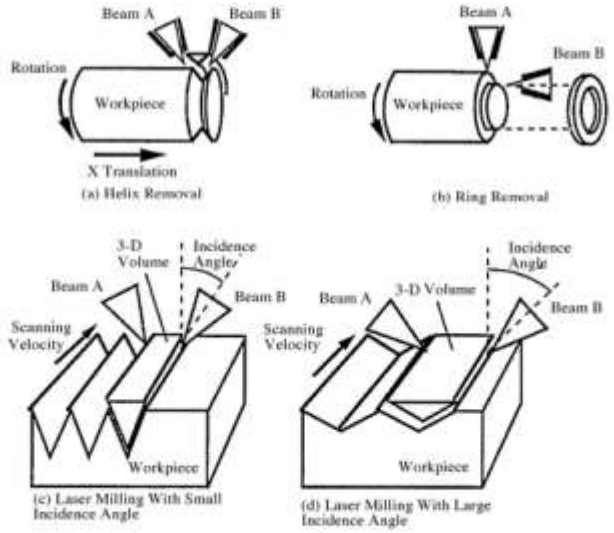

Fig. 19. Three-dimensional laser machining. (After Chryssolouris[34] with kind permission of Springer Science + Business Media.)

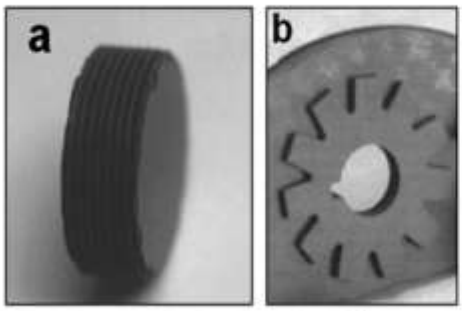

Fig. 20. (a) Turning of threads in Si_3N_4. (After Liu et al.[77] with permission. Copyright Elsevier.) (b) A gear shape cut in SiC_w18/Al_2O_3 composite. (After Islam[78] with kind permission of Springer Science + Business Media.)

The threshold energy density (the minimum energy density required for material removal) for drilling gold-coated alumina by ruby lasers (400 J/cm^2) was less than the energy density for drilling uncoated alumina (750–1000 J/cm^2). This drop in energy density could be attributed to the relatively high thermal conductivity of gold.[82] Drilling of 0.25 mm diameter holes in 0.1 mm thick alumina workpiece was performed by Coherent, Inc. at a machining speed of 0.1 s/hole using a pulsed CO_2 laser at a pulse frequency of 500 Hz and pulse duration of 200 ms.[83] Chryssolouris and Bredt[84] drilled blind holes (depths varying from 0.02 to 1 cm) using a 1.2 kW CW CO_2 laser with energy densities ranging from 2 to 500 kJ/cm^2. CO_2 and Nd:YAG lasers with power densities between 10^6 and 10^8 W/cm^2 were used to drill holes in alumina upto 0.25 mm diameter and it was found that the holes drilled by CO_2 laser showed a noticeable taper compared to the holes made by Nd:YAG laser.[85]

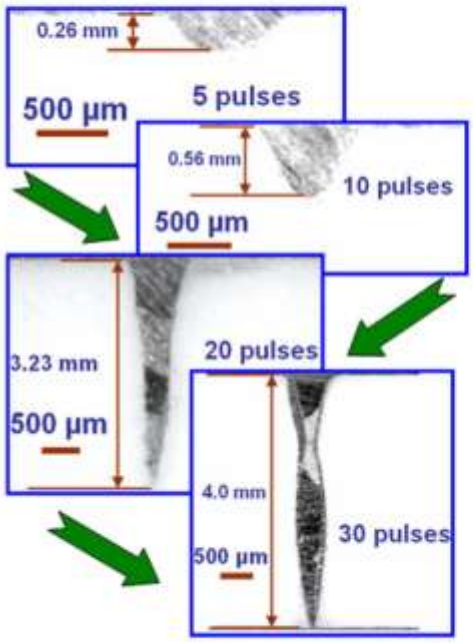

Fig. 21. Drilling in dense alumina ceramic. (After Samant and Dahotre[51]).

Common defects associated with laser drilling (Microcracks and spatter[86–89]) were prevented by a drilling technique based on gelcasting.[90] For gelcasting, the ceramic slurry made by dispersing the powders in a pre-mixed monomer solution is cast in a mold of desired shape. After addition of a suitable initiator, the entire system is polymerized in situ and green bodies with improved mechanical properties are produced. As the green body has relatively loose structures compared with sintered ceramics, spatter-free holes with more uniform shapes and without microcracks can be drilled (Fig. 22).

A computer controlled Nd:YAG laser was used to obtain good quality kerfs and cuts without cracks in alumina substrates for embedded MCM-Ds (Multi Chip Modules, deposited) and water-cooled heat sinks for single chips, multi chip modules or laser diodes. A laser energy of 1.7 J, pulse duration of 0.4 ms, pulse frequency of 250 Hz, nitrogen as process gas and a feed rate of 150 mm/min were used for machining these substrates.[91] Alumina has also been machined with a KrF excimer laser with laser fluence (1.8 and 7.5 J/cm^2), pulse duration (25 ns), number of pulses (1–500), frequency (1–120 Hz), and the corresponding microstructural changes were examined.[92] At low fluence (1.8 J/cm^2), the melting/resolidification produced scales on the surface while at high fluence (7.5 J/cm^2), there were no continuous scales as the material was removed by vaporization. The depth of material removed was directly proportional to the number of pulses.[65,92] However, this laser treatment was not suitable for reducing the roughness as can be seen from Fig. 23 that the values of Ra (surface roughness) and Rt (peak-to-valley distance) varied slightly compared to the starting values. Moreover, Femtosecond near-infrared (NIR) optical pulses have been used for microstructuring alumina with improved edge quality at scanned intensities less than 50 W/cm^2.[78] The surface showed no discoloration unlike the processing done by nanosecond UV lasers at 248 nm wavelength by Sciti et al.[92]

3D Laser Carving is an emerging technique in industries for manufacturing ceramic components of complex shapes. Initially, a 3D CAD model is sliced in a particular direction to obtain profile information of the slice. The focused laser beam is then used for scanning and engraving the ceramic surface as per the profile information, producing two-dimensional layer patterns. Finally, the Z-axis of the table is raised to a designated height to locate the carving surface at the focal plane. This process is repeated several times until the whole model is completely sliced and the 3D graphics is engraved on the workpiece (Fig. 24).[93] Thus, alumina ceramic has been laser machined in one, two and three dimensions by using different types of lasers for several applications.

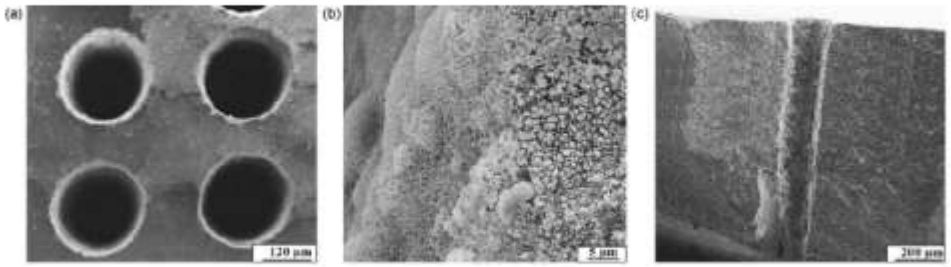

Fig. 22. Holes drilled on gelcast green body of alumina. (a) Top view, (b) hole edge, (c) cross-section of hole. (After Guo et al.[97] with permission. Copyright Elsevier.)

4.2. Silicon nitride

Silicon nitride is widely used for machining purposes in automotive, semi-conductor and aerospace industries. Cams, bearings, piston rings and rocker arms can be made by machining this ceramic.[94,95] A 0.1 mm hole drilled at the Integrated Manufacturing Technologies Institute (IMTI), National Research Council Canada (NRC) through a 6 mm thick silicon nitride cutting tool insert is presented in Fig. 25.[72] Harrysson et al. drilled holes in Si_3N_4 using CO_2 and Nd:YAG lasers. High thermal stresses produced intense cracking in CO_2 laser drilled samples while the cracking was limited only to the recast layer (about 0.02 mm) by using a Nd:YAG laser.[96] A pulsed Nd:YAG laser at a pulse energy of 4 J, pulse width of 0.5 ms and a repetition rate of 20 Hz was used for drilling holes of varying depths in Si_3N_4 by applying different number of pulses (Fig. 26).[62]

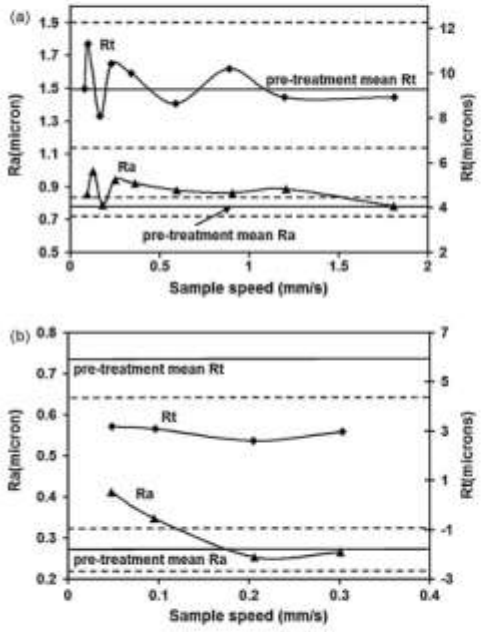

Fig. 23. Surface roughness after laser treatment for (a) raw Al_2O_3 at fluence of 1.8 J/cm^2 and (b) polished Al_2O_3 at fluence of 7.5 J/cm^2. (After Sciti et al.[92] with kind permission of Springer Science + Business Media.)

The decomposition of Si_3N_4 into N_2 gas and Si liquid (Eq. (12))[97] at the sublimation temperature of Si_3N_4 followed by the expulsion of the liquid silicon was proposed as the material removal mechanism.[98,99]

$$Si_3N_4 = 3Si(l) + 2N_2(g) \quad (12)$$

There were some evaporative losses at the surface and a combination of melting, dissociation and evaporation lead to machining in silicon nitride (Table 3).[62] In excimer laser processing by ArF, KrF and XeF excimer lasers, decomposition of Si_3N_4 into Si (gas) and nitrogen along with ionized silicon produced excellent quality of the processed ceramic without deposition of any decomposed material.[100] Shigematsu et al. machined Si_3N_4 in different atmospheres (N_2, O_2 gas and air) by a multi-mode CO_2 laser and the particles suspended in the chamber after machining were studied.[101] The infrared spectra of the gases and the suspended particles inside the chamber are presented in Fig. 27. No absorption peaks were observed in N_2 and all the liquid silicon formed by Eq. (12) above was deposited on the ceramic surface. The energy density of the CO_2 laser was insufficient to vaporize the free silicon. Machining in O_2 or air formed SiO vapor by the oxidation decomposition of Si_3N_4:

$$2Si_3N_4(s) + 3O_2 = 6SiO(g) + 4N_2(g) \quad (13)$$

The SiO vapor immediately oxidized and formed solid phase SiO_2 seen in the absorption spectrum:

$$SiO(g) + 1/2O_2(g) = SiO_2(s) \quad (14)$$

Machining in O_2 also released NO_2 gas:

$$Si_3N_4(s) + 11/2O_2 = 3SiO(g) + 4NO_2(g) \quad (15)$$

Such an analysis of the constituents released during machining can help in the selection of an appropriate machining environment and laser machining parameters.

CO_2 laser was operated in continuous and pulsed mode for cutting Si_3N_4 and it was found that deep and narrow cuts were produced by pulsed mode as compared to continuous mode of

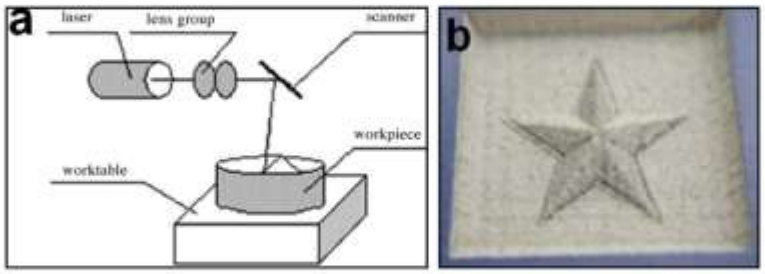

Fig. 24. 3D Laser Carving (a) schematic layout (b) 3D star in alumina ceramic. (After Wang and Zeng[32] with permission. Copyright Elsevier.)

operation. Reducing the traverse speed avoided fracture of the ceramic and it was more effective than increasing the laser power for machining thicker plates (6–8 mm).[102] Firestone et al. used a 15 kW CO_2 laser to machine silicon nitride without fracturing at 996 °C and the machining rates achieved were ten times that of conventional diamond grinding.[103] This ceramic has also been machined by Lavrinovich et al. in two regimes: with free generation where the width of the laser pulse was 4 ms and with Q-factor modulation where the pulse width was 3×10^{-7} s.[104] Q-factor modulation was able to form an oxide film on the surface when exposed to a defocused laser beam. This method also helped to minimize the residual microcracks.

Apart from the above applications of laser machining of silicon nitride, laser milling is a newly developed method of producing wide variety of complex parts from ceramics such as silicon nitride directly using the CAD data, thus making it possible to machine Si_3N_4 in one, two and three dimensions.[105]

4.3. Silicon carbide

Silicon carbide is another structural ceramic that has been widely machined by lasers for different purposes. Using a pulsed Nd:YAG laser (1064 nm wavelength) at an input energy of 6 J, pulse duration of 0.5 ms, and repetition rate of 50 Hz, a through cavity was machined in a 2 mm thick SiC plate in approximately 25 pulses while it took about 125 pulses to machine through the entire thickness of a 3 mm thick plate (Fig. 28).[66] Sciti and Bellosi used a pulsed CO_2 laser with laser powers of 0.5 and 1 kW for drilling the ceramic surface.[74] The beam was incident on the surface at an angle of 90° and three different focal lengths of 95.3, 63.5, and 31.8 mm were used for machining. The hole depth increased with the pulse duration and also the input power for a given focal length because of increase in laser light intensity. Even though the hole diameters remained constant with pulse duration, they were affected by the lens focal length that governed the size of the laser spot (Fig. 29).

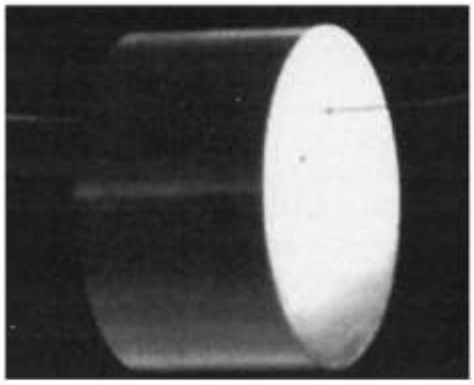

Fig. 25. A 0.1 mm diameter hole drilled in 6 mm thick Si_3N_4 cutting tool insert. Wire passing through the hole is also seen. (After Islam[72] with kind permission of Springer Science + Business Media.)

Metallic silicon particles were found on the surface of the silicon carbide ceramics machined in N_2, O_2, or air.[101] CO_2 formed by the oxidization of free carbon released by the dissociation of SiC was also detected in the machining atmosphere (Eqs. (16)–(18)).[101]

$$SiC(s) = Si(l) + C(s) \quad (16)$$

$$2C(s) + O_2(g) = 2CO(g) \quad (17)$$

$$2CO(g) + O_2(g) = 2CO_2(g) \quad (18)$$

Furthermore, machining in air or O_2 and in N_2 produced SiO_2 (Eqs. (19)–(20)) and toxic cyanogen respectively (Eq. (21)).[101]

$$2SiC + O_2(g) = 2SiO(g) + 2C(s) \quad (19)$$

$$2SiO(g) + O_2(g) = 2SiO_2(s) \quad (20)$$

$$2C + N_2(g) = (CN)_2(g) \quad (21)$$

Looking at the released constituents can assist in choosing a suitable working atmosphere based on safety and health requirements. A 400 W Nd:YAG laser with pulse frequencies upto 200 Hz and pulse width of 250 to 1000 ms was capable of drilling holes (0.25–1.5 mm diameter) in 3–3.5 mm thick SiC plates along with other ceramics such as silicon nitride and alumina.[106] It was found that SiC required the highest pulse energy of all ceramics and corresponding holes produced had the most irregular shape.

Affolter et al. cut 5 mm thick SiC plates with a 10 kW Nd:YAG laser at a cutting speed of 40 mm/min[107] while a 15 kW

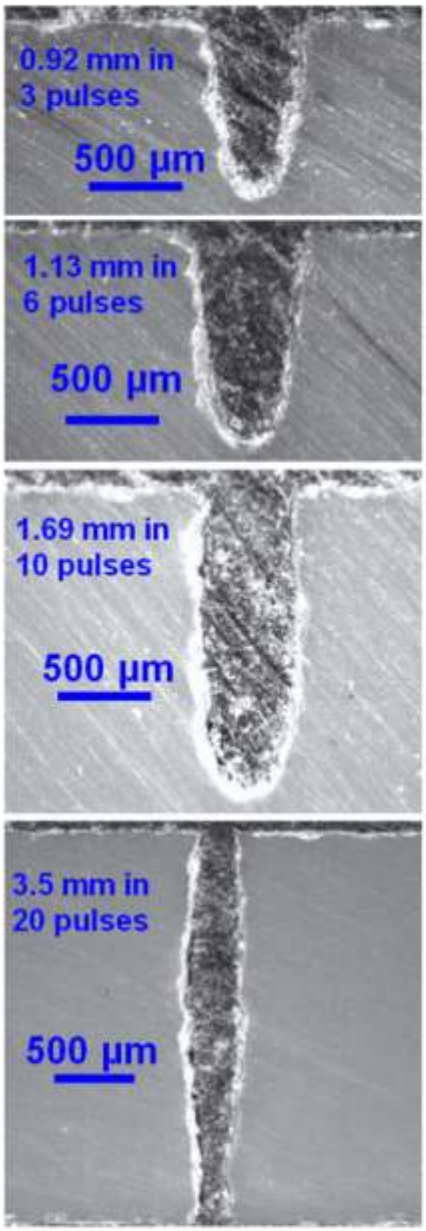

Fig. 26. Drilled holes in silicon nitride. (After Samant and Dahotre[92]).

CW CO_2 laser with a spot diameter of 2.7 mm was used by Firestone et al.[103] for the cutting process. The workpieces were initially heated to 1400 °C in a furnace to reduce the cracks and a gas jet minimized oxidation and plasma formation.[103] For SiC processed by KrF excimer lasers, ablation depth varied linearly with number of pulses and the surface showed flat as well as rough areas, debris deposit and thin scale formation.[92]

Three-dimensional contours have been made on SiC ceramic by a 450 W CW CO_2 laser by machining overlapping grooves for material removal. The grooves were formed by directing the beam tangential to the workpiece. Decreasing the groove depth on successive overlapping passes controlled the surface roughness of the finished components. This technique is similar to electrical-discharge machining and was used for generating flat or threaded surfaces on the workpiece.[108]

4.4. Aluminum nitride

Aluminum nitride (AlN) is commonly used in microelectronic substrates and packages because of its high thermal conductivity and small thermal expansion mismatch with silicon.[109] Lines and single – layer pockets were machined on AlN surface with an ultraviolet (UV) and near-infrared lasers and the effect of pulse overlap and pulse frequency on material removal rate and wall angle was predicted. However, there is no work reported that could explain the physical processes governing the machining in this ceramic. Maximum material removal rates (MRR) of 0.011 and 0.094 mm^3/s were achieved by UV and NIR lasers, respectively.[110] The steepest wall angle for an UV (Fig. 30a) and NIR laser (Fig. 30b) was 86° and 88°, respectively. Walls with steeper angles were produced at 95% overlap with NIR laser and at lower overlaps for UV laser.

Heat sinks were made out of AlN with laser machined cooling channels, the width and depth of which were controlled by

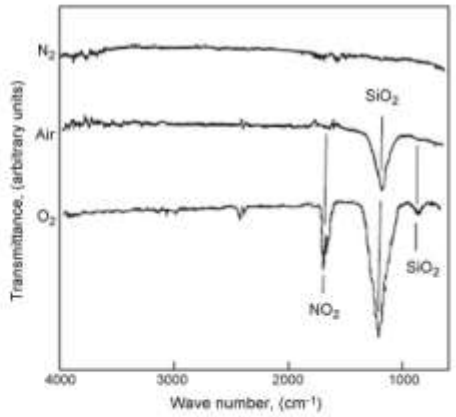

Fig. 27. Infrared absorption spectrum of atmosphere after laser machining of Si_3N_4. (After Shigematsu et al.[101] with kind permission of Springer Science + Business Media.)

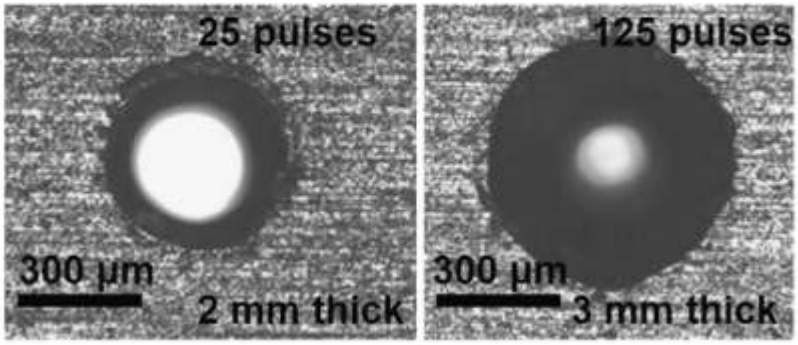

Fig. 28. Machining in 2 and 3 mm thick SiC plates. (After Samant et al.[90]).

the pulse width, the spot size and distance between the beam focus and the substrate. Laser energy of 7.5 J, pulse width of 0.9 ms, speed of 150 mm/min, and a pulse frequency of 60 Hz were used with nitrogen as a process gas for machining these

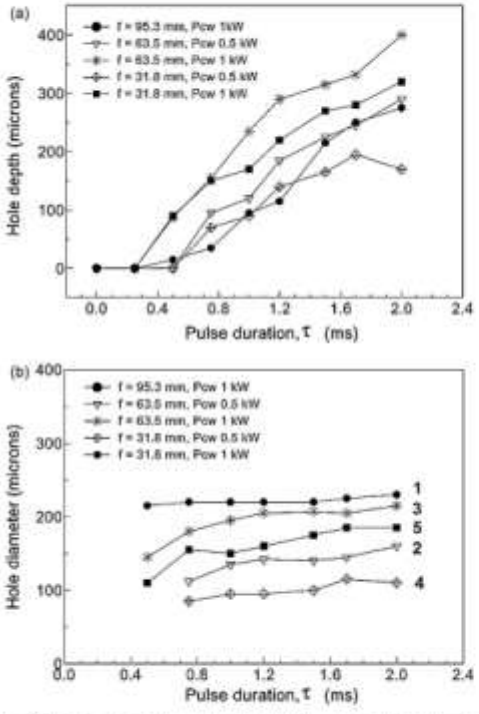

Fig. 29. Variation of (a) hole depth and (b) hole diameter with pulse duration for SiC drilling. (After Sciti and Bellosi[74] with permission. Copyright Elsevier.)

cooling channels.[91] A Lambda Physik LPX 210icc excimer laser was used for fabricating small diameter and high aspect ratio holes at designated locations in AlN ceramic. The ablation depth increased with decreasing pressure (Fig. 31a) and increasing fluence (Fig. 31b). The effective ablation rate saturated at high fluences due to attenuation by plasma and re-ablation of redeposited debris from earlier pulses. Plasma reduced the effective energy reaching the ceramic surface, thus removing less material per pulse. Also, redeposition generated an error in the depth measurement as the coating of the previously ablated material made the hole appear shallower.[109]

4.5. Zirconia

Low thermal conductivity, low coefficient of friction, excellent corrosion and wear resistance, high fracture toughness, and good thermal shock resistance make zirconia suitable for use in bearings, pH meters, fuel cells, infrared radiators, thread guides, pressure sensors, and oxygen sensors.[111] A pulsed Nd:YAG laser was used for drilling zirconia ceramic and the observations were input to MINITAB software for optimizing the parameters to obtain minimum heat-affected zone (HAZ) and taper. It was found that minimum HAZ thickness of 0.0675 mm (Fig. 32) could be obtained when the lamp current, pulse frequency, assisted air pressure, and pulse width are set at 17 A, 2 kHz, 2 kg/cm^2 and 2% of the duty cycle, respectively. The corresponding optimum parameters to attain a minimum taper of 0.0319 were lamp current of 17 A, pulse frequency of 2 kHz, air pressure of 0.6 kg/cm^2 and pulse width of 2% of the duty cycle (Fig. 33).

Using a 10 kW Nd:YAG laser, at a power density of 5 MW/cm^2, 1.3 mm thick ZrO_2 samples were machined at 200 mm/min.[107] Laser cutting of magnesia-stabilized zirconia (PSZ) was also investigated using a 15 kW CW CO_2 laser by preheating at 660 and 957 °C with single and multiple passes. The power varied from 2 to 6 kW with cutting speeds varying from 9100 to 16,000 mm/min and the resultant depth of cut ranged from 0.13 to 0.9 mm.[103] ZrO_2 was machined by excimer

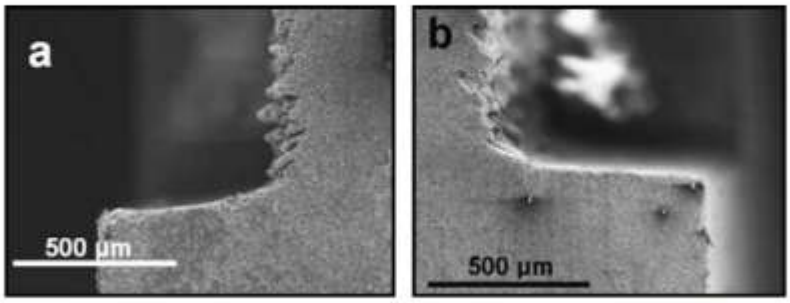

Fig. 30. Pocket edges machined in AlN with (a) UV laser with a 93% overlap and (b) NIR laser with a 95% overlap. (After Gilbert et al.[110] with permission. Copyright Elsevier.)

lasers and the mechanism for material removal was proposed to be melting and vaporization without the additional mechanism of dissociation that takes place in the case of SiC and Si_3N_4. Nevertheless, XeF laser machined surface demonstrated a porous structure and slower processing rate. ZrO_2 is transparent to 351 nm wavelength (wavelength of XeF laser) and the grain boundaries selectively absorbed the incident energy during laser processing. This selectively etched the grain boundaries and the processed surface appeared porous.[100]

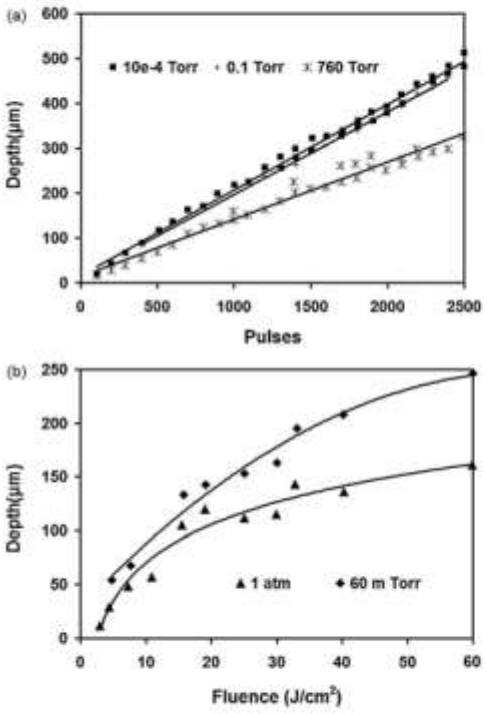

Fig. 31. (a) Variation of ablation depth with number of pulses at 40 J/cm^2 and for different pressures (b) variation of ablation depth with laser fluence at 60 mTorr and 760 Torr (1 atm).[109]

4.6. Magnesia

To the best of the present knowledge based on available literature, no significant work has been reported in the laser machining of pure MgO ceramic which has several industrial applications as mentioned earlier in this study. Samant and Dahotre have made an attempt in machining this ceramic with a pulsed Nd:YAG laser and the physical phenomena during the laser–ceramic interaction have been studied.[65] For pulse energy of 4 J, repetition rate of 20 Hz and pulse width of 0.5 ms, different number of pulses were applied to 3 mm thick MgO plates and the corresponding depth of the machined cavity was measured. Cavities that were 0.25, 0.86, 1.54 and 3 mm deep were formed when 3, 6, 9 and 20 pulses were incident on the ceramic. Instantaneous temperatures reached at the surface during laser machining are very high (higher than 2850 °C[116], the melting/decomposition/vaporization temperature of magnesia). At these high temperatures, magnesia dissociates as per the following reaction:[112,113]

$$MgO \rightarrow Mg(s) + O(g) \quad (22)$$

The melting and vaporization temperatures of magnesium are 649 °C[114] and 1090 °C[115], respectively. The decomposition temperature of magnesia being much higher than both the melting and vaporization temperatures of magnesium, Mg(s) generated by the above reaction instantaneously vaporizes. Hence, at high temperatures reached during laser machining, the material losses in magnesia take place solely by the vaporization of magnesium. Thus, in MgO, the dissociation of the ceramic followed by evaporation is responsible for material removal.[65]

As the material evaporates, it exerts a force over the machined area and material removal takes place by corresponding pressure (vapor pressure) acting upwards and proportional to the laser fluence (input energy/beam cross-sectional area):

$$\text{Vapor pressure} = \frac{\text{laser fluence}}{\text{machined depth}} \quad (23)$$

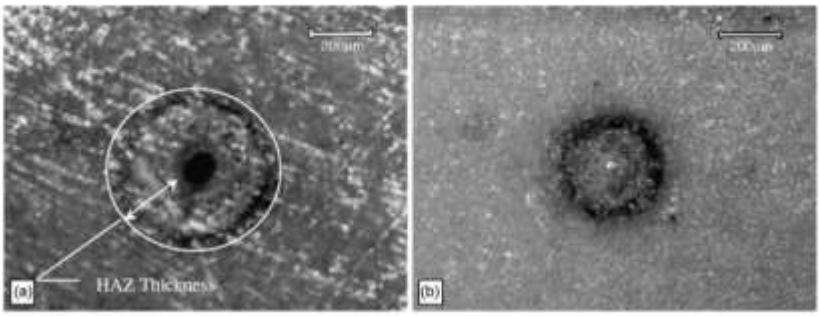

Fig. 32. Minimum HAZ thickness in ZrO_2: (a) top surface, (b) bottom surface. (After Kuar et al.[23] with permission. Copyright Elsevier.)

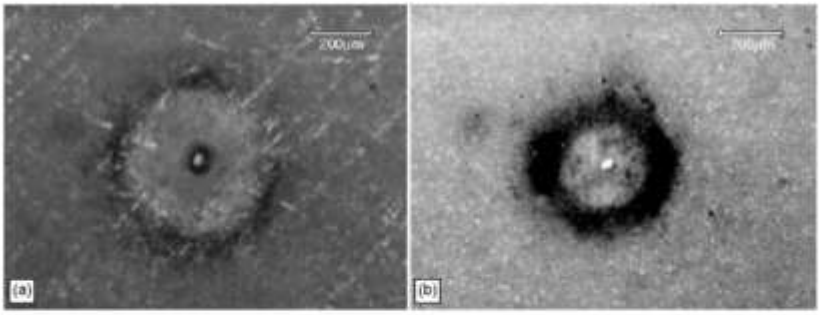

Fig. 33. Hole drilled in ZrO_2 with minimum taper: (a) top surface, (b) bottom surface. (After Kuar et al.[23] with permission. Copyright Elsevier.)

Moreover, the evaporated material is also subjected to gravitational pull acting downwards and given by ρgh, where ρ is density of the ceramic, g is the acceleration due to gravity (9.8 m/s^2) and h is the machined depth. The cavity formation is governed by the effect of these counteracting pressures (vapor pressure and gravitational pressure) and a clean cavity (Fig. 34) is formed when the vapor pressure exceeds the gravitational pressure.[65]

In addition to the above-mentioned illustrations, there would be several studies of laser machining of these and other structural ceramics. However, these few specific examples suffice the purpose of explaining the effects in laser machining of ceramics

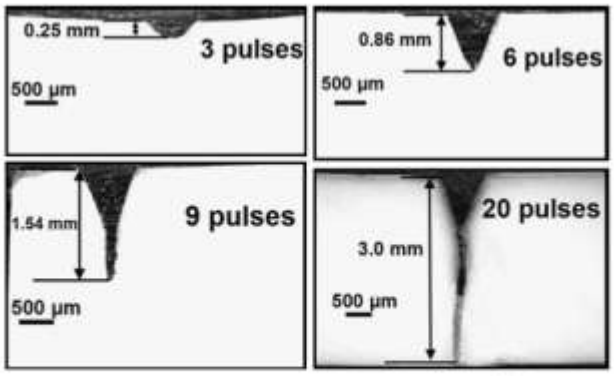

Fig. 34. Machining in MgO ceramic. (After Samant and Dahotre[65]).

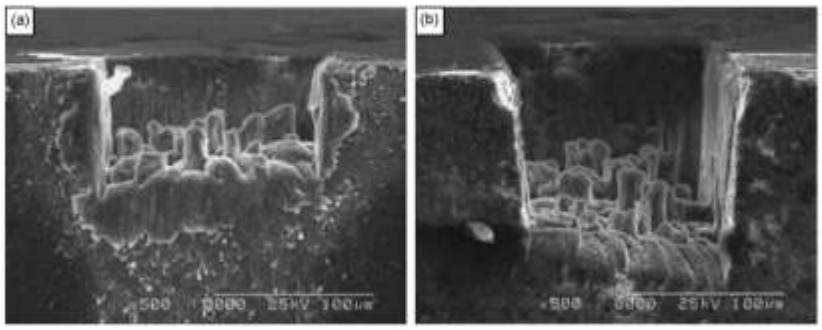

Fig. 35. Cross-section of craters formed in Al_2O_3–TiC after treatment at 10 J/cm^2 with (a) 500 and (b) 1000 laser pulses. (After Oliveira et al.[119] with kind permission of Springer Science + Business Media.)

based on combinations of various physical phenomena. Finally, the next section briefly looks at some of the recent advances in the field of laser micromachining.

5. Laser micromachining

There is an increasing demand for producing parts with micro and meso scale features in the field of semi-conductors, biomedical devices and optics.[117] In light of this demand, several techniques such as mechanical micromachining (micro-grooving, micro-milling), focused ion-beam micromachining, laser micromachining are being used in microfabrication. Laser micromachining is a comparatively new technique and provides improved flexibility in dimensional design of microproducts[49] and they can produce kerfs with depth and width smaller than 100 μm. Nd:YAG lasers are more widely used than CO_2 lasers because of their high energy density and small focused spot.[36] Material removal in laser micromachining mainly takes place by ablation and laser-assisted chemical etching. The growing demand for structural ceramics for different applications requires novel machining technologies with high accuracy and efficiency. Some work in the field of laser micromachining has been carried out by Oliveira et al.[118,119] who have machined Al_2O_3–34 wt.% TiC ceramics which are being increasingly used for high precision parts such as magnetic head sliders (Fig. 35).

However, no detailed studies on the physics behind laser micromachining of structural ceramics have been found in open literature. The common problems associated with conventional micromachining are tool wear and force-induced damage on ceramic components.[120] These problems can be adequately addressed by using thermal softening by a laser heat source during micro-machining. Thus, laser micro-machining of structural ceramics is still a gray area and has immense potential for research and applications.

6. Conclusion

In this study, an attempt has been made to cover the laser machining of several structural ceramics such as alumina, silicon nitride, silicon carbide, aluminum nitride, zirconia and magnesia after thoroughly understanding the physical phenomena associated with the machining process. The mechanism governing the material removal is a function of the material properties and the laser processing conditions. Laser micromachining of ceramics can also be used for producing parts at micro and meso scale. Overall, it seems that laser processing being a rapid, non-contact and flexible process, machining of structural ceramics by lasers is a budding field with tremendous applications in the future.

References

1. *New Structural Materials Technologies: Opportunities for the Use of Advanced Ceramics and Composites – A Technical Memorandum*, U.S. Congress, 1986.
2. Tsendey, I. P., Jawaid, A. and Pashby, I. R., Review: various methods of machining advanced ceramic materials. *J. Mater. Process. Technol.*, 1994, **42**(4), 377–390.
3. Schwartz, M., *Handbook of Structural Ceramics*, McGraw-Hill, New York, 1992, ISBN: 0070557195.
4. Vikulin, V., Kelina, I., Shutalin, A. and Rusanova, L., Advanced ceramic structural materials. *Refractories Ind. Ceram.*, 2004, **45**, 383–386.
5. Wang, H., Wang, C. A., Yao, X. and Fang, D., Processing and mechanical properties of zirconium diboride-based ceramics prepared by spark plasma sintering. *J. Am. Ceram. Soc.*, 2007, **90**, 1992–1997.
6. Kim, J. D., Lee, E. S. and Lee, C. Y., Crack generation and the effect of in-process electro-discharge dressing in grinding single crystal MgO. *Int. J. Mech. Sci.*, 1995, **37**, 569–583.
7. Kim, J. D. and Lee, E. S., A study on the micro-like grinding of MgO single crystal with various diamond wheels. *J. Mater. Process. Technol.*, 1997, **72**, 1–10.
8. Kalpakjian, S. and Schmid, S. R., *Manufacturing Engineering and Technology*, Prentice Hall, Upper Saddle River, NJ, 2001, ISBN: 0201361310.
9. König, W. and Wagemann, A., Machining of ceramic components—process-technological potentials. *Machining Adv. Mater.*, 1993, **847**, 3–16 [NIST Special Publication].
10. Chryssolouris, G., Anifantis, N. and Karagiannis, S., Laser assisted machining: an overview. *J. Manuf. Sci. Eng.*, 1997, **119**(4B), 766–769.
11. Koepke, B. G. and Stokes, R. J., A study of grinding damage in magnesium oxide single crystals. *J. Mater. Sci.*, 1970, **5**(3), 240–247.
12. Kirchner, H. P., Damage penetration at elongated machining grooves in hot-pressed Si_3N_4. *J. Am. Ceram. Soc.*, 1984, **67**(2), 127–132.
13. Zhang, B., Precision grinding regime of advanced ceramics. In *Proceedings of Annual Meeting of American Society of Precision Engineering*, 1993, pp. 225–229.

14. Xu, H. H. K. and Jahanmir, S., Microfracture and material removal in scratching of alumina. *J. Mater. Sci.*, 1995, **30**(9), 2235–2247.
15. Zhang, B., Zheng, X. L., Tokura, H. and Yoshikawa, M., Grinding induced damage in ceramics. *J. Mater. Process. Technol.*, 2003, **132**, 353–364.
16. Thoe, T. B., Aspinwall, D. K. and Wise, M. L. H., Review on ultrasonic machining. *Int. J. Mach. Tools Manuf.*, 1998, **38**(4), 239–255.
17. Choi, J. P., Jeon, B. H. and Kim, B. H., Chemical-assisted ultrasonic machining of glass. *J. Mater. Process. Technol.*, 2007, **191**(1–3), 153–156.
18. Gudimetla, P., Wang, J. and Wong, W., Kerf formation analysis in the abrasive waterjet cutting of industrial ceramics. *J. Mater. Process. Technol.*, 2002, **128**(1–3), 123–129.
19. Park, J. M., Jeong, S. C., Lee, H. W., Jeong, H. D. and Lee, E., A study on the chemical mechanical micro-machining (CSM) process and its application. *J. Mater. Process. Technol.*, 2002, **130–131**, 390–395.
20. Puertas, I. and Luis, C. J., A study on the electrical discharge machining of conductive ceramics. *J. Mater. Process. Technol.*, 2004, **153–154**, 1033–1038.
21. Chak, S. K. and Rao, P. V., Tirpanning of Al_2O_3 by electro-chemical discharge machining (ECDM) process using abrasive electrode with pulsed DC supply. *Int. J. Mach. Tools Manuf.*, 2007, **47**(14), 2061–2070.
22. Horio, K., Terabayashi, T. and Taniguchi, N., Beam defocus effect in electron beam machining of green ceramic sheet. *CIRP Ann. – Manuf. Technol.*, 1987, **36**(1), 95–98.
23. Kuar, A. S., Doloi, B. and Bhattacharyya, B., Modelling and analysis of pulsed Nd:YAG laser machining characteristics during micro-drilling of zirconia (ZrO_2). *Int. J. Mach. Tools Manuf.*, 2006, **46**(12–13), 1301–1310.
24. Jia, Z. X., Zhang, J. H. and Ai, X., High quality machining of engineering ceramics. *Key Eng. Mater.*, 1995, **108–110**, 155–164.
25. Shih, H. and Shu, K., A study of electrical discharge grinding using a rotary disk electrode. *Int. J. Adv. Manuf. Technol.*, 2008, **38**, 59–67.
26. Bäuerle, D., *Laser Processing and Chemistry*, Springer, New York, 2000, ISBN: 3540668918.
27. Lei, S., Shin, Y. C. and Incropera, F. P., Experimental investigation of thermo-mechanical characteristics in laser-assisted machining of silicon nitride ceramics. *J. Manuf. Sci. Eng.*, 2001, **123**, 639–646.
28. Rozzi, J. C., Pfefferkorn, F. E., Incropera, F. P. and Shin, Y. C., Transient, three-dimensional heat transfer model for the laser assisted machining of silicon nitride. I. Comparison of predictions with measured surface temperature histories. *Int. J. Heat Mass Transfer*, 2000, **43**(8), 1409–1424.
29. Rozzi, J. C., Pfefferkorn, F. E., Incropera, F. P. and Shin, Y. C., Transient thermal response of a rotating cylindrical silicon nitride workpiece subjected to a translating laser heat source. Part I. Comparison of surface temperature measurements with theoretical results. *J. Heat Transfer*, 1998, **120**, 899–906.
30. Rozzi, J. C., Incropera, F. P. and Shin, Y. C., Transient thermal response of a rotating cylindrical silicon nitride workpiece subjected to a translating laser heat source. Part II. Parametric effects and assessment of a simplified model. *J. Heat Transfer*, 1998, **120**, 907–915.
31. Rozzi, J. C., Incropera, F. P. and Shin, Y. C., Transient, three-dimensional heat transfer model for the laser assisted machining of silicon nitride. II. Assessment of parametric effects. *Int. J. Heat Mass Transfer*, 2000, **43**(8), 1425–1437.
32. Lei, S., Shin, Y. C. and Incropera, F. P., Deformation mechanisms and constitutive modeling for silicon nitride undergoing laser-assisted machining. *Int. J. Mach. Tools Manuf.*, 2000, **40**(15), 2213–2233.
33. Pfefferkorn, F. E., Shin, Y. C., Tian, Y. and Incropera, F. P., Laser-assisted machining of magnesia-partially-stabilized zirconia. *J. Manuf. Sci. Eng.*, 2004, **126**, 42–51.
34. Chang, C. W. and Kuo, C. P., An investigation of laser-assisted machining of Al_2O_3 ceramics planning. *Int. J. Mach. Tools Manuf.*, 2007, **47**(3–4), 452–461.
35. www.laserchevalfeleng/subcontracting.php.
36. Chryssolouris, G., *Laser Machining Theory and Practice*. Springer-Verlag, New York, 1991.
37. Albright, C., *Laser Welding, Machining and Materials Processing*. IFS (Publications) Ltd. and Springer-Verlag, New York, 1985.
38. Pandey, P. C. and Shan, H. S., *Modern Machining Processes*. McGraw Hill, New Delhi, 1980.
39. Sun, S., Durandet, Y. and Brandt, M., Parametric investigation of pulsed Nd:YAG laser cladding of stellite 6 on stainless steel. *Surf. Coat. Technol.*, 2005, **194**(2–3), 225–231.
40. Islam, M. U. and Campbell, G., Laser machining of ceramics: A review. *Mater. Manuf. Processes*, 1993, **8**(6), 611–630.
41. Ki, H., Mohanty, P. S. and Mazumder, J., Multiple reflection and its influence on keyhole evolution. *J. Laser Appl.*, 2002, **14**, 39–45.
42. Bang, S. Y. and Modest, M. F., Multiple reflection effects on evaporative cutting with a moving CW laser. *J. Heat Transfer*, 1991, **113**, 663–669.
43. Zhao, J., *Numerical Simulation of High Intensity Laser Drilling of Metals*. Masters Thesis. The University of Tennessee, Knoxville, TN, 1999.
44. Minamida, K., Takafuji, H., Hamada, N., Haga, H. and Mizuhashi, N., Wedge shape welding with multiple reflection effects of high power CO_2 laser beam. In *Proceedings of the 5th Int. Congress on Applications of Lasers and Electro-optics*, 1986, pp. 97–104.
45. Rahman, F. A., Takahashi, K. and Teik, C. H., Theoretical analysis of coupling between laser diodes and conically lensed single-mode fibres utilising ABCD matrix method. *Opt. Commun.*, 2003, **215**(1–3), 61–68.
46. Bang, S. Y., Roy, S. and Modest, M. F., CW laser machining of hard ceramics-II. Effects of multiple reflections. *Int. J. Heat Mass Transfer*, 1993, **36**(14), 3529–3540.
47. Modest, M. F., Effects of multiple reflections on hole formation during short-pulsed laser drilling. *J. Heat Transfer*, 2006, **128**(7), 653–661.
48. Baily, A. W. and Modak, A., Numerical simulation of laser ablation with cavity reflections. *J. Thermophys. Heat Transfer*, 1989, **3**, 42–45.
49. Dahotre, N. B. and Harimkar, S. P., *Laser Fabrication and Machining of Materials*. Springer, New York, NY, 2008.
50. Andrews, J. G. and Atthey, D. R., Hydrodynamic limit to penetration of a material by a high-power beam. *J. Phys. D: Appl. Phys.*, 1976, **9**, 2181–2194.
51. Mazumdar, J. and Steen, W. M., Heat transfer model for CW laser material processing. *J. Appl. Phys.*, 1980, **51**, 941.
52. Steen, W. M., *Laser Materials Processing*. Springer, London, 1991.
53. Dubey, A. K. and Yadava, V., Experimental study of Nd:YAG laser beam machining—An overview. *J. Mater. Process. Technol.*, 2008, **195**(1–3), 15–26.
54. Salonitis, K., Stournaras, A., Tsoukantas, G., Stavropoulos, P. and Chryssolouris, G., A theoretical and experimental investigation on limitations of pulsed laser drilling. *J. Mater. Process. Technol.*, 2007, **183**(1), 96–103.
55. Morita, N., Ishida, S., Fujimori, Y. and Ishikawa, K., Pulsed laser processing of ceramics in water. *Appl. Phys. Lett.*, 1988, **52**(23), 1965–1966.
56. Kovalenko, V. S. and Laurinovich, A. V., Laser machining of ceramic materials. In *Proceedings of 6th Int. Conf. on Production Engineering*, 1987, pp. 627–631.
57. Kim, M. J., 3D Finite element analysis of evaporative laser cutting. *Appl. Math Model.*, 2005, **29**(10), 938–954.
58. Kim, M. J. and Zhang, J., Finite element analysis of evaporative cutting with a moving high energy pulsed laser. *Appl. Math Model.*, 2001, **25**(3), 203–220.
59. Modest, M. F. and Abakian, H., Heat conduction in a moving semi-infinite solid subjected to pulsed laser irradiation. *ASME J. Heat Transfer*, 1986, **108**, 602–607.
60. Abakian, H. and Modest, M. F., Evaporative cutting of a semi-transparent body with a moving CW laser. *ASME J. Heat Transfer*, 1988, **110**, 924–930.
61. Modest, M., Laser machining of ablating/decomposing materials through cutting and drilling models. *J. Laser Appl.*, 1997, **9**, 137–145.
62. Samant, A. N. and Dahotre, N. B., Ab initio physical analysis of single dimensional laser machining of silicon nitride. *Adv. Eng. Mater.*, 2008, **10**, 978–981.
63. Samant, A. N. and Dahotre, N. B., Computational predictions in single dimensional laser machining of alumina. *Int. J. Mach. Tools Manuf.*, 2008, **48**, 1345–1353.
64. Samant, A. N. and Dahotre, N. B., Differences in physical phenomena governing laser machining of structural ceramics. *Ceram. Int.*, in press, corrected proof, doi:10.1016/j.ceramint.2008.11.013.

65. Samant, A. N. and Dahotre, N. B., An integrated computational approach to single dimensional laser machining of magnesia. *Opt. Lasers Eng.*, in press, corrected proof, doi:10.1016/j.optlaseng.2008.10.001.
66. Samant, A. N., Daniel, C., Chand, R. H., Blue, C. A. and Dahotre, N. B., Computational approach to photonic drilling of silicon carbide. *Int. J. Adv. Manuf. Technol.*, under review.
67. Semak, V. V., Knorovsky, G. A., MacCallum, D. O. and Roach, R. A., Effect of surface tension on melt pool dynamics during laser pulse interaction. *J. Phys. D: Appl. Phys.*, 2006, **39**, 590–595.
68. Semak, V. V., Knorovsky, G. A. and MacCallum, D. O., On the possibility of microwelding with laser beams. *J. Phys. D: Appl. Phys.*, 2003, **36**, 2170–2174.
69. Anisimov, S. I., Vaporization of metal absorbing laser radiation. *Sov. Phys. JETP*, 1968, **27**, 182–183.
70. Tönshoff, H. K. and Kappel, H., Surface modification of ceramics by laser machining. *CIRP Ann. – Manuf Technol.*, 1998, **47**(1), 471–474.
71. Tönshoff, H. K., Hesse, D. and Gonschior, M., Microstructuring with excimer lasers and reduction of deposited ablation products using a special gas nozzle with a vacuum system. In *Proceedings of ICALEO*, 1994, pp. 333–342.
72. Islam, M. U., An overview of research in the fields of laser surface modification and laser machining at the Integrated Manufacturing Technologies Institute, NRC. *Adv. Perform. Mater.*, 1996, **3**, 215–238.
73. Lunde, L. D., Ogeret, C., Jadin, A. and Kolev, K., Excimer laser ablation of Y SiAlON. *Appl. Surf. Sci.*, 1998, **127–129**, 848–851.
74. Sciti, D. and Bellosi, A., Laser-induced surface drilling of silicon carbide. *Appl. Surf. Sci.*, 2001, **180**, 92–101.
75. Dubey, A. K. and Yadava, V., Optimization of kerf quality during pulsed laser cutting of aluminium alloy sheet. *J. Mater. Process. Technol.*, 2008, **204**(1–3), 412–418.
76. Tsai, C. H. and Chen, H. W., Laser cutting of thick ceramic substrates by controlled fracture technique. *J. Mater. Process. Technol.*, 2003, **136**(1–3), 166–173.
77. Liu, J. S., Li, L. J. and Jin, X. Z., Accuracy control of three-dimensional Nd:YAG laser shaping by ablation. *Opt. Laser Technol.*, 1999, **31**, 419–423.
78. Perrie, W., Rushton, A., Gill, M., Fox, P. and O'Neill, W., Femtosecond laser micro-structuring of alumina ceramic. *Appl. Surf. Sci.*, 2005, **248**(1–4), 213–217.
79. Longfellow, J., High speed drilling in alumina substrates with a CO_2 laser. *Am. Ceram. Soc. Bull.*, 1971, **50**(3), 251–253.
80. Saifi, M. A. and Bonetta, R., Optimization of pulsed CO_2 laser parameters for Al_2O_3 scribing. *Ceram. Bull.*, 1975, **54**, 986–989.
81. Ananthapadmanabhan, P. V., Thiyagarajan, T. K., Sreekumar, K. P. and Venkatramani, N., Formation of nano-sized alumina by in-flight oxidation of aluminium powder in a thermal plasma reactor. *Scr. Mater.*, 2004, **50**(1), 143–147.
82. Wagner, R. E., Laser drilling mechanics. *J. Appl. Phys.*, 1974, **45**(10), 4631–4637.
83. Coherent, Inc., *Lasers-Operation, Equipment, Application, and Design*, McGraw Hill, New York, 1980.
84. Chryssolouris, G. and Bredt, J., Machining of ceramics using a laser lathe. In *Proceedings of Intersociety Symp. on Machining of Adv. Ceram. Mater. and Components*, ed. R. E. Barks, K. Subramanian, and K. E. Ball, Pittsburgh, PA, 1987, pp. 70–72.
85. Hamann, C. and Rosen, H., Laser machining of ceramic and silicon. *Industrial Laser Annual Handbook*. Penwell Pub., Tulsa, OK, 1986.
86. Tönshoff, H. K. and Emmelmann, E., *Laser Processing of Ceramics*. International Power Beam Conference, San Diego, CA, 1988.
87. Tönshoff, H. K. and Semau, H., Laser beam machining in new fields of application. In *Conference on Research and Technology Development in Non-Traditional Machining*, 1988.
88. Tönshoff, H. K., Butje, R., Konig, W. and Trasser, F. J., Excimer laser in material processing. *Ann. CIRP*, 1988, **37**(2), 681–684.
89. Tönshoff, H. K. and Emmelmann, E., Laser cutting of advanced ceramics. *Ann. CIRP*, 1989, **38**(1), 219–222.
90. Guo, D., Cai, K., Yang, J. and Huang, Y., Spatter-free laser drilling of alumina ceramics based on gelcasting technology. *J. Eur. Ceram. Soc.*, 2003, **23**(8), 1263–1267.
91. Glaw, V., Hahn, R., Paredes, A., Hein, U., Ehrmann, O. and Reichl, H., Laser machining of ceramics and silicon for MCM-D applications. In *Proceedings of the 3rd International Symposium on Adv. Packaging Mater.*, 1997, pp. 173–176.
92. Sciti, D., Melandri, C. and Bellosi, A., Excimer laser-induced microstructural changes of alumina and silicon carbide. *J. Mater. Sci.*, 2000, **35**, 3799–3810.
93. Wang, C. and Zeng, X., Study of laser carving three-dimensional structures on ceramics: quality controlling and mechanisms. *Opt. Laser Technol.*, 2007, **39**(7), 1400–1405.
94. Kelly, A. and Macmillan, N. H., *Strong Solids*. Oxford University Press, New York, 1986.
95. Wachtman, J. B., *Mechanical Properties of Ceramics*. John Wiley & Sons, New York, 1996.
96. Harrysson, R. and Herbertsson, H., Machining of high performance ceramics and thermal etching of glass by laser. In *Proceedings of the 4th International Conference on Lasers in Manufacturing*, 1987, pp. 211–219.
97. Murray, J. P., Flamant, G. and Roos, C. J., Silicon and solar-grade silicon production by solar dissociation of Si_3N_4. *Sol. Energy*, 2006, **80**(10), 1349–1354.
98. Copley, S. M., Laser shaping of materials. In *Proceedings of ASM Conference on Lasers in Materials Processing*, 1983, pp. 82–92.
99. Copley, S. M., Shaping ceramics with lasers. *Interdisciplinary Issues Mater. Process. Manuf.*, 1987, 631.
100. Miyamoto, I. and Maruo, H., Processing of ceramics by excimer lasers. *SPIE-Laser Assist. Process. II*, 1990, **1279**, 66.
101. Shigematsu, I., Kanayama, K., Tange, A. and Nakamura, M., Analysis of constituents generated with laser machining of Si_3N_4 and SiC. *J. Mater. Sci. Lett.*, 1998, **17**, 737–739.
102. Yamamoto, J. and Yamamoto, Y., Laser machining of silicon nitride. In *Proceedings of LAMP' 87*, 1987, p. 297.
103. Firestone, R. F. and Vesely Jr., E. J., High power laser beam machining of structural ceramics. In *Proceedings of the ASME Symposium on Machining of Adv. Ceram. Mater. & Components*, 1988, pp. 215–227.
104. Lavrinovich, A. V., Kryl, Y. A., Androsov, I. M. and Artemyuk, S. A., Effect of dimensional laser machining on the structure and properties of silicon nitride. *Powder Metall. Met. Ceram.*, 1990, **29**(4), 328–332.
105. Pham, D. T., Dimov, S. S. and Petkov, P. V., Laser milling of ceramic components. *Int. J. Mach. Tools Manuf.*, 2007, **47**(3–4), 618–626.
106. Polk, D. H., Banas, C. M., Frye, R. W. and Gregonz, R. A., Laser processing of materials. *Ind. Heat Exchangers*, 1986, 357–364.
107. Affolter, P. and Schmid, H. G., Processing of new ceramic materials with solid state laser radiation. *SPIE-High Power Lasers Ind. Appl.*, 1987, **801**, 120–129.
108. Copley, S., Bass, M., Jan, B. and Wallace, R., Shaping materials with lasers. *Laser Mater. Proc.*, 1983, 297–336.
109. Lumpp, K., Excimer laser machining and metallization of vias in aluminium nitride. *Mater. Sci. Eng., B*, 1997, **45**(1–3), 208–212.
110. Gilbert, T., Krstic, V. D. and Zak, G., Machining of aluminium nitride with ultra-violet and near-infrared Nd:YAG lasers. *J. Mater. Process. Technol.*, 2007, **189**(1–3), 409–417.
111. Liang, X. Y. and Dutta, S. P., Application trend in advanced ceramic technologies. *Technovation*, 2001, **21**, 61–65.
112. Yabe, T., Mohamed, M. S., Uchida, S., Baasandash, C., Sato, Y., Tsuji, M. and Mori, Y., Noncatalytic dissociation of MgO by laser pulses towards sustainable energy cycle. *J. Appl. Phys.*, 2007, **101**, 123106–1-7, doi:10.1063/1.2743730.
113. Brewer, L. and Porter, R. F., A thermodynamic and spectroscopic study of gaseous magnesium oxide. *J. Chem. Phys.*, 1954, **22**, 1867–1877.
114. Weimin, Z., Yong, S., Haipeng, L. and Chunyong, L., The effects of some elements on the igniting temperature of magnesium alloys. *Mater. Sci. Eng.: B*, 2006, **127**(2–3), 105–107.
115. Massalski, T. B., Okamoto, H., Subramanian, P. R. and Kacprzak, L., *Binary Alloy Phase Diagrams*. ASM International, Materials Park, OH, 1990.
116. Bhushan, B. and Gupta, B. K., *Handbook of Tribology (Materials, Coatings and Surface Treatments)*. Mc Graw Hill, New York, 1991.

117. Singh, R., Alberts, M. J. and Melkote, S. N., Characterization and prediction of the heat-affected zone in a laser-assisted mechanical micromachining process. *Int. J. Mach. Tools Manuf.*, 2008, **48**(9), 994–1004.

118. Oliveira, V., Vilar, R., Conde, O. and Freitas, P., Laser micromachining of Al_2O_3 – TiC ceramic. *J. Mater. Res.*, 1997, **12**(12), 3206–3209.

119. Oliveira, V., Simoes, F. and Vilar, R., Column-growth mechanisms during KrF laser micromachining of Al_2O_3–TiC ceramics. *Appl. Phys. A*, 2005, **81**, 1157–1162.

120. Chen, T. C. and Darling, R. B., Laser micromachining of the materials using in microfluidics by high precision pulsed near and mid-ultraviolet Nd:YAG lasers. *J. Mater. Process. Technol.*, 2008, **98**, 248–253.

ADVANCED ENGINEERING MATERIALS

COMMUNICATION

DOI: 10.1002/adem.200900056

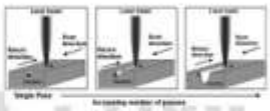

Physical Effects of Multipass Two-Dimensional Laser Machining of Structural Ceramics

*A. N. Samant, N. B. Dahotre**

Effect of multiple laser passes on cavities machined in structural ceramics is presented. Multiple laser passes machined cavities with reduced thermal stresses and cracks. Thermal model based on temperature dependent absorptivity and thermophysical properties along with defocusing of laser beam, multiple track induced preheating effect, and heat transfer was developed to incorporate effect of multiple passes on machined cavity. Predicted and experimentally measured values of physical attributes showed decent match.

ADV. ENG. MATER. 2009, 00 1–7

DOI: 10.1002/adem.200900056

Physical Effects of Multipass Two-Dimensional Laser Machining of Structural Ceramics**

By Anoop N. Samant and Narendra B. Dahotre*

High hardness and thermal stability, low electrical conductivity along with high wear resistance have made structural ceramics such as alumina (Al_2O_3), silicon nitride (Si_3N_4), silicon carbide (SiC), and magnesia (MgO) useful for several applications in aerospace, automotive, and semiconductor industries.[1–4] Laser machining is one of the promising machining techniques because of several advantages such as reduced manufacturing costs, automation, and efficient material utilization. Even though, in two-dimensional laser machining, desired depth of cavity in a given ceramic can be attained by a single pass of the laser beam with different processing conditions (varying scanning speed, repetition rate, frequency, energy), scanning ceramic surface with multiple laser passes with appropriate parameters is, however, likely to machine the ceramic for the same dimensions with minimal thermal stresses and cracking. To the authors' knowledge, there is a paucity of work reported in open literature that identify physical processes and their effects on two-dimensional laser machining of ceramics. In light of this, various physical effects that stir up during this process such as phase transition, variation of thermophysical properties and absorptivity with temperature, preheating due to multiple tracks, defocusing of laser beam with increased machined depth, and heat transfer via the three basic modes (conduction, convection, and radiation) were incorporated into a thermal model considered in the present work.

This model is capable of predicting machining attributes such as depth and width of cavity generated in a ceramic after exposure to multiple passes of the laser beam under a given set of processing conditions. Values of these attributes estimated from computational model were in turn compared with actual measurements from the micrographs. Such study is expected to assist in advance predictions of machining features (depth and width) and save considerable amount of energy and time.

[*] Dr. A. N. Samant, Prof. N. B. Dahotre
[Q2] Please check title
Laboratory for Laser Materials Synthesis and Fabrication
Department of Materials Science and Engineering
The University of Tennessee, Knoxville, TN 37996, USA
E-mail: ndahotre@utk.edu

[**] The authors acknowledge the financial support under NSF CMMI-0825240 grant.

Experimental

Dense Al_2O_3, Si_3N_4, SiC, and MgO coupons (25.4 mm × 25.4 mm × 4.5 mm) were exposed to a 1.06 μm wavelength JK 701 pulsed Nd:YAG laser. Initially, a 15-mm long cavity was machined by scanning the surface with a single pass of the laser beam at repetition rate of 20 Hz, pulse energy of 4 J, pulse width of 0.5 ms, and scanning speed of 5 in min^{-1} (2.11 mm s^{-1}) with air as cover gas at a pressure of 80 psi (5.5 bar). This was followed by exposing the cavity to different number of laser passes (3, 5, and 7 passes for Al_2O_3, 2, 3, and 4 passes for Si_3N_4, 2, 3, and 5 passes for SiC, and 3, 4, and 5 passes for MgO) under the same set of machining parameters as that employed for single cavity machining in order to study effect of multiple passes on dimensions of depth and width of machined cavity with minimal thermal stresses. However, evaluation of thermal stress is not the part of present study and will be presented in future publication. For every subsequent pass, the laser beam was again brought to same position from where the preceding cavity was started. A CNC program developed in FlashCut CNC[76] was used to facilitate repeated to and from motion of laser beam.

The laser beam was delivered by a fiber optic system and a 120-mm focal length convex lens so that a defocused spot diameter of roughly 0.5 mm was generated on the surface at the beginning of first pass. The focusing lens configuration provided a uniform beam distribution, in temporal and spatial evolution and it was assumed that the energy was evenly distributed across the pulse. Using a lens of longer focal length and longer focal waist reduced the tapering effect. Although, in the present study, the scanning speed, *S* of 5 in min^{-1} (2.11 mm s^{-1}) was chosen based on prior experience, the approach adopted in the study can be extended to any desirable processing speed. A schematic of effect of multiple pass laser processing on depth and width evolution of cavity on the surface of a ceramic is represented in Figure 1.

The laser beam starts processing from point A for every pass and one pass is complete when the laser reaches point B. Then, the laser is switched off and no processing is done when the laser returns back with the same scanning speed from point B to point A. It is observed that machined depth and width increases with increase in number of passes. The physical phenomena responsible for this trend will be discussed in detail in later part of this study. Although, the number of passes chosen for different ceramics were based on prior experience and for the purpose to demonstrate feasibility of the approach in predicting the dimensions of

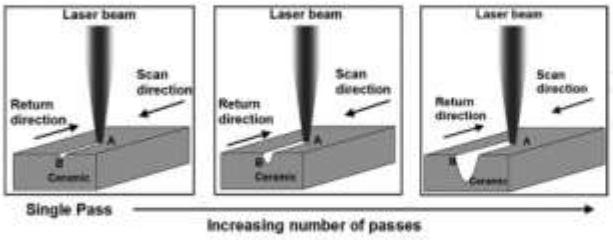

Fig. 1. Schematic illustrating the effect of multiple passes on the depth and width of machined cavity.

machined cavity, the approach can be extended to machining a cavity of desired dimensions and corresponding number of passes in any ceramic.

Three coupons of each ceramic were machined under these laser conditions with three cavities machined in each coupon by different number of passes in random sequence (e.g., in alumina, 3, 5, 7 passes in first coupon followed by 3, 7, 5 passes in second and then 7, 5, 3 passes in the third coupon). Machining several cavities on different coupons in the same sequence of multiple passes would have caused lurking variables such as surrounding temperature and relative humidity to affect machined depth and width. This course of action incorporated randomization, which is one of the basic principles of any statistical design of experiments.[5] The machined cavities were then cross-sectioned to measure depth and width using ImageJ.[TM] software (Fig. 2).

Cavities machined in some ceramics for a certain number of passes (3 and 5 passes in SiC and for 4 and 5 passes in MgO) were a little asymmetric around the bottom tip of the cavity and a portion of the cavity also chipped off from33 top. This cracking can be attributed to thermal stresses generated in some of these brittle ceramics under certain set of laser machining parameters. In light of this, as seen in Figure 2, in order to determine actual width of these cavities, their profile was reconstructed by assuming symmetry around the marked centerline and corresponding width was reported. Attempts are ongoing to minimize cracks generated during machining of these ceramics and they will be presented in the future. On the other hand, cavities in Al_2O_3 and Si_3N_4 did not experience thermal stress cracking under the present machining conditions. The depth and width of cavities for different number of passes are marked in Figure 2 and also listed in Table 1 along with the scatter in measured data.

As schematically illustrated in Figure 1 earlier, for all ceramics, the machined depth increased with increase in number of passes as each pass removed material by absorbing

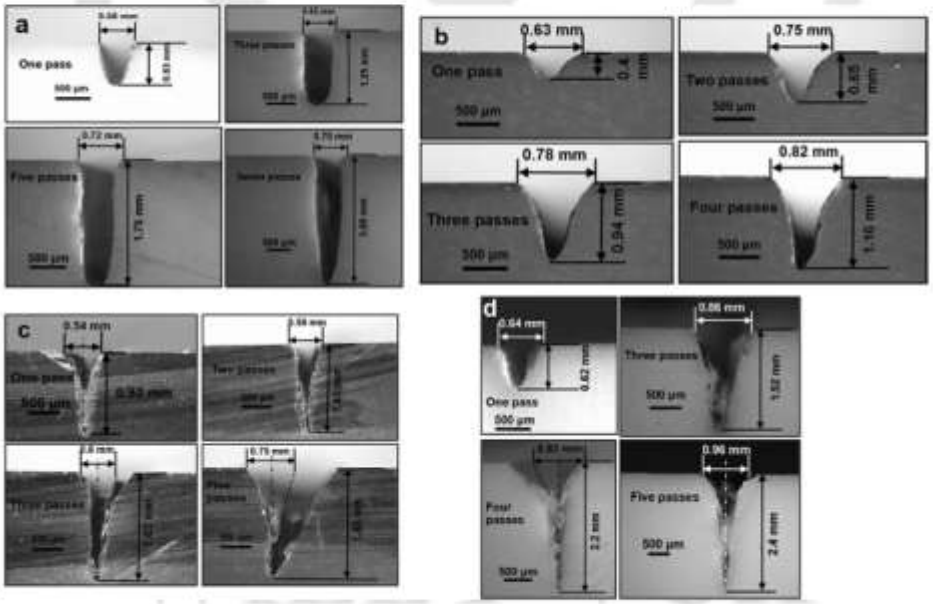

Fig. 2. Cross-sectional views of cavities machined in (a) Al_2O_3, (b) Si_3N_4, (c) SiC, and (d) MgO for different number of passes.

Table 1. Measured and predicted attributes of machined cavity (depth and width) for different number of passes in all ceramics.

Ceramic	Number of passes	$Depth_{measured}$ [mm]	$Depth_{predicted}$ [mm]	$Width_{measured}$ [mm]	$Width_{predicted}$ [mm]
Al_2O_3	1	0.63 ± 0.034	0.63	0.56 ± 0.060	0.60
	3	1.25 ± 0.015	1.70	0.62 ± 0.080	0.70
	5	1.75 ± 0.021	2.69	0.72 ± 0.046	0.77
	7	2.62 ± 0.030	3.59	0.75 ± 0.067	0.82
Si_3N_4	1	0.4 ± 0.011	0.40	0.63 ± 0.10	0.57
	2	0.65 ± 0.020	0.69	0.75 ± 0.07	0.66
	3	0.94 ± 0.015	0.92	0.78 ± 0.05	0.69
	4	1.16 ± 0.005	1.27	0.82 ± 0.07	0.72
SiC	1	0.92 ± 0.005	0.92	0.54 ± 0.040	0.61
	2	1.43 ± 0.010	1.75	0.52 ± 0.066	0.66
	3	1.62 ± 0.040	2.65	0.60 ± 0.033	0.70
	5	1.85 ± 0.025	3.40	0.75 ± 0.120	0.77
MgO	1	0.62 ± 0.011	0.62	0.64 ± 0.002	0.59
	3	1.52 ± 0.060	1.50	0.86 ± 0.025	0.70
	4	2.20 ± 0.030	1.89	0.93 ± 0.074	0.74
	5	2.40 ± 0.045	2.27	0.96 ± 0.150	0.78

energy and added to the total machined depth. Furthermore, as discussed later, the laser beam became defocused with the evolution of machined cavity and diameter of beam on the bottom surface of the cavity at the end of a given pass (assumed to be equal to the width of cavity) increased with multiple passes as also presented in Figure 1.[6]

In separate experiments, absorptivity values were determined for these ceramics in low temperature range (700–1150 K) using thermocouple-based techniques under similar laser processing conditions.[7] The details associated with these measurements are presented in the reference. Following this, attempts were also made to develop a model in COMSOL's[TM] heat transfer mode for predicting absorptivity transitions at high temperatures (>1150 K) in two-dimensional laser machining by a single pass of the laser beam.[8] The present study extends this work in single pass machining[7,8] to machining by multiple laser passes with incorporation of additional effects such as defocusing of laser beam and preheating of ceramic surface as discussed in next section. As physical phenomena occurring during laser machining by a single laser pass have been elaborately described by Samant and Dahotre elsewhere,[8] this study only briefly covers the same in anticipation of changes in machined cavity when ceramic surface is exposed to multiple scans.

As the laser beam interacts with the surface during the first pass, a major portion is absorbed while the remaining fraction is transmitted, scattered, refracted, and reflected. However, 100% of incident energy cannot be absorbed because of reflection or transmission from the open kerf as laser beam moves along a cutting front.[9] Even though ceramic is initially at room temperature (300 K), absorption of energy raises temperature and the temperature evolution is governed by time of exposure of the surface to laser beam (residence time, t_{res})[10] given by:

$$\text{Residence time} = \frac{\text{Repetition rate} \times \text{Pulse width} \times \text{Beam diameter}}{\text{Scanning speed}} \quad (1)$$

The energy input to the material being machined depends on residence time and this input energy also affects the temperature evolution. Hence, the residence time was input to the model along with peak power density per unit cross-sectional area given by:

$$\text{Peak power density} = \frac{\text{Incident energy}}{\text{Pulse width} \times \text{Area of incident beam}} \quad (2)$$

Giving this peak power density as an input to the model along with residence time for which it was incident on the surface implemented the control of residence time on energy input. As stated earlier, a beam distribution in both temporal and spatial evolution being uniform, under the processing conditions used in this study, the residence time was 2.36 ms and peak power density was 4.07×10^6 W cm^{-2} for the first pass and corresponding to a beam diameter of 0.5 mm at the surface. In this study, the laser beam is considered as a quasi-stationary heat source with the coordinate system translating with it. Thus the effect of a moving laser beam was equivalent to that of a stationary beam interacting with surface for a time equal to residence time.[11–13] The absorbed energy is converted into heat which then conducts according to Fourier's heat transfer law and simultaneously radiates from surface and convects from the bottom surface of ceramic.[14–16] All these effects and corresponding equations have been built into a computational model for prediction of temperature rise. The details of the model adopted in the present study have been elaborately discussed elsewhere by Samant and Dahotre.[8]

Laser machining being an extremely rapid process, the thermophysical properties change rapidly over a large range of temperature. For improved accuracy in calculations, these properties and laser beam (1.06 μm wavelength) absorptivity were included as a function of temperature. Within the low temperature range until the first phase transition temperature (melting/sublimation/dissociation) absorptivity of the ceramics considered in the present study tends to decrease with

increasing temperature due to the intraband absorption.[7] However, above first phase transition temperature, absorptivities of these ceramics increase with increase in temperature due to physical entrapment of the beam and its multiple reflections within the machined cavity.[8] The material removal mechanisms (MRMs) during laser based machining of the ceramic are influenced by various physical processes. These MRMs are extensively discussed by Samant and Dahotre[9] and briefly explained in the following section for the ceramics (Al_2O_3, Si_3N_4, SiC, and MgO). Single pass machining (20 Hz, 0.5 ms, 4 J and 2.11 mm s^{-1}) was considered in the present study as it is the precursor for multiple pass machining.

Single Pass Machining

Material removal in alumina takes place by a combination of melting, dissociation, and evaporation.[17–20] In light of this, absorptivity drops to $a_1 = 0.041$ at 1165 K[9] for which corresponding surface temperature (T_{surf}) at end of residence time (t_{res}) is melting point (MP) of alumina (2327 K)[17] and material is removed by melting and expulsion of melt. Following this, absorptivity increases to $a_2 = 0.05$[9] so that surface temperature is the dissociation/vaporization temperature (VT) (3250 K)[17,7] and vaporization causes machining. Finally, absorptivity jumps to $a_3 = 0.32$ and remains constant at this value till a depth of 0.63 mm was machined in 2.36 ms (residence time predicted above) by vaporization.[9] The final absorptivity of 0.32 was obtained by tracking highest phase change temperature (VT) during iteration of the thermal model[9] to the depth that matched the depth from the cross-sections in Figure 2 (corresponding to processing by a single laser pass). Similar procedure was applied for all ceramics mentioned below and this caused predicted depth to be equal to measured depth as seen later.

Combination of melting, dissociation, and evaporation are governing MRMs in Si_3N_4.[13,19,21] Due to similar reasons mentioned above for alumina, absorptivity first decreases to $a_1 = 0.031$ at 1723 K[7] to attain melting/sublimation point of Si_3N_4 (2173 K)[22] at end of residence time and material is removed by melting and dissociation into liquid silicon and its expulsion. The absorptivity then increases to $a_2 = 0.07$ so that boiling point of silicon (3514 K)[23] is reached and vaporization of silicon leads to machining.[9] Further increase in absorptivity to $a_3 = 0.19$ machines a depth of 0.4 mm in 2.36 ms.[9]

Melting, dissociation, and evaporation are also the MRMs in SiC.[13,19] Accordingly, absorptivity drops to $a_1 = 0.054$ at 1473 K[9] so that surface temperature at end of residence time is melting/decomposition temperature of SiC (3103 K)[22] and melting/expulsion of silicon removes material. Silicon vapor governs machining when absorptivity increases to $a_2 = 0.07$ and depth of 0.92 mm is machined in 2.36 ms when absorptivity further increases to $a_3 = 0.79$.[9]

At high temperatures attained in laser machining, dissociation followed by evaporation is responsible for material removal in magnesia.[13,19,24] Hence, absorptivity first decreases to $a_2 = 0.06$ at 1263 K and temperature on surface reaches vaporization/decomposition temperature of magnesia (3123 K[22]). A depth of 0.62 mm is machined in 2.36 ms as absorptivity rises to $a_3 = 0.25$.[9]

Multiple Pass Machining

In multiple pass machining, the laser first interacts with ceramic surface for time equivalent to residence time (Eq. 1) for laying first track on the surface. Then the laser is switched off and it returns back to starting point (point A in Fig. 1) for laying next track by again moving till the end of the track (point B in Fig. 1). This to and fro motion is controlled by the CNC program. As seen later, the total time taken by the beam to come back to the starting point (from the instant it starts laying the preceding track) to lay the next track is summation of time for machining a single track (t_{res}) and time for which laser is switched off during return (t_{cut}). The heat transfer phenomena, associated MRMs (melting, dissociation, vaporization based on the type of ceramic) and absorptivity transitions mentioned above for Al_2O_3, Si_3N_4, SiC, and MgO occur during each laser pass on that ceramic and can be implemented for every pass by using the model developed earlier by Samant and Dahotre for single pass low aspect ratio machining.[9] In addition, few additional effects such as beam defocusing and surface preheating play a role in multiple pass machining and will be incorporated in the existing model as discussed in next section. It should be noted that a certain depth of cavity achieved by multiple laser passes can also be attained by a single laser pass with large energy input. However, as the high energy single laser pass would induce large thermal stresses and cracking of ceramic as mentioned above, multiple laser passes are preferred for machining deeper cavities.

Laser Beam Defocusing

As the machined cavity evolves with successive passes, the beam gets defocused on the bottom surface of each cavity with increase in machined depth[6] and does not remain of the same size as it was at the beginning of that pass, d_{start}. The diameter at the end of a pass, d_{end} ($< d_{start}$) is given by:[6]

$$d_{end} = d_{start}\left[1 + \left(\frac{4\lambda(z_t + \delta_f)}{\pi d_{start}^2}\right)^2\right]^{1/2} \quad (3)$$

where λ is the laser wavelength (1.06 μm), δ_f is the focal length (120 mm), z_t is the predicted depth of cavity at the end of that pass. As mentioned earlier, width of cavity and beam diameter at the bottom of the cavity in the end of a given pass, d_{end} were assumed to be same and the successive pass was processed with d_{end}. The diameter of beam at beginning of first pass was adjusted to 0.5 mm as an out of focus beam diameter on the surface. The diameter of the beam, d_{end} predicted by Equation (3) above for each (i^{th}) pass was used to predict the residence time and peak power density for the next [$(i+1)^{th}$] pass using Equations (1) and (2), respectively. These values were constantly updated at the end of each pass and were input for consecutive passes. Thus defocusing of the beam reduced

the peak power density input to the system and increased the residence time for successive passes.

Preheating Effect

A series of pulses are incident on the ceramic surface when one complete track is machined. The total number of pulses required to machine a cavity of given length, L (15 mm in this case) was given by dividing the length of machined cavity by beam diameter for that pass (d_{eff}). As each pulse is active for residence time (2.36 ms), the total on time for the laser (t_{on}) was given by multiplying the total number of pulses by residence time. As mentioned earlier, the laser is switched off after machining a track and the time it takes to come back to machine the next track (t_{off}) was obtained by dividing the length of cavity, L by return speed [same as scanning speed, S (2.11 mm s^{-1}) in this study]. The total time it takes for laser beam to come back to starting point is summation of t_{on} and t_{off}. Thus, after i^{th} pass, laser beam comes back to starting point (point A in Fig. 1) for the next $(i+1)^{th}$ pass in a time, $t_{cooling}$ given by:

$$t_{cooling} = t_{on} + t_{off} = \frac{L \times t_{on}}{d_{eff}} + \frac{L}{S} \quad (4)$$

The temperature at the start of this $(i+1)^{th}$ pass is temperature of staring point of i^{th} pass (point A in Fig. 1) at time equal to $t_{cooling}$. This temperature was noted from the cooling curve of i^{th} pass at time = $t_{cooling}$ and input as an initial temperature for $i+1^{th}$ pass.

Computations were then carried out by using this initial temperature along with residence time and peak power density updated above after considering a defocused laser beam (Eqs. 1 and 2). The depth machined by each laser pass

Fig. 3. Flowchart for predicting depth and width of machined cavity after multiple laser passes.

was predicted by tracking maximum phase transition temperature for different ceramics as described by Samant and Dahotre earlier.[18] Once the depth was estimated, the corresponding width of cavity was also predicted by determining the changed diameter of laser beam, d_{mod} and considering it to be equal to the cavity width as mentioned above (Eq. 3). The final depth at the end of multiple passes was the summation of depths machined after individual passes.

Thus the region where the $i+1^{th}$ track will be machined is preheated by earlier i^{th} track and temperature at beginning of a pass (except for the first one) is greater than room temperature (300 K) due to this preheating effect. The temperature at the beginning of first pass was assumed to be equal to room temperature. This preheating facilitates machining of deeper cavities for the same input energy as surface is already heated prior to next interaction with laser thereby saving the energy utilized in further raising surface temperature. Incorporation of laser beam defocusing and preheating effect into computations is illustrated in a flow chart in Figure 3.

Considering experimentally determined absorptivity values for low temperatures (700–1150 K)[17] followed by transitions in absorptivity at higher temperatures (>1150 K)[18] and incorporating beam defocusing and surface preheating effects mentioned above, the total predicted depth machined for different number of passes on all ceramics and corresponding predicted width are listed in Table 1. Furthermore, a comparison between predicted and measured depth and width of cavity has also been made in Figures 4 and 5, respectively.

The measured and predicted depth machined by a single laser pass on all ceramics (Fig. 4) showed a perfect match because of the procedure mentioned above in determining final absorptivity required to machine a certain depth in a single pass.[18] For other passes, some deviation in values (depth and/or width) can be attributed to limitations of method employed in measuring machined parameters from optical micrographs using ImageJ^{TM} software as mentioned

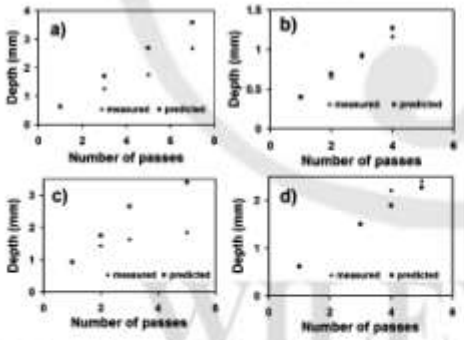

Fig. 4. Comparison between predicted and measured depth of cavity in (a) Al_2O_3, (b) Si_3N_4, (c) SiC, and (d) MgO for different number of passes.

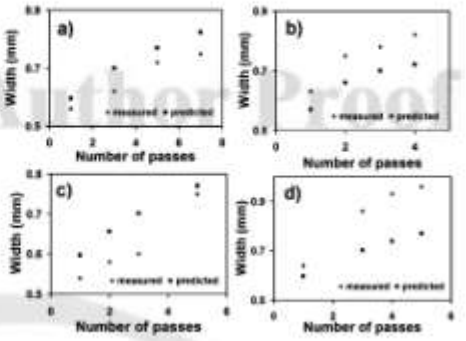

Fig. 5. Comparison between predicted and measured width of cavity in (a) Al_2O_3, (b) Si_3N_4, (c) SiC, and (d) MgO for different number of passes.

above. It should be noted that even though physical phenomena occurring in every laser pass are same, the depth machined at the end of each pass was different (Table 1 and Fig. 4). As discussed above, a defocused beam reduces energy input to the system while on the contrary, preheating saves energy by removing more material for same input energy. Thus, the depth machined by any laser pass is governed by the resultant of these two counter effects. Furthermore, in addition to heat transfer, preheating, transition in absorptivity, and beam defocusing, there could be some other phenomena that are unknown at this time and not considered in this study may affect cavity dimensions (depth and width). Identification and incorporation of these physical processes in computational predictions will be dealt with in future. In general, this study enables in advance prediction of the laser processing parameters and number of passes required for machining desired depth in any ceramic.

Conclusions

An integrated multilevel approach to laser machining of structural ceramics, Al_2O_3, Si_3N_4, SiC, and MgO by multiple laser passes has been successfully developed. Multiple laser passes was able to machine the ceramic with reduced thermal stresses and cracking of ceramic. Cavities were machined with depths varying from 0.63 to 2.68 mm (for number of passes varying from 1 to 7) in Al_2O_3 and from 0.4 to 1.16 mm (for variation in number of passes from 1 to 4) in Si_3N_4. Corresponding widths varied from 0.56 to 0.75 mm in Al_2O_3 and from 0.63 to 0.82 mm Si_3N_4. On the other hand, cavities 0.9–1.85 mm (for variation from 1 to 5 passes) and 0.62–2.4 mm (for variation from 1 to 5 passes) deep were machined in SiC and MgO, respectively. Widths of these cavities varied from 0.54 to 0.75 mm in SiC and from 0.64 to 0.96 mm in MgO. For processing conditions employed in this study, the cavities in Al_2O_3 and Si_3N_4 machined by multiple passes were clean (without any material deposition within the

cavity) and symmetrical compared to those produced in SiC and MgO. Physical phenomena such as heat transfer by all modes (conduction, convection, and radiation), variation of thermophysical properties and absorptivity with temperature, absorptivity transitions above phase change temperature, defocusing of laser beam and preheating of surface due to multiple passes were incorporated. For successive passes, a defocused beam reduced the effective input energy while preheating assisted in removing more material for the same input energy. Such a study would make the machining process more efficient as a desired depth and width of cavity can be obtained by multiple passes under same set of laser parameters with induction of minimal thermal stress that are very critical for machining brittle ceramics.

Received: February 10, 2009
Final Version: March 3, 2009
Published online: XX XX XX

[1] A. J. Pyzik, D. F. Carroll, *Annu. Rev. Mater. Sci.* 1994, *24*, 189.
[2] A. Kelly, N. H. Macmillan, *Strong Solids*, Oxford University Press, New York 1986.
[3] J. B. Wachtman, *Mechanical Properties of Ceramics*, John Wiley & Sons, New York 1996.
[4] I. P. Tuersley, A. Jawaid, I. R. Pashby, *J. Mater. Process. Technol.* 1994, *42*, 377.
[5] D. C. Montgomery, *Design and Analysis of Experiments*, Wiley, New York 1997.
[6] K. Salonitis, A. Stournaras, G. Tsoukantas, P. Stavropoulos, G. Chryssolouris, *J. Mater. Process. Technol.* 2007, *183*, 96.
[7] A. N. Samant, N. B. Dahotre, *J. Appl. Phys.* 2008, under review■Please update■.
[8] A. N. Samant, N. B. Dahotre, *Int. J. Appl. Ceram. Technol.* 2008, under review■Please update■.
[9] J. F. Ready, *LIA Handbook of Laser Materials Processing*, Magnolia Publishing/Springer, Berlin 2002.
[10] A. N. Samant, S. P. Harimkar, N. B. Dahotre, *J. Appl. Phys.* 2007, *102*, 123105.
[11] J. Ahlström, B. Karlsson, S. Niederhauser, *J. Phys. IV France* 2004, *210*, 405.
[12] N. Arnold, R. Kullmer, D. Bäuerle, *Microelectron. Eng.* 1998, *20*, 31.
[13] R. Patwa, Y. C. Shin, *Int. J. Mach. Tools. Manuf.* 2007, *47*, 307.
[14] S. P. Harimkar, A. N. Samant, N. B. Dahotre, *J. Appl. Phys.* 2007, *101*, DOI: 054911. ■Please provide the page number■
[15] S. Z. Shuja, B. S. Yilbas, *Appl. Surf. Sci.* 2000, *167*, 134.
[16] B. S. Yilbas, S. B. Mansoor, *J. Phys. D: Appl. Phys.* 2006, *39*, 3863.
[17] P. V. Ananthapadmanabhan, T. K. Thiyagarajan, K. P. Sreekumar, N. Venkatramani, *Sci. Mater.* 2004, *50*, 143.
[18] A. N. Samant, N. B. Dahotre, *Ceram. Int.* in press ■Please update■ corrected proof, doi:10.1016/j.ceramint.2008.11.013.
[19] A. N. Samant, N. B. Dahotre, *J. Eur. Ceram. Soc.* 2009, *29*, 969.
[20] A. N. Samant, N. B. Dahotre, *Int. J. Mach. Tools Manuf.* 2008, *48*, 1345.
[21] A. N. Samant, N. B. Dahotre, *Adv. Eng. Mater.* 2008, *10*, 978.
[22] B. Bhushan, B. K. Gupta, *Handbook of Tribology (Materials, Coatings and Surface Treatments)*, Mc Graw Hill, New York 1991.
[23] C. L. Yaws, *Chemical Properties Handbook*, Mc Graw Hill, New York 1991.
[24] A. N. Samant, N. B. Dahotre, *Opt. Lasers Eng.* 2009, *47*, 570.

Q1: Please clarify throughout the article all editorial/technical requests marked by black boxes.

WILEY InterScience®
Early View publication on www.interscience.wiley.com
(issue and page numbers not yet assigned; citable using Digital Object Identifier – DOI)

Phys. Status Solidi A, 1–7 (2009) / DOI 10.1002/pssa.200925108

physica status solidi a
applications and materials science

In-situ surface absorptivity prediction during 1.06 μm wavelength laser low aspect ratio machining of structural ceramics

Anoop N. Samant[1], Baoshuai Du[1, 2], and Narendra B. Dahotre*[, 1]

[1] Laboratory for Laser Materials Synthesis and Fabrication, Department of Materials Science and Engineering, University of Tennessee, Knoxville, TN, 37996, USA
[2] Current address: School of Materials Science and Engineering, Shandong University, Jinan 250061, P.R. China

Received 4 March 2009, revised 1 April 2009, accepted 21 April 2009
Published online ■■

PACS 81.05.Je, 81.20.Wk

* Corresponding author: e-mail ndahotre@utk.edu, Phone: 865-974-3609, Fax: 865-974-4115

This study predicts the variation of surface absorptivity with temperature for structural ceramics such as magnesia (MgO), alumina (Al_2O_3), silicon nitride (Si_3N_4), and silicon carbide (SiC). In-situ temperatures reached during pulsed 1.06 μm Nd:YAG laser low aspect ratio cavity machining of the ceramics under various number of pulses were sensed by a K-type thermocouple. A thermal model was calibrated by varying the absorptivity to match the computed temperature to that with the measured temperature in the ranges of 860–980 K (MgO), 1020–1120 K (Al_2O_3), 900–1150 K (Si_3N_4), and 700–950 K (SiC) at a given distance from center of the laser beam. Such absorptivity predictions are critical for accurate predictions of suitable machining parameters and in determining actual energy absorbed during low aspect ratio laser machining of structural ceramics.

1 Introduction Chemical stability, high thermal resistance and hardness have made structural ceramics such as alumina (Al_2O_3), magnesia (MgO), silicon nitride (Si_3N_4) and silicon carbide (SiC) popular in electronic, medical and automotive fields [1]. Valves, medical implants, machine tool inserts, heat resistant packings and substrate in hybrid circuits are made from Al_2O_3. On the other hand, Si_3N_4 is extensively machined for making cams, bearings and piston rings. SiC is being widely used for high power, high frequency and high temperature applications while thermocouple housings and brake linings are made from MgO. Hard and brittle nature of these ceramics pose a serious problem in using traditional methods based on mechanical grinding and fracturing for machining them. Laser machining has emerged as one of the promising techniques due to its low production costs, automation, efficient material utilization and contact less processing [2–5].

Reflection, absorption, and transmission are the different physical phenomena that take place when the laser beam interacts with the surface of the material (ceramic). In general, part of the irradiated beam will be reflected away, a fraction will be absorbed and the rest will be transmitted through the workpiece. Significant of all these effects is absorption which is an interaction of the electromagnetic radiation with electrons of the material and it depends on the wavelength of laser used for processing, spectral absorptivity characteristics of the ceramic being machined, surface roughness, orientation of the material surface with respect to beam direction and temperature attained during processing [2, 6]. Absorptivity, a is defined as ratio of absorbed part of incoming radiation to total incoming radiation and it varies between the values 0 and 1 [7]. The amount of energy absorbed by the ceramic surface governs the temperature evolution and it is high enough to cause material removal at surface and sub surface region. The ensuing effects such as machined depth, machining time and energy required for machining a certain depth will be governed by this temperature evolution. Thus the energy absorbed by the surface decides if machining is likely to take place. In light of this, in order to efficiently predict these effects and hence corresponding machining parameters, it is critical to determine variation of absorp-

2091336 physica 206/7 WordXP Art.: W25108/Samant V:\p_2\pha\pha20607_25108-vm3\pha25108u.doc
&R610; ingesamt 7 Seiten Diskette 15.05.2009 Bearb.: Weishaar

tivity with temperature during laser processing. To the best of authors' knowledge, except for LIA Handbook of Laser Materials Processing [7], there is paucity of the data in open literature representing the variation of absorptivity with temperature for structural ceramics processed at a given wavelength. This study, therefore, aims at predicting the absorptivity of commonly used structural ceramics such as Al_2O_3, MgO, Si_3N_4, and SiC as a function of temperature by measuring in-situ machining temperatures with the aid of thermocouples and correlating them with temperatures predicted from a thermal model as described later. Furthermore, the energy absorbed at the surface is maximum and it decays because of several phenomena as it propagates through the bulk of the material. In certain ceramics which have a multi-crystalline nature, the incident energy will be multiply scattered inside the material and this would affect the variation of absorptivity with depth. However, laser processing being an extremely rapid process (interaction time of the order of a few ms), it is extremely difficult to determine decay of absorptivity in bulk material. Prediction of absorptivity decay (drop in absorptivity per unit length) is not a focus of this study and will be covered in future publications.

In this study, the temperatures were measured for the workpiece machined with low aspect ratio (depth to width <1) because for cavities with high aspect ratios (>1), multiple beam reflections along the cavity wall affect the amount of absorbed energy [8, 9] and the absorptivity rapidly changes to 1. Moreover, thermal conductivity of ceramics generally being less than majority of metals, the portion of absorbed incident energy builds up rapidly to raise the temperature within surface and subsurface regions for machining of ceramics via various physical processes such as melting, dissociation/decomposition and vaporization [10, 11]. Also, due to phase change (solid-liquid transformation above melting point or liquid-vapor/solid-vapor transformation above vaporization/dissociation temperature of ceramic), the absorptivity rapidly increases and entire incident energy is instantaneously absorbed by the ceramic. Hence, although the absorptivity was predicted for low aspect ratio machining of the ceramic, the respective values can be very useful for estimating absorbed energy and corresponding machining parameters in the initial stages of any machining where there is no phase change which is often followed by high aspect ratio machining where absorptivity of 1 can be assumed for the incident energy. It should be noted in this study that even though the workpiece was assumed to be multi-crystalline and not a single crystal, the complex phenomenon of scattering (reflections) at the several interfaces was not incorporated and will be implemented in due course of time.

2 Experimental Coupons of dimensions 5 mm × 5 mm × 8 mm were made from dense Al_2O_3, MgO, Si_3N_4 and SiC. In order to sense the temperature rise during laser interaction, a K-type thermocouple was glued to the coupons using a high temperature ceramic adhesive (Cerama-bond™ 516 from Aremco Products, Inc) followed by curing at 373 K for one hour. K-type thermocouple is a nickel based alloy composed of chromel (90 wt% Ni and 10 wt% Cr) and alumel (95 wt% Ni, 2 wt% Mn, 2 wt% Al, and 1 wt% Si) with capability to sense temperatures as high as 1623 K [12]. The thermocouple was calibrated using a temperature-controlled furnace. The temperature recorded by the thermocouple for a preset temperature of the furnace is presented in Fig. 1. The linear fit law ($T_{actual} = 0.9768\ T_{thermocouple} + 10.241$) was used to convert the measured temperature into actual temperature. Slope of linear fit (0.9768) was close to 1 and these set of temperature values differed only maximum of 2% from each other.

JK 701 pulsed Nd:YAG laser (1.06 μm wavelength) was used to machine the ceramic coupon with a low aspect ratio (<1) cavity during thermocouple based temperature measurement by applying different number of pulses (400 pulses to 700 pulses) with pulse width of 2.0 ms, repetition rate of 20 Hz, and pulse energy of 4 J corresponding to an average power, Q of 80 W (repetition rate (20 Hz) × pulse energy (4 J)). Three temperatures were recorded for each set of pulses to minimize errors. The number of pulses were applied in a random sequence (500, 700, 600, 400 followed by 700, 400, 500, 600 and then 400, 600, 500, 700 pulses). Absorptivity was predicted for each case using the procedure elaborated later. If several runs had been performed with the same sequence of the number of pulses, then lurking variables such as surrounding temperature and relative humidity could affect maximum temperatures reached and the predicted absorptivity. In this manner, randomization, which is one of the basic principles of any statistical design of experiments, was implemented in the present study [13]. The laser beam was defocused on the surface and pulses were applied as close as possible to the thermocouple tip to minimize losses of heat to the surrounding environment and enable effective sensing of the maximum temperatures attained during machining. A very small fraction of the incident energy is scattered towards the thermocouple tip and magnitude of energy directly absorbed by the tip is extremely small. Hence no significant

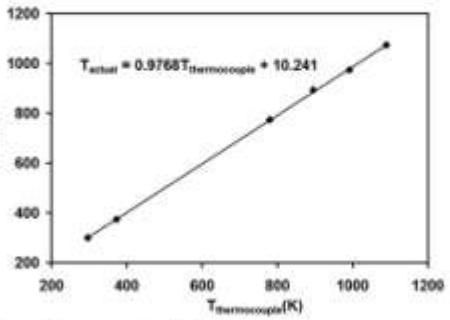

Figure 1 Thermocouple calibration.

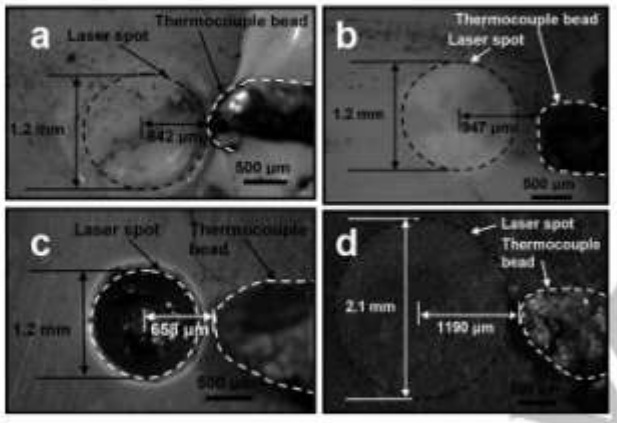

Figure 2 Top views of thermocouple glued to the ceramic surface in a) Al_2O_3, b) MgO, c) Si_3N_4, and d) SiC.

temperature rise can be caused due to scattering and subsequent direct absorption of incident energy by thermocouple tip at the surface. The out of focus beam diameter, d and distance between the center of the laser beam and the thermocouple tip, r were measured from the top views of the machined ceramic coupons (Fig. 2). These values are represented in Table 1 along with densities (kg/m^3) of different ceramics and will be used for thermal calculations discussed later [14]. As the laser beam was positioned near the thermocouple by mere visual observation and judgement, the distance r between the center of the laser beam and the thermocouple tip was not the same for all ceramics.

Furthermore, a surface becomes more absorptive (less reflective) as the roughness increases because the incident laser beam may undergo multiple reflections off local peaks and valleys (resulting in increased absorption) before leaving the surface of workpiece into an off-specular direction [7]. Thus, as surface roughness affects absorptivity of the ceramic, it was measured for all ceramics using a Mahr Federal Perthometer (Model M1) with a tip scan distance of 5.6 mm and these values have also been represented in Table 1. The absorptivities predicted later were corresponding to these roughness values and they may change significantly with roughness. As long as surface roughness is less than beam wavelength (1.06 μm), the incident beam will not suffer multiple reflections as mentioned above and the surface will be considered to be flat [15]. However, for higher roughness values, the effect of surface roughness on absorptivity could be a very complex phenomena and absorptivity could differ by more than an order of magnitude depending on magnitude of surface roughness. The effect of change of surface roughness on absorptivity is not the focus of this study and will be presented in the future.

The laser beam was defocused on the surface of ceramic to achieve the formation of low aspect ratio (<1) machined cavity. In case of Al_2O_3, MgO, and Si_3N_4 such defocused beam diameter that raised the surface temperature sufficiently high was 1.2 mm whereas it was 2.1 mm for SiC due to its inherently high absorption characteristic for 1.06 μm wavelength laser beam [7]. The in-situ machining temperatures were recorded using LabVIEW (La-

Table 1 Physical parameters corresponding to experimental conditions and ceramics used in computational model.

ceramic	out of focus beam diameter d (mm)	distance of thermocouple tip from laser beam center r (μm)	surface Roughness R_a (μm)	density ρ (kg/m^3) [14]
Al_2O_3	1.2	842	0.913 ± 0.15	3800
MgO	1.2	947	0.527 ± 0.12	3580
Si_3N_4	1.2	658	0.249 ± 0.10	2370
SiC	2.1	1190	0.283 ± 0.03	3100

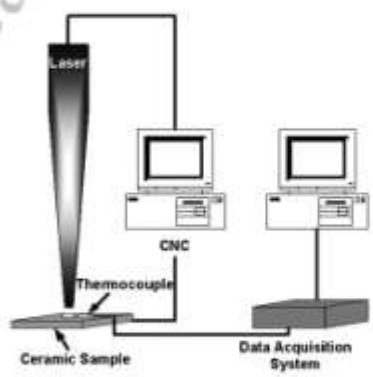

Figure 3 Setup for temperature measurement using thermocouple.

boratory Virtual Instrument Engineering Workbench), a commercially available package for data acquisition and visualization [16]. A schematic of the entire setup used for temperature measurement is represented in Fig. 3. The maximum temperature measured by the thermocouple at the surface for each ceramic was used as a benchmark for predicting temperatures using a thermal model [17] and iteration method [18] described in the next section. Similar approach can be extended for bulk absorptivity determination by inserting the thermocouple at different depths and then iterating the model discussed below to predict absorptivity as function of depth. However, the present study assumes a constant absorptivity through the bulk of material and only considers variation of absorptivity at the surface as function of temperature.

3 Thermal Model During laser machining, the ceramic surface absorbs a part of incident energy and this affects the temperature distribution and machining parameters. In light of this, a model based on Fourier's second law of heat transfer in COMSOL's [TM] heat transfer transient mode was used for predicting the temporal evolution:

$$\frac{\partial T(x,y,z,t)}{\partial t} = \frac{k(T)}{\rho C_p(T)} \times \left[\frac{\partial^2 T(x,t)}{\partial x^2} + \frac{\partial^2 T(y,t)}{\partial y^2} + \frac{\partial^2 T(z,t)}{\partial z^2}\right], \quad (1)$$

where $C_p(T)$ and $k(T)$ are variations in specific heat and thermal conductivity as a function of temperature, ρ is density (Table 1), T is temperature field, t is time and x, y, and z are spatial directions. In order to improve accuracy of calculations, variation of thermophysical properties such as specific heat and thermal conductivity were considered as a function of temperature [14] and are represented in Fig. 4 for different ceramics considered in this study. The latent heat term was accounted for by incorporating the variation of specific heat as a function of temperature.

At time $t = 0$, the initial temperature was assumed to be $T = T_0 = 300$ K. The balance between the absorbed laser energy at the surface and the radiation losses was given by:

$$-k(T)\left(\frac{\partial T(x,y,0,t)}{\partial x} + \frac{\partial T(x,y,0,t)}{\partial y} + \frac{\partial T(x,y,0,t)}{\partial z}\right) = \frac{A\delta\alpha Q}{\pi d^2} - \varepsilon\sigma(T(x,y,0,t)^4 - T_0^4)$$

$$\delta = 1 \quad \text{if} \quad 0 \le t \le t_{on}$$

$$\delta = 0 \quad \text{if} \quad t > t_{on}, \quad (2)$$

where $k(T)$ is temperature dependent thermal conductivity of the ceramic, α is absorptivity which will be predicted later and it is the same as ε (emissivity for thermal radiation) for a given material and processing condition [19], Q is incident average power (80 W), d is diameter of defo-

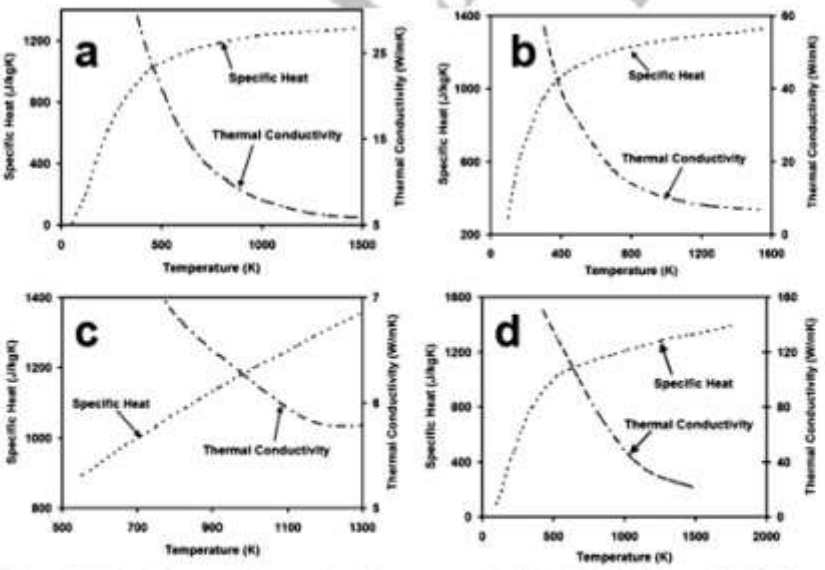

Figure 4 Variation of thermophysical properties with temperature of a) Al_2O_3, b) MgO, c) Si_3N_4, and d) SiC [14].

cused laser beam on the surface (measured from Fig. 2 and represented in Table 1), t_{on} is total time for which pulses were applied (number of pulses/frequency = 20, 25, 30 and 35 seconds for 400, 500, 600 and 700 pulses, respectively), and σ is Stefan–Boltzman constant (5.67×10^{-8} W/m^2 K^4). The term δ takes a value of 1 when t is less than t_{on} and it is 0 when t exceeds t_{on}. Thus the value of δ depends on time and it ensures that energy is input to the system only when pulses are being applied on the ceramic. Even though a pulsed laser was used in this study, it was assumed that drop in temperature during the pulse OFF-time was negligible for these ceramics as also seen by Samant et. al. [20–24] and Salonitis et. al. [25] and it did not have any significant effect on the temperature profile.

Sufficiently thick samples (5 mm thick) were used in this study and convection losses from the bottom surface of these coupons could be neglected by assuming them to be a semi-infinite body. However, similar to Shuja and Yilbas [26], in order to improve accuracy of calculations, convection taking place only at the bottom surface of the ceramic coupon was considered:

$$-k(T)\left(\frac{\partial T(x,y,H,t)}{\partial x}+\frac{\partial T(x,y,H,t)}{\partial y}+\frac{\partial T(x,y,H,t)}{\partial z}\right) = h(T(x,y,H,t)-T_0), \quad (3)$$

where H is thickness of coupon (5 mm) and h is heat transfer coefficient (W/m^2 K) which was included as a function of temperature [27]. Furthermore, convection losses (either from upper or bottom surface of the coupon) are negligible and do not have a significant effect on surface temperature [26, 28, 29] and hence effect of convection from the upper surface was neglected. The value of a (absorptivity) was iterated in the above set of (Eqs. (1) to (3) to obtain a solution for the maximum predicted surface temperature at distance r from the laser beam center that matched the temperature measured by the thermocouple at the same distance for any given number of pulses [18]. The absorptivity for the maximum surface temperature corresponding to a particular number of pulses was thus obtained (Table 2) and is further discussed in the following section. These predicted absorptivity values govern the temperature evolution which can be tracked for melting/dissociation/evaporation based material removal (machining) which has been elaborately discussed elsewhere by Samant and Dahotre [30, 31].

Table 2 Computed values of absorptivity corresponding to experimentally measured temperature for all ceramics.

ceramic	number of pulses	T average (K)	absorptivity
Al_2O_3	400	1039	0.25 ± 0.002
	500	1051	0.19 ± 0.001
	600	1086	0.17 ± 0.001
	700	1102	0.15 ± 0.001
MgO	400	866	0.32 ± 0.007
	500	912	0.26 ± 0.002
	600	938	0.23 ± 0.003
	700	965	0.20 ± 0.002
Si_3N_4	400	927	0.34 ± 0.020
	500	1039	0.30 ± 0.004
	600	1105	0.29 ± 0.003
	700	1136	0.25 ± 0.001
SiC	400	735	0.85 ± 0.022
	500	787	0.72 ± 0.031
	600	847	0.71 ± 0.018
	700	914	0.66 ± 0.006

4 Absorptivity The variation of absorptivity of different ceramics with temperature is represented in Fig. 5. As mentioned above, three temperature measurements were made for each set of pulses and corresponding absorptivity was predicted. The average maximum surface temperature for each case along with standard deviation in absorptivity is presented in Table 2. For all the ceramics, it was seen that there was no significant variation in absorptivity predicted for the different readings corresponding to a given number of pulses. This ensured that the temperature measurements for the processing conditions used in this study were repeatable. The absorptivity of SiC was the highest of all the structural ceramics considered in this study (varying from 0.66 to 0.85 with change in temperature from 914 K to 735 K). This high absorptivity of SiC, as mentioned earlier, made it essential for the beam on the surface to defocus more (2.5 mm diameter) compared to that for Al_2O_3, MgO, and Si_3N_4 (1.2 mm diameter) without creating a cavity of high aspect ratio (>1).

Contrary to many established notions, a very interesting fact was observed that for the 1.06 μm wavelength of

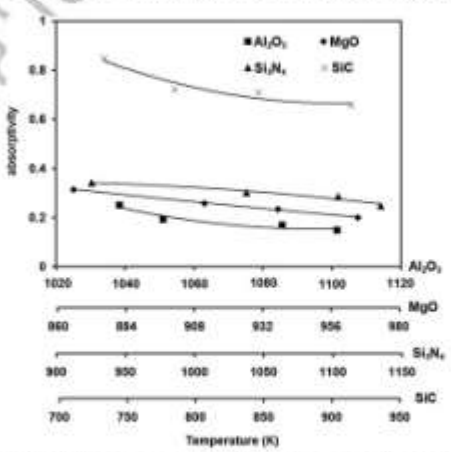

Figure 5 Variation of absorptivity with temperature for different ceramics.

laser beam used in this study, absorptivity of all structural ceramics decreased with increase in temperature as also noticed by Riethof et. al in some other ceramics [32]. In reality, there is a wavelength for which the absorptivity is constant with temperature and this wavelength is termed as X-point beyond which an opposite trend is observed and absorptivity increases with rise in temperature [33]. However, machining the ceramics at a wavelength greater than 1.06 μm for observing the trend in absorptivity variation and predicting X-point is not a part of this study and will be dealt in future publications. As discussed next, the mechanism of energy absorption depends on the wavelength of processing energy (laser beam) and it governs the trend observed in variation of absorptivity with temperature.

The free carrier absorption mechanism (intraband absorption) plays a dominant role in energy absorption in ceramics in the short wavelength range while in the long wavelength range (>10 μm), photons contribute to absorptivity changes (interband absorption) [34, 35]. In any solid (ceramics), free carriers/electrons are relegated to bands that are separated from each other by energy gaps. Incompletely filled bands are termed conduction bands while the full bands are valence bands [36]. In intraband absorption, the free carriers are transferred to higher energy levels in the same band (conduction or valence) by absorption of incident radiation and this mechanism is dominant for absorption of radiations with frequencies lower than those which give rise to interband transitions [37]. Decrease in half-width of absorption band of free carriers with increase in temperature at short wavelength leads to a drop in absorptivity. Furthermore, due to the increase in vibrations of free carriers with temperature, the mean free path also increases for short wavelength of incident energy [38]. This reduces the associated scattering of the laser beam and hence the absorptivity.

On the other hand, in interband absorption observed at longer wavelengths of processing, the electron jumps from the band at lower energy to the one above it by absorbing a photon [37, 39]. The conservation of energy for the interband transition is given by:

$$E_f = E_i + \hbar\omega, \tag{4}$$

where E_i is energy of the electron in the lower band, E_f is energy of the final state in the upper band, and $\hbar\omega$ is the photon energy. The number of photons increases with temperature and this causes more number of electrons to transit from lower to higher energy band and an increase in absorptivity with temperature is observed. This is also in accordance with the Hagen-Rubens relationship which postulates that absorptivity is proportional to $1/\sqrt{\sigma_{dc}}$ where σ_{dc} is electrical conductivity of the material which is approximately inversely proportional to the temperature. Thus, the absorptivity is proportional to the square root of absolute temperature for longer wavelengths, and an increase in absorptivity with temperature is observed [7]. The absorptivities of Al_2O_3, MgO, Si_3N_4 and SiC for room temperature at the wavelength of CO_2 laser (10.6 μm) were 0.9 to 0.99, 0.93 to 0.98, 0.9 and 0.8 to 0.9 respectively [7].

It can be seen from this study that the mechanism of absorption of energy depends on the wavelength of processing laser beam. Laser machining is a thermal process and different machining parameters such as machining time, depth of machined cavity, and number of pulses are heavily dependent on the temperature evolution which is a function of the absorbed energy. Below the phase change temperatures (melting/vaporization/sublimation/dissociation temperature depending on the type of ceramic) and for low aspect ratio cavity machining, the absorbed energy can be calculated using the predicted absorptivity values (Table 2 and Fig. 5). Above this temperature and high aspect ratio cavity machining, 100% of the incident energy can be assumed to be absorbed ($a = 1$) by the ceramic on account of multiple reflections and low thermal conductivity. Such a study would assist in better designing of the laser machining process.

5 Conclusion Variation of absorptivity with temperature during low aspect ratio (<1) machining of structural ceramics such as Al_2O_3, MgO, Si_3N_4, and SiC were successfully predicted by measuring in-situ surface temperatures by thermocouples and then calibrating a thermal model against this measured temperature. Similar approach could also be extended to determine the absorptivity at the surface or the bulk of other structural ceramics or materials (metals, polymers, composites or inter-metallic compounds). Intraband absorption was the cause for drop in absorptivity with increasing temperature for short wavelength while the opposite trend of rise in absorptivity with increase in temperature at long wavelength (>10 μm) could be attributed to interband absorption. SiC had the highest absorptivity of all the ceramics considered in this study (0.85 at a temperature of 735 K). On the other hand, for the observed range of temperatures, it was seen that maximum absorptivity for Al_2O_3, MgO, and Si_3N_4 were 0.25 at 1039 K, 0.32 at 866 K, and 0.34 at 927 K, respectively. Having an insight into the absorptivity variation and their governing mechanism for different materials would assist in controlling the laser machining process more efficiently.

Acknowledgements Authors acknowledge financial support from the National Science Foundation (NSF-CMMI-0825244).

References

[1] I. P. Tuersley, A. Jawaid, and I. R. Pashby, J. Mater. Process. Technol. 42(4), 377 (1994).
[2] G. Chryssolouris, Laser Machining: Theory and Practice (Springer-Verlag, New York, 1991).
[3] K. Salonitis, P. Stavropoulos, A. Stournaras, and G. Chryssolouris, in: Proceedings of the 5th Laser Assisted Net Shape Engineering (Erlangen, Germany, 2007), pp. 825–835.
[4] P. Stavropoulos, K. Salonitis, A. Stournaras, K. Euthimiou, and G. Chryssolouris, in: Proceedings of the 10th CIRP In-

national Workshop on Modeling of Machining Operations (Calabria, Italy, 2007), pp. 549–553.
[5] A. Stournaras, K. Salonitis, P. Stavropoulos, and G. Chryssolouris, in: Proceedings of the 10th CIRP International Workshop on Modeling of Machining Operations (Calabria, Italy, 2007), pp. 563–570.
[6] M. U. Islam and G. Campbell, Mater. Manuf. Process. **8**(6), 611 (1993).
[7] J. F Ready, LIA Handbook of Laser Materials Processing (Magnolia Publishing, Inc., Orlando, 2002).
[8] H. Ki, P. S. Mohanty, and J. Mazumder, J. Laser Appl. **14**, 39 (2002).
[9] S. Y. Bang and M. F. Modest, J. Heat Transfer **113**, 663 (1991).
[10] J. G. Andrews and D. R. Atthey, J. Phys. D, Appl. Phys. **9**, 2181 (1976).
[11] J. Mazumdar and W. M. Steen, J. Appl. Phys. **51**, DOI: 10.1063/1.327672 (1980).
[12] D. R. Buttsworth, Exp. Therm. Fluid Sci. **25**, 409 (2001).
[13] D. C. Montgomery, Design and analysis of experiments (Wiley, New York, 1997).
[14] Y. S. Touloukian, Thermophysical Properties of High Temperature Materials (IFI/Plenum, New York, 1967).
[15] W. M. Steen, Laser Material Processing (Springer, New York, 2003).
[16] K. D. Kim and Rizwan-uddin, Nucl. Eng. Des. **237**, 1185 (2007).
[17] A. N. Samant, S. P. Harimkar, and N. B. Dahotre, J. Appl. Phys. **102**, 123105 (2007).
[18] R. Singh, M. J. Alberts, and S. M. Melkote, Int. J. Mach. Tools Manuf. **48**, 994 (2008).
[19] M. D. Sturge, Statistical and Thermal Physics, Fundamentals and Applications (A. K. Peters Ltd., Natick, MA, 2003).
[20] A. N. Samant and N. B. Dahotre, Int. J. Mach. Tools Manuf. **48**, 1345 (2008).
[21] A. N. Samant and N. B. Dahotre, Adv. Eng. Mater. **10**, 978 (2008).
[22] A. N. Samant and N. B. Dahotre, Opt. Lasers Eng. **47**, 570 (2009).
[23] A. N. Samant and N. B. Dahotre, Ceram. Int. in press, DOI:10.1016/j.ceramint.2008.11.013.
[24] A. N. Samant, C. Daniel, R. H. Chand, C. A. Blue, and N. B. Dahotre, Int. J. Adv. Manuf. Technol., in press (2009).
[25] K. Salonitis, A. Stournaras , G. Tsoukantas, P. Stavropoulos, and G. Chryssolouris, J. Mater. Process. Technol. **183**, 96 (2007).
[26] S. Z. Shuja and B. S. Yilbas, Appl. Surf. Sci. **167**, 134 (2000).
[27] F. P. Incropera and D. P. Dewitt, Fundamentals of Heat and Mass Transfer (Wiley, New York, 2002).
[28] M. F. Modest, J. Laser Appl. **9**, 137 (1997).
[29] M. F. Modest and H. Abakians, J. Heat Transfer **108**, 602 (1986).
[30] A. N. Samant, N. B. Dahotre, Adv. Eng. Mater., in press.
[31] A. N. Samant, N. B. Dahotre, Int. J. Appl. Ceram. Technol., under review.
[32] T. R. Riethof, and V. J. DeSantis, Measurement of Thermal Radiation Properties of Solids, edited by J. C. Richmond (National Aeronautics and Space Administration, Washington, D.C., 1963).
[33] D. J. Price, Proc. Phys. Soc. **59**, 131 (1947).
[34] N. M. Ravindra, S. Abedrabbo, W. Chen, F. M. Tong, A. K. Nanda, and A. C. Speranza, IEEE Trans. Semicond. Manuf. **11**, 30 (1998).
[35] N. M. Ravindra, F. M. Tong, S. Abedrabbo, W. Chen, W. Schmidt, A. Nanda, T. Speranza, and A. M. Tello, in: Proceedings of Fourth Int. Conf. Rapid Thermal Processing (Boise, ID, 1996), pp. 190–204.
[36] M. W. Barsoum, Fundamentals of Ceramics (Institute of Physics Publishing, Philadelphia, PA, 1997).
[37] C. C. Wu, J. Tsai, and C. J. Lin, Phys. Rev. B **43**, 7328 (1991).
[38] W. D. Kingery, H. K. Bowen, and D. R. Uhlmann, Introduction to Ceramics (Wiley & Sons, New York, 1976).
[39] M. Fox, Optical Properties of Solids (Oxford University Press Inc., New York, 2001).

Appl. Phys. A 90, 493–499 (2008)
DOI: 10.1007/s00339-007-4311-3

Applied Physics A
Materials Science & Processing

A.N. SAMANT
N.B. DAHOTRE✉

Multilevel residual stress evaluation in laser surface modified alumina ceramic

Department of Materials Science and Engineering, The University of Tennessee, Knoxville, TN 37996, USA

Received: 6 August 2007 / Accepted: 21 September 2007
Published online: 31 October 2007 •

ABSTRACT The type and extent of residual stresses within laser surface modified alumina ceramic were investigated. Macro stresses were predicted with the help of the OOF2 simulation package, developed at the National Institute of Standards and Technology. The software utilizes a meshing technique to discretize the surface microstructure into a mesh suitable for finite-element analysis, which leads to stress determination. Micro stresses were estimated by the prediction of full width at half-maximum of the peaks from the X-ray diffraction patterns of processed samples. Under the present set of laser processing parameters, the ceramic was devoid of any major cracks, making it ideal for several applications. This study provides a tool for rapid evaluation and hence for controlling the stresses through tailoring the laser process parameters to suit a particular application.

PACS 61.30.Hn; 81.40.-z; 81.05.Je; 79.20.Ds

1 Introduction

Lasers became a significant material processing tool since the 1960s, following which a lot of theoretical and experimental work has been done to inspect the laser heating of materials and the corresponding generated residual stresses [1]. Residual stresses are the internal stresses which become evenly balanced by themselves and exist in a free body that has no external forces or constraints acting on its boundary. They are mainly formed in laser surface treatments due to the extreme temperature difference between the surface and the bulk of the material [2]. Energy absorption from a laser causes very high temperatures to be reached over a very short period of time. As there is rapid movement of heated material against the restriction of colder and deforming surrounding material, thermal stresses are produced [3]. Residual stresses have a significant effect on the material properties such as fatigue strength, anti-stress corrosion, and dimensional stability, which may affect the lifetime of the material [4].

The capability of foreseeing and controlling these thermal stresses is vital in laser processing as very high thermal/residual stresses may lead to surface and subsurface cracking of a component, thus affecting its performance. This is catastrophic, especially for brittle ceramics such as alumina. They may also cause strain interference and excessive deformation of the components [5, 6]. Residual stresses are produced mainly during the solidification stage of the melt and they can prove to be either unfavorable or advantageous to performance. If the shrinkage of the melt pool is more than the expansion effects generated by other phase transformations, tensile residual stresses predominate and the surface may crack if these exceed the fracture stress [7]. On the other hand, generation of compressive residual stresses due to a thermal expansion, often due to phase transformation at the cooling stage, can be used for several advantageous applications one of which could be the ceramic tile grout sealing process which has been pioneered by Lawrence et al. [8–10]. This sealing procedure using high power diode lasers (HPDLs) facilitates the easy cleaning of tile grouts and thus prevents future contamination. Thermal stress predictions by using finite-element techniques in laser processing, which lead to melting/resolidifying of the processed materials, gained significant importance since the 1990s [6, 11–13]. These predictions will help to establish guidelines for appropriate beam parameters and thus finally achieve the desired material properties.

Based on the length scale, the stresses can be classified into three types. Macro stresses remain homogeneous over a large number of grains and equilibrium of forces is assumed over a large number of crystals. The second type of stress remains homogeneous within one grain and the forces are assumed to be in balance among adjoining grains. Finally, the third type is homogeneous over some interatomic distances and the internal forces remain in equilibrium around crystalline defects. The second and the third types of stresses mentioned above together form the micro stresses [7].

As mentioned above, macro stresses are global and extend over a large number of grains. These stresses are strongly associated with macroscopic structures such as grain size, grain shape, grain boundary area, porosity, cracks, and several other features. In the present investigation, attempts are made to predict the state of residual stress in correlation with the microstructural features (porosity and grain/crystallite size) in laser-irradiated alumina ceramic under various input energies. The approach of finite-element modeling of real microstruc-

✉ Fax: +1-865-974-4115, E-mail: ndahotre@utk.edu

tures, which was developed at the National Institute of Standards and Technology (NIST) in the form of a package named as 'OOF2' (object-oriented finite-element analysis), was used in the macro stress analysis [14]. This software tool has been used in a variety of microstructural level analyses [15–19]. OOF2 is a software that does not predict microstructures but rather uses microstructures of the processed samples and predicts the stresses from them by performing a finite-element analysis on the micrograph.

Conventional X-ray diffraction (XRD) techniques can also be employed to predict the residual stresses, as done by Kadolkar et al. [2]. However, this method involves a tedious and careful sample preparation procedure which becomes even more cumbersome for a ceramic due to its extremely hard surface. Collection of stress data using the XRD technique involves scanning of the sample over a wide range of angles with very small increments in angle. In addition to the procedural difference, there are also some other differences in the measurement of stress by using OOF2 and XRD. Deeper depths of the order of 1 μm to 5 μm can be probed by the XRD technique, while OOF2 is confined to the surface only. There is no limitation on the surface area to be considered by the OOF2 method, as OOF2 takes into account surface microstructural features. Such fundamental differences may provide different values for macro stresses evaluated by using the XRD and OOF2 techniques. Furthermore, some differences between the X-ray and finite-element predictions could be due to variations between the actual material properties and those prescribed in the model. Although the objective of the present work was to rapidly determine surface macro stresses, efforts are also ongoing to compare these stresses with that determined using the conventional XRD technique and will be reported in a future publication.

OOF2 software was preferred over the conventional method as it uses already obtained micrographs for its analysis, hence leading to easy determination of the stress state. Equivalent to the procedure of taking several scans over the surface by the XRD technique for stress determination, micrographs of several regions on the surface were taken and the ones that were representative for that particular fluence condition were used for the stress analysis by the OOF2 software. As the software uses micrographs for its analysis, the effect of all the microscopic features (porosity and grain/crystallite size) mentioned above that affect the stress values will automatically be taken into account. These microstructural features are either directly or indirectly linked to many other features such as melt depth and volume that are not considered in the present work. Such additional features are also expected to influence the state of residual stress.

There is a significant difference between the grains affecting the macro stresses and the crystallites governing the micro stress formation. A part of the specimen which diffracts the X-ray beam coherently is referred to as a coherently diffracting domain. Crystallite size is nothing but this coherent diffraction domain in the material, whereas the grains are always larger than crystallites and are formed by several of them. Crystallite size is usually predicted by X-ray diffraction methods, while the grain size can be approximated by other characterization methods like scanning electron microscopy (SEM), transmission electron microscopy (TEM), or atomic force microscopy (AFM) [20]. Microscopic stresses which are treated as scale properties of the material are generated due to imperfections in the crystal lattice. These stresses evolve due to disparity in strain between the crystallites surrounded by dislocation tangles within the grains, acting over a distance less than the dimensions of the crystals [4]. Estimation of micro stresses helps to determine a material's residual life. Micro stresses vary from point to point within the crystals, generating a range of lattice spacing and broadening of the diffraction peak. Hence, in this approach, the micro stresses were determined by predicting the peak broadening or the full width at half-maximum (FWHM) from the observed XRD data.

As the mechanical properties of the material are associated with crystallinity, orientation, macro stresses, dimension of the crystallite, lattice distortion, and micro stresses, it is necessary to look at the macro as well as the micro stresses generated in a material due to processing. As mentioned above, as several crystallites form a grain, both macro and micro residual stresses are related. Hence, a combined study of both is vital and has been carried out in this study. The sign and magnitude of these stresses depend on the type of the material and on the parameters of the applied processing technology. The nature of these stresses affects the functionality of the component. Compressive stresses foster the fatigue limit and improve wear resistance, while tensile stresses decrease fatigue strength and destroy the surfaces [21].

2 Laser surface processing

A 4 kW HAAS continuous-wave Nd:YAG (1.06-μm wavelength) laser with fiber optically delivered beam was used to irradiate the surface of alumina ceramic compacts which were obtained from a commercial source (MSC Industrial Supply Co., Melville, NY). Laser fluences in the range of 459–611 J cm^{-2} were used to modify the surface of a 2.5-cm-thick and flat ceramic compact of area 5 × 5 cm^2. The effects of laser irradiation on the ceramic surface were observed by taking micrographs of the irradiated surface. A Hitachi S3500 SEM was employed for characterizing the surface features [22]. Higher resolutions of SEM images provide better accuracy in physical definitions of the surface features.

3 Finite-element analysis

Two-dimensional finite-element simulations were carried out using the program OOF2 that is a public domain program available for free downloading via the Internet at http://www.ctcms.nist.gov/oof/oof2/ [23]. The program OOF2 is capable of reading an image file such as a micrograph. The alumina ceramic that was used for the study had 40% by volume porosity. This is the porosity generated during sintering of the material and such high porosity is desired as such highly porous alumina is prepared for grinding operations. Hence, the two main characteristic features that made up the micrograph were the alumina grains and the porosity. Although the microstructures for finite-element analysis were considered from the top surface, it also represented an overall microstructure throughout the modified region as extensively studied in earlier work [22, 24, 25]. Such minimal

Elastic modulus (GPa)	Poisson's ratio	Thermal conductivity (W/mK)	CTE (/°C)
408	0.32	35	7.5×10^{-6}

TABLE 1 Mechanical and thermophysical properties of dense alumina

or no variation in the modified surface region may be due to inherently low thermal conductivity associated with alumina ceramic (35 W/mK). The micrograph was divided into two pixel groups corresponding to the grains and the pores, respectively, by using the burn tool. After forming these groups, the material properties such as Young's modulus, Poisson's ratio, thermal conductivity, and coefficient of thermal expansion were assigned. The properties of dense alumina are listed in Table 1 [26].

It has been documented in the past by Harimkar and Dahotre that the surface solidification porosity generated during the solidification of laser-treated alumina ceramic decreases [27] and the surface grain size increases with increase in laser fluence (corresponding to a decreasing cooling rate) [28]. To predict the effect of porosity on the different thermophysical properties, the rule of mixtures was used as follows:

$$P = (1-\varphi)P_1 + \varphi P_2 ,$$

in which φ is the volume fraction porosity of the processed sample, P_1 is the property of dense aluminum oxide (thermal conductivity, elastic modulus, coefficient of thermal expansion), and P_2 is the property of air (pores). The thermal conductivity of air being very small (~ 0.03 W/mK), zero conductivity was assumed within the void areas [16]. The modulus of elasticity of the pores was also assumed to be zero [29]. The modified properties and corresponding depths of surface modified regions (melt depths) listed in Table 2 were used for analysis.

The microstructures were then converted into binary images consisting of groups corresponding to the microstructural features (grains, phases, cracks, porosity, etc.). Although several of these microstructural features collectively influence the residual stresses, in the present case only the distinct and dominant features such as grains and pores were considered for creation of binary images. This digitized image was then converted into a finite-element mesh using the object oriented finite (OOF) element method. An initial mesh comprising 2600 nodes and 5000 triangular elements was laid on the micrograph corresponding to a laser fluence of 459 J/cm^2. Similar meshes were also laid on the micrographs corresponding to the other laser fluences. The adaptive mesh refinement modifier was then used, which facilitated the subdivision of the elements and movement of nodes to conform to the microstructure. This helped in minimizing the energy functional parameter of the mesh, which was further reduced by an 'annealing' procedure at the conclusion of the meshing operation. After the adaptive mesh refinement, a mesh comprising 9000 nodes and 18 000 elements was generated. The elements corresponding to the grains were grouped together as a single unit and had a coarser mesh, while the pores formed another group and were meshed extremely finely [31, 32]. After meshing and applying the material properties to the different elements of the micrograph, the simulations were run to predict the stress state in each element and to obtain corresponding contour plots. The different steps involved in predicting the residual stress state starting with an initial micrograph for alumina processed at a laser fluence of 459 J/cm^2 are shown in Fig. 1.

The stress distribution diagram represents the minimum and maximum values of the stress reached and how the stress values vary in that range for a given fluence. However, the representative macro stress for a given processing condition was obtained by taking the mean value of the stresses at all the elements, thus yielding the resultant stress as either tensile or compressive. The standard deviation in the stress values was also predicted in order to account for the non-homogeneity within the specimens.

4 Micro stress determination

A Norelco (Philips Electronics Instruments, New York) X-ray diffractometer was used to carry out the X-ray diffraction analysis (Fig. 2) of the laser surface modified alumina compacts with Cu K_α ($\lambda = 1.54$ Å) radiation at 20 kV and 10 mA and diffraction angles varying between 20° and 100°. The shape, particularly the width, of the diffraction peaks is a measure of the amplitude of thermal oscillations of the atoms at their regular lattice sites. It can also be a measure of the plastic deformation and the stress generation. Crystallite size can lead to peak broadening and this can be easily calculated as a function of peak width (specified as full width at half-maximum (FWHM)). Peak Paint software was used to identify the FWHM (B_r) for each of the peaks in the X-ray spectrum and the corresponding Bragg angles were also noted. According to Scherrer equation mentioned in [33], the broadening of X-ray diffraction peaks due only to small crystallite sizes is given by

$$B_{\text{crystallite}} = \frac{k\lambda}{M\cos\theta}, \quad (1)$$

where λ is the wavelength of the X-rays used (0.154056 nm for Cu K_α radiation), θ is the Bragg angle, M is the 'average'

Laser fluence (J/cm^2)	Melt depth [30] (μm)	Elastic modulus (GPa)	Thermal conductivity (W/mK)	CTE $\times 10^{-6}$ (/°C)
459	510	342.7	29.4	6.3
497	600	359.0	30.8	6.6
535	710	371.2	31.8	6.8
573	780	377.4	32.3	6.9
611	850	387.6	33.2	7.1

TABLE 2 Mechanical and thermophysical properties of laser-processed alumina

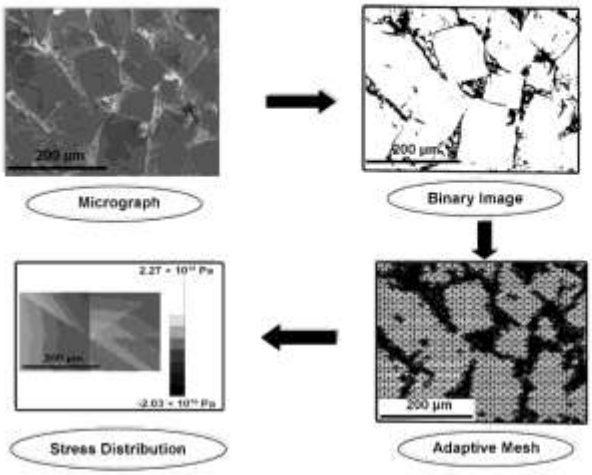

FIGURE 1 Flow chart for macro stress determination

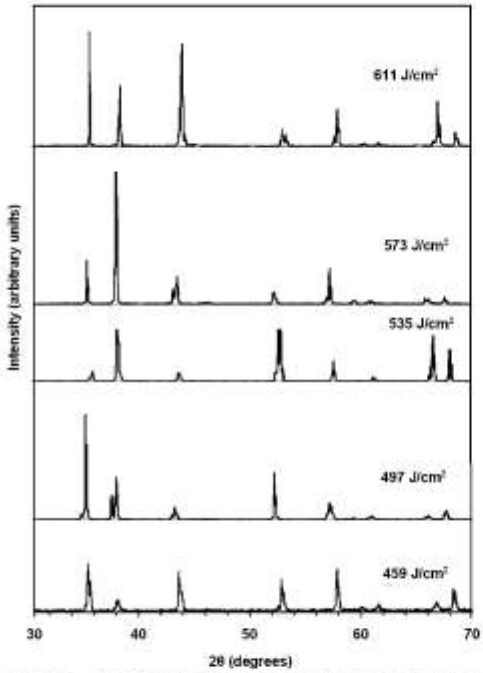

FIGURE 2 X-ray diffraction patterns of laser surface modified alumina at different laser fluences [22]

crystallite size measured perpendicular to the specimen surface, and k is a constant that varies between 0.89 and 1.39, but is generally taken close to unity. The precision of crystallite-size analysis by this method being $\pm 10\%$, the assumption that $k = 1.0$ is acceptable [33]. The lattice strain in the material also leads to peak broadening given by

$$B_{\text{strain}} = \eta \tan\theta \,. \tag{2}$$

where η is the material strain. Thus, the width B_t of the diffraction peak is given by the sum of widths due to small crystallite sizes and lattice strains:

$$B_t \cos\theta = \frac{k\lambda}{M} + \eta \sin\theta \,. \tag{3}$$

Thus, as can be seen from (3), a plot of $B_t \cos\theta$ against $\sin\theta$ can yield the lattice strain from the slope of the graph, while the crystallite size can be predicted from the Y-axis intercept. Thus, this method was capable of yielding both the crystallite-size distribution and the lattice micro strain for different laser fluences. The micro stress was then obtained by multiplying the micro strain with the elastic modulus of the laser-processed alumina.

5 Results and discussion

A schematic of the coordinate system representing the relative positions of the axes considered for defining the stress fields is shown in Fig. 3. As per the sign convention placed in Fig. 3, the x axis is along the direction of traverse of the laser beam, the y axis is perpendicular to the traverse direction, and both are along the surface, while the z axis is located along the depth of the specimen and perpendicular to the surface. The corresponding stresses acting along these directions are axial stress σ_{xx}, lateral stress σ_{yy}, normal stress σ_{zz}, and shear stress σ_{xy}. The mean values of these stresses as predicted by the OOF2 software are listed in Table 3, where the values in parenthesis are estimated standard deviations. As mentioned earlier, as the laser fluence has an effect on percentage porosity and grain size, these values are also mentioned in the table in order to help to correlate the microscopic features with the

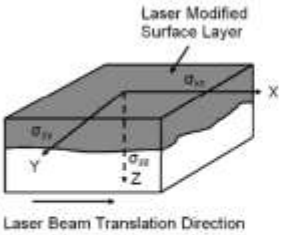

FIGURE 5 Schematic of the coordinate system adopted in stress field evaluations

stress values. The standard deviation values are large as compared to the average values, as few elements in the mesh have large stress values. The high stress values could be due to the stress concentration in certain regions such as the pores or the grain boundaries. These localized stresses could be the cause of isolated local cracking on the surface, as can be observed in the microstructure (Fig. 4).

Since the two principal stresses, axial stress σ_{xx} and lateral stress σ_{yy} along and transverse to the laser traverse, respectively, are the primary stresses of interest, only those along with shear stress σ_{xy} were considered in the discussion. Furthermore, even though the other components of the shear stresses, σ_{yz} and σ_{xz}, were also predicted, they were not reported due to their negligible values. The stresses in Table 3 have tensile (positive) as well as compressive (negative) values. The macro stress was plotted against the laser fluence in Fig. 5 to identify the working envelopes comprising the range of laser fluence that causes compressive stresses and the range that produces tensile stresses. The effects of porosity and grain size as a direct function of the laser fluence (and indirectly as a function of cooling rate) on macro stress are represented in Fig. 6.

Typically, in a system comprising a substrate (unprocessed alumina) and a coating (processed alumina surface region), the stresses generated in the coating are tensile in nature if the coefficient of thermal expansion of the coating is greater than the coefficient of thermal expansion of the substrate, and compressive stresses are generated if the thermal expansion coefficient of the coating is less than that of the substrate [2, 35]. Since the substrate had 40% by volume porosity, the elastic modulus and the coefficient of thermal expansion (CTE) of the unprocessed alumina were calculated using the weighted average method as 244.8 GPa and 4.5×10^{-6}/°C and using the properties of dense alumina mentioned in Table 1. From Table 2, it can be observed that the CTE of the processed surface region of alumina (or coating) is higher than that of the unprocessed alumina. Using the standard expression for thermal stresses as a function of material properties [2, 35] and material constants listed in Table 2 for a 510 μm [30] coating thickness (melt depth) corresponding to a laser fluence of 459 J/cm^2 on a 3.57-mm-thick substrate (unprocessed alumina) (taking the original coupon thickness to be eight times the melt depth of the processed alumina [2, 36] and then considering the substrate (unprocessed alumina) thickness to be the thickness of the original coupon minus the melt depth), a tensile stress of 2961.86 MPa was estimated for a maximum temperature of 3918 K attained during processing [30]. Thus, based on only the difference in CTE, a tensile stress is predicted in the present material system during laser surface modification. However, in the present case, as the laser fluence increased, the stresses gradually became less tensile and eventually they entered into the compressive regime (Fig. 5). Among many other factors, this can be mainly attributed to the extensive annealing experienced at higher fluences. During laser processing of alumina, several subsequent tracks were laid for coverage of a large surface treatment. Due to the extensive temperature rise in the track being laid down, temperatures of the neighboring tracks laid earlier also substantially rise, leading to release of the residual stresses (annealing) within them and exerting compressive forces on the track being processed through physical expansion of the material. A similar phenomenon is also expected to take place at lower laser fluences. However, as the cooling rates encountered at lower fluences are high [24], the annealing effects within the earlier tracks are less and lead to retention of the tensile stresses of higher magnitude. Thus, the above-mentioned phenomenon explains the generation of the tensile stress regime at lower fluences (corresponding to higher cooling rates) and the formation of the compressive stress regime at higher laser fluences (corresponding to lower cooling rates). The compressive stresses are advantageous for long life of the components, as mentioned before.

As observed from Table 3 and Fig. 5, shear stress σ_{xy} values corresponding to all laser fluences are negligible and also marginally vary as a function of laser fluence, indicating no significant plastic deformation within the area of analysis. Similar observations were experienced in the TiC ceramic phase of TiC/Al composite coating synthesized using laser-based processing [2]. High-resolution TEM observations of these samples indicated no dislocation structures or stacking fault defects in TiC [2]. Ceramics such as alumina and TiC being covalently and/or ionically bonded and complex in crystal structures, they provide a limited number of slip systems for deformation even under extreme thermal

Laser fluence (J/cm^2)	Solidification porosity [27] (%)	Grain size [28] (μm)	σ_{xx} (MPa)	σ_{yy} (MPa)	σ_{zz} (MPa)	σ_{xy} (MPa)
459	16	100	83.1 (±1580)	−1055.9 (±10 050.7)	−854.79 (±8541.2)	31.89 (±202.94)
497	12	142.8	162.7 (±2066.1)	336.6 (±3135.9)	217.6 (±1570.2)	41.4 (±283.3)
535	9	185.7	168.0 (±1433.0)	−118.27 (±1906.7)	−54.7 (±686.9)	−17.09 (±193.7)
573	7.5	214.2	113.3 (±2138.1)	−3.67 (±2151.0)	39.49 (±473.8)	2.01 (±257.96)
611	5	242.8	45.93 (±2390.6)	−176.16 (±2376.6)	−46.04 (±517.06)	37.89 (±267.58)

TABLE 3 Mean macro stress components for laser-modified alumina ceramic

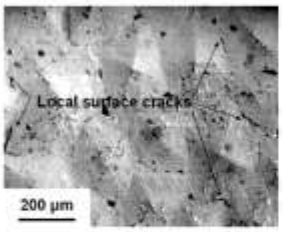

FIGURE 4 Local surface cracks [34]

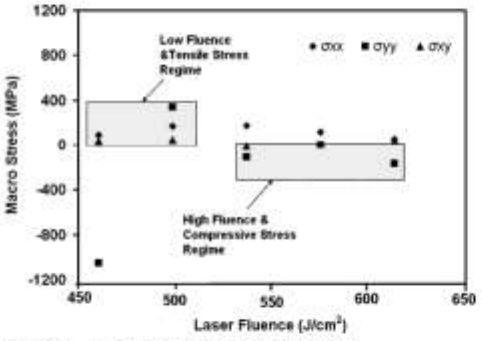

FIGURE 5 Variation of macro stress with laser fluence

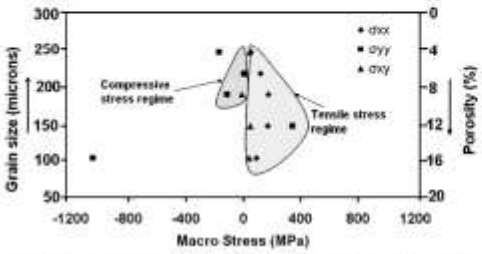

FIGURE 6 Macro stress variation as a function of grain size and porosity

conditions (rapid heating/cooling) of laser processing. Such marginal shear stresses ensure longer life of the processed components.

Since laser fluence has a significant effect on the microscopic features like grain size and porosity, changing the fluence will affect the state of the stress. As observed in Fig. 6, the stress values are in the compressive regime for increased grain sizes associated with decreasing cooling rates due to increasing laser fluences [28]. On the contrary, the tensile stresses are generated with the generation of small grains with high cooling rates associated with lower laser fluences [28]. As all the grains are disoriented and not aligned in the same direction, they have a tendency to align themselves. This process of alignment of the grains leads to the stress formation, which will be more for smaller grains [37]. As the grains become larger (in the present case, approximately greater than 150 µm), the grain-boundary region reduces, which leads to smaller stresses as can be observed in Fig. 6 in the tensile and the compressive regimes.

The generation of compressive stresses can also at the microscopic level be a function of differences in the thermal conductivity and coefficient of thermal expansion of different grains [38]. As the different grains may possess different thermophysical properties, they try to attain a state of equilibrium, thus leading to the stress generation in the process. In the present case, the maximum compressive stress observed is ~ 1055 MPa and it is less than 3400 MPa, the theoretical compressive strength of alumina [39], thus ensuring the limited possibilities of failure of the ceramic. On the contrary, the maximum tensile stress of ~ 336 MPa is slightly greater than 300 MPa, the theoretical tensile strength of alumina [39]. This can be manifested in isolated minor cracking on the surface (Fig. 4).

Such stress data gives an estimate of the laser fluence range to avoid the generation of stresses from exceeding the tensile/compressive strength and obtain a crack-free surface. The compressive stress regime is advantageous for certain applications that involve sealing, as mentioned earlier. The seals have been used as lining in furnaces [40], where it is necessary to prevent penetration of molten slag, and they can also act as thermal barriers in heat exchangers in severe operating conditions. Compressive stresses are capable of inhibiting slip and delaying the crack nucleation. If the laser-treated alumina ceramic is used for certain applications like grinding, the compressive stresses formed due to the laser processing of the ceramic will further assist in increasing the fatigue endurance limits of the components, thus enhancing the grinding efficiency [41].

The solidification porosity has a significant effect on the stresses generated. The contribution of pores is to increase the internal friction of the material and the mechanism by which this takes place can be interpreted in terms of defect effects. This can be attributed to the formation of inhomogeneous stress regions followed by the dissipation of this stress. Due to the variation in the loading, the inhomogeneous strain and stress conditions become intensified and form high dislocation densities at the pore boundaries. The atoms within these distorted regions are forced to redistribute, causing the stress to reduce. Thus, the high dislocation densities help to disperse the intense energy prevailing near the pores, thus effectively reducing the stress. Hence, porous materials will show an increased tendency to dissipate the stress and hence lower values of stresses. As can be seen from Fig. 6, stresses reduce with increase in porosity due to the above-mentioned phenomena [42–45]. Thus, the porosity of the ceramic can be controlled by adjusting the laser fluence, which in turn would control the stresses developed as required by the application.

As mentioned earlier, the grains and crystallites are two different microscopic features with the micro stress being affected by the crystallite size. As can be seen in Fig. 7, the laser fluence changes the crystallite size and hence the associated micro stresses. For a particular stress regime, it can be observed that an increase in laser fluence corresponding to lower cooling rates leads to the formation of larger crystallites. This is a similar trend as that reported in the past, wherein higher fluences provided lower cooling rates and larger grain sizes [24, 28, 34]. Furthermore, as observed in Fig. 5 for the

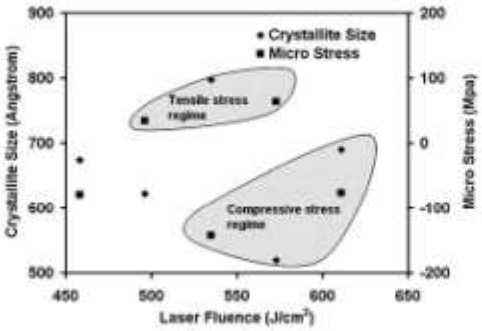

FIGURE 7 Variation of crystallite size and micro stress with laser fluence

macro stresses, higher laser fluence causes compressive micro stresses, while lower fluence generates tensile micro stresses (Fig. 7). The phenomenon causing the changes in the micro stress due to the changes in crystallite size has been explained earlier. As many crystallites club together to form a grain, the crystallite-size variations produce changes in the grain size and associated porosity because of which the generation of macro stresses and micro stresses follow the same general trend as a function of laser fluence (Figs. 5 and 7). Thus, this scrutiny helps to lay out the processing regimes for generation of tensile and compressive stresses. It also helps to bring out the relation between macro and micro stresses and to tailor these residual stresses to possibly improve the fatigue strength and wear resistance of the material, which will be follow up efforts.

6 Conclusion

Residual stress analysis of laser surface modified alumina ceramic was carried out using the object-oriented finite-element analysis technique for determining the macro stress and the FWHM method for predicting the micro stress. The macro stress values were in the compressive regime for increased grain sizes associated with decreasing cooling rates due to increasing laser fluences, and the tensile macro stresses were generated with generation of small grains with high cooling rates associated with lower laser fluences. As many crystallites club together to form a grain, the generation of macro stresses and micro stresses follow the same general trend as a function of laser fluence. Types and magnitudes of residual stresses generated using the set of processing parameters employed in the present work modified the surface of alumina ceramic without any major surface failure (cracks). Thus, this study gives an insight into how a systematic control of the laser processing conditions can be exercised to control grain size and porosity for generation of a desired type and magnitude of stresses in the ceramic component to suit a particular application.

ACKNOWLEDGEMENTS The authors would like to thank Dr. Andrew Reid of the Center for Theoretical and Computational Material Science, NIST, for his help in installation and understanding the basic simulation procedure of the OOF2 software.

REFERENCES

1 T. Maiman, Nature (London) **187**, 493 (1960)
2 P. Kadolkar, T. Watkins, J. De Hosson, B. Kooi, N. Dahotre, Acta Mater. **55**, 1203 (2007)
3 F. Tehrani, L. Hector, R. Hetmaniki Jr., M. Enlami, Trans. ASME **68**, 480 (2001)
4 A. Zhang, Q. He, L. Gao, J. Polym. Sci. B **42**, 3759 (2004)
5 A. Solina, M. de Sanctis, L. Pagnotti, P. Coppa, J. Heat Treat. **4**, 272 (1986)
6 K. Dai, L. Shaw, Acta Mater. **49**, 4171 (2001)
7 U. De Oliveira, V. Ocelik, J. De Hosson, Surf. Coat. Technol. **201**, 6363 (2007)
8 J. Lawrence, L. Li, J. Spencer, Opt. Laser Technol. **30**, 205 (1998)
9 J. Lawrence, L. Li, J. Spencer, Opt. Laser Technol. **30**, 215 (1998)
10 J. Lawrence, L. Li, J. Laser Appl. **12**, 116 (2000)
11 R. Chin, J. Beuth, C. Amon, Mech. Mater. **24**, 257 (1996)
12 K. Dai, L. Shaw, Acta Mater. **52**, 69 (2004)
13 C. Amon, J. Beuth, R. Merz, F. Prinz, L. Weiss, ASME J. Manuf. Sci. Eng. **120**, 656 (1998)
14 F. Mishlik, C. Berndt, Surf. Coat. Technol. **201**, 2369 (2006)
15 A. Kulkarni, Z. Wang, T. Nakamura, S. Sampath, A. Goland, H. Herman, J. Allen, J. Ilavsky, G. Long, J. Frahm, R. Steinbrech, Acta Mater. **51**, 2457 (2003)
16 Z. Wang, A. Kulkarni, S. Deshpande, T. Nakamura, H. Herman, Acta Mater. **51**, 5319 (2003)
17 V. Vedula, S. Glass, D. Saylor, G. Rohrer, W. Carter, S. Langer, E. Fuller Jr., J. Am. Ceram. Soc. **84**, 2947 (2001)
18 C. Hsueh, J. Haynes, M. Lance, P. Becher, M. Ferber, E.R. Fuller, S.A. Langer, W.C. Carter, W.R. Cannon, J. Am. Ceram. Soc. **82**, 1073 (1999)
19 A. Zimmermann, W. Carter, E. Fuller, Acta Mater. **49**, 127 (2001)
20 J. Ares, A. Pascual, I. Ferrer, C. Sánchez, Thin Solid Films **480–481**, 477 (2005)
21 M. Cherkashky, N. Ganev, J. Bansal, J. Drahokoupil, E. Kolářík, Z. Kristallogr. **23**, 369 (2006)
22 S. Harimkar, N. Dahotre, Adv. Appl. Ceram. **105**, 304 (2006)
23 S. Langer, W. Carter, E. Fuller Jr., *OOF* (NIST, Gaithersburg, MD, 1997)
24 S. Harimkar, N. Dahotre, J. Appl. Phys. **100**, 034901 (2006)
25 A. Khanger, E. Kenik, N. Dahotre, Ceram. Int. **31**, 621 (2005)
26 W. Gitzen, *Alumina as a Ceramic Material* (The American Ceramic Society, Westerville, OH, 1970)
27 S. Harimkar, N. Dahotre, Phys. Stat. Solidi A **204**, 1105 (2007)
28 S. Harimkar, N. Dahotre, Int. J. Appl. Ceram. Technol. **3**, 375 (2006)
29 T. Zhdanova, O. Smishchenko, I. Morgin, O. Borushko, R. Khodakovskaya, Glass Ceram. **42**, 446 (1985)
30 S. Harimkar, A. Samant, N. Dahotre, J. Appl. Phys. **101**, 054913 (2007)
31 A. Saigal, E. Fuller Jr., Comput. Mater. Sci. **21**, 149 (2001)
32 A. Jadhav, N. Padture, E. Jordan, M. Gell, P. Miranzo, E. Fuller Jr., Acta Mater. **54**, 3343 (2006)
33 C. Suryanarayana, M.G. Norton, *X-Ray Diffraction – A Practical Approach* (Plenum, New York, 1998)
34 S. Harimkar, A. Samant, A. Khanger, N. Dahotre, J. Phys. D Appl. Phys. **39**, 1642 (2006)
35 S. Albert, G. Schajer, *Surface Engineering* (ASM Handb. **5**) (ASM, Materials Park, OH, 1998)
36 L. Karipelli, A. Agarwal, N. Dahotre, Mater. Sci. Eng. A **289**, 34 (2000)
37 M. Seabaugh, I. Kerrdit, G. Messing, J. Am. Ceram. Soc. **80**, 1181 (1997)
38 P. Sedek, J. Brozda, L. Wang, P. Withers, Int. J. Pressure Vessels Piping **80**, 705 (2003)
39 B. Bhushan, B. Gupta, *Handbook of Tribology (Materials, Coatings and Surface Treatments)* (McGraw-Hill, New York, 1991)
40 L. Bradley, L. Li, P. Stott, Appl. Surf. Sci. **138–139**, 233 (1999)
41 K. Carlsson, G. Kardomateas, *An Introduction to Fatigue in Metals and Composites* (Chapman & Hall, London, 1996)
42 L. Nielsen, J. Am. Ceram. Soc. **67**, 93 (1984)
43 P. Puri, S. Cowin, J. Elasticity **15**, 167 (1985)
44 J. Zhang, M. Gungor, E. Lavernia, J. Mater. Sci. **28**, 1515 (1993)
45 M. Kearns, P. Blenkinsop, A. Barber, T. Farthing, Int. J. Powder Metall. **24**, 59 (1988)

Laser beam operation mode dependent grain morphology of alumina

Anoop N. Samant, Sandip P. Harimkar, and Narendra B. Dahotre[a)]
Department of Materials Science and Engineering, The University of Tennessee, Knoxville, Tennessee 37996, USA

(Received 23 August 2007; accepted 24 October 2007; published online 19 December 2007)

The effect of laser beam operation mode on transition of grain morphology was studied during surface modification of alumina ceramic. A 4 kW HL 4006D continuous wave Nd:yttrium-aluminum-garnet (YAG) laser and a JK 701 pulsed Nd:YAG laser were employed to conduct surface modification of alumina. The laser beam operated in continuous wave mode generated faceted grain structure on the surface of the ceramic while the beam operated in pulsed mode produced nonfaceted grain structure. Such transition in grain morphology is mainly attributed to different levels of undercooling which is a function of cooling rates encountered in two different modes of laser operation. © *2007 American Institute of Physics*. [DOI: 10.1063/1.2825403]

I. INTRODUCTION

Lasers have been extensively used to improve the surface properties of different materials such as ceramics because the high cooling rates encountered in laser processing can provide different morphologies on the surface.[1–4] Alumina is a ceramic with excellent mechanical and thermal properties and is used in environments involving high temperatures and aggressive operating conditions. Surface modified alumina can increase the life of linings utilized in heat exchangers and furnaces by reducing the surface porosity. Porous alumina has also been widely used as a grinding wheel material and laser dressing of these wheels is gaining importance, as it is a noncontact process providing better automation and control.[5–10] Porosity is maintained in alumina for various reasons including but not limited to thermal expansion, thermal conductivity, toughness, and for lodging of metal particles during grinding operation.

By controlling the processing parameters during surface modification, convenient control can be obtained over the final surface microstructure. The laser can be operated in continuous wave (cw) or the pulsed mode (PM). Both these modes of laser operation can be used to modify the ceramic surface depending on the type of final microstructure desired on the surface. In a cw laser, the laser is pumped continuously and incessant light is emitted, while in a pulsed laser, there is a laser power-off period between two pulses.[11] cw lasers have been extensively used for porous alumina surface modification and generated microstructures have been diligently discussed in the past.[5–10] However, the effect of pulsed laser processing on surface microstructure of porous alumina ceramic has not been carefully studied yet. Hence, the present study aims at comparing the microstructures in surface modified region of porous alumina due to PM laser operation with those obtained by cw laser operation and understanding the physical phenomena underlying these two processes which could cause the transition in microstructure. This study will help to select an appropriate mode of laser operation in tailoring a desired surface microstructure.

a)Author to whom correspondence should be addressed. Telephone: 865-974-3609. FAX: 865-974-4115. Electronic mail: adahotre@utk.edu.

II. LASER SURFACE PROCESSING

Alumina ceramic compacts having 40% by volume porosity were obtained from MSC Industrial Supply Co., Melville, NY. Sintering of the material introduced the porosity in the ceramic, which is desirable for grinding operation. The surface area of these coupons was 5×5 cm^2 and their thickness was 2.54 cm. The surface of some of the ceramic coupons were exposed to a 4 kW HL 4006D cw Nd:yttrium-aluminum-garnet (YAG) (1.06 μm wavelength) laser with fiber optically delivered beam from TRUMPF, Schramberg, Germany, while some compacts were irradiated by a JK 701 pulsed Nd:YAG laser (1.06 μm wavelength) from GSI Lumonics, Rugby, England. The laser used for cw laser operation displayed the input energy in terms of power supplied in watts while the laser used for PM laser operation provided the input energy in terms of energy supplied in joules. The laser process parameters (input energy, repetition rate, and traverse speed) were systematically varied and the interaction between the laser beam and the ceramic surface was observed. Therefore, the laser processing parameters (power or input energy, transverse speed, etc.) selected and employed in the present study represent a range of parameters outside of which the parameters were unable to create any interaction (for lower input energies) with the ceramic surface or unable to cause surface melting (instead for higher input energies vaporization occurred). For the continuous wave laser, power densities varying from 2.03×10^4 to 2.71×10^4 W/cm^2 and laser traverse speed of 100 cm/min were employed to dress the ceramic surface. For the PM laser operation, power densities varying from 0.08×10^6 to 1.13×10^6 W/cm^2 and velocities ranging from 5.08 to 7.62 cm/min were employed. Hitachi S3500 scanning electron microscopy characterized the surface features for both the processing modes.

III. THERMAL PREDICTIONS

Microstructure (grain structure/morphology) formed on surface due to laser processing depends on the temperature distribution and the cooling rates associated with the process.[5] cw and PM laser operations are bound to generate different thermal conditions and associated cooling rates

within the material. Hence, in order to correlate the microstructure (grain morphology) with cooling rates, it was necessary to first determine the cooling rates attained during the process. For this purpose, a three-dimensional heat flow model was developed using COMSOL's heat transfer transient mode[7] based on Fourier's second law of heat transfer,

$$\frac{\partial T(x,y,z,t)}{\partial t} = \alpha\left[\frac{\partial^2 T(x,t)}{\partial x^2} + \frac{\partial^2 T(y,t)}{\partial y^2} + \frac{\partial^2 T(z,t)}{\partial z^2}\right], \quad (1)$$

where α is the thermal diffusivity of the material and is given by $K/\rho C_p$, ρ is density of 2280 kg/m^3,[7] K is thermal conductivity of 14.6 W/mK,[7] and C_p is the specific heat of 800 J/kg K.[7] At time $t=0$, the initial temperature of $T=T_0$ =298 K was applied. At the sample surface, the equilibrium between the laser energy absorbed by the sample and the radiation losses is given by

$$-K\left[\frac{\partial T(x,y,0,t)}{\partial x} + \frac{\partial T(x,y,0,t)}{\partial y} + \frac{\partial T(x,y,0,t)}{\partial z}\right] = \delta AI - \varepsilon\sigma[T(x,y,0,t)^4 - T_0^4],$$

$$\delta = 1 \text{ if } 0 \le t \le t_p,$$

$$\delta = 0 \text{ if } t > t_p, \quad (2)$$

where ε is emissivity for thermal radiation=0.7,[12] I is laser power intensity, t_p is residence time, T_0 is ambient temperature (298 K), σ is Stefan–Boltzman constant=5.67 $\times 10^{-8}$ W/m^2 K^4, and A is absorptivity=0.8.[13] Convection taking place at the bottom surface of the sample is given by

$$-K\left[\frac{\partial T(x,y,L,t)}{\partial x} + \frac{\partial T(x,y,L,t)}{\partial y} + \frac{\partial T(x,y,L,t)}{\partial z}\right] = h[T(x,y,L,t) - T_0], \quad (3)$$

where h is the convective heat transfer coefficient =200 W/m^2 K [14] and L is the thickness of the sample =2.54 cm. It is assumed that no heat loss takes place through the other surfaces. The maximum cooling rates encountered in both the processing modes were estimated after solving this model. In order to explore the possible correlation between the melt depth and the formed microstructure, the melt depth was predicted using the thermal profiles developed by the earlier mentioned model [Eqs. (1)–(3)] by tracking the depth at which the melting point of alumina (2323 K) was reached.

The amount of energy going into material surface and the time for which this energy is supplied (residence time) affect the maximum surface temperature reached during processing and, hence, the corresponding maximum cooling rates. In order to solve the model for cooling rates, it was necessary to input the energy density and the time for which it is being supplied to the material. As the traverse speed dictates the time of interaction between the material surface and beam, the residence time was determined using the traverse speed.

For cw laser operation, the beam was elliptical in cross section with major and minor axes dimensions of 0.5 and 0.15 cm, respectively. As the beam continuously emits energy without the power being shut off during surface processing, the residence time of cw operation was determined by dividing the minor axis of the beam by the traverse speed, the minor axis being in the direction of beam traverse. On the contrary, for the pulsed laser the beam was circular in cross section (diameter of 0.04 cm) and there was a power off period between two consecutive pulses. Therefore, the pulse width and repetition rate of the laser pulses are also taken into account to determine the residence time, the time for which the laser beam interacts with the surface. In light of this, the residence time for the pulse mode was calculated by using the following relation:

$$\text{Residence time (s)} = \frac{\text{pulse width (s)} \times \text{beam diameter (cm)} \times \text{repetition rate (Hz)}}{\text{traverse speed (cm/s)}}. \quad (4)$$

The amount of total energy going into the material depends on the traverse speed as it decides the time of interaction (residence) between the beam and material. Such energy can be expressed as energy per unit beam cross-sectional area per unit beam interaction (residence) time, which also can be termed as energy density per unit time and expressed as

$$\text{Energy density per unit time (W/cm}^2\text{)} = \frac{\text{incident energy (J)}}{\text{residence time (s)} \times \text{area of incident beam (cm}^2\text{)}}. \quad (5)$$

Expressing the input energy in this form maintained consistency in units even though the energies were displayed differently by the different lasers as mentioned before in Sec. II. In the case of cw mode of laser operation, incident energy is given by the following equation:

$$\text{Incident energy (J)} = \text{incident power (W)} \times \text{residence time (s)}. \quad (6)$$

This energy density per unit residence time and the residence time were input to the model for determining the cooling rate. The parameters that were employed for cw and PM laser processing and the parameters that were provided as an

TABLE I. Parameters associated with cw laser operation.

Energy density per unit residence time, E_{cw} (W/cm^2)	Traverse Speed (cm/min)	Residence time, t_{cw} (ms)	Cooling rate, R_{cw} (K/s)	Laser beam penetration depth, D_{cw} (μm)
2.03×10^6	100	90	594	558
2.20×10^6			502	609
2.37×10^6			362	659
2.54×10^6			260	700
2.71×10^6			197	742

input for the thermal model discussed earlier (energy density per unit residence time and the residence time) are listed in Tables I and II, respectively. These tables also include the cooling rates and melt depths predicted by this model. The effects of the cooling rates on the surface microstructure, however, will be discussed in the subsequent sections.

IV. RESULTS AND DISCUSSION

The representative surface microstructures obtained by the cw laser processing of alumina are illustrated in Fig. 1 for energy densities per unit time of 2.2×10^4, 2.3×10^4, and 2.5×10^4 W/cm^2 (corresponding to 1300, 1400, and 1500 W, respectively). The microstructures indicate the presence of extremely faceted morphology for surface grains. The formation of these facets has been extensively discussed by Harimkar *et al.*[5,6,15] on the basis of van der Drift model. This theory assumes that every grain cultivates with a crystallographic facet moving with a certain normal velocity until it meets the surface of another developing grain, thus leading to the formation of grain boundaries because of the impingement of the different grains on each other. Especially, the faceting of surface grains is mainly due to the competitive augmentation of different crystallographic planes, which predicts the energetically favorable shape of the grains during solidification. The facets generate due to the difficulties in kinetics encountered while new planes of atoms are being formed. Interface kinetics and anisotropic surface energy are the motivating forces for the preferred dendritic directions in faceted morphology.[16] In laser surface modified porous alumina, it has been documented by Harimkar *et al.*[15] that the facets are formed due to the evolution of intense crystallographic texture related to {110} and {211} planes which correspond to maximum texture coefficients for these planes.

The representative surface microstructures corresponding to PM laser operation are illustrated in Fig. 2 for energy densities per unit time of 1.13×10^6, 0.47×10^6, and 0.99×10^6 W/cm^2 (corresponding to 25, 15, and 5 J, respectively). As the process parameters for the PM operation were different from those used in the cw mode of laser operation, the energy density per unit time values were also different without any correlation between each other. Unlike the grain morphology corresponding to cw laser operation (Fig. 1) the grains corresponding to PM laser operation failed to show the faceted morphology. However, the grain morphology remained the same for a particular mode of operation (i.e., the grains showed facets for the cw mode of laser operation while they were nonfaceted for the PM mode) even though the different process parameters were varied for a particular mode. It can be seen from Fig. 2 that different processing conditions of the PM laser operation generate grains of different shapes. The possible causes behind the formation of different shapes of the grains as a result of PM operation are currently under investigation and will be documented in subsequent publications. Optimizing the PM laser process parameters to optimize any desirable material property (such as grain size or porosity) will also be a separate study and will be presented in due course of time. On the contrary, the current efforts aim to focus on the transition of faceted to nonfaceted surface grains with a change in laser processing from cw to PM operation along with an explanation of possible thermal conditions behind such transition.

The high cooling rates (10^2–10^8 K/s) encountered during the rapid solidification process such as laser surface processing generate near or nonequilibrium conditions,[9] which can lead to solidification of the melt at a temperature different from the equilibrium melting temperature of alumina (~2323 K). The difference between the melting point of the ceramic and the temperature at which actual solidification occurs is the undercooling. Certain materials undergo a transition from faceted to nonfaceted morphology due to the dif-

TABLE II. Parameters associated with PM laser operation.

Energy density per unit residence time, E_{PM} (W/cm^2)	Traverse speed (cm/min)	Pulse width (ns)	Repetition rate (Hz)	Residence time, t_{PM} (ms)	Cooling rate, R_{PM} (K/s)	Laser beam penetration depth, D_{PM} (μm)
1.13×10^6	7.62	7	8	17.6	78.9×10^3	910
0.84×10^6	5.08	4	10	18.9	101.7×10^3	900
0.47×10^6	5.08	4	13.3	25.1	118.9×10^3	960
0.08×10^6	5.08	4	20	37.8	133.7×10^3	790
0.99×10^6	7.11	0.5	20	3.3	195.5×10^3	360

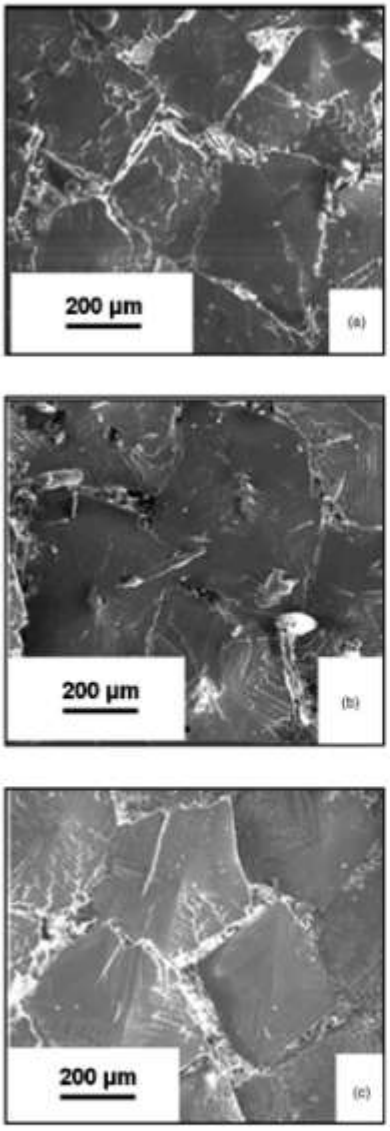

FIG. 1. Faceted grains observed on alumina surface processed by a cw laser at (a) 2.2×10^4, (b) 2.3×10^4, and (c) 2.5×10^4 W/cm^2.

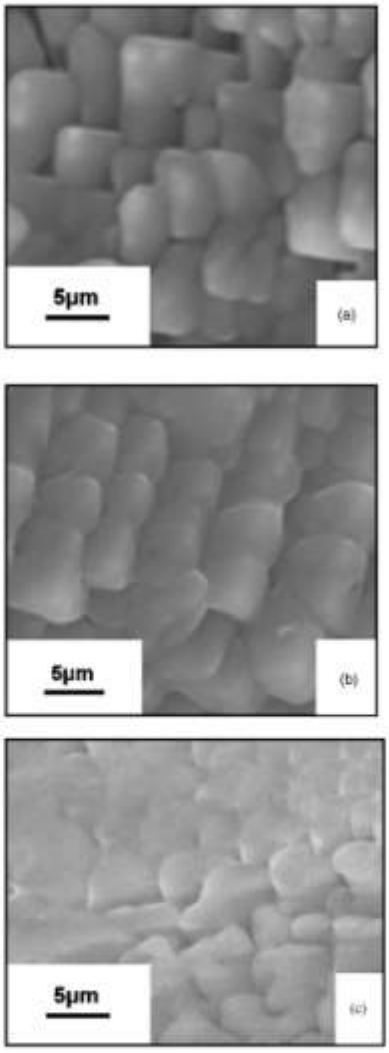

FIG. 2. Surface micrographs for PM laser operation at (a) 1.13×10^6, (b) 0.47×10^6, and (c) 0.99×10^6 W/cm^2.

ference in undercooling experienced under different processing conditions.[17] It has been reported by Li *et al.*[17] that small undercooling forms faceted structures while nonfaceted features are a result of large undercooling. A cooling rate has a strong bearing on the undercooling of melts.[18–20] Hence, it was necessary to bring out a relationship between the cooling rate and undercooling to correlate the observed microstructures with the cooling rates and associated undercoolings of cw and PM laser conditions. A cooling rate in terms of undercooling can be expressed as[21,22]

$$R = M\Delta T^n, \tag{7}$$

where M is a constant of proportionality that depends upon the factors such as nucleation rate constant, solidification

TABLE III. Values of dimensionless cooling rate and undercooling.

cw laser operation		PM laser operation	
Dimensionless cooling rate, R^*_{cw}	Dimensionless undercooling, ΔT^*_{cw}	Dimensionless cooling rate, R^*_{PM}	Dimensionless undercooling, ΔT^*_{PM}
0.89×10^{-3}	2.98×10^{-2}	1	1
1.37×10^{-3}	3.69×10^{-2}	1.29	1.14
1.80×10^{-3}	4.24×10^{-2}	1.51	1.23
2.50×10^{-3}	4.50×10^{-2}	1.69	1.30
3.30×10^{-3}	5.74×10^{-2}	2.48	1.57

rate, and concentration change.[21] The parameter "n" which is referred to the order of nucleation is strictly an empirical parameter related to the nucleation process and has no fundamental significance.[21,22]

It can be observed from Tables I and II that the cooling rates for the PM laser processing are much higher (three orders of magnitude) compared to the cooling rates for the cw laser processing. These cooling rates can be employed in Eq. (7) to predict corresponding undercooling. However, the constant of proportionality M from Eq. (7) is not easily available in the open literature. In light of this, the cooling rate values were nondimensionalized and the corresponding dimensionless undercooling values were predicted for cw and PM operations. As mentioned earlier, the order of nucleation (n) being purely empirical with no fundamental significance, a value of 2 commonly quoted in the literature was used.[23] Dimensionless cooling rates (R^*) were obtained by dividing cooling rates with the cooling rate corresponding to the energy density per unit residence time of 1.13×10^6 W/cm^2 for PM laser operations. Thus, an equation that can be generated from Eq. (7) using dimensionless parameters is given as

$$(R^*) = (\Delta T^*)^n. \tag{8}$$

The values of the dimensionless cooling rate R^* and the corresponding dimensionless undercooling ΔT^* computed using Eq. (8) for both cw and PM laser operations are presented in Table III. The relationships between R^* and ΔT^* for cw and PM laser operations are illustrated in Figs. 3 and 4, respectively. In both cw and PM laser operations, the cooling rate and undercooling hold a polynomial relationship (Figs. 3 and 4). It can also be realized from Table III and Figs. 3 and 4

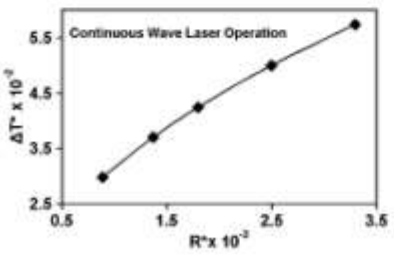

FIG. 3. Dimensionless undercooling and cooling rate variation for cw laser operation.

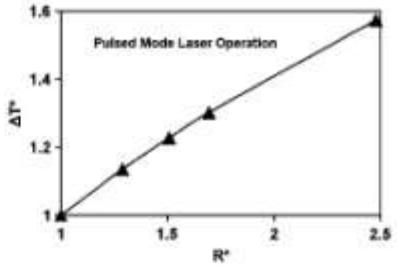

FIG. 4. Dimensionless undercooling and cooling rate variation for PM laser operation.

that the undercooling values for PM laser operation are nearly two orders of magnitude higher compared to that corresponding to cw operation.

As mentioned earlier, the magnitude of the cooling rate and corresponding undercooling have a strong bearing on the generation of faceted and nonfaceted grains during solidification. Furthermore, the physical phenomenon by which undercooling governs faceting has been explained by Cahn *et al.*[24] The free energy that is associated with the solid-liquid interface can be considered to be periodic in nature and this period is a function of the lattice spacing. Thus, an energy barrier has to be tackled while shifting from one atomic position to the next. For low undercooling, as experienced in cw laser operation, the driving force for surmounting this barrier appears to be inadequate to incessant interface motion to occur, hence, leading to a generation of stepped or faceted interface (Fig. 1). This was also further explained using the van der Drift model by Harimkar *et al.*[5,8,15] for formation of faceted grains in surface modified alumina using cw laser operation. On the other hand, if the undercooling is large as experienced in PM laser operation (>2 orders of magnitude compared to cw laser operation), then uninterrupted motion of the interface is likely to take place and thus provide a diffuse and nonfaceted interface as observed in Fig. 2. In addition to the extent of driving force, the time associated with the cooling rate is expected to control the grain morphology. Thus, extremely high cooling rates associated with PM laser operation (>3 orders of magnitude compared to cw laser operation) (Table III, Fig. 3) provided inadequate time for the facets to grow thereby forming nonfaceted grains.[11] In addition, during the pulse mode operation, the disintegration of dendrites is also likely to take place due to the stirring effect generated by the impact of the pulse with the ceramic surface.[11] As a result of this fragmentation, the dendrites are prevented from growing into the faceted grains.

The predicted melt depths for the PM operation were higher for a majority of the energy densities (Tables I and II) as compared to the cw mode of laser operation. In the PM operation, higher energy densities were supplied for a shorter period of time, thus melting more material in a majority of the cases as compared to the cw mode of laser operation where smaller magnitudes of energy densities were supplied for a longer period of time. Thus, the melt depth was a function of the input energy and the time for which it was sup-

plied (residence time) without much direct bearing on the undercooling. On the contrary, the undercooling is directly affected by the cooling rate, which in turn is affected by the mode of laser energy delivery. Therefore, although the melt depths in PM operation are larger than the melt depth in cw operation, the cooling rates of PM operation are three orders of magnitude higher than the cooling rates of cw operation.

V. CONCLUSION

Surface modification in porous alumina by cw and PM laser operations produced faceted and nonfaceted grains, respectively. Cooling rates and undercoolings for PM operation are of several orders of magnitude higher compared to that of cw laser operation. Unobstructed motion of the solid-liquid interface due to high cooling rates and undercooling in PM laser operation created nonfaceted grains. On the contrary, slow cooling rates responsible for small undercooling during cw laser operation were responsible for the formation of faceted grain morphology.

ACKNOWLEDGMENTS

The authors would like to thank Sameer R. Paital at the University of Tennessee, Knoxville for his help in adjusting the laser parameters and successfully processing the porous alumina ceramic samples using the pulsed mode laser.

[1]J. D. Majumdar, B. R. Chandra, B. L. Mordike, R. Galun, and I. Manna, Surf. Coat. Technol. **179**, 297 (2004).
[2]B. J. Kooi, Y. T. Pei, J. Th, and M. De Hosson, Acta Mater. **51**, 831 (2003).
[3]A. Agarwal and N. B. Dahotre, Int. J. Refract. Met. Hard Mater. **17**, 283 (1999).
[4]P. Kadolkar and N. B. Dahotre, Appl. Surf. Sci. **199**, 222 (2002).
[5]S. P. Harimkar and N. B. Dahotre, Int. J. Appl. Ceram. Technol. **3**, 375 (2006).
[6]S. P. Harimkar and N. B. Dahotre, Adv. Appl. Ceram. **105**, 304 (2006).
[7]S. P. Harimkar, A. N. Samant, and N. B. Dahotre, J. Appl. Phys. **101**, 054911 (2007).
[8]A. A. Khangar, E. A. Kenik, and N. B. Dahotre, Ceram. Int. **31**, 621 (2005).
[9]A. N. Samant, S. P. Harimkar, and N. B. Dahotre, JOM **59**, 35 (2007).
[10]S. P. Harimkar, A. N. Samant, A. A. Khangar, and N. B. Dahotre, J. Phys. D **39**, 1642 (2006).
[11]S. Sun, Y. Durandet, and M. Brandt, Surf. Coat. Technol. **194**, 225 (2005).
[12]Y. S. Touloukian, *Thermophysical Properties of High Temperature Material* (IFI/Plenum, New York, 1967).
[13]W. H. Gitzen, *Alumina as a Ceramic Material* (The American Ceramic Society, Westerville, OH, 1970).
[14]F. P. Incropera and D. P. DeWitt, *Fundamentals of Heat and Mass Transfer* (Wiley, New York, 1990).
[15]S. P. Harimkar and N. B. Dahotre, J. Appl. Phys. **100**, 024901 (2006).
[16]M. C. Flemings, *Solidification Processing* (McGraw-Hill, New York, 1974).
[17]D. Li and D. M. Herlach, Europhys. Lett. **34**, 423 (1996).
[18]Z. Zhou, J. Zhao, and W. Wang, J. Mater. Res. **15**, 4 (2000).
[19]W.-B. Guan, Y.-L. Gao, Q.-J. Zhai, and K.-D. Xu, Mater. Lett. **59**, 1701 (2005).
[20]Y. Wang, X. Zeng, W. Ding, A. A. Luo, and A. K. Sachdev, Metall. Mater. Trans. A **38**, 1358 (2007).
[21]J. W. Mullin, *Crystallization* (Butterworth Heinemann, Woburn, MA, 2001).
[22]K. W. Smith, F. W. Cain, and G. Talbot, Eur. J. Lipid Sci. Technol. **107**, 583 (2005).
[23]Ch. Charbon and R. Le Sar, Modell. Simul. Mater. Sci. Eng. **5**, 53 (1997).
[24]J. W. Cahn, Acta Metall. **8**, 554 (1960).

G Model
PROTEC-12529; No. of Pages 8
ARTICLE IN PRESS

Journal of Materials Processing Technology xxx (2009) xxx–xxx

Contents lists available at ScienceDirect

Journal of Materials Processing Technology

journal homepage: www.elsevier.com/locate/jmatprotec

Pulsed laser surface treatment of magnesium alloy: Correlation between thermal model and experimental observations

Anoop N. Samant [a], Baoshuai Du [a,b], Sameer R. Paital [a], S. Kumar [c], Narendra B. Dahotre [a,*]

[a] Department of Material Science and Engineering, The University of Tennessee, Knoxville, TN 37996, USA
[b] School of Materials Science and Engineering, Shandong University, Jinan 250061, China
[c] Department of Materials Engineering, Indian Institute of Science, Bangalore 560012, India

ARTICLE INFO

Article history:
Received 31 October 2008
Received in revised form 20 January 2009
Accepted 7 February 2009
Available online xxx

Keywords:
Pulsed laser
Thermal modeling
MRI 153M Mg alloy
Microhardness
Melt depth

ABSTRACT

The effect of deposition of Al + Al_2O_3 on MRI 153 M Mg alloy processed using a pulsed Nd:YAG laser is presented in this study. A composite coating with metallurgical joint to the substrate was formed. The microstructure and phase constituents were characterized and correlated with the thermal predictions. The laser scan speed had an effect on the average melt depth and the amount of retained and/or reconstituted alumina in the final coating. The coating consisted of alumina particles and highly refined dendrites formed due to the extremely high cooling rates (of the order of 10^6 K/s). The microhardness of the coating was higher and several fold improvement of wear resistance compared to the substrate was observed for the coatings. These microstructural features and physical properties were correlated with the effects predicted by a thermal model.

1. Introduction

The increasing demand of light structural materials in commercial applications, such as automobile and aerospace, has driven the rapid development of Mg alloys due to their low density and high specific strength (Cao et al., 2006). However, the inherent hexagonal close-packed (HCP) crystal structure of Mg and its inability to form a dense oxidation layer on the surface lead to the restricted mechanical properties of Mg alloys and thereby limit their applications in wear and corrosion environments. In light of these limitations, modification of the bulk materials through alloying and forming Mg-matrix composites (fiber reinforced and particulate reinforced) has been attempted (Volkova, 2006; Ye and Liu, 2004). Nevertheless, the improvement of wear and corrosion resistance of Mg alloys can also be achieved by modifying chemical and/or physical properties of the surface, since the failure through wear and corrosion often begin at the surface of components. A number of coating technologies (e.g. CVD, PVD, plasma spraying, electron beam vaporization, magnetron sputtering, microwave oxidation and laser assisted technique) have been tried to modify the surface properties of Mg alloys (Gray and Luan, 2002).

Among various surface modification techniques, laser surface treatment of Mg alloys has attracted significant interests. The key feature of this process is localized melting and solidification within a short time and shallow depth, while the bulk material remains cool and serves as an infinite heat sink. Thus, a wide variety of chemical and microstructural states can be retained owing to this rapid quench effect (Draper and Ewing, 1984). Moreover, short processing time, flexibility in operation, economy in time/energy/material consumption, shallow heat affected zone and precision are the important advantages of laser surface engineering over conventional processes (Majumdar et al., 2004). In the past, laser remelting and cladding has been reported to improve the wear and corrosion resistance of Mg and its alloys (Abbas et al., 2005; Mondal et al., 2008; Yue et al., 2007; Yue and Su, 2007; Yue and Lin, 2008; Wang et al., 1993). It is also found that hard ceramic reinforcement can be introduced into metal matrix to form a composite coating on Mg alloys by simultaneous laser melting of a precursor and a portion of the substrate. Composite coatings reinforced by Al_2O_3, SiC and Mg_2Si have been deposited on Mg alloys by laser surface engineering and it was shown that by forming such a composite coating wear and corrosion resistance can be significantly improved (Majumdar et al., 2004, 2003; Gao et al., 2006; Volovitch et al., 2008). Although continuous wave laser has been extensively investigated in terms of laser surface modification of Mg alloys, there is a lack of study about pulsed laser. Compared with continuous wave laser, the high peak power of a single pulse produced by the pulse laser can readily reach the threshold of high absorbtivity of Mg which is around the melting point, thus resulting in better absorption. The short duration time of laser pulse which means short heating time can also contribute

* Corresponding author. Tel.: +1 865 974 3609; fax: +1 865 974 4115.
E-mail address: ndahotre@utk.edu (N.B. Dahotre).

0924-0136/$ – see front matter © 2009 Elsevier B.V. All rights reserved.
doi:10.1016/j.jmatprotec.2009.02.004

Please cite this article in press as: Samant, A.N., et al., Pulsed laser surface treatment of magnesium alloy: Correlation between thermal model and experimental observations. J. Mater. Process. Tech. (2009), doi:10.1016/j.jmatprotec.2009.02.004

to higher cooling rates and subsequent grain refinement and formation of non-equilibrium phases. Besides, by adjusting the duration time, repetition rate, pulse energy, a flexible processing window can be obtained for tailoring and patterning the microstructure and properties of the coating.

The aim of this study was to examine the effect of processing speed on the depth of coating and explore the feasibility of improving wear resistance of Mg alloy using a pulsed laser by forming a ceramic particle reinforced composite coating. A powder mixture of Al_2O_3 (95 wt.%) + Al (5 wt.%) was used as the precursor owing to the ultra hardness and superior tribological properties of alumina (Dong and Bell, 1999). 5 wt.% of aluminum was added to improve the interfacial strength and the wetting behavior between magnesium and alumina (Majumdar et al., 2004). Phase constituents and microstructure was characterized. Furthermore, thermal modeling was carried out to understand the effects of thermal cycle experienced by the materials during the laser treatment and further control over such processing.

2. Experimental

Permanent mould cast (PM) MRI 153 M alloy (Al 7.95, Ca 0.98, Zn < 0.01, Mn 0.2, Sr 0.27, Sn <0.01, Mg bal. wt.%) plates with dimensions of 45 mm × 45 mm × 4 mm were used as a substrate. The precursor comprising of 95 wt.% Al_2O_3 (99.0% purity, polygonal in shape with an average particle size of 10 μm) and 5 wt.% Al (99.5% purity, 10 μm particle size) was mixed with a proprietary organic binder (LISI WI5853, Warren Paint and Color Company, Nashville, TN) and spray deposited to an average thickness of approximately 120 μm on the substrate. The Al_2O_3 and Al particles were evenly distributed in the precursor. JK 701 pulsed Nd:YAG laser with an average power of 400 W was used for laser processing. The laser beam was delivered by a fiber optic system and a 120 mm focal length convex lens providing a defocused spot diameter of 500 μm on the surface of substrate. The configuration of the focusing lens assembly provided a uniform beam distribution, in both temporal as well as spatial evolution. Hence it was assumed that the energy is evenly distributed across the pulse. Several laser tracks were laid with minimal overlap (<5%) to cover the entire surface area. As the overlap was very small, no significant overlap effects were observed. The scanning speeds of 21 mm/s, 42 mm/s, 63 mm/s, and 84 mm/s were employed for laser processing at a pulse width of 0.5 ms, repetition rate of 20 Hz, and pulse energy of 4 J using Ar as a cover gas at a pressure of 80 psi (5.5 bar).

Structural characterization was conducted by employing a Philips Norelco X-ray Diffractometer (XRD) with CuK_α radiation (wavelength 1.5418 Å) operating at 20 kV and 10 mA. The scanning angle (2θ) ranged from 20° to 100° with a step size of 0.02° and count time of 1 s. Samples for microstructure observation were cut transverse to the laser track by a low speed diamond saw under oil-cooling condition. These samples were then successively polished with 600, 800, and 1200 grit emery papers. Final polishing was conducted with 0.3 μm alumina suspension on a microcloth and followed by etching with a mixture of 100 ml ethanol, 10 ml acetic acid, 6 ml picric acid, and 20 ml distilled water. A LEO 1525 scanning electron microscope (SEM) was used to observe the microstructure. Microhardness tests were performed with a load of 50 g for 12 s duration by a Vickers microhardness tester (Buehler, Model Number: 1600-6300).

Wear tests were performed by using a pin-on-disc wear and friction monitor (Model: No. TR201EV) according to the ASTM G-99 standard. The experiment was conducted under dry sliding condition at room temperature. The disc with diameter of 100 mm and hardness of HRC 58 was made from EN 32 steel. Cylindrical specimens of 6 mm diameter and 5 mm height were machined from the coated sample and used as the pin. During the wear testing, the pin was placed at a distance 40 mm from the center of the disc rotating at 200 rpm, corresponding to a linear velocity of 0.837 m/s. In the present investigation the total sliding distance was kept constant at 1 km while the load was varied from 5 N to 40 N. The wear rate (mm^3/m) was presented as the total volume lost within the wear track over the entire sliding distance.

3. Computational

The various physical attributes such as depth of melting and other microstructural features during laser processing depend on the temperature distribution and associated cooling rates through the coating and substrate. For this purpose, a thermal model was built in COMSOL's™ heat transfer transient mode to correlate the observed attributes with the laser processing conditions (Harimkar et al., 2006; Harimkar et al., 2007; Basu et al., 2008; Du et al., 2008a; Chen et al., 2008). Geometry in the form of a cube corresponding to the precursor (45 mm × 45 mm × 120 μm) was coupled with another cube representing the substrate (45 mm × 45 mm × 4 mm). The temperature evolution and cooling rates are governed by the energy input to the system and the time for which the surface is exposed to this laser energy (irradiation time). The repetition rate and the pulse width of the laser beam of diameter, 500 μm were taken into account to determine the irradiation time because there was a power off period between two successive pulses. The residence time was estimated using the following relation (Samant et al., 2007):

$$\text{Residence time (s)} = \frac{\text{Repetition rate (Hz)} \times \text{Pulse width (s)} \times \text{Beam diameter (cm)}}{\text{Traverse speed (cm/s)}} \quad (1)$$

Laser processing speeds of 21 mm/s, 42 mm/s, 63 mm/s, and 84 mm/s corresponded to irradiation times of 236.3 μs, 118.0 μs, 78.8 μs, and 59.1 μs respectively. Thus, in this study, the laser beam was considered a quasi-stationary heat source and the coordinate system could be translated along with this heat source. The effect of a moving laser beam was considered to be the same as a stationary beam that is interacting with the surface for a time equal to the residence time. Similar approach has been considered in the past by Harimkar et al. (2006), Du et al. (2008a), Chen et al. (2008), Basu et al. (2008), Ahlström et al. (2004), Arnold et al. (1993) and Patwa and Shin (2007). The residence time predicted for different speeds was input to the model along with the energy density per unit beam cross-sectional area given by:

$$\text{Energy density (W/cm}^2\text{)} = \frac{\text{Incident energy (J)}}{\text{Pulse width (s)} \times \text{Area of incident beam (cm}^2\text{)}} \quad (2)$$

Assuming a uniform beam distribution in both the temporal and spatial evolution, the energy density corresponding to input energy of 4 J, pulse width of 0.5 ms and beam cross-sectional area of 1.96×10^{-3} cm^2 was 4.07×10^6 W/cm^2.

The heat transfer taking place during laser processing was modeled using Fourier's second law of heat transfer:

$$\frac{\partial T(x,y,z,t)}{\partial t} = \frac{k(T)}{\rho C_p(T)}\left[\frac{\partial^2 T(x,y,z,t)}{\partial x^2} + \frac{\partial^2 T(x,y,z,t)}{\partial y^2} + \frac{\partial^2 T(x,y,z,t)}{\partial z^2}\right] \quad (3)$$

where $k(T)$ and $C_p(T)$ are the variations in thermal conductivity and specific heat as a function of temperature (Fig. 1), ρ is the density, T is the temperature field, t is the time and x, y and z are the

Please cite this article in press as: Samant, A.N., et al., Pulsed laser surface treatment of magnesium alloy: Correlation between thermal model and experimental observations. J. Mater. Process. Tech. (2009), doi:10.1016/j.jmatprotec.2009.02.004

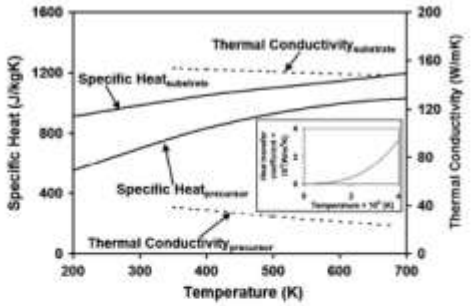

Fig. 1. Variation of thermal conductivity and specific heat of the precursor and substrate with temperature. Inset: Variation of heat transfer coefficient with temperature.

spatial directions. Using the law of mixtures, the density of precursor was computed to be 3278 kg/m^3 that also took into account the porosity of the precursor layer (~12% from the optical micrographs using Image J[IM] software) while the density of the substrate (MRI 153 M Mg) was found to be 1774.24 kg/m^3. As laser surface melting is a rapid heating and cooling process, the thermophysical properties of materials under laser irradiation change rapidly over a large temperature range. Hence, variation of thermal conductivity and specific heat were considered as a function of temperature for both the precursor and the substrate for improving the accuracy of simulations (Fig. 1) (Touloukian, 1967). The latent heat of solidification was accounted for by incorporating the variation of specific heat as a function of temperature. This took into consideration the phase change due to melting. At time $t=0$, the initial temperature of $T-T_0=300$ K was applied.

The balance between the absorbed laser energy at the surface and the losses due to radiation was given by:

$$-k(T)\left(\frac{\partial T(x,y,0,t)}{\partial x}+\frac{\partial T(x,y,0,t)}{\partial y}+\frac{\partial T(x,y,0,t)}{\partial z}\right) = \delta a I-\varepsilon\sigma(T(x,y,0,t)^4-T_0^4) \quad (4)$$

$\delta=1$ when $0\le t\le t_r$

$\delta=0$ when $t>t_r$

where I is the laser energy density predicted above in Eq. (2), $k(T)$ is the temperature dependent thermal conductivity of the material (Fig. 1), ε is the emissivity for thermal radiation, t_r is the irradiation time (Eq. (1)), σ is Stefan–Boltzman constant (5.67×10^{-8} W/m^{2}K^4), and a is the absorptivity of the material. The term δ takes a value of 1 when time, t is less than irradiation time, t_r and it is 0 when time, t exceeds irradiation time. Thus the value of δ depends on the pulse on time and ensures that the energy is input to the system only during the irradiation time and cuts off the energy supply after that during pulse off time. The laser energy is incident on the precursor and it is then transferred to the substrate by different heat transfer phenomena. Hence, only the absorptivity of the precursor was considered for calculations. Furthermore, as the reflection of a mixture of opaque particles is a function of the relative surface area (Schatz, 1967), the surface-area percent of the precursor was used to evaluate the absorptivity of the precursor. In order to determine the surface-area percent, the weight percent of the components of the precursor (Al_2O_3 and Al) was converted into volume percent. The size of all the particles being same, it was assumed that volume percent was the same as surface-area percent. Thus, considering 12% porosity, 95 wt.% Al_2O_3 and 5 wt.% Al were equivalent to 82 and 6 area % respectively. In situ absorptivity measurements in short duration high energy density dynamic process such as laser–material interaction being extremely difficult, values of absorptivity of precursor components (0.8 for Al_2O_3 and 0.17 for Al at 1.06 μm wavelength) commonly found in literature (Touloukian, 1967) along with their surface-area percent mentioned above were used for calculations yielding an absorptivity value for the precursor of 0.66. Nonetheless, attempts are ongoing for measuring absorptivity under laser processing conditions similar to the ones employed in this study and they will be incorporated in future simulations. Also, as for a given material and processing condition, the absorptivity is equal to the emissivity (Sturge, 2003), emissivity was also taken as 0.66.

The convection at the bottom surface of the sample was given by:

$$-k(T)\left(\frac{\partial T(x,y,D,t)}{\partial x}+\frac{\partial T(x,y,D,t)}{\partial y}+\frac{\partial T(x,y,D,t)}{\partial z}\right) = h(T(x,y,L,t)-T_0), \quad (5)$$

where D is the thickness of the sample which was taken as 4.12 mm (120 μm for the precursor +4 mm for the substrate) and $h(T)$ is the heat transfer coefficient (W/m^2 K) which was included as a function of temperature (inset in Fig. 1) (Incropera and Dewitt, 2002). Even though the sample was sufficiently thick (4.12 mm), it was not assumed to be a semi-infinite body and convection from bottom surface was not neglected in order to improve accuracy of calculations by considering all modes of heat transfer on the laser process as also done by Shuja and Yilbas (2000) and by Yilbas and Mansoor (2006). A non-uniform grid was used for simulations with a finer mesh under the laser beam as compared to the rest of the geometry where temperatures and their gradients are highest (Patwa and Shin, 2007). The grid independence test was conducted and mesh size of approximately 53,000 elements resulted in a grid independent solution. The temperature profiles were obtained by running the simulations with extremely small time steps of 10 μs in order to incorporate the changes in surface temperature during the residence time due to laser scanning speed. The corresponding cooling rates (slope of the cooling curve at different time instants) and depth of melting were obtained from these computations and their correlations with the processing conditions are discussed in the later part of this study.

4. Results and discussion

The microstructure and structural characterization of the laser processed samples was carried out and an attempt was made to correlate them with the thermal modeling predictions as discussed in this section.

4.1. Structural characterization

Structural characterization of the coating was carried out in order to see the effect of laser processing on the phase distribution and corresponding microstructure in the surface and subsurface regions. In light of this, the overlay of XRD patterns obtained from the surface of the sample is shown in Fig. 2. The major phases present in the coating are α-Mg and Al_2O_3, and some minor peaks belonging to $Al_{0.9}Mg_{3.1}$ and MgO were also detected. In general, the coatings produced using different laser scan speeds have similar XRD patterns, and only the peak intensity of each phase varied, illustrating that a relatively broad processing window can be used without affecting the phase constituents of the composite coating considered in the present work. The laser–material interaction leads to the melting of the precursor (Al + Al_2O_3) and a portion of the substrate (MRI 153 M Mg). The subsequent cooling and solidification result in evolution of the phases listed above. The formation

Please cite this article in press as: Samant, A.N., et al., Pulsed laser surface treatment of magnesium alloy: Correlation between thermal model and experimental observations. J. Mater. Process. Tech. (2009), doi:10.1016/j.jmatprotec.2009.02.004

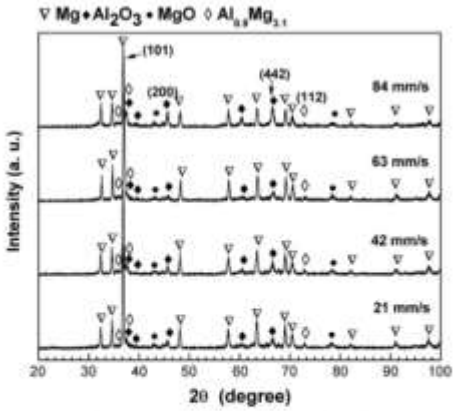

Fig. 2. XRD patterns of the laser processed samples.

of MgO is attributed to the following reaction (Ragone, 1995):

$$\begin{aligned} &Mg + O = MgO \quad \Delta G = -603,960 + 142.05T - 5.36T \ln T \,(298\,K \le T \le 923\,K) \\ &\Delta G = -608,140 + 112.76T - 0.44T \ln T \,(923\,K \le T \le 1380\,K) \end{aligned} \tag{6}$$

From the Gibbs free energy of the above reaction, it can be found that Mg possesses a high affinity to O, which can come from the environment and/or dissociated/melted Al_2O_3 due to the high temperature attained during the process. However, the presence of Al_2O_3 in XRD patterns corresponding to all four processing speeds may be due to resolidification of melted Al_2O_3 and/or reconstitution of decomposed/dissociated Al_2O_3 through the following reaction

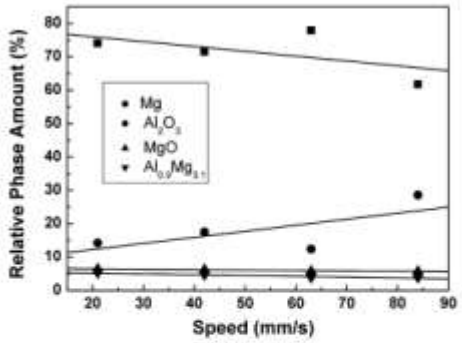

Fig. 3. Relative phase amount as a function of laser processing speed.

(Gaskell, 1995):

$$2Al_{(l)} + 1.5O_{2(g)} = Al_2O_{3(s)}$$

$$\Delta G = -1,687,200 + 326.8T \,(993 \le T \le 2327\,K) \tag{7}$$

A semiquantitative analysis of the relative amount of each phase was conducted using the following formula (Greish and Brown, 2003; Du et al., 2008b):

$$\%I_i = \frac{I_i}{\sum_1^4 I_i} \tag{8}$$

where I_i is integrated peak intensity of the phase in concern and $\sum_1^4 I_i$ corresponds to the sum of integrated peak intensity of each of the four phases in the present composite coating. The corresponding plans of the peaks used in the calculation are indicated in Fig. 2 and the result of semiquantitative analysis is shown in Fig. 3. A

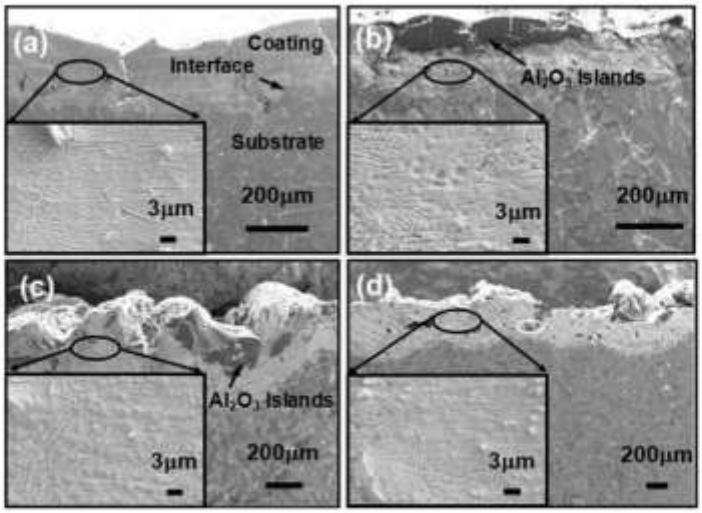

Fig. 4. SEM images of the laser processed samples: (a) 21 mm/s, (b) 42 mm/s, (c) 63 mm/s, and (d) 84 mm/s. (Inset: High magnification image of the coating showing the secondary dendrites.)

Please cite this article in press as: Samant, A.N., et al., Pulsed laser surface treatment of magnesium alloy: Correlation between thermal model and experimental observations. J. Mater. Process. Tech. (2009), doi:10.1016/j.jmatprotec.2009.02.004

Table 1
Variation of measured melt depth, residence time, diffusion length, maximum cooling rate and microhardness (in coating and substrate) with processing speed.

Speed (mm/s)	Average measured melt depth (μm)	Residence time (μs)	Diffusion length (μm)	Maximum cooling rate × 10^6 (K/s)	Average microhardness in coating (HV)	Average microhardness in substrate (HV)
21	363 ± 100.26	236.3	28.2	0.96	117.52 ± 3.97	80.87 ± 5.17
42	317 ± 114.35	118.0	19.9	1.23	114.24 ± 8.37	93.1 ± 4.81
63	279 ± 55.29	78.8	16.2	1.89	110.04 ± 12.23	83.56 ± 0.64
84	224 ± 68.88	59.1	14.1	1.98	120.46 ± 9.09	102.4 ± 2.19

decreasing trend of the Mg-containing phases (α-Mg, $Al_{0.9}Mg_{3.1}$ and MgO) with the increasing laser scan speed is observed while the relative amount of Al_2O_3 showed a reverse trend. With the fact that the precursor thickness was same (120 μm) for all processing speeds, the laser material interaction time decreased with increasing speed leading to observed trend in the phase content. It also appeared that although Mg may have suffered some evaporative losses during laser processing due to its low boiling point (Li et al., 1993), it had a marginal effect on the trend of relative amount of phases in the coating. As seen later, based on the thermal modeling and experimental observation, it is found that the measured coating thickness decreased from 363 μm to 224 μm with increased laser processing speed from 21 mm/s to 84 mm/s due to the corresponding decrease in laser–material interaction time.

4.2. Microstructural evolution and thermal predictions

Cross-sectional views of the samples treated at different laser processing speeds are shown in Fig. 4. The composite coating on the surface has a wavy surface texture due to the overlap pulse processing. The distinct interface between the coating and substrate shows a sound metallurgical joint. Moreover, it can be found that the heat affected zone (HAZ) is practically negligible, which is indicative of localized heating associated with the laser beam.

Due to the uneven profile, the depth of melting was measured at ten different locations in three different cross-sectional areas and the average value was reported for each processing speed along with the standard deviation corresponding to the scatter in measurements (Table 1). An increase in the processing speed from 21 mm/s to 84 mm/s reduced the residence time from 236.3 μs to 59.1 μs respectively. As the effective laser energy going into the material system reduced with residence time, less material melted and average melt depth decreased with increased speed. These measured melt depths were compared with values predicted using temperature distribution profiles as seen later in this study.

The coating mainly consisted of polygonal particles (indicated by white circle in Fig. 4d) in addition to highly refined cellular dendritic grain structure (insets in Fig. 4). The EDS analysis on these polygonal particles provided an Al to O ratio close to 0.67, thus confirming that they are Al_2O_3 particles from the precursor. The highly refined cellular dendritic grain structure is attributed to extremely high cooling rates associated with laser processing. The average composition of the cellular dendrite measured by EDS is 83 at.% Mg, 11.1 at.% Al, 2.4 at.% O, 1.0 at.% Ca, 1.4 at.% Mn, 0.6 at.% Zn, 0.4 at.% Sn and 0.1 at.% Sr, illustrating that it is mainly a solid solution of α-Mg with other elements. In order to see the effect of the laser processing speed on the formation of dendrites, the average SDAS (secondary dendrite arm spacing) values corresponding to each processing speed were obtained using the linear intercept method (Fig. 5a). This method involves measuring the distances (spacings) between secondary dendrite arms along a line normal to the dendrite arms. This procedure was repeated for five different image frames and the average SDAS is represented in Fig. 5b along with the corresponding error bars (Harimkar et al., 2006). The correlation between the measured SDAS and the predicted cooling rates is discussed later.

The temperature profiles for different processing speeds obtained from Eqs. (1)–(5) above are presented in Fig. 6. The decrease in residence time and corresponding input laser energy with increase in processing speed reduced the maximum surface temperature. As the temperature distribution into the material evolves as a function of time, maximum melt depth corresponds to the residence time for each of the processing speeds. The maximum temperatures reached under all four processing speeds are sufficiently higher than the melting point of alumina (2323 K (Touloukian, 1967)). Hence, the total melt depth was predicted by tracing the location of melting point of magnesium (923 K (Touloukian, 1967)), the lowest melting component of the system) in the temperature distribution within the material (Fig. 7a) because the content of magnesium in substrate (~90 wt.%) was more than the other elements.

Although, the maximum temperatures reached under all four processing speeds were sufficiently higher than melting point of alumina (2323 K (Touloukian, 1967)) (Fig. 6), the residence time varied for all speeds which in turn decides if alumina particles

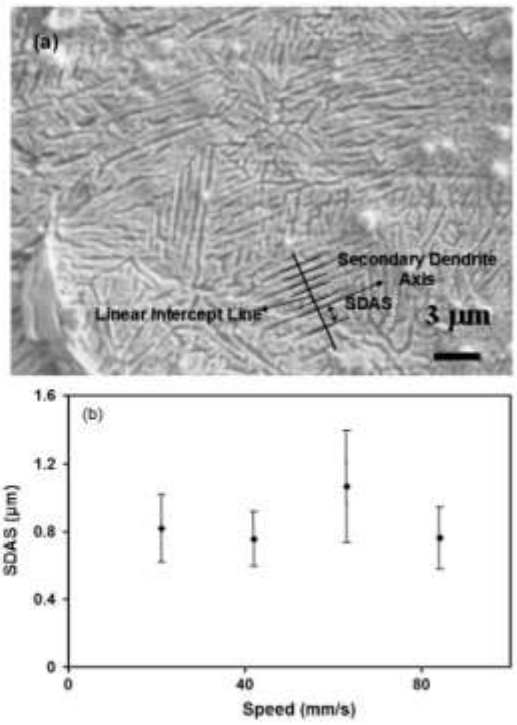

Fig. 5. (a) Secondary dendrite arm spacing (SDAS) measurement from a high magnification SEM image using linear intercept method. (b) Variation of SDAS with processing speed.

Please cite this article in press as: Samant, A.N., et al., Pulsed laser surface treatment of magnesium alloy: Correlation between thermal model and experimental observations. J. Mater. Process. Tech. (2009), doi:10.1016/j.jmatprotec.2009.02.004

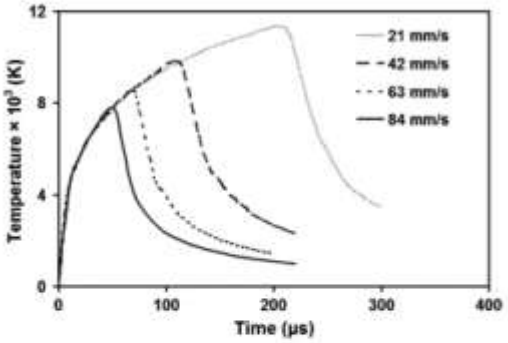

Fig. 6. Surface temperature profiles for different processing speeds.

of average size 10 μm in the original precursor are likely to completely melt. Hence in order to determine if the processing speeds employed in the present work were capable of melting the alumina particles through their core (i.e. reaching melting temperature at the center) in the precursor, the spatial decay in the temperature distribution (diffusion length) at the melting point of alumina was predicted for each case and was compared with the radius of the alumina particles (5 μm). For directional heat flow problems, the diffusion length, l_H can be approximated using the thermal diffusivity, χ given by $k(T)/\rho C_p(T)$, and the residence time t_r as follows (Daniel et al., 2008; Bäuerle, 2000):

$$l_H = 2\sqrt{\chi t_r} \tag{9}$$

At the melting point of alumina its thermal diffusivity is 8.43×10^{-7} m²/s, density is 3800 kg/m³ (Touloukian, 1967), thermal conductivity is 6.27 W/mK and specific heat is 1958 J/kg K. It is seen from Table 1 that the predicted diffusion length for each processing speed is much more than the radius of an alumina particle. Thus, for all the cases considered in this study, temperatures higher than the melting point of alumina were attained at the core (center) of the particle and alumina seen in the melted region (Fig. 2) for all speeds; may have reconstituted, as mentioned earlier, through resolidification and/or reaction between Al and O. Furthermore, majority of such reconstituted alumina particles within the matrix of coating are refined (Fig. 4) due to the rapid cooling rates (as explained later) associated with all processing speeds employed in the present work where as few particles are reconstituted as islands in the near surface region (Fig. 4b and c).

Also, the melting point of alumina which is much higher than that of aluminum (933 K (Touloukian, 1967)) was traced to estimate the quantity of melted and reconstituted alumina from the original precursor layer under different processing speeds (Fig. 7b). It can be observed from Fig. 7b that for the processing speeds of 21, 42, and 63 mm/s the melting temperature of alumina reached to the depth equal to or greater than 120 μm indicating that all alumina particles within the original precursor layer of 120 μm thickness completely melted and reconstituted in the final melt region. Where as for the fastest speed (84 mm/s) the melting temperature of alumina can be traced only to the depth of 95 μm (Fig. 7b) suggesting that the alumina particles within the bottom 25 μm thick precursor layer were retained without undergoing any melting in the final melt region. As the original precursor mixture contained 95 wt.% (82 volume%) alumina, only 19.8 wt.% (17 volume%) unmelted alumina was retained in the final melt region corresponding to the fastest speed (84 mm/s). In essence, due to the extremely rapid cooling rates associated with all laser processing speeds (as explained later) first three speeds produced very fine reconstituted alumina and the fastest speed provided a mixture of reconstituted (83 volume%) and retained (unmelted) (17 volume%) alumina (Fig. 4). Thus the laser processing speed can be varied to control the content of retained and/or reconstituted alumina in the coating. It can be observed from Fig. 8 that the final melt depths predicted using the model proposed earlier were in close match with experimentally measured values. Furthermore,

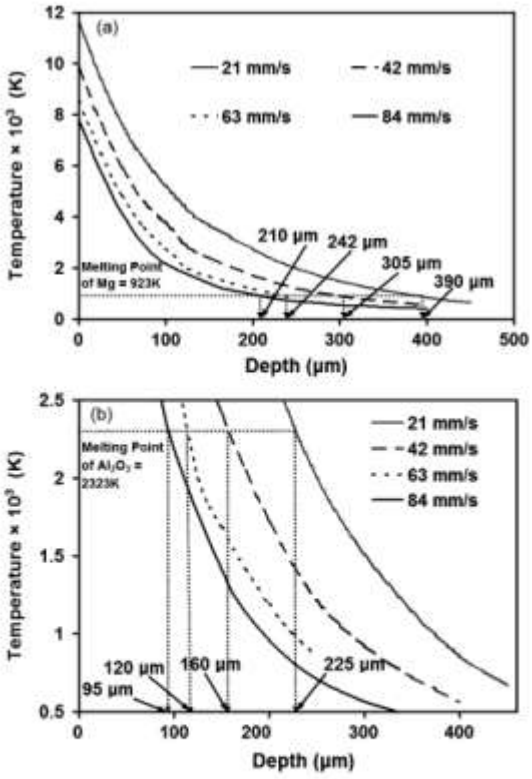

Fig. 7. (a) Prediction of total (final) melt depth. (b) Prediction of melt depth corresponding to the melting point of alumina for different processing speeds.

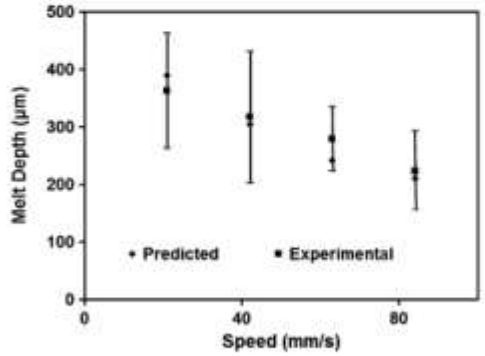

Fig. 8. Comparison between experimental and predicted final melt depth.

Please cite this article in press as: Samant, A.N., et al., Pulsed laser surface treatment of magnesium alloy: Correlation between thermal model and experimental observations. J. Mater. Process. Tech. (2009), doi:10.1016/j.jmatprotec.2009.02.004

as explained above, similar to experimental values, predicted final melt depth also decreased with increase in processing speed. Slight discrepancy between predicted and experimental values could be due to non-uniform nature of the melt pool as mentioned earlier and limitations of the software (Image J™) employed for conducting these measurements.

The slope of the temperature profiles discussed earlier (Fig. 6) gave the cooling rates presented in Table 1. An increase in processing speed from 126 cm/min to 508 cm/min increased the maximum cooling rate from 0.96×10^8 K/s to 1.98×10^8 K/s. Thus, even though the cooling rates were extremely high (of the order of 10^8 K/s), there was a marginal difference in the magnitudes of cooling rates for different processing speeds. According to solidification theory, SDAS is a function of the cooling rate (Kurz and Fisher, 1998). Hence marginal variation in cooling rates (Table 1) was responsible for minor changes in SDAS values observed for different processing speeds (Fig. 5b). Furthermore, the manifestation of marginal variation in these physical attributes of the melted regions produced under the present set of laser processing parameters is also realized in the mechanical properties of the coating.

Thus the size of the melt pool and associated properties of the precursor could be controlled/modified by varying the laser processing speed and a thermal model can be used to successfully predict the solidification characteristics during pulsed laser surface treatment of MRI 153 M Mg alloy.

4.3. Microhardness and wear resistance

Microhardness was measured on the cross-sectional plane transverse to the laser track. The variation of microhardness distributions for melt regions corresponding to all processing speeds remained within the same range and, in general the hardness of melt region was 1.5–2.0 times higher than the substrate (Fig. 9). The interface between the melt pool and the substrate (melt depth) is also shown in Fig. 9 for all the processing speeds to illustrate the depth from which there is a drop in hardness corresponding to the unmelted substrate. The average values of the microhardness for the coating and the substrate are represented in Table 1 along with the corresponding scatter in data. Thus, the precursor composition of 95 wt.% Al_2O_3 and 5 wt.% Al was able to improve the hardness of MRI 153 M Mg alloy.

Wear rate at different applied load for both the as-received substrate and laser treated samples are shown in Fig. 10. As expected, the wear rate increased with the increase in applied load for both materials. Compared with the substrate, a substantial reduction of wear rate of the laser treated samples was observed at all loads, indicating an improvement of wear resistance for the coatings. This was also in accordance with the increase of microhardness in laser

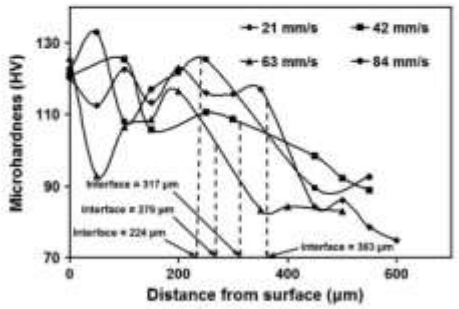

Fig. 9. Microhardness variation for different processing speeds.

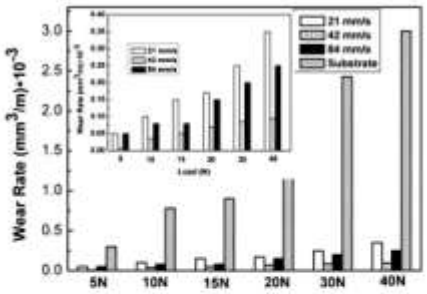

Fig. 10. Wear rate of substrate and laser treated samples at different applied load. (Inset: Detailed view of wear rate of the coatings.)

processed coatings (Fig. 9), since hardness plays an important role in wear behavior for materials and is generally used as a measurement of wear resistance (Chen et al., 2009). This improvement of wear resistance in the laser treated samples could be explained by considering its different wear mechanisms from that of the substrate. It has been shown in the literature (Mondal et al., 2008; Chen et al., 2009) that micro grooving and micro cutting are the dominant wear mechanisms for Mg alloys, and due to the low microhardness and poor ductility a high wear loss is expected for Mg alloys. Nevertheless, for the laser processed coatings which are composite in nature, both the hard reinforcement (predominantly Al_2O_3) and the highly refined Mg matrix considerably improved the wear resistance (Du et al., 2008c). The Al_2O_3 particles can effectively prevent grooving and ploughing during the wear process, while the highly refined dendrites of Mg play the role of strong and ductile metal matrix.

In order to explore the influence of laser processing parameters on the wear behavior of the laser treated samples, a detailed comparison of the wear resistance of the composite coatings were shown in the inset in Fig. 10. In comparison, the coatings processed with laser scan speeds of 21 mm/s, 84 mm/s, and 42 mm/s experienced the high, medium and low wear rates respectively. In the current investigation the processing parameter varied was laser scan speed, which is the predominant factor affecting the temperature of melting pool and cooling rate. As explained earlier, the level of temperature determined the extent of retained Al_2O_3 particles whereas the cooling rate controlled the level of refinement in grain size (SDAS) and the size of reconstituted Al_2O_3. From Table 1 it can be seen that the sample processed with 21 mm/s was associated with the lowest cooling rate (0.98×10^8 K/s) among all the laser processed samples and the SDAS of this sample (Fig. 5) showed a relatively higher value. This coating consisted of relatively coarser dendrites and reconstituted Al_2O_3 particles, thus experiencing the high wear rate. Nevertheless, it is interesting to note that the sample processed with 84 mm/s experienced lower temperature (Fig. 4) and the highest cooling rate (Table 1) that were responsible for retention of Al_2O_3 along with formation of refined and reconstituted Al_2O_3 leading to medium wear rate. On the other hand, the samples processed with 42 mm/s (medium cooling rate: 0.98×10^8 K/s) contained only refined and reconstituted Al_2O_3 due to which it exhibited the lowest wear rate of 0.095×10^{-3} mm³/m at the applied load of 40 N which was approximately 30 times less than that of as-received substrate (3×10^{-3} mm³/m). Such contrast behavior is attributable to the refinement of the grain structure and presence of retained Al_2O_3. It is likely that retained Al_2O_3 particles may cause detrimental effect to wear resistance of the composite coatings. Coating with retained Al_2O_3 particles may lead to less wear resistance because of the their coarse size inherited from the

Please cite this article in press as: Samant, A.N., et al., Pulsed laser surface treatment of magnesium alloy: Correlation between thermal model and experimental observations. J. Mater. Process. Tech. (2009), doi:10.1016/j.jmatprotec.2009.02.004

precursor powder (10 μm) and their poor interface with the Mg matrix compared with that of in situ formed (reconstituted) Al_2O_3 particles. Such poor interface between particles and matrix might cause pulling out of the particles. As a result, although the coating processed at 84 mm/s is associated with the highest cooling rate and finest microstructure, it showed a medium wear resistance due to retained Al_2O_3. On the contrary, coating produced at 42 mm/s exhibited the highest wear resistance as it consisted of a combination of fully reconstituted and refined Al_2O_3 and it was associated with a moderately high cooling rate. This result also provided an indication that processing parameters that lead to fully reconstituted Al_2O_3 particles as well as fine microstructure should be considered for tailoring and optimizing the wear properties of such composite coating.

5. Conclusion

MRI 153 M Mg alloy was successfully coated with 95 wt.% Al_2O_3 and 5 wt.% Al by using a pulsed Nd:YAG laser. Structural characterization showed that the coating consisted of α-Mg, Al_2O_3, $Al_{0.9}Mg_{3.1}$ and MgO. The average measured melt depth decreased from 363 μm to 224 μm as the laser processing speed increased from 126 cm/min to 508 cm/min due to the decrease in residence time (from 236.3 μs to 59.1 μs). Thermal predictions showed that only the sample processed with 84 mm/s had retained alumina along with major portion of reconstituted alumina, while other processing speeds lead to coatings with only the reconstituted alumina. The maximum predicted cooling rate increased from 0.96×10^8 K/s to 1.98×10^8 K/s with increase in speed from 21 to 84 mm/s. These extremely high cooling rates were responsible for the formation of fine dendrites which had secondary dendrite arm spacing (SDAS) of around 1 μm. Microhardness increased from ~80 HV for the substrate to ~120 HV for the coating. Due to the presence of hard Al_2O_3 particles and highly refined Mg grains the wear rate decreased substantially compared with that of the substrate (3×10^{-3} mm^3/m) and the sample processed with 42 mm/s showed the best resistance to wear (0.095×10^{-3} mm^3/m).

References

Abbas, G., Liu, Z., Skeldon, P., 2005. Corrosion behavior of laser-melted magnesium alloys. Appl. Surf. Sci. 247, 347–353.
Ahlström, J., Karlsson, B., Niederhauser, S., 2004. Modelling of laser cladding of medium carbon steel—a first approach. J. Phys. IV France 210, 405–412.
Arnold, N., Kullmer, R., Bäuerle, D., 1993. Simulation of growth in pyrolytic laser-CVD of microstructures-I. One dimensional approach. Microelectron. Eng. 20, 31–41.
Basu, A., Samant, A.N., Harimkar, S.P., Majumdar, J.D., Manna, I., Dahotre, N.B., 2008. Laser surface coating of Fe–Cr–Mo–Y–B–C bulk metallic glass composition on AISI 4140 steel. Surf. Coat. Technol. 202, 2623–2631.
Bäuerle, D., 2000. Laser Processing and Chemistry. Springer, Berlin.
Cao, X., Jahazi, M., Immarigeon, J.P., Wallace, W., 2006. A review of laser welding techniques for magnesium alloys. J. Mater. Process. Technol. 171, 188–204.
Chen, Y., Samant, A., Balani, K., Dahotre, N.B., Agarwal, A., 2008. Effect of laser melting on plasma sprayed aluminum oxide coatings reinforced with carbon nanotubes. Appl. Phys. A 94, 861–870.
Chen, T.J., Ma, Y., Li, R., Li, Y.D., Hao, Y., 2009. Effects of processing parameters on wear behaviors of thixoformed AZ91D magnesium alloys. Mater. Des. 30, 235–244.
Daniel, C., Armstrong, B.L., Howe, J.Y., Dahotre, N.B., 2008. Controlled evolution of morphology and microstructure in laser interference-structured zirconia. J. Am. Ceram. Soc. 91, 2138–2142.
Dong, H., Bell, T., 1999. Tribological behavior of alumina sliding against Ti6Al4 V in unlubricated contact. Wear 225–229, 874–884.
Draper, C.W., Ewing, C.A., 1984. Laser surface alloying: a bibliography. J. Mater. Sci. 19, 1815–1825.
Du, R., Samant, A.N., Paital, S.R., Dahotre, N.B., 2008a. Pulsed laser synthesis of ceramic–metal composite coating on steel. Appl. Surf. Sci. 255, 3188–3194.
Du, R., Paital, S.R., Dahotre, N.B., 2008b. Phase constituents and microstructure of laser synthesized TiB_2–TiC reinforced composite coating on steel. Scr. Mater. 59, 1147–1150.
Du, R., Zou, Z., Wang, X., Qu, S., 2008c. Laser cladding of in situ TiB_2/Fe composite coating on steel. Appl. Surf. Sci. 254, 6489–6494.
Gao, Yali, Wang, Cunshan, Lin, Qi, Liu, Hongbin, Yao, Man, 2006. Broad-beam laser cladding of Al–Si alloy coating on AZ91HP magnesium alloy. Surf. Coat. Technol. 201, 2701–2706.
Gaskell, D.R., 1995. Introduction to Thermodynamics of Materials. Taylor Francis, Washington, DC.
Gray, J.E., Luan, B., 2002. Protective coatings on magnesium and its alloys—a critical review. J. Alloy Compd. 336, 88–113.
Greish, Y., Brown, P., 2003. Phase evolution during the formation of stoichiometric hydroxyapatite at 37.4 °C. J. Biomed. Mater. Res. 67, 632–637.
Harimkar, S.P., Samant, A.N., Khangar, A.A., Dahotre, Narendra, B., 2006. Prediction of solidification microstructures during laser dressing of alumina-based grinding wheel material. J. Phys. D: Appl. Phys. 39, 1642–1649.
Harimkar, S.P., Samant, A.N., Dahotre, N.B., 2007. Temporally evolved recoil pressure driven melt infiltration during laser surface modifications of porous alumina ceramic. J. Appl. Phys. 101, 054911.
Incropera, F.P., Dewitt, D.P., 2002. Fundamentals of Heat and Mass Transfer. J. Wiley, New York.
Kurz, W., Fisher, D.J., 1998. Fundamentals of Solidification. Trans Tech Publications, Zurich.
Li, G.H., Gill, H.S., Varin, R.A., 1993. Magnesium silicide intermetallic alloys. Metall. Trans. A 24, 2382–2391.
Majumdar, J.D., Chandra, B.R., Modike, B.L., Galun, R., Manna, I., 2004. Laser surface engineering of a magnesium alloy with Al + Al_2O_3. Surf. Coat. Technol. 179, 297–305.
Majumdar, J.D., Chandra, B.R., Galun, R., Modike, B.L., Manna, I., 2003. Laser composite surfacing of a magnesium alloy with silicon carbide. Surf. Coat. Technol. 63, 771–778.
Mondal, A.K., Kumar, S., Blawert, C., Dahotre, N.B., 2008. Effect of laser surface treatment on corrosion and wear resistance of ACM720 Mg alloy. Surf. Coat. Technol. 202, 3187–3198.
Patwa, R., Shin, Y.C., 2007. Predictive modeling of laser hardening of AISI 5160 steels. Int. J. Mach. Tools Manuf. 47, 307–320.
Ragone, D.V., 1995. Thermodynamics of Materials. J. Wiley & Sons, New York.
Samant, A.N., Harimkar, S.P., Dahotre, N.B., 2007. Laser beam operation mode dependent grain morphology of alumina. J. Appl. Phys. 102, 123105.
Schatz, E.A., 1967. Reflectance of compacted powder mixtures. J. Opt. Soc. Am. 57, 941–942.
Shuja, S.Z., Yilbas, B.S., 2000. 3-Dimensional conjugate laser heating of a moving slab. Appl. Surf. Sci. 167, 134–148.
Sturge, M.D., 2003. Statistical and Thermal Physics, Fundamentals and Applications. A.K. Peters Ltd., Natick.
Touloukian, Y.S., 1967. Thermophysical Properties of High Temperature Materials. IFI/Plenum, New York.
Volkova, E.L., 2006. Modern magnesium-base deformable alloys and composite materials (a review). Met. Sci. Heat Treat. 48, 473–478.
Volovitch, P., Masse, J.E., Fabre, A., Barrallier, L., Saikaly, W., 2008. Microstructure and corrosion resistance of magnesium alloy ZE41 with laser surface cladding by Al–Si powder. Surf. Coat. Technol. 202, 4901–4914.
Wang, A.A., Sircar, S., Mazumder, J., 1993. Laser cladding of Mg–Al alloys. J. Mater. Sci. 28, 5113–5122.
Ye, H.Z., Liu, X.Y., 2004. Review of recent studies in magnesium matrix composites. J. Mater. Sci. 39, 6153–6171.
Yilbas, B.S., Mansoor, S.B., 2006. Laser evaporative heating of surface: simulation of flow field in the laser produced cavity. J. Phys. D: Appl. Phys. 39, 3863–3875.
Yue, T.M., Su, Y.P., Yang, H.O., 2007. Laser cladding of $Zr_{52}Al_{10}Ni_{13}Cu_{15}$ amorphous alloy on magnesium. Mater. Lett. 61, 209–212.
Yue, T.M., Lin, T., 2008. Laser cladding of Ni/Cu/Al functionally graded coating on magnesium substrate. Surf. Coat. Technol. 202, 3043–3049.
Yue, T.M., Su, Y.P., 2007. Laser multi-layer cladding of $Zr_{52}Al_{10}Ni_{13}Cu_{15}$ amorphous alloy on magnesium substrates. J. Mater. Sci. 42, 6153–6160.

Please cite this article in press as: Samant, A.N., et al., Pulsed laser surface treatment of magnesium alloy: Correlation between thermal model and experimental observations. J. Mater. Process. Tech. (2009), doi:10.1016/j.jmatprotec.2009.02.004

JOURNAL OF MATERIALS PROCESSING TECHNOLOGY 203 (2008) 498–504

journal homepage: www.elsevier.com/locate/jmatprotec

Process optimization in laser surface structuring of alumina

*Anoop N. Samant, Sameer R. Paital, Narendra B. Dahotre**

Department of Materials Science and Engineering, The University of Tennessee, Knoxville, TN 37996, United States

ARTICLE INFO

Article history:
Received 31 July 2007
Received in revised form
11 September 2007
Accepted 23 October 2007

Keywords:
Taguchi method
Nd:YAG laser
Alumina
Optimization
Ceramic

ABSTRACT

The efficacy of pulsed Nd:YAG laser for the laser surface structuring (dressing) of porous alumina ceramic was optimized using the Taguchi analytical procedure. The laser processing parameters like the pulse width, repetition rate and the scanning speed were evaluated and the factors essential to optimize the interdendritic porosity and grain size were predicted. The analysis of variance (ANOVA) helped to identify the processing parameters that contributed the most to minimize the porosity and maximize the grain size. The pulse repetition rate was the most significant factor in minimizing the interdendritic porosity while the scanning speed played a vital role in increasing the grain size. The Taguchi method could yield a combination of different process parameters that could be used to optimize the microstructural features.

1. Introduction

Ceramics such as alumina are seeking increased applications as sophisticated engineering materials where surface alterations are vital (Nicolas et al., 1997; Queiroz et al., 2004). The surface modification processes have a substantial effect on the microstructural properties of the ceramics (Gahr and Schneider, 2000; Cappelli et al., 2000). Such surface modified alumina have increasing applications as they can be used to improve the life of ceramic linings in furnaces (Bradley et al., 1999) and also surface modified abrasive wheels can rejuvenate the surface topography required for precise material machining (Harimkar et al., 2006). Hence, coming up with optimum processing parameters to manipulate the microstrutural features formed during surface modification is extremely vital. Even though modified ceramics have many applications, detailed studies related to microstructure evolution are limited (Harimkar and Dahotre, 2006). Keeping this objective in mind, the current study aims at coming up with laser parameters that can optimize any desirable material property. Pulsed Nd:YAG lasers were used for processing the ceramic as they are capable of delivering superior peak powers with excellent beam quality due to which they are widely used in the manufacturing industries (Bandyopadhyay et al., 2005). Taguchi's method was employed to recognize and configure the experimental parameters for optimum output material properties (interdendritic porosity and grain size). Being a statistically vigorous method (Ross, 1989; Bendell et al., 1989), it requires fewer experiments to be carried out and the inferences can be associated with statistical level of confidence. In addition to this, also the method is more versatile than the standard design of experiments (DOE)

* Corresponding author. Tel.: +1 865 974 3609; fax: +1 865 974 4115.
E-mail address: ndahotre@utk.edu (N.B. Dahotre).
0924-0136/$ – see front matter © 2007 Elsevier B.V. All rights reserved.
doi:10.1016/j.jmatprotec.2007.10.055

Table 1 – Levels for different factors

Factor symbol	Factor name	Levels						
		1	2	3	4	5	6	7
W	Pulse width (ms)	0.5	2	4	5	6	7	8
R	Repetition rate (Hz)	8	10	13.3	16	20	25	–
S	Speed (cm/min)	2.87	5.08	6.35	7.11	7.62	–	–

technique (Montgomery, 1991). Tremendous applications of Taguchi method have enhanced several processes and product reliability and quality (Phadke et al., 1983; Phadke and Dehnad, 1988; Pan et al., 2005). In this approach, an attempt was made to minimize the interdendritic porosity and maximize the grain size of porous alumina ceramic just to demonstrate the ability of the method without any specific application in mind. Similar study can also be carried out to maximize the porosity and/or minimize the grain size.

The alumina that was used for the analysis had 40% by volume porosity. Sintering of the material caused the porosity in the ceramic and such high porosity is required as it could be used for grinding operation. As the laser pulse interacts with the surface of the material, the high cooling rates and corresponding temperature changes in the material will cause the material to solidify with dendritic structures. Such laser-material interaction also affects the porosity between these dendrites. An attempt has been made to optimize this interdendritic porosity so that it could be used for different applications as each application may require variable levels of porosity. Laser processing also produces significant changes in the grain size that would have significant influence on the mechanical properties of the material; hence, optimization of grain size as function of laser process has also been considered.

2. Laser surface processing

A JK 701 pulsed Nd:YAG laser (1064 nm wavelength) from GSI Lumonics, Rugby, England was used for irradiating the surface of alumina ceramic compacts which were obtained from commercial source (MSC Industrial Supply Co., Melville, NY). The laser was capable of providing pulse energy in the range of 0.1–55 J, repetition rates varying from 0.2 to 500 Hz and pulse width could be varied from 0.3 to 20 ms. Effects of laser irradiation on the ceramic surface were observed by taking micrographs of the irradiated surface. Hitachi S3500 SEM was employed for characterizing the surface features.

Variables (control factors) that were selected for parametric study were: pulse width (W), repetition rate (R), and scanning speed (S). The causes (materials and processing parameters) and their key effects (materials properties) related to alumina ceramic are represented in Fig. 1. The illustration clearly emphasizes that causes in various combinations can be controlled for realization of prime effects associated with surface modification of alumina ceramic for required application. As explained later, the correlation between cause and effect can be designed for desired outcome through Taguchi analysis. The repetition rate (R) and the pulse width (W) were varied starting from the lowest possible value to the highest value for different scan speeds and the corresponding effects on the surface microstructure were observed. For certain sets of combination of parameters there was no interaction of the laser beam with the ceramic surface while for certain other combinations, laser cutting (extensive vaporization) occurred on the surface. The main focus of this study was to come up with those parameters that caused surface melting and study the associated porosity and grain size. Hence, the parameters that failed to create any interaction or failed to cause surface melting were not reported in this study. Using this procedure, pulse widths of 0.5, 2, 4, 5, 6, 7, and 8 ms were used for the study along

Table 2 – Experimental layout using an L15 orthogonal array

Trial number	Factors			Factor values		
	W	R	S	Pulse width (ms)	Repetition rate (Hz)	Speed (cm/min)
1	4	1	1	5	8	2.87
2	4	1	5	5	8	7.62
3	4	1	3	5	8	6.35
4	1	5	5	0.5	20	7.62
5	1	5	4	0.5	20	7.11
6	1	5	2	0.5	20	5.08
7	5	1	5	6	8	7.62
8	6	1	5	7	8	7.62
9	7	1	5	8	8	7.62
10	3	2	2	4	10	5.08
11	3	3	2	4	13.3	5.08
12	3	5	2	4	20	5.08
13	2	4	5	2	16	7.62
14	2	5	5	2	20	7.62
15	2	6	5	2	25	7.62

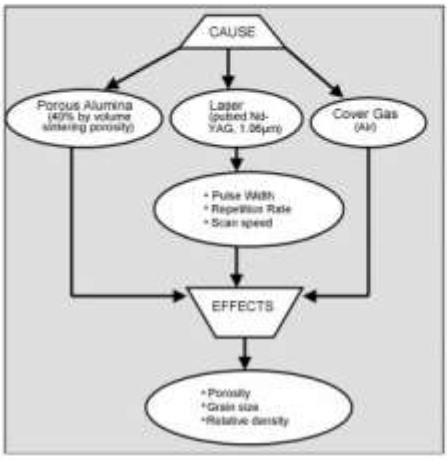

Fig. 1 – Cause-and-effect diagram for laser processing.

with repetition rates of 8, 10, 13.3, 16, 20, and 25 Hz. In addition to these parameters, laser beam scanning speeds of 2.87, 5.08, 6.35, 7.1, and 7.6 cm/min were used. Keeping one parameter constant, others were varied to give the different sets of processing conditions. Table 1 summarizes the values (levels) assigned to the various processing parameters (factors). The combinations of these factors and factor values (levels) provided the conditions of trial runs as indicated later in Table 2. It was observed that surface melting occurred for the combination of the mentioned seven levels of pulse width, six levels of repetition rate and for five levels of scan speed. The progressive reduction of subsequent number of parameters was merely a coincidence without any particular intention to do so. Using these parameters, the experiments were then randomly run and not in any systematic order. By randomizing, the experiment is protected from the influence of lurking variables or noise, such as change of relative humidity, change of ambient temperature and so on which may significantly affect the response. Hence, the standard methodology of randomizing the experimental runs was followed in this study.

Surface micrographs of the processed porous ceramic were recorded for each of the combinations of the different process parameters. ImageJ™ software, a public domain JAVA image processing program inspired by National Institutes of Health (NIH) Image™, was used for analyzing these micrographs to determine the volume percent intendendritic porosity. For this purpose around five micrographs from different locations on the surface were taken for each set of the processing condition. The contrast in the image was enhanced and the image was sharpened using the software following which a binary image was formed from the micrograph. This procedure ensured clear visual distinction between the grains and the pores, thus

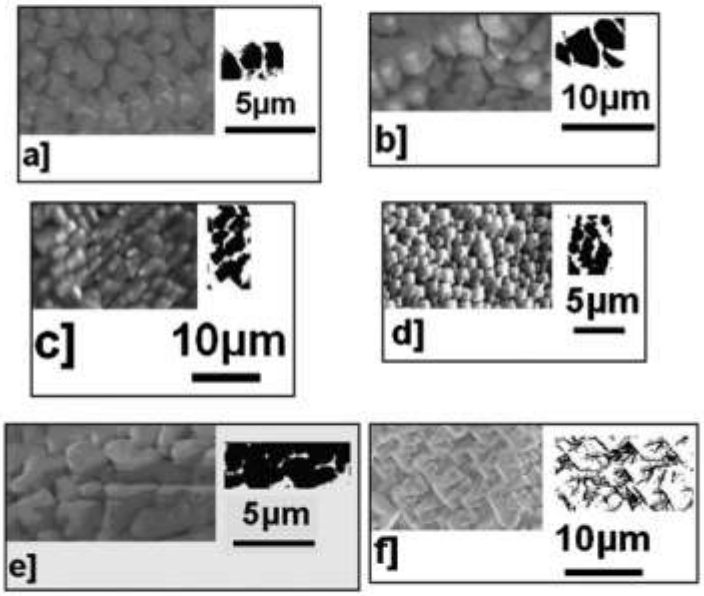

Fig. 2 – Surface SEM images of laser surface modified alumina ceramic. Binary images employed for porosity measurements are displayed on the right side of the SEM image. (a) W = 5 ms, R = 8 Hz, S = 7.62 cm/min, (b) W = 7 ms, R = 8 Hz, S = 7.62 cm/min, (c) W = 4 ms, R = 20 Hz, S = 5.08 cm/min, (d) W = 2 ms, R = 16 Hz, S = 7.62 cm/min, (e) W = 0.5 ms, R = 20 Hz, S = 7.11 cm/min, and (f) W = 0.5 ms, R = 20 Hz, S = 5.08 cm/min.

Table 3 – Results of parametric variation

Experiment	Pulse width (ms)	Repetition rate (Hz)	Speed (in./min)	Grain size (μm)	Interdendritic porosity (vol.%)	Density (g/cm³)	Relative density
Variable speed							
1	5	8	1.133	0.933	33.65	2.52	0.66
2	5	8	3	3.93	23.50	2.90	0.76
3	5	8	2.5	3.1	33.26	2.53	0.66
4	0.5	20	3	1.2	31.48	2.60	0.68
5	0.5	20	2.8	1.81	32.83	2.55	0.67
6	0.5	20	2	4.69	18.52	3.09	0.81
Variable pulse width							
7	6	8	3	3.73	34.71	2.48	0.65
8	7	8	3	4.73	29.70	2.67	0.70
9	8	8	3	1.91	22.86	2.93	0.77
Variable repetition rate							
10	4	10	2	3.97	22.14	2.95	0.77
11	4	13.3	2	3.51	19.24	3.06	0.80
12	4	20	2	2.85	32.56	2.56	0.67
13	2	16	3	3.16	37.45	2.37	0.62
14	2	20	3	1.52	28.05	2.73	0.71
15	2	25	3	2.45	22.86	2.93	0.77

ensuring precise porosity measurements by the software. The mean porosity value was reported by performing calculations for the different micrographs and this value was assumed as representative of the entire volume of the ceramic. Furthermore, the mean grain size was also predicted by the software by measuring the sizes of around 10 grains of roughly the same size in each of the micrographs. This way it ensured that the grain size which was representative for that particular processing condition was calculated. The density of the porous ceramic was calculated using the theoretical density of dense alumina (3.8 g/cm³) (Gitzen, 1970) by using the relation

$$\text{Density of porous ceramic} = (\text{Theoretical density of dense alumina}) \times (1 - \text{pore fraction}) \quad (1)$$

The relative density was given by the ratio of density of porous to fully dense alumina. The micrographs and the corresponding binary images required for calculations are represented in Fig. 2. In Fig. 2, for cases a–e, the black regions in the binary images indicates the grains, while the white region indicates the porosity except in the last case (case f) where the white portion represents the grains with the black regions being the porosity.

3. Taguchi analysis

3.1. Design of orthogonal array and signal-to-noise analysis

The three types of variables that are generally encountered when applying the Taguchi method are signal factors that affect the average response, control factors that affect the extent of variability about the average response and noise factors that have an influence over a response but cannot be controlled in actual applications (Tam et al., 1993). When simulated experiments are performed, the results need to be converted into a signal-to-noise-ratio (S/N) which helps to recognize the optimum conditions of operation. The higher-the-better, the lower-the-better, and, the nominal-the-better are the three categories of quality characteristics. Regardless of the category of the quality characteristic, a greater S/N ratio is essential for better quality characteristics. The degree of freedom (DOF) indicates the amount of information contained in a data set. For each factor, DOF is one less than the number of factor values (levels). In the present case, the total number of degrees of freedom is 15 (6 DOF for pulse width, 5 DOF for repetition rate, and 4 DOF for scanning speed). The number of experiments should be equal to or greater than the number of degrees of freedom (Ross, 1989). A special arrangement of orthogonal arrays was made in order to examine all the designed parameters at a relatively low cost. Orthogonality implies that the factors can be assessed separately and the effect of one factor does not interfere with the estimation of the influence of another factor (Ross, 1989). Hence, an L15 orthogonal array was employed as it could provide the minimum degrees of freedom required for the experimental exploration. The column assignment and experimental layout are shown in Table 2.

S/N ratio was calculated in order to measure the quality characteristic deviating from the desired value. The S/N ratio η is given by $\eta = -10\log(\text{M.S.D.})$, where M.S.D. is the mean square deviation for the output characteristic. The mean-square-deviation (M.S.D.) for the lower-the-better quality characteristic can be expressed as (Yang and Tarng, 1998)

$$\text{M.S.D} = \frac{1}{m}\sum_{i=1}^{m} Y_i^2. \quad (2)$$

Table 4 – Raw data and S/N ratios

Trial number	Porosity 1	Porosity 2	S/N^P	Grain size 1	Grain size 2	S/N^G
1	34.2	33.1	−30.5409	1.3	0.93	10.12751
2	27.4	19.6	−27.5394	4.86	4.07	22.43675
3	32.2	34.32	−30.4429	2.45	3.33	18.45716
4	24.1	38.86	−30.1931	1.05	1.03	9.794257
5	31.6	34.06	−30.3315	1.84	1.76	14.64144
6	14.04	23.01	−25.6025	4.38	4.21	22.19659
7	31.02	38.4	−30.8579	3.33	2.94	19.41674
8	30.9	28.5	−29.4622	4.8	4.47	22.84691
9	20.26	25.47	−27.2594	1.48	2.13	14.24714
10	21.35	22.94	−26.9111	2.76	3.48	19.25366
11	24.4	14.09	−25.9873	3.08	2.68	18.66739
12	34	31.13	−30.2454	3.24	2.88	19.21174
13	37.01	37.9	−31.4708	2.69	3.16	18.78075
14	28.9	27.2	−28.9626	1.52	1.58	13.34418
15	26.84	18.89	−27.3127	2.06	2.62	16.73974

S/N^P—S/N values for porosity. S/N^G—S/N values for grain size.

where m is the number of tests and P_i is the value of the measured output quantity for the i^{th} test while the M.S.D. for the higher-the-better quality characteristic is given by

$$\text{M.S.D.} = \frac{1}{m}\sum_{i=1}^{m}\frac{1}{P_i^2} \tag{3}$$

3.2. Analysis of variance (ANOVA)

The technique of ANOVA enabled to establish the relative significance of the individual processing factors on the inter-dendritic porosity and the grain size. The ANOVA was based on the variance (V), the degree of freedom (D_f), the sum of the squares (SS), and the percentage of contribution to the total variation (C) (Ma et al., 2007). The parameters used in ANOVA are calculated by the following equations

(1) Total sum of squares,

$$SS_T = \sum_{i=1}^{m}\beta_i^2 - \frac{1}{k}\left[\sum_{i=1}^{k}\beta_i\right]^2 \tag{4}$$

where k is the total number of experiments and β_i is the S/N ratio of the i^{th} test.

(2) The sum of squares from the tested factors

$$SS_p = \sum_{j=1}^{r}\frac{(S_{pj})^2}{r} - \frac{1}{k}\left(\sum_{i=1}^{k}\beta_i\right)^2 \tag{5}$$

where p represents one of the tested factors, j is the level number of this specific factor p, r is the repetition of each level of the factor p and S_{pj} is the sum of the S/N ratio involving this factor and level j.

(3) Degree of freedom (D_f) for each factor is the number of its levels minus one.

(4) Variance

$$V = \frac{SS_p}{D_p} \tag{6}$$

(5) Percentage of contribution to the total variation

$$C\ (\%) = \frac{SS_p}{SS_T} \times 100 \tag{7}$$

4. Results and discussion

Two sets of values for porosity and grain size were obtained using ImageJ™ software by considering two different micrographs of the surface. Using these sets of data for porosity and grain size, the average value was predicted. Table 3 sum-

Table 5 – ANOVA of S/N ratios

Factor	DOF	SS^P	SS^G	V^P	V^G	C^P	C^G
Pulse width	6	12.69	66.23	2.1157	11.03	24.49	27.76
Repetition rate	5	22.89	21.17	4.57	4.23	44.19	8.87
Speed	4	19.27	85.54	4.81	21.38	37.20	35.85

D—degrees of freedom defined earlier; SS^P—sum of squares for porosity calculations; SS^G—sum of squares for grain size calculations; V^P—variance for porosity calculations; V^G—variance for size calculations; C^P—contribution towards porosity; C^G—contribution towards grain size.

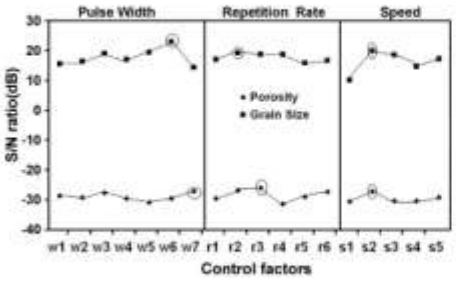

Fig. 3 – Response graph.

marizes the average measured grain size, and average volume percent interdendritic porosity along with predicted density and relative density of the alumina ceramic processed using various combinations of process parameters. It is obvious from the table that apparently there are no distinct trends in relating causes to effects in the present effort. The realization of any trend is further complicated due to employment of a large number of variable process parameters. In light of this, adoption of Taguchi analysis to define the process regimes for appropriate outcome is justified.

The raw data for each of the experiments and the calculated S/N value for each case is represented in Table 4. Utilizing the calculated S/N values, a response graph was generated (Fig. 3) which showed the variation in the S/N ratio due to the variation of the different control factors. This graph showed the average value of the S/N ratio that each control factor produced for both minimizing the porosity and also for maximizing the grain size. Thus, even though 15 trials were available, the number of control factors were 18 as can be seen from Table 1. Hence, 18 points were plotted corresponding to the 18 control factors for optimizing the porosity and similarly 18 points were plotted to optimize the grain size. This graph was created for minimizing porosity and maximizing grain size for the alumina ceramic for any desirable application.

From Fig. 3, it can be illustrated that highest yield of the S/N ratio for percentage porosity, hence minimum porosity could be attained for the combined settings of W_7, R_3 and S_2, i.e. for a pulse width of 8 ms, repetition rate of 13.3 Hz and scanning speed of 5.08 cm/min. Similarly, for maximum grain size, the highest yield of the S/N ratio can be achieved for the combined settings of W_6, R_2 and S_2, i.e. for a pulse width of 7 ms, repetition rate of 10 Hz and scanning speed of 5.08 cm/min. As these combinations of parameter settings were not tested in the experiment, it assures that the orthogonal experiment is able to identify the optimum parameters in the multi-dimensional parameter space. The circled values in Fig. 3 represent the parameters required to attain minimum porosity and maximum grain size. Presently, the experiments are on going to validate the optimization of process parameters predicted by the Taguchi analysis. So far, the preliminary efforts have indicated encouraging observations and detailed efforts and observations will be reported in a separate follow up paper in due course of time.

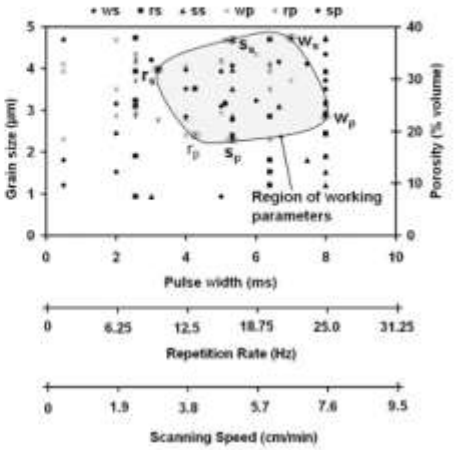

Fig. 4 – Regime identification plot (suffix p corresponds to parameters causing minimum porosity, suffix s corresponds to parameters producing maximum grain size).

The results of ANOVA for minimizing porosity and maximizing grain size are shown in Table 5 wherein the calculations were done manually and by using the software Analysis Lab™ to determine the sum of squares and variance. The repetition rate plays a leading role in affecting the interdendritic porosity (44.19% contribution). The laser beam scanning speed (35.85% contribution) governs the grain size variation significantly. Table 5 also indicates the contribution of each of the other parameters towards porosity and grain size. The change in interdendritic porosity and grain size with the different parameters such as repetition rate, scan speed and pulse width is represented in the regime identification plot in Fig. 4.

The parameters causing minimum porosity and maximum grain size predicted from the response graph in Fig. 3 were identified in Fig. 4. The region encompassed by the curve passing through these parameters causing minimum interdendritic porosity and maximum grain size defined the region of working parameters and it provided the regime of parameters wherein minimum porosity and/or maximum grain size can be achieved. Similar curves could also be generated if we need to maximize the porosity and/or minimize the grain size depending on the application for which the processed alumina ceramic would be used for. Thus, as the application of Taguchi analysis can predict the regime of parameters to go with in order to maximize or minimize any material property, this analysis turns out to be very useful.

5. Conclusion

The laser process parameters such as repetition rate, scanning speed and pulse width influenced the interdendritic porosity and grain size. The Taguchi method for the design

of experiment was employed to identify a combination of process parameters for optimized physical attributes of the ceramic and contribution (influence) of each of these parameters toward these attributes. Due to this ability, it would be possible to control the laser-assisted process more efficiently and effectively and, thus enabling the use of these porous alumina ceramics for several applications including grinding wheels.

REFERENCES

Bandyopadhyay, S., Gokhale, H., Sarin Sundar, J.K., Sundararajan, G., Joshi, S.V., 2005. A statistical approach to determine process parameter impact in Nd:YAG laser drilling of IN718 and Ti–6Al–4V sheets. Opt. Lasers Eng. 43, 163–182.

Bendell, A., Disney, J., Pridmore, W.A., 1989. Taguchi Methods: Applications in World Industry. IFS Publication, UK.

Bradley, L., Li, L., Stott, F.H., 1999. Flame-assisted laser surface treatment of refractory materials for crack-free densification. Mater. Sci. Eng. A 278A, 204–212.

Cappelli, E., Orlando, S., Sciti, D., Montozzi, M., Pandolfi, L., 2000. Ceramic surface modifications induced by pulsed laser treatment. Appl. Surf. Sci. 154, 682–688.

Gahr, K.H., Schneider, J., 2000. Surface modification of ceramics for improved tribological properties. Ceram. Int. 26, 363–370.

Gitzen, W.H., 1970. Alumina as Ceramic Material. American Ceramic Society, Westerville, OH.

Harimkar, S.P., Dahotre, N.B., 2006. Effect of laser fluence on surface microstructure of alumina ceramic. Adv. Appl. Ceram. 105, 304–308.

Harimkar, S.P., Samant, A.N., Khangar, A.A., Dahotre, N.B., 2006. Prediction of solidification microstructures during laser dressing of alumina-based grinding wheel material. J. Phys. D 39D, 1642–1649.

Ma, Y., Hu, H., Northwood, D., Nie, X., 2007. Optimization of the electrolytic plasma oxidation processes for corrosion protection of magnesium alloy AM50 using the Taguchi method. J. Mater. Proc. Technol. 182, 58–64.

Montgomery, D.C., 1991. Design and Analysis of Experiments, 3rd ed. Wiley, NY.

Nicolas, G., Autric, M., Marine, W., Shafeev, G.A., 1997. Laser induced surface modifications on ZrO_2 ceramic. Appl. Surf. Sci. 109, 289–292.

Pan, L.K., Wang, C.C., Hsiao, Y.C., Ho, K.C., 2005. Optimization of Nd:YAG laser welding onto magnesium alloy via Taguchi analysis. Opt. Laser Technol. 37, 33–42.

Phadke, M.S., Dehnad, K., 1988. Optimization of product and process design for quality and cost. Qual. Rel. Eng. Int. 4, 105–112.

Phadke, M.S., Kackar, R.N., Speeney, D.V., Grieco, M.J., 1983. Off-line quality control integrated circuit fabrication using experimental design. Bell Syst. Tech. J. 62, 1273–1309.

Queiroz, A.C., Santos, J.D., Vilar, R., Eugénio, S., Monteiro, F.J., 2004. Laser surface modification of hydroxyapatite and glass-reinforced hydroxyapatite. Biomaterials 25, 4607–4614.

Ross, P.J., 1989. Taguchi Techniques for Quality Engineering. McGraw-Hill, NY.

Tam, S.C., Yeo, C.Y., Jana, S., Lau, M.W.S., Lira, L.E.N., Yang, L.J., Md. Noor, Y., 1993. Optimization of laser deep-hole drilling of Inconel 718 using the Taguchi method. J. Mater. Proc. Technol. 37, 741–757.

Yang, W.H., Tarng, Y.S., 1998. Design optimization of cutting parameters for turning operations based on the Taguchi method. J. Mater. Proc. Technol. 84, 122–129.

The Laser Surface Modification of Advanced Ceramics: A Modeling Approach

Anoop N. Samant, Sandip P. Harimkar, and Narendra B. Dahotre

A numerical approach for predicting microstructures during the laser surface modification of ceramics has been proposed. Laser surface modification is a near-non-equilibrium or non-equilibrium process involving high cooling rates (10^6–10^9 K/s) leading to rapid solidification. As the basic governing solidification theory behind conventional processes like casting and laser processing is the same, the approach and the theory behind the conventional processes can be extended to such near-non-equilibrium processes by adequately modifying the conventional models. This study looks at various challenges in modeling the laser processing phenomena and elaborates on present efforts and future modeling goals.

INTRODUCTION

Ceramics are a vital class of material with tremendous applications in various fields such as the biomedical, automotive, aerospace, chemical, petrochemical, and electronics industries. Surface engineering of ceramics implies the modification and design of a surface to improve heat resistance, wear resistance, or other desirable properties depending on the application for which the modified surface will be utilized. For example, surface-modified ceramics offer an innovative approach to the well-established challenges of drug delivery.[1] Laser surface modification has been shown to increase the surface area of hydroxyapatite and glass-reinforced hydroxyapatite, which can, in turn, increase the reactivity and drug delivery capability of both materials.[2] The growth of a crystalline oxide ceramic layer on the surface of titanium implants has improved the properties of these implants.[3] Surface-modified polycrystalline alumina also has wide applications in dental medicine.[4]

Laser treatment offers a potential solution to ceramic processing and machining of pieces into required shapes. As the process is non-contacting, tool wear and high contact stresses between the tool and machined samples are avoided. Thus, lasers are significantly used in the milling, drilling, cutting, or marking of ceramics.[5] The surface modification of commercially available alumina has been carried out by laser irradiation to reduce friction and wear, thus enhancing its tribological properties.[6] Laser modification plays a vital role in recrystallizing to obtain preferred grain orientation at the surface layer of oxide ceramics. This technique can be used to generate high-quality productive electronic ceramics.[7,8]

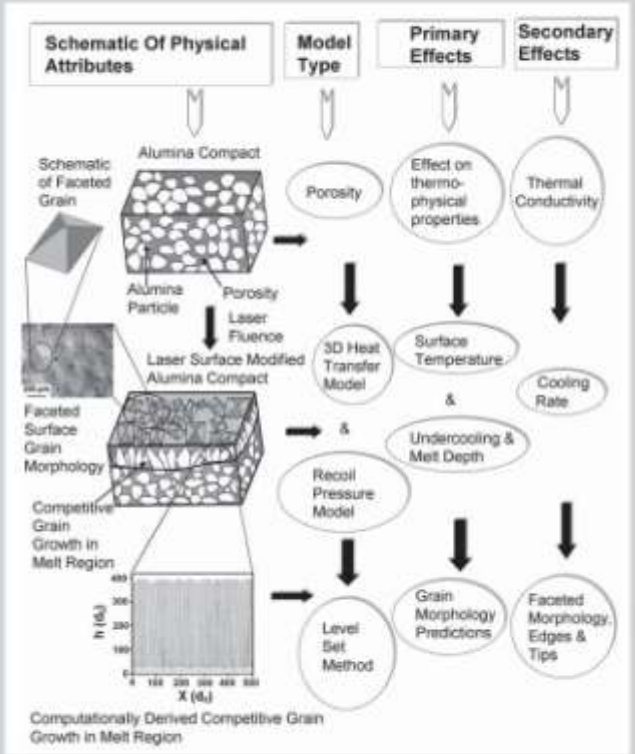

Figure 1. An integrated modeling approach

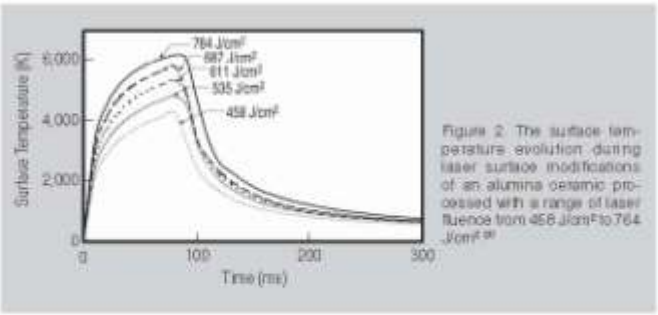

Figure 2. The surface temperature evolution during laser surface modifications of an alumina ceramic processed with a range of laser fluence from 458 J/cm² to 764 J/cm².[20]

Laser irradiation of ZrO_2 ceramic significantly modifies its surface and produces good adherence of metal deposits onto the ceramic surface.[7] Alumina ceramic possesses outstanding thermal and mechanical properties, which make it a preferred material for use in structural components that require minimum porosity. Laser processing can be used to densify the surface porosity of these ceramics in applications where the ceramics are exposed to high temperatures and severe environments.[10] The surface modification technique can be applied for several innovative purposes, such as the dressing of grinding wheels, first proposed by N.R. Babu et al.[11–14] This non-contact process increases productivity, maintains a constant quality of wheel surface topography, and provides better automation.

Optimizing the laser processing parameters in order to obtain the desired surface topography is a challenging task. To make the optimization process less complicated, modeling techniques can be used to evaluate the relationship between the surface microstructure and the laser processing parameters such as power intensity and laser speed. Hence, modeling is essential for studying surface-modified ceramics and will be the main focus of this paper.

MODELING APPROACH

Surface modification using lasers involves melting the material that interacts with the laser beam followed by the solidification of this molten material. During the cooling cycle (i.e., after the laser irradiation time is over), the solidification of the molten material leads to the formation of different microstructural features depending on several factors such as cooling rate and laser fluence. Hence, considering basic theories of solidification is extremely vital while modeling the laser processing phenomena. Solidification in conventional processes is mainly governed by the rate at which the latent heat is taken away from the interface. In this case, the crystal growth occurs slowly enough so that the solid and liquid immediately on either side of the interface can be considered to be in local equilibrium. Such a simplification is permissible in the case of metals solidifying at the rates encountered in normal casting operations, typically on the order of 10°C/s.[15] The compositions can be obtained from the solidus and liquidus on the phase diagram.

At very high growth rates (V > 100 mm/s),[16] such as those that occur in rapid solidification processing, conditions of local equilibrium no longer exist. Rapid solidification has attained a regime of crystal growth speed where the deviations from local equilibrium are important, in which interface motion cannot be thought of as heat flow or diffusion limited. Initial work in the area of solidification has been directed toward macroscopic modeling (i.e., analytical or numerical solutions of the continuity equations in the presence of a phase change).[17] On the contrary, past modeling efforts in the field of laser processing were focused toward determining the influence of operating conditions on the temperature distribution within the heated work piece without including the prediction of microstructures generated for different processing conditions.[18,19] This study looks at the different modeling aspects of laser processing phenomena, the challenges faced, and attempts made to predict surface microstructure in terms of grain morphology and to correlate surface features with processing parameters.

Modeling Challenges

After the interaction of the laser beam with the solid, the solid surface is heated which is followed by material melting and rapid evaporation.[20] Several factors need to be accounted for when modeling the laser processing phenomena and it is cumbersome to include all the factors into the model at the same time. This leads to the step-wise development of the modeling efforts. Laser processing is highly influenced by thermophysical properties such as melting temperature, thermal conductivity, diffusivity, and latent heat, which need to be accounted for during the modeling and tailoring of the process. Hence an integrated modeling technique based on a modular approach has to be considered that will take into account the thermo-physical properties prior to and after laser processing of a material.

The different properties of the ceramic, such as thermal conductivity and specific heat, vary with temperature. But the variation of these properties with temperature or any function governing the variation cannot be easily obtained. Hence, most of the modeling efforts assume a constant value of a certain property. In addition, ceramics such as alumina possess porosity which is intro-

Equations

$$-k\left(\frac{\partial T(x,y,0,t)}{\partial x}+\frac{\partial T(x,y,0,t)}{\partial y}+\frac{\partial T(x,y,0,t)}{\partial z}\right) = \delta A\left(-\varepsilon\sigma\left(T(x,y,0,t)^4-T_a^4\right)\right)$$
$$\delta = 1 \quad \text{for } 0 \le t \le t_p$$
$$\delta = 0 \quad \text{for } t > t_p \qquad (1)$$

$$-k\left(\frac{\partial T(x,y,L,t)}{\partial x}+\frac{\partial T(x,y,L,t)}{\partial y}+\frac{\partial T(x,y,L,t)}{\partial z}\right) = h\left(T(x,y,L,t)-T_a\right) \qquad (2)$$

$$\frac{dp}{dz} = -\frac{180\mu\, s\,(1-\varepsilon)^2}{d_s^2\,\varepsilon^3} \qquad (3)$$

$$\Sigma = \{x \mid \varphi(x) = 0\} \qquad (4)$$

$$\frac{\partial \varphi}{\partial t} + v\cdot\nabla\varphi = 0 \qquad (5)$$

duced during sintering. This porosity ranges from a fraction of one percent to several percent depending upon the intended use, and affects material properties such as thermal conductivity and density.

Laser processing also results in phase changes in the material, which significantly affects properties. Taking into account this phase change effect in the modeling efforts is also a challenging task. The cooling rates encountered in laser processing are extremely high and these high cooling rates have a distinguished effect on the grain morphology. Hence, it is vital to consider these high cooling rates in modeling efforts. Significant loss of heat takes place by convection and radiation effects, and these losses need to be accounted for to ensure accurate temperature predictions. Absorptivity is the fraction of the incident radiation that is absorbed by the body surface. Exact experimental determination of this absorptivity value needs to be done for precise modeling. Figure 1 represents the multiscale changes in alumina ceramic during laser processing and the corresponding models that could be applicable at different stages.

Current Efforts in Modeling

The density of porous alumina was considered by applying a weighted average method to fully dense alumina (ρ = 3,800 kg/m^{-3}) and porosity (for example, 40% by volume). Porosity also has an effect on the thermal conductivity; hence, the thermal conductivity corresponding to 40 vol.% porous alumina (K =14.6 W/mK) was considered.[21]

After considering the effect of porosity on the different thermo-physical properties, the next step was the precise determination of the melt depth that enabled accurate surface temperature predictions. This is essential for the precise grain evolution, which depends on the temperature and cooling rate at a given time. The application of laser fluence on the surface of the ceramic dissipates heat throughout the surface and develops a temperature gradient throughout the substrate, with maximum temperature reached at the surface. The temperature values and the size of the melt pool depend on the thermo-physical properties of the ceramic, making it necessary to consider the porosity model first.

Fourier's second law, as depicted in Equation 1 (all equations are shown in the Equations table), was used to model the heat transfer phenomena during laser processing of alumina ceramic, where A is absorptivity of alumina; I is laser power intensity; ε is emissivity of alumina for thermal radiation; σ is Stefan–Boltzman constant; and t_p is irradiation time. The convective boundary condition at the bottom surface of the sample was given by Equation 2, where h is convective heat transfer coefficient and L is the thickness of the sample. The other surfaces were considered to be insulated. A three-dimensional heat flow model was developed using the *COMSOL Multiphysics*™ modeling package. The temperature distribution within the material and the melt depth from the surface was predicted from this model. The melt depth was calculated by tracing the melting point in the temperature vs. distance from surface profiles for different times. High laser fluence caused the surface of the ceramic to melt and subsequently solidify into a highly dense recast layer. The variations of surface temperature calculated from this model are presented in Figure 2 as a function of time for various laser fluences.

Significant loss of heat takes place by convection and radiation effects, and these losses need to be accounted for to ensure accurate temperature predictions.

All the factors that lead to the generation of the melt pool, such as the recoil pressure, need to be accounted for. This pressure is created due to the rapid evaporation at the surface of the melt, which drives the flow of molten material into the porous substrate, thus further extending the melt depth. The evaporation of the material that takes place at such a high rate on the surface generates an extremely strong recoil pressure to counterbalance this high evaporation, which drives the molten material further down. The macroscopic melt depth predictions do not take into account the recoil pressure effect on the melt depth. Carman–Kozeny equations (Equation 3) were employed to analyze the effect of recoil pressure on the depth of infiltration, and were subsequently integrated with the calculated depth of melting from the thermal model, where dp/dz is the pressure gradient across the melt, μ is dynamic viscosity, u is the flow rate, ω is the porosity, and d_s is the average alumina particle diameter. As shown in Figure 3, the calculated depth of melting increases with laser processing fluence due to the melting front advancing deeper into the material with increasing laser processing fluence.

The variation of surface cooling rates with laser fluence is also represented in Figure 3. This figure clearly indicates a decreasing cooling rate with increasing laser fluence, which also goes well with the universal theories of solidifica-

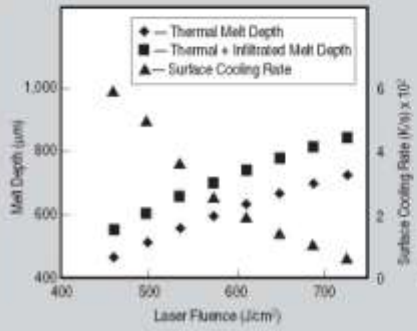

Figure 3. The variation of melt depth and cooling rate with laser fluence.[21,22]

tion.[22]

Considering detailed aspects of the process such as the infiltration melt depth leads to refinement in the model output and enhances the melt depth calculated from the three-dimensional (3-D) heat flow model, as can be observed from Figure 3. Thus, so far the modeling efforts have been able to predict the surface temperature profiles, the associated surface cooling rates, and certain features like the melt depth. These computed parameters have a significant effect on the surface microstructure evolution and form the basis for modeling the laser processing phenomena, as also can be seen in Figure 1. Following the prediction of these features, the next step would be to study the evolution of the surface microstructures such as the morphology of the grains that are formed on the surface during the solidification process.

Future Modeling Goals

Under certain conditions, ceramics like alumina solidify with characteristic physical nature such as faceted crystals (Figure 1). Surface features like the faceted morphology of the surface grains are greatly affected by the evolution of crystallographic texture.[23] Each facet has a plane associated with it that moves with a given normal speed which may be different for different facets, the boundaries of which will be determined by the intersection of the planes. Models such as the Van der Drift model[24] consider that each crystallite or grain grows with each crystallographic facet moving with a known normal velocity until a facet meets the surface of another growing crystallite, leading to the formation of grain boundaries due to the impingement of the grains on each other.

The development of facets in laser-surface-modified alumina was experimentally observed by A.A. Khangar et al.[25] and a phenomenological explanation for this development was provided by S.P Harimkar et al.[23] based on the Van der Drift model of faceted growth. However, a numerical approach has not yet been developed that enables one to foresee the effects of thermal aspects of laser processing on the morphology of the surface grains. A level-set method[26,27] for the motion of faceted interfaces can be utilized to predict the faceted growth observed in laser-processed ceramics such as alumina. In the level-set method, a continuous function $\varphi(x,t)$ could be introduced such that the crystal interface Σ will be given by Equation 4. The velocity field can then be used to evolve the phase φ according to Equation 5.

On solving the above equation using finite differences, the zero level set of $\varphi(x,t)$ could generate the evolution of the interface. Thus, this work aims at modeling the evolution of surface grain structure in laser surface modification phenomena and the associated microstructure development using minimal experimental techniques only for microstructural analysis and heavy computational techniques to optimize the laser processing parameters.

References

1. N. Kossovsky et al., "Surface-Modified Nanocrystalline Ceramics for Drug Delivery Applications," *Biomaterials*, 15 (1994), pp. 1201–1207.
2. Ana C. Queiroz et al., "Laser Surface Modification of Hydroxyapatite and Glass-Reinforced Hydroxyapatite," *Biomaterials*, 25 (2004), pp. 4607–4614.
3. G. Szabo et al., "A New Advanced Surface Modification Technique—Titanium Oxide Ceramic Surface Implants: The Background and Long-Term Results," *J. Long Term Eff. Med. Implants*, 9 (3) (1999), pp. 247–259.
4. Robert P. Kusy et al., "Coefficient of Friction Characterization of Surface-Modified Polycrystalline Alumina," *Journal of the American Ceramic Society*, 76 (2) (1993), p. 336.
5. E. Cappelli et al., "Ceramic Surface Modifications Induced by Pulsed Laser Treatment," *Applied Surface Science*, 154–155 (2000), pp. 682–688.
6. K.-H. Zum Gahr and J. Schneider, "Surface Modification of Ceramics for Improved Tribological Properties," *Ceramics International*, 26 (2000), pp. 353–370.
7. Mamoru Okutomi et al., "Surface Modification and Characterization of Functional Ceramics Using CO_2 Laser," *Nuclear Instruments and Methods in Physics Research B*, 169 (2000), pp. 6–11.
8. D. Damjanovic et al., "Properties and Applications of Modified Lead Titanate Ceramics" (Presentation at the IEEE International Frequency Control Symposium, Pasadena, California, 1998).
9. G. Nicolas et al., "Laser Induced Surface Modifications on ZrO Ceramics," *Applied Surface Science*, 109-110 (1997), pp. 289–292.
10. S. Harimkar and N. B. Dahotre, "Laser Assisted Densification of Surface Porosity in Structural Alumina Ceramic," *phys. stat. sol. (a)* (1007), pp. 1– 9.
11. N.R. Babu, V. Radhakrishnan, and Y.V.G.S. Murti, "Investigations on Laser Dressing of Grinding Wheels—Part I: A Preliminary Study," *ASME J. Eng. Ind.*, 111 (1989), pp. 244–252.
12. N.R. Babu and V Radhakrishnan, "Investigations on Laser Dressing of Grinding Wheels—Part II: Grinding Performance of a Laser Dressed Aluminum Oxide Wheel," *ASME J. Eng. Ind.*, 111 (1989), pp. 253–261.
13. N.R. Babu and V. Radhakrishnan, "Influence of Dressing Feed on the Performance of Laser Dressed Al_2O_3 Wheel in Wet Grinding," *Int. J. Mach. Tools Manuf.*, 35 (1995), pp. 661–671.
14. V. Phanindranath and N.R. Babu, "A Theoretical Model for Prediction of Groove Geometry on Laser Dressed Grinding Wheel Surface," *Int. J. Mach. Tools Manuf.*, 36 (1996), pp. 1–16.
15. L. Nastac and D.M. Stefanescu, "Macrotransport-Solidification Kinetics Modeling of Equiaxed Dendritic Growth: Part 1. Model Development and Discussion," *Metallurgical and Materials Transactions A*, 27A (1996), pp. 4061–4074.
16. W. Kurz and D.J. Fisher, *Fundamentals of Solidification* (Rockport, MA: Trans Tech Publications, 1986).
17. Laurentiu Nastac, *Modeling and Simulation of Microstructure Evolution in Solidifying Alloys* (New York: Kluwer Academic Publishers, 2004).
18. J.C. Rozzi, F.P. Incropera, and Y.C. Shin, "Transient, Three-Dimensional Heat Transfer Model for the Laser Assisted Machining of Silicon Nitride: II—Assessment of Parametric Effects," *International Journal of Heat and Mass Transfer*, 43 (2000), pp. 1425–1437.
19. S. Lei, Y.C. Shin, and F.P. Incropera, "Experimental Investigation of Thermo-Mechanical Characteristics in Laser Assisted Machining of Silicon Nitride Ceramics," *Transactions ASME, Journal of Manufacturing Science and Engineering*, 123 (2001), pp. 639–646.
20. Sandip P. Harimkar, Anoop N. Samant, and Narendra B. Dahotre, "Temporally Evolved Recoil Pressure Driven Melt Infiltration during Laser Surface Modifications of Porous Alumina Ceramic," *Journal of Applied Physics*, 101 (2007), p. 054911.
21. W.H. Gitzen, *Alumina as Ceramic Material* (Westerville, OH: American Ceramic Society, 1970).
22. Anoop N. Samant and N.B. Dahotre, "Computational Prediction of Grain Size during Rapid Laser Surface Modification of Al-O Ceramic," *phys. stat. sol.* (2006), pp. 1–3.
23. S.P. Harimkar and N.B. Dahotre, "Crystallographic and Morphologic Textures in Laser Surface Modified Alumina Ceramic," *J. App. Phys.*, 100 (2006), p. 024901.
24. Van der Drift, "Evolutionary Selection, A Principle Governing Growth Orientation in Vapour-Deposited Layers," *Philips Research Reports*, 22 (1967), p. 267.
25. A.A. Khangar, E.A. Kenik, and N.B. Dahotre, "Microstructure and Microtexture in Laser-Dressed Alumina Grinding Wheel Material," *Ceramics International*, 31 (2005), pp. 621–629.
26. G. Russo and P. Smereka, "A Level-Set Method for the Evolution of Faceted Crystals," *Siam. J. Sci. Comput.*, 21 (6) (2000), pp. 2073–2095.
27. D.J. Paritosh et al., "Simulation of Faceted Film Growth in 2D: Microstructure, Morphology and Texture," *Acta Materialia*, 47 (1999), pp. 2269–2281.

Anoop N. Samant, Sandip P. Harimkar, and Narendra B. Dahotre are with the Department of Materials Science and Engineering, the University of Tennessee, Knoxville, Tennessee 37996. Dr. Dahotre can be reached at (865) 974-3609; fax (865) 974-4115; e-mail ndahotre@utk.edu.

VITA

Anoop N. Samant was born on October 9, 1979 in Pune, India. He completed his Bachelor of Engineering Degree in Mechanical Engineering from the University of Pune, India in 2001. He then worked for Bajaj Auto Limited, Akurdi, India for a brief period of six months after which he went abroad to the United States of America for higher education. He obtained his Masters Degree in Mechanical Engineering from the University of Connecticut, Storrs, CT in 2004. Anoop is currently pursuing his doctorate in Materials Science and Engineering at the University of Tennessee, Knoxville, TN.